frontiers | Research Topics

Advanced technologies for oral and craniomaxillofacial therapy

Edited by
Dan Lin, Nicholas G. Fischer and Bolei Cai

Published in
Frontiers in Bioengineering and Biotechnology

ISSN 1664-8714
ISBN 978-2-8325-7420-1
DOI 10.3389/978-2-8325-7420-1

Generative AI statement
Any alternative text (Alt text) provided alongside figures in the articles in this ebook has been generated by Frontiers with the support of artificial intelligence and reasonable efforts have been made to ensure accuracy, including review by the authors wherever possible. If you identify any issues, please contact us.

About Frontiers

Frontiers is more than just an open access publisher of scholarly articles: it is a pioneering approach to the world of academia, radically improving the way scholarly research is managed. The grand vision of Frontiers is a world where all people have an equal opportunity to seek, share and generate knowledge. Frontiers provides immediate and permanent online open access to all its publications, but this alone is not enough to realize our grand goals.

Frontiers journal series

The Frontiers journal series is a multi-tier and interdisciplinary set of open-access, online journals, promising a paradigm shift from the current review, selection and dissemination processes in academic publishing. All Frontiers journals are driven by researchers for researchers; therefore, they constitute a service to the scholarly community. At the same time, the *Frontiers journal series* operates on a revolutionary invention, the tiered publishing system, initially addressing specific communities of scholars, and gradually climbing up to broader public understanding, thus serving the interests of the lay society, too.

Dedication to quality

Each Frontiers article is a landmark of the highest quality, thanks to genuinely collaborative interactions between authors and review editors, who include some of the world's best academicians. Research must be certified by peers before entering a stream of knowledge that may eventually reach the public - and shape society; therefore, Frontiers only applies the most rigorous and unbiased reviews. Frontiers revolutionizes research publishing by freely delivering the most outstanding research, evaluated with no bias from both the academic and social point of view. By applying the most advanced information technologies, Frontiers is catapulting scholarly publishing into a new generation.

What are Frontiers Research Topics?

Frontiers Research Topics are very popular trademarks of the *Frontiers journals series*: they are collections of at least ten articles, all centered on a particular subject. With their unique mix of varied contributions from Original Research to Review Articles, Frontiers Research Topics unify the most influential researchers, the latest key findings and historical advances in a hot research area.

Find out more on how to host your own Frontiers Research Topic or contribute to one as an author by contacting the Frontiers editorial office: frontiersin.org/about/contact

Advanced technologies for oral and craniomaxillofacial therapy

Topic editors

Dan Lin — Shanghai University of Medicine and Health Sciences, China

Nicholas G. Fischer — University of Pennsylvania, United States

Bolei Cai — The Fourth Military Medical University, China

Citation

Lin, D., Fischer, N. G., Cai, B., eds. (2026). *Advanced technologies for oral and craniomaxillofacial therapy*. Lausanne: Frontiers Media SA.

doi: 10.3389/978-2-8325-7420-1

Table of contents

frontiers | Frontiers in Bioengineering and Biotechnology

TYPE Editorial
PUBLISHED 12 January 2026
DOI 10.3389/fbioe.2026.1759125

OPEN ACCESS

EDITED AND REVIEWED BY
Candan Tamerler,
University of Kansas, United States

*CORRESPONDENCE
Nicholas G. Fischer,
nfi@seas.upenn.edu
Bolei Cai,
caibolei1020@126.com
Dan Lin,
lind@sumhs.edu.cn

RECEIVED 02 December 2025
REVISED 02 December 2025
ACCEPTED 05 January 2026
PUBLISHED 12 January 2026

CITATION
Fischer NG, Cai B and Lin D (2026) Editorial: Advanced technologies for oral and craniomaxillofacial therapy.
Front. Bioeng. Biotechnol. 14:1759125.
doi: 10.3389/fbioe.2026.1759125

Editorial: Advanced technologies for oral and craniomaxillofacial therapy

Nicholas G. Fischer[1,2,3]*, Bolei Cai[4]* and Dan Lin[5,6]*

[1]Department of Bioengineering, University of Pennsylvania, Philadelphia, PA, United States, [2]Center for Precision Engineering for Health, University of Pennsylvania, Philadelphia, PA, United States, [3]Center for Innovation and Precision Dentistry, University of Pennsylvania, Philadelphia, PA, United States, [4]State Key Laboratory of Oral and Maxillofacial Reconstruction and Regeneration, National Clinical Research Center for Oral Diseases, Shaanxi Clinical Research Center for Oral Diseases, Department of Oral and Maxillofacial Surgery, School of Stomatology, The Fourth Military Medical University, Xi'an, China, [5]Intelligent Inspection and Diagnostics Health Service Platform, Shanghai University of Medicine and Health Sciences, Shanghai, China, [6]Shanghai University of Medicine and Health Sciences Affiliated Zhoupu Hospital, Shanghai, China

KEYWORDS

artificial intelligence, biomaterials, dental materials, digital dentistry, interdisciplinary collaboration

Editorial on the Research Topic
Advanced technologies for oral and craniomaxillofacial therapy

Interdisciplinary collaboration is fundamental to advancing dental biomaterials research. Oral and craniomaxillofacial health challenges span the entire human lifespan and involve extraordinarily diverse tissues. From congenital craniofacial developmental anomalies to caries, periodontal disease, bone loss, and age-related degeneration, clinicians face continuous demands for intelligent, functional, and bioactive materials that regenerate, protect, or restore both soft and hard tissues across the craniofacial complex. Many of these clinical problems cannot be solved by any single discipline. For example, persistent gaps remain in producing dental materials with reliable anti-microbial, anti-fouling, abrasion-resistant, and self-healing properties, or engineering materials that can concurrently address infection, inflammation, aging, or osteoporosis. These needs highlight the necessity of integrating material science, oral biology, and clinical insights to design patient-specific solutions.

The mechanical and biological environment of the oral cavity is uniquely complex, with dynamic loading, fluid exposure, microbiome interaction, and rapid tissue turnover. Challenges such as uncontrolled force transmission during orthodontics or prosthodontics, unpredictable bone remodeling around implants, and biomaterial-related complications arise from the lack of precise biomechanical control and inadequate understanding of multiscale mechanisms. Interdisciplinary teams—uniting engineers, biologists, clinicians, and computational modelers—are essential for uncovering the cellular and molecular pathways involved in tissue integration. Such collaborations enable the development of immunoregulatory scaffolds, biomolecule-modified biomaterials, and next-generation polymers capable of resisting microbial colonization and mechanical wear.

As digitalization and artificial intelligence (AI) rapidly transform biomedical innovation, interdisciplinary collaboration again becomes crucial. AI-driven imaging,

predictive modeling, and automated design pipelines now make it possible to optimize orthodontic biomechanics, personalize prosthodontic devices, guide surgical planning, and accelerate the discovery of new biomaterials. Similarly, digital dentistry workflows allow clinicians and engineers to refine therapeutic procedures, improving accuracy, efficiency, and patient outcomes. Together, these converging disciplines are redefining what is possible in oral and craniomaxillofacial therapy.

Here, in this Research Topic, we assembled a group of manuscripts that push the field forward through interdisciplinary research, including next-generation photothermal therapies to combat antibiotic resistance (Wang et al.), finite element analysis for optimizing orthodontic treatment (Zeng et al.), and advanced materials systems such as drug-loaded chitosan nanoparticles (Li et al.), imidazolate framework-8 composite nanofibrous membranes (Wang et al.), MXene nanomaterials (Li et al.), and self-healing resin composites (Han et al.). Furthermore, interdisciplinary efforts have yielded anti-cancer biomaterials (Wen et al. and Wen et al.), enhanced computer-assisted surgical systems (Wu et al., Bao et al., and Miadili et al.), refined surgical techniques for implant site preparation (López-Valverde et al.), and AI-aided decision support for orthodontic extractions (Huang et al.). These studies also address rising societal challenges, such as aging populations (Fu et al.), demonstrating the expansive impact of cross-disciplinary approaches (Zhou et al., Liu et al., and Wang et al.).

The studies collected in this Research Topic demonstrate how interdisciplinary collaboration is no longer optional but foundational to meaningful progress in dental and craniomaxillofacial biomaterials. By integrating engineering, biology, clinical expertise, and emerging digital and AI-driven technologies, and smart materials, these works demonstrate how complex challenges may be addressed more effectively than any single field could achieve alone. As the oral health landscape continues to evolve, such collaborations will remain essential for translating fundamental discoveries into innovative, patient-centered, personalized medicine solutions that elevate the standards of care across the lifespan.

Author contributions

NF: Writing – review and editing, Writing – original draft. BC: Writing – original draft, Writing – review and editing. DL: Writing – review and editing, Writing – original draft.

Funding

The author(s) declared that financial support was not received for this work and/or its publication.

Conflict of interest

The author(s) declared that this work was conducted in the absence of any commercial or financial relationships that could be construed as a potential conflict of interest.

Generative AI statement

The author(s) declared that generative AI was not used in the creation of this manuscript.

Any alternative text (alt text) provided alongside figures in this article has been generated by Frontiers with the support of artificial intelligence and reasonable efforts have been made to ensure accuracy, including review by the authors wherever possible. If you identify any issues, please contact us.

Publisher's note

frontiers | Frontiers in Bioengineering and Biotechnology

TYPE Original Research
PUBLISHED 14 October 2024
DOI 10.3389/fbioe.2024.1483230

OPEN ACCESS

EDITED BY
Bolei Cai,
The Fourth Military Medical University, China

REVIEWED BY
Chun Ouyang,
Fudan University, China
Nishant Kumar,
K L University, India
Meritxell Sanchez Molins,
University of Barcelona, Spain
Nuno Gustavo Correia d'Oliveira,
University of Barcelona, Spain, in collaboration with reviewer MS

*CORRESPONDENCE
Congchong Yang,
yangcongchong1987@126.com
Yichen Pan,
602752877@qq.com

RECEIVED 19 August 2024
ACCEPTED 04 October 2024
PUBLISHED 14 October 2024

CITATION
Huang J, Chan I-T, Wang Z, Ding X, Jin Y, Yang C and Pan Y (2024) Evaluation of four machine learning methods in predicting orthodontic extraction decision from clinical examination data and analysis of feature contribution. *Front. Bioeng. Biotechnol.* 12:1483230. doi: 10.3389/fbioe.2024.1483230

Evaluation of four machine learning methods in predicting orthodontic extraction decision from clinical examination data and analysis of feature contribution

Jialiang Huang[1,2], Ian-Tong Chan[3], Zhixian Wang[4], Xiaoyi Ding[4], Ying Jin[4], Congchong Yang[5,6,7]* and Yichen Pan[6,7,8]*

[1]Department of Orthodontics, Shanghai Stomatological Hospital and School of Stomatology, Fudan University, Shanghai, China, [2]Shanghai Key Laboratory of Craniomaxillofacial Development and Diseases, Fudan University, Shanghai, China, [3]School of Stomatology, Fudan University, Shanghai, China, [4]School of Medical Technology, Shanghai University of Medicine and Health Sciences, Shanghai, China, [5]Department of Cariology and Endodontology, College of Stomatology, Shanghai Ninth People's Hospital, Shanghai Jiao Tong University School of Medicine, Shanghai, China, [6]National Clinical Research Center for Oral Diseases, National Center for Stomatology, Shanghai, China, [7]Shanghai Key Laboratory of Stomatology and Shanghai Research Institute of Stomatology, Shanghai, China, [8]Department of Oral and Maxillofacial-Head Neck Oncology, College of Stomatology, Shanghai Ninth People's Hospital, Shanghai Jiao Tong University School of Medicine, Shanghai, China

Introduction: The study aims to predict tooth extraction decision based on four machine learning methods and analyze the feature contribution, so as to shed light on the important basis for experts of tooth extraction planning, providing reference for orthodontic treatment planning.

Methods: This study collected clinical information of 192 patients with malocclusion diagnosis and treatment plans. This study used four machine learning strategies, including decision tree, random forest, support vector machine (SVM) and multilayer perceptron (MLP) to predict orthodontic extraction decisions on clinical examination data acquired during initial consultant containing Angle classification, skeletal classification, maxillary and mandibular crowding, overjet, overbite, upper and lower incisor inclination, vertical growth pattern, lateral facial profile. Among them, 30% of the samples were randomly selected as testing sets. We used five-fold cross-validation to evaluate the generalization performance of the model and avoid over-fitting. The accuracy of the four models was calculated for the training set and cross-validation set. The confusion matrix was plotted for the testing set, and 6 indicators were calculated to evaluate the performance of the model. For the decision tree and random forest models, we observed the feature contribution.

Results: The accuracy of the four models in the training set ranges from 82% to 90%, and in the cross-validation set, the decision tree and random forest had higher accuracy. In the confusion matrix analysis, decision tree tops the four models with highest accuracy, specificity, precision and F1-score and the other three models tended to classify too many samples as extraction cases. In the feature contribution analysis, crowding, lateral facial profile, and lower incisor inclination ranked at the top in the decision tree model.

Conclusion: Among the machine learning models that only use clinical data for tooth extraction prediction, decision tree has the best overall performance. For tooth extraction decisions, specifically, crowding, lateral facial profile, and lower incisor inclination have the greatest contribution.

KEYWORDS

orthodontic treatment, tooth extraction decision, decision tree, machine learning, cross validation

1 Introduction

Whether to extract teeth is one of the most important decisions in orthodontic treatment planning. Its frequency has fluctuated over the years, the extraction percentage was 30% in 1953, reached 76% in 1968, and declined to 28% in 1993, this variation was due to considerations in outcome stability, facial esthetics, and technological changes (Proffit, 1994). To date, scholars have been studying and exploring orthodontic extraction decisions to obtain healthier, more stable and more esthetic orthodontic outcomes (Jackson et al., 2017; Proffit, 1994). Occlusion, stability and esthetics are the three goals for a successful treatment plan, but no single rule can give the orthodontist a simple way to decide how to reach these goals, the extraction decision is multi-factorial, involving crowding (Janson et al., 2014; Boley et al., 2003), overjet and overbite (Janson et al., 2003), Bolton ratio (Hasija et al., 2014), Angle and skeletal classifications (Ker et al., 2008), transverse dimension (midline discrepancy, facial asymmetries) (Chang et al., 2011), incisors angulation, presence of root resorption (Maués et al., 2015), soft-tissue profile (Konstantonis et al., 2013), etc. The extraction plan embodies the experience and wisdom of orthodontists, which is difficult and confusing for young or general practitioners (Liu et al., 2021).

With the popularization of big data and artificial intelligence, more and more studies are trying to use machine learning algorithms to assist in extraction decision-making (Khanagar et al., 2021). Commonly used machine learning methods in decision prediction include linear regression (Köktürk et al., 2024), tree models (Köktürk et al., 2024; Etemad et al., 2021; Suhail et al., 2020), support vector machines (Köktürk et al., 2024), neural networks (Köktürk et al., 2024; Jung and Kim, 2016; Li et al., 2019; Xie et al., 2010), etc. from simple to complex. They usually included model measurements and cephalometric data to train the models. Different validation strategies for over-fitting were applied in the previous studies. We took categorical variables that are often recorded in clinical diagnosis, so we chose tree models, support vector machines, and neural networks. Since the number of variables in this study is not very large, we hope to include features to the maximum extent, so we chose the random forest while also trying the decision tree.

The current study aimed to predict tooth extraction decision based on four machine learning methods and analyze the feature contribution. This study invited senior specialists of the orthodontic department of Shanghai Stomatological Hospital to note down the diagnosis and tooth extraction plan of the patients, and applied four machine learning method for prediction of extraction decision-making. We used cross-validation to measure the generalization ability of the model and avoid over-fitting, and calculated feature contribution to explain the key variables that clinicians value when determining extraction planning.

2 Materials and methods

2.1 Data collection

The clinical materials were collected from consecutive patients visiting the department of orthodontics of Shanghai Stomatological Hospital from 2018 to 2020, including pre-treatment plaster models, clinical examination data, and treatment plans for malocclusion. Plaster models were scanned and stored in STL format.

Two senior doctors were asked to fill in a standardized form to record the patient's Angle classification, skeletal classification, maxillary and mandibular crowding, overjet, overbite, upper and lower incisor inclination, vertical growth pattern, lateral facial profile. Angle's classification, crowding, overbite and overjet were measured from dental models. And lateral facial profile was observed from facial photographs. Skeletal classification, upper/lower incisor inclination, and vertical growth pattern were measured in the cephalometric radiographs, using Steiner analysis (SNA SNB ANB U1-SN U1-NA L1-NB MP-SN), Tweed analysis (FMA IMPA FMIA), Wit's appraisal, Ricketts's analysis (lower lip to E plane). Experts' decisions were comprehensive judgments based on the combination of objective measurement indicators and clinical observations.

As for the extraction decisions, only the consensus of the two experts was recorded, otherwise a third expert was invited and the majority opinion prevailed. An endodontic expert was invited to evaluate the preservation value of the residual crown. We marked the non-extraction cases, and then for the extraction cases, we recorded the specific teeth that are to be extracted, although the prediction of the extraction pattern was not involved in this study. The research plan has been approved by the Institutional Review Board of Shanghai Stomatological Hospital [Hu Kou Fang Lun Shen (2017) No. 0005]. Written informed consent was obtained from all the participants.

2.2 Inclusion and exclusion criteria

(1) Complete permanent dentition;
(2) No congenitally missing teeth or impacted teeth;
(3) The tooth extraction in the treatment plan is the classic extraction mode, that is, symmetric extraction of premolars;
(4) Complete pre-treatment model, clinical examination data and orthodontics treatment plan information;
(5) Informed consent signed by the patient or the parent (for teenager under 18).

In total, 192 patients with complete information were included, among whom, 30% were randomly selected as testing set and the rest were divided as training set (Figure 1).

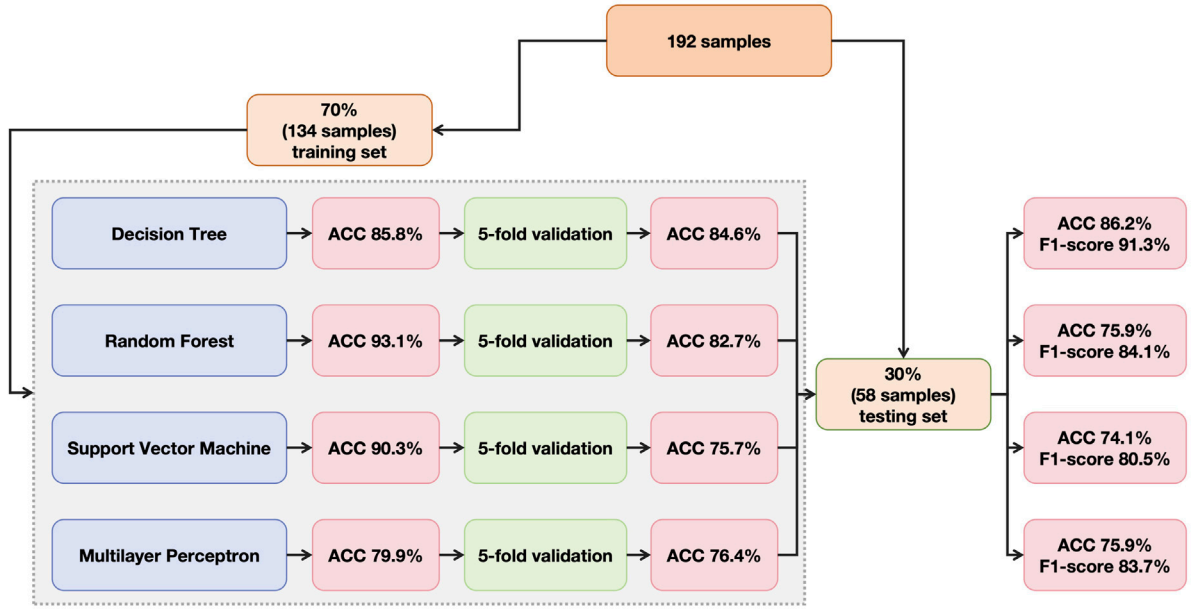

FIGURE 1
Flowchart of data allocation, model training, cross-validation and model testing.

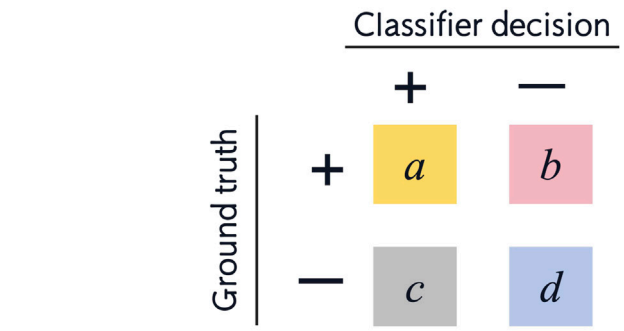

$$Accuracy = \frac{a+d}{a+b+c+d} \qquad Balanced\ accuracy = \frac{\frac{a}{a+b}+\frac{d}{c+d}}{2}$$

$$Sensitivity = \frac{a}{a+b} \qquad Specificity = \frac{d}{c+d}$$

$$Precision = \frac{a}{a+c} \qquad F1\text{-}score = \frac{2a}{2a+b+c}$$

FIGURE 2
Confusion matrix and six measurements for evaluation of model performance (positive cases represent extraction classification and negative cases represent non-extraction classification).

2.3 Model training

Four machine learning frameworks were applied for prediction of extraction and non-extraction planning, including decision tree (DT), random forest (RF), support vector machine (SVM) and multilayer perceptron (MLP) (Figure 1).

Decision Trees are built by continuously splitting the data into binary nodes that acquire the largest information gain until the terminal node outputs the predictions of classification (Suhail et al., 2020).

Random Forest is an ensemble of decision trees. Each decision tree performs the same classification prediction individually, and the

TABLE 1 Definitions of nine feature variables.

Variables	Labels	Definitions
Angle's classification	1	Class I
	2	Class II
	3	Class III
Skeletal classification	1	Class I
	2	Class II
	3	Class III
Crowding	0	Less than 2 mm
(Maximum of upper and lower crowding)	1	2–4 mm
	2	4–8 mm
	3	Over 8 mm
	4	Spacing
Overbite	0	Less than 1/3 overlap
	1	1/3–1/2 overlap
	2	1/2–2/3 overlap
	3	Over 2/3 overlap
	4	Open bite
Overjet	0	Less than 3 mm
	1	3–5 mm
	2	5–8 mm
	3	Over 8 mm
	4	Edge to edge
	5	Cross bite
Upper incisor inclination	1	Buccal inclination
	2	Vertical
	3	Lingual inclination
Lower incisor inclination	1	Buccal inclination
	2	Vertical
	3	Lingual inclination
Vertical growth pattern	1	Hyperdivergent
	2	Normal
	3	Hypodivergent
Lateral facial profile	1	Convex
	2	Straight
	3	Concave

final classification, or output, is determined by taking the most common predictions for discrete variables or the average of predictions for continuous variables (Etemad et al., 2021). The number of trees was set to 1,000 in our study.

Support Vector Machine (SVM) can efficiently perform a non-linear classification using what is called the kernel trick, representing the data only through a set of pairwise similarity comparisons between the original data points using a kernel function, which transforms them into coordinates in the higher dimensional feature space (Leavitt et al., 2023).

Multilayer Perceptron (MLP) is one of the simplest forms of artificial neural network (ANN), composed of input layer, output layer and hidden layer(s). Each layer consists of multiple nodes, called neuron, fully connected with nodes at adjacent layers (Etemad et al., 2021).

Due to the limited number of features, we removed data containing missing values. And convert continuous data into discrete data using the commonly used classification in orthodontics. Since age and gender nearly had no contribution (0%) to the model in the preliminary experiment, they were removed from the features in the formal study. Finally, nine feature variables were Angle's classification, skeletal classification, crowding, overbite, overjet, upper and lower incisor inclination, vertical growth pattern and lateral facial profile (Table 1) and one classification variable was extraction/non-extraction decision.

Since there is a difference between the proportion of tooth extraction cases (144 cases) and non-tooth extraction cases (48 cases) in the dataset, in order to deal with the problem of imbalanced classification, we adopted the threshold moving method (Collell et al., 2018). According to the ROC curve of the training set, we select the optimal classification threshold to prevent the model from being "occupied" by the classification with more data.

2.4 Cross-validation

Cross-validation is often used to measure the generalization ability of a model (Jonathan et al., 2000; Karkkainen, 2014). In order to ensure adequate number of samples in the cross-validation set, this study used a five-fold cross-validation method. It divided the dataset into five parts, taking turns to use four of them as training set and one as validation set. In each validation, the four training sets will generate a model, and the validation set will be input into the model for classification task. The proportion of the number of times the classifier decision matches the ground truth to the total number of tests is calculated as the accuracy of each validation. The average accuracy of the five validations is taken as the accuracy of a five-fold cross-validation.

2.5 Model testing

In the dataset, 30% (58 samples) of all patients were randomly selected as the testing set. The above four machine learning models were used for testing. The results of the testing set were represented by confusion matrix, and the following indicators were calculated (Figure 2):

- Accuracy: correctly classified data points in the testing set.
- Balanced accuracy: the average of sensitivity and specificity.
- Sensitivity/recall: positive data points correctly classified as positive.
- Specificity: negative data points correctly classified as negative.
- Precision: data points classified as positive that are actually positive.

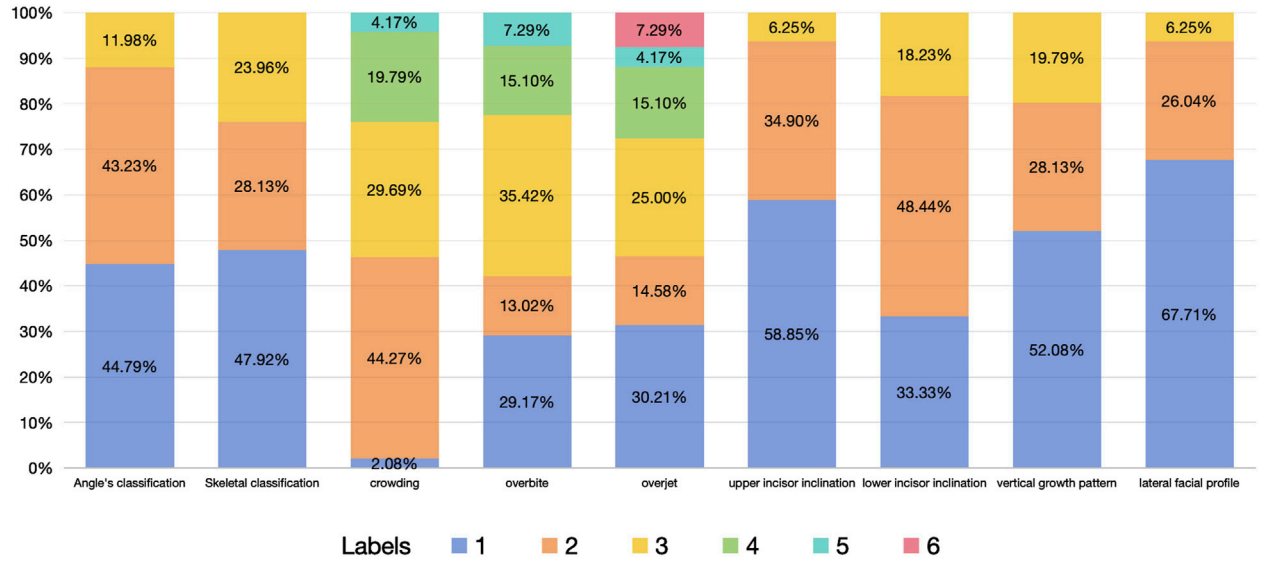

FIGURE 3
Proportion of each feature variables.

- F1-score: the harmonic mean of precision and sensitivity. Precision and sensitivity may affect each other. Although it is ideal for both to be high, but in reality, it is often the case that the precision is high and the sensitivity is low, or otherwise. Therefore, F1-score is an indication of both at the same time.

We also plotted the receiver operating characteristic (ROC) curve to visually demonstrate the performance of the model and calculated the area under the curve (AUC).

2.6 Feature contribution

Feature contribution in tree models can be measured by the number of times a feature participates in building the tree and the cumulative value of information gain when it is used as a split node. In the process of building a tree, the more times the feature is used to split nodes, the more important role the feature plays in the decision process. Cumulative value of information gain represents the amount of reduction in information entropy when the feature is used for node splitting. The greater the information gain, the greater the contribution of the feature to improving the predictive ability of the model. In addition, early participation of a feature (at the upper nodes of the tree) is usually considered more important than late participation and the cumulative sum was calculated in a weighted manner to reflect the contribution of the features.

3 Results

3.1 Descriptive statistics

The dataset of this study includes 48 non-extraction cases and 144 extraction cases. The proportion of each feature variables is shown in Figure 3.

Since crowding often changes in similar directions in the upper and lower dentitions, we combined it into one variable-crowding, by calculating the maximum of crowding in upper and lower dentitions. However, the inclination of the upper and lower anterior teeth can appear completely opposite trends, such as buccal inclination in upper incisor and lingual inclination in lower incisor, so they were considered separately in this study. Open bite and deep overbite reflect different degrees of vertical discrepancy of the upper and lower anterior teeth in different directions, so they were combined into one variable as overbite (Table 1; Figure 3).

3.2 Evaluation of model accuracy

The accuracy of the four models in the training set and cross-validation set is shown in Figure 4. The accuracy of the four models in the training set ranges from 80% to 93%, and in the cross-validation set, the decision tree and random forest had higher accuracy. We can evaluate the generalization ability of the model by comparing the difference between the accuracy of cross-validation set and training set. Generally, over-fitting is often seen if the accuracy in the cross-validation set is significantly lower than that in the training set, but there is not a definite border (Xu and Goodacre, 2018). In this study, random forest and SVM showed a tendency of, but not absolute, over-fitting. The performance of decision tree and MLP was acceptable, and the accuracy of decision tree was greater than that of MLP.

For the testing set, we list the confusion matrices of the four models, in which, positive cases represent extraction classification and negative cases represent non-extraction classification (Figure 5). In the random forest and SVM, the accuracy of the testing set was also significantly lower than the training set (Figures 4, 6). Among the performance of these four models, the decision tree showed the best overall prediction performance with the best accuracy, balanced

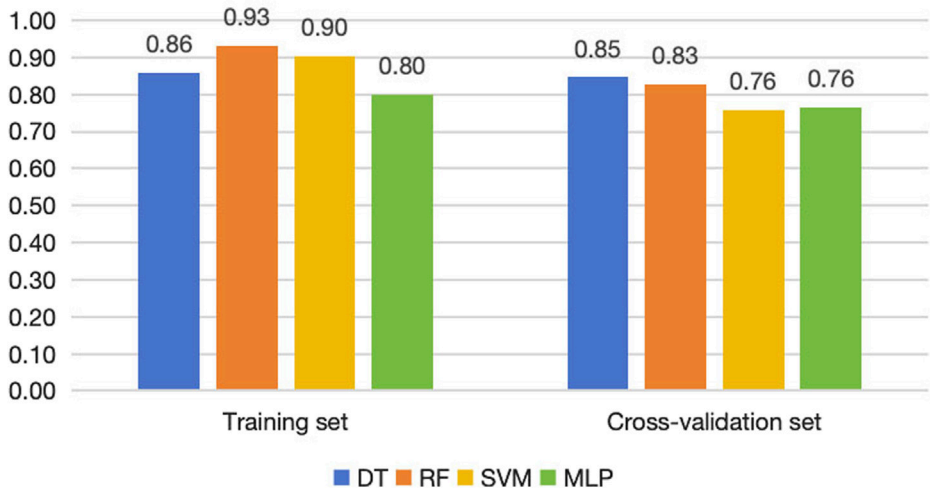

FIGURE 4
Accuracy of the four machine learning models in training sets, cross-validation sets and testing sets.

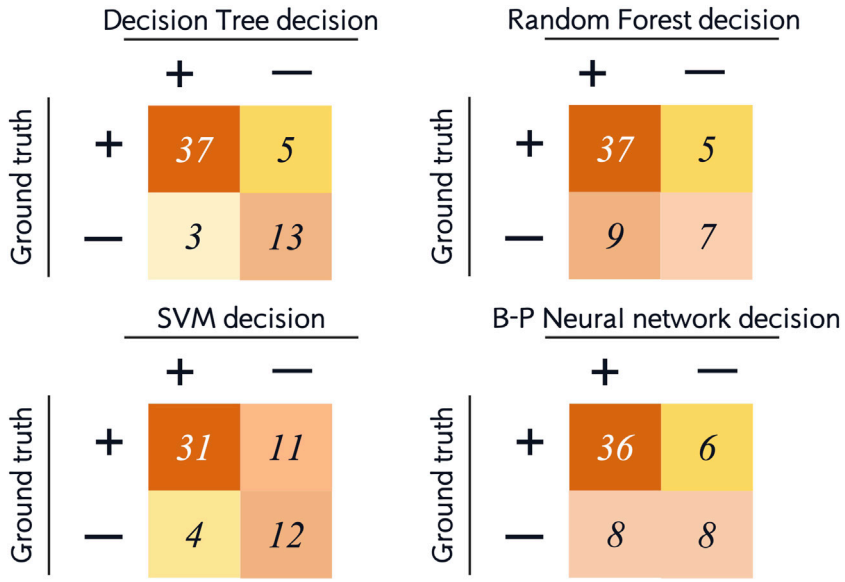

FIGURE 5
Confusion matrix of the testing sets of the four machine learning models.

accuracy, specificity, precision and F1-score (Figure 6). It is worth noting that in a more detailed analysis, RF and MLP showed a low specificity, indicating that they tended to classify too many non-extraction cases into extraction group (Figure 6).

From the ROC curve, we can see that the decision tree model performs best, followed by SVM, and MLP is the weakest (Figure 7).

3.3 Evaluation of feature contribution

The tree model has strong interpretability and is significantly better than support vector machines and neural networks. In the decision tree model, crowding is the most important indicator for tooth extraction (30.20%), followed by lateral facial profile (26.00%), lower incisor inclination (13.30%), overbite (9.20%), upper anterior lip inclination (8.10%), and skeletal classification (7.30%) (Figure 8). In the random forest model, the most important indicator is lateral facial profile (29.4%), followed by overbite (6.80%), crowding (11.90%), upper (10.9%) and lower incisor inclination (10.20%), vertical growth pattern (7.90%), etc. (Figure 8).

Figure 9 shows one of the decision tree models generated in this study, which facilitates intuitive analysis of the specific role of each feature. The feature selection standard of the decision tree in this study is set to information gain (entropy). Entropy represents the uncertainty of the information of the node, taking a value between 0 and 1. The larger the entropy, the greater the uncertainty. That is to

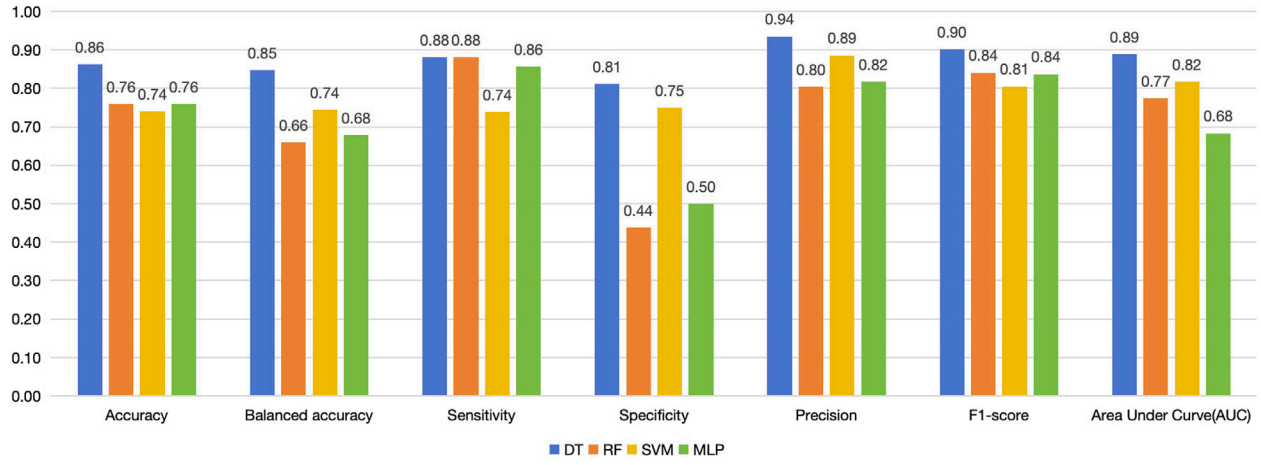

FIGURE 6
Performance of the four models in testing set.

say, for the training set of this tree, the closer the entropy is to 0, the greater the confidence of this classification.

The root node, or 0-layer node, used in the tree in Figure 9 are lateral facial profile, upper and lower incisor inclination, crowding, overbite, vertical growth pattern, skeletal classification. The root node is the lateral facial profile. The model is divided into two categories according to straight, convex and concave lateral facial profile. However, it is unable to make a tooth extraction prediction based on the lateral facial profile alone, so node splits into two branches as first-layer nodes. A more detailed analysis shows that the most commonly used feature was crowding (grey box in Figure 9), and when we look at the most left and right boxes in the second-level nodes, if the crowding score was between 1 and 3 (larger than 2 mm crowding), it tends to extraction decision, and when it is greater than 3 or equal to 4 (spacing), it tends to non-extraction decision. For vertical growth pattern (orange box in the third-level node), a score over 2 (hypodivergent) indicates non-extraction decision. Moreover, Class II and Class III classification (pink box, scored 2 and 3) points to tooth extraction and buccal incisor inclination (blue box in the fourth-level node, scored 1) suggests the tendency to tooth extraction.

4 Discussion

Orthodontic treatment planning embodies experience and wisdom of orthodontists, and the formulation of tooth extraction plans is one of the most critical decisions in orthodontic practice, and it is also one of the biggest challenges for young doctors and general practitioners (Liu et al., 2021). Although there are many factors that may influence orthodontic tooth extraction decisions. For most orthodontic cases, orthodontic experts have relatively consistent judgments on tooth extraction planning (Suhail et al., 2020; Xu and Huang, 2002). In this context, it is meaningful to perform automatic decision-making assisted by machine learning.

Because natural prevalence of different categories of malocclusion differs among different populations (Lombardo et al., 2020). At the same time, patients' motivation to seek orthodontic treatment also varies. For example, Chinese patients may have stronger will to correct convex facial profile (Yin et al., 2014). Therefore, each category of malocclusion in this study cannot be completely balanced. If the proportion of each category of malocclusion is calibrated during the inclusion process, randomization cannot be ensured, and it may be difficult for the model to adapt to clinical reality.

Classification algorithm is an important technology in data mining. In this study, the decision tree was very effective in classifying the sample set. In orthodontic tooth extraction decisions, random forests usually perform better than decision trees (Prasad et al., 2022; Etemad et al., 2021). Random forests may randomly select a certain proportion of features to be included in each model (Belgiu and Dragut, 2016). When the scale of the decision tree is too large, it may lead to over-fitting. Therefore, this study appropriately limited the depth and number of nodes of the tree during the parameter adjustment process. Random forest is suitable for most types of datasets, but in this study, no matter how the parameters are adjusted, random forest still shows some over-fitting tendency. Neural networks are more suitable for large and complex datasets. In the analysis of the confusion matrix, RF, SVM and MLP all showed low specificity (<0.4) at the first experiment, showing a strong preference to the tooth extraction decision. This may be attributed to the imbalance of the classification variable of the dataset. Among the consecutive patients in our hospital, the number of extraction treatment is larger than non-extraction, resulting in more positive cases in the testing set. Therefore, we adopted threshold moving method to select an optimal classification threshold (Collell et al., 2018). As a result, the specificity improved in SVM. Still, in RF and MLP models, adding the judgment of the extraction decision may improve the accuracy, resulting in decision bias. However, the decision tree shows better discernment of non-extraction cases. The more complex the model, the greater the possibility of over-fitting. Decision tree is more resistible to uneven category in this study. Decision tree is based on information entropy for classification, so it essentially looks at the correlation between features and categories. Even if there is little data in this category, as long as its correlation with the features

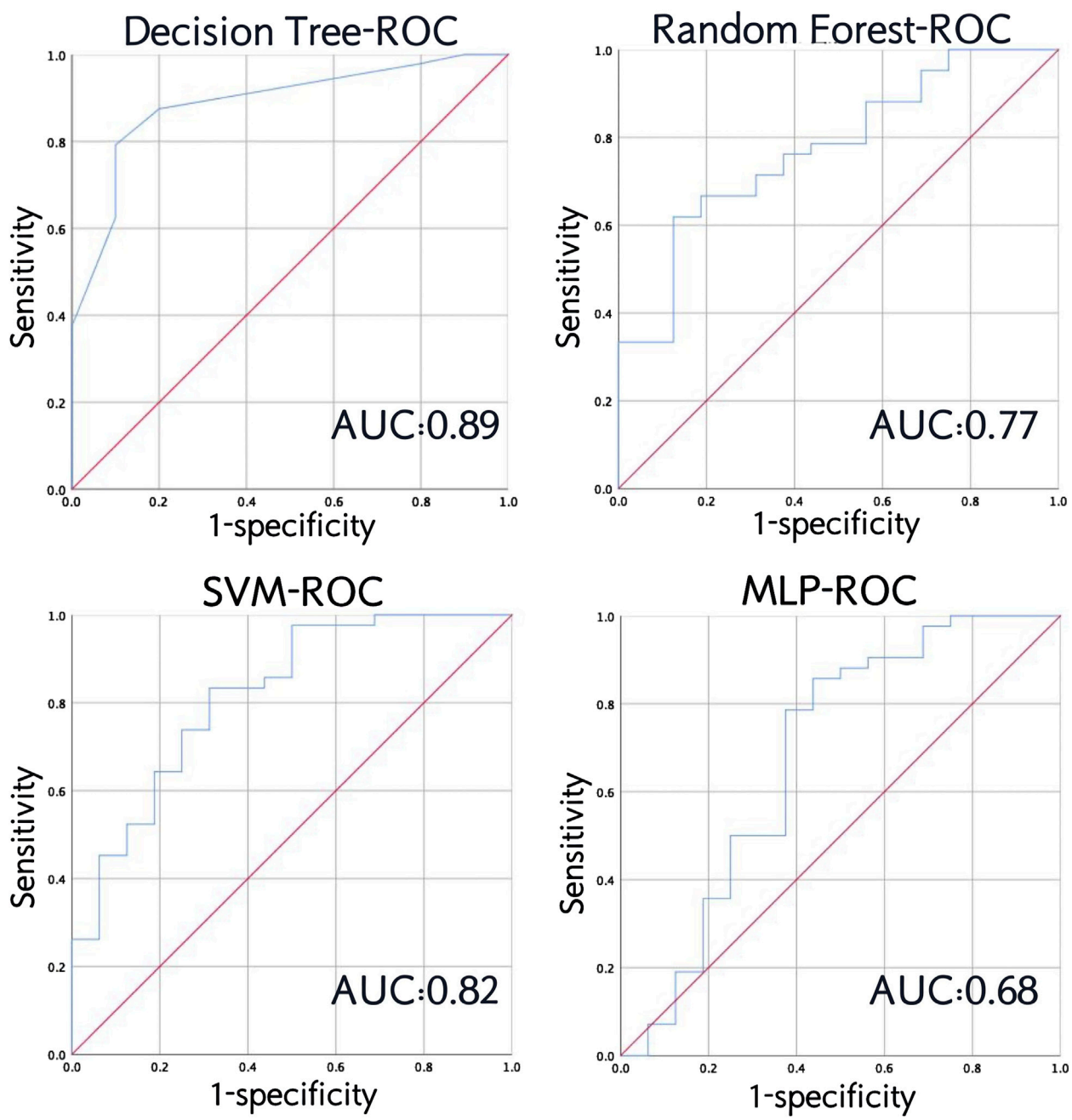

FIGURE 7
Receiver operating characteristic (ROC) curve and area under the curve (AUC) of the four models in testing set.

is strong, it will not be misclassified. Random forest has a step of random sampling of data. If the category distribution is uneven, this class may not exist in some sub-sampling, which will affect the results.

There is occasionality in the generation of the model, and high accuracy in a single test does not mean stable performance of the model. In order to evaluate the generalization of the model, we conducted cross-validation. In cross-validation, each sample will appear once in the validation set, therefore, the model needs to have good generalization ability for all samples in the dataset in order to achieve a high average cross-validation accuracy (Jonathan et al., 2000; Karkkainen, 2014). Xie et al. (2010) used an artificial neural network model to predict the extraction plan and obtained an accuracy of 100% in the training set and 80% in the testing set, indicating over-fitting of the model. Köktürk et al. (2024) used multiple machine learning methods for tooth extraction decision-making, and the best algorithm was Gradient Boosted Trees, with an accuracy of 83.3%. We obtained an accuracy of 81.5% using MLP. Li et al. (2019) and Jung and Kim (2016) both used deep neural networks to train tooth extraction prediction models on samples of 156 and 302 patients, respectively, achieving an accuracy rate of over 93%, but their study did not specify the validation method they

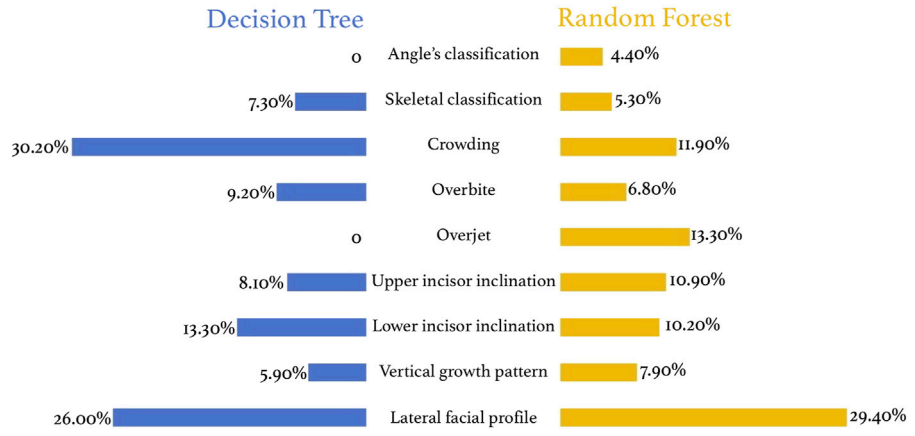

FIGURE 8
Feature contribution in decision tree and random forest models.

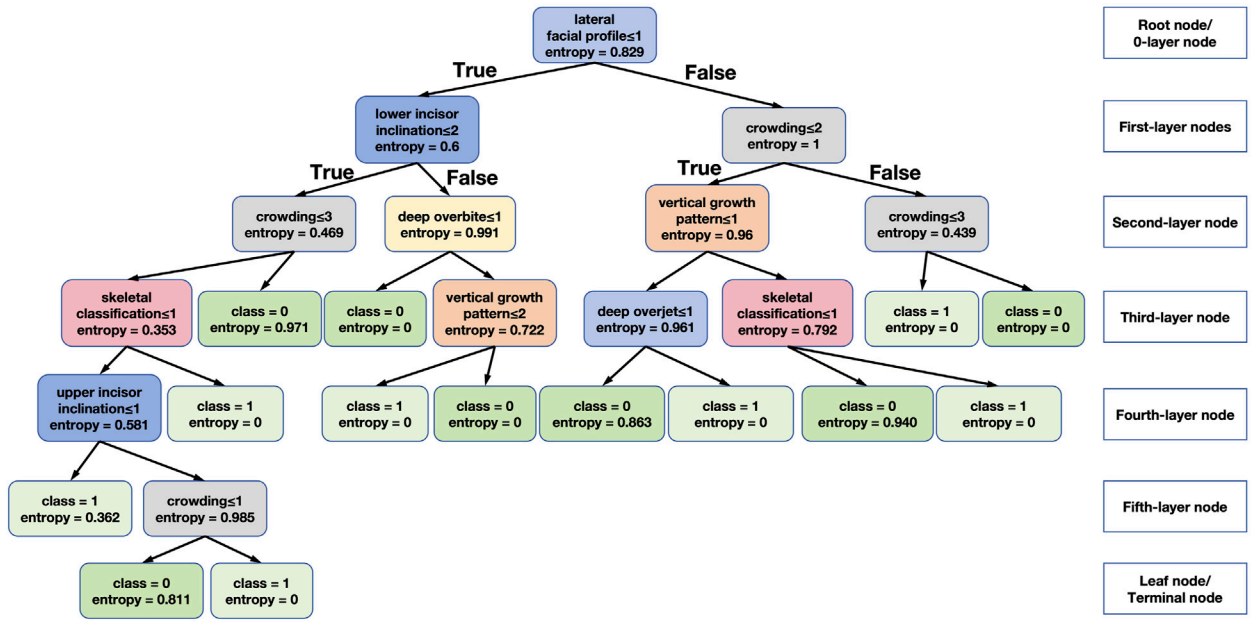

FIGURE 9
One example of a decision tree generated in our study.

used. However, Köktürk et al. (2024), Etemad et al. (2021) and the current study also used the MLP method, but none of the accuracy exceeded 82%. They further divided the dataset into a correctly predicted group and an incorrectly predicted group according to the classification results of this preliminary model, and used the same method to calculate the accuracy, which was improved in both groups (Etemad et al., 2021). However, such a division has no clinical implication, and therefore impossible to find the corresponding external testing set, so it cannot be said that this result can be generalized. Interestingly, Etemad et al. (2021) found that the accuracy of the model obtained by using 117 variables did not improve compared with that using 22 variables. Our study only used 9 variables and obtained an accuracy exceeding their study. Suhail et al. (2020), unlike previous studies, significantly reduced the number of diagnostic features (nineteen) and demonstrated that finite feature sets and machine learning algorithms can accurately predict the extraction process. The ensemble of simpler models outperforms more complex models, like neural network.

There is a huge difference in the tooth extraction rate between Eastern and Western people. The tooth extraction and correction rate of Western people is around 10%–30%, much lower than that of East Asian people (Jackson et al., 2017). Economic, psychological, physiological and anatomical conditions may cause various extraction rate and complex influencing factors among different countries (Del Real et al., 2022), resulting in distinct difficulty of model training. Del Real et al. (2022) obtained an accuracy of more

than 90% in one of their models in a Chilean population, but in their sample, cases of skeletal class I accounted for 65%, and skeletal class III only 6%, and the average angle cases were also close to 50%, the proportion of normal facial type was significantly higher than in our study.

Tooth extraction plan can be affected by the patient's own factors. Some patients strongly resist tooth extraction, which may lead to the actual number of tooth extraction classifications in the final included data being less than the number of tooth extraction classifications that should be, which may be one of the reasons for the misclassification of the prediction model. Therefore, in this study, we recorded the experts' preferred plans rather than the actual plans in the final dataset to predict the tooth extraction plan.

The interpretability of the tree models significantly outperforms other models like deep neural networks. Since the decision tree model worked better in this study, and a tendency of over-fitting occurred in the random forest, the results of the decision tree should be referred to in the feature contribution analysis. The most important indicators of extraction treatment were crowding, lateral facial profile, and lower incisor inclination. These features can all reflect the tooth-bone volume discrepancy. On the other hand, indicators such as Angle's classification and overjet may reflect the sagittal discrepancy of maxilla and mandible and does not influence orthodontic extraction decisions from our study. Li et al. (2019) found out that upper and lower crowding, and U1-NA°, are the three most important features. Su et al. (2022) studied the tooth extraction pattern of patients with skeletal Class II average angle and deep overjet and showed that deep overjet and distal molar relationship are the main reasons for tooth extraction in Class II patients. Guo et al. (2014) founded that lower anterior crowding, molar relationship, and growth pattern were the three most relevant influential factors to the extraction decisions for Angle's class II division 1 malocclusions. The above three studies all found that crowding is the most important influencing factor in determining tooth extraction decisions, but other factors are slightly different from this study. However, Bishara et al. (1995) pointed out that tooth size-arch length discrepancy and lip protrusion are the main reference factors for tooth extraction correction, which is highly consistent with the results of our study.

It should be noted that the purpose of introducing machine learning to assist in the classification of orthodontic tooth extraction plans is not to pursue a wiser judgment than that of orthodontists in critical cases, because whether it is expert judgment or machine learning classifier, the plan formulation of critical cases needs to weigh non-orthodontic indicators such as periodontal conditions, patient's own will, and public aesthetics, rather than just the accuracy as a measurement standard. Machine learning methods should be able to better summarize the logic and ideas of experts, explain the causes and nature of malocclusion, and help doctors formulate more comprehensive treatment plans. Any mathematical principle that affects decision-making cannot be isolated from clinical examination and communication.

5 Conclusion

The decision tree algorithm in machine learning outperformed other machine learning models in predicting orthodontic extraction plans, with an average accuracy of 86%. Crowding is the most important factor for experts to decide on extraction treatment, followed by lateral facial profile and lower incisor inclination, indicating that tooth extraction is an important treatment method for tooth-bone volume discrepancy. Clinically, lack of space, protrusive anterior lips and convex facial profile indicates the need for tooth extraction. Machine learning should not replace but help doctors formulate more comprehensive treatment plans.

Data availability statement

The raw data supporting the conclusions of this article will be made available by the authors, without undue reservation.

Ethics statement

The studies involving humans were approved by the Institutional Review Board of Shanghai Stomatological Hospital. The studies were conducted in accordance with the local legislation and institutional requirements. Written informed consent for participation was not required from the participants or the participants' legal guardians/next of kin in accordance with the national legislation and institutional requirements.

Author contributions

JH: Conceptualization, Data curation, Formal Analysis, Funding acquisition, Investigation, Project administration, Resources, Software, Supervision, Validation, Writing–original draft, Writing–review and editing. I-TC: Data curation, Formal Analysis, Investigation, Writing–review and editing. ZW: Data curation, Formal Analysis, Investigation, Writing–review and editing. XD: Data curation, Formal Analysis, Investigation, Writing–review and editing. YJ: Data curation, Formal Analysis, Investigation, Writing–review and editing. CY: Conceptualization, Formal Analysis, Funding acquisition, Supervision, Writing–review and editing. YP: Conceptualization, Data curation, Formal Analysis, Investigation, Methodology, Project administration, Resources, Software, Supervision, Validation, Writing–original draft, Writing–review and editing.

Funding

The author(s) declare that financial support was received for the research, authorship, and/or publication of this article. The research was supported by National Natural Science Foundation of China (82001104).

Acknowledgments

The authors would like to thank all the doctors of Department of Orthodontics, Shanghai Stomatological Hospital who have provided clinical materials and Yibin Liu, vision engineer of Changzhou Changchuan Technology Co., Ltd. for technical support.

Conflict of interest

The authors declare that the research was conducted in the absence of any commercial or financial relationships that could be construed as a potential conflict of interest.

The reviewer CO declared a shared affiliation with the authors JH and I-TC to the handling editor at the time of review.

Publisher's note

References

Belgiu, M., and Dragut, L. (2016). Random forest in remote sensing: a review of applications and future directions. *Isprs J. Photogramm.* 114, 24–31. doi:10.1016/j.isprsjprs.2016.01.011

Bishara, S. E., Cummins, D. M., and Jakobsen, J. R. (1995). The morphologic basis for the extraction decision in Class II, division 1 malocclusions: a comparative study. *Am. J. Orthod. Dentofac. Orthop.* 107, 129–135. doi:10.1016/s0889-5406(95)70127-3

Boley, J. C., Mark, J. A., Sachdeva, R. C., and Buschang, P. H. (2003). Long-term stability of Class I premolar extraction treatment. *Am. J. Orthod. Dentofac. Orthop.* 124, 277–287. doi:10.1016/s0889-5406(03)00448-7

Chang, C. A., Fields, H. W., Jr., Beck, F. M., Springer, N. C., Firestone, A. R., Rosenstiel, S., et al. (2011). Smile esthetics from patients' perspectives for faces of varying attractiveness. *Am. J. Orthod. Dentofac. Orthop.* 140, e171–e180. doi:10.1016/j.ajodo.2011.03.022

Collell, G., Prelec, D., and Patil, K. R. (2018). A simple plug-in bagging ensemble based on threshold-moving for classifying binary and multiclass imbalanced data. *Neurocomputing* 275, 330–340. doi:10.1016/j.neucom.2017.08.035

Del Real, A., Del Real, O., Sardina, S., and Oyonarte, R. (2022). Use of automated artificial intelligence to predict the need for orthodontic extractions. *Korean J. Orthod.* 52, 102–111. doi:10.4041/kjod.2022.52.2.102

Etemad, L., Wu, T. H., Heiner, P., Liu, J., Lee, S., Chao, W. L., et al. (2021). Machine learning from clinical data sets of a contemporary decision for orthodontic tooth extraction. *Orthod. Craniofac Res.* 24 (Suppl. 2), 193–200. doi:10.1111/ocr.12502

Guo, Y., Han, X., Xu, H., Ai, D., Zeng, H., and Bai, D. (2014). Morphological characteristics influencing the orthodontic extraction strategies for Angle's class II division 1 malocclusions. *Prog. Orthod.* 15, 44. doi:10.1186/s40510-014-0044-y

Hasija, N., Bala, M., and Goyal, V. (2014). Estimation of tooth size discrepancies among different malocclusion groups. *Int. J. Clin. Pediatr. Dent.* 7, 82–85. doi:10.5005/jp-journals-10005-1242

Jackson, T. H., Guez, C., Lin, F. C., Proffit, W. R., and Ko, C. C. (2017). Extraction frequencies at a university orthodontic clinic in the 21st century: demographic and diagnostic factors affecting the likelihood of extraction. *Am. J. Orthod. Dentofac. Orthop.* 151, 456–462. doi:10.1016/j.ajodo.2016.08.021

Janson, G., Araki, J., Estelita, S., and Camardella, L. T. (2014). Stability of class II subdivision malocclusion treatment with 3 and 4 premolar extractions. *Prog. Orthod.* 15, 67. doi:10.1186/s40510-014-0067-4

Janson, G., Valarelli, F. P., Henriques, J. F., de Freitas, M. R., and Cançado, R. H. (2003). Stability of anterior open bite nonextraction treatment in the permanent dentition. *Am. J. Orthod. Dentofac. Orthop.* 124, 265–276. doi:10.1016/s0889-5406(03)00449-9

Jonathan, P., Krzanowski, W. J., and Mccarthy, W. V. (2000). On the use of cross-validation to assess performance in multivariate prediction. *Statistics and Comput.* 10, 209–229. doi:10.1023/a:1008987426876

Jung, S. K., and Kim, T. W. (2016). New approach for the diagnosis of extractions with neural network machine learning. *Am. J. Orthod. Dentofac. Orthop.* 149, 127–133. doi:10.1016/j.ajodo.2015.07.030

Karkkainen, T. (2014). On cross-validation for MLP model evaluation. *Int. Workshop Stat. Tech. Pattern Recognit.*, 291–300. doi:10.1007/978-3-662-44415-3_30

Ker, A. J., Chan, R., Fields, H. W., Beck, M., and Rosenstiel, S. (2008). Esthetics and smile characteristics from the layperson's perspective: a computer-based survey study. *J. Am. Dent. Assoc.* 139, 1318–1327. doi:10.14219/jada.archive.2008.0043

Khanagar, S. B., Al-Ehaideb, A., Vishwanathaiah, S., Maganur, P. C., Patil, S., Naik, S., et al. (2021). Scope and performance of artificial intelligence technology in orthodontic diagnosis, treatment planning, and clinical decision-making - a systematic review. *J. Dent. Sci.* 16, 482–492. doi:10.1016/j.jds.2020.05.022

Köktürk, B., Pamukçu, H., and Gözüaçik, Ö. (2024). Evaluation of different machine learning algorithms for extraction decision in orthodontic treatment. *Orthod. Craniofac Res.* doi:10.1111/ocr.12811

Konstantonis, D., Anthopoulou, C., and Makou, M. (2013). Extraction decision and identification of treatment predictors in Class I malocclusions. *Prog. Orthod.* 14, 47. doi:10.1186/2196-1042-14-47

Leavitt, L., Volovic, J., Steinhauer, L., Mason, T., Eckert, G., Dean, J. A., et al. (2023). Can we predict orthodontic extraction patterns by using machine learning?. *Orthod. Craniofac Res.* 26, 552–559. doi:10.1111/ocr.12641

Li, P., Kong, D., Tang, T., Su, D., Yang, P., Wang, H., et al. (2019). Orthodontic treatment planning based on artificial neural networks. *Sci. Rep.* 9, 2037. doi:10.1038/s41598-018-38439-w

Liu, J., Chen, Y., Li, S., Zhao, Z., and Wu, Z. (2021). Machine learning in orthodontics: challenges and perspectives. *Adv. Clin. Exp. Med.* 30, 1065–1074. doi:10.17219/acem/138702

Lombardo, G., Vena, F., Negri, P., Pagano, S., Barilotti, C., Paglia, L., et al. (2020). Worldwide prevalence of malocclusion in the different stages of dentition: a systematic review and meta-analysis. *Eur. J. Paediatr. Dent.* 21, 115–122. doi:10.23804/ejpd.2020.21.02.05

Maués, C. P. R., Nascimento, R. R. D., and Vilella, O. D. V. (2015). Severe root resorption resulting from orthodontic treatment: prevalence and risk factors. *Dent. Press J. Orthod.* 20, 52–58. doi:10.1590/2176-9451.20.1.052-058.oar

Prasad, J., Mallikarjunaiah, D. R., Shetty, A., Gandedkar, N., Chikkamuniswamy, A. B., and Shivashankar, P. C. (2022). Machine learning predictive model as clinical decision support system in orthodontic treatment planning. *Dent. J. (Basel)* 11, 1. doi:10.3390/dj11010001

Proffit, W. R. (1994). Forty-year review of extraction frequencies at a university orthodontic clinic. *Angle Orthod.* 64, 407–414. doi:10.1043/0003-3219(1994)064<0407:FROEFA>2.0.CO;2

Su, H., Han, B., Wang, X., and Xu, T. (2022). Analysis of craniofacial features of patients with skeletal Class II average angle deepoverjet in three different tooth extraction modes. *Chin. J. Orthod.* 29, 24–28. doi:10.3760/cma.j.cn115797-20211112-22105

Suhail, Y., Upadhyay, M., Chhibber, A., and Kshitiz, (2020). Machine learning for the diagnosis of orthodontic extractions: a computational analysis using ensemble learning. *Bioengineering* 7, 55. doi:10.3390/bioengineering7020055

Xie, X., Wang, L., and Wang, A. (2010). Artificial neural network modeling for deciding if extractions are necessary prior to orthodontic treatment. *Angle Orthod.* 80, 262–266. doi:10.2319/111608-588.1

Xu, T., and Huang, W. (2002). Interclinician agreement on the decision of extraction or non-extraction orthodontic treatment. *Chin. J. Orthod.* 9, 14–16. doi:10.3760/cma.j.issn.1674-5760.2002.02.004

Xu, Y., and Goodacre, R. (2018). On splitting training and validation set: a comparative study of cross-validation, bootstrap and systematic sampling for estimating the generalization performance of supervised learning. *J. Anal. Test.* 2, 249–262. doi:10.1007/s41664-018-0068-2

Yin, L., Jiang, M., Chen, W., Smales, R. J., Wang, Q., and Tang, L. (2014). Differences in facial profile and dental esthetic perceptions between young adults and orthodontists. *Am. J. Orthod. Dentofac. Orthop.* 145, 750–756. doi:10.1016/j.ajodo.2014.01.021

frontiers | Frontiers in Bioengineering and Biotechnology

TYPE Original Research
PUBLISHED 04 December 2024
DOI 10.3389/fbioe.2024.1507525

OPEN ACCESS

EDITED BY
Nicholas G. Fischer,
University of Minnesota Twin Cities,
United States

REVIEWED BY
Yuan Gao,
Sichuan University, China
Hector Flores,
Autonomous University of San Luis Potosí,
Mexico

*CORRESPONDENCE
Di Wu,
prinsiss2009@163.com

RECEIVED 07 October 2024
ACCEPTED 13 November 2024
PUBLISHED 04 December 2024

CITATION
Wang L, Feng B, Shi S, Sun D and Wu D (2024) The effect of different activation irrigations on intracanal smear layer removal: a vitro study. *Front. Bioeng. Biotechnol.* 12:1507525. doi: 10.3389/fbioe.2024.1507525

The effect of different activation irrigations on intracanal smear layer removal: a vitro study

Lingxiang Wang, Bo Feng, Shaojing Shi, Degang Sun and Di Wu*

Department of Cariology and Endodontology, Qingdao Stomatological Hospital Affiliated to Qingdao University, Qingdao, Shandong, China

Objective: To compare the effect of syringe irrigation technique, passive ultrasonic activation technique, EDDY activation technique and Er,Cr,YSGG laser activation technique on smear layer removal in root canals *in vitro*.

Methods: Forty mandibular first premolars with single canal were collected from patients in Qingdao Stomatological Hospital affiliated to Qingdao University. After root canal preparation with ProTaper Universal to F3, they were randomly divided into four groups (n = 10) according to different activation irrigations for the final washing: syringe irrigation (SI), passive ultrasonic activation (PU), EDDY activation (EDDY) and Er,Cr,YSGG laser activation (YSGG). Finally, all the crowns of them were cut off and the root length was trimmed to 15 mm. The roots were split longitudinally and observed with scanning electron microscope (SEM) for assessment of smear layer removal in different parts of the root canal.

Results: All groups showed similar effects for cleaning the root canals in the coronal thirds ($P > 0.05$). For cleaning the root canals in the middle thirds, PU group, EDDY group and YSGG group showed similar effects, ($P > 0.05$). They were more effective than SI group ($P < 0.05$). For cleaning the root canals in the apical thirds, PU group and EDDY group showed similar effects ($P > 0.05$). They were more effective than SI group ($P < 0.05$). YSGG group was more effective than other groups ($P < 0.05$).

Conclusion: Er,Cr,YSGG laser activation technique can remove smear layer of root canals effectively. The cleaning effect of the passive ultrasonic activation technique, EDDY activation technique is better than that of syringe irrigation technique.

KEYWORDS

smear layer, ultrasonic technique, ER, Cr, YSGG laser, EDDY activation technique, scanning electron microscope

1 Introduction

Infection control is the core of root canal treatment. At present, the infection control of root canal mainly depends on the combination of mechanical and chemical preparation of the root canal. The mechanical preparation of a root canal results in a large amount of smear layer (thickness of 2–5 μm) formation mixed with inorganic calcified tissues, organic matrix, and dentinal debris. Smear layer formation leads to a number of unfavorable consequences such as blocking the surface of dentinal tubules as well as the penetration of irrigants, medications, and filling materials into the dentinal tubules (Widbiller et al., 2021; Chavate et al., 2024). In endodontics, there is a great emphasis on removal of the smear layer

and using different intra-canal irrigators. However, studies have shown that the traditional syringe irrigation technique is difficult to effectively remove the smear layer of the root canal wall, especially the root apex section (Xinyu and Xue, 2022; Drukteinis et al., 2024). Therefore, the use of the new auxiliary root canal irrigation activation technology has important clinical significance.

Kinetic energy irrigation technique can transfer different forms of energy to the root canal solution, which can effectively and fully transport the solution to the root canal system, improve the depth of its entry into the root canal, and activate the active components (Kaur et al., 2024). In recent years, the kinetic energy irrigation technique include sonic, ultrasonic, and laser-activated irrigation and so on. The traditional syringe irrigation technology is difficult to effectively deliver the solution to the root tip area due to the "air lock effect" in the apical area (Haupt et al., 2020). The sonic and ultrasonic activated irrigation technique can play a role through acoustic-streaming-effect, unltrasonic cavitation effect and thermal effect. For example, VDW's EDDY sonic device can operate at a frequency of 6 kHz and an amplitude of 346 μm (Tomson and Simon, 2016), thus achieving the purpose of deeper removal of smear layers and tissue debris. Different kinds of laser-activated irrigation can be achieved by acoustic-streaming-effect, unltrasonic cavitation effect and thermal effect. The steam bubbles can be formed in their working process, and the volume change caused by the bubble bursting can cause the movement of the root tube flushing liquid, so as to achieve a better cleaning effect of the smear layer (Meire and De Moor, 2024).

Therefore, the aim of the present study was to evaluate the effectiveness of the syringe irrigation technique, passive ultrasonic activation technique, EDDY activation technique and Er,Cr,YSGG laser activation technique on smear layer removal in root canals during chemomechanical preparation.

2 Materials and methods

2.1 Materials

This experimental study was performed on caries-free mandibular first premolars (n = 40) extracted due to orthodontic treatment need. The extracted teeth were examined carefully to ensure that they met the following criteria (Grischke et al., 2014): fully developed teeth with a completely closed apex, length of the teeth ranging from 20 to 25 mm, and the root length greater than 10 mm. Any teeth treated endodontically or presenting with dysplasia, calcification, or root resorption were excluded. The Institutional Ethics Research Committee (NO.2023KQYX037) approved the design of this study, and an informed written consent to participate was obtained from all patients. All teeth were cleaned and stored in 0.9% normal saline at 40°C until further experimentation.

The irrigation reagents used in the present study included NaOCl (Chlorex, Durham, United Kingdom), EDTA gel and solution (17%) (Chlorex, Durham, United Kingdom). The instruments used in the present study included X-Smart motor, K-type files, ProTaper Universal (Denstply-Maillefer, Ballaigues, Switzerland), 27-gauge Monoject endodontic needles (Ultradent, South Jordan, UT, United States), sonic S motor, EDDY (VDW, Germany), K25-21 ultrasonic file (Acteon, France), Er,Cr,YSGG waterlaser (Biolase, San Clemente, America) and scanning electron microscope (Vega3 Twscan, Czech Republic).

2.2 Specimen preparation

Pulp tissue remnants were removed from each root canal with fine, barbed broaches (Maillefer, Ballaigues, Switzerland) before the biomechanical preparations. An ISO#15 K-type file was inserted into the root canal until it was visible at the apical foramen, and the working length of each root canal was established at 1 mm from the apical foramen. All teeth were prepared using ProTaper Universal to F3. During the canal preparation, the canals were prepared using 17% EDTA gel and irrigated with 2 mL of 2% NaClO irrigants between each filing.

All mandibular first premolars were divided randomly into four groups (n = 10 for each group). The canals were irrigated as detailed in Table 1, and irrigation with 2 mL of normal saline was performed between each irrigant.

Syringe irrigation (SI): a 27-gauge Monoject endodontic needle attached to a Luer-Loc syringe with 17% EDTA solution were placed 2 mm away from the apical stop and washed the whole root canal at a constant and slow speed for 15 s. The needle was then used to wash the root canal with 2% NaClO solution for 15s.

Passive ultrasonic activation (PU): 17% EDTA solution was pre-injected into the root canal and the K25-21 was placed 2 mm away from the apical stop and washed the whole root canal at a constant and slow speed for 15 s. The K25-21 was then used to wash the root canal with 2% NaClO solution for 15s.

EDDY activation (EDDY): 17% EDTA solution was pre-injected into the root canal and the EDDY (25#06) was placed 2 mm away from the apical stop and washed the whole root canal at a constant and slow speed for 15 s.The EDDY was then used to wash the root canal with 2 %NaClO solution for 15s.

Er,Cr,YSGG laser activation (YSGG): 17% EDTA solution was pre-injected into the root canal. Set the water laser operator to the root canal treatment mode (H mode) and place the RFT2 and RFT3 laser fiber (power 0.75W, 20% air, 30% water, pulse frequency 20 Hz) 2 mm away from the apical stop and washed the whole root canal at a constant and slow speed for 15 s. The laser fibers were then used to wash the root canal with 2% NaClO solution for 15s.

Finally, the teeth were rinsed free of agents with normal saline and transferred to the fixative (2.5% glutaraldehyde).

2.3 Scanning electron microscopy (SEM) and debris scoring

All roots were removed from the fixative, and gutta-percha cones were inserted into the root canals. The objective was to avoid any intrusion of the cutting disc into the canals, which would pollute the samples by splattering cutting debris into the root canal system.To yield root specimens of uniform length (15 mm), the teeth were decoronated at the level of the

TABLE 1 Description of the various study groups and the corresponding irrigation treatments.

Group	Preparation	Final washing
SI group	17% EDTA gel +2% NaOCl	17% EDTA solution + SI+ 2% NaOCl
PU group	17% EDTA gel +2% NaOCl	17% EDTA solution + PU+2% NaOCl
EDDY group	17% EDTA gel +2% NaOCl	17% EDTA solution + EDDY+2% NaOCl
YSGG group	17% EDTA gel +2% NaOCl	17% EDTA solution + YSGG+2% NaOCl

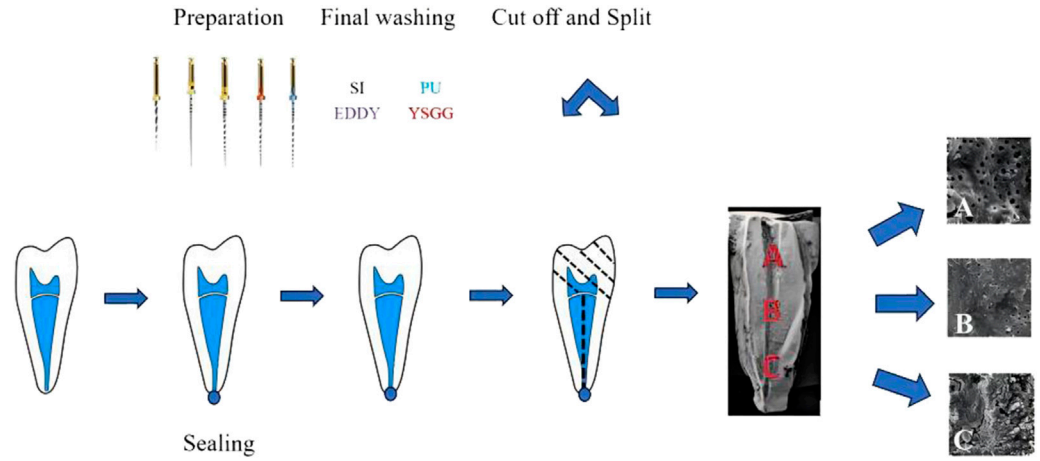

FIGURE 1
Schematic presentation of the fragment preparation process and the various segments. **(A)** Coronal third, **(B)** middle third, **(C)** apical third.

cementoenamel junction using a bone chisel and hammer. The grooves were demarcated by a diamond disk along the buccal and lingual surfaces to mark three parts: coronal, middle, and apical thirds. The roots were then split into two halves with a hammer and a microtome blade. For each root, the half containing the most visible prepared parts were used in the study, returned to fresh fixative solution (2.5% glutaraldehyde), and incubated overnight at 4°C. The specimens were rinsed with sterile water and sequentially dehydrated using a gradient of ethanol (30%, 50%, 70%, 80%, 90%, and 100%, v/v) at 15-min intervals. The dehydrated specimens were transferred to a critical point dryer (Tsousimis Autosamdri®-815 Series A, United States) with absolute alcohol as the intermediate fluid and liquid CO_2 as the transition fluid. Following mounting and gold sputter coating (EikoIB-3 ion sputter coater, Japan), the surface morphology of the specimens was analyzed using SEM (Vega3 Twscan, Czech Republic). At the observation stage, the canal walls in the apical, middle, and coronal thirds were examined, and photomicrographs of representative areas were taken at ×2000 magnification as in Figure 1.

The quantitative scoring of the canal wall debris was evaluated using the protocol described by Faras et al. (2016), as follows:

1. No smear layer and open dentinal tubules;
2. A small amount of smear layer and open dentinal tubules;
3. A thin smear layer and partially open dentinal tubules;
4. Partial covering of dentinal tubules with a thick smear layer;
5. Full covering of dentinal tubules with a thick smear layer.

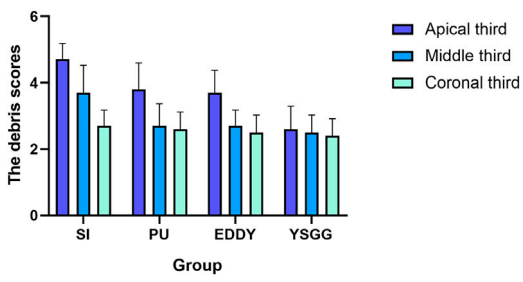

FIGURE 2
Scores for smear layer removal in all groups according to the quantitative scoring of the canal wall debris by Faras et al. (2016). SI = syringe irrigation, EDDY = EDDY activation, PU = passive ultrasonic activation, YSGG = Er,Cr,YSGG laser activation.

2.4 Statistical analysis

All statistical analyses were performed with SPSS 26.0 software (IBM-SPSS Inc., Chicago). First, the full set of samples was independently and blindly evaluated by two observers, and Cohen K scores were calculated to determine the inter-examiner reliability. Second, the debris scores for different irrigants were analyzed by the nonparametric Kruskal–Wallis test and the Mann–Whitney rank sum test for pairwise comparisons. The level of statistical significance was set at $P < 0.05$ (Do and Gaudin, 2020).

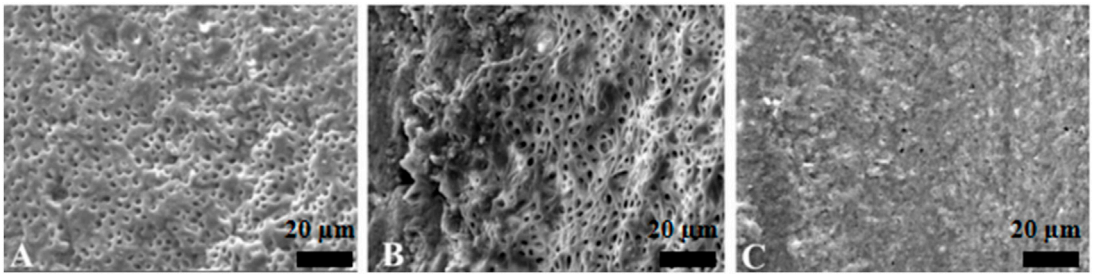

FIGURE 3
Representative scanning electron microscopy images showing the surface morphology in syringe irrigation group. The opening of dentinal tubules as a result of debris removal is apparent in the coronal **(A)** and middle **(B)** thirds, and it was less effective in the apical thirds **(C)** of the root canals (scale bar = 20 μm).

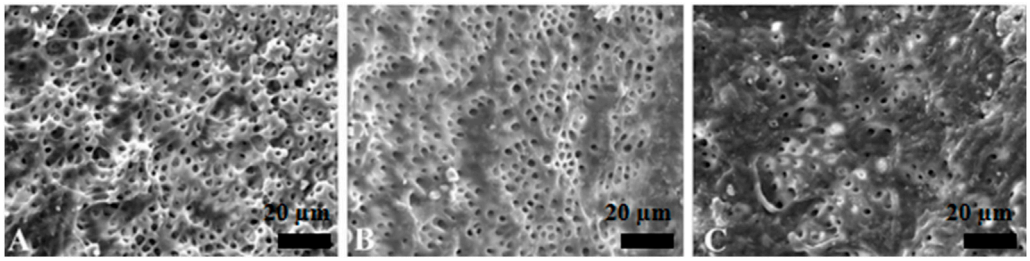

FIGURE 4
Representative scanning electron microscopy images showing the surface morphology in passive ultrasonic irrigation group. The opening of dentinal tubules as a result of debris removal is apparent in the coronal **(A)** and middle **(B)** thirds, and it was less effective in the apical thirds **(C)** of the root canals (scale bar = 20 μm).

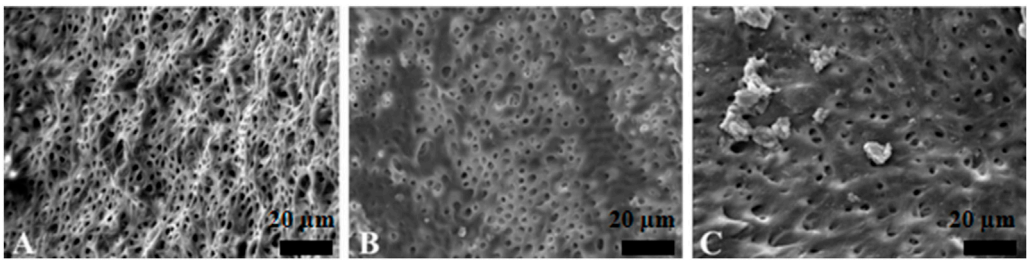

FIGURE 5
Representative scanning electron microscopy images showing the surface morphology in EDDY irrigation group. The opening of dentinal tubules as a result of debris removal is apparent in the coronal **(A)** and middle **(B)** thirds, and it was less effective in the apical thirds **(C)** of the root canals (scale bar = 20 μm).

3 Results

In terms of the root canal sections, a similar trend was observed for four groups in the coronal thirds ($P > 0.05$). In the middle thirds: the PU group, the EDDY group and the YSGG group had a similar effective ($P > 0.05$), but they cleaned significantly ($P < 0.05$) better than the SI group. In the apical thirds: the PU group and the EDDY group had a similar effective ($P > 0.05$), but they cleaned significantly ($P < 0.05$) better than the SI group. The YSGG group was significantly ($P < 0.05$) more effective than all of the other groups (Figure 2).

The PU group and the EDDY group had a similar effect of activation irrigations on intracanal smear layer removal, better than the SI group (Figures 3–5).

The YSGG group was significantly more effective than all of the other groups, showing that Er,Cr,YSGG laser irrigation has a better capability to remove the canal debris and to open the dentinal tubules (Figure 6).

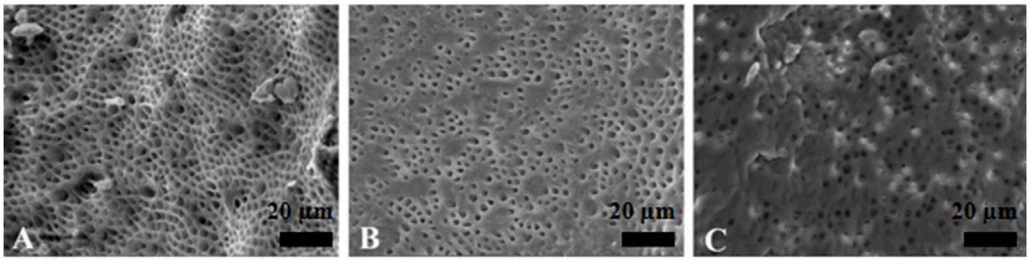

FIGURE 6
Representative scanning electron microscopy images showing the surface morphology in Er,Cr,YSGG laser irrigation group. The opening of dentinal tubules as a result of debris removal is apparent in the coronal **(A)** and middle **(B)** thirds, and it was less effective in the apical thirds **(C)** of the root canals (scale bar = 20 μm).

4 Discussion

The main purpose of root canal treatment is to remove the infection, which is mainly caused by microbial infection and the smear layer generated during root canal preparation (Iandolo et al., 2020). The 2~5 μm thick smear layer will cover the root canal wall and block the dentin tubules, and the filling material will not be in close contact with the root canal wall, which will affect the root canal treatment effect (Chavate et al., 2024). In order to effectively remove root canal infection, root canal preparation devices and chemical preparation drugs have been updated, but studies have shown that preparation devices can only reach about 50% of the root canal anatomy, and those small, narrow structures remain inaccessible (Li et al., 2020). At present, there is no ideal irrigation agent, because sodium hypochlorite can sterilize and dissolve organic matter and necrotic tissue in the root canal, and EDTA can soften and dissolve inorganic matter in the smear layer, so they are often used in combination in clinical practice (Dentistry, 2019). However, traditional irrigators have the limitation of not being able to fully deliver the irrigation to the anatomically complex areas. In addition, due to the tapered shape of the root canal system, there is an "airlock effect" within the root canal system, which prevents the irrigation agent from entering the apical thirds (Rodrigues et al., 2021). Therefore, improving the distribution of the irrigation agent so that it is adequately irrigated throughout the root canal system is essential for the effectiveness of the irrigation.

In recent years, kinetic irrigation has received extensive attention, which can transfer energy into the irrigation agent, deliver the irrigation agent more comprehensively into the root canal system, improve the distribution of the irrigation agent, and activate the active ingredients of the irrigation agent to make it work (Betancourt et al., 2020). Kinetic energy flushing makes up for the shortcomings of traditional flushing devices and plays a role in both chemical and mechanical aspects. The chemical effect of root canal irrigation is mainly achieved by sodium hypochlorite, while the mechanical effect is mainly achieved by the shear stress exerted by the flowing irrigation agent on the biofilm and residual tissue debris (Boutsioukis et al., 2022). Sonic and ultrasonic kinetic energy flushing devices work through acoustic flow effects, cavitation effects, and thermal effects, and their flushing effects have been demonstrated in several studies (Dashtimoghadam et al., 2020; Klyn et al., 2010). The intensity of the sound flow depends mainly on the speed of the sound flow, which is closely related to the frequency and amplitude of the working tip (Ahmad et al., 1988). The ultrasound working tip typically operates at a frequency of 30 kHz and an amplitude of 75 μm (Boutsioukis and Arias, 2022), while the EDDY operating tip operates at a frequency of 6 kHz and an amplitude of 346 μm. The motion of the ultrasonic working tip is a plane, and the motion of the EDDY rotates around its axis in a three-dimensional space (Tomson and Simon, 2016). In my experiment, there was no significant difference in the score of the smear layer between the four groups in the coronal thirds, which proved that the four groups of auxiliary irrigation technology could achieve good cleaning effect in the thick region. In the middle thirds and the apical thirds, the cleaning effect of the passive ultrasonic group, the EDDY group, and the YSGG group were better than that of the syringe irrigation group, because of their agitation activates the system to accelerate the flow of fluid in the root canal, which can effectively break through the area of "airlock effect", and the resulting temperature rise can activate the activity of sodium hypochlorite, which is consistent with the results of other studies (Wimonchit et al., 2002). Therefore, kinetic energy flushing equipment is more effective than traditional irrigators when cleaning irregular, deep areas. The results of a meta-analysis study (Virdee et al., 2018) also support the idea that kinetic irrigation can create cleaner root canals compared to traditional irrigation. There was no significant difference in the cleaning effect of the smear layer in the comparison between passive ultrasonic group and EDDY group, which may be due to the large amplitude of EDDY washing, which exceeded the diameter of the root canal, and frequent tube wall contact would reduce its efficiency (Urban et al., 2017).

Lasers are characterized by low pain, minimally invasiveness, and less bleeding, and have become an important treatment tool in clinical practice in recent years. The wavelength of the Er,Cr,YSGG laser is 2.78 μm, which is close to the absorption peak of water (3 μm) (Kirmali et al., 2015). It can be found from the results of this experiment that Er,Cr,YSGG laser showed the best cleaning effect of the smear layer in the whole section of the root canal. Because when the laser energy is transferred to the coaxial air-water mixture, water mist particles can be generated in the atomization area at the front of the treatment handle, because these water mist particles carry the energy imparted by the laser, and can release energy from the reaction zone 1–2 mm away from the tip of the laser to make them have high-speed kinetic energy and rapidly expand in volume, the high-energy water molecules destroy the target cells and break through the "airlock effect" area of the root apical segment, so that the irrigation solution can fully flow in the root canal system to achieve the effect of disinfection and removal of the smear layer

(Blanken et al., 2009). It has been reported (Dentistry, 2019; Betancourt et al., 2019) that the application of Er,Cr,YSGG laser in the root canal can melt the inorganic components in the dentin, which can effectively remove debris and dirt from the root canal wall. Rosalin and Yosvimol Kuphasuk (2017) took transparent isolated teeth as the research object, and used Er,Cr,YSGG laser (1.5 W, 20 HZ, 30% water, 50% air) to wash the root canal and then perform root canal filling to fill more lateral root canals and root canal isthmus, indicating that the Er,Cr,YSGG laser can effectively remove the smear layer and open the lateral branch root canal. In addition, studies have shown that the Er,Cr,YSGG laser treatment system has less smear layer and no charring phenomenon after irradiation of the tooth surface, and has a low chance of thermal damage to periodontal tissues (Asnaashari et al., 2022). Although the laser has obvious advantages, there are also some shortcomings that need our attention. Widbiller M et al. found that the surface disintegration of root canal dentine was observed with the additional activation of EDTA and particularly after laser-based techniques (Widbiller M et al., 2023). Even though it was not observed in our study, it cannot be excluded that thermal effects may still occur locally, which should be considered as a drawback for this method of activation.

This experiment is based on several commonly used methods for removing the smear layer after root canal preparation in clinical practice. The aim is to preliminarily evaluate the advantages and disadvantages of different treatment techniques, provide initial guidance for future clinical work, and offer directions for further research in the future. Currently, various methods for studying the smear layer and observing dentine tubules are emerging, such as SEM, AFM, and COSM (De-Deus et al., 2011). These methods excel in certain aspects (e.g., imaging speed, quantitative analysis, data statistics, longitudinal comparison), each with its own advantages and disadvantages. However, there is still no ideal experimental model. Although SEM has certain limitations, such as qualitative comparison, slow imaging speed, operator bias, and field of view restrictions, it remains the most commonly used method for obtaining information on the surface of dentin at this stage, as evidenced by multiple relevant literature reviews. Considering the experimental objectives and methods of this study, quantitative analysis was not involved. Instead, the focus was on comparing the effectiveness of different techniques in removing the smear layer. To minimize errors, multiple sites were evaluated using a double-blind method with two trained evaluators. Some studies have shown that SEM is difficult to distinguish between the smear layer and sclerotic dentin, which is a physiological change that occurs with age (Dewi et al., 2020; Sudhakar et al., 2023). Therefore, young teeth extracted for orthodontic purposes were selected in this study to reduce the interference of sclerotic dentin.

5 Conclusion

In summary, when facing the complex area of the root canal, it is necessary not only to have an effective irrigation solution but also to combine kinetic irrigation to achieve a more ideal irrigation effect. The root canal system is complex and changeable, so kinetic irrigation is indispensable for root canal treatment.In clinical application, the appropriate kinetic energy irrigation method should be selected according to the actual situation of the affected tooth, root canal infection, root canal curvature, and patient's opening degree, so as to provide guarantee for the efficacy of root canal treatment.

Data availability statement

The raw data supporting the conclusions of this article will be made available by the authors, without undue reservation.

Ethics statement

The studies involving humans were approved by The ethical committee of Qingdao Stomatological Hospital affiliated to Qingdao University. The studies were conducted in accordance with the local legislation and institutional requirements. Written informed consent for participation in this study was provided by the participants' legal guardians/next of kin.

Author contributions

LW: Methodology, Writing–original draft. BF: Data curation, Investigation, Writing–original draft. SS: Methodology, Visualization, Writing–original draft. DS: Data curation, Writing–original draft. DW: Resources, Supervision, Writing–review and editing.

Funding

The author(s) declare that financial support was received for the research, authorship, and/or publication of this article. This work was supported by Qingdao Key Health Discipline Development Fund (2022-2024), Qingdao Clinical Research Center for Oral Diseases (22-3-7-lczx-7-nsh) and Shandong Provincial Key Medical and Health Discipline of Oral Medicine (Qingdao University Affiliated Qingdao Stomatological Hospital) (2024-2026).

Acknowledgments

This study was approved by the ethical committee of Qingdao Stomatological Hospital affiliated to Qingdao University (NO.2023KQYX037).

Conflict of interest

The authors declare that the research was conducted in the absence of any commercial or financial relationships that could be construed as a potential conflict of interest.

Generative AI statement

The authors declare that no Generative AI was used in the creation of this manuscript.

Publisher's note

References

Ahmad, M., Ford, T. R. P., Crum, L. A., and Walton, A. J. (1988). Ultrasonic debridement of root canals: acoustic cavitation and its relevance. *J. Endod.* 14, 486–493. doi:10.1016/s0099-2399(88)80105-5

Asnaashari, M., Sadeghian, A., and Hazrati, P. (2022). The effect of high-power lasers on root canal disinfection: a systematic review. *J. Lasers Med. Sci.* 13, 66. doi:10.34172/jlms.2022.66

Betancourt, P., Merlos, A., Sierra, J. M., Arnabat-Dominguez, J., and Viñas, M. (2020). Er,Cr:YSGG laser-activated irrigation and passive ultrasonic irrigation: comparison of two strategies for root canal disinfection. *Laser Surg.* 38, 91–97. doi:10.1089/photob.2019.4645

Betancourt, P., Merlos, A., Sierra, J. M., Camps-Font, O., Arnabat-Dominguez, J., and Viñas, M. (2019). Effectiveness of low concentration of sodium hypochlorite activated by Er,Cr:YSGG laser against *Enterococcus faecalis* biofilm. *Med. Sci.* 34, 247–254. doi:10.1007/s10103-018-2578-6

Blanken, J., De Moor, R. J. G., Meire, M., and Verdaasdonk, R. (2009). Laser induced explosive vapor and cavitation resulting in effective irrigation of the root canal. Part 1: a visualization study. *Lasers Surg. Med.* 41, 514–519. doi:10.1002/lsm.20798

Boutsioukis, C., and Arias-, M. T. (2022). Present status and future directions–irrigants and irrigation. *Int. Endod. J.* 55, 588–612. doi:10.1111/iej.13739

Boutsioukis, C., Arias-Moliz, M. T., and Chávez de Paz, L. E. (2022). A critical analysis of research methods and experimental models to study irrigants and irrigation systems. *Int. Endod. J.* 55, 295–329. doi:10.1111/iej.13710

Chavate, P. R., Ponnappa, K. C., and Nanjappa, A. S. (2024). Comparative evaluation of the effect of ultrasonic and rotary agitation of herbal irrigating solutions on smear layer: a SEM study. *J. Conserv. Dent. Endod.* 27, 164–169. doi:10.4103/jcde.jcde_277_23

Dashtimoghadam, E., Johnson, A., Fahimipour, F., Malakoutian, M., Vargas, J., Gonzalez, J., et al. (2020). Vibrational and sonochemical characterization of ultrasonic endodontic activating devices for translation to clinical efficacy. *Mater. Sci. Eng. C* 109, 110646. doi:10.1016/j.msec.2020.110646

De-Deus, G., Reis, C., and Paciornik, S. (2011). Critical appraisal of published smear layer-removal studies: methodological issues. *Oral Med. Oral Pathol. Oral Radiol. Endodontology* 112, 531–543. doi:10.1016/j.tripleo.2011.01.046

Dentistry, P. (2019). Pedodontics and preventive Dentistry, 37, 1–6.

Dewi, A., Upara, C., Chaiariyakul, D., and Louwakul, P. (2020). Smear layer removal from root canal dentin and antimicrobial effect of citric acid-modified chlorhexidine. *Eur. Endod. J.* 5, 257–263. doi:10.14744/eej.2020.38258

Do, Q. L., and Gaudin, A. (2020). The efficiency of the ER: YAG laser and photon-induced photoacoustic streaming (PIPS) as an activation method in endodontic irrigation: a literature review. *J. Lasers Med. Sci.* 11, 316–334. doi:10.34172/jlms.2020.53

Drukteinis, S., Rajasekharan, S., and Widbiller, M. (2024). Advanced materials for clinical endodontic applications: current status and future directions. *J. Funct. Biomater.* 15, 31. doi:10.3390/jfb15020031

Faras, F., Abo-Alhassan, F., Sadeq, A., and Burezq, H. (2016). Complication of improper management of sodium hypochlorite accident during root canal treatment. *J. Int. Soc. Prev. Community Dent.* 6, 493–496. doi:10.4103/2231-0762.192939

Grischke, J., Müller-Heine, A., and Hülsmann, M. (2014). The effect of four different irrigation systems in the removal of a root canal sealer. *Clin. Oral Investig.* 18, 1845–1851. doi:10.1007/s00784-013-1161-6

Haupt, F., Meinel, M., Gunawardana, A., and Hülsmann, M. (2020). Effectiveness of different activated irrigation techniques on debris and smear layer removal from curved root canals: a SEM evaluation. *Aust. Endod. J.* 46, 40–46. doi:10.1111/aej.12342

Iandolo, A., Abdellatif, D., Amato, M., Pantaleo, G., Blasi, A., Franco, V., et al. (2020). Dentinal tubule penetration and root canal cleanliness following ultrasonic activation of intracanal-heated sodium hypochlorite. *Aust. Endod. J.* 46, 204–209. doi:10.1111/aej.12393

Kaur, M., Singla, M., Kaur, H., Mittal, L., Gupta, S., and Joseph, M. M. (2024). Comparative evaluation of smear layer removal by using different irrigant activation techniques: an *in vitro* scanning electron microscopic study. *J. Conserv. Dent. Endod.* 27, 257–261. doi:10.4103/jcde.jcde_254_23

Kirmali, O., Kustarci, A., Kapdan, A., and Er, K. (2015). Effects of dentin surface treatments including Er,Cr:YSGG laser irradiation with different intensities on the push-out bond strength of the glass fiber posts to root dentin. *Acta Odontol. Scand.* 73, 380–386. doi:10.3109/00016357.2014.968872

Klyn, S. L., Kirkpatrick, T. C., and Rutledge, R. E. (2010). *In vitro* comparisons of debris removal of the EndoActivator TM system, the F file TM, ultrasonic irrigation, and NaOCl irrigation alone after hand-rotary instrumentation in human mandibular molars. *J. Endod.* 36, 1367–1371. doi:10.1016/j.joen.2010.03.022

Li, Q., Zhang, Q., Zou, X., and Yue, L. (2020). Evaluation of four final irrigation protocols for cleaning root canal walls. *Int. J. Oral Sci.* 12, 29. doi:10.1038/s41368-020-00091-4

Meire, M., and De Moor, R. J. G. (2024). Principle and antimicrobial efficacy of laser-activated irrigation: a narrative review. *Int. Endod. J.* 57, 841–860. doi:10.1111/iej.14042

Rodrigues, C. T., EzEldeen, M., Jacobs, R., Lambrechts, P., Alcalde, M. P., and Hungaro Duarte, M. A. (2021). Cleaning efficacy and uncontrolled removal of dentin of two methods of irrigant activation in curved canals connected by an isthmus. *Aust. Endod. J.* 47, 631–638. doi:10.1111/aej.12534

Rosalin, H., and Yosvimol Kuphasuk, K. R. (2017). Effectiveness of platelet-rich fibrin in the management of pain and delayed wound healing. *Eur. J. Dent.* 11, 192–195. doi:10.4103/ejd.ejd

Sudhakar, S., Gupta, N., Ghambir, N., Singh, R., and Singh, D. (2023). Comparative evaluation of intracanal smear layer removal by different root canal irrigants: a scanning electron microscope study. *Int. J. Clin. Pediatr. Dent.* 16, 633–638. doi:10.5005/jp-journals-10005-2648

Tomson, P. L., and Simon, S. R. (2016). Contemporary cleaning and shaping of the root canal system. *Prim. Dent. J.* 5, 46–53. doi:10.1308/205016816819304196

Urban, K., Donnermeyer, D., Schäfer, E., and Bürklein, S. (2017). Canal cleanliness using different irrigation activation systems: a SEM evaluation. *Clin. Oral Investig.* 21, 2681–2687. doi:10.1007/s00784-017-2070-x

Virdee, S. S., Seymour, D. W., Farnell, D., Bhamra, G., and Bhakta, S. (2018). Efficacy of irrigant activation techniques in removing intracanal smear layer and debris from mature permanent teeth: a systematic review and meta-analysis. *Int. Endod. J.* 51, 605–621. doi:10.1111/iej.12877

Widbiller, M., Keim, L., Schlichting, R., Striegl, B., Hiller, K. A., Jungbauer, R., et al. (2021). Debris removal by activation of endodontic irrigants in complex root canal systems: a standardized in-vitro-study. *Appl. Sci.* 11, 7331. doi:10.3390/app11167331

Widbiller, M., Rosendahl, A., Schlichting, R., Schuller, C., Lingl, B., Hiller, K. A., et al. (2023). Impact of endodontic irrigant activation on smear layer removal and surface disintegration of root canal dentine *in vitro*. *Healthc* 11, 376. doi:10.3390/healthcare11030376

Wimonchit, S., Timpawat, S., and Vongsavan, N. (2002). *Scientific articles A comparison of techniques for assessment of*, 1–4.

Xinyu, C., and Xue, M. (2022). Evaluation of root-canal isthmus debridement efficacy of 3 kinds of activated irrigation technique. *Hua Xi Kou Qiang Yi Xue Za Zhi* 40, 554–559. doi:10.7518/hxkq.2022.05.008

frontiers | Frontiers in Bioengineering and Biotechnology

TYPE Original Research
PUBLISHED 11 December 2024
DOI 10.3389/fbioe.2024.1485437

OPEN ACCESS

EDITED BY
Bolei Cai,
The Fourth Military Medical University, China

REVIEWED BY
Kaili Lin,
Shanghai Jiao Tong University, China
Dan Lin,
Shanghai University of Medicine and Health Sciences, China

*CORRESPONDENCE
Jianping Ruan,
ruanjp@xjtu.edu.cn

RECEIVED 23 August 2024
ACCEPTED 25 November 2024
PUBLISHED 11 December 2024

CITATION
Li J, Fan Z, Guan Z and Ruan J (2024) Injectable MXene/Ag-HA composite hydrogel for enhanced alveolar bone healing and mechanistic study.
Front. Bioeng. Biotechnol. 12:1485437.
doi: 10.3389/fbioe.2024.1485437

Injectable MXene/Ag-HA composite hydrogel for enhanced alveolar bone healing and mechanistic study

Jialing Li[1,2], Zilu Fan[3], Zhenju Guan[2] and Jianping Ruan[1,4]*

[1]Key Laboratory of Shaanxi Province for Craniofacial Precision Medicine Research, College of Stomatology, Xi'an Jiaotong University, Xi'an, Shaanxi, China, [2]Nanchong Central Hospital (Nanchong Hospital of Beijing Anzhen Hospital,Capital Medical University), the Second Clinical College of North Sichuan Medical College, Nanchong, Sichuan, China, [3]Nanchong Mental Health Center Of Sichuan Province, Nanchong Second People's Hospital, Nanchong Senior Hospital, Nanchong, Sichuan, China, [4]Center of Oral Public Health, College of Stomatology, Xi'an Jiaotong University, Xi'an, Shaanxi, China

Introduction: Alveolar bone defects pose significant challenges in dentistry. Due to the complexity of alveolar bone anatomy and insufficient repair mechanisms, large bone defects are difficult for the body to heal naturally. Clinical treatment typically involves the use of bone substitute materials. However, current substitutes often suffer from limitations such as insufficient osteoinductivity, rapid degradation, inflammatory responses, and poor mechanical properties. Additionally, the irregular morphology of alveolar bone defects complicates the application of solid bone substitutes, potentially leading to secondary damage at the repair site.

Methods: To address these challenges, this study introduces an innovative approach by integrating MXene nanomaterials into Ag-HA/GelMA hydrogels to create an injectable MXene/Ag-HA composite hydrogel. MXene nanomaterials are renowned for their excellent biocompatibility, antibacterial properties, and mechanical strength.

Results: The results indicate that the MXene/Ag-HA composite hydrogel exhibits satisfactory mechanical and biological properties. Specifically, it demonstrates excellent antibacterial, antioxidant, and osteogenic activities. Gene expression analysis further reveals that the MXene composite hydrogel promotes osteogenesis by regulating the expression of Dmp1 and Dusp1.

Discussion: The findings of this study suggest that the MXene/Ag-HA composite hydrogel is a promising candidate for alveolar bone repair and regeneration. The integration of MXene nanomaterials into the hydrogel enhances its mechanical and biological properties, making it well-suited for the treatment of irregular alveolar bone defects. Furthermore, the study underscores the vast potential of MXene nanomaterials in the biomedical field, hinting at potential applications beyond alveolar bone repair.

KEYWORDS

alveolar bone defect, osteoinductivity, MXene, hydrogel, osteogenesis

1 Introduction

Alveolar bone defects refer to the loss or destruction of alveolar bone tissue, most commonly caused by chronic alveolar bone resorption due to periodontitis (Li et al., 2023). Due to the complex anatomy of the alveolar bone and insufficient repair mechanisms, when bone defects exceed a certain size, the body struggles to self-repair (Ramezanzade et al., 2023; Wang et al., 2022), thus clinical intervention is necessitated.

At present, the application of artificial bone replacement in treating alveolar bone defects is becoming increasingly widespread. Ideal artificial bone substitute materials must possess various properties such as favorable biodegradability as well as biocompatibility, concordant mechanical strength to bone tissue, and a porous network construction conducive for the cell growth (Iocca et al., 2017; Faour et al., 2011; Toosi et al., 2024). Hydroxyapatite (HA), a primary component of natural bone, can increase local Ca^{2+} concentration, thereby activating osteoblast proliferation and promoting the discrepancy and growth of mesenchymal stem cells (MSCs) (Zhao et al., 2017; Ren et al., 2023). Due to its non-immunogenicity, acceptable osteoconductivity, and bioactivity, HA has been frequently applied in bone repair (Yu et al., 2022; Shi et al., 2021). Interestingly, the crystal structure of HA facilitates various ion substitutions. This ion exchange affects the concentration, size, and interaction type of the HA lattice, improving its physicochemical properties by altering its electron density and surface conditions, thereby optimizing its performance (Daniel Arcos and Vallet-Regí, 2020). Within a low silver loading range of 0.5%–2% (wt), Ag-HA exhibits excellent antibacterial activity along with outstanding biocompatibility and bone-binding capacity (Mirzaee et al., 2016).

Gelatin methacryloyl (GelMA) is a typical synthetic hydrogel formulation widely employed in biomedical fields (Kurian et al., 2022) with low antigenicity, significant biocompatibility, and cellular response properties. It can be crosslinked and solidified into a gel in the presence of a photoinitiator due to the double-bond modified gelatin feature under UV or visible light illumination. While introduced as a scaffold in bone repair systems, GelMA owns synthetic and natural characteristics of biomaterials (Yue et al., 2015; Zhang et al., 2020), its three-dimensional structure also benefits for the cell growth and differentiation.

MXene, a two-dimensional transition metal carbide nitride discovered and synthesized in 2011, exhibits excellent photothermal effects, bioimaging capabilities, conductivity, biocompatibility, and antibacterial properties, making it widely popular in the design of biomaterials and extensively applied in photodynamic therapy, biosensors, and drug delivery systems (Gazzi et al., 2019; Sinha et al., 2018; Ye et al., 2024). It also demonstrates a wide range of applications in the field of osteogenesis; its excellent antibacterial performance and ability to promote bone regeneration and angiogenesis have been verified. Furthermore, due to its efficient photothermal conversion and stimulation of bone regeneration, it has also been explored for applications in osteosarcoma (Yin et al., 2021; Wang et al., 2023).

This study was dedicated to developing an innovative injectable hydrogel for alveolar bone regeneration. In constructing the composite hydrogel, we chose GelMA as the three-dimensional scaffold material, which provided a suitable porous structure that promoted cell proliferation and differentiation. We incorporated a low concentration of Ag-HA into GelMA and innovatively introduced MXene materials. These additions not only overcame the high brittleness of Ag-HA but also significantly enhanced the hydrogel's antibacterial, mechanical, and osteogenic properties. Through comprehensive physical characterization and *in vitro* and *in vivo* anti-inflammatory osteogenesis experiments, the results demonstrated that the 0.3% MXene/Ag-HA composite hydrogel exhibited excellent mechanical properties, biodegradability, biocompatibility, anti-inflammatory, antioxidant, and osteogenic properties. Therefore, this composite hydrogel was expected to become an ideal material in the next-generation of bone repair and regeneration, offering a new solution for treating bone diseases such as alveolar bone defects.

2 Materials and methods

2.1 Cells and materials

For the Cell culture, MC3T3-E1 and RAW 264.7 cells (acquired from the Kunming Cell Bank, Chinese Academy of Sciences) were cultured in a 5% CO_2 humidified incubator under 37°C. For the materials, the following reagents were purchased from Sigma-Aldrich: $(NH_4)\ H_2PO_4$, $Ca(NO_3)_2$, HCl, $AgNO_3$, NH_4OH, gelatin, methacrylic anhydride, LAP, and Ti_3AlC_2. The CCK-8 kit and qPCR kit were obtained from Vazyme Biotech. The live/dead cell staining kit and ROS detection kit were purchased from Beyotime Biotechnology. Antibodies for CD206, iNOS, OPN, OCN, and VEGF were acquired from Abcam. The ALP staining kit and ARS staining kit were also obtained from Sigma-Aldrich.

2.2 Preparation of MXene/Ag-HA composite hydrogel

10 g of gelatin were weighed and placed into a round-bottom flask, followed by the addition of 100 mL PBS solution. The mixture was stirred at 45°C in a water bath for 12 h. Then, 6 g of methacrylic anhydride were added dropwise, and the reaction continued for 2 h. Then, the supernatant was collected for dialysis after the centrifuging the mixture. Upon completion of dialysis, the material was freeze-dried to obtain a 10% concentration of GelMA hydrogel, which was stored at 4°C in the dark.

To prepare Ag-HA, using the chemical formula $Ag_xCa_{10-x}(PO)_4(OH)_2$, a certain concentration of $(NH_4)H_2PO_4$ and $Ca(NO_3)_2$ solution was mixed. $AgNO_3$ was dissolved in the $Ca(NO_3)_2$ solution to achieve a 1% Ag content, where Ag^+ replaced Ca^{2+} in the reaction, preparing Ag-loaded HA. Subsequently, the prepared Ag-HA was added to the GelMA solution at 3 w/v% of concentration, along with 0.25 w/v% for LAP photoinitiator. The mixture was thoroughly stirred to ensure uniform dispersion, forming GelMA/HA composite hydrogel (Abbreviated as AG).

Next, TI_3AlC_2 was etched with HCl to synthesize the MXene required for the experiment. MXene was then mixed with AG hydrogel at different mass molar ratios, thoroughly stirred to achieve homogeneity, and resulted in MXene/Ag-HA/GelMA

composite hydrogels with MXene proportions of 0.1%, 0.3%, and 0.5% (Abbreviated as MAG).

2.3 Characterization analysis

The samples were divided into five groups: Control groups included GelMA group and AG group, target groups included 0.1%, 0.3%, and 0.5% of MAG. The hydrogel solutions were then injected into cylindrical molds with a height of 15 mm (n = 3 per group) and a diameter of 10 mm, respectively. The composite hydrogels were treated under 405 nm blue light illumination for 30 s to allow for setting. After curing, the samples were frozen in liquid nitrogen for 1 min and then freeze-dried for 48 h to prepare them for subsequent experiments. The morphology, elemental composition, mechanical properties, and conductivity of the hydrogels in each group were investigated and discussed. Results are presented as mean ± standard deviation. Quantitative data were analyzed using one-way ANOVA with GraphPad Prism 9.0, and a p-value of <0.05 was considered statistically significant.

2.4 Evaluation of the *in vitro* biological properties of hydrogels

2.4.1 Biocompatibility

The hydrogels seeded with MC3T3-E1 cells were kept in 24-well plates, and the culture medium was changed at an interval of 2 days. On the first, fourth, and seventh days, three samples from each group were taken, and 200 μL of culture medium containing 10% CCK-8 was introduced to each well. After incubating the samples for 2 h at 37°C, 100 μL of the corresponding incubation solution was then moved to a 96-well plate. Additionally, on the fourth day, live/dead cell staining was performed, and the samples were investigated under a fluorescence microscope. The optical density (OD) was measured at 450 nm.

2.4.2 Antibacterial properties

MXene can rapidly absorb light energy and convert it into heat (Parajuli et al., 2022), significantly increasing its surface temperature, which is beneficial for antibacterial activity. In this study, NIR illumination was applied for 4 min, and the temperature change of the hydrogel was recorded to explore the photothermal conversion potential of the composite hydrogel after the addition of MXene. Subsequently, the antibacterial performance of various hydrogel groups against *staphylococcus aureus* was evaluated using the plate-counting method. Selected samples were divided into two groups: one group received NIR illumination, while the other group was not proceeded. The samples were then co-cultured with bacterial suspension for 12 h and incubated for 48 h under 37°C. Bacterial colony growth can be observed after incubation, moreover, the antibacterial performance of each hydrogel group was compared.

2.4.3 Anti-inflammatory and antioxidant properties

The samples from each group were co-cultured with RAW 264.7 for 48 h, followed by fixation with 4% paraformaldehyde. After fixation, the cells were blocked and subjected to antibody staining, and the signals for CD206 and iNOS were detected using a fluorescence filter. Subsequently, the samples were co-cultured with MC3T3-E1 cells for 48 h to measure the ROS levels.

2.4.4 Osteogenic performance *in Vitro*

To observe the angiogenesis of MC3T3-E1 co-cultured with hydrogels lasting for 6 h, immunofluorescence detection of VEGF, OCN, and OPN was conducted at specific time points (2 or 4 days) to assess the expression of osteogenic proteins. Additionally, ALP as well as ARS staining were employed to detect osteogenic differentiation and calcium nodule deposition, while qPCR measured the expression of the osteogenic-corresponded genes OPN, OCN and ALP in MC3T3-E1 cells. These experiments comprehensively evaluated the osteogenic performance of the different hydrogel groups.

2.4.5 *In vivo* biological performance of hydrogels

A rat calvarial defect model with a diameter of about 5 mm on both sides of the skull was established to simulate a bone defect environment, into which hydrogels with different materials were implanted. At 4 and 8 weeks of post-surgery, the influence of these materials on bone regeneration as well as osseointegration were evaluated via Micro-CT scanning, immunohistochemical staining, and histological analysis.

2.4.6 Investigation of the molecular mechanisms and signaling pathways of osteogenesis regulated by MAG composite hydrogels

RNA-seq sequencing combined with bioinformatics analysis was used to screen for differentially expressed genes in rat MC3T3-E1 cells treated with MAG and AG hydrogels. The relevant osteogenic mechanisms were explored based on these findings.

3 Results and discussion

3.1 Synthesis of MXene

As depicted in Figure 1, SEM (Scanning electron microscope) image from Figure 1A and TEM (Transmission electron microscope) image from Figure 1B reveal a stacked flake-like structure forming the multilayered configuration. AFM image from Figure 1C observations of the synthesized MXene material's surface morphology also indicate that the successful preparation of multilayer MXene, with a sample thickness of approximately 15 nm.

3.2 Microstructure of hydrogels

The microstructure of hydrogels possesses a significant impact on their overall performance. The internal structure is obliged to not only provide stable support but also create an appropriate micro-environment for cell proliferation. In this experiment, SEM was employed to observe the surface morphology for the hydrogels in each group, as exhibited in Figure 1D. With the addition of Ag-HA and MXene, the pore structure of GelMA changed significantly, with thicker and rougher pore walls, which markedly improved the

10.3389/fbioe.2024.1485437

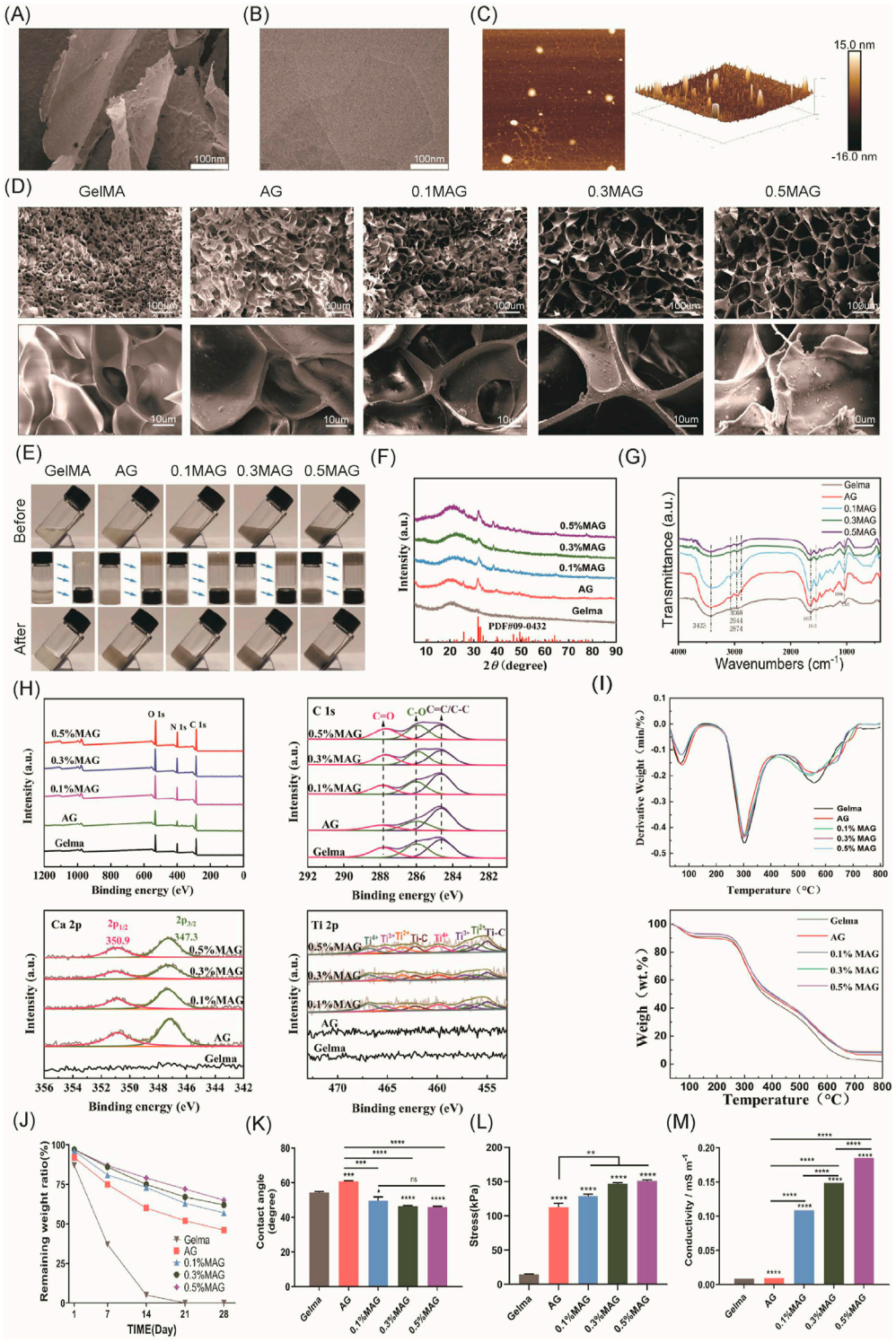

FIGURE 1
(A) SEM images, **(B)** TEM images, and **(C)** AFM images of MXene; **(D)** SEM images of each hydrogel group; **(E)** Macroscopic images of each hydrogel group before and after exposure to blue light; **(F)** XRD spectra of each hydrogel group; **(G)** FT-IR spectra of each hydrogel group; **(H)** XPS spectra and peak fitting of each hydrogel group; **(I)** TGA and DTG curves of each hydrogel group; **(J)** *In vitro* degradation curves of each hydrogel group; **(K)** Contact angle analysis of each hydrogel group; **(L)** Compressive strength results of each hydrogel group.; **(M)** Conductivity of each hydrogel group.

mechanical properties of the hydrogels. Furthermore, the widened pore size facilitated cell proliferation and material exchange, and the connectivity of the materials was also enhanced. Both of the 0.3% and 0.5% MAG groups demonstrated larger pore sizes; However, in the 0.5% group, the increased MXene content resulted in more graphene-like wrinkled layered structures on some pore walls,

blocking the pore entrances, which might adversely affect cell proliferation.

3.3 Macroscopic Appearance and injectability

As shown in Figure 1E, the GelMA group is visually observed as a colorless and transparent gel. With the addition of Ag-HA, the color changes to light gray, and upon further addition of MXene, the color deepens to dark gray. Injectable hydrogels, due to their tunable properties, have become one of the most attractive types of hydrogels (Lin et al., 2018; Li et al., 2021). To verify the injectability of the samples in this experiment, we recorded the state of the hydrogels before and after exposure to 405 nm blue light. Before illumination, the materials in the bottles were in a liquid state and could flow, with the liquid surface parallel to the ground when the bottle was tilted. After illumination, due to the crosslinking reaction, the materials in the bottles became solid; when the bottle was tilted or inverted, the shape of solid material was retained. This result indicated that the fluidity of the MAG hydrogel was crucial for filling complex alveolar bone defects.

3.4 Composition analysis of hydrogel

To investigate the chemical composition of various hydrogel groups, a series of tests including XRD (X-ray diffraction), FT-IR, XPS (X-ray photoelectron spectroscopy), and thermogravimetric analysis were conducted.As shown in Figure 1F . In the XRD measurement, GelMA combined with Ag-HA showed characteristic diffraction peaks of HA at 2θ = 31°–33°, indicating successful incorporation of HA. However, no distinct MXene peaks were observed in the MAG hydrogel group, likely due to the low concentration and good dispersion of MXene within the hydrogel.

As shown in Figure 1G, in the infrared spectra of the GelMA samples, a series of infrared vibration peaks were observed. The 3,423 cm^{-1} and 3,068 cm^{-1} peaks indicate the stretching vibrations of the N-H bonds in the amide A and B bands, while the 2,944 cm^{-1} and 2,874 cm^{-1} peak are attributed to C-H vibrations at different positions on the GelMA surface. The peak at 1,635 cm^{-1} mainly results from the C=O vibration within the conjugated amide groups, and the peak at 1,543 cm^{-1} corresponds to the coupled C-N stretching vibration as well as N-H bending vibration. These peaks confirm the presence of GelMA. After combining GelMA with Ag-HA, new peaks appeared at 1,035 cm^{-1}, 871 cm^{-1}, 603 cm^{-1}, and 564 cm^{-1}, corresponding to the characteristic absorption peaks of the PO_4^{3-} group, suggesting the presence of hydroxyapatite. Upon further combination with different concentrations of MXene, the characteristic peaks of GelMA and hydroxyapatite remained, while the peak intensity at 3,423 cm^{-1} gradually decreased, and the peak at 1,085 cm^{-1} disappeared, leaving the C-O-C stretching peak at 1,035 cm^{-1}. This demonstrates that GelMA is connected to the MXene surface's oxygen-containing functional groups via amide bonds. Furthermore, no other extraneous peaks were observed, indicating the successful combination of these materials while maintaining their original chemical structures.

As shown in Figure 1H, The XPS survey spectrum revealed characteristic peaks of C, N, and O elements. However, due to the low concentration and even dispersion of Ti in the hydrogel, its presence was not well reflected in the survey spectrum. We performed peak fitting for C, Ca, and Ti elements, as shown in the figures. With the increase for MXene concentration, the intensity of the C-O peak at 287.8 eV as well as the C=O peak at 286 eV was also improved, and these characteristic peaks shifted towards lower binding energies, specifically to 287.6 eV and 285.9 eV, which indicated that in the MAG hydrogel, the rich functional groups on the MXene surface chemically reacted and interacted with the carbon and hydroxyl groups in GelMA, forming enriched C-O and C=O bonds. When fitting the Ca peak, the MAG group showed specific peaks at 347.3 eV and 350.9 eV corresponding to Ca $2p_{3/2}$ and Ca $2p_{1/2}$, respectively, while this observation was not detected in the GelMA group, confirming the successful incorporation of hydroxyapatite into the composite hydrogel. In the Ti peak fitting, the MAG group exhibited Ti-C bonds, with increasing peak intensity correlating with the MXene concentration, demonstrating the presence of MXene in the MAG composite hydrogel and its effective bonding with the other components via Ti-C bonds.

As shown in Figure 1I, Thermogravimetric analysis is used to distinguish the organic and inorganic components of the samples. The experiments showed that the weight of the five hydrogel groups decreased with increasing temperature from room temperature to 800°C. Moreover, the organic components in the hydrogels rapidly decomposed at 300°C and they were completely decomposed by approximately 600°C. Ultimately, the MAG group retained the highest weight close to 10%, while the GelMA group retained less than 2%, illustrating the successful preparation of composite hydrogels with varying mass percentages of MXene.

3.5 Mechanical properties of hydrogel

Appropriate degradation of bone regeneration scaffolds was crucial for their temporary support function. Herein, we evaluated the *in vitro* degradation performance for each group of composite hydrogels via immersed in PBS solution, and the degradation curves were shown in Figure 1J. With the addition of low concentrations of HA and MXene, the hydrogels remained essentially intact in the early 1–2 weeks, providing sufficient mechanical support to stabilize the wound site and support cell adhesion and early tissue repair. By the 3rd to 4th week, MAG hydrogels gradually degraded, providing space for osteogenic cells and newly formed matrix. As exhibited in Figure 1K, for the hydrogels in 5 groups, the MAG group exhibited a lower water contact angle, indicating good wettability of the material with cells or organisms. This was beneficial for cell adhesion, growth, and tissue repair.

Compression tests were used to evaluate the compressive performance of hydrogels, aiming to understand their deformation characteristics and strength under pressure. As shown in Figure 1L, the maximum compressive stress reached 151.01 ± 1.52 kPa after the addition of HA and MXene, which was more than 10 times higher compared to the GelMA group, significantly enhancing the compressive strength of the composite

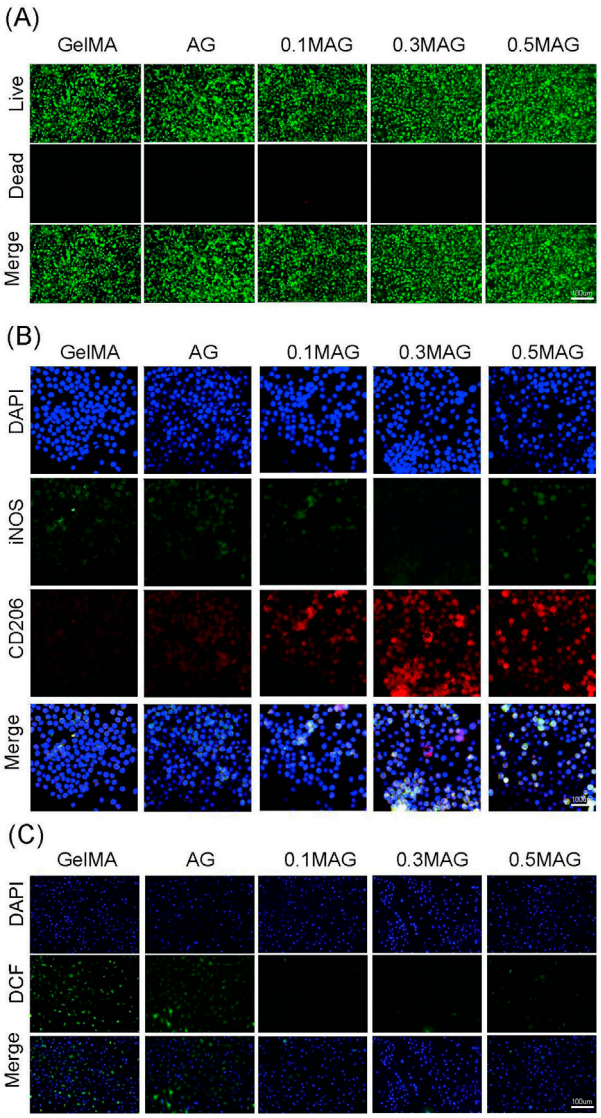

FIGURE 2
(A) Live (green)/dead (red) staining of MC3T3-E1 cells co-cultured with hydrogels for 4 days from each group; **(B)** Immunofluorescence staining of iNOS (green) and CD206 (red) in RAW264.7 cells co-cultured with hydrogels for 2 days from each group, the cell nuclei are labeled in blue; **(C)** ROS levels in MC3T3-E1 cells co-cultured with hydrogels for 2 days from each group, detected using the fluorescent probe DCFH-DA.

hydrogel. This enhancement can be attributed to the filling effect and physical crosslinking of HA and MXene, optimizing the microstructure of the hydrogel and forming a more ordered network, thus improving the material's mechanical strength and stability.

3.6 Electrical conductivity

Conductive materials have vast prospects in bone tissue engineering, as they can significantly promote bone regeneration by regulating cell proliferation, differentiation, and mineralization. However, hydrogels typically exhibit poor mechanical strength and limited electrical conductivity (Li et al., 2022). Recent studies have found that MXenes not only sense cellular electrophysiology but also significantly enhance the electrical conductivity of hydrogels (Wang et al., 2024; Jervis et al., 2021). Hu et al. prepared an electroactive hydrogel based on regenerated silk fibroin and MXene, and found that the material showed good biocompatibility *in vivo* and animal experiments under electrical stimulation, and significantly promoted bone regeneration, mineralization, and angiogenesis. Through RNA sequencing, studies have shown that electrical stimulation can upregulate genes related to biomineralization, tissue development, and calcium signaling pathways, especially the CALM gene (calmodulin gene). This indicates that the osteogenic effect induced by electrical stimulation is closely related to the activation of Ca^{2+}/CALM signaling in BMSCs (Hu et al., 2023). This study explored the effect of incorporating MXenes on the electrical conductivity of composite hydrogels. As shown in Figure 1M, the introduction of MXenes significantly modified the electrical conductivity of the hydrogels. Additionally, the conductivity increases further with higher concentrations of MXenes. The 0.5% MAG hydrogel group achieved a conductivity of 0.185 S/mm, categorizing it as a high-conductivity hydrogel. This enhanced conductivity is beneficial for promoting the proliferation and differentiation of osteoblasts, thereby facilitating bone regeneration.

3.7 *In vitro* cell biocompatibility studies

We further investigate the biocompatibility of each hydrogel group, as seen in Figure 2A, cells in all groups exhibited good growth, maintained high viability, and showed no significant cell death, indicating that all hydrogels had no obvious toxic effects.

To evaluate the anti-inflammatory properties, we performed fluorescence staining for iNOS and CD206 on the five sample groups. The results, shown in Figure 2B, indicated that the fluorescence intensity of iNOS in the 0.3% MAG group was remarkably lower, which suggested that an appropriate concentration of MXene helps to suppress the expression of the pro-inflammatory factor iNOS, thereby promoting tissue repair and regeneration. Furthermore, the fluorescence signal of CD206 in the 0.3% MAG group was observed to be significantly higher than in the other groups, implying the material facilitates the polarization of macrophages from the M1 to M2 type, which was beneficial for anti-inflammatory responses and indirect osteogenesis.

The antioxidant results, shown in Figure 2C, demonstrated that the ROS scavenging capacity of the MAG group was more preferable than that of the AG and GelMA group, while the 0.1% and 0.3% MAG groups displayed the best results. This indicated that the addition for low concentrations of MXene to the hydrogel aids in removing excess ROS, reducing oxidative stress, and maintaining extracellular matrix stability, thereby positively impacting the osteogenesis process.

The healing of extraction sockets involves inflammation, cell proliferation, and tissue reconstruction, making it crucial to evaluate the antibacterial properties of bone tissue engineering scaffolds. We co-cultured the hydrogels with MC3T3-E1 cells and performed an antibacterial assay against *Staphylococcus aureus* using the plate coating method combined with NIR photothermal experiments. The

10.3389/fbioe.2024.1485437

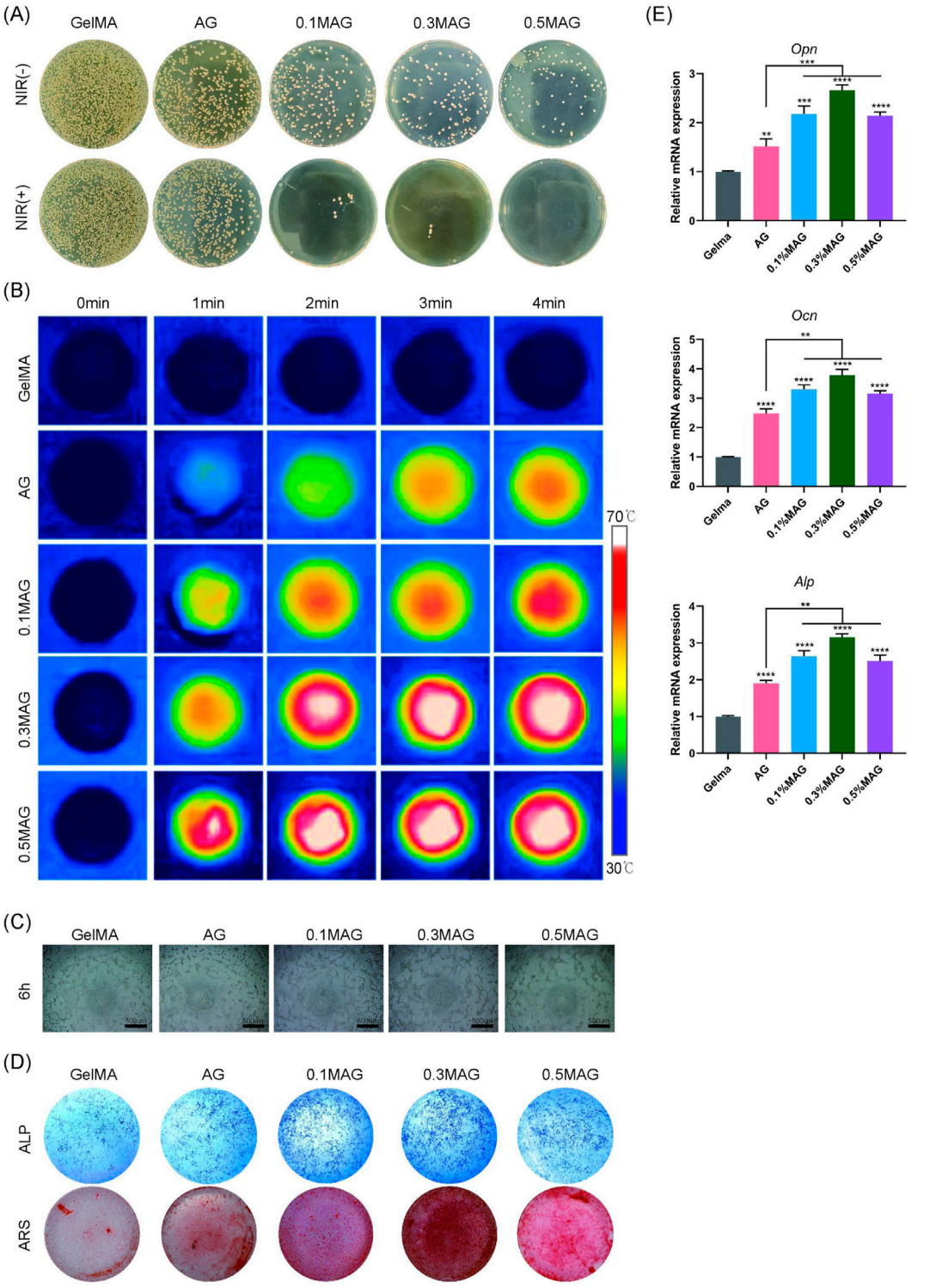

FIGURE 3
(A) Colony images showing the antibacterial effect of hydrogels from each group against *Staphylococcus aureus* without and with NIR illumination; **(B)** Infrared thermal images of hydrogels; **(C)** Angiogenesis of MC3T3-E1 cells co-cultured with hydrogels from each group at 6 h; **(D)** ALP staining at the seventh day and ARS staining at the 21st day of MC3T3-E1 cells co-cultured with hydrogels from each group; **(E)** PCR analysis of osteogenic-related genes OPN, OCN, and ALP expression in MC3T3-E1 cells co-cultured with hydrogels for 4 days from each group (****$p < 0.0001$; ***$p < 0.001$; **$p < 0.01$; *$p < 0.05$).

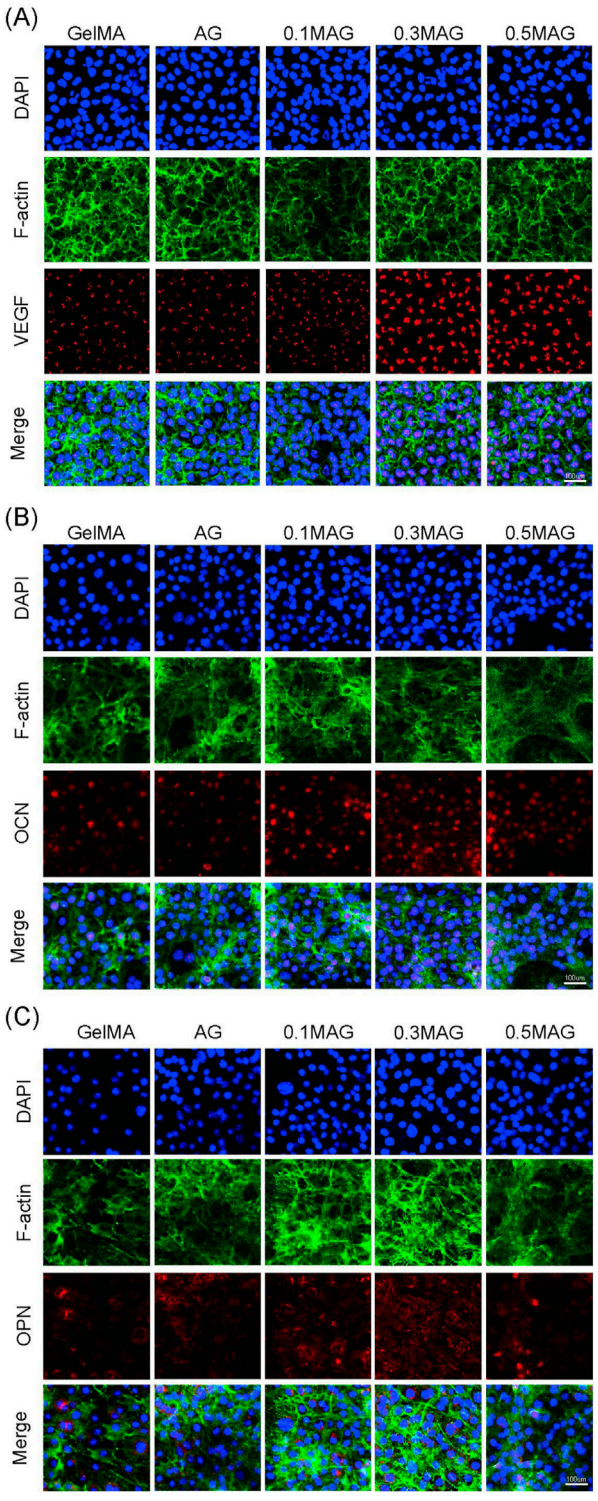

FIGURE 4
(A) Immunofluorescence staining of VEGF in MC3T3-E1 cells, **(B)** Immunofluorescence staining of OCN in MC3T3-E1 cells, and **(C)** Immunofluorescence staining of OPN in MC3T3-E1 cells co-cultured with hydrogels from each group at day 2, 4, and 4 respectively.

results, shown in Figure 3A, indicated that the MAG hydrogels exhibited excellent antibacterial properties, which were further enhanced after NIR illumination. This antibacterial effect resulted from several factors: the mechanical disruption of bacterial membranes by nano-MXene, and the ability of MXene materials to efficiently convert light energy into heat energy under near-infrared light illumination (Avinashi et al., 2024). Through localized heating, MXene can effectively kill pathogenic microorganisms, thereby reducing the use of antibiotics and lowering the emergence of resistant strains (Seidi et al., 2023). The incorporation of low concentrations of Ag (Rai et al., 2009) also contributed to the antibacterial activity.

Moreover, this photothermal conversion can also promote bone regeneration. Local thermal stimulation enhances cellular metabolic activity, promotes the generation and mineralization of the extracellular matrix, and further accelerates bone tissue repair (Abdulghafor et al., 2024). We further explored the photothermal conversion capabilities of the composite hydrogels. As shown in Figure 3B, the addition of MXene endows the hydrogels with excellent photothermal conversion capabilities, allowing them to rapidly reach temperatures of 50°C–55°C under NIR illumination, thereby promoting the process of osteogenesis.

Angiogenesis is critical for wound healing and new bone formation. This study used angiogenesis assays to investigate the effects of each hydrogel group on promoting angiogenesis. As shown in Figure 3C, the 0.3% MAG hydrogel group had the highest amount of new blood vessels Additionally, we assessed the ability of the hydrogels to induce osteogenic differentiation and calcium deposition through ALP and ARS staining. The results shown in Figure 3D, suggest that, in compared with the GelMA group, the rest of four groups exhibited deeper staining, with the 0.3% MAG group showing the best results. RT-PCR was employed to measure the expression levels of osteogenesis-related genes ALP, OPN, and OCN. As shown in Figure 3E, the 0.3% MAG hydrogel significantly promoted osteogenesis by upregulating the expression of the osteogenic genes ALP, OPN, and OCN, thereby enhancing the proliferation, differentiation, and calcium deposition of osteoblasts.

The results of immunofluorescence staining showed, as shown in Figure 4A, that the VEGF fluorescence signal was the strongest, indicating that an appropriate amount of MXene promotes the formation of new blood vessels and osteogenesis. The immunofluorescence staining for OPN and OCN further validated this result. As seen in Figures 4B, C, the 0.3% MAG group exhibited the strongest and most uniform fluorescence.

3.8 *In vivo* osteogenesis study

The overall design of the animal experiment is demonstrated in Figure 5A. Learning from the *in vitro* cell experiments, we selected the 0.3% MAG hydrogel group as the experimental group, with the AG group and GelMA hydrogel group as control groups for the animal experiments. At 4 and 8 weeks post-implantation into rat cranial bone defects, bone repair was observed via Micro-CT scanning. The results showed that the bone healing effects *in vivo* were highly consistent with the *in vitro* experiment results, with the MAG group demonstrating significant osteogenic advantages. This trend was also reflected in the trabecular number (Tb.N), bone

10.3389/fbioe.2024.1485437

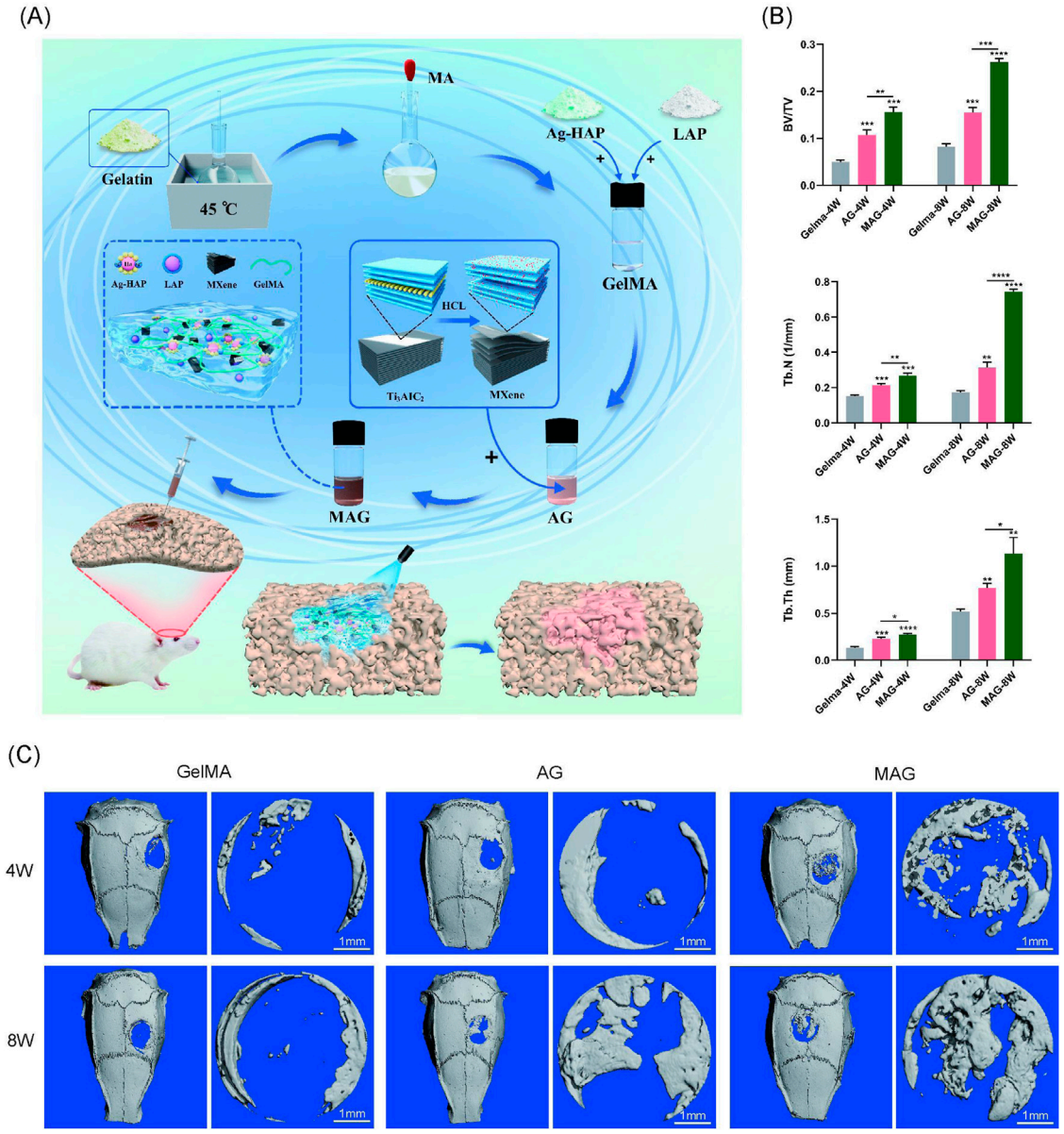

FIGURE 5
(A) Experimental design flowchart; **(B)** Quantitative analysis of bone volume fraction (BV/TV), trabecular number (Tb.N), and trabecular thickness (Tb.Th); **(C)** Micro-CT 3D reconstruction images of bone defect areas filled with hydrogels from each group at 4 and 8 weeks (****p < 0.0001; ***p < 0.001; **p < 0.01; *p < 0.05).

volume fraction (BV/TV), and trabecular thickness (Tb.Th),as shown in Figure 5B.

At 4 weeks, the pure GelMA group exhibited the poorest bone repair, with only a few new bones forming at the edges of circular bone defect. The MAG group showed the best osteogenic effect, with the CT images revealing substantial bone bridging, indicating that the incorporation of MXene into the hydrogel promotes early new bone formation, consistent with the previous *in vitro* cell experiment results. At 8 weeks, the micro-CT results showed a similar trend, with the MAG group continuing to achieve the best bone repair, forming extensive new bone regeneration in the center of the defect, as shown in Figure 5C.

H&E staining, Masson staining, and immunohistochemical staining further confirmed these findings, as shown in Figures 6A, B. The inclusion of MXene promoted high expression of ALP and OCN, and the composite hydrogel exhibited extensive new bone formation around its periphery and in its gaps. Mature bone tissue formation and high collagen content were observed, demonstrating excellent bone integration and osteogenic potential, providing strong support for its future clinical applications. Meanwhile, the H&E staining results for various organs indicate that the MAG composite hydrogel has good biocompatibility *in vivo*, providing evidence for its safety in future clinical applications (Figure 6C).

10.3389/fbioe.2024.1485437

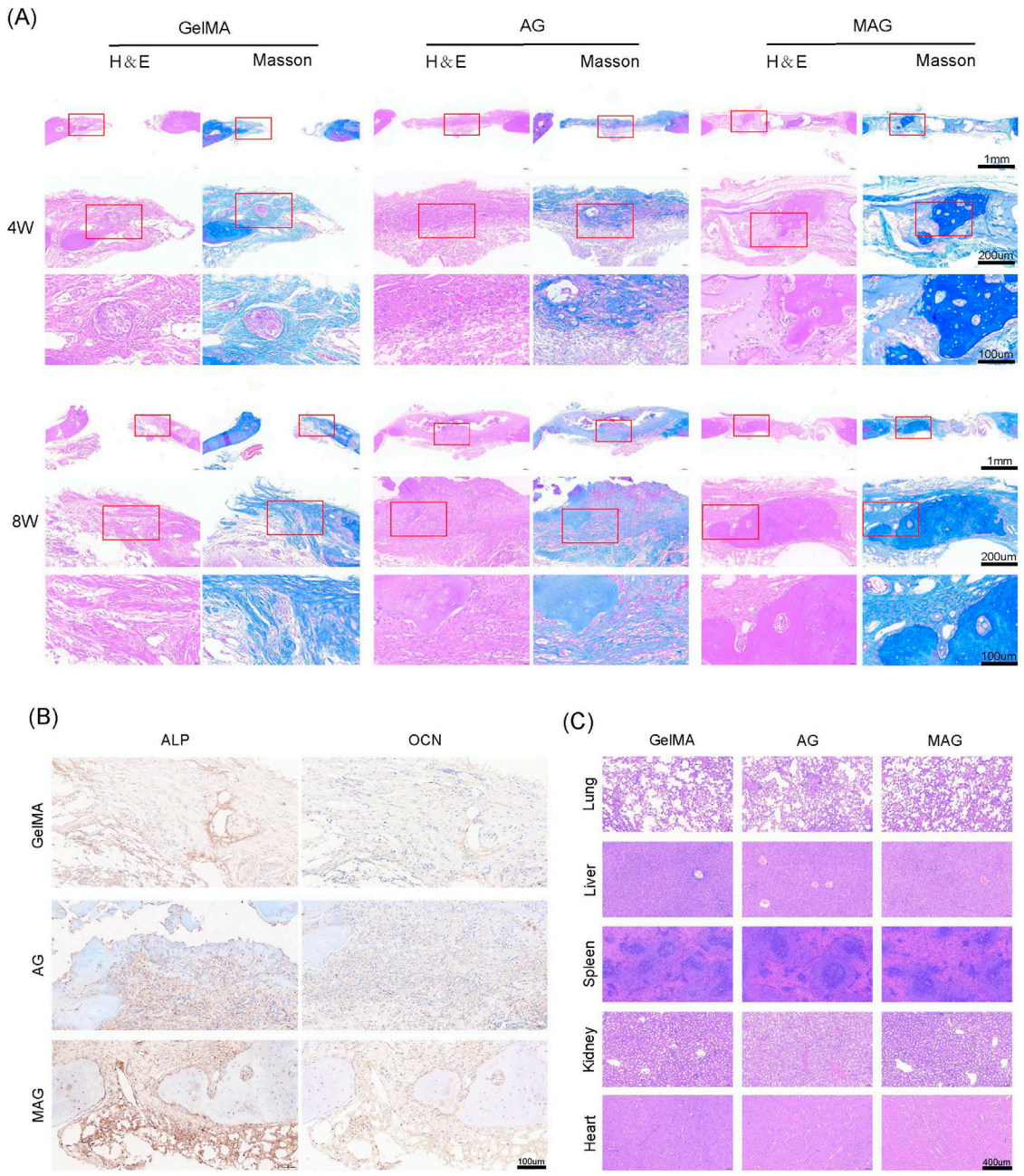

FIGURE 6
(A) HE and Masson staining of bone defect areas implanted with hydrogels from each group at 4 and 8 weeks; **(B)** ALP and OCN staining of bone defect areas implanted with hydrogels from each group at 8 weeks; **(C)** HE staining results of the heart, liver, spleen, lung, and kidney of rats after 8 weeks of hydrogel implantation in each group.

3.9 Osteogenic gene mechanism study

In both of *in vitro* and *in vivo* studies, we demonstrated that the incorporation of MXene into hydrogels exhibited remarkable osteoinductive effects, showing significant advantages in bone regeneration and integration. In this study, we selected the 0.3% MAG group hydrogel as the experimental group, with AG hydrogel as the control group, and systematically analyzed the expression differences between these two composite hydrogels at the cellular and molecular levels. We delved into the osteogenic mechanism and signaling pathways of the MAG group, revealing its potential mechanisms in promoting bone regeneration.

We set the significance level for differential gene selection at $q < 0.05$ and $|\log2(FC)| > 1$. As illustrated in Figure 7A, the expression levels of these differentially expressed genes were analyzed using hierarchical clustering heatmaps. Compared to the AG group, the MAG group showed upregulated expression of non-collagenous matrix protein Dmp1, the MMP inhibition gene Timp4, and the cytoskeletal component ACTBL2. Moreover, the MAG group

10.3389/fbioe.2024.1485437

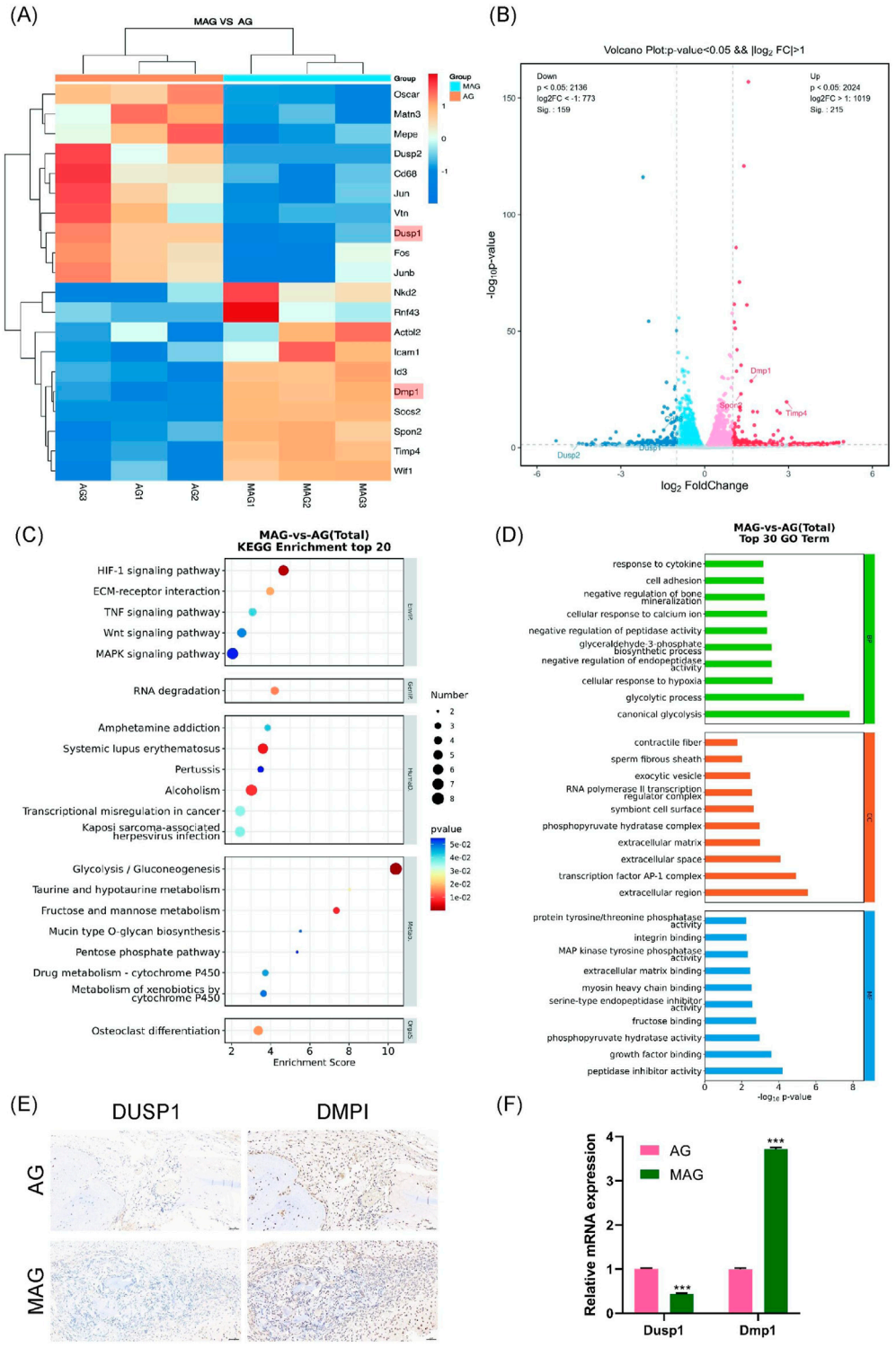

FIGURE 7
(A) Heatmap of differentially expressed gene expression levels; **(B)** Volcano plot of differentially expressed genes; **(C)** KEGG pathway enrichment analysis of differentially expressed genes; **(D)** GO enrichment analysis of differentially expressed genes between the groups; **(E)** DMP1 and DUSP1 staining of bone defect areas implanted with MAG and AG hydrogels at 8 weeks; **(F)** Verification of Dmp1 and Dusp1 Gene Expression Changes in MC3T3-E1 Cells Co-cultured with AG and MAG Hydrogels Using qPCR (*p < 0.001).

exhibited increased expression of genes related to cell movement (such as SPON2, Icam1, and Id3), which collectively enhanced osteogenesis.

Notably, the MAG group also significantly downregulated genes unfavorable to osteogenesis. For example, the expression of Dusp1, a negative regulator of the MAPK signaling pathway, was

downregulated, which may enhance MAPK pathway activity. These findings were visually represented using volcano plots, highlighting gene expression differences between the two hydrogel materials (Figure 7B).

In the KEGG pathway analysis (Figure 7C), osteogenesis-related differential pathways were identified, including the Wnt and MAPK signaling pathways. Similarly, GO enrichment analysis (Figure 7D) indicated that MAG hydrogel could promote cell adhesion and calcium ion binding, enhance glycolysis to supply energy and metabolic intermediates, and regulate osteoblast proliferation, differentiation, and bone mineralization, thereby supporting osteoblast growth and function.

We selected Dmp1 and Dusp1 for experimental validation based on KEGG pathway analysis, GO enrichment analysis, and hierarchical clustering heatmaps, as these genes exhibited significant expression changes in the MAG group and played crucial roles in osteogenesis. Dmp1 activates the Wnt/β-catenin signaling pathway, regulating osteogenic genes such as Runx2 and OPN. Additionally, Dmp1 promotes osteoblast differentiation, contributing to bone mineralization and improving bone mechanical strength and stability (Kongkiatkamon et al., 2021). In contrast, Dusp1, a phosphatase that dephosphorylates and inactivates key molecules in the MAPK signaling pathway (Peng et al., 2017), such as ERK, JNK, and p38, was downregulated in the MAG group. This downregulation increases the activity of MAPKs, enhancing the transmission of the MAPK signaling pathway, and ultimately promoting osteoblast proliferation and differentiation.

As shown in Figure 7E, immunohistochemical staining in animal models was used to validate gene expression. The results demonstrated that the MAG hydrogel significantly upregulated Dmp1 expression while downregulating Dusp1 expression, thus facilitating osteoblast proliferation, differentiation, and mineralization. This trend was further confirmed by qPCR results (Figure 7F).

4 Conclusion

This study successfully prepared injectable MXene/Ag-HA composite hydrogel scaffolds. Physical characterization revealed uniform distribution of MXene in the composite hydrogel, demonstrating excellent mechanical properties, conductivity, and appropriate biodegradability of the scaffold. Through a series of *in vitro* and *in vivo* experiments, it was verified that the 0.3% concentration of MXene/Ag-HA hydrogel exhibits outstanding antibacterial properties, clears excessive ROS, induces macrophage polarization, promotes vascularization, and demonstrates excellent osteogenic capabilities. Genomic analysis revealed that MXene/Ag-HA upregulates Dmp1 and downregulates Dusp1 expression, activating the Wnt/β-catenin and MAPK signaling pathways, respectively, thereby regulating osteogenesis. Therefore, the studied MXene/Ag-HA composite hydrogel represents a promising bone repair material for use in bone regeneration and repair.

Data availability statement

The original contributions presented in the study are included in the article/supplementary material, further inquiries can be directed to the corresponding author.

Author contributions

JL: Conceptualization, Formal Analysis, Investigation, Writing–original draft. ZF: Formal Analysis, Investigation, Writing–original draft. ZG: Data curation, Investigation, Writing–review and editing. JR: Conceptualization, Supervision, Writing–review and editing.

Funding

The author(s) declare that financial support was received for the research, authorship, and/or publication of this article. This work was supported by the Scientific Research Project of Sichuan Provincial Medical and Health Promotion Association of China (KY2023QN0239), and the City-School Cooperation Project of Nanchong Science and Technology Bureau of China (22SXQT0390).

Acknowledgments

We would like to express our sincere gratitude to all colleagues, institutions, and funding agencies that supported this research.

Conflict of interest

The authors declare that the research was conducted in the absence of any commercial or financial relationships that could be construed as a potential conflict of interest.

Publisher's note

References

Abdulghafor, M. A., Mahmood, M. K., Tassery, H., Tardivo, D., Falguiere, A., and Lan, R. (2024). Biomimetic coatings in implant dentistry: a quick update. *J. Funct. Biomater.* 15, 15. doi:10.3390/jfb15010015

Avinashi, S. K., Mishra, R. K., Singh, R., Fatima, Z., and Gautam, C. R. (2024). Fabrication methods, structural, surface morphology and biomedical applications of MXene: a review. *ACS Appl. Mater. Interface* 16, 47003–47049. doi:10.1021/acsami.4c07894

Daniel Arcos, D., and Vallet-Regí, M. (2020). Substituted hydroxyapatite coatings of bone implants. *J. Mater. Chem. B* 8, 1781–1800. doi:10.1039/C9TB02710F

Faour, O., Dimitriou, R., Cousins, C. A., and Giannoudis, P. V. (2011). The use of bone graft substitutes in large cancellous voids: any specific needs? *Injury* 42, 87–S90. doi:10.1016/j.injury.2011.06.020

Gazzi, A., Fusco, L., Khan, A., Bedognetti, D., Zavan, B., Vitale, F., et al. (2019). Photodynamic therapy based on graphene and MXene in cancer theranostics. *Front. Bioeng. Biotech.* 7, 295. doi:10.3389/fbioe.2019.00295

Hu, Z., Lu, J., Zhang, T., Liang, H., Yuan, H., Su, D., et al. (2023). Piezoresistive MXene/silk fibroin nanocomposite hydrogel for accelerating bone regeneration by Re-establishing electrical microenvironment. *Bioact. Mater.* 22, 1–17. doi:10.1016/j.bioactmat.2022.08.025

Iocca, O., Farcomeni, A., Lopez, S. P., and Talib, H. S. (2017). Alveolar Ridge preservation after tooth extraction: a bayesian network meta-analysis of grafting materials efficacy on prevention of bone height and width reduction. *J. Clin. Periodontol.* 44, 104–114. doi:10.1111/jcpe.12633

Jervis, P. J., Amorim, C., Pereira, T., Martins, J. A., and Ferreira, P. M. T. (2021). Dehydropeptide supramolecular hydrogels and nanostructures as potential peptidomimetic biomedical materials. *Int. J. Mol. Sci.* 22, 2528. doi:10.3390/ijms22052528

Kongkiatkamon, S., Ramachandran, A., Knoernschild, K. L., Campbell, S. D., Sukotjo, C., and George, A. (2021). Dentin matrix protein 1 on titanium surface facilitates osteogenic differentiation of stem cells. *Molecules* 26, 6756. doi:10.3390/molecules26226756

Kurian, A. G., Singh, R. K., Patel, K. D., Lee, J.-H., and Kim, H.-W. (2022). Multifunctional GelMA platforms with nanomaterials for advanced tissue therapeutics. *Bioact. Mater.* 8, 267–295. doi:10.1016/j.bioactmat.2021.06.027

Li, J., Gao, L., Xu, R., Ma, S., Ma, Z., Liu, Y., et al. (2022). Fibers reinforced composite hydrogels with improved lubrication and load-bearing capacity. *Friction* 10, 54–67. doi:10.1007/s40544-020-0389-9

Li, T., Zeng, X., Zou, S., Xu, Y., and Duan, P. (2023). Recent advances in horizontal alveolar bone regeneration. *Biomed. Mater.* 18, 052004. doi:10.1088/1748-605X/acd672

Li, Y., Yang, H., and Lee, D. (2021). Advances in biodegradable and injectable hydrogels for biomedical applications. *J. Control Release* 330, 151–160. doi:10.1016/j.jconrel.2020.12.008

Lin, H., Chen, Y., and Shi, J. (2018). Insights into 2D MXenes for versatile biomedical applications: current advances and challenges ahead. *Adv. Sci.* 5, 1800518. doi:10.1002/advs.201800518

Mirzaee, M., Vaezi, M., and Palizdar, Y. (2016). Synthesis and characterization of silver doped hydroxyapatite nanocomposite coatings and evaluation of their antibacterial and corrosion resistance properties in simulated body fluid. *Mater. Sci. Eng.* 69, 675–684. doi:10.1016/j.msec.2016.07.057

Parajuli, D., Murali, N., Kc, D., Karki, B., Samatha, K., Kim, A., et al. (2022). Advancements in MXene-polymer nanocomposites in energy storage and biomedical applications. *Polymers* 14, 3433. doi:10.3390/polym14163433

Peng, H., Yun, Z., Wang, W., and Ma, B. (2017). Dual specificity phosphatase 1 has a protective role in osteoarthritis fibroblast-like synoviocytes via inhibition of the MAPK signaling pathway. *Mol. Med. Rep.* 16, 8441–8447. doi:10.3892/mmr.2017.7617

Rai, M., Yadav, A., and Gade, A. J. Ba. (2009). Silver nanoparticles as a new generation of antimicrobials. *Biotechnol. Adv.* 27, 76–83. doi:10.1016/j.biotechadv.2008.09.002

Ramezanzade, S., Aeinehvand, M., Ziaei, H., Khurshid, Z., Keyhan, S. O., Fallahi, H. R., et al. (2023). Reconstruction of critical sized maxillofacial defects using composite allogeneic tissue engineering: systematic review of current literature. *Biomimetics* 8, 142. doi:10.3390/biomimetics8020142

Ren, S., Lin, Y., Liu, W., Yang, L., and Zhao, M. (2023). MSC-exos: important active factor of bone regeneration. *Front. Bioeng. Biotechnol.* 11, 1136453. doi:10.3389/fbioe.2023.1136453

Seidi, F., Shamsabadi, A. A., Firouzjaei, M. D., Elliott, M., Saeb, M. R., Huang, Y., et al. (2023). MXenes antibacterial properties and applications: a review and perspective. *Small* 19, 2206716. doi:10.1002/smll.202206716

Shi, H., Zhou, Z., Li, W., Fan, Y., Li, Z., and Wei, J. (2021). Hydroxyapatite based materials for bone tissue engineering: a brief and comprehensive introduction. *Crystals* 11, 149. doi:10.3390/cryst11020149

Sinha, A., Zhao, H., Huang, Y., Lu, X., Chen, J., and Jain, R. (2018). MXene: an emerging material for sensing and biosensing. *Trac-Trend Anal. Chem.* 105, 424. doi:10.1016/j.trac.2018.05.021

Toosi, S., Javid-Naderi, M. J., Tamayol, A., Ebrahimzadeh, M. H., Yaghoubian, S., and Mousavi Shaegh, S. A. (2024). Additively manufactured porous scaffolds by design for treatment of bone defects. *Front. Bioeng. Biotechnol.* 11, 1252636. doi:10.3389/fbioe.2023.1252636

Wang, B., Feng, C., Liu, Y., Mi, F., and Dong, J. (2022). Recent advances in biofunctional guided bone regeneration materials for repairing defective alveolar and maxillofacial bone: a review. *Jpn. Dent. Sci. Rev.* 58, 233–248. doi:10.1016/j.jdsr.2022.07.002

Wang, H., Hsu, Y.-C., Wang, C., Xiao, X., Yuan, Z., Zhu, Y., et al. (2024). Conductive and enhanced mechanical strength of $Mo_2Ti_2C_3$ MXene-based hydrogel promotes neurogenesis and bone regeneration in bone defect repair. *ACS Appl. Mater. Interfaces* 16, 17208–17218. doi:10.1021/acsami.3c19410

Wang, H., Mu, N., He, Y., Zhang, X., Lei, J., Yang, C., et al. (2023). Ultrasound-controlled MXene-based Schottky heterojunction improves anti-infection and osteogenesis properties. *Theranostics* 13, 1669–1683. doi:10.7150/thno.81511

Ye, S., Zhang, H., Lai, H., Xu, J., Yu, L., Ye, Z., et al. (2024). MXene: a wonderful nanomaterial in antibacterial. *Front. Bioeng. Biotechnol.* 12, 1338539. doi:10.3389/fbioe.2024.1338539

Yin, J., Pan, S., Guo, X., Gao, Y., Zhu, D., Yang, Q., et al. (2021). Nb_2C MXene-functionalized scaffolds enables osteosarcoma phototherapy and angiogenesis/osteogenesis of bone defects. *Nano-Micro Lett.* 13, 30. doi:10.1007/s40820-020-00547-6

Yu, F., Lian, R., Liu, L., Liu, T., Bi, C., Hong, K., et al. (2022). Biomimetic hydroxyapatite nanorods promote bone regeneration via accelerating osteogenesis of BMSCs through T cell-derived IL-22. *ACS Nano* 16, 755–770. doi:10.1021/acsnano.1c08281

Yue, K., Santiago, G. T., Alvarez, M. M., Tamayol, A., Annabi, N., and Khademhosseini, A. (2015). Synthesis, properties, and biomedical applications of gelatin methacryloyl (GelMA) hydrogels. *Biomater* 73, 254. doi:10.1016/j.biomaterials.2015.08.045

Zhang, Y., Wu, D., Zhao, X., Pakvasa, M., Tucker, A. B., Luo, H., et al. (2020). Stem cell-friendly scaffold biomaterials: applications for bone tissue engineering and regenerative medicine. *Front. Bioeng. Biotechnol.* 8, 598607. doi:10.3389/fbioe.2020.598607

Zhao, R., Xie, P., Zhang, K., Tang, Z., Chen, X., Zhu, X., et al. (2017). Selective effect of hydroxyapatite nanoparticles on osteoporotic and healthy bone formation correlates with intracellular calcium homeostasis regulation. *Acta Biomater.* 59, 338–350. doi:10.1016/j.actbio.2017.07.009

frontiers | Frontiers in Bioengineering and Biotechnology

TYPE Original Research
PUBLISHED 14 January 2025
DOI 10.3389/fbioe.2024.1526877

OPEN ACCESS

EDITED BY
Dan Lin,
Shanghai University of Medicine and Health Sciences, China

REVIEWED BY
Mahmoud Ebrahimi,
University of Maragheh, Iran
Sharanabasava V. Ganachari,
KLE Technological University, India

*CORRESPONDENCE
You Fu,
fuyou91@alumni.sjtu.edu.cn
Xingping Zhou,
xpzhou@dhu.edu.cn

†These authors have contributed equally to this work

RECEIVED 12 November 2024
ACCEPTED 30 December 2024
PUBLISHED 14 January 2025

CITATION
Wen J, Wang J, Wang S, Zhou X and Fu Y (2025) Characterization and application of fluorescent hydrogel films with superior mechanical properties in detecting iron(III) ions and ferroptosis in oral cancer.
Front. Bioeng. Biotechnol. 12:1526877.
doi: 10.3389/fbioe.2024.1526877

Characterization and application of fluorescent hydrogel films with superior mechanical properties in detecting iron(III) ions and ferroptosis in oral cancer

Jinxi Wen[1†], Jian Wang[2†], Siqi Wang[1], Xingping Zhou[1*] and You Fu[3*]

[1]College of Biological Science and Medical Engineering, Donghua University, Shanghai, China, [2]Department of General Dentistry, Shanghai Ninth People's Hospital, Shanghai Jiao Tong University School of Medicine, College of Stomatology, Shanghai Jiao Tong University, National Center for Stomatology, National Clinical Research Center for Oral Diseases, Shanghai Key Laboratory of Stomatology and Shanghai Research Institute of Stomatology, Research Unit of Oral and Maxillofacial Regenerative Medicine, Chinese Academy of Medical Sciences, Shanghai, China, [3]Department of Orthodontics, Shanghai Ninth People's Hospital, Shanghai Jiao Tong University School of Medicine, College of Stomatology, Shanghai Jiao Tong University, National Center for Stomatology, National Clinical Research Center for Oral Diseases, Shanghai Key Laboratory of Stomatology and Shanghai Research Institute of Stomatology, Research Unit of Oral and Maxillofacial Regenerative Medicine, Chinese Academy of Medical Sciences, Shanghai, China

A one-step hydrothermal method was applied to prepare carbon dots (CDs) with superior fluorescence properties using chitosan as a carbon source. The as-prepared carbon dots were then grafted onto a sodium alginate-gelatin hydrogel film to form a fluorescent hydrogel film (FHGF), emitting at 450 nm under excitation of 350 nm light. In comparison to the CDs, the fluorescence intensity of this film was maintained over 90.0% and the luminescence position remained basically unchanged, caused by the unchanged surface light-emitting structure of the CDs, due to the existence of electrostatic repulsion between the CDs and the hydrogel. Moreover, the tensile-stress of the fluorescent film with 1.0 wt.% of the CDs was increased by 200% to 10.3 Mpa, and the strain was increased from 117% to 153%. The above experimental results are attributed to the hydrogen bonding between the CDs and the sodium alginate-gelatin hydrogel from analyses of the FT-IR spectra. Interestingly, Fe^{3+} exerted a great quenching effect on this fluorescent film in the concentration range of 0–1.8 μM. The film can be basically used recyclically to detect Fe^{3+} in solution with a detection limit as low as 0.043 μM. In a word, this work demonstrated an enormous potential of carbon dots in fabricating mechanical and fluorescent properties of the hydrogel and proposed a new detection platform for Fe^{3+}. In view of the promising Fe^{3+} detection capacity, this hydrogel film can also be applied in oral bacteria surveillance and semi-quantification of ferroptosis in oral cancer.

KEYWORDS

carbon dots, fluorescent hydrogel film, Fe^{3+}, mechanical properties, ferroptosis

Introduction

Hydrogel is a polymer system with a three-dimensional network structure, which has received extensive attention due to its good biocompatibility (Chang et al., 2019) and biodegradability (Hao et al., 2019). Nowadays, hydrogel has been applied in the fields of tissue-engineering (Liu et al., 2020), drug-delivery (Plappert et al., 2019), a portable probe (Li et al., 2024a) and the like. Meanwhile, research on the fluorescent hydrogel is attracting more attention due to its special usages in bioimaging (Mehwish et al., 2019) and environment arraying (Dai and Fidalgo de Cortalezzi, 2019). Scientists have attempted to combine fluorescent materials such as rare-earth compounds (Liu et al., 2019), organic fluorescent dyes (Nishiyabu et al., 2014), and semiconductor quantum dots (Sahiner et al., 2011) with hydrogels to obtain fluorescent hydrogels with some specific properties. However, the above materials usually limit the application range of fluorescent hydrogels due to their toxicity and high cost. Then, with the advent of carbon dots (CDs), scientists have seen ways to solve this problem. They have tried to combine CDs with hydrogels based on the biocompatibility (Ni et al., 2019), low toxicity (Gate et al., 2019) and excellent optical properties (Wang et al., 2010). Besides, the combination of CDs and hydrogels can be widely used in fields such as bioimaging (Zhu et al., 2013) and metal ion probes (Zhang and Chen, 2014). Surprisingly, the addition of CDs can also replace the traditional crosslinkers to enhance the mechanical properties of the hydrogel (Hu et al., 2015). For example, in 2018, Hu et al. (2016) found that adding carbon dots as physical crosslinkers into the polyacrylamide (PAM) hydrogel can greatly improve its mechanical properties. Recently, Wang J. et al. (2018) also found the same phenomenon in synthesizing new p (HEMA-co-AA) fluorescent hydrogels.

Owing to the sensitivity and selectivity of carbon dots to metal ions (Wei et al., 2012), efforts are being made to develop CDs as a completely new metal ion probe. Fortunately, the carbon dots also give the similar performance while being grafted to fluorescent hydrogels (Konwar et al., 2015). Therefore, the use of fluorescent hydrogel as a new ion detection platform has become a new field of exploration (Guo et al., 2017). For instance, in 2018, the PVAm-g-N-CDs/PAM synthesized by Yu et al. (2017) was highly sensitive to Hg^{2+} with a detection limit of 0.089 μM. Moreover, Geng et al. (2015) synthesized fluorescent chitosan hydrogel (3D-FCH), which had a detection function for Hg^{2+} with a very low detection limit. The above all indicated the possibility of fluorescent hydrogels to be a metal ion detection platform.

Generally, iron is an indispensable element for human body and its content in drinking water should be controlled within a certain range. At present, the content of Fe^{3+} in solution is generally determined based on inductively coupled plasma-atomic emission spectroscopy (ICP-AES) and chemical titration. However, the above method is strenuous and cumbersome. Therefore, it becomes very important to explore a new simple method for monitoring iron content. Fortunately, scientists have discovered that Fe^{3+} can cause fluorescence quenching of carbon dots (Qu et al., 2013), implying the possibility of establishing a superior Fe^{3+} detection platform by the use of the CDs-grafted hydrogel. More importantly, from aspect of the promising Fe^{3+} detection capacity, this kind of hydrogel film can also be applied in oral bacteria surveillance and ferroptosis bioimaging (Li X. et al., 2024). Herein, CDs were firstly prepared with excellent fluorescence intensity and then grafted into the hydrogel film. Then, the properties of the composite film were checked including the fluorescence properties and mechanical properties, to investigate effects of the CDs on the film. Importantly, the relationship between the Fe^{3+} concentration and the fluorescence intensity and effects of various metal ions on its fluorescence intensity were also carried out, for exploring the feasibility of fluorescent hydrogels film as a Fe^{3+} detection platform and accelerating the application of CDs, especially in application of oral bacteria surveillance and ferroptosis bioimaging.

Materials and methods

Chitosan (deacetylation degree ≥95%, viscosity 100 ~ 200 mpa·s), gelatin (glue strength ~240 g Bloom), and sodium alginate (viscosity 200 ± 20 mpa·s) were purchased from Aladdin. Glycerol (Purity ≥99.0%) was purchased from Greagent and quinine sulfate (purity ≥99%) was purchased from Acros. Salts of $FeCl_3{\cdot}6H_20$, Ni $(NO_3)_2{\cdot}H_2O$, $MgSO_4{\cdot}7H_20$, Ca $(NO_3)_2{\cdot}4H_2O$, KCl, Pb $(NO_3)_2$, $ZnSO_4{\cdot}7H_2O$, $AgNO_3$, NH_4Cl, $CuSO_4{\cdot}5H_20$, and EDTA were purchased from Sinopharm Chemical Reagent Co., Ltd., China. None of the above chemicals were further purified. The deionized water used was supplied by the lab.

Synthesis of carbon dots (CDs)

Chitosan of 1.0 g was dissolved in deionized water of 50 mL, and the resultant was transferred to a high-pressure hydrothermal reaction vessel in an oven, followed by aging at 200°C for 6 h. After the treatments of filtration, centrifugation, dialysis and freeze-drying, brown yellow powder of carbon dots was obtained as received.

Preparation of fluorescent hydrogel film (FHGF)

Sodium alginate of 2.0 g and gelatin of 0.5 g were dissolved in deionized water of 50 mL and then stirred at 50°C for 4 h. After that, glycerol of 3.0 mL and a certain amount of carbon dots were added to the above solution and then the mixture was agitated at room temperature for 4 h. Hereafter, the resulting suspension was poured into a mold and placed in an oven at 60°C, maintained for 24 h to obtain a dried gel film. Finally, a calcium chloride solution (5.0 wt.%) prepared in advance was sprayed on the surface of the film. After crosslinking for 10 min, the composite film was peeled off to be as a fluorescent hydrogel film (FHGF).

Cycling experiment of FHGF

The FHGF was soaked in 10–5 M Fe^{3+} solution for 5 min, and then rinsed for 3 times with deionized water to remove the Fe^{3+} remained on the surface. After that, it was further immersed in 10–5 M EDTA solution for 5 min, and then rinsed for 3 times with deionized water. The fluorescence intensity of the FHGF was then measured. The above steps were repeated for 5 times.

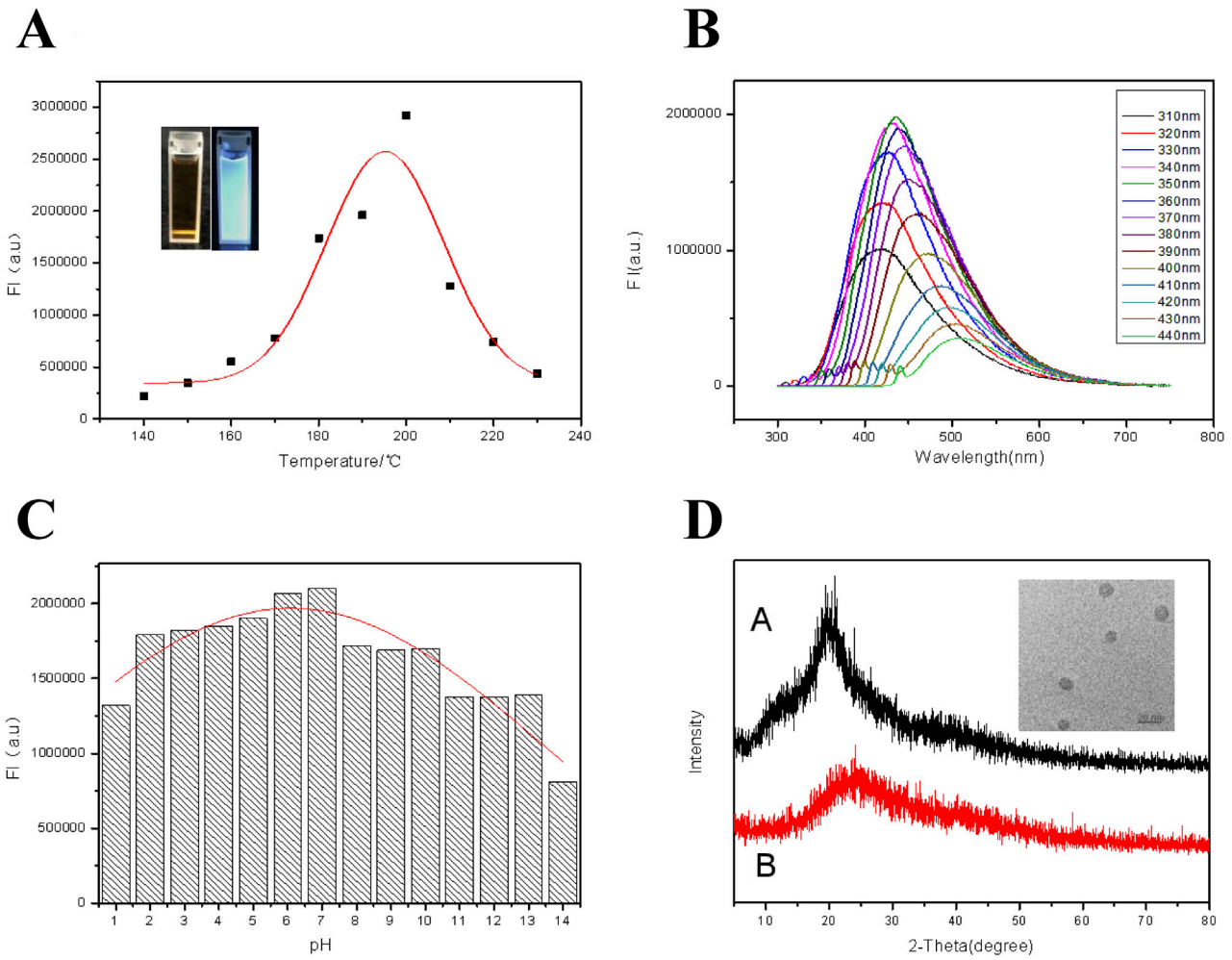

FIGURE 1
(A) Fluorescence intensities of CDs at different reaction temperatures when excited by ultraviolet light of 350 nm. Inset: From left to right are photos of the CDs suspension in natural light and 365 nm UV light. **(B)** Fluorescence emission spectra of the CDs under excitation with different wavelengths. **(C)** Effect of solution pH on fluorescence intensity of the CDs. **(D)** XRD patterns of chitosan (Curve A) and the CDs (Curve B). Inset: TEM image of the CDs.

Characterizations

X-ray diffraction (XRD) of CDs was measured using a D/max-2550 PC X-ray powder diffractometer. Optical properties of CDs and FHGF were analyzed using a V-530 UV-visible spectrophotometer and an F-4500 fluorescence spectrophotometer. To obtain material composition information, Fourier transform infrared (FT-IR) spectra of samples were obtained on an Aavatar-380 FT-IR spectrometer. The zeta potential of the samples was analyzed by using the Zestasizer Nano ZS ZEN3600 (Japan). In addition, the surface morphology and structure of the FHGF were analyzed on a Hitachi S-4800 scanning electron microscope (SEM) at an accelerating voltage of 10 kV, and on a JEM-2100 microscope transmission electron microscope (TEM).

Malondialdehyde (MDA) assay

Ferroptosis was induced by erastin (Absin, China) in the oral squamous cell carcinoma cell line HN4. MDA concentration was measured using MDA Assay Kit (Beyotime, China) following the manufacture's instruction.

Results and discussion

Preparation and characterization of carbon dots (CDs)

As shown in Figure 1A, based on the luminescing ability, the optimized reaction temperature for synthesizing carbon dots was 20°C with the chitosan concentration of 2.0 wt.% and the reaction time of 6 h. From the inset of Figure 1A, the CDs suspension appeared dark brown when exposed to sunlight, and appeared bright blue when illuminated with 365 nm UV light. Figure 1B shows the fluorescence spectra of CDs under different excitation wavelengths. It can be easily seen that, when the excitation wavelength moved from 310 nm to 440 nm, a red shift (Qu et al., 2015) occurred in the emission peak. While the ultraviolet light excitation wavelength was 350 nm, the strongest emission peak appeared at 450 nm. The fluorescence of the CDs was also checked in

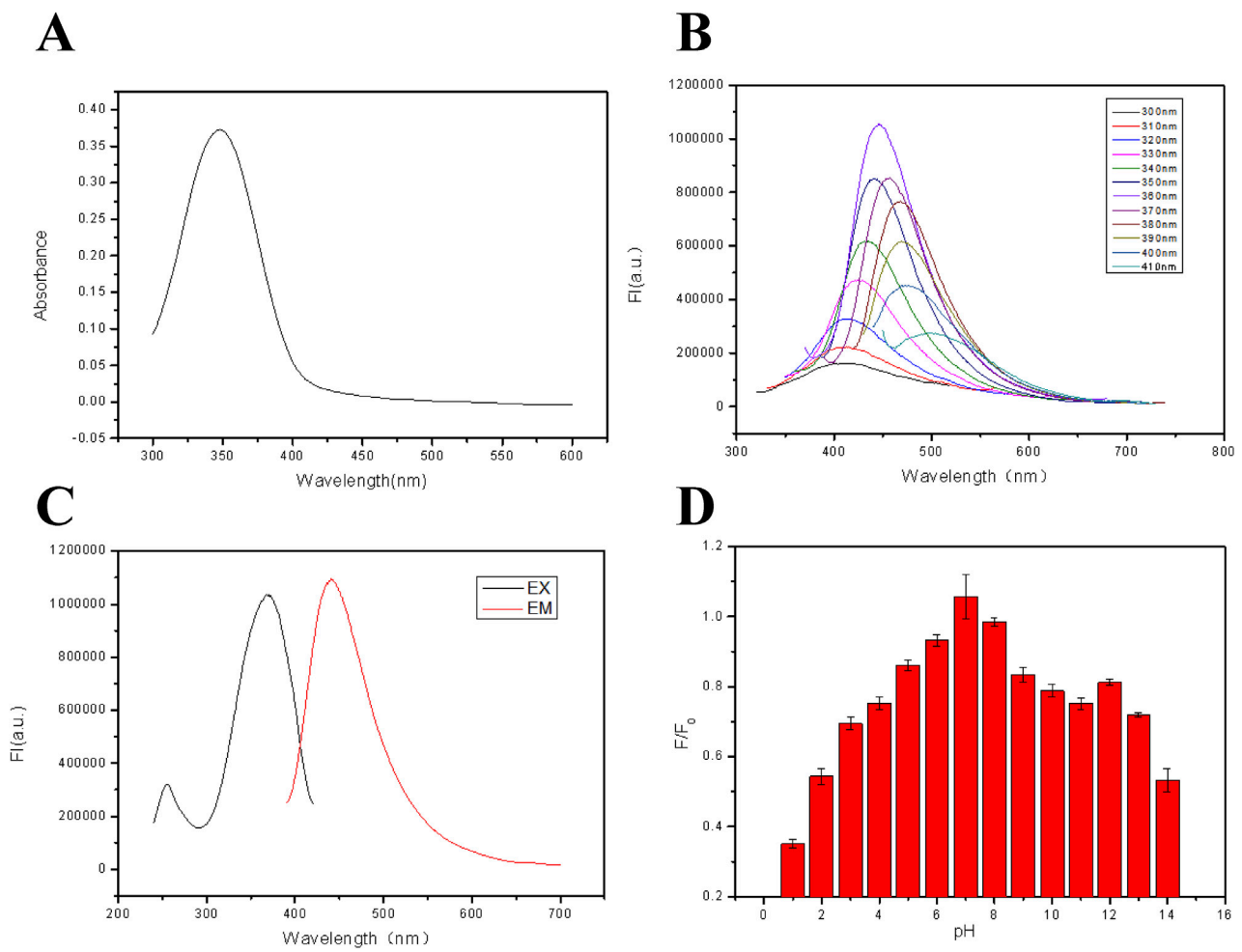

FIGURE 2
(A) UV-vis absorption spectra of the FHGF. **(B)** Excitation and emission spectra of FHF (λ_{EX} = 365 nm, λ_{EM} = 450 nm). **(C)** Fluorescence emission spectra of FHF under excitation with different wavelengths. **(D)** Effect of solution pH on the fluorescence intensity of FHGF. All of the samples were excited at 350 nm.

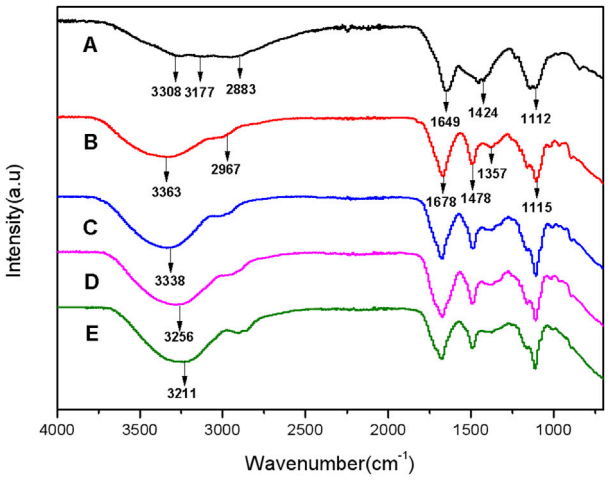

FIGURE 3
FT-IR spectra of CDs **(A)**, hydrogel films without grafted CDs **(B)**, FHGF with 1.0 wt.% CDs **(C)**, FHGF with 5.0 wt.% CDs **(D)**,and FHGF with 15 wt.% CDs **(E)**.

suspension with different pH and the results were shown in Figure 1C. Obviously, in the pH range of 2.0 and 10.0, the fluorescence intensity was basically kept constant. However, the strong acidic or alkaline environment exerted a significant effect on the fluorescence intensity of the CDs, probably resulted from by the broken exiting group on the surface of the CDs under strong acidic and alkaline conditions (Jia et al., 2012). On the other hand, XRD pattern of the CDs was displayed in Figure 1D, together with that of chitosan. The chitosan possessed crystallization characteristics and the CDs were mainly in the form of amorphous carbon, displaying their relatively high purity. Besides, according to the TEM imagine inserted in Figure 1D, the particle with an average diameter of 8.3 nm was spherical with a narrow size-distribution. In a word, the synthesized CDs have good optical properties with good acid and alkali resistances.

Composition and characterization of FHGF

The optical properties of the fluorescent hydrogel are shown in Figures 2A–C. From Figure 1A, a strong UV absorption peak appeared at 345 nm, probably being attributed to the n–π*

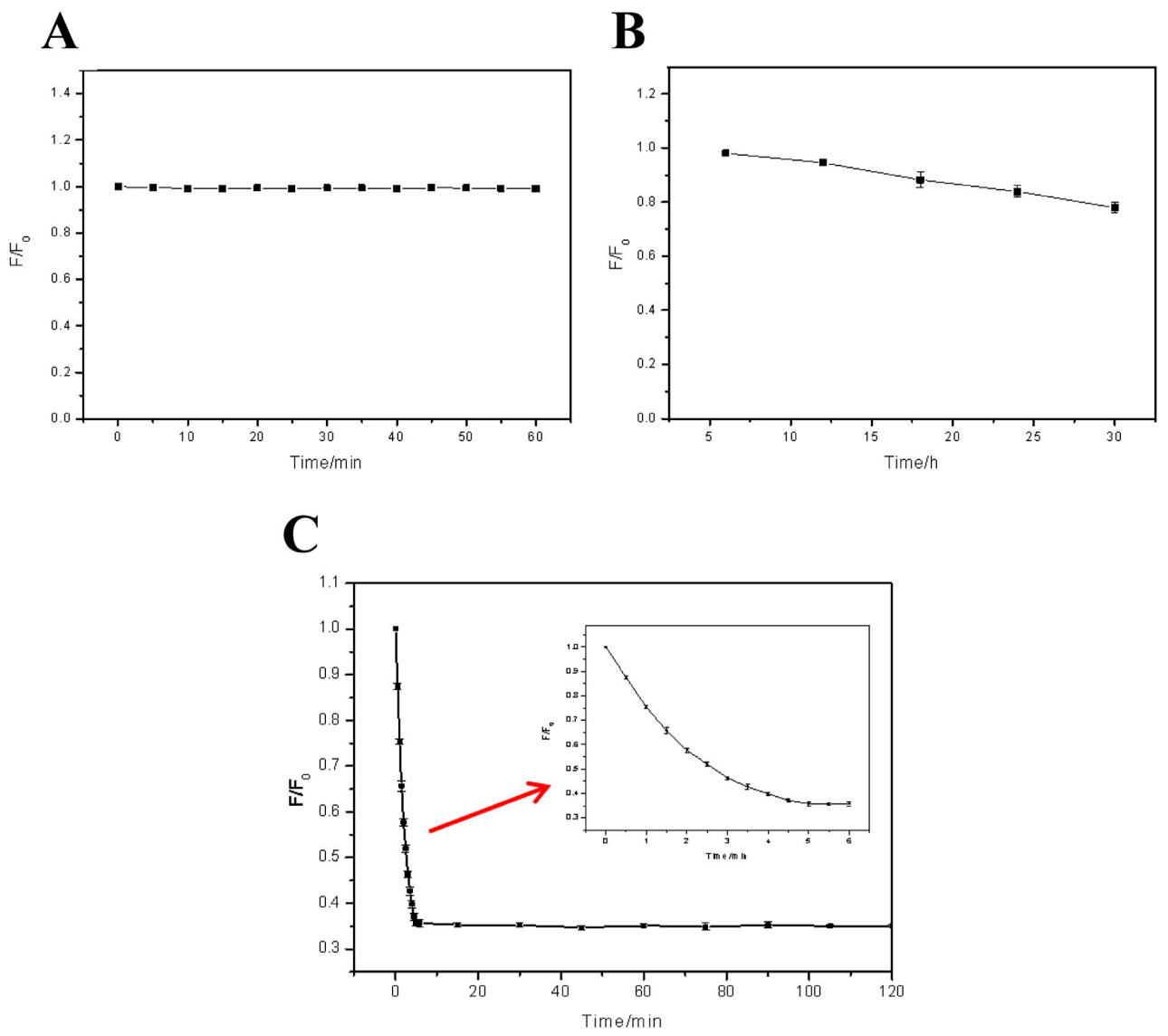

FIGURE 4
Effect of soaking time on the fluorescence intensity: **(A)** That of FHGF immersed in deionized water for a short time (0min~60 min); **(B)** That of FHGF immersed in deionized water for a long time (5h~30 h); **(C)** Relationship between FHF fluorescence and the response time in Fe^{3+} solution with a concentration of 10^{-5} M. All of the samples were excited at 350 nm.

transition of a C=O bond (Baker and Baker, 2010). In Figure 2B, when the excitation wavelength was altered from 300 nm to 410 nm, the emission peak position of the film moved from 410 nm to 510 nm. Meanwhile, a red shift phenomenon of the fluorescent hydrogel occurred due to the "Stoke shift," proving the down-converting luminescence (Ren et al., 2017) property of the film. The dependence of the fluorescent properties on the excitation wavelength is attributed to the naturality of these carbon dots. The fluorescence excitation and emission spectra of the fluorescent film are displayed in Figure 2C. From this figure, when the excitation wavelength is 345 nm, a strong emission peak can be observed at about 450 nm. In addition, the effect of solution pH on the fluorescence intensity of fluorescent films was also explored and the results are revealed in Figure 2D. It is found that when the pH is between 5.0 and 13.0, the fluorescence intensity of the film is relatively strong, but in the strong acid environment, the fluorescence intensity of the film is reduced. This is due to the fact that sodium alginate can react with proton in an acidic environment to form water-insoluble alginic acid, adhering to the surface of the fluorescent film to reduce its fluorescence intensity. The reaction equation is as follows:

$$\mathrm{NaAlg + HCI \rightarrow Halg \downarrow + NaCI}$$

Figure 3 shows FT-IR spectra of the CDs and the hydrogel films with and without CDs to characterize the structure and composition. The characteristic absorption bands of -OH at 3,308 cm^{-1} and -NH at 3,177 cm^{-1} of the CDs are obtained in Curve A, indicating the presence of an amide group on the surface of the CDs (Fan et al., 2019). The peaks at 2,883 cm^{-1}, 1,649 cm^{-1}, 1,424 cm^{-1}, and 1,112 cm^{-1} are attributed to the stretching vibration of -CH,

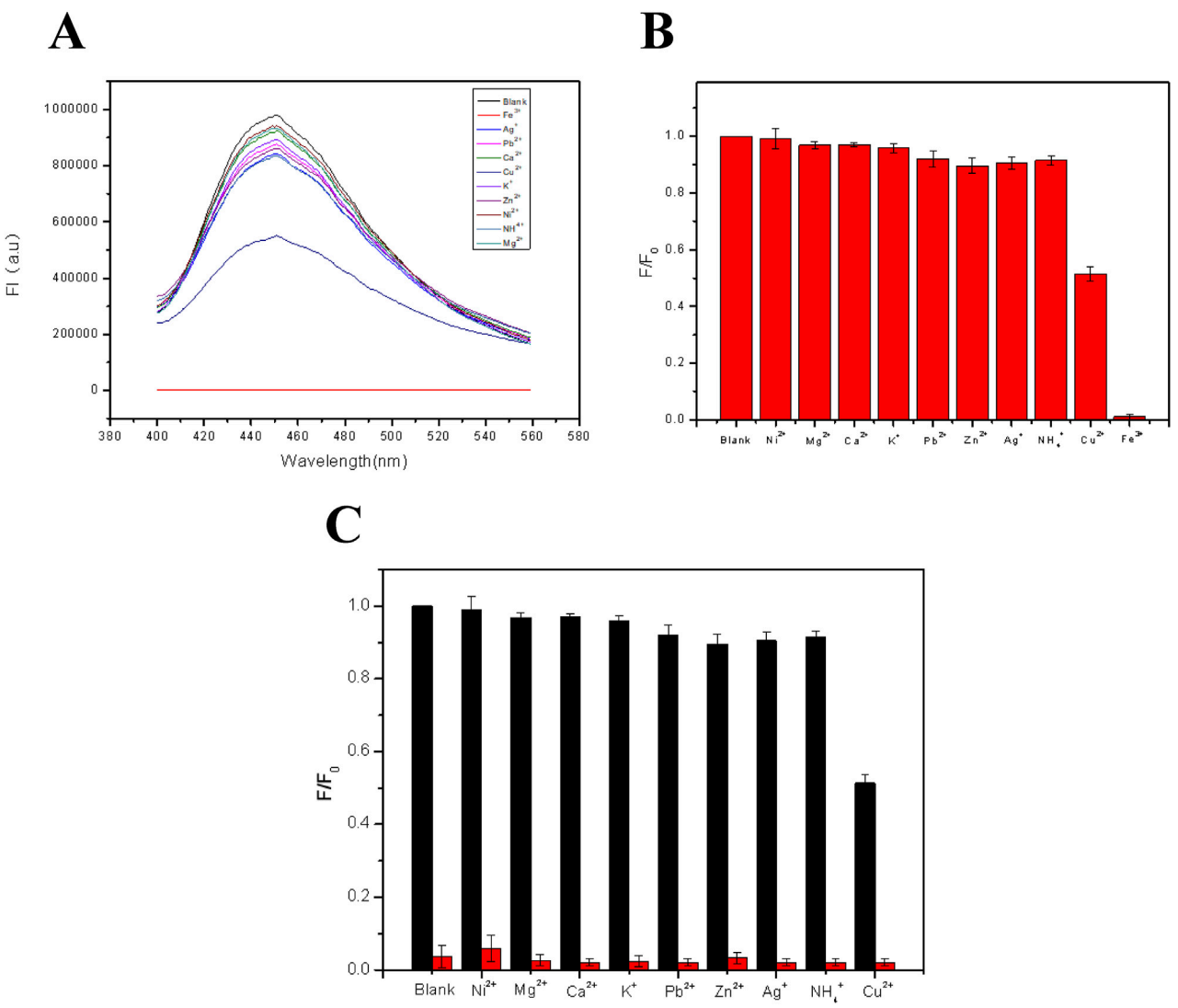

FIGURE 5
(A) Fluorescence patterns of the FHGF soaked in solutions with different metal ions. **(B)** Histogram of the effect of metal ions on the fluorescence intensity of the FHGF. **(C)** Selectivity of the FHGF in the presence of interference cations. All of the samples were excited at 350 nm.

C=O, -CH_2^-, and -C-O-C- (Zhang et al., 2015; Wang et al., 2014), respectively. Besides, Curve B shown in Figure 3 presents FT-IR spectrum of the hydrogel film (HGF) without CDs. HGF has strong and broad peaks at 3,363 cm^{-1}, probably caused from the characteristic absorption bands of -OH and -NH-. The peaks at 2,967 cm^{-1}, 1,678 cm^{-1}, 1,478 cm^{-1}, 1,357 cm^{-1} and 1,115 cm^{-1} are attributed to the stretching vibration of -CH-, -C=O, -CH_2-, -C-$(CH_3)_3$, and -C-O-C- (Sachdev et al., 2016), respectively. Unexpectedly, the peak at 3,363 cm^{-1} in Curve B is significantly red-shifted to the peak at 3,338 cm^{-1} according to Curve C, which shows the FT-IR spectra of FHGF with 1.0 wt.% content of CDs. This indicates the presence of hydrogen bonds between CDs and HGF (Jemmis and Jemmis, 2007). To further confirm the above speculation, the FT-IR spectra of the other two FHGFs containing 5.0 wt.% and 15.0 wt.% CDs were respectively tested and the results were shown on Curves D and E. Obviously, from Curves D and E, as the CDs concentration increased, the red-shifted characteristic absorption band of -NH and -OH became more pronounced, from the peak at 3,256 cm^{-1} to that at 3,211 cm^{-1}. In summary, hydrogen bonds were formed between the CDs and the hydrogel film and became stronger along with the increase in CDs content.

Most working environment of the FHGF is aqueous system, so it is quite important to explore the soaking effect in aqueous environment. Figure 4A indicates the effect of water to the FHGF fluorescence intensity after a short-term immersion. It can be seen from the figure that the aqueous solution does not have a significant effect on the fluorescence intensity of the film in a short time such as less than 1 h, which makes it possible to use the film as a metal ion detection platform. Besides, it can be seen from Figure 4B that when the FHGF is immersed in an aqueous solution for a long time, the fluorescence intensity of the film will be significantly reduced in several 10 h. As the immersion time was 30 h, the fluorescence intensity was decreased by 20%. In a long time, the water molecules can enter the interior of the hydrogel film through the film pores and bind to the CDs in the film by hydrogen bond (Li et al., 2018), and then carry the CDs out of the FHGF, causing the decrease of

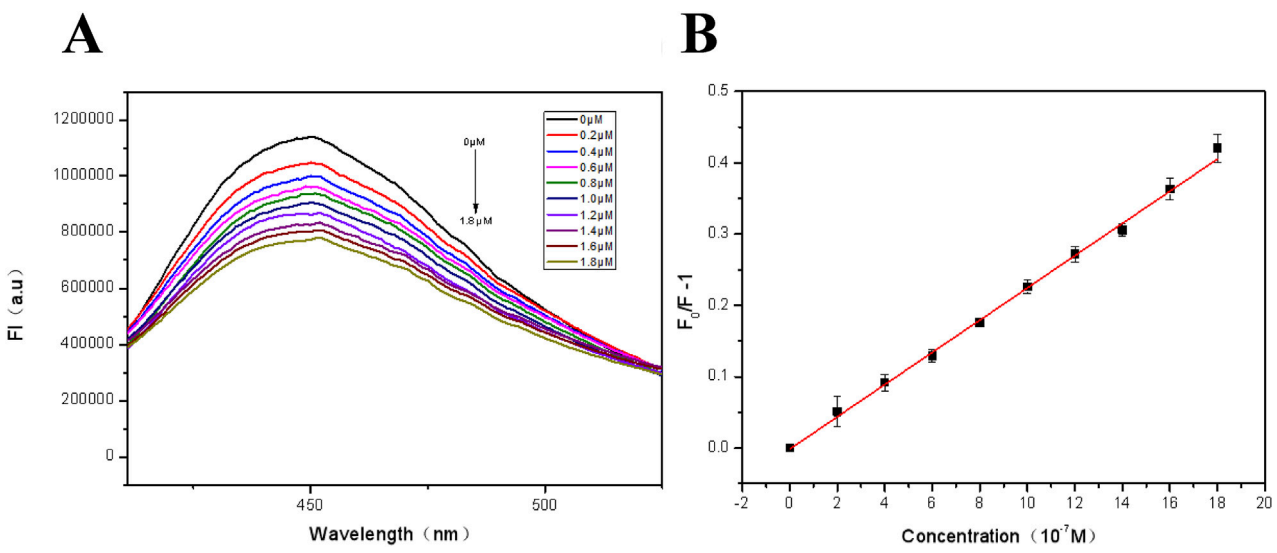

FIGURE 6
(A) Fluorescence spectra of the FHGF at different concentrations of Fe^{3+} (0~1.8 μM); **(B)** Fluorescence linear equation of FHGF in response to Fe^{3+} concentration. All of the samples were excited at 350 nm.

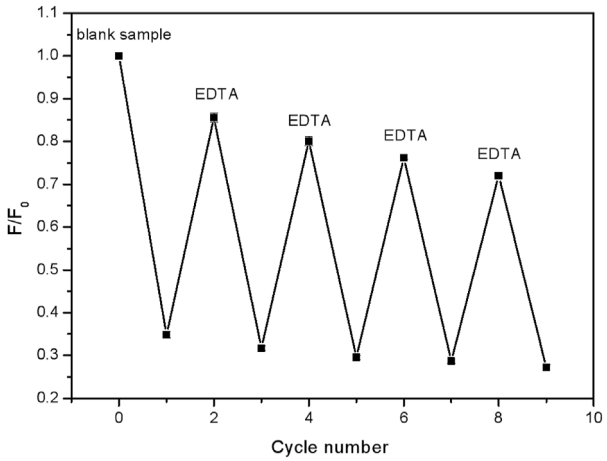

FIGURE 7
Fluorescence intensity changes of the FHGF after cyclically soaking in Fe^{3+} (10^{-5} M) and EDTA (10^{-5} M) in solution.

fluorescence intensity of the film. Figure 4C shows the film soaked in a 10^{-5} M Fe^{3+} solution to investigate the effect of soaking time and determine the optimal reaction time. It can be seen from the figure that the fluorescence intensity of the film markedly decreased in 5 min and remained substantially unchanged while the immersion time exceeded 5 min, indicating that the optimal reaction time was 5 min.

Metal ion selectivity is also a very important factor for detecting metal ions. For checking the selectivity, the fluorescent film was immersed in solutions with different metal ion (Fe^{3+}, Ag^{+}, Pb^{2+}, Ca^{2+}, Cu^{2+}, K^{+}, Zn^{2+}, Ni^{2+}, NH^{4+}, and Mg^{2+}) at a fixed concentration of 10^{-4} M. Then, the film was irradiated with a 350 nm UV light for measuring the emission intensities of different samples. It was found from Figures 5A, B that the quenching effect of Fe^{3+} on the fluorescence of the film was mostly obvious, along with a much weaker effect of Cu^{2+}, while other metal ions had no obvious effect on the fluorescence. Figure 5C shows the fluorescence intensities of 10^{-4} M Fe^{3+} solution in the presence of different metal ions with the same concentration for checking the anti-interference ability. It has been shown from Figure 5B that the effect of each kind of metal ion on the fluorescence intensity of FHGF before mixing with Fe^{3+} was weak. However, from Figure 5C, with the addition of Fe^{3+}, the fluorescence intensity of the film decreased sharply, indicating that the FHGF has unique selectivity to Fe^{3+} and good anti-interference to other metal ions. This is probably due to that Fe^{3+} and CDs in the FHGF can easily form a stable chelate in comparison to the other metal ions with low charges and reduce the fluorescence intensity (Ju and Chen, 2014). In conclusion, the fluorescent film has unique selectivity to Fe^{3+} and good anti-interference to the other metal ions, which is very indispensable for establishing a novel metal ion detection platform.

For the sensitivity study of fluorescent films, Fe^{3+} concentration in the range from 0 to 1.8 μM was selected for investigation. As shown in Figure 6A, the intensity of the FHGF at 450 nm decreased with increasing Fe^{3+} concentration, displaying that there is a negative relativity and this detection system has a good sensitivity to Fe^{3+}. Then, the fluorescence quenching were quantifically further analyzed using the Stern-Volmer equation (Friedl et al., 2015).

$$F_0/F_{-1} = k_{sv}C$$

where F0 and F−1 are the fluorescence intensities of the fluorescent film at 450 nm without and with the addition of Fe^{3+} respectively, ksv is the Stern-Volmer quenching coefficient, and C is the concentration of the analyte (Fe^{3+}). As shown in Figure 6B, the Stern-Volmer equation exhibited an excellent linear relationship in the concentration range of 0–1.8 μM. The correlation coefficient (R2) = 0.9923, and the detection limit (3σ/s) was 0.043 μM, where σ

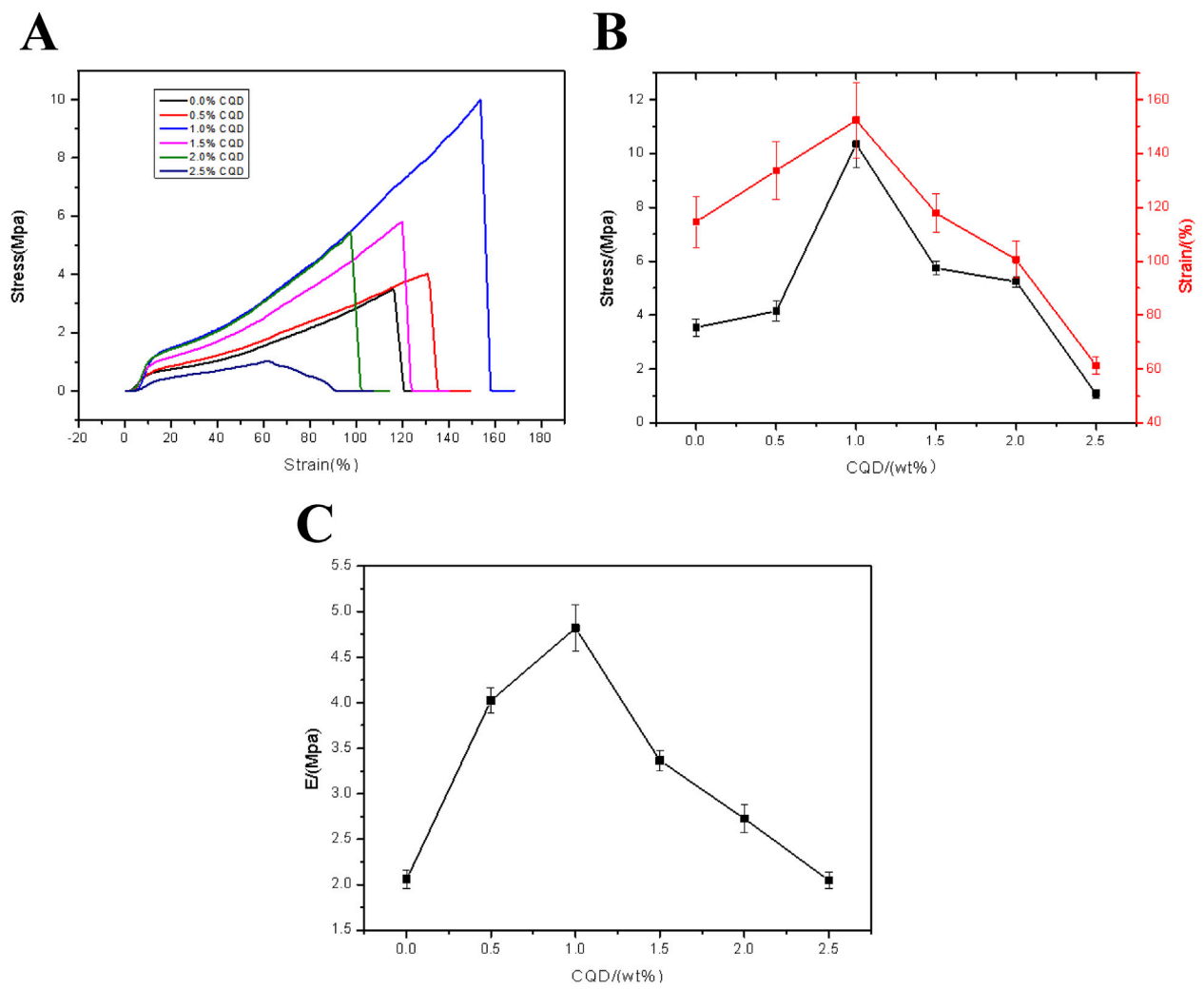

FIGURE 8
(A) Tensile strain-stress curve of the FHGF with different CDs content. **(B)** Stresses and strains of the FHGF as a function of the CDs content. **(C)** Relationship between Young's Modulus of the FHGF and CDs content.

TABLE 1 Zeta potentials of CDs and Chitosan- algin.

Sample	Zeta potential value (mV)
CDs	−8.18
Chitosan- algin solution	−4.57

represents the standard deviation of 10 blank measurements and s is the slope of the calibration curve.

The above results have described a potential arraying detection route to Fe^{3+}. Then, for the practical usage, repeated application tests are also quite important. To get it, EDTA was used to complex completely with Fe^{3+} ions and then the CDs were released (Wang N. et al., 2018). As shown in Figure 7, when the FHGF was soaked in a 10^{-5} M Fe^{3+} solution, the fluorescence intensity of the FHGF was found to drop sharply. After the addition of EDTA (10^{-5} M), the fluorescence increased significantly, although it could not be restored completely to the original level. Besides, the fluorescence intensity of the FHGF was reduced gently from the previous one after each time EDTA was used. In a word, after four cycles, the FHGF still maintained 76% of the original fluorescence intensity, indicating that this novel platform for detecting Fe^{3+} concentration can be basically used recyclically.

For the practical application of the FHGF, the mechanical properties are also important. To investigate the effect of CDs on the mechanical properties of the fluorescent films, stress and strain tests at different carbon dots content were conducted. As shown in Figure 8A, the stress and strain of the FHGF increased firstly and then decreased with the addition of CDs, exhibiting an obvious influence from the CDs on the mechanical properties of the FHGF. When the carbon dots content was increased from 0% to 1.0%, the tensile-stress is increased by 200% to 10.3 Mpa and the tensile-strain strength was increased by 36%–152%, as displayed in Figure 8B. However, when the CDs content increased from 1.0 wt.% to 2.5 wt.%, the mechanical properties of the film declined, proving that the mechanical properties of the film were optimal at 1.0 wt.% of the CDs. Additionally, from Figure 8C, when the content of CDs was increased from 0 to 1.0 wt.%, the Young's modulus of the film was

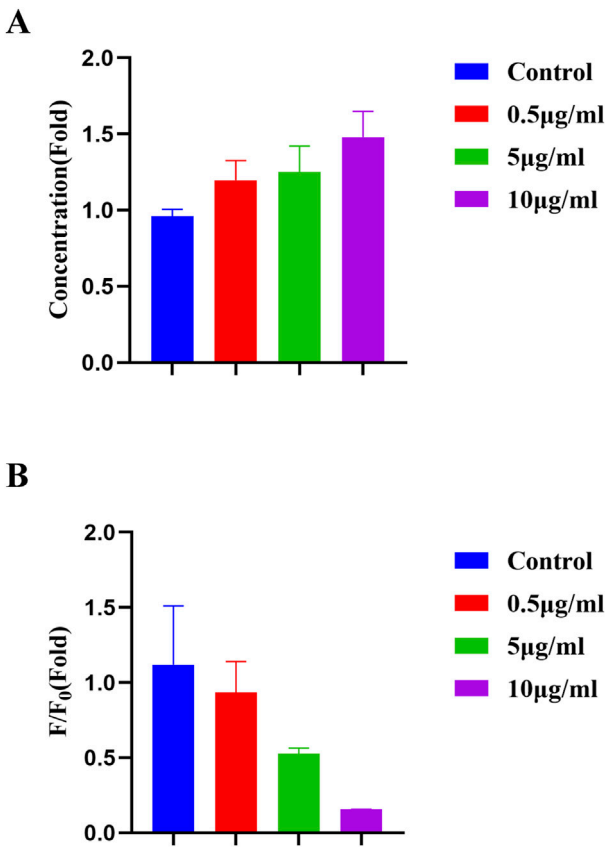

FIGURE 9
(A) MDA concentration of HN4 cells after erastin induction. **(B)** Fluorescence intensity of the FHGF incubated with HN4 cells after erastin induction.

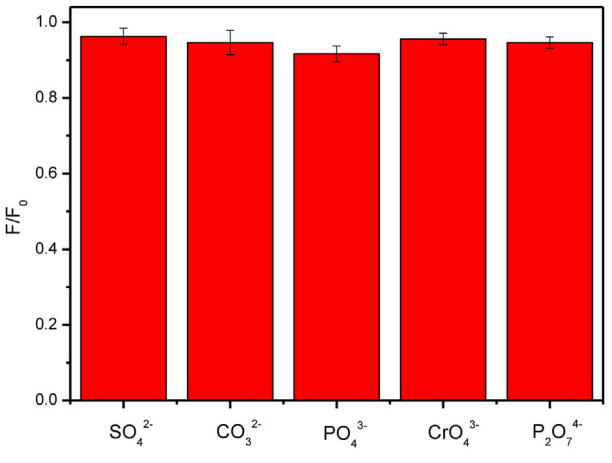

FIGURE 10
Histogram showing the effect of anions on the fluorescence intensity of the FHGF.

increased by 150% to 4.8 MPa, and then decreased with the increase of CDs content. In order to explain this phenomenon, the Zeta electrical potentials of the CDs and the film in the mixed solution were determined, and the data were listed in Table 1. According to this table, the Zeta potential value of the CDs was −8.18 mV, and that of the film in the mixed solution was −4.57 mV. This indicates that they all have negative charges and they will be repulsive each other. Combined with the previous FT-IR data, it is suggested that due to the hydrogen bond action between the CDs and FHGF, the mechanical properties of the film are enhanced as the content of CDs increases. However, when the content of the CDs is more than 1.0 wt.%, the repulsive effect between them is greater than the connection effect from the hydrogen bond action, resulting in the weakened mechanical properties of the film in this case.

Ferroptosis is a novel form of programmed cell death resulting from iron-dependent accumulation of lipid peroxides. The mechanism of ferroptosis includes disorder of iron metabolism, imbalance of amino acid antioxidant system, and accumulation of lipid peroxides. Ferroptosis was proved to be related to several diseases, such as stroke, tumor, degenerative diseases and cerebral hemorrhage. It was reported that CDs was utilized to induce ferroptosis of tumor cells and enhance antitumor immunity (Li et al., 2024c; Liu et al., 2024). CDs were also applied to observe and inhibit oral bacterial biofilm formation due to its good biocompatibility and bioimaging capacity (Yao et al., 2022). Fe^{3+} usually binds to transferrin and enters into the cells through the transferrin channel, and then participates in a variety of subsequent biochemical processes (Wang et al., 2021). Therefore, Fe^{3+} is an important indicator to determine the occurrence of ferroptosis. Ferroptosis was induced in oral squamous cell carcinoma cell line HN4 by erastin (Guang et al., 2024). Malondialdehyde (MDA) was reported to be a biomarker for ferroptosis (Jiang et al., 2023; Kong et al., 2023). In Figure 9A, MDA concentration exhibited a dose-dependent increase in HN4 cells. Accordingly, because the concentration of Fe^{3+} increased during ferroptosis, the fluorescence intensity of the film decreased also following a dose-dependent way in Figure 9B. In this study, the hydrogel synthesized was of a promising property for Fe^{3+} detection, leading to an ideal tool for ferroptosis tracing and ferroptosis-based therapy.

From the above discussion, it is revealed that the surface charges of CDs and the relative materials are a key factor to affect the properties of the composite materials doped with the CDs. Although there have been a lot of reports on the research of CDs composites, the fluorescence or some other properties of the composite materials are not satisfied. In this work, the fluorescent properties of the FHGF were well maintained, which was probably attributed to the negative charge of both the carbon dots and the hydrogel. To further confirm the above idea, the effect of various anions on the fluorescence intensity of the FHGF was tested. As shown in Figure 10, when the FHGF was immersed in an anion solution with the same concentration (10^{-4} M) of SO_4^{2-}, CO_3^{2-}, PO_4^{3-}, CrO_4^{2-}, and $P_2O_7^{4-}$, respectively, the fluorescence intensity of the FHGF was substantially unchanged. The above phenomenon indicates that these anions do not have much influence on the fluorescence performance of the film. This further proves the fact that the CDs in the film and ions with the same charge will repel each other, leading to that the light-emitting structure on the surface of the carbon dots is not destroyed and then the fluorescence performance of the CDs is well maintained.

Conclusion

In this paper, carbon dots (CDs) with good optical properties were synthesized by a one-step hydrothermal method and then grafted into the hydrogel successfully, maintaining their basic optical properties. This is due to the presence of electrostatic repulsion between the CDs and hydrogel, which does not alter the surface morphology of the carbon dots after recombination. Besides, FHGFs obtained by using CDs as crosslinker, not only served as a kind of fluorescent probe for detecting Fe^{3+} content in solution but also had excellent mechanical properties. The synthesized FHGFs are of good sensitivity and selectivity to Fe^{3+} in aqueous solution, achieving that the detection limit of the obtained fluorescent probe is as low as 0.043 μM. The reason for the selectivity is mainly attributed to the positive charge of Fe^{3+} ions, altering the surface charge of negatively charged CDs and thus quenching CDs. Further, the mechanical properties of the film are obviously promoted, due to the comprehensive action of hydrogen bonding and electrostatic interaction between the CDs and hydrogels. The above testing indicates that the addition of CDs greatly enhances the mechanical properties of FHGF and will broaden their application range. Previous studies also demonstrated that CDs could be utilized for oral bacterial biofilm observing and ferroptosis inducing. Most importantly, the results have made it possible to detect Fe^{3+} in solution more conveniently and demonstrate the feasibility of carbon dots as crosslinker. In addition, this hydrogel film could provide a promising strategy for identification of ferroptosis in oral cancer and ferroptosis-based therapy.

Data availability statement

The raw data supporting the conclusions of this article will be made available by the authors, without undue reservation.

Author contributions

JWe: Writing–original draft. JWa: Data curation, Writing–review and editing. XZ: Writing–review and editing. YF: Conceptualization, Writing–review and editing.

Funding

The author(s) declare that no financial support was received for the research, authorship, and/or publication of this article.

Conflict of interest

The authors declare that the research was conducted in the absence of any commercial or financial relationships that could be construed as a potential conflict of interest.

Generative AI statement

The author(s) declare that no Generative AI was used in the creation of this manuscript.

Publisher's note

References

Baker, S. N., and Baker, G. A. (2010). Luminescent carbon nanodots: emergent nanolights. *Angew. Chem. Int. Ed. Engl.* 49 (38), 6726–6744. doi:10.1002/anie.200906623

Chang, K. C., Lin, D. J., Wu, Y. R., Chang, C. W., Chen, C. H., Ko, C. L., et al. (2019). Characterization of genipin-crosslinked gelatin/hyaluronic acid-based hydrogel membranes and loaded with hinokitiol: *in vitro* evaluation of antibacterial activity and biocompatibility. *Mater Sci. Eng. C Mater Biol. Appl.* 105, 110074. doi:10.1016/j.msec.2019.110074

Dai, J., and Fidalgo de Cortalezzi, M. (2019). Influence of pH, ionic strength and natural organic matter concentration on a MIP-Fluorescent sensor for the quantification of DNT in water. *Heliyon* 5 (6), e01922. doi:10.1016/j.heliyon.2019.e01922

Fan, Y., Yang, X., Yin, C., Ma, C., and Zhou, X. (2019). Blue- and green-emitting hydrophobic carbon dots: preparation, optical transition, and carbon dot-loading. *Nanotechnology* 30 (26), 265704. doi:10.1088/1361-6528/ab0b14

Friedl, F., Krah, N., and Jähne, B. (2015). Optical sensing of oxygen using a modified Stern–Volmer equation for high laser irradiance. *Sensors Actuators B Chem.* 206, 336–342. doi:10.1016/j.snb.2014.09.073

Gate, L., Knudsen, K. B., Seidel, C., Berthing, T., Chézeau, L., Jacobsen, N. R., et al. (2019). Pulmonary toxicity of two different multi-walled carbon nanotubes in rat: Comparison between intratracheal instillation and inhalation exposure. *Toxicol. Appl. Pharmacol.* 375, 17–31. doi:10.1016/j.taap.2019.05.001

Geng, Z., Zhang, H., Xiong, Q., Zhang, Y., Zhao, H., and Wang, G. (2015). A fluorescent chitosan hydrogel detection platform for the sensitive and selective determination of trace mercury(ii) in water. *J. Mater. Chem. A* 3 (38), 19455–19460. doi:10.1039/c5ta05610a

Guang, L., Mao, C., Horbath, A. D., Yan, Y., Cai, S., Yao, J., et al. (2024). BRCA1-Mediated dual regulation of ferroptosis exposes a vulnerability to GPX4 and PARP Co-inhibition in BRCA1-deficient cancers. *Cancer Discov.* 14 (8), 1476–1495. doi:10.1158/2159-8290.cd-23-1220

Guo, J., Zhou, M., and Yang, C. (2017). Fluorescent hydrogel waveguide for on-site detection of heavy metal ions. *Sci. Rep.* 7 (1), 7902. doi:10.1038/s41598-017-08353-8

Hao, Y., He, J., Ma, X., Feng, L., Zhu, M., Zhai, Y., et al. (2019). A fully degradable and photocrosslinked polysaccharide-polyphosphate hydrogel for tissue engineering. *Carbohydr. Polym.* 225, 115257. doi:10.1016/j.carbpol.2019.115257

Hu, M., Gu, X., Hu, Y., Wang, T., Huang, J., and Wang, C. (2016). Low chemically cross-linked PAM/C-dot hydrogel with robustness and superstretchability in both as-prepared and swelling equilibrium states. *Macromolecules* 49 (8), 3174–3183. doi:10.1021/acs.macromol.5b02352

Hu, M., Yang, Y., Gu, X., Hu, Y., Du, Z., and Wang, C. (2015). Novel nanocomposite hydrogels consisting of C-dots with excellent mechanical properties. *Macromol. Mater. Eng.* 300 (11), 1043–1048. doi:10.1002/mame.201500141

Jemmis, J. J. E. D., and Jemmis, E. D. (2007). Red-Blue-or No-shift in hydrogen bonds A unified explanation. *J. Am. Chem. Soc.* 129 (15), 4620–4632. doi:10.1021/ja067545z

Jia, X., Li, J., and Wang, E. (2012). One-pot green synthesis of optically pH-sensitive carbon dots with upconversion luminescence. *Nanoscale* 4 (18), 5572–5575. doi:10.1039/c2nr31319g

Jiang, M., Jike, Y., Liu, K., Gan, F., Zhang, K., Xie, M., et al. (2023). Exosome-mediated miR-144-3p promotes ferroptosis to inhibit osteosarcoma proliferation, migration, and invasion through regulating ZEB1. *Mol. Cancer* 22, 113. doi:10.1186/s12943-023-01804-z

Ju, J., and Chen, W. (2014). Synthesis of highly fluorescent nitrogen-doped graphene quantum dots for sensitive, label-free detection of Fe (III) in aqueous media. *Biosens. Bioelectron.* 58, 219–225. doi:10.1016/j.bios.2014.02.061

Kong, P. C., Yang, M., Wang, Y., Yu, K., Wu, L., and Han, W. (2023). Ferroptosis triggered by STAT1- IRF1-ACSL4 pathway was involved in radiation-induced intestinal injury. *Redox Biol.* 66, 102857–112317. doi:10.1016/j.redox.2023.102857

Konwar, A., Gogoi, N., Majumdar, G., and Chowdhury, D. (2015). Green chitosan-carbon dots nanocomposite hydrogel film with superior properties. *Carbohydr. Polym.* 115, 238–245. doi:10.1016/j.carbpol.2014.08.021

Li, H., Dou, Y., Yang, H., Xing, H., Zhu, C., Wang, T., et al. (2024c). Ce6-modified Fe ions-doped carbon dots as multifunctional nanoplatform for ferroptosis and photodynamic synergistic therapy of melanoma. *J. Nanobiotechnology* 22, 100–123. doi:10.1186/s12951-024-02346-2

Li, H., Wu, Y., Xu, Z., and Wang, Y. (2024a). Controllable preparation of a Cu NCs@ Zn-mof hybrid with dual emission induced by an ion exchange strategy for the detection of explosives. *ACS Sensors* 9 (9), 4701–4710. doi:10.1021/acssensors.4c01093

Li, Q., Zhou, M., Yang, M., Yang, Q., Zhang, Z., and Shi, J. (2018). Induction of long-lived room temperature phosphorescence of carbon dots by water in hydrogen-bonded matrices. *Nat. Commun.* 9 (1), 734. doi:10.1038/s41467-018-03144-9

Li, X., Luo, J. Q., Liao, X. Q., Zhang, S., Yang, L. F., Wu, T., et al. (2024b). Allicin inhibits the growth of HONE-1 and HNE1 human nasopharyngeal carcinoma cells by inducing ferroptosis. *Neoplasma* 71 (03), 243–254. doi:10.4149/neo_2024_240108n8

Liu, J., Fan, Y. Q., Zhang, Q. P., Yao, H., Zhang, Y. M., Wei, T. B., et al. (2019). Super metal hydrogels constructed from a simple tripodal gelator and rare earth metal ions and its application in highly selective and ultrasensitive detection of histidine. *Soft Matter* 15 (5), 999–1004. doi:10.1039/c8sm02319k

Liu, J., Yang, B., Li, M., Li, J., and Wan, Y. (2020). Enhanced dual network hydrogels consisting of thiolated chitosan and silk fibroin for cartilage tissue engineering. *Carbohydr. Polym.* 227, 115335. doi:10.1016/j.carbpol.2019.115335

Liu, Y., Zhao, Y., Guo, S., Qin, D., Yan, J., Cheng, H., et al. (2024). Copper doped carbon dots modified bacterial cellulose with enhanced antibacterial and immune regulatory functions for accelerating wound healing. *Carbohydr. Polym.* 346, 122656–122677. doi:10.1016/j.carbpol.2024.122656

Mehwish, N., Dou, X., Zhao, Y., and Feng, C. L. (2019). Supramolecular fluorescent hydrogelators as bio-imaging probes. *Mater. Horizons* 6 (1), 14–44. doi:10.1039/c8mh01130c

Ni, P., Li, Q., Xu, C., Lai, H., Bai, Y., and Chen, T. (2019). Optical properties of nitrogen and sulfur co-doped carbon dots and their applicability as fluorescent probes for living cell imaging. *Appl. Surf. Sci.* 494, 377–383. doi:10.1016/j.apsusc.2019.07.196

Nishiyabu, R., Ushikubo, S., Kamiya, Y., and Kubo, Y. (2014). A boronate hydrogel film containing organized two-component dyes as a multicolor fluorescent sensor for heavy metal ions in water. *J. Mater. Chem. A* 2 (38), 15846–15852. doi:10.1039/c4ta03268c

Plappert, S. F., Liebner, F. W., Konnerth, J., and Nedelec, J. M. (2019). Anisotropic nanocellulose gel-membranes for drug delivery: tailoring structure and interface by sequential periodate-chlorite oxidation. *Carbohydr. Polym.* 226, 115306. doi:10.1016/j.carbpol.2019.115306

Qu, D., Zheng, M., Li, J., Xie, Z., and Sun, Z. (2015). Tailoring color emissions from N-doped graphene quantum dots for bioimaging applications. *Light Sci. and Appl.* 4 (12), e364. doi:10.1038/lsa.2015.137

Qu, K., Wang, J., Ren, J., and Qu, X. (2013). Carbon dots prepared by hydrothermal treatment of dopamine as an effective fluorescent sensing platform for the label-free detection of iron(III) ions and dopamine. *Chemistry* 19 (22), 7243–7249. doi:10.1002/chem.201300042

Ren, Z., Liu, X., Chu, H., Yu, H., Xu, Y., Zheng, W., et al. (2017). Carbon quantum dots decorated MoSe2 photocatalyst for Cr(VI) reduction in the UV-vis-NIR photon energy range. *J. Colloid Interface Sci.* 488, 190–195. doi:10.1016/j.jcis.2016.10.077

Sachdev, A., Matai, I., and Gopinath, P. (2016). Carbon dots incorporated polymeric hydrogels as multifunctional platform for imaging and induction of apoptosis in lung cancer cells. *Colloids Surf. B Biointerfaces* 141, 242–252. doi:10.1016/j.colsurfb.2016.01.043

Sahiner, N., Sel, K., Meral, K., Onganer, Y., Butun, S., Ozay, O., et al. (2011). Hydrogel templated CdS quantum dots synthesis and their characterization. *Colloids Surfaces A Physicochem. Eng. Aspects* 389 (1-3), 6–11. doi:10.1016/j.colsurfa.2011.09.006

Wang, G., Xie, L., Li, B., Sang, W., Yan, J., Li, J., et al. (2021). A nanounit strategy reverses immune suppression of exosomal PD-L1 and is associated with enhanced ferroptosis. *Nat. Commun.* 12 (1), 5733. doi:10.1038/s41467-021-25990-w

Wang, J., Ma, X., Wei, L., Zhu, X., Zhu, Y., Wang, G., et al. (2018a). Construction of high-strength p(HEMA-co-AA) fluorescent hydrogels based on modified carbon dots as chemically crosslinkers. *Colloid Polym. Sci.* 296 (4), 745–752. doi:10.1007/s00396-018-4287-x

Wang, K., Yuan, X., Guo, Z., Xu, J., and Chen, Y. (2014). Red emissive cross-linked chitosan and their nanoparticles for imaging the nucleoli of living cells. *Carbohydr. Polym.* 102, 699–707. doi:10.1016/j.carbpol.2013.10.100

Wang, N., Chai, H., Dong, X., Zhou, Q., and Zhu, L. (2018b). Detection of Fe(III) EDTA by using photoluminescent carbon dot with the aid of F(-) ion. *Food Chem.* 258, 51–58. doi:10.1016/j.foodchem.2018.03.050

Wang, X., Cao, L., Yang, S.-T., Lu, F., Meziani, M. J., Tian, L., et al. (2010). Bandgap-like strong fluorescence in functionalized carbon nanoparticles. *Angew. Chem. Int. Ed. Engl.* 49 (31), 5310–5314. doi:10.1002/anie.201000982

Wei, W., Xu, C., Ren, J., Xu, B., and Qu, X. (2012). Sensing metal ions with ion selectivity of a crown ether and fluorescence resonance energy transfer between carbon dots and graphene. *Chem. Commun. (Camb)* 48 (9), 1284–1286. doi:10.1039/c2cc16481g

Yao, L., Zhao, M. M., Luo, Q. W., Zhang, Y. C., Liu, T. T., Yang, Z., et al. (2022). Carbon quantum dots-based nanozyme from coffee induces cancer cell ferroptosis to activate antitumor immunity. *Acs Nano* 16 (6), 9228–9239. doi:10.1021/acsnano.2c01619

Yu, S., Chen, K., Wang, F., Zhu, Y., and Zhang, X. (2017). Polymer composite fluorescent hydrogel film based on nitrogen-doped carbon dots and their application in the detection of Hg(2+) ions. *Luminescence* 32 (6), 970–977. doi:10.1002/bio.3279

Zhang, H., Fei, J., Yan, X., Wang, A., and Li, J. (2015). Enzyme-responsive release of doxorubicin from monodisperse dipeptide-based nanocarriers for highly efficient cancer treatment *in vitro*. *Adv. Funct. Mater.* 25 (8), 1193–1204. doi:10.1002/adfm.201403119

Zhang, R., and Chen, W. (2014). Nitrogen-doped carbon quantum dots: facile synthesis and application as a "turn-off" fluorescent probe for detection of Hg2+ ions. *Biosens. Bioelectron.* 55, 83–90. doi:10.1016/j.bios.2013.11.074

Zhu, S., Meng, Q., Wang, L., Zhang, J., Song, Y., Jin, H., et al. (2013). Highly photoluminescent carbon dots for multicolor patterning, sensors, and bioimaging. *Angew. Chem. Int. Ed. Engl.* 52 (14), 3953–3957. doi:10.1002/anie.201300519

frontiers | Frontiers in Bioengineering and Biotechnology

TYPE Original Research
PUBLISHED 05 February 2025
DOI 10.3389/fbioe.2025.1535245

OPEN ACCESS

EDITED BY
Dan Lin,
Shanghai University of Medicine and Health Sciences, China

REVIEWED BY
Christiane Laranjo Salgado,
Universidade do Porto, Portugal
Martha Elena Diaz Hernandez,
Emory University, United States

*CORRESPONDENCE
Ji Chen,
jim117cj@sohu.com
Fang Jin,
jinfang@fmmu.edu.cn
Bing-Dong Sui,
bingdong@fmmu.edu.cn

†These authors have contributed equally to this work

RECEIVED 27 November 2024
ACCEPTED 15 January 2025
PUBLISHED 05 February 2025

CITATION
Liu J-N, Tian J-Y, Liu L, Cao Y, Lei X, Zhang X-H, Zhang Z-Q, He J-X, Zheng C-X, Ma C, Bai S-F, Sui B-D, Jin F and Chen J (2025) The landscape of cell regulatory and communication networks in the human dental follicle.
Front. Bioeng. Biotechnol. 13:1535245.
doi: 10.3389/fbioe.2025.1535245

The landscape of cell regulatory and communication networks in the human dental follicle

Jia-Ning Liu[1,2†], Jiong-Yi Tian[1†], Lu Liu[1,2], Yuan Cao[1,2], Xiao Lei[1,2], Xiao-Hui Zhang[1,2], Zi-Qi Zhang[1,2], Jun-Xi He[1,2], Chen-Xi Zheng[1], Chao Ma[1], Sheng-Feng Bai[1], Bing-Dong Sui[1*], Fang Jin[2*] and Ji Chen[1,3*]

[1]State Key Laboratory of Oral & Maxillofacial Reconstruction and Regeneration, National Clinical Research Center for Oral Diseases, Shaanxi International Joint Research Center for Oral Diseases, Center for Tissue Engineering, School of Stomatology, The Fourth Military Medical University, Xi'an, Shaanxi, China, [2]State Key Laboratory of Oral & Maxillofacial Reconstruction and Regeneration, National Clinical Research Center for Oral Diseases, Shaanxi Clinical Research Center for Oral Diseases, Department of Orthodontics, School of Stomatology, The Fourth Military Medical University, Xi'an, Shaanxi, China, [3]Department of Oral Implantology, School of Stomatology, The Fourth Military Medical University, Xi'an, Shaanxi, China

Introduction: The dental follicle localizes the surrounding enamel organ and dental papilla of the developing tooth germ during the embryonic stage. It can differentiate and develop to form the periodontal ligament, cementum, and alveolar bone tissues. Postnatally, the dental follicle gradually degenerates, but some parts of the dental follicle remain around the impacted tooth. However, the specific cellular components and the intricate regulatory mechanisms governing the postnatal development and biological function of the dental follicle have not been completely understood.

Methods: We analyzed dental follicles with single-cell RNA sequencing (scRNA-seq) to reveal their cellular constitution molecular signatures by cell cycle analysis, scenic analysis, gene enrichment analysis, and cell communication analysis.

Results: Ten cell clusters were identified with differential characteristics, among which immune and vessel-related cells, as well as a stem cell population, were revealed as the main cell types. Gene regulatory networks (GRNs) were established and defined four regulon modules underlying dental tissue development and microenvironmental regulation, including vascular and immune responses. Cell–cell communication analysis unraveled crosstalk between vascular and immune cell components in orchestrating dental follicle biological activities, potentially based on COLLAGAN-CD44 ligand–receptor pairs, as well as ANGPTL1-ITGA/ITGB ligand–receptor pairs.

Conclusion: We establish a landscape of cell regulatory and communication networks in the human dental follicle, providing mechanistic insights into the cellular regulation and interactions in the complex dental follicle tissue microenvironment.

KEYWORDS

dental follicle, single-cell RNA sequencing, gene regulatory networks, cell–cell communication, vasculature, immune

1 Introduction

The dental follicle is a layer of loose connective tissue that surrounds the developing tooth germ or the impacted tooth (Zeng et al., 2022). During the embryonic stage, the dental follicle surrounding the enamel organ and dental papilla is composed of ectomesenchymal cells that are derived from the neural crest cells (Zeng et al., 2022; Zhou et al., 2019). These cells, known as dental follicle cells (DFCs), are multipotent stem cells capable of differentiating into various cell types and finally to form the periodontal ligament, cementum, and alveolar bone tissues (J et al., 2021). In addition, the dental follicle is essential for tooth eruption as it regulates the resorption of bone to form an eruption pathway and provides the driving force for the tooth to move toward its functional position in the oral cavity (Shiyan et al., 2016; Wise, 2009). Postnatally, the dental follicle gradually degenerates, and the periodontal tissues differentiate and mature. Some parts of the dental follicle remain due to the impacted state (Yang et al., 2019). However, the specific cellular components and the intricate regulatory mechanisms governing the post-natal development and function of the dental follicle are not yet completely understood.

Single-cell RNA sequencing (scRNA-seq) has emerged as a powerful tool for dissecting cellular heterogeneity within complex tissues, allowing for a comprehensive understanding of cellular subpopulations and their functional roles (Vallejo et al., 2021; Wen et al., 2022). So far, scRNA-seq has been employed to investigate the human tooth germ derived from the developing third molar (Shi et al., 2021). A large number of immune cells were discovered in the tooth germ of the human third molar, highlighting the significant immune characteristics of the human third molar in the adult stage, and these cells regulate other dental cells through signaling pathways such as TGF-β, TNF, and IL-1 (Shi et al., 2021). Comparative analysis between human and mouse teeth revealed both parallels and divergences in tissue heterogeneity, emphasizing the molecular differences and species-specific cell subtypes (Krivanek et al., 2020). These findings underscored the utility of scRNA-seq in elucidating the intricate signaling networks that govern essential biological processes in human teeth postnatally.

The dental follicle, a reservoir of odontogenic mesenchymal stem cells, plays a pivotal role in tooth development and periodontal tissue regeneration (Yang et al., 2019; Guo et al., 2009). Under physiological conditions, these dental MSCs contribute to angiogenesis, a critical process in tissue regeneration (Li et al., 2022). Conversely, in pathological states, they participate in immune modulation, highlighting their dual role in maintaining homeostasis and tissue regeneration (Li et al., 2023). Moreover, vascular and immune cell components also collaborate and contribute to dental tissue homeostasis, but the specific mechanisms remain not fully understood (Zarubova et al., 2022). Understanding the transcriptomic landscape of the dental follicle is not only essential for uncovering the molecular regulatory mechanisms but also harnessing its regenerative potential (Zarubova et al., 2022; Azari et al., 2023). The ability to modulate the behavior of dental follicle cells offers a promising avenue for developing novel therapeutic strategies in regenerative dentistry and medicine. By identifying key regulatory nodes within the dental follicle transcriptome, we can potentially direct cells toward desired lineage commitments, enhancing vascularization, and immune modulation for tissue repair.

In this study, we aimed to explore the transcriptome heterogeneity, cell regulatory network, and cell–cell communication of the dental follicle to uncover the molecular signatures associated with its angiogenesis and immunomodulatory functions. We performed scRNA-seq analysis of the human dental follicle and revealed the cellular composition and heterogeneity of this tissue. We further identified specific regulons governing the progenitor cell destiny and discovered immune and vascular cell components with reciprocal signaling to maintain the dental follicle niche. Collectively, our results unravel the previous unrecognized cellular landscape of the dental follicle at the postnatal stage and provide a comprehensive understanding of the potential mechanisms governing cellular biological activities and cell communication to function synergistically, highlighting the potential intervention targets like COLLAGAN-CD44 and ANGPTL1-ITGA/ITGB ligand–receptor pairs to promote tissue regeneration.

2 Materials and methods

2.1 Data availability

The raw sequence data analyzed in this research have been uploaded into Genome Sequence Archive (Chen et al., 2021) in National Genomics Data Center (Xue et al., 2022), China National Center for Bioinformation/Beijing Institute of Genomics, Chinese Academy of Sciences, and the data under accession HRA008022 will be available on 2026-07-12 automatically or will be made available at https://ngdc.cncb.ac.cn/search/specific?db=hra&q=HRA008022 upon publication.

2.2 Human tissue harvest and preparation

All donors were patients in the School of Stomatology, The Fourth Military Medical University, and have signed informed consent to this study. Experimental procedures of human samples were approved by the Ethics Committee of The Fourth Military Medical University with the approval number IRB-REV-2022187. We collected dental follicle tissues from six impacted third molars of patients aged 18–22 years. Dental follicles were harvested based on inclusion criteria as follows: patients had no history of pain or infection around the impacted teeth, and clinical examination showed no swelling, redness, or tenderness in the pericoronal tissues of the third molars (Table 1; Figures 1A, B). All the patients were examined by oral panorama before surgery, and radiographic examination revealed no abnormal low- or high-density shadows around the crown (Figure 1C). By flap reflection, bone removal, tooth sectioning, and luxation, we obtained the third molars with attached dental follicle tissue, which were immediately immersed in 10% alpha-minimum essential medium (α-MEM; 12571-048, Invitrogen, United States) and delivered to the laboratory in an ice box.

TABLE 1 Clinical characteristics of participants.

Sample	Gender	Age	Tooth location	Pain or infection history	Redness or swelling	Low-density shadow on oral panorama
1	Female	20	48	No	No	No
2	Male	19	48	No	No	No
3	Male	20	48	No	No	No
4	Female	21	38	No	No	No
5	Female	20	38	No	No	No
6	Male	20	38	No	No	No

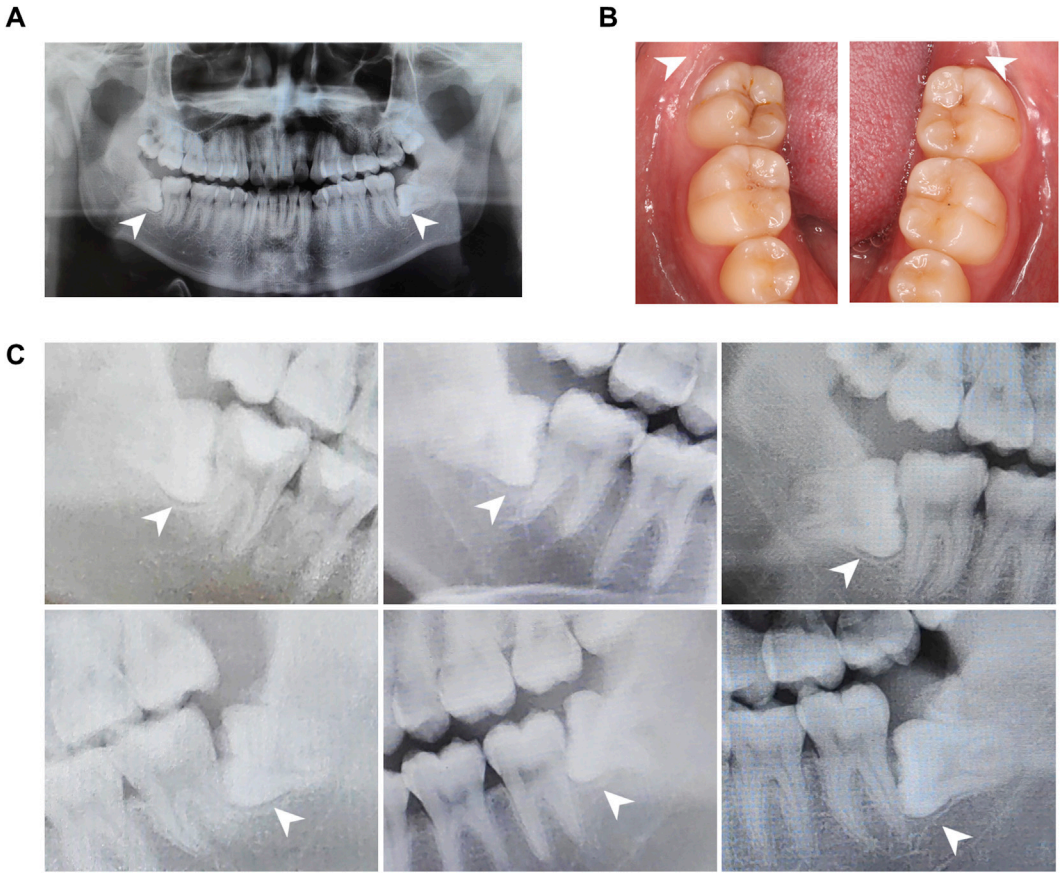

FIGURE 1
Panoramic radiographs and clinical views of the human dental follicle tissue. **(A)** A representative panoramic radiograph. **(B)**. Intraoral images illustrate non-inflammatory infiltration. **(C)**. Parts of panoramic radiographs of the human dental follicle tissue from a bite-wing perspective. Dental follicles from six wisdom teeth were identified without an abnormal low-density shadow.

2.3 ScRNA-seq analysis

Dental follicles were obtained by cutting off soft tissues around the teeth. The tissues were sectioned into 2-mm^3 pieces and rinsed twice with phosphate-buffered saline (PBS; P5493, Sigma-Aldrich, United States) before dental follicle tissues were initially dissociated into single cells using 0.02% Type I collagenase (17018029, Gibco, United States). Cells were barcoded with 10× gel beads and encapsulated in oil to form single-cell gel beads-in-emulsion (GEMs). Reverse transcription reactions were engaged barcoded full-length cDNA, followed by the disruption of emulsions using the recovery agent. Single-cell 3′ Reagent v3 Kits (1000268, 10× Genomics, United States) were used for scRNA-seq library construction. The sequencing was performed on Illumina Nova 6000 PE150 platform (Illumina, United States). Cell Ranger (version 7.0.1) software (10× Genomics, United States) was employed for

quality control and through comparisons between reads to the genome by the spliced transcript alignment to a reference (STAR) aligner. The cells that did not meet the criteria were discarded: 1) gene numbers >200, unique multiplex index (UMI) > 1000 and log10GenesPerUMI >0.7; 2) the UMI of mitochondrial genes <15% and hemoglobin genes <5%. Subsequently, the DoubletFinder package (version 2.0.3) was used to identify potential doublets (McGinnis et al., 2019). To obtain the normalized gene expression data, library size normalization was processed using the NormalizeData function. Specifically, the global-scaling normalization method "LogNormalize" normalized the gene expression measurements for each cell by the total expression, multiplied by a scaling factor (10,000 by default), and log-transformed the results.

2.4 Dimensionality reduction and clustering

Top 2000 highly variable genes (HVGs) were calculated using the Seurat function FindVariableGenes (mean.function = FastExpMean, dispersion.function = FastLogVMR). Principal component analysis (PCA) was performed to reduce the dimensionality with RunPCA function. Graph-based clustering was performed to cluster cells according to their gene expression profile with the FindClusters function. Cells were visualized using a 2-dimensional t-distributed stochastic neighbor embedding (t-SNE) algorithm with the RunTSNE function. The FindAllMarkers function (test.use = presto) was used to identify marker genes of each cluster. Differentially expressed genes (DEGs) were selected using the function FindMarkers (test.use = presto). *P* value <0.05 and |log2foldchange| > 0.58 were set as the thresholds for significantly differential expression.

2.5 Cell type annotation

By employing the SingleR package (version 1.4.1) based on a public reference dataset, we calculate the correlation between the expression profiles of the cells to be identified and the reference dataset, assigning the most correlated cell type from the reference dataset to the cells in question, thereby largely eliminating subjective human factors. The principle of identification involves calculating the Spearman correlation between the expression profiles of each cell in the sample and each annotated cell in the reference dataset, selecting the cell type with the highest expression correlation in the dataset as the final identified cell type. Finally, we manually correct the cell types based on the characteristic expression genes of common cells according to the previous acknowledgments made by the authorities.

2.6 Cell proportion analysis

The cell abundance is determined based on the number of cells included in each cell population. Data visualization libraries plotAbundance in the R package (4.0.3) is used to create a stacked bar chart that represents the proportion of each cell population.

2.7 Cell cycle analysis

The cell cycle phase of individual cells was inferred by Seurat (Butler et al., 2018) with CellCycleScoring function. The function in the Seurat package is designed to calculate cell cycle scores to individual cells based on the expression of classic genes that are indicative of different phases of the cell cycle, particularly the S phase and the G2/M phase. Concisely, these marker gene sets are inversely correlated with their expression levels; cells that do not express these marker genes are likely to be in the G1 phase.

2.8 Single-cell regulatory network inference and clustering (SCENIC) analysis

The SCENIC analysis, a tool for reconstructing gene regulatory networks (GRNs) and identifying cell states, was performed by the motifs database for RcisTarget and GRNboost (SCENIC (Aibar et al., 2017) version 1.1.2.2, which corresponds to RcisTarget 1.2.1 and AUCell 1.4.1) with the default parameters. In detail, we identified potential targets for each transcription factor based on the co-expression relationships between genes. Next, we identified TF binding motifs over-represented on a gene list with the RcisTarget package. Lastly, the activity of each group of regulons in each cell was scored by the AUCell package.

To evaluate the cell-type specificity of each predicted regulon, we calculated the regulon specificity score (RSS) which was based on the Jensen–Shannon divergence (JSD), a measure of the similarity between two probability distributions. Specifically, we calculated the JSD between each vector of binary regulon activity which overlaps with the assignment of cells to a specific cell type (Suo et al., 2018). The connection specificity index (CSI) for all regulons was calculated with the scFunctions (https://github.com/FloWuenne/scFunctions/) package.

2.9 Gene enrichment analysis

Gene enrichment analysis, specifically Gene Ontology (GO) enrichment analysis, is widely used to test the enrichment of certain functions or characteristics within a set of genes. It compares genes with the GO database to identify significantly enriched GO terms, thereby inferring the functions and relationships of genes with other genes. GO terms are categorized into three main aspects, namely, molecular function, biological process, and cellular component, which provide a broad visualization of gene activities and help us extract biological meaning after numerous hypothesis tests accurately. Product properties of regulons from each CSI module were analyzed based on the GO dataset. GO enrichment analysis was performed using the oeCloud tools at https://cloud.oebiotech.com.

2.10 Cell communication analysis

CellChat (Jin et al., 2021) (version 1.1.3) R package was used for prediction of cell–cell interactions in the dental follicle. After

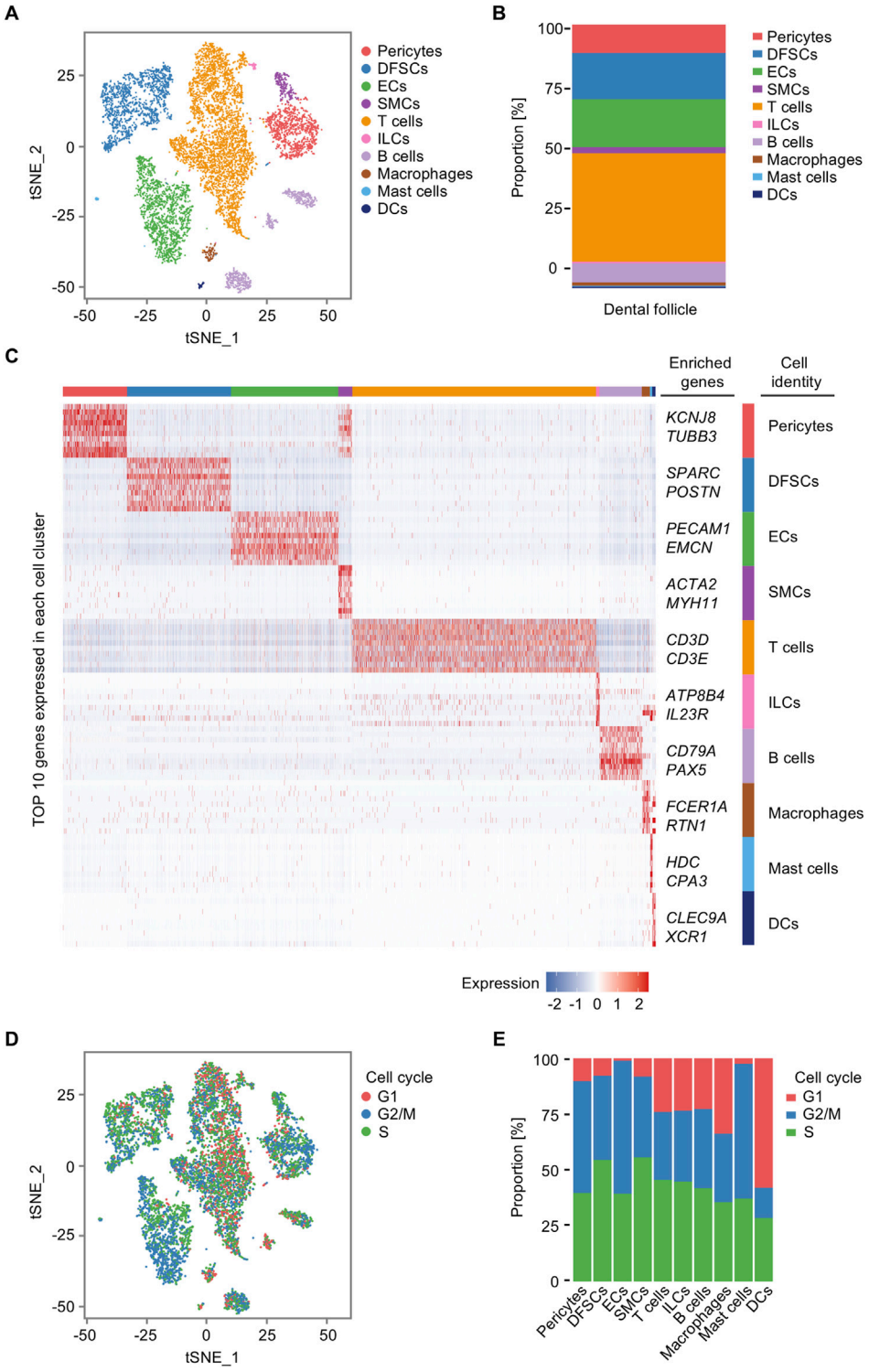

FIGURE 2
Single-cell transcriptomic profiling of the human dental follicle tissue. **(A)** t-distributed stochastic neighbor embedding (t-SNE) plot of 9,947 cells from the dental follicle colored by 10 cell-type annotations. **(B)** Bar plot of the relative abundance of different cell types in the dental follicle. **(C)** Heatmap of expression of top 10 genes in each cell cluster. **(D)** t-SNE plot of cell cycle analysis for all cells colored by G1, G2/M, and S annotations. **(E)** Bar plot of cell cycle states of each cell cluster in the dental follicle.

creating a CellChat object using the createCellChat function, the data were preprocessed with the identifyOverExpressedGenes, identifyOverExpressedInteractions, and projectData functions. Potential ligand–receptor interactions were inferred according to the calculated results of the computeCommunProb, filterCommunication, and computeCommunProbPathway

functions. Finally, the aggregateNet function was employed to aggregate the intercellular interaction network.

2.11 Immunofluorescence staining

For acquired human dental follicles, tissues were first fixed with 4% PFA for 12 h and dehydrated in 30% sucrose solution (Sigma-Aldrich, United States). Embedded in the O.C.T compound (4583, Sakura Finetek, United States), tissues were made to obtain 10-μm frozen sections by a freezing microtome (Leica, Germany). After permeabilization with 0.3% Triton X-100 (X100PC, Sigma-Aldrich, United States) and blocking with the goat serum (AR0009, BOSTER, China), sections were incubated with primary antibodies for FOXO3 (12829, CST, United States; diluted 1:400), RUNX3 (sc-376591, Santa Cruz, United States; diluted 1:100), CD31 (FAB3628G, R&D Systems, United States; diluted 1:100), CD31 (3528, CST, United States; diluted 1:400), F4/80 (14-4801-82, eBioscience, United States; diluted 1:100), COL1 (72026, CST, United States; diluted 1:100), CD44-PE (553134, BD Pharmingen, United States; diluted 1:100), CD20 (sc-7735, Santa Cruz, United States; diluted 1: 100), ANGPTL (sc-365146, Santa Cruz, United States; diluted 1: 100), and ITGB-FITC (11-0299-42, eBioscience, United States; diluted 1:100) at 4°C for 14 h. Fluorescence-conjugated secondary antibodies were then stained at 37°C for 1 h, followed by DAPI staining for 10 min or directly sealing slides with AntiFade Mounting Medium (HY-K1042, MedChemExpress, United States). The fluorescence images were captured with CLSM (Nikon, Japan).

3 Results

3.1 Profiling at the single-cell level depicts a landscape of human dental follicle cell population

At the beginning, we analyzed the diversification of cell populations in the representative postnatal human dental follicle. Through unsupervised marker analysis and manually rectified based on the characteristic expression genes, cells were identified into 10 clusters, including pericytes, dental follicle stem cells (DFSCs), endothelial cells (ECs), smooth muscle cells (SMCs), T cells, innate lymphoid cells (ILCs), B cells, macrophages, mast cells, and dendritic cells (DCs) (Figure 2A). Relative abundance of cell populations revealed an enrichment of T cells and B cells, along with ECs, pericytes, and DFSCs, as the main cell types in the dental follicle tissue (Figure 2B). The large proportion of T cells indicated that although the third molar is in an impacted state, immune cells in the dental follicle tissue may not be in silence and still be activated to assist in the tooth eruption. The profiles of gene expression were displayed as follows: *potassium inwardly rectifying channel subfamily J member 8 (KCNJ8)* and *tubulin beta 3 (TUBB3)* for pericytes (Ando et al., 2022), *secreted protein acidic and cysteine rich (SPARC)* and *periostin (POSTN)* for DFSCs (Shi et al., 2023; Wei et al., 2023), *platelet endothelial cell adhesion molecule 1 (PECAM1)* and *endomucin (EMCN)* for ECs (Cheung et al., 2015; Zhang et al., 2018; Zahr et al., 2016), *actin alpha 2 (ACTA2)* and *myosin heavy chain 11 (MYH11)* for SMCs (Yuan, 2015; von Kleeck et al., 2021), *CD3D* and *CD3E* for T cells (Liu et al., 2024), *ATPase phospholipid transporting 8B4 (ATP8B4)* and *interleukin 23 receptor (IL23R)* for ILCs (Sewell and Kaser, 2022; Croft et al., 2022), *CD79A* and *paired box 5 (PAX5)* for B cells (Küppers and Bräuninger, 2006; Xue et al., 2016), *Fc epsilon receptor Ia (FCER1A)* and *reticulon 1 (RTN1)* for macrophages (Dong et al., 2022), *histidine decarboxylase (HDC)* and *carboxypeptidase A3 (CPA3)* for mast cells (Takai et al., 2019; Atiakshin et al., 2022), and *C-type lectin domain-containing 9A (CLEC9A)* and *X-C motif chemokine receptor 1 (XCR1)* for DCs (Caminschi et al., 2008; Heger et al., 2023) (Figure 2C). Aside from the well-known markers in cell populations, we first defined based on the top 10 genes expressions that novel cell markers like *RTN* for macrophages, *ATP8B4* for ILCs, and *TUBB3* for pericytes. The proliferation activity of each cluster differed slightly (Figure 2D), and the ratio of cells in the S phase in DFSCs and SMCs was higher compared to that of other cell types (Figure 2E). The S phase is the stage of the cell cycle where DNA replication occurs (Bertoli et al., 2013); therefore, a higher proportion of DFSCs and SMCs in the S phase indicated that these cell populations have a greater proliferative potential and play a more important role in tissue regeneration. Taken together, these results identify the cellular composition and cell-specific states in the human dental follicle.

3.2 Gene regulatory networks (GRNs) are identified to dictate the biological processes in the adult dental follicle

GRNs play a critical role in the regulation of cell activity. A collection of genes called regulon is regulated as a unit by the same regulatory element, typically a transcription factor (TF). SCENIC analysis was employed to depict the multiple cell type-specific regulons, thus comprehensively constructing GRNs in the dental follicle. In addition, regulon analysis has two metrics including the regulon-specific score (RSS) and the high regulon activity score (RAS). The RSS measures the specificity of a regulon to a particular cell type, indicating how unique the expression of a regulon is to that cell type. It is crucial for identifying cell type-specific regulatory programs. The RAS measures the activity of a regulon across cells, providing insights into which regulatory programs are active in different cellular contexts. As a result, TFs with high RAS were discovered in cell clusters in the adult dental follicle. For example, Forkhead box (FOX) members, such as FOXN3, FOXO3, and FOXP1, were highly enriched in ECs, T cells, and B cells, indicating that immune and vascular components were determined to regulate postnatal dental follicle development, functioning like the other FOX family members indispensable for the differentiation of periodontal tissue (Jing et al., 2022). Furthermore, CAMP responsive element-binding protein (CREB) family members, including CREB3L2 and CREB3L1, were enriched in DFSCs and B cells, and Kruppel-like factor (KLF) families, such as KLF3 and KLF5, were enriched in ECs and mast cells, also suggesting cross-cell-type regulations between

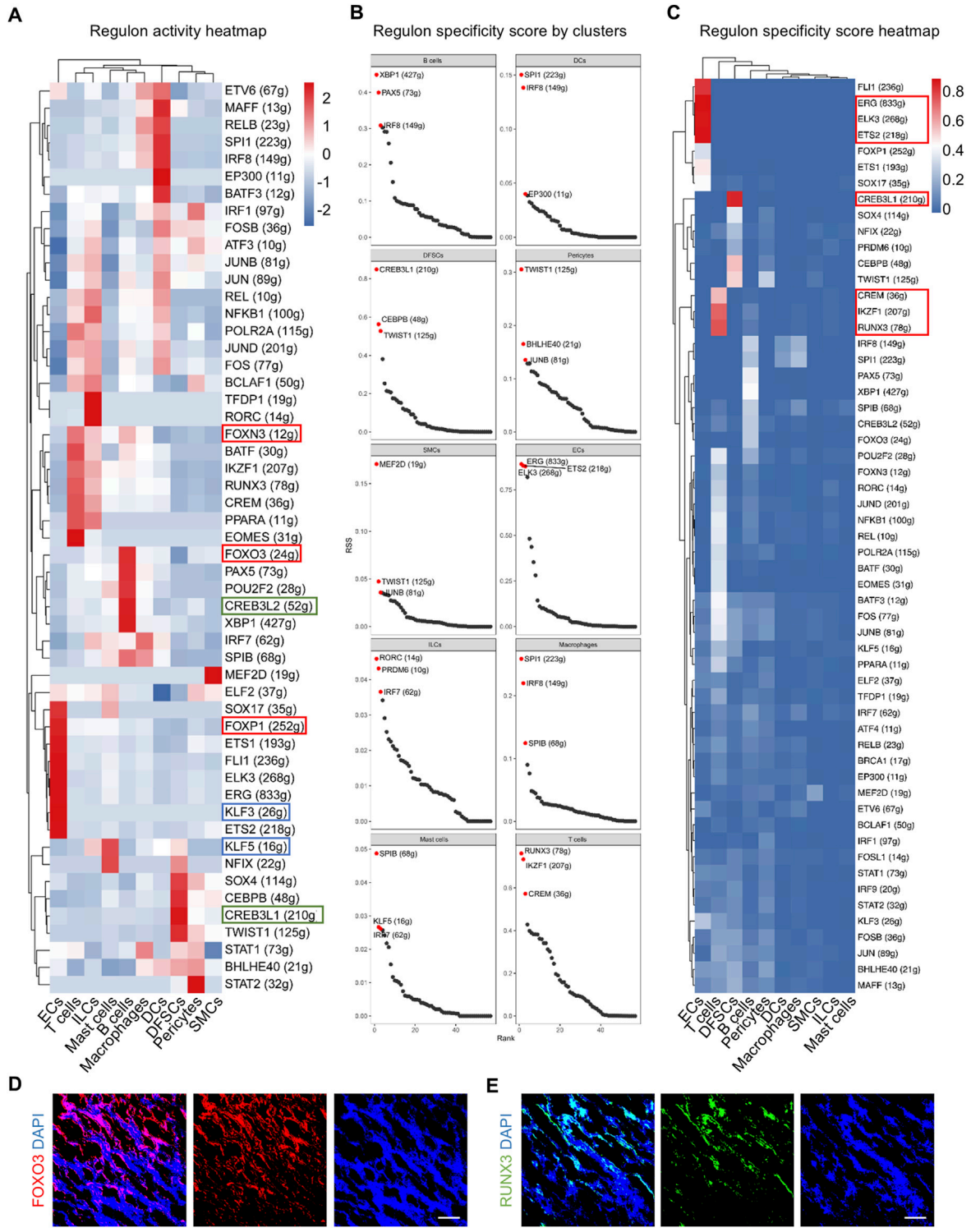

FIGURE 3
Identification of major regulons in the human dental follicle by SCENIC. **(A)** Heatmap of regulon activity score (RAS) for each cell cluster. **(B)** Scatter plot of regulon specificity score (RSS) for the regulons with the highest specific correlation in each cell cluster. Red dots indicating the top three regulons with the highest RSS. **(C)** Heatmap of RSS in each cell cluster. **(D)** Immunofluorescence images showing validation of FOXO3 expressed in the dental follicle. Scale bar, 100 μm. **(E)** Immunofluorescence images showing validation of RUNX3 expressed in the dental follicle. Scale bar, 100 μm.

vascular cells and immune cells (Figure 3A). Specific regulons to each cell cluster were also identified based on the RSS (Figure 3B). Especially, regulons of ECs were among the most specific in cell populations, such as E-26 transformation-specific (ETS) transcription factors (Figure 3C). T cells were specifically governed by IKAROS family zinc finger 1 (IKZF1) and Runt-

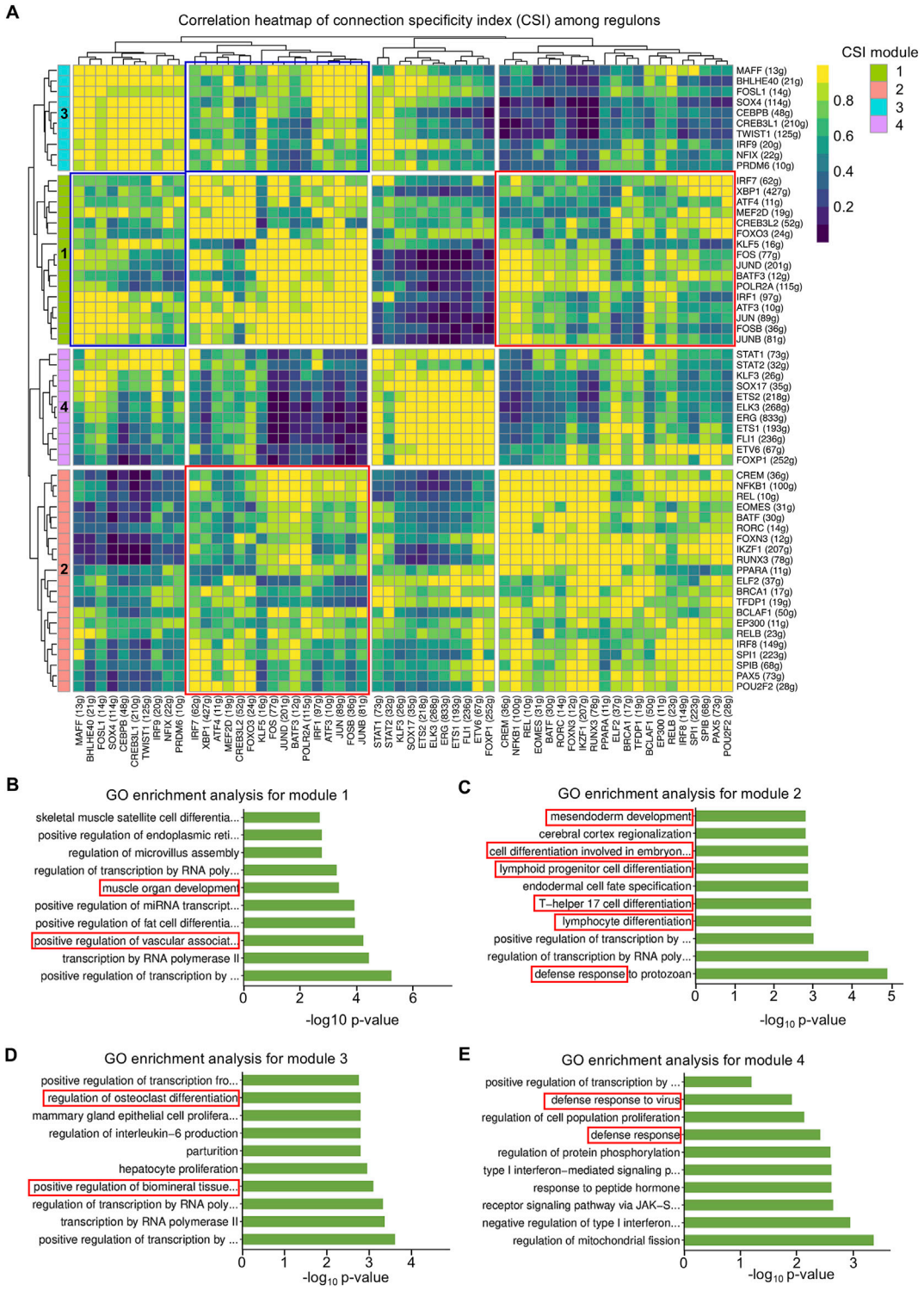

FIGURE 4
Regulon modules function in similar modes to regulate the downstream effect. **(A)** Matrix of inter-regulon expression correlation analysis showing four modules according to the connection specificity index (CSI). **(B)** Bar plot of Gene Oncology (GO) enrichment analysis for transcription factors (TFs) in module 1. **(C)** Bar plot of GO enrichment analysis for TFs in module 2. **(D)** Bar plot of GO enrichment analysis for TFs in module 3. **(E)** Bar plot of GO enrichment analysis for TFs in module 4.

related transcription factor 3 (RUNX3), and DFSCs were governed specifically by CREB3L1 (Figure 3C). It is inferred that CREBL3L might regulate B cells and DFSCs to participate in periodontal bone tissue differentiation under the immune responses. Immunofluorescence images confirmed the FOXO3 and RUNX3 expressed widely in the dental follicle

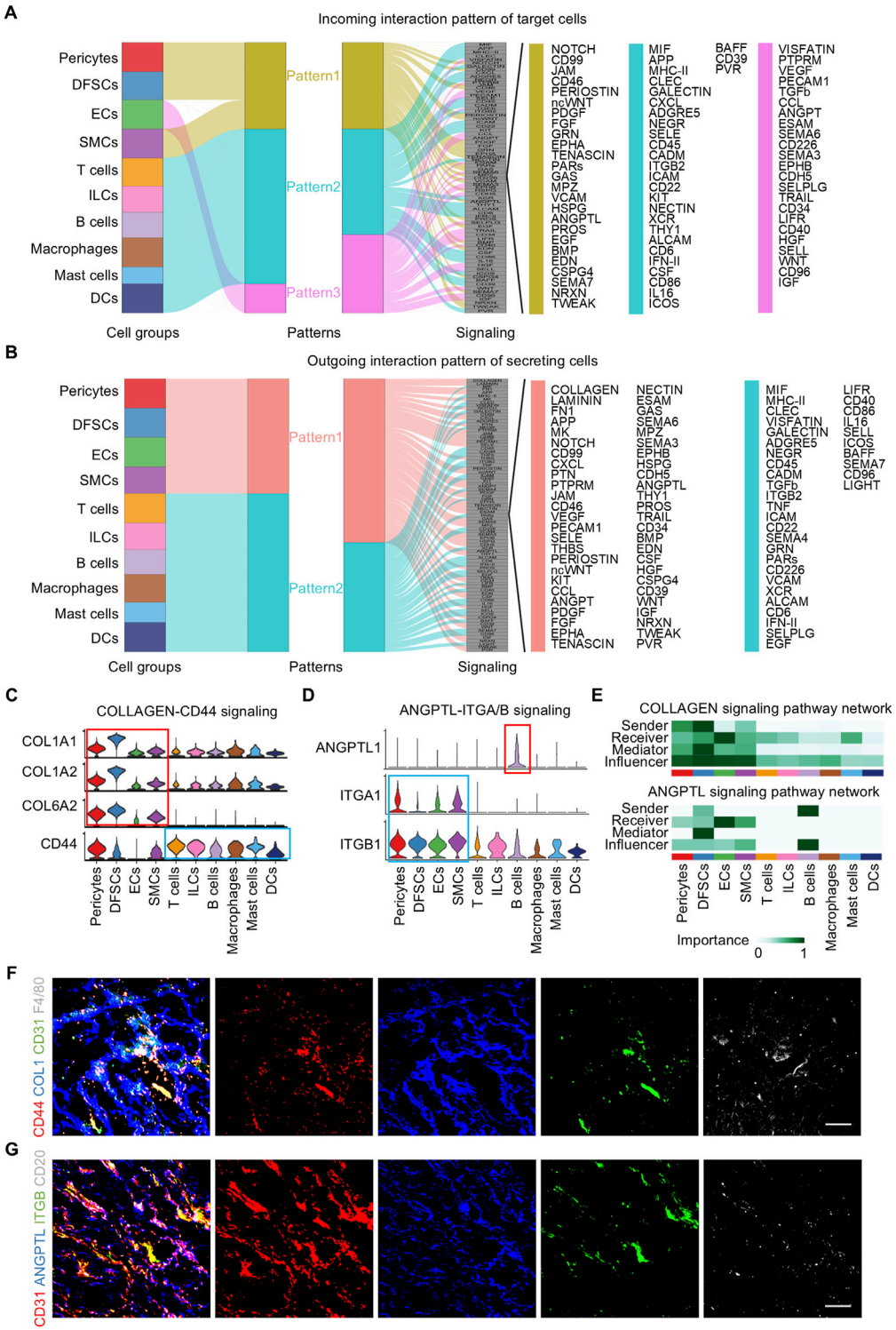

FIGURE 5
Pattern of cell communication in the human dental follicle. **(A)** Inferred incoming communication pattern of target cells. **(B)** Inferred outgoing communication pattern of secreting cells. **(C)** Expression distribution of COLLAGEN signaling genes. **(D)** Expression distribution of ANGPTL signaling genes. **(E)** Heatmap of the relative importance of each cell cluster based on the computed network centrality measures of COLLAGEN and ANGPTL signaling. **(F)** Immunofluorescence images showing validation of COL1 (blue), CD31 (green), F4/80 (gray), and CD44 (red) in dental follicles. Scale bar, 100 μm. **(G)** Immunofluorescence images showing validation of CD31 (red), ANGPTL (blue), ITGB (green), and CD20 (gray) in dental follicles. Scale bar, 100 μm.

(Figures 3D, E). Collectively, GRNs are identified in the postnatal human dental follicle, which dictate the complex cellular activities.

3.3 Regulon modules are classified to synergistically perform specific functions

Next, regulons were divided into four modules according to specific functions. The high connection specificity index (CSI) provides information about the co-regulation and potential collaboration of different regulons. Regulons with high CSI values are likely to be involved in similar cellular functions and may co-regulate downstream genes and cell function (Figure 4A). In detail, module 1 contained CSI regulons in roles characterized by muscle organ development and vascular-associated differentiation (Figures 4A, B). Module 2 was involved in regulating mesendoderm development and lymphoid progenitor differentiation (Figures 4A, C). Module 3 was discovered to take part in the mineralization process, as well as osteoclast differentiation (Figures 4A, D). Finally, module 4 was unraveled to contribute to immune responses (Figures 4A, E). In addition, modules 1 and 2 had a close correlation which might reflect the synergistic effect between vascular and immune cell development (Figure 4A), and modules 1 and 3 potentially cooperated to regulate the coupling of vascular and biomineralized activities (Figure 4A). It was supported that VEGF factors secreted by ECs influence the activity of osteoblasts and osteoclasts, further integrating vascular and biomineralized activities (Song et al., 2023). Importantly, vascular ECs influence immune cell migration and activation, while immune cells affect vascular function and remodeling. This interaction is particularly involved in processes such as inflammation, wound healing, and tissue regeneration (Silberman et al., 2021). Together, regulon modules are defined according to biological functions, part of which has concerted actions in the dental follicle tissue.

3.4 Communication pattern analysis reveals the interrelationship between immune and vascular niche components

Cell–cell communication patterns refer to the various ways in which cells interact and communicate with each other, which is essential for the coordination of cellular activities in multicellular organisms. Outgoing patterns reveal how sender cells (cells as signal sources) coordinate with each other and with certain signaling pathways to transmit messages to target cells. Incoming patterns show how target cells (cells as signal receivers) coordinate with each other and with certain signaling pathways to react to the signals they receive. To explore how multiple cell clusters and signaling pathways collaborate in the dental follicle, CellChat analysis was employed which uncover three communication patterns for the incoming signaling pathway of target cells and two patterns for the outgoing signaling pathway of secreting cells (Figures 5A, B). Specifically, incoming signaling of pericytes, DFSCs, and SMCs was driven by pattern #1, which included pathways including NOTCH, PERIOSTIN, fibroblast growth factor (FGF), angiopoietin (ANGPT), and BMP, which guided angiogenesis and osteogenesis (Figure 5A) (Ramasamy et al., 2014; Rahman et al., 2015). All immune cells were characterized by pattern #2 of incoming signaling, represented by C-X-C motif chemokine ligand (CXCL), Integrin subunit beta 2 (ITGB2), and interferon-II (IFN-II) pathways (Figure 5A), which mediated immune cell activation and migration (Zhang et al., 2021). ECs solely dictated pattern #3 of incoming signaling, including vascular endothelial growth factor (VEGF), PECAM1, and ANGPT pathways (Figure 5A), which were known for their importance in vessel formation (Eklund and Saharinen, 2013; Luo et al., 2023). For outgoing signaling, pericytes, DFSCs, SMCs, and ECs were categorized into pattern #1, while immune cells were grouped into pattern #2 (Figure 5B).

Considering that immune and vascular cells represent critical niche components of the dental follicle tissue and that they were regulated by several overlapping regulons, immune and vascular interactions were further investigated. The inferred ligand–receptor pairs were shown (Figures 5C, D). In detail, the COLLAGEN vascular signaling also participated in launching downstream immune reactions via the CD44 receptor (Figure 5C). In turn, immune cells sent signals to vascular components. B cells were the representative secreting cells of vessel-regulating ANGPTL1 (Figure 5D). CellChat analysis enables the identification of dominant senders, receivers, mediators, and influencers in cell–cell communication networks by multiple network centrality analysis for each cell population. Network centrality analysis of the inferred communication signaling confirmed that ECs were the most prominent source of COLLAGEN and ANGPTL ligands for immunomodulation (Figure 5E). Notably, ECs were also the dominant mediator of regulating immune responses and the receiver of immunoregulatory information (Figure 5E), suggesting its role as a gatekeeper of cell–cell communication in the adult dental follicle microenvironment. Within the immune cells, B cells were the main signal senders functioning in ANGPTL signaling interactions (Figure 5E). Immunofluorescence validated that the reciprocal co-localization of CD44 on macrophages labeled with F4/80 and COL1 secreted by ECs labeled with CD31, as well as ITGB on ECs labeled with CD3 and ANGPTL secreted by B cells labeled with CD20 (Figures 5F, G), strongly confirming the interactions between the aforementioned receptor–ligand pairs and the interactions between ECs and immune cells. Taken together, these results reveal the interrelationship between immune and vascular components of the dental follicle tissue, which potentially regulates the niche homeostasis and responses.

4 Discussion

The heterogeneity of cells, cell–cell interactions and their gene regulatory networks construct a complicated but elaborate information landscape. However, the specific mechanisms of coordination among diverse cell populations in the specific cellular components and the intricate regulatory mechanisms governing the postnatal biological activities and function of the dental follicle remain unclarified. In this study, we performed scRNA-seq analysis to reveal the cell composition within the dental follicle tissue and highlight the importance of GRNs and cell–cell interactions in the dental follicle microenvironment.

Through a cohort of bioinformatic experiments, we showed the gene regulatory and signaling network underlying cell lineage diversification and crosstalk. These results serve as an important cornerstone for future studies in the mechanisms regulating dental tissue regeneration through regulating immune and vascular reactions.

GRNs are complex networks consisting of interacting molecules that dictate the biological activities in tissues and organs. Different tissues and organs have their own specific GRNs, and these networks control tissue-specific gene expression patterns. Previous studies have identified that GRNs are pivotal for tooth development and patterning in the enamel knot of the dental epithelium and dental mesenchyme, especially known as Eda signaling, DLX signaling, and FOX signaling (Jing et al., 2022; Tucker et al., 2000). In this study, we have focused on GRNs in the adult dental follicle across the human third molar for the first time. Consistent with previous findings, we revealed that FOX, KLF, and CREB3L families function importantly in the tissue homeostasis through regulating DFSCs, ECs, T cells, and B cells in the dental follicle (Lam et al., 2013). In the view of evolutionary conservativeness of FOX across different species, we complement that FOX families are crucial for regulating a wide variety of biological functions both in mouse dental development and in the human postnatal dental follicle (Golson and Kaestner, 2016). However, it is controversial that FOXO1 is beneficial or detrimental for alveolar bone reconstruction. On one hand, patients suffered from periodontitis had a low expression of FOXO1 and the combination of FOXO1 to METTL3 regulates PDLSCs to promote osteogenesis through the PI3K/AKT signaling pathway (Wang Q. et al., 2023). On the other hand, FOXO1 deficiency greatly rescued osteoblast differentiation and prevented the progression of age-related alveolar bone resorption (Wang et al., 2023b). On the basis of SCENIC analysis, we uncover that FOXN3 and FOXO3 may play vital roles in immune cell regulation in the dental follicle tissue (Zhu et al., 2022), FOXP1 might function to affect the vascular microenvironment. In addition, CREBL3L might participate in periodontal bone tissue differentiation in accordance with its ability to promote bone morphogenesis and regulate the expression of hypoxia-inducible factor-1α (HIF-1α) improving bone angiogenesis (Zhao et al., 2024; Cao, 2021). Furthermore, we found that FOXO3 is expressed widely in the dental follicle, which meant its large requirement in maintaining tissue homeostasis. Nevertheless, the specific effect of FOX families within adult dental follicle should be emphasized deeply so as to achieve precise regulation for medical practice. Accordingly, systematic explanations for GRNs contribute to understand the key mechanisms of coordinated and orderly regulation of biological process, which also enlighten potential new strategies for regenerative medicine and disease treatment (Sadier et al., 2020).

Noticeably, various immune cells are involved and exert important functions, yet their specific signaling of function remains poorly understood. A previous report has analyzed human tooth germs comparatively at two different stages at the single-cell level, which indicates T cells, neutrophils, and macrophages as the main immune cell types in human developing tooth germs (Shi et al., 2021). In line with their findings, we also defined various immune cells within the dental follicle at the postnatal stage, and particularly T cells had the largest proportion. However, intercellular interaction patterns are only focused on the limited subpopulations of T cells or non-T immune cell subpopulations, revealing that T cells exhibited strong communication with osteoclasts specifically by signals from CCL3/CCL4/CCL5 to CCR1/CCR5 (Shi et al., 2021). Complementary to the communication pattern contributing to bone resorption, we provided a novel perspective on the interaction relationship between immune cells and vascular cells, on the basis of collaborated CSI regulon modules 1 and 2 potentially regulating their development. The recruitment of immune cells has been underscored remarkably playing a role in inflammatory responses, angiogenesis, and tissue remodeling (Zarubova et al., 2022). The collaboration of neutrophils and macrophages leads to a sufficient revascularization of implanted biomaterials (Lin et al., 2017). Moreover, M2 macrophages produce MMP-9 to remodel the ECM and release proangiogenic factors like VEGF, TGF-β, and PDGF important for vascular cell recruitment and consequent blood vessel stabilization (Ebrahem et al., 2010; Kwee and Mooney, 2015). Recently, proangiogenic macrophages (PraM), a new subpopulation in macrophages, has been found widely distributed around vessels in multiple organs and play an important role in regulating angiogenesis (Wang et al., 2023c). In addition, monocytes have been recognized as the pioneer to lead and prepare a favorable microenvironment for angiogenesis through migrasomes enriched in angiogenic factors (Zhang et al., 2022). However, there is still lack of evidence about vascular microenvironment modulating the formation or recruitment of immune cells during human tissue repair. In our study, ligand–receptor pair analysis and immunofluorescence staining outcome indicated that ECs are co-localized with macrophages. Collagen as a major component of the ECM of the vessel wall is not only crucial for maintaining vascular integrity and elasticity (He et al., 2022), but it can be inferred that COL1 originating from ECs interacted with receptor ITGB on the macrophages and induced reciprocal recruitment to form an assembly. Importantly, the ECM could shape immune cell phenotypes (Jürgensen et al., 2020), beneficial for regeneration accompanied by modulation of the immune response in the host (Xie et al., 2021). Our analysis also discovered the role of B cells communicating with ECs through ANGPTL-ITGA/B ligand–receptor pairs in regeneration promotion effect. In accordance with previous findings, it has been illuminated that mature naïve B cells enhance angiogenesis and accelerate tissue regeneration by either secreting pro-angiogenic mediators such as VEGF or TGF-β (Yang et al., 2013; Iwata et al., 2009). Future research studies are still necessitated to provide direct evidence to validate the vascular cells regulating the immune cells when applied to tissue regeneration with target regulation.

It should be noted that there is variability in the sample collecting stages. Despite our efforts to select samples that met similar criteria, the fact that they were not acquired completely homogenous since tooth developmental stages exhibit heterogeneity, and it is difficult to ensure all eligible samples collected simultaneously could introduce biases into our analysis. This non-uniformity may have limitations on detecting lowly expressed genes, potentially leading to the loss of significant information. Furthermore, although our study detected a substantial number of immune cells and explored their interactions with vascular cells, the possibility of inflammatory infiltration in the dental follicle cannot be overlooked. Despite

these limitations, our study provides valuable insights into the complex interplay between immune cells and vascular components within the adult dental follicle. We hope that future research studies can build upon the conclusions drawn in this study to conduct further validation experiments, thereby obtaining a more comprehensive landscape of vascular and immune components in the dental follicle tissue.

5 Conclusion

This study depicts a detailed landscape of GRNs and cell–cell communication networks in the adult human dental follicle. Ten cell clusters are revealed by dimension reduction and clustering annotation. A series of complex GRNs and cell–cell communication networks are uncovered by SCENIC and CellChat analysis. Significantly, we emphasize the close connection between vascular and immune cells regulated by a similar set of regulons involved in vascular and immune cell development, specifically COLLAGAN-CD44 ligand–receptor pairs and ANGPTL1-ITGA/ITGB ligand–receptor pairs constructed the information bridge between immune cells and vascular cells, potentially promoting angiogenesis and immunoregulatory effect during tissue regeneration. These findings will inspire further application of dental follicle tissue in tissue engineering regeneration, as well as the potential targets for regulating the regenerative microenvironment through the mutual modulation of vessels and immunity.

Data availability statement

The datasets presented in this study can be found in online repositories. The names of the repository/repositories and accession number(s) can be found at: https://ngdc.cncb.ac.cn/search/specific?db=hra&q=HRA008022.

Ethics statement

The studies involving humans were approved by the Ethics Committee of The Fourth Military Medical University. The studies were conducted in accordance with the local legislation and institutional requirements. The participants provided their written informed consent to participate in this study.

Author contributions

J-NL: formal analysis, investigation, methodology, and writing–original draft. J-YT: formal analysis, investigation, methodology, and writing–original draft. LL: data curation, validation, and writing–review and editing. YC: data curation, validation, and writing–review and editing. XL: data curation, validation, and writing–review and editing. X-HZ: data curation, validation, and writing–review and editing. Z-QZ: data curation, validation, and writing–review and editing. J-XH: data curation, validation, and writing–review and editing. C-XZ: funding acquisition and writing–review and editing. CM: software, visualization, and writing–review and editing. S-FB: software, visualization, and writing–review and editing. B-DS: conceptualization, funding acquisition, project administration, resources, supervision, and writing–review and editing. FJ: conceptualization, funding acquisition, project administration, resources, supervision, and writing–review and editing. JC: conceptualization, funding acquisition, project administration, resources, supervision, and writing–review and editing.

Funding

The author(s) declare that financial support was received for the research, authorship, and/or publication of this article. This work was supported by grants from the National Natural Science Foundation of China (82170988, 82301028, 82471011, and 82371020), the Shaanxi Provincial Health Research and Innovation Platform Construction Plan (2024PT-04), the Young Science and Technology Rising Star Project of Shaanxi Province (2023KJXX-027 and 2024ZC-KJXX-122), the Key Research and Development Program of Shaanxi Province (2023-YBSF-489), the China Postdoctoral Science Foundation (BX20230485), and the "Rapid Response" Research projects (2023KXKT017 and 2023KXKT090).

Acknowledgments

The authors thank Shanghai OE Biotech Co., Ltd. for providing support in data analysis.

Conflict of interest

The authors declare that the research was conducted in the absence of any commercial or financial relationships that could be construed as a potential conflict of interest.

Generative AI statement

The author(s) declare that no Generative AI was used in the creation of this manuscript.

Publisher's note

References

Aibar, S., González-Blas, C. B., Moerman, T., Huynh-Thu, V. A., Imrichova, H., Hulselmans, G., et al. (2017). SCENIC: single-cell regulatory network inference and clustering. *Nat. Methods* 14, 1083–1086. doi:10.1038/nmeth.4463

Ando, K., Tong, L., Peng, D., Vázquez-Liébanas, E., Chiyoda, H., He, L., et al. (2022). KCNJ8/ABCC9-containing K-ATP channel modulates brain vascular smooth muscle development and neurovascular coupling. *Dev. Cell* 57, 1383–1399.e7. doi:10.1016/j.devcel.2022.04.019

Atiakshin, D., Kostin, A., Trotsenko, I., Samoilova, V., Buchwalow, I., and Tiemann, M. (2022). Carboxypeptidase A3—a key component of the protease phenotype of mast cells. *Cells* 11, 570. doi:10.3390/cells11030570

Azari, Z., Gorgani, S., Hosseini, S. A., Wang, A. Z., Kim, H. W., and Kargozar, S. (2023). The role of immune cells in therapeutic angiogenesis: concepts in tissue engineering. *Curr. Opin. Biomed. Eng.* 28, 100470. doi:10.1016/j.cobme.2023.100470

Bertoli, C., Skotheim, J. M., and de Bruin, R. A. M. (2013). Control of cell cycle transcription during G1 and S phases. *Nat. Rev. Mol. Cell Biol.* 14, 518–528. doi:10.1038/nrm3629

Butler, A., Hoffman, P., Smibert, P., Papalexi, E., and Satija, R. (2018). Integrating single-cell transcriptomic data across different conditions, technologies, and species. *Nat. Biotechnol.* 36, 411–420. doi:10.1038/nbt.4096

Caminschi, I., Proietto, A. I., Ahmet, F., Kitsoulis, S., Shin Teh, J., Lo, J. C. Y., et al. (2008). The dendritic cell subtype-restricted C-type lectin Clec9A is a target for vaccine enhancement. *Blood* 112, 3264–3273. doi:10.1182/blood-2008-05-155176

Cao, Y. (2021). The impact of the hypoxia-VEGF-vascular permeability on COVID-19-infected patients. *Explor. (Beijing)* 1, 20210051. doi:10.1002/EXP.20210051

Chen, T., Chen, X., Zhang, S., Zhu, J., Tang, B., Wang, A., et al. (2021). The genome sequence archive family: toward explosive data growth and diverse data types. *Genomics Proteomics Bioinforma.* 19, 578–583. doi:10.1016/j.gpb.2021.08.001

Cheung, K., Ma, L., Wang, G., Coe, D., Ferro, R., Falasca, M., et al. (2015). CD31 signals confer immune privilege to the vascular endothelium. *Proc. Natl. Acad. Sci. U. S. A.* 112, E5815–E5824. doi:10.1073/pnas.1509627112

Croft, C. A., Thaller, A., Marie, S., Doisne, J.-M., Surace, L., Yang, R., et al. (2022). Notch, RORC and IL-23 signals cooperate to promote multi-lineage human innate lymphoid cell differentiation. *Nat. Commun.* 13, 4344. doi:10.1038/s41467-022-32089-3

Dong, K., Chen, W., Pan, X., Wang, H., Sun, Y., Qian, C., et al. (2022). FCER1G positively relates to macrophage infiltration in clear cell renal cell carcinoma and contributes to unfavorable prognosis by regulating tumor immunity. *BMC Cancer* 22, 140. doi:10.1186/s12885-022-09251-7

Ebrahem, Q., Chaurasia, S. S., Vasanji, A., Qi, J. H., Klenotic, P. A., Cutler, A., et al. (2010). Cross-talk between vascular endothelial growth factor and matrix metalloproteinases in the induction of neovascularization *in vivo*. *Am. J. Pathology* 176, 496–503. doi:10.2353/ajpath.2010.080642

Eklund, L., and Saharinen, P. (2013). Angiopoietin signaling in the vasculature. *Exp. Cell Res.* 319, 1271–1280. doi:10.1016/j.yexcr.2013.03.011

Golson, M. L., and Kaestner, K. H. (2016). Fox transcription factors: from development to disease. *Development* 143, 4558–4570. doi:10.1242/dev.112672

Guo, W., He, Y., Zhang, X., Lu, W., Wang, C., Yu, H., et al. (2009). The use of dentin matrix scaffold and dental follicle cells for dentin regeneration. *Biomaterials* 30, 6708–6723. doi:10.1016/j.biomaterials.2009.08.034

He, W., Wang, Q., Tian, X., and Pan, G. (2022). Recapitulating dynamic ECM ligand presentation at biomaterial interfaces: molecular strategies and biomedical prospects. *Explor. (Beijing)* 2, 20210093. doi:10.1002/EXP.20210093

Heger, L., Hatscher, L., Liang, C., Lehmann, C. H. K., Amon, L., Lühr, J. J., et al. (2023). XCR1 expression distinguishes human conventional dendritic cell type 1 with full effector functions from their immediate precursors. *Proc. Natl. Acad. Sci. U. S. A.* 120, e2300343120. doi:10.1073/pnas.2300343120

Iwata, Y., Yoshizaki, A., Komura, K., Shimizu, K., Ogawa, F., Hara, T., et al. (2009). CD19, a response regulator of B lymphocytes, regulates wound healing through hyaluronan-induced TLR4 signaling. *Am. J. Pathology* 175, 649–660. doi:10.2353/ajpath.2009.080355

J, C., O, P., Cg, P., V, A., C, M., and D, D. (2021). Dental follicle cell differentiation towards periodontal ligament-like tissue in a self-assembly three-dimensional organoid model. *Eur. Cells and Mater.* 42, 20–33. doi:10.22203/eCM.v042a02

Jin, S., Guerrero-Juarez, C. F., Zhang, L., Chang, I., Ramos, R., Kuan, C.-H., et al. (2021). Inference and analysis of cell-cell communication using CellChat. *Nat. Commun.* 12, 1088. doi:10.1038/s41467-021-21246-9

Jing, J., Feng, J., Yuan, Y., Guo, T., Lei, J., Pei, F., et al. (2022). Spatiotemporal single-cell regulatory atlas reveals neural crest lineage diversification and cellular function during tooth morphogenesis. *Nat. Commun.* 13, 4803. doi:10.1038/s41467-022-32490-y

Jürgensen, H. J., van Putten, S., Nørregaard, K. S., Bugge, T. H., Engelholm, L. H., Behrendt, N., et al. (2020). Cellular uptake of collagens and implications for immune cell regulation in disease. *Cell Mol. Life Sci.* 77, 3161–3176. doi:10.1007/s00018-020-03481-3

Krivanek, J., Soldatov, R. A., Kastriti, M. E., Chontorotzea, T., Herdina, A. N., Petersen, J., et al. (2020). Dental cell type atlas reveals stem and differentiated cell types in mouse and human teeth. *Nat. Commun.* 11, 4816. doi:10.1038/s41467-020-18512-7

Küppers, R., and Bräuninger, A. (2006). Reprogramming of the tumour B-cell phenotype in Hodgkin lymphoma. *Trends Immunol.* 27, 203–205. doi:10.1016/j.it.2006.03.001

Kwee, B. J., and Mooney, D. J. (2015). Manipulating the intersection of angiogenesis and inflammation. *Ann. Biomed. Eng.* 43, 628–640. doi:10.1007/s10439-014-1145-y

Lam, E. W.-F., Brosens, J. J., Gomes, A. R., and Koo, C.-Y. (2013). Forkhead box proteins: tuning forks for transcriptional harmony. *Nat. Rev. Cancer* 13, 482–495. doi:10.1038/nrc3539

Li, P., Ou, Q., Shi, S., and Shao, C. (2023). Immunomodulatory properties of mesenchymal stem cells/dental stem cells and their therapeutic applications. *Cell Mol. Immunol.* 20, 558–569. doi:10.1038/s41423-023-00998-y

Li, Z., Wu, M., Liu, S., Liu, X., Huan, Y., Ye, Q., et al. (2022). Apoptotic vesicles activate autophagy in recipient cells to induce angiogenesis and dental pulp regeneration. *Mol. Ther.* 30, 3193–3208. doi:10.1016/j.ymthe.2022.05.006

Lin, R.-Z., Lee, C. N., Moreno-Luna, R., Neumeyer, J., Piekarski, B., Zhou, P., et al. (2017). Host non-inflammatory neutrophils mediate the engraftment of bioengineered vascular networks. *Nat. Biomed. Eng.* 1, 0081. doi:10.1038/s41551-017-0081

Liu, D., Hu, X., Chen, Z., Wei, W., and Wu, Y. (2024). Key links in the physiological regulation of the immune system and disease induction: T cell receptor -CD3 complex. *Biochem. Pharmacol.* 227, 116441. doi:10.1016/j.bcp.2024.116441

Luo, Z., Yao, J., Wang, Z., and Xu, J. (2023). Mitochondria in endothelial cells angiogenesis and function: current understanding and future perspectives. *J. Transl. Med.* 21, 441. doi:10.1186/s12967-023-04286-1

McGinnis, C. S., Murrow, L. M., and Gartner, Z. J. (2019). DoubletFinder: doublet detection in single-cell RNA sequencing data using artificial nearest neighbors. *Cell Syst.* 8, 329–337.e4. doi:10.1016/j.cels.2019.03.003

Rahman, M. S., Akhtar, N., Jamil, H. M., Banik, R. S., and Asaduzzaman, S. M. (2015). TGF-β/BMP signaling and other molecular events: regulation of osteoblastogenesis and bone formation. *Bone Res.* 3, 15005–15020. doi:10.1038/boneres.2015.5

Ramasamy, S. K., Kusumbe, A. P., Wang, L., and Adams, R. H. (2014). Endothelial Notch activity promotes angiogenesis and osteogenesis in bone. *Nature* 507, 376–380. doi:10.1038/nature13146

Sadier, A., Santana, S. E., and Sears, K. E. (2020). The role of core and variable Gene Regulatory Network modules in tooth development and evolution. *Integr. Comp. Biol.* 63, 162–175. doi:10.1093/icb/icaa116

Sewell, G. W., and Kaser, A. (2022). Interleukin-23 in the pathogenesis of inflammatory bowel disease and implications for therapeutic intervention. *J. Crohns Colitis* 16, ii3–19. doi:10.1093/ecco-jcc/jjac034

Shi, S., Li, Q., Liu, Y., Zhang, R., and Chen, H. (2023). SPARC promotes fibroblast proliferation, migration, and collagen production in keloids by inactivation of p53. *J. Dermatological Sci.* 109, 2–11. doi:10.1016/j.jdermsci.2023.01.002

Shi, Y., Yu, Y., Zhou, Y., Zhao, J., Zhang, W., Zou, D., et al. (2021). A single-cell interactome of human tooth germ from growing third molar elucidates signaling networks regulating dental development. *Cell Biosci.* 11, 178. doi:10.1186/s13578-021-00691-5

Shiyan, H., Nanquan, R., Shuhao, X., and Xiaobing, L. (2016). Research progress on the cellular and molecular mechanisms of tooth eruption. *Hua Xi Kou Qiang Yi Xue Za Zhi* 34, 317–321. doi:10.7518/hxkq.2016.03.020

Silberman, J., Jha, A., Ryan, H., Abbate, T., and Moore, E. (2021). Modeled vascular microenvironments: immune-endothelial cell interactions *in vitro*. *Drug Deliv. Transl. Res.* 11, 2482–2495. doi:10.1007/s13346-021-00970-1

Song, S., Zhang, G., Chen, X., Zheng, J., Liu, X., Wang, Y., et al. (2023). HIF-1α increases the osteogenic capacity of ADSCs by coupling angiogenesis and osteogenesis via the HIF-1α/VEGF/AKT/mTOR signaling pathway. *J. Nanobiotechnol* 21, 257. doi:10.1186/s12951-023-02020-z

Suo, S., Zhu, Q., Saadatpour, A., Fei, L., Guo, G., and Yuan, G.-C. (2018). Revealing the critical regulators of cell identity in the mouse cell atlas. *Cell Rep.* 25, 1436–1445.e3. doi:10.1016/j.celrep.2018.10.045

Takai, J., Ohtsu, H., Sato, A., Uemura, S., Fujimura, T., Yamamoto, M., et al. (2019). Lipopolysaccharide-induced expansion of histidine decarboxylase-expressing Ly6G+ myeloid cells identified by exploiting histidine decarboxylase BAC-GFP transgenic mice. *Sci. Rep.* 9, 15603. doi:10.1038/s41598-019-51716-6

Tucker, A. S., Headon, D. J., Schneider, P., Ferguson, B. M., Overbeek, P., Tschopp, J., et al. (2000). Edar/Eda interactions regulate enamel knot formation in tooth morphogenesis. *Development* 127, 4691–4700. doi:10.1242/dev.127.21.4691

Vallejo, J., Cochain, C., Zernecke, A., and Ley, K. (2021). Heterogeneity of immune cells in human atherosclerosis revealed by scRNA-Seq. *Cardiovasc Res.* 117, 2537–2543. doi:10.1093/cvr/cvab260

von Kleeck, R., Castagnino, P., Roberts, E., Talwar, S., Ferrari, G., and Assoian, R. K. (2021). Decreased vascular smooth muscle contractility in Hutchinson–Gilford Progeria Syndrome linked to defective smooth muscle myosin heavy chain expression. *Sci. Rep.* 11, 10625. doi:10.1038/s41598-021-90119-4

Wang, Q., Shi, W., Lin, S., and Wang, H. (2023a). FOXO1 regulates osteogenic differentiation of periodontal ligament stem cells through the METTL3 signaling pathway. *J. Orthop. Surg. Res.* 18, 637. doi:10.1186/s13018-023-04120-w

Wang, Z., Wu, Z., Wang, H., Feng, R., Wang, G., Li, M., et al. (2023c). An immune cell atlas reveals the dynamics of human macrophage specification during prenatal development. *Cell* 186, 4454–4471.e19. doi:10.1016/j.cell.2023.08.019

Wang, Z., Zhou, F., Feng, X., Li, H., Duan, C., Wu, Y., et al. (2023b). FoxO1/NLRP3 inflammasome promotes age-related alveolar bone resorption. *J. Dent. Res.* 102, 919–928. doi:10.1177/00220345231164104

Wei, X., Guo, S., Liu, Q., Liu, L., Huo, F., Wu, Y., et al. (2023). Dental follicle stem cells promote periodontal regeneration through periostin-mediated macrophage infiltration and reprogramming in an inflammatory microenvironment. *Int. J. Mol. Sci.* 24, 6353. doi:10.3390/ijms24076353

Wen, L., Li, G., Huang, T., Geng, W., Pei, H., Yang, J., et al. (2022). Single-cell technologies: from research to application. *Innov. (Camb)* 3, 100342. doi:10.1016/j.xinn.2022.100342

Wise, G. E. (2009). Cellular and molecular basis of tooth eruption. *Orthod. Craniofac Res.* 12, 67–73. doi:10.1111/j.1601-6343.2009.01439.x

Xie, L., Wang, G., Wu, Y., Liao, Q., Mo, S., Ren, X., et al. (2021). Programmed surface on poly(aryl-ether-ether-ketone) initiating immune mediation and fulfilling bone regeneration sequentially. *Innov. (Camb)* 2, 100148. doi:10.1016/j.xinn.2021.100148

Xue, Y., Bao, Y., Zhang, Z., Zhao, W., Xiao, J., He, S., et al. (2022). Database resources of the national Genomics data center, China national center for bioinformation in 2022. *Nucleic Acids Res.* 50, D27–D38. doi:10.1093/nar/gkab951

Xue, K., Song, J., Yang, Y., Li, Z., Wu, C., Jin, J., et al. (2016). PAX5 promotes pre-B cell proliferation by regulating the expression of pre-B cell receptor and its downstream signaling. *Mol. Immunol.* 73, 1–9. doi:10.1016/j.molimm.2016.03.007

Yang, C., Lee, H., Pal, S., Jove, V., Deng, J., Zhang, W., et al. (2013). B cells promote tumor progression via STAT3 regulated-angiogenesis. *PLOS ONE* 8, e64159. doi:10.1371/journal.pone.0064159

Yang, X., Ma, Y., Guo, W., Yang, B., and Tian, W. (2019). Stem cells from human exfoliated deciduous teeth as an alternative cell source in bio-root regeneration. *Theranostics* 9, 2694–2711. doi:10.7150/thno.31801

Yuan, S.-M. (2015). α-Smooth muscle Actin and ACTA2 gene expressions in vasculopathies. *Braz J. Cardiovasc Surg.* 30, 644–649. doi:10.5935/1678-9741.20150081

Zahr, A., Alcaide, P., Yang, J., Jones, A., Gregory, M., dela Paz, N. G., et al. (2016). Endomucin prevents leukocyte–endothelial cell adhesion and has a critical role under resting and inflammatory conditions. *Nat. Commun.* 7, 10363. doi:10.1038/ncomms10363

Zarubova, J., Hasani-Sadrabadi, M. M., Ardehali, R., and Li, S. (2022). Immunoengineering strategies to enhance vascularization and tissue regeneration. *Adv. Drug Deliv. Rev.* 184, 114233. doi:10.1016/j.addr.2022.114233

Zeng, L., He, H., Sun, M., Gong, X., Zhou, M., Hong, Y., et al. (2022). Runx2 and Nell-1 in dental follicle progenitor cells regulate bone remodeling and tooth eruption. *Stem Cell Res. Ther.* 13, 486. doi:10.1186/s13287-022-03140-3

Zhang, C., Li, T., Yin, S., Gao, M., He, H., Li, Y., et al. (2022). Monocytes deposit migrasomes to promote embryonic angiogenesis. *Nat. Cell Biol.* 24, 1726–1738. doi:10.1038/s41556-022-01026-3

Zhang, F., Mears, J. R., Shakib, L., Beynor, J. I., Shanaj, S., Korsunsky, I., et al. (2021). IFN-γ and TNF-α drive a CXCL10+ CCL2+ macrophage phenotype expanded in severe COVID-19 lungs and inflammatory diseases with tissue inflammation. *Genome Med.* 13, 64. doi:10.1186/s13073-021-00881-3

Zhang, Y.-Y., Kong, L.-Q., Zhu, X.-D., Cai, H., Wang, C.-H., Shi, W.-K., et al. (2018). CD31 regulates metastasis by inducing epithelial-mesenchymal transition in hepatocellular carcinoma via the ITGB1-FAK-Akt signaling pathway. *Cancer Lett.* 429, 29–40. doi:10.1016/j.canlet.2018.05.004

Zhao, Y., Yu, Z., Song, Y., Fan, L., Lei, T., He, Y., et al. (2024). The regulatory network of CREB3L1 and its roles in physiological and pathological conditions. *Int. J. Med. Sci.* 21, 123–136. doi:10.7150/ijms.90189

Zhou, T., Pan, J., Wu, P., Huang, R., Du, W., Zhou, Y., et al. (2019). Dental follicle cells: roles in development and beyond. *Stem Cells Int.* 2019, 1–17. doi:10.1155/2019/9159605

Zhu, D., Liu, S., Huang, K., Wang, Z., Hu, S., Li, J., et al. (2022). Intrapericardial exosome therapy dampens cardiac injury via activating Foxo3. *Circ. Res.* 131, e135–e150. doi:10.1161/CIRCRESAHA.122.321384

frontiers | Frontiers in Bioengineering and Biotechnology

TYPE Original Research
PUBLISHED 24 February 2025
DOI 10.3389/fbioe.2025.1552661

OPEN ACCESS

EDITED BY
Dan Lin,
Shanghai University of Medicine and Health Sciences, China

REVIEWED BY
Gaofeng Zeng,
Chinese Academy of Sciences (CAS), China
Yun-Zhi Feng,
Central South University, China
Shuo Wang,
Zhengzhou University, China

*CORRESPONDENCE
Ling Zhang,
topgun1128@163.com
Huaming Mai,
huamingmai@163.com

†These authors have contributed equally to this work

RECEIVED 28 December 2024
ACCEPTED 10 February 2025
PUBLISHED 24 February 2025

CITATION
Wen X, Zhou Q, Lin S, Mai H and Zhang L (2025) Selenium-modified hydroxyapatite titanium coating: enhancing osteogenesis and inhibiting cancer in bone invasion by head and neck squamous cell carcinoma.
Front. Bioeng. Biotechnol. 13:1552661.
doi: 10.3389/fbioe.2025.1552661

Selenium-modified hydroxyapatite titanium coating: enhancing osteogenesis and inhibiting cancer in bone invasion by head and neck squamous cell carcinoma

Xutao Wen[1,2,3,4†], Qin Zhou[2,5†], Sihan Lin[2,3,6], Huaming Mai[4*] and Ling Zhang[1,2,7*]

[1]Department of Oral and Maxillofacial-Head and Neck Oncology, Shanghai Ninth People's Hospital, Shanghai Jiao Tong University School of Medicine, Shanghai, China, [2]Shanghai Key Laboratory of Stomatology, National Center for Stomatology, National Clinical Research Center for Oral Diseases, College of Stomatology, Shanghai Research Institute of Stomatology, Shanghai Jiao Tong University, Shanghai, China, [3]Shanghai Engineering Research Center of Advanced Dental Technology and Materials, Shanghai Key Laboratory of Stomatology, Shanghai Research Institute of Stomatology, Shanghai, China, [4]Department of Oral and Maxillofacial Surgery, College and Hospital of Stomatology, Guangxi Medical University, Nanning, China, [5]Department of Oral Surgery, Shanghai Ninth People's Hospital, Shanghai Jiao Tong University School of Medicine, Shanghai, China, [6]Department of Prosthodontics, Shanghai Ninth People's Hospital, Shanghai Jiao Tong University School of Medicine, Shanghai, China, [7]Department of Oral and Maxillofacial Surgery, Kashgar Prefecture Second People's Hospital, Xinjiang, China

Introduction: Head and neck squamous cell carcinoma (HNSCC) frequently invades the jaw, and surgical treatment often leads to bone defects requiring reconstruction with titanium plates. To enhance the anti-tumor and bone regeneration properties of titanium, a selenium-modified hydroxyapatite coating was developed on titanium surfaces.

Methods: Selenium-modified hydroxyapatite coatings was fabricated using micro-arc oxidation (MAO). The coating properties were characterized by SEM, XPS, AFM, Contacting angle test and ICP-OES. Cell proliferation assays were performed using rBMSCs and Cal27 cells. The osteogenic potential of the materials was assessed via ALP and OCN immunofluorescence staining and quantitative polymerase chain reaction (qPCR). Apoptosis in Cal27 cells was analyzed through flow cytometry, and ROS levels in rBMSCs and Cal27 cells were measured using ROS fluorescent probes.

Results: A coating was successfully formed on the surface of titanium with a porous structure via MAO. The atomic percentages of calcium, phosphorus and selenium on the coating surface were 42.47%, 45.43% and 12.3%, respectively, and the ion components could be released steadily and slowly. *In vitro*, 0.2 μg/mL selenium had toxic effects on Cal27 and promoted osteogenic differentiation of rBMSCs. PCR showed that selenium increased the expression of genes related to osteogenic differentiation of rBMSCs by 3–5 times. ROS detection found differences in intracellular ROS content between Cal27 and rBMSCs.

Discussion: By incorporating selenium-modified coatings, titanium implant materials can simultaneously promote osteogenesis and inhibit tumor growth, offering a promising strategy for postoperative functional recovery in HNSCC patients.

KEYWORDS

antitumor, osteogenesis, titanium, micro-arc oxidation, selenium

1 Introduction

Head and neck squamous cell carcinoma (HNSCC) is one of the most prevalent malignant tumors, characterized by aggressive and invasive growth (Chuang et al., 2008; Buim et al., 2010; Li et al., 2023). Statistics indicate that approximately half of HNSCC cases involve invasion into adjacent jaw tissue (Brown et al., 2002; Jo et al., 2017). Currently, surgery remains the primary treatment for HNSCC, frequently requiring extensive resection of the tumor and affected jaw (Chamoli et al., 2021). However, jaw resection not only significantly compromises the patient's quality of life but is also associated with a poor prognosis. Studies have shown that the survival rate of patients with jaw invasion after surgery is markedly lower than that of patients without bone invasion (DeAngelis et al., 2019). The free fibular flap has become the standard of care, and its combination with bridging plates effectively restores jaw morphology (Kammerer and Al-Nawas, 2023). Nevertheless, it is associated with certain risks, including prolonged operation duration and complex preparation processes, and while it primarily addresses bone defect repair, a considerable risk of recurrence persists following tumor resection. Consequently, researchers have begun to investigate biomaterials capable of simultaneously repairing bone defects and inhibiting tumor recurrence.

Hydroxyapatite (HA) is the primary inorganic component of bones and teeth, recognized for its superior biocompatibility and bioactivity compared to other materials (Fendi et al., 2024). HA surface modification of prosthetic metal implants is widely used to enhance bone stability (Zhang et al., 2019; Popkov et al., 2023). Notably, HA can be functionalized with ion substitutions to improve its reparative properties (Salam and Gibson, 2022). For instance, doping with magnesium, strontium, or zinc ions enhances bone regeneration (Hou et al., 2023). The incorporation of silver ions imparts localized antimicrobial capabilities (Ivankovic et al., 2023; Piecuch et al., 2023). Similarly, the addition of cerium ions provides effective anti-inflammatory and antioxidative effects (Kim and Kim, 2022). Recent studies have demonstrated that introducing anionic selenium into HA can effectively inhibit osteosarcoma (Barbanente et al., 2021; Huang et al., 2024). While selenium frequently exerts an inhibitory effect on cancer when used in conjunction with chemotherapeutic agents, often resulting in a systemic response (Zhang et al., 2024). Thus, selenium-modified HA coatings on titanium implants not only inhibit HNSCC, but also achieve the effect of reducing systemic reactions. This approach offers a promising strategy for restoring bone continuity and reducing local recurrence in postoperative HNSCC patients.

Micro-arc oxidation (MAO) enhances the biocompatibility of materials by applying high voltage to induce an oxidation reaction on the anodized metal surface, forming a ceramic-like oxide film (Sheng et al., 2022). Our previous studies successfully utilized MAO to create ceramic coatings on titanium surfaces incorporating magnesium and zinc ions (Li et al., 2020a; Zhou et al., 2022; Yu et al., 2023). Historically, MAO research has primarily focused on the incorporation of specific cations into metal surfaces, with relatively limited exploration of anion incorporation. In this study, selenite was successfully introduced into the titanium surface coating by optimizing the electrolyte composition and instrument parameters, enabling an investigation of its osteogenic and anti-tumor properties.

To our knowledge, no experimental studies have investigated selenium-doped hydroxyapatite for head and neck squamous cell carcinoma (HNSCC), nor has there been substantial research on incorporating anions into titanium surface coatings via micro-arc oxidation (MAO). In this study, selenite was successfully incorporated into a porous hydroxyapatite coating on titanium using MAO. The resulting selenium-modified coating exhibited excellent structural properties and biocompatibility, effectively inhibiting HNSCC growth and promoting bone regeneration. Using human tongue squamous cell carcinoma cell lines and rat mesenchymal stem cells, the anti-tumor and osteogenic effects were further explored *in vitro*, offering a promising material for postoperative repair in patients with jaw invasion by HNSCC.

2 Materials and methods

2.1 Sample and coating preparation

Round pure titanium plates (10 mm in diameter, 1 mm thick, TA1) were used as substrates for the porous coating. The oxide layer on the titanium surface was removed using abrasive paper, followed by sequential ultrasonic cleaning with acetone, anhydrous ethanol, and deionized water for 5 min each. For the experimental group (SeHAMAO), the electrolyte consisted of 0.05 mol/L calcium acetate monohydrate ($C_4H_6CaO_4{\cdot}H_2O$, Aladdin, Shanghai, China), 0.02 mol/L sodium β-glycerophosphate pentahydrate ($C_3H_7Na_2O_6P{\cdot}5H_2O$, Aladdin, Shanghai, China), and 0.01 mol/L sodium selenite (Na_2SeO_3, Aladdin, Shanghai, China). The negative control group (HAMAO) used the same electrolyte without sodium selenite. Porous ceramic coatings were applied to the titanium plates using micro-arc oxidation (MAO, WHD-20, Harbin, China). The MAO process was performed under a constant current of 0.8 A for 8 min, with a pulse frequency of 1,000 Hz and a duty cycle of 10%. After treatment, the samples were rinsed with deionized water and air-dried.

2.2 Characterization

The surface morphology and elemental distribution of the coatings were analyzed using scanning electron microscopy (SEM, ZEISS Gemini SEM 300, Germany). The chemical compositions of the HAMAO and SeHAMAO coatings were determined by X-ray photoelectron spectroscopy (XPS, Thermo Fisher Nexsa, United States). Ionic components of the coatings and electrolytes were quantified using inductively coupled plasma optical emission spectroscopy (ICP-OES, Agilent 5,110, United States). The wetting properties of the coating surfaces were measured with a contact angle meter (SDC-350KS, China), and surface roughness was evaluated using atomic force microscopy (AFM, Bruker Dimension Icon, Germany).

2.3 Cell culture of rBMSCs and Cal27

Rat bone marrow mesenchymal stem cells (rBMSCs) were isolated and purified from the long bone marrow of 3-week-old Sprague Dawley (SD) rats. The SD rats were sourced from the Animal Centre of the Ninth People's Hospital of Shanghai Jiao Tong University, with all procedures approved by the institutional animal ethics committee. Second to fourth passage rBMSCs were used for subsequent experiments. Both Cal27 cells and rBMSCs were cultured and expanded in Dulbecco's Modified Eagle's Medium (DMEM, Gibco, United States) supplemented with 10% fetal bovine serum (FBS) and 1% penicillin/streptomycin (Gibco, United States).

2.4 Preparation of HAMAO and SeHAMAO extract

Ion Release: Titanium plates from the HAMAO and SeHAMAO groups were immersed in equal volumes (5 mL) of deionized water and placed in a 37°C shaker at 75 rpm. The solution was extracted on days 1, 3, 5, and 7. After each extraction, an equal volume of fresh deionized water was added to continue the immersion process. The concentrations of Ca, P, and Se in the extracts were analyzed using inductively coupled plasma optical emission spectroscopy (ICP-OES).

Selenium-Containing Extract: Titanium plates from the HAMAO and SeHAMAO groups were immersed in 5 mL of Dulbecco's Modified Eagle's Medium (DMEM) and placed in a 37°C shaker at 75 rpm for 1 day. The original extract, referred to as "1," was collected and divided into 20 aliquots for subsequent experiments.

2.5 Live/dead fluorescence staining and cell counting Kit-8 (CCK-8) assay

To evaluate the effects of the coatings on Cal27 and rBMSCs, 2.5×10^5 Cal27 cells and 5×10^4 rBMSCs were seeded onto the titanium plates from each group. After 24 h of incubation, cells were treated with a Calcein/PI Live/Dead Viability/Cytotoxicity Assay Kit (Beyotime, China) and observed using confocal laser scanning microscopy (CLSM, Leica, Germany).

To determine the optimal synergistic concentrations of the extracts *in vitro*, 5×10^4 Cal27 cells and 1×10^4 rBMSCs were seeded into 96-well plates and treated with different concentrations of the extracts, divided into 20 groups. After 24 h, the medium was mixed with CCK-8 reagent (DOJINDO, Japan) in a 10:1 ratio, added to the wells, and incubated for 2 h. Absorbance was measured at 450 nm using a microplate reader. All experiments were performed in triplicate.

To explore the time-dependent effects of the extracts, equal concentrations of HAMAO and SeHAMAO extracts were applied to Cal27 cells for 6, 12, 18, 24, and 48 h. Cell viability was then assessed using the CCK-8 assay.

2.6 Alkaline phosphatase (ALP) staining

The osteogenic properties of the coating materials were evaluated using alkaline phosphatase (ALP) staining. Third-passage (P3) rBMSCs were seeded onto the surfaces of three sets of titanium slices, with fresh medium replaced regularly. In parallel, rBMSCs were treated with extracts under the same conditions. After 5 days, the culture medium was aspirated, and the samples were washed with phosphate-buffered saline (PBS) and fixed in 4% paraformaldehyde for 30 min. Following fixation, the samples were washed again with PBS. ALP staining solution was then added, and the samples were incubated for 30 min. After the staining solution was aspirated, the samples were washed with PBS, and the reaction was terminated by placing them on a shaker with gentle shaking for 3 min. Finally, the stained rBMSCs were photographed to observe ALP activity.

2.7 Immunofluorescence staining

The osteogenic ability of the extract was examined by immunofluorescence staining with ALP (RD, AF2910, United States) and OCN (RD, MAB1419, United States). rBMSCs were inoculated at a density of 5×10^4 in 35 mm confocal dishes and the solution was changed every 2 days. After 5 days, the culture was aspirated and discarded, washed with phosphate buffer, and fixed for 0.5 h by adding a fixative. And then, 0.5% Triton (Sigma, United States) was permeabilized at room temperature for 20 min, followed by adding 5% fetal bovine serum for 2 h. The primary antibody was added and placed in the refrigerator at four degrees overnight. The fluorescent secondary antibody (Alexa Fluor 594, 1: 200, Yeasen, Shanghai, China) was added the next day and protected from light for 1 h at room temperature. Finally, FITC (Yeasen, Shanghai, China) staining and DAPI (Yeasen, Shanghai, China) staining were performed to determine the cytoskeletal morphology and cytosolic status of rBMSCs. Follow-up fluorescence photography was performed using a laser scanning confocal microscope (Leica, Germany).

2.8 Osteogenic gene expression

rBMSCs were seeded into 6-well plates at a density of 2×10^5 cells/well and allocated into four groups according to the culture medium: DMEM, osteogenic medium (OM), HAMAO extract (ex-HAMAO), and SeHAMAO extract (ex-SeHAMAO). Fresh medium

was replaced regularly. After 5 days of culture, the expression levels of osteogenesis-related genes in each group of rBMSCs were analyzed using quantitative PCR (qPCR). The primer sequences used in these experiments are listed below: rGAPDH forward: CAG GGCTGCCTTCTCTTGTG, reverse: AACTTGCCGTGGGTAGAG TC; rBmp2 forward: ACCGTGCTCAGCTTCCATCAC, reverse: TTCCTGCATTTGTTCCCGAAA; rCol1 forward: CATGTTCAG CTTTGTGGACCT, reverse: GCAGCTGACTTCAGGGATGT; rOPN forward: GAGGAGAAGGCGCATTACAG, reverse: ATG GCTTTCATTGGAGTTGC; rRUNX2 forward: CCTTCCCTC CGAGACCCTAA, reverse: ATGGCTGCTCCCTTCTGAAC.

2.9 Flow cytometry of Cal27

Cal27 cells were seeded into 6-well plates at a density of 2×10^5 cells/well and divided into three groups: DMEM, ex-HAMAO, and ex-SeHAMAO. After 48 h of culture, cell viability was assessed by flow cytometry using an Annexin V-FITC Apoptosis Detection Kit (BD Biosciences, United States), following the manufacturer's instructions. In parallel, Cal27 cells were seeded into confocal culture dishes at a density of 1×10^4 cells/dish. After 48 h of culture under the same conditions, the cells were treated as described above and then observed using a laser confocal microscope.

2.10 Detection of reactive oxygen species

Cal27 and rBMSCs were seeded into 6-well plates at a density of 2×10^5 cells/well and allocated into four groups: DMEM, ROS, ex-HAMAO, and ex-SeHAMAO. After 48 h of culture, cells were treated with a Reactive Oxygen Species Assay Kit (Yeasen, Shanghai) according to the manufacturer's instructions, then observed and photographed under a fluorescence microscope. In parallel, Cal27 and rBMSCs were also seeded into 96-well plates (Corning, 3875, United States) at a density of 1×10^4 cells/well. After 48 h, cell viability was assessed using the CCK-8 assay, followed by ROS detection using the ROS Assay Kit. Fluorescence intensity was measured with a microplate reader, and the average intracellular ROS fluorescence intensity was calculated.

2.11 Statistical analysis

Data from this study were analyzed using one-way ANOVA in GraphPad Prism to determine statistical significance. ImageJ and Origin software were used to generate figures. Statistical significance levels were set at $^*P < 0.05$, $^{**}P < 0.01$, $^{***}P < 0.001$, and $^{****}P < 0.0001$.

3 Results

3.1 Characterization

Micro-arc oxidation (MAO) successfully produced a coating on the titanium surface. Among the three groups tested, the two groups subjected to MAO formed a uniformly distributed, micron- and nano-scale porous structure (Figure 1A). Energy-dispersive X-ray spectroscopy (EDS) analysis of the titanium surface and its coatings confirmed the successful incorporation of Ca, P, and Se into the coatings (Figure 1B). In the SeHAMAO group, the primary elemental atomic percentages were approximately Ca 84.25%, P 15.39%, and Se 0.36%. To reduce measurement errors, the elemental composition was further quantified using X-ray photoelectron spectroscopy (XPS), which detected O, Ti, Ca, P, C, and Se in the SeHAMAO group. The three main elements identified by XPS were Ca (42.27%), P (45.43%), and Se (12.3%) (Figure 1C). Analysis of binding energies revealed that C exhibited three peaks at 286.73 eV, 284.80 eV, and 288.94 eV; Ca had two peaks at 347.66 eV and 351.23 eV; P had a single peak at 133.79 eV; and Se had a single peak at 59.28 eV (Figure 1C).

The contact angles of the Ti, HAMAO, and SeHAMAO groups were $53.17^\circ \pm 1.39^\circ$, $14.16^\circ \pm 1.56^\circ$, and $6.59^\circ \pm 1.22^\circ$, respectively (Figures 2A, B). Compared with the Ti group, the HAMAO-treated group exhibited a smaller contact angle. Moreover, the Se-doped coating (SeHAMAO) demonstrated an even smaller contact angle and stronger hydrophilicity. Ion release measurements showed that Ca, P, and Se concentrations increased linearly and gradually over time, indicating continuous ion release from the coating. After 7 days, the ion concentrations in the SeHAMAO extract were 458.37 μg/mL for Ca, 0.08 μg/mL for P, and 0.21 μg/mL for Se. In contrast, the HAMAO extract contained 432.10 μg/mL of Ca and 9.47 μg/mL of P (Figure 2C). Two-dimensional and three-dimensional atomic force microscopy (AFM) images of the three groups confirmed these findings (Figure 2D).

3.2 Cytotoxicity and proliferation

Live-dead cell staining of rBMSCs and Cal27 cells cultured on the three groups of samples revealed that, except for a large number of dead Cal27 cells on the SeHAMAO group, cells in all other groups remained viable (Figure 3A). When treated with the extracts, the CCK-8 proliferation assay demonstrated that extracts containing selenium had a significant inhibitory effect on rBMSCs after surpassing a certain concentration (Figures 3B,C). In contrast, for Cal27 cells, the inhibitory effect increased continuously with the concentration of the selenium-containing extract (Figures 3D,E). Statistical analysis identified a selenium concentration of 0.2 μg/mL as suitable for testing on Cal27 cells. Over a 48-h period, Cal27 cell viability declined with time when compared to the control group (Figure 3F).

3.3 Effect of coating surface on osteogenesis

After confirming that the coating material was non-toxic to rBMSCs, we examined its effects on osteogenic differentiation. Compared with the control, cells treated with the selenium-containing extract showed elevated ALP expression, although this increase was less pronounced than that observed in cells cultured with osteogenic medium (Figures 4A, B). ALP staining of rBMSCs grown on the material's surface indicated that both HAMAO and SeHAMAO coatings enhanced ALP expression, with the Se-modified coating exerting a stronger effect (Figure 4C).

10.3389/fbioe.2025.1552661

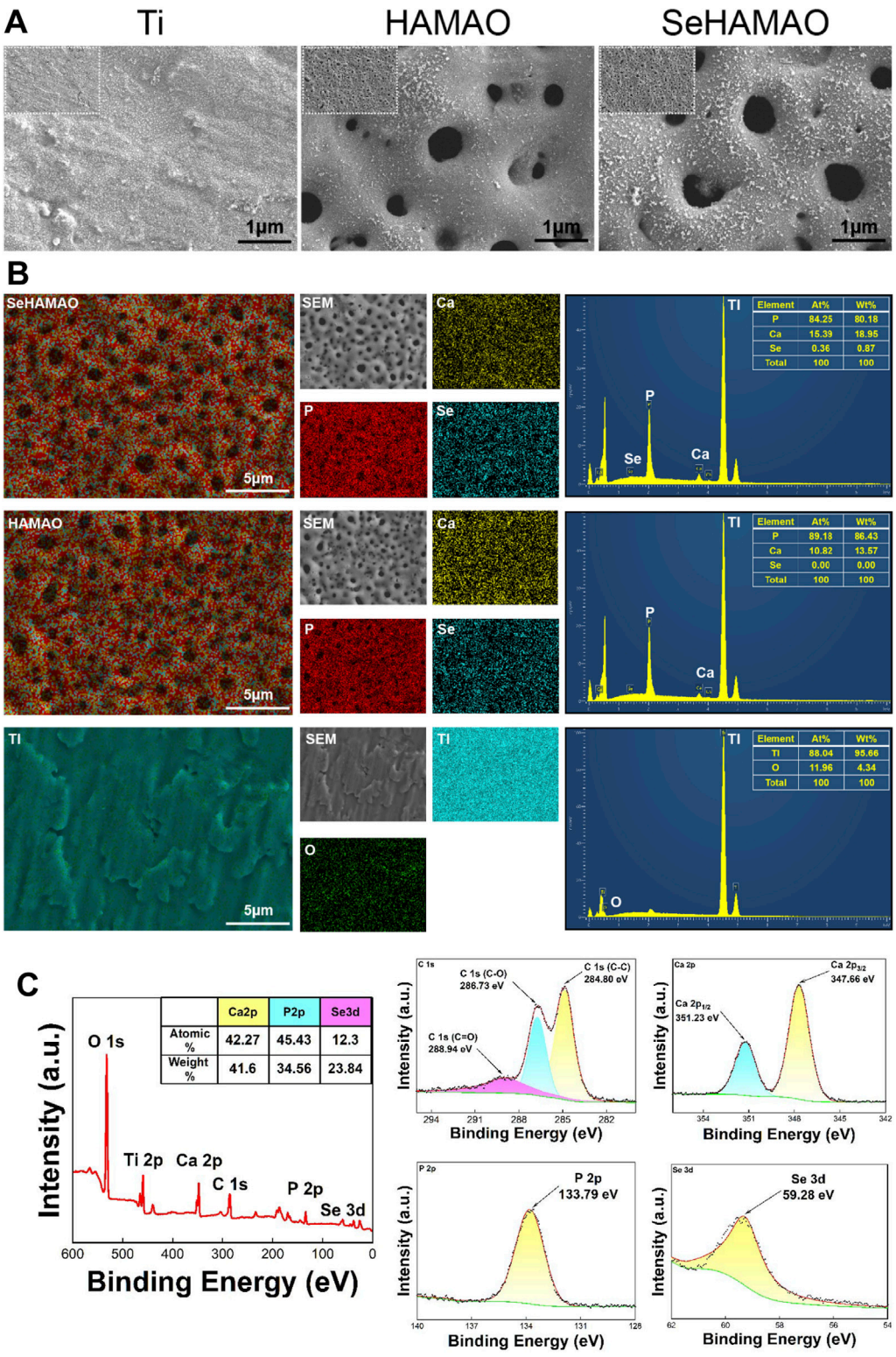

FIGURE 1
(A) Scanning electron microscopy images showing the morphological structures of the three groups of materials. **(B)** Elemental distribution and proportions in the three groups of materials, as determined by EDS. **(C)** X-ray photoelectron spectroscopy (XPS) analysis of the SeHAMAO group, showing the binding energies of each element.

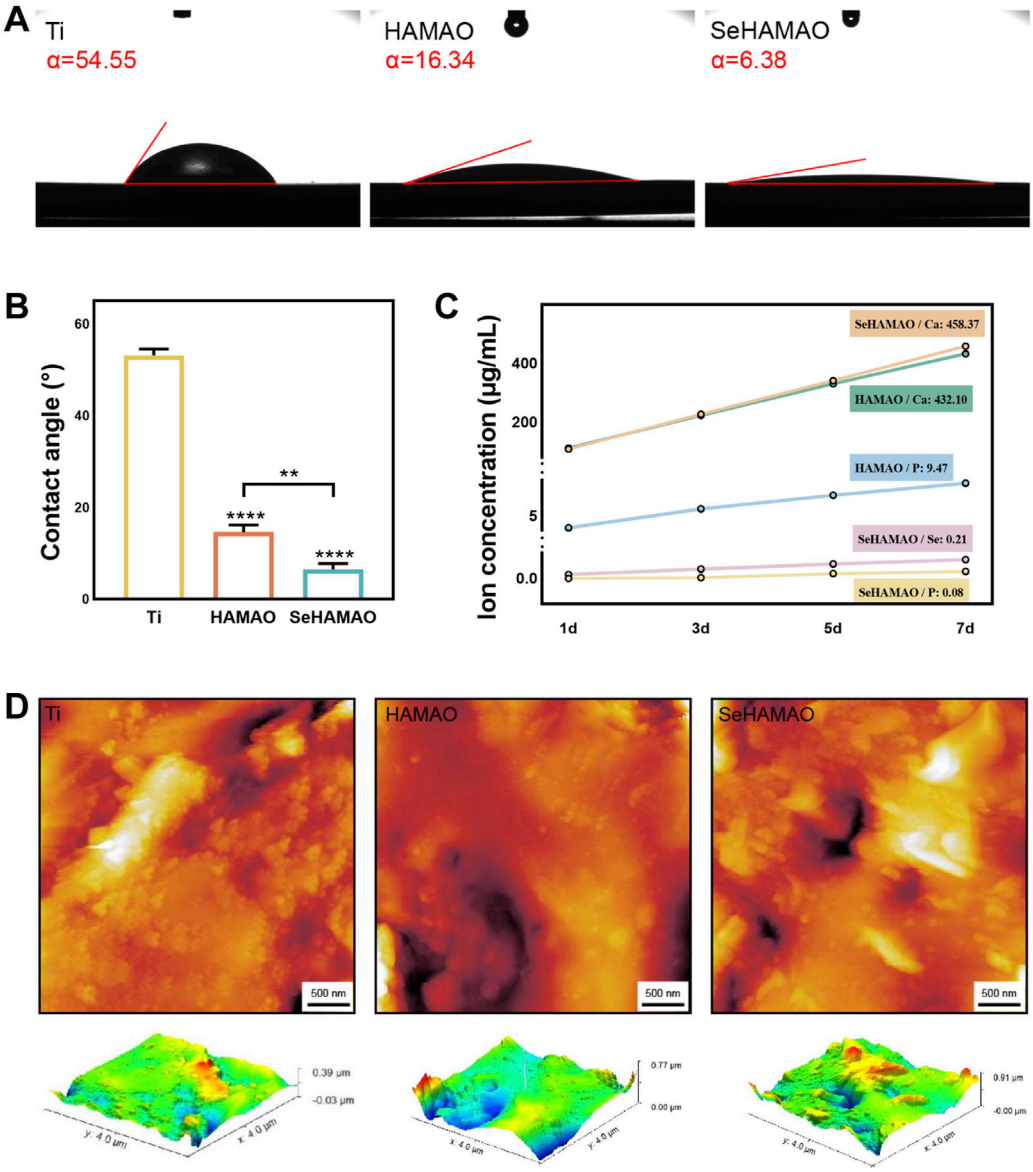

FIGURE 2
(A, B) Contact angles of the four groups of materials. **(C)** Ion release profiles of three groups at 1, 3, 5, and 7 days **(D)** Two-dimensional (2D) and three-dimensional (3D) atomic force microscopy (AFM) images of the three groups. **P < 0.01 and ****P < 0.0001 indicate statistically significant differences.

We next examined OCN expression in rBMSCs. Immunofluorescence staining revealed that OCN expression was significantly enhanced in cells treated with the selenium-containing extract, although it remained lower than that observed in cells cultured with osteogenic medium (Figure 5A). Semi-quantitative gene expression analysis showed that the relative expression levels of BMP2, Col1, OPN, and RUNX2 were all elevated in the selenium-containing extract group (Figures 5B–E).

3.4 Reactive oxygen species detection and apoptosis flow cytometry

To investigate the underlying reasons for the differential effects of the selenium-containing extract on cells, we measured ROS levels in both cell types. Cal27 cells treated with the selenium-containing extract exhibited abnormal cell morphology and increased intracellular ROS levels, whereas no significant changes were observed in the other groups (Figures 6A, D, E). Flow cytometry analysis of apoptosis in Cal27 cells further revealed that the selenium-containing extract led to a marked increase in apoptotic and necrotic cells compared with normal conditions (Figures 6B, C).

4 Discussion

Currently, coating modifications on titanium surfaces are predominantly applied in implants, enhancing osseointegration and reducing infection and inflammation (Wu et al., 2021; Costa

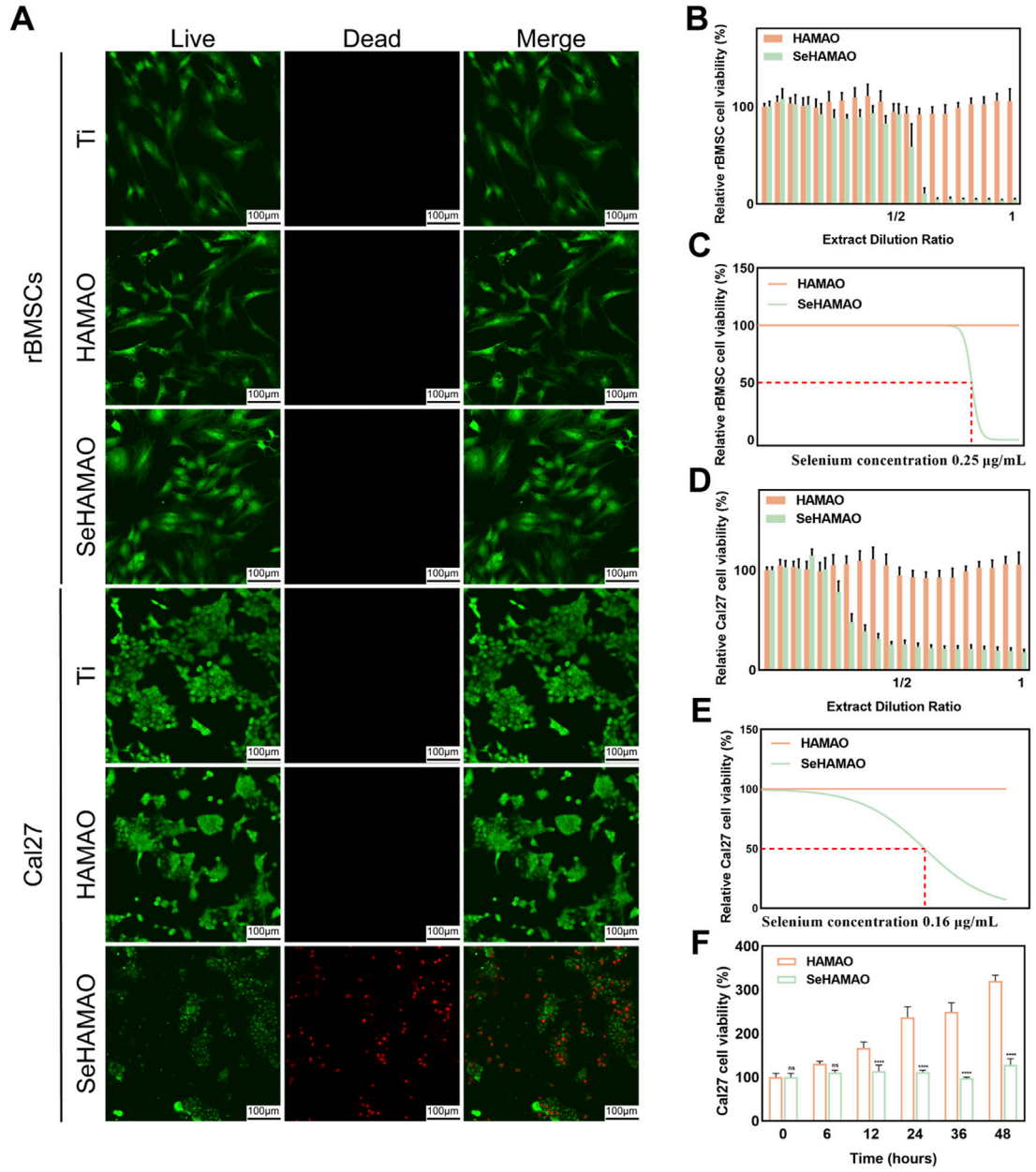

FIGURE 3
(A) Live-dead staining of rBMSCs and Cal27 cells cultured on three different titanium surfaces. **(B)** The effects of various extract concentrations on rBMSC viability. **(C)** Fitting curves and IC_{50} values for rBMSCs under different extract concentrations. **(D)** The effects of various extract concentrations on Cal27 cell viability. **(E)** Fitting curves and IC_{50} values for Cal27 cells under different extract concentrations. **(F)** Time-dependent changes in Cal27 cell viability at an extract concentration containing 0.2 μg/mL of Se.

et al., 2023; Feng et al., 2023) However, in cases of bone defects resulting from maxillofacial tumor surgeries, both bone repair and the prevention of postoperative tumor recurrence are necessary. In recent years, materials with dual antitumor and bone regeneration properties have primarily targeted osteosarcoma (Li et al., 2020b; Jing et al., 2024). Given the epidemiological and structural characteristics of the head and neck, squamous cell carcinoma frequently invades the jaw (Yao, 2020). Therefore, we combined selenium-doped hydroxyapatite, previously shown to be effective against osteosarcoma, with titanium plates to successfully produce a selenium-modified hydroxyapatite titanium coating. Furthermore, we demonstrated its capacity to inhibit head and neck squamous cell carcinoma and promote bone regeneration *in vitro*.

Micro-arc oxidation (MAO) facilitates the incorporation of electrolyte-derived elements into the surface coating of titanium substrates. In this study, sodium selenite was added to the electrolyte. Although flocculation was observed within the solution, we proceeded to analyze the electrolyte composition using inductively coupled plasma-optical emission spectroscopy (ICP-OES), which revealed the following concentrations: Ca 1,600 mg/L, P 421 mg/L, and Se 225 mg/L. Subsequently, the elemental composition present on the titanium surface was

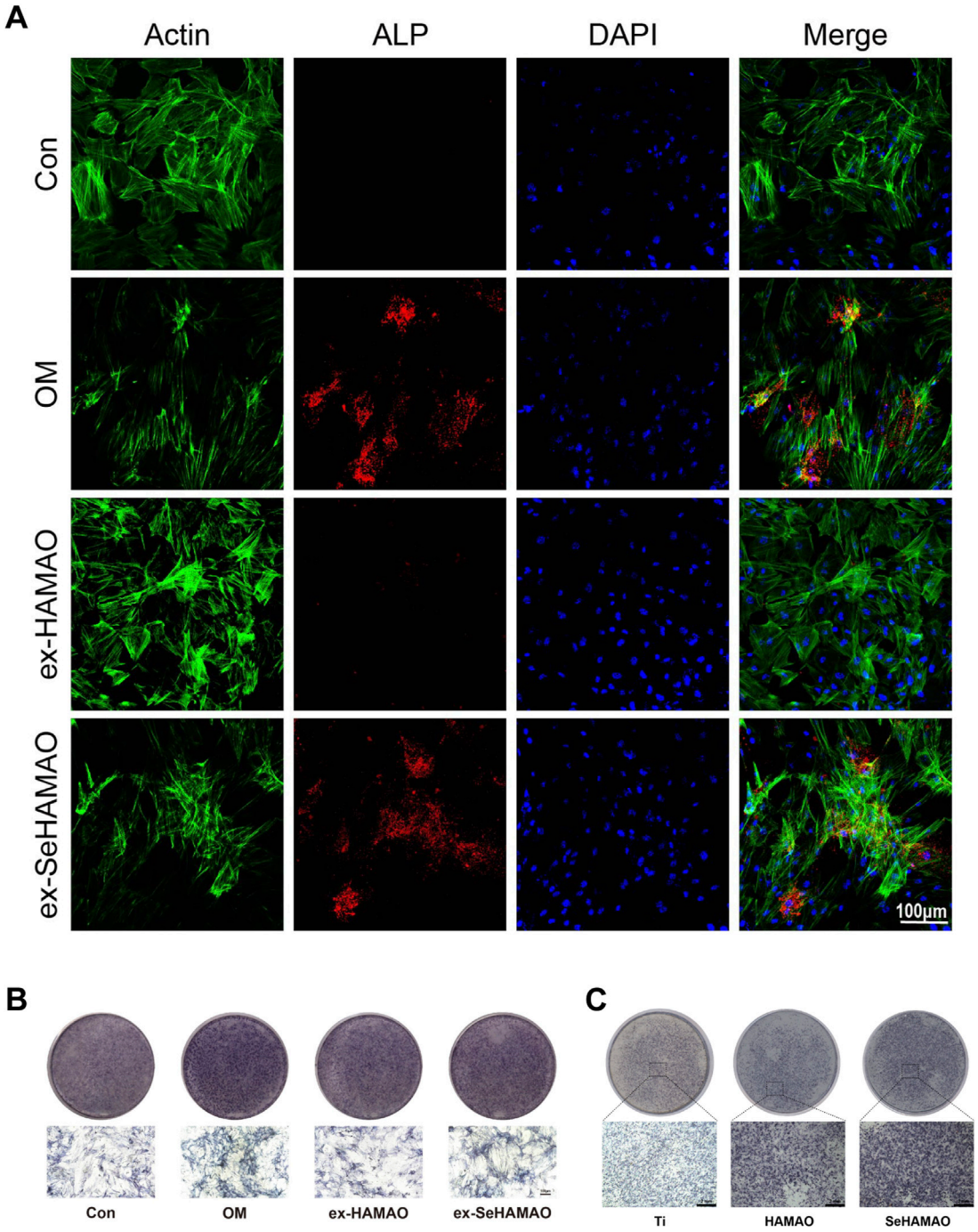

FIGURE 4
(A) Immunofluorescence staining showing ALP expression. **(B)** ALP staining of rBMSCs treated with different media. **(C)** ALP staining of rBMSCs cultured on different substrates.

examined by X-ray photoelectron spectroscopy (XPS). The binding energy (BE) of the P 2p peak was measured at 133.79 eV, indicating that phosphorus predominantly exists in the form of phosphate. Similarly, the BE of the Se 3d peak, at 59.28 eV, confirmed that selenium is present as selenite (Figure 1C). (Zhang et al., 2017; Chubar, 2023)

MAO can create a multi-porous coating on the titanium surface, facilitating cell adhesion (Figure 2D). When we seeded cells on the coated material, the SeHAMAO group showed greater cytotoxicity towards Cal27 cells. Considering that rBMSCs are of mesenchymal origin while Cal27 cells are epithelial in origin, their structures and morphologies differ. To exclude the influence of the porous structure on the cells, we applied the material extract directly and obtained similar results. Thus, we believe that selenite plays a crucial role in tumor suppression. Consistent with previous findings, selenite exerts significant antitumor effects, including reduced

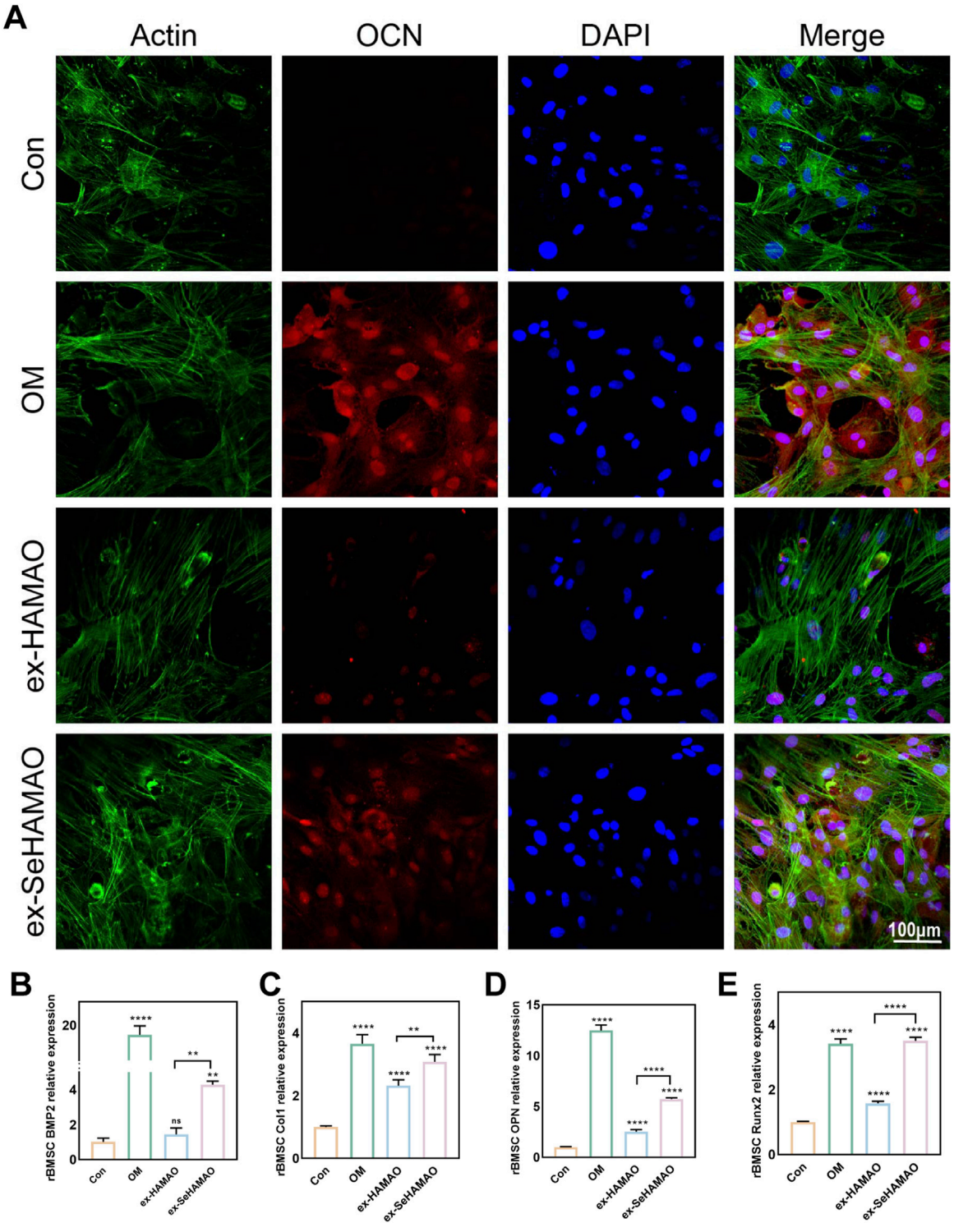

FIGURE 5
(A) OCN expression in rBMSCs as detected by immunofluorescence staining. **(B–E)** Relative expression levels of osteogenesis-related genes (BMP2, Col1, OPN, and Runx2) in rBMSCs. **P < 0.01 and ****P < 0.0001 indicate statistically significant differences, while ns denotes no significant differences between groups.

cancer incidence, inhibition of tumor invasion and metastasis, and potential clinical applications in combination with radiation and chemotherapy (Kim et al., 2021). Clinical studies have also indicated that selenite can be employed as an anticancer agent with low drug resistance (Brodin et al., 2015). As observed, selenite is more toxic to cancer cells (Figure 3A). Previous studies (Radomska et al., 2021) suggest that cancer cells, characterized by high metabolic activity, tend to absorb more selenium, which may contribute to their higher

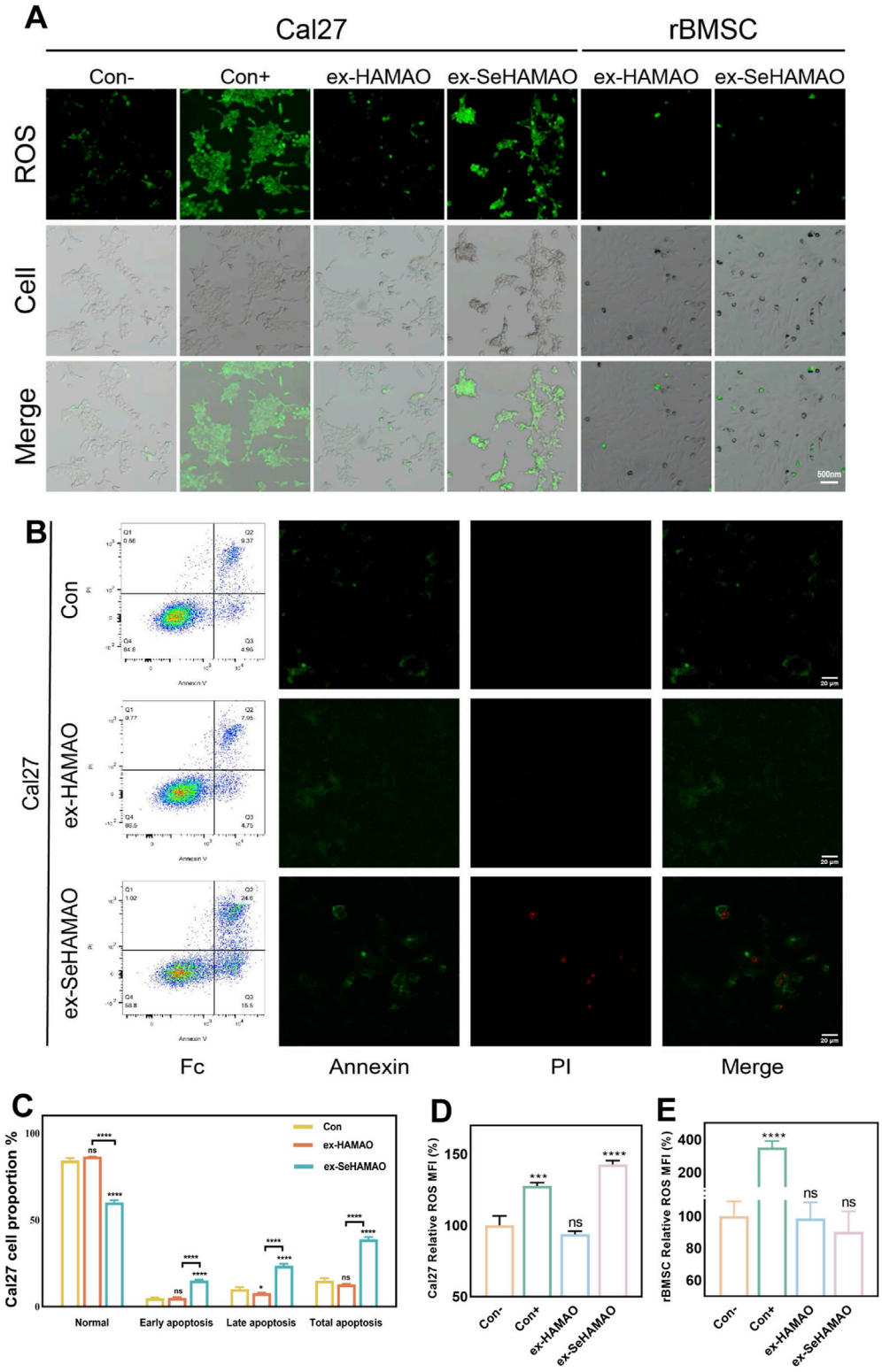

FIGURE 6
(A) Fluorescence detection of intracellular ROS in rBMSCs and Cal27 cells. **(B)** Annexin V-FITC flow cytometry analysis of Cal27 cells, showing the proportion of apoptotic cells and the distribution of intracellular fluorescence. **(C)** Statistical analysis of percentage of apoptotic cells in Cal27. **(D)** Statistical analysis of the mean fluorescence intensity of ROS in Cal27 cells. **(E)** Statistical analysis of the mean fluorescence intensity of ROS in rBMSCs. *P < 0.05 and ****P < 0.0001 indicate statistically significant differences, while ns denotes no significant differences between groups.

sensitivity to selenium toxicity, whereas normal cells exhibit lower uptake and are less affected. It has been reported that high ROS levels induce cancer cell death, (Hayes et al., 2020), while low levels of ROS can be used as signal molecules to enhance osteogenic differentiation of MSCs (Bai et al., 2021). Unexpectedly, under the same Se concentration, Cal27 cell viability appeared unchanged (Figure 3F). To determine whether this result reflects inhibited proliferation or induced cell death, we performed apoptosis flow cytometry on Cal27. This analysis revealed a significant increase in both apoptotic and necrotic cells (Figures 6B,C). We suspect that Se suppresses tumours by promoting apoptosis in Cal27 cells. Previous reports show that sodium selenite induces apoptosis in cervical cancer cells via ROS generation and in breast cancer cells through endoplasmic reticulum stress and oxidative stress (Cao et al., 2021; Lv et al., 2024). Our results suggest that Se also promotes apoptosis in HNSCC. Furthermore, high doses of Se compounds inhibit neoplastic growth by producing ROS, (Wallenberg et al., 2014), consistent with our findings (Figure 6A).

The formation of a multi-porous (nano-micron scale) structure on the titanium surface increases surface roughness, alters its hydrophobicity, and provides more binding sites for cells (Jemat et al., 2015; Lorenzetti et al., 2015). Studies have also reported that the pore size of tissue engineering scaffolds can regulate stem cell fate. When the pore size exceeds 250 μm, it promotes the terminal differentiation of BMSCs (Swanson et al., 2021). In our study, even without selenium, the HAMAO coating enhanced ALP expression in rBMSCs (Figure 4C), which may be attributed to its pore size. At the gene expression level, the selenium-containing medium also promoted the osteogenic differentiation of rBMSCs. In the classical signal pathway of MSCs during osteogenic differentiation, BMP2 functions as a pivotal initiating factor that mediates the upregulation of RUNX2 via the BMP/Smad, thereby modulating the expression of downstream osteogenic genes such as COL1 and OPN (Hwang et al., 2023). Ultimately, the progression of osteogenic differentiation can be assessed by evaluating the expression levels of ALP and OCN (Figures 5B–E). It is well known that selenite can exert anti-oxidative stress effects, for instance, by protecting rBMSCs from oxidative stress through activation of the Nrf2 pathway (Rahimi et al., 2023). One potential mechanism involves the Nrf2 (nuclear factor erythroid 2-related factor 2) pathway, a key regulator of oxidative stress. Under high ROS conditions, Nrf2 activation is impaired, leading to reduced antioxidant and increased apoptosis in cancer cells. Conversely, in normal cells such as rBMSCs, controlled ROS levels may act as secondary messengers to promote differentiation via pathways such as Wnt/β-catenin or BMP/Smad signal. Excessive oxidative stress damages osteoblasts, but reducing such stress enhances osteogenesis (Yang et al., 2023). We also found that ROS levels in rBMSCs slightly decreased compared with the control group (Figure 6E), which may protect the cells and further support osteogenesis.

To further establish the clinical potential of this material, the vivo studies are essential to evaluate its long-term biocompatibility, osseointegration, and tumor-suppressive effects in a physiological environment. While our research sheds light on the role of selenium in modulating ROS production and apoptosis, the precise molecular mechanisms driving its osteogenic and antitumor effects remain unclear. Future research should delve deeper into the specific signal pathways involved, which would strengthen the foundation for clinical translation. Addressing these gaps will help advance selenium-modified titanium coatings toward practical applications, providing a dual-functional biomaterial for maxillofacial reconstruction in HNSCC patients.

5 Conclusion

In this study, we successfully fabricated a selenium-modified hydroxyapatite coating on titanium using micro-arc oxidation. We verified that this coating possesses favorable surface physical properties, enhances the osteogenic differentiation of MSCs, and promotes the apoptosis of head and neck squamous cell carcinoma cells. Thus, selenium-modified hydroxyapatite titanium coatings offer a promising strategy for repairing jaw defects following tumor surgery. Nonetheless, further investigation is required to elucidate the specific molecular mechanisms and signaling pathways by which selenium exerts its effects, potentially guiding novel therapeutic approaches in the future.

Data availability statement

The original contributions presented in the study are included in the article/supplementary material, further inquiries can be directed to the corresponding authors.

Ethics statement

The animal study was approved by The Animal Care and Experiment Committee of the Ninth People's Hospital. The study was conducted in accordance with the local legislation and institutional requirements.

Author contributions

XW: Data curation, Investigation, Methodology, Resources, Visualization, Writing–original draft. QZ: Formal Analysis, Funding acquisition, Methodology, Resources, Writing–original draft. SL: Project administration, Resources, Validation, Writing–original draft. HM: Conceptualization, Supervision, Writing–review and editing. LZ: Conceptualization, Funding acquisition, Supervision, Writing–review and editing.

Funding

The author(s) declare that financial support was received for the research, authorship, and/or publication of this article. This work was supported by grants from the National Natural Science Foundation of China (81771127 and 32000973), and the Natural Science Foundation of Xinjiang Uygur Autonomous Region (2022D01C15).

Acknowledgments

The authors express their gratitude to the National Natural Science Foundation of China for its financial support of this research. We also sincerely thank Professor Wenjie Zhang and his team for their invaluable guidance and assistance throughout this study.

Conflict of interest

The authors declare that the research was conducted in the absence of any commercial or financial relationships that could be construed as a potential conflict of interest.

Generative AI statement

The author(s) declare that no Generative AI was used in the creation of this manuscript.

Publisher's note

All claims expressed in this article are solely those of the authors and do not necessarily represent those of their affiliated organizations, or those of the publisher, the editors and the reviewers. Any product that may be evaluated in this article, or claim that may be made by its manufacturer, is not guaranteed or endorsed by the publisher.

References

Bai, J., Li, L., Kou, N., Bai, Y., Zhang, Y., Lu, Y., et al. (2021). Low level laser therapy promotes bone regeneration by coupling angiogenesis and osteogenesis. *Stem Cell Res. Ther.* 12 (1), 432. doi:10.1186/s13287-021-02493-5

Barbanente, A., Palazzo, B., Esposti, L. D., Adamiano, A., Iafisco, M., Ditaranto, N., et al. (2021). Selenium-doped hydroxyapatite nanoparticles for potential application in bone tumor therapy. *J. Inorg. Biochem.* 215, 111334. doi:10.1016/j.jinorgbio.2020.111334

Brodin, O., Eksborg, S., Wallenberg, M., Asker-Hagelberg, C., Larsen, E. H., Mohlkert, D., et al. (2015). Pharmacokinetics and toxicity of sodium selenite in the treatment of patients with carcinoma in a phase I clinical trial: the SECAR study. *Nutrients* 7 (6), 4978–4994. doi:10.3390/nu7064978

Brown, J. S., Lowe, D., Kalavrezos, N., D'Souza, J., Magennis, P., and Woolgar, J. (2002). Patterns of invasion and routes of tumor entry into the mandible by oral squamous cell carcinoma. *Head. Neck* 24 (4), 370–383. doi:10.1002/hed.10062

Buim, M. E., Lourenco, S. V., Carvalho, K. C., Cardim, R., Pereira, C., Carvalho, A. L., et al. (2010). Downregulation of CD9 protein expression is associated with aggressive behavior of oral squamous cell carcinoma. *Oral Oncol.* 46 (3), 166–171. doi:10.1016/j.oraloncology.2009.11.009

Cao, L., Zhang, J., Du, Y., Sun, M., Xiang, Y., Sheng, Y., et al. (2021). Selenite induced breast cancer MCF7 cells apoptosis through endoplasmic reticulum stress and oxidative stress pathway. *Chem. Biol. Interact.* 349, 109651. doi:10.1016/j.cbi.2021.109651

Chamoli, A., Gosavi, A. S., Shirwadkar, U. P., Wangdale, K. V., Behera, S. K., Kurrey, N. K., et al. (2021). Overview of oral cavity squamous cell carcinoma: risk factors, mechanisms, and diagnostics. *Oral Oncol.* 121, 105451. doi:10.1016/j.oraloncology.2021.105451

Chuang, H. C., Su, C. Y., Huang, H. Y., Huang, C. C., Chien, C. Y., Du, Y. Y., et al. (2008). Active matrix metalloproteinase-7 is associated with invasion in buccal squamous cell carcinoma. *Mod. Pathol.* 21 (12), 1444–1450. doi:10.1038/modpathol.2008.99

Chubar, N. (2023). XPS determined mechanism of selenite (HSeO3−) sorption in absence/presence of sulfate (SO42−) on Mg-Al-CO3 Layered double hydroxides (LDHs): solid phase speciation focus. *J. Environ. Chem. Eng.* 11 (3), 109669. doi:10.1016/j.jece.2023.109669

Costa, R. C., Nagay, B. E., Dini, C., Borges, M. H. R., Miranda, L. F. B., Cordeiro, J. M., et al. (2023). The race for the optimal antimicrobial surface: perspectives and challenges related to plasma electrolytic oxidation coating for titanium-based implants. *Adv. Colloid Interface Sci.* 311, 102805. doi:10.1016/j.cis.2022.102805

DeAngelis, A., Breik, O., Angel, C., Goh, C., Iseli, T., Nastri, A., et al. (2019). Can radiological examination of mandibular bone invasion accurately predict the need for mandibular resection in oral squamous cell carcinoma? *Int. J. Oral Maxillofac. Surg.* 48 (5), 576–583. doi:10.1016/j.ijom.2018.12.007

Fendi, F., Abdullah, B., Suryani, S., Usman, A. N., and Tahir, D. (2024). Development and application of hydroxyapatite-based scaffolds for bone tissue regeneration: a systematic literature review. *Bone* 183, 117075. doi:10.1016/j.bone.2024.117075

Feng, Y., Wu, D., Knaus, J., Kessler, S., Ni, B., Chen, Z., et al. (2023). A bioinspired gelatin-amorphous calcium phosphate coating on titanium implant for bone regeneration. *Adv. Healthc. Mater* 12 (20), e2203411. doi:10.1002/adhm.202203411

Hayes, J. D., Dinkova-Kostova, A. T., and Tew, K. D. (2020). Oxidative stress in cancer. *Cancer Cell* 38 (2), 167–197. doi:10.1016/j.ccell.2020.06.001

Hou, H. H., Lee, B. S., Liu, Y. C., Wang, Y. P., Kuo, W. T., Chen, I. H., et al. (2023). Vapor-induced pore-forming atmospheric-plasma-sprayed zinc-strontium-and magnesium-doped hydroxyapatite coatings on titanium implants enhance new bone formation-an *in vivo* and *in vitro* investigation. *Int. J. Mol. Sci.* 24 (5), 4933. doi:10.3390/ijms24054933

Huang, H., Qiang, L., Fan, M., Liu, Y., Yang, A., Chang, D., et al. (2024). 3D-printed tri-element-doped hydroxyapatite/polycaprolactone composite scaffolds with antibacterial potential for osteosarcoma therapy and bone regeneration. *Bioact. Mater* 31, 18–37. doi:10.1016/j.bioactmat.2023.07.004

Hwang, Y. J., Hwang, H. J., Go, H., Park, N., and Hwang, K. A. (2023). Sword bean (Canavalia gladiata) pods induce differentiation in mc3t3-E1 osteoblast cells by activating the BMP2/SMAD/RUNX2 pathway. *Nutrients* 15 (20), 4372. doi:10.3390/nu15204372

Ivankovic, T., Turk, H., Hrenovic, J., Schauperl, Z., Ivankovic, M., and Ressler, A. (2023). Antibacterial activity of silver doped hydroxyapatite toward multidrug-resistant clinical isolates of Acinetobacter baumannii. *J. Hazard Mater* 458, 131867. doi:10.1016/j.jhazmat.2023.131867

Jemat, A., Ghazali, M. J., Razali, M., and Otsuka, Y. (2015). Surface modifications and their effects on titanium dental implants. *Biomed. Res. Int.* 2015, 1–11. doi:10.1155/2015/791725

Jing, Z., Yuan, W., Wang, J., Ni, R., Qin, Y., Mao, Z., et al. (2024). Simvastatin/hydrogel-loaded 3D-printed titanium alloy scaffolds suppress osteosarcoma via TF/NOX2-associated ferroptosis while repairing bone defects. *Bioact. Mater* 33, 223–241. doi:10.1016/j.bioactmat.2023.11.001

Jo, G. D., Yi, W. J., Heo, M. S., Lee, S. S., Choi, S. C., and Huh, K. H. (2017). CT evaluation of underlying bone sclerosis in patients with oral squamous cell carcinoma: a preliminary retrospective study. *Imaging Sci. Dent.* 47 (4), 255–259. doi:10.5624/isd.2017.47.4.255

Kammerer, P. W., and Al-Nawas, B. (2023). Bone reconstruction of extensive maxillomandibular defects in adults. *Periodontol. 2000* 93 (1), 340–357. doi:10.1111/prd.12499

Kim, H. W., and Kim, Y. J. (2022). Effect of silicon or cerium doping on the anti-inflammatory activity of biphasic calcium phosphate scaffolds for bone regeneration. *Prog. Biomater.* 11 (4), 421–430. doi:10.1007/s40204-022-00206-6

Kim, S. J., Choi, M. C., Park, J. M., and Chung, A. S. (2021). Antitumor effects of selenium. *Int. J. Mol. Sci.* 22 (21), 11844. doi:10.3390/ijms222111844

Li, C., Guan, R., Li, W., Wei, D., Cao, S., Chang, F., et al. (2023). Analysis of myosin genes in HNSCC and identify MYL1 as a specific poor prognostic biomarker, promotes tumor metastasis and correlates with tumor immune infiltration in HNSCC. *BMC Cancer* 23 (1), 840. doi:10.1186/s12885-023-11349-5

Li, X., Wang, M., Zhang, W., Bai, Y., Liu, Y., Meng, J., et al. (2020a). A magnesium-incorporated nanoporous titanium coating for rapid osseointegration. *Int. J. Nanomedicine* 15, 6593–6603. doi:10.2147/IJN.S255486

Li, X., Wang, Y., Chen, Y., Zhou, P., Wei, K., Wang, H., et al. (2020b). Hierarchically constructed selenium-doped bone-mimetic nanoparticles promote ROS-mediated autophagy and apoptosis for bone tumor inhibition. *Biomaterials* 257, 120253. doi:10.1016/j.biomaterials.2020.120253

Lorenzetti, M., Dogsa, I., Stosicki, T., Stopar, D., Kalin, M., Kobe, S., et al. (2015). The influence of surface modification on bacterial adhesion to titanium-based substrates. *ACS Appl. Mater Interfaces* 7 (3), 1644–1651. doi:10.1021/am507148n

Lv, C., Zeng, Q., Qi, L., Wang, Y., Li, J., Sun, H., et al. (2024). Sodium selenite induces autophagy and apoptosis in cervical cancer cells via mitochondrial ROS-activated AMPK/mTOR/FOXO3a pathway. *Antioxidants (Basel)* 13 (8), 1004. doi:10.3390/antiox13081004

Piecuch, A., Targonska, S., Rewak-Sorczynska, J., Ogorek, R., and Wiglusz, R. J. (2023). New silicate-substituted hydroxyapatite materials doped with silver ions as potential antifungal agents. *BMC Microbiol.* 23 (1), 193. doi:10.1186/s12866-023-02930-w

Popkov, A., Kononovich, N., Dubinenko, G., Gorbach, E., Shastov, A., Tverdokhlebov, S., et al. (2023). Long bone defect filling with bioactive degradable 3D-implant: experimental study. *Biomimetics (Basel)* 8 (2), 138. doi:10.3390/biomimetics8020138

Radomska, D., Czarnomysy, R., Radomski, D., and Bielawski, K. (2021). Selenium compounds as novel potential anticancer agents. *Int. J. Mol. Sci.* 22 (3), 1009. doi:10.3390/ijms22031009

Rahimi, B., Panahi, M., Lotfi, H., Khalili, M., Salehi, A., Saraygord-Afshari, N., et al. (2023). Sodium selenite preserves rBM-MSCs' stemness, differentiation potential, and immunophenotype and protects them against oxidative stress via activation of the Nrf2 signaling pathway. *BMC Complement. Med. Ther.* 23 (1), 131. doi:10.1186/s12906-023-03952-7

Salam, N., and Gibson, I. R. (2022). Lithium ion doped carbonated hydroxyapatite compositions: synthesis, physicochemical characterisation and effect on osteogenic response *in vitro*. *Biomater. Adv.* 140, 213068. doi:10.1016/j.bioadv.2022.213068

Sheng, X., Wang, A., Wang, Z., Liu, H., Wang, J., and Li, C. (2022). Advanced surface modification for 3D-printed titanium alloy implant interface functionalization. *Front. Bioeng. Biotechnol.* 10, 850110. doi:10.3389/fbioe.2022.850110

Swanson, W. B., Omi, M., Zhang, Z., Nam, H. K., Jung, Y., Wang, G., et al. (2021). Macropore design of tissue engineering scaffolds regulates mesenchymal stem cell differentiation fate. *Biomaterials* 272, 120769. doi:10.1016/j.biomaterials.2021.120769

Wallenberg, M., Misra, S., Wasik, A. M., Marzano, C., Bjornstedt, M., Gandin, V., et al. (2014). Selenium induces a multi-targeted cell death process in addition to ROS formation. *J. Cell Mol. Med.* 18 (4), 671–684. doi:10.1111/jcmm.12214

Wu, S., Xu, J., Zou, L., Luo, S., Yao, R., Zheng, B., et al. (2021). Long-lasting renewable antibacterial porous polymeric coatings enable titanium biomaterials to prevent and treat peri-implant infection. *Nat. Commun.* 12 (1), 3303. doi:10.1038/s41467-021-23069-0

Yang, S., Ni, G., Xia, M., Li, H., and Gao, Z. (2023). Mussel inspired multifunctional bovine serum albumin (BSA) coatings loaded with Baicalein (Bai) to enhance osteogenesis and resist oxidative stress for potential application on implant. *Int. J. Biol. Macromol.* 229, 752–765. doi:10.1016/j.ijbiomac.2022.12.285

Yao, C. M. K. L. (2020). *Jatin shah's head and neck surgery and oncology*. 5th edition. New York, NY: JatinShah, SnehaPatel, BhuvaneshSingh, RichardWongElsevier, 896. $399.99. Head and Neck-journal for The Sciences and Specialties of The Head and Neck.

Yu, L., Yin, Y., Guo, Z., Fei, Y., Wen, X., Wang, J., et al. (2023). A functional study of zinc-titanium coatings and exploration of the intrinsic correlation between angiogenesis and osteogenesis. *J. Mater Chem. B* 11 (14), 3236–3251. doi:10.1039/d3tb00119a

Zhang, B., Wei, X., and Li, J. (2024). Selenomethionine suppresses head and neck squamous cell carcinoma progression through TopBP1/ATR and TCAB1 signaling. *Histol. Histopathol.* 39 (7), 877–887. doi:10.14670/HH-18-665

Zhang, K., Zhou, Y., Xiao, C., Zhao, W., Wu, H., Tang, J., et al. (2019). Application of hydroxyapatite nanoparticles in tumor-associated bone segmental defect. *Sci. Adv.* 5 (8), eaax6946. doi:10.1126/sciadv.aax6946

Zhang, Y., Fu, M., Wu, D., and Zhang, Y. (2017). Immobilization of selenite from aqueous solution by structural ferrous hydroxide complexes. *RSC Adv.* 7 (22), 13398–13405. doi:10.1039/c6ra26225b

Zhou, Y., Wang, G., Wang, T., Wang, J., Wen, X., Sun, H., et al. (2022). Multidynamic osteogenic differentiation by effective polydopamine Micro-Arc oxide manipulations. *Int. J. Nanomedicine* 17, 4773–4790. doi:10.2147/IJN.S378387

frontiers | Frontiers in Bioengineering and Biotechnology

TYPE Original Research
PUBLISHED 25 February 2025
DOI 10.3389/fbioe.2025.1536957

OPEN ACCESS

EDITED BY
Nicholas G. Fischer,
University of Minnesota Twin Cities,
United States

REVIEWED BY
Mahboubeh Nabavinia,
The Research Institute at Nationwide Children's Hospital, United States
Sharanabasava V. Ganachari,
KLE Technological University, India

*CORRESPONDENCE
Yiming Gao,
drgaoym@163.com
Jianfei Zhang,
555zjf@163.com

†These authors have contributed equally to this work and share first authorship

RECEIVED 29 November 2024
ACCEPTED 04 February 2025
PUBLISHED 25 February 2025

CITATION
Miadili M, Li X, Zhang Y, Ruan D, Liu W, Zhang J and Gao Y (2025) The impact of jawbone regions (molar area, premolar area, anterior area) and bone density on the accuracy of robot-assisted dental implantation: a preliminary study.
Front. Bioeng. Biotechnol. 13:1536957.
doi: 10.3389/fbioe.2025.1536957

The impact of jawbone regions (molar area, premolar area, anterior area) and bone density on the accuracy of robot-assisted dental implantation: a preliminary study

Mirealimu Miadili[1,2†], Xiaoman Li[1†], Yan Zhang[1], Danping Ruan[3], Wei Liu[4], Jianfei Zhang[2*] and Yiming Gao[1*]

[1]Shanghai Jiao Tong University School of Medicine, Institute of Ruijin Hospital, Shanghai, China, [2]Department of Oral and Cranio-maxillofacial Surgery, Shanghai Ninth People's Hospital, Shanghai Jiao Tong University School of Medicine, Shanghai, China, [3]Department of Stomatology, Minhang Central Hospital Fudan University, Shanghai, China, [4]The Fourth Affiliated Hospital of Inner Mongolia Medical University, Baotou, China

Robotic-assisted dental implantation represents a transformative innovation in modern dentistry, offering enhanced surgical precision and reduced variability. Despite its clinical adoption, the impact of anatomical and bone-related factors on placement accuracy remains underexplored. This retrospective study evaluated 54 implants placed in 30 patients using cone-beam computed tomography (CBCT) and virtual planning software to analyze deviations in crown position, apex position, and angulation. Significant regional variations in accuracy were observed, with higher angular deviations in the anterior maxilla (mean ± SD: 3.21° ± 2.22°) and greater positional deviations in the posterior mandible (1.09 mm ± 0.51 mm) ($p < 0.05$). Implant diameter significantly influenced global deviation ($p = 0.019$), while implant length and bone density (classified by Misch's system) showed no significant effects ($p > 0.05$). However, denser bone types (D1) exhibited a trend toward increased deviations, potentially due to insertion resistance. These findings underscore the need for region-specific and bone-quality considerations in robotic-assisted implantation. Refining robotic navigation and feedback mechanisms is critical to optimizing accuracy, particularly in anatomically complex regions.

KEYWORDS

robot-assisted, implantation, accuracy, bone density, jawbone

Introduction

With continuous advancements in technology, robotic-assisted dental implantation has emerged as a promising approach to enhance surgical precision, stability, and reduce trauma (Block and Emery, 2016). Compared to freehand procedures, robotic systems have demonstrated significantly improved accuracy in implant placement. However, current evidence suggests that this precision may vary depending on anatomical regions—such as the anterior, premolar, and molar areas—and differences in bone density. These variations could be attributed to factors such as anatomical structure, cortical bone thickness, and

10.3389/fbioe.2025.1536957

TABLE 1 Demographic and clinical characteristics of the included patients.

Personal details		
Age	22–75	43
Gender	Male	19
	Female	11
Implant position		
Maxillary	Anterior	10
	Premolar	9
	Molar	9
Mandibular	Anterior	9
	Premolar	8
	Molar	9
Implant system	Straumann	54
Implant diameter	3.3	24
	4.1	18
	4.8	12
Implant length	8	7
	10	19
	12	28
Bone density	D1	9
	D2	23
	D3	13
	D4	9

operational angulation, which can influence implant positioning (Wu et al., 2024). Despite these potential challenges, limited studies have systematically investigated how these site-specific characteristics impact the accuracy of robotic-assisted implantation (Jorba-García et al., 2021).

In conventional implant surgery, the precision of implant positioning largely relies on the clinician's skill and experience, leading to variability across complex anatomical regions (D'Haese et al., 2017). Robotic systems theoretically mitigate these challenges by offering advanced navigation and real-time feedback, yet achieving uniform accuracy across all jawbone areas remains uncertain (Wang M. et al., 2024). This uncertainty is particularly pronounced in regions with dense cortical bone, thinner bone structures, or steep angulations, which may contribute to positional deviations during implant placement (Howashi et al., 2016).

Currently, clinical investigations on the relationship between bone density and robotic-assisted implant precision remain scarce. While imaging modalities such as Cone Beam Computed Tomography (CBCT) provide valuable diagnostic data, they lack the resolution to accurately quantify bone density (Visconti et al., 2013). To address this limitation, bone classification systems such as Misch's system are widely employed to categorize bone quality (Misch, 1990). Nevertheless, significant differences in density and bone types across jaw regions may still impact implant accuracy, requiring further exploration (Putra et al., 2020).

This study aims to investigate how specific jawbone regions—namely the anterior, premolar, and molar areas—affect the precision of robotic-assisted dental implantation. By examining these regional variations, this study seeks to provide insights that can guide clinical decision-making and optimize implant outcomes across diverse anatomical scenarios.

Materials and methods

Study design and patient selection

This retrospective study included a cohort of 30 patients who underwent robot-assisted dental implant surgeries at RuiJin Hospital from 1 January 2022 to 31 December 2023. The study included 19 males and 11 females, aged 22–75 years, with an average age of 43 years, comprised a total of 54 implant placements, each of which was performed using a robot-assisted surgical system specifically designed for dental implantology (Table 1). The inclusion criteria for patient selection were as follows: (1) patients over the age of 18, (2) requiring one or more dental implants, (3) without significant systemic health conditions that could affect bone metabolism (e.g., osteoporosis or uncontrolled diabetes), and (4) having sufficient bone volume for implant placement without the need for advanced grafting procedures. Patients with craniofacial deformities, history of radiation therapy to the head or neck, or those on medications affecting bone density (e.g., bisphosphonates) were excluded. All patients provided informed consent, and the study protocol was approved by the institutional review board (IRB) of Ruijin Hospital Ethics Committee, Shanghai Jiaotong University School of Medicine.

Sample size calculation

The sample size for this study was determined using an evidence-based design approach. *A priori* statistical power analysis was performed using G*Power 3.1 (Heinrich-Heine University Düsseldorf, Germany) with a significance level (α) of 0.05 and statistical power (1−β) of 0.80. Based on previous studies on dental implants, a large effect size (Cohen's d = 0.8) was anticipated, and a two-tailed independent samples t-test calculated the minimum required sample size for each group to be 25. Additionally, the sample size was adjusted considering the following factors: to ensure clinical independence, an average of 1–2 implants per patient was considered a reasonable protocol; the number of eligible patients at the center over the past 2 years ensured practical feasibility; and the sample size was designed to ensure representativeness and generalizability of the results. This approach balanced statistical rigor with clinical and practical considerations.

Ultimately, 30 patients and 54 implants (28 maxillary and 26 mandibular) were included in the study, exceeding the minimum sample size required for adequate statistical power (25 per group). While this sample size was sufficient to detect large effect size differences, subgroup analyses by implant position (e.g., maxillary anterior: 10 implants, maxillary premolar: 9 implants, maxillary molar: 9 implants; mandibular

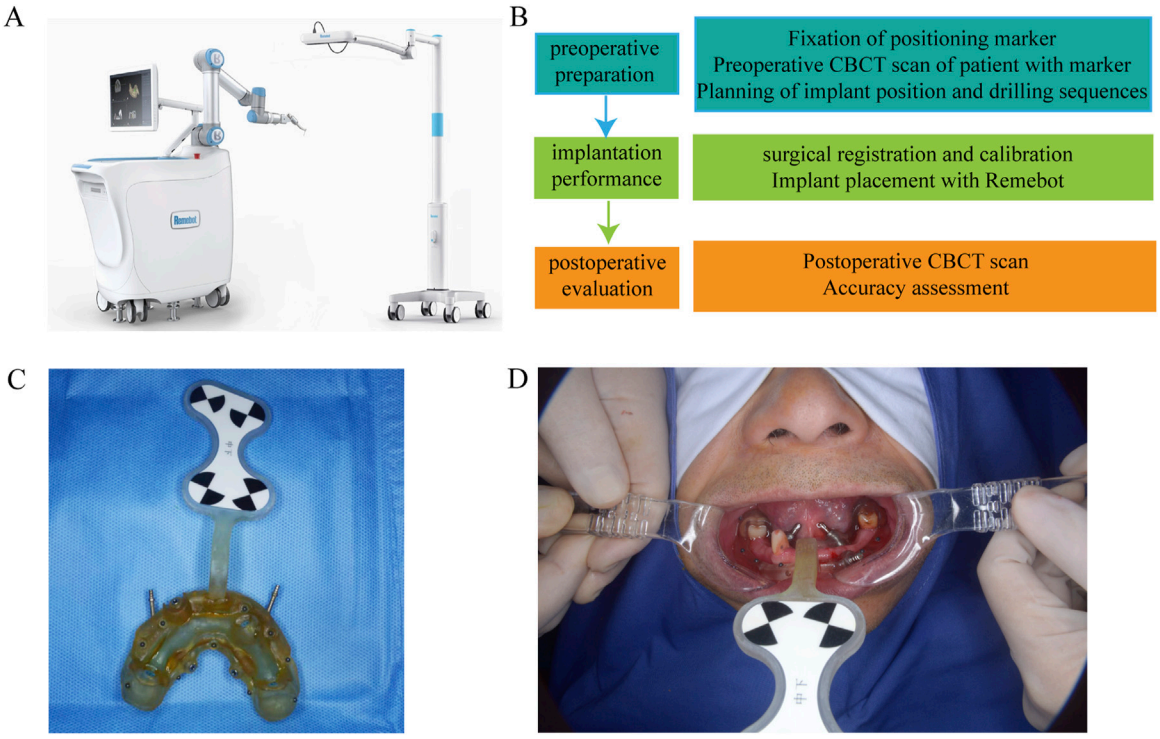

FIGURE 1
(A) RemebotDent1.0 navigation system. **(B)** Preoperative Assessment and Surgical Planning. **(C)** A printed prosthesis with marked ceramic beads. **(D)** Install the prosthesis and match the implantation plan file.

anterior: 9 implants, mandibular premolar: 8 implants, mandibular molar: 9 implants) may have limited statistical power. These subgroup analyses should therefore be interpreted as exploratory.

Preoperative assessment and surgical planning

Prior to surgery, all patients underwent detailed preoperative assessments using cone-beam computed tomography (CBCT) scans to evaluate the morphology and density of the jawbone at the planned implant sites. All CBCT scans were acquired using standardized parameters, including tube voltage (90.0 kV), tube current (6.0 mA), and resolution (0.500 × 0.500 voxel), ensuring consistency and comparability of imaging data. The CBCT data was imported into specialized three-dimensional (3D) planning software (RemebotDent1.0 navigation system), which allowed for precise virtual surgical planning. Since the Hounsfield Unit (HU) values derived from Cone-Beam Computed Tomography (CBCT) do not directly correlate with the density of the jawbone, an alternative and indirect method was employed to address this limitation (Hu et al., 2024) (Figures 1A–D). Specifically, we utilized Misch's jawbone classification system to categorize implant sites, and the detailed classification methodology is elaborated in the subsequent section on classification. By adopting this method, we aimed to achieve a more reliable evaluation of the bone quality at the implant site, ensuring a robust basis for clinical decision-making. All the implant sites were catalogued into three anatomical regions: the anterior region (incisors and canines), premolar region, and molar region.

For each implant, the optimal positioning, angulation, and depth were planned virtually, with the goal of ensuring proper primary stability and avoiding critical anatomical structures such as the inferior alveolar nerve, maxillary sinus, and adjacent tooth roots. The planned implant positions served as the reference standard against which the actual postoperative positions would be compared (de Almeida et al., 2010). To ensure consistency and minimize operator-dependent variability, all preoperative planning and surgical procedures were performed by the same experienced clinician. This approach maximized the elimination of potential operator-related errors, ensuring the accuracy and reproducibility of the study results.

Surgical procedure

Robot-assisted dental implant surgeries were performed using the Remebot, (Beijing Baihui Weikang Technology Co., Ltd., Beijing, China),a precision-guided robotic system that provides real-time feedback and automated controls to enhance the accuracy of implant placement. Following the preoperative planning, the surgical robot was calibrated to execute the implant placement according to the 3D virtual plan (Figure 2). The robot-guided system allowed for controlled drilling and precise insertion of the implants. All procedures were performed by experienced surgeons with expertise in robot-assisted dental surgery, ensuring consistency across the patient cohort (Bahrami et al., 2024).

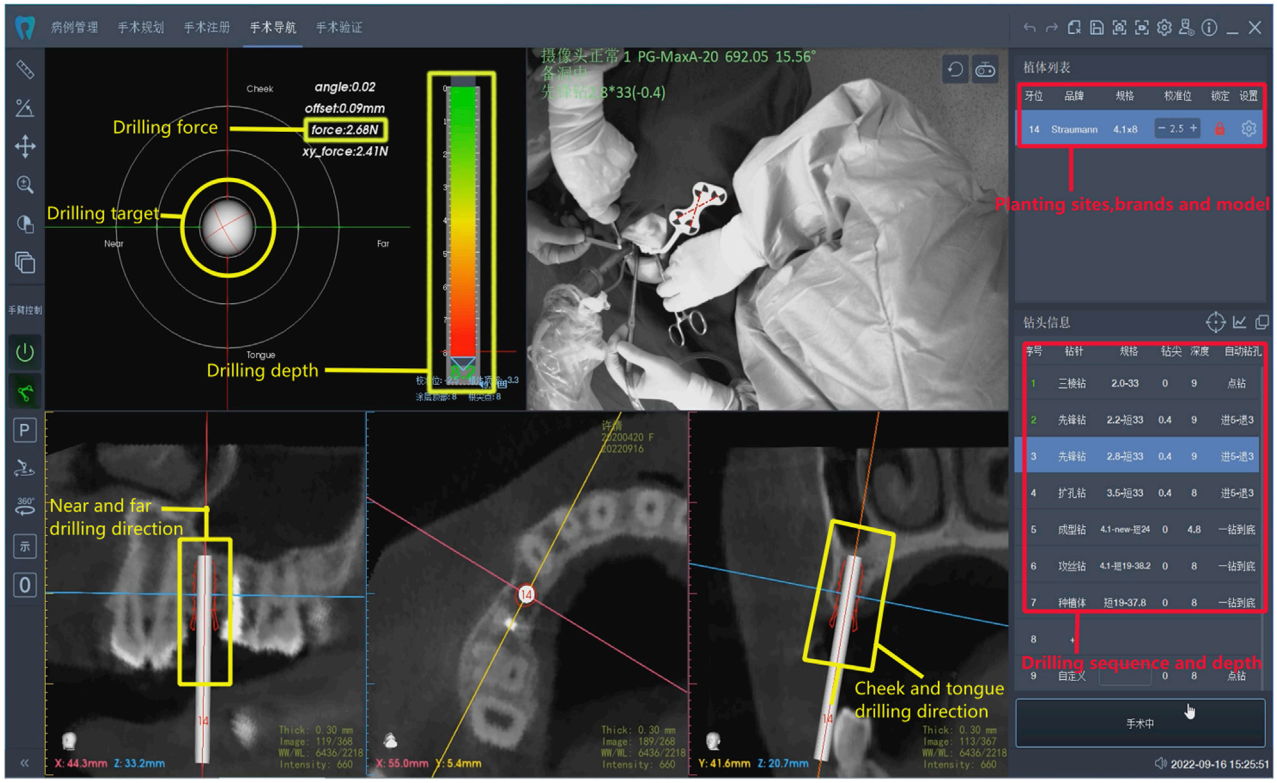

FIGURE 2
Robotic system that provides real-time feedback and automated controls.

Postoperative evaluation

Postoperative CBCT scans were performed immediately after surgery to assess the actual implant positions. Using the same 3D software, the postoperative implant positions were compared with the preoperative virtual plan to measure deviations. Deviations were measured in three primary domains: (1) Crown Position Deviation: Measured in both lateral (buccolingual/mesiodistal) and depth (vertical) dimensions at the level of the implant crown. (2) Apex Position Deviation: Similarly, deviations in the apex (root) position were measured in lateral and depth dimensions. (3) Angulation Deviation: The angular deviation was measured as the difference between the planned and actual angulation of the implant in degrees (Takács et al., 2023).

Each deviation (Figure 3) was precisely calculated using the digital measurement tools provided by the 3D software, ensuring high accuracy and reproducibility of measurements (Figures 4A–I). The results were recorded in millimeters (mm) for positional deviations and degrees (°) for angular deviations (Shi et al., 2024).

Bone density analysis using Misch's classification

Bone density was assessed using Misch's classification system, which categorizes bone into four types based on cortical and trabecular characteristics. CBCT imaging served as the primary diagnostic tool, providing detailed visualization of the maxilla and mandible. Experienced clinicians reviewed the CBCT scans, incorporating their expertise to classify bone quality into Type I (dense cortical bone), Type II (dense cortical and trabecular bone), Type III (thin cortical with dense trabecular bone), or Type IV (thin cortical and sparse trabecular bone). All classifications were documented systematically for subsequent analysis. This approach integrates advanced imaging with expert interpretation to enhance the precision of bone density evaluation (Misch, 1989).

Statistical analysis

All data were analyzed using SPSS 20.0 statistical software (IBM Corp., Armonk, NY, USA). Descriptive statistics, including mean values, standard deviations, and 95% confidence intervals (CI), were calculated for all measured deviations (crown, apex, and angulation). One-way analysis of variance (ANOVA) was employed to evaluate discrepancies in implant accuracy under various conditions, including maxillary and mandibular implant accuracy, regional implant accuracy within the maxilla and mandible (categorized into anterior, premolar, and molar regions), implant length, implant diameter, and bone density. Jawbone density was classified according to Misch's classification system, and ANOVA was used to determine whether bone density significantly influenced implant accuracy. A trend indicating higher deviations in denser bone types was observed and further assessed. To control for the accumulation of Type I error due to multiple comparisons, Bonferroni corrections were applied. Specifically, for comparisons involving six tooth positions, three implant diameters,

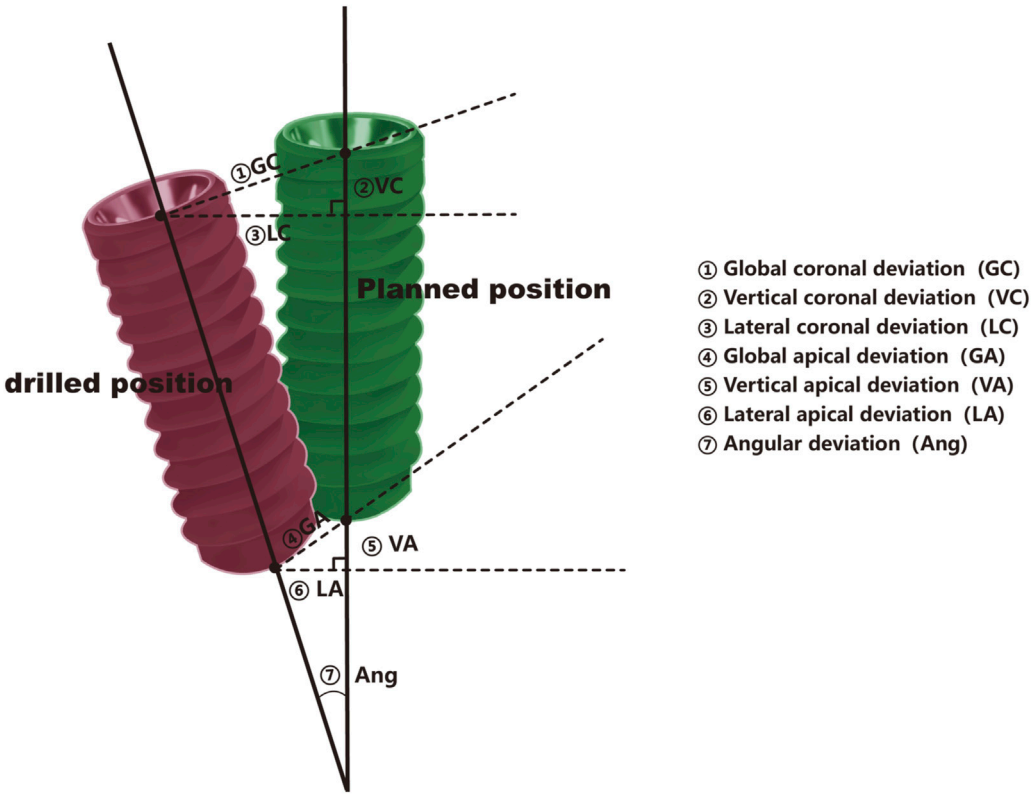

FIGURE 3
Pattern diagram, the pattern is divided into planned position (green)and drilling position (red).

three implant lengths, and four bone density categories, the adjusted significance thresholds were α' = 0.008, 0.017, 0.017, and 0.0125, respectively. An independent samples t-test was used to compare maxillary and mandibular groups, with a significance level of α = 0.05 and *p*-values derived from two-tailed tests. Effect sizes were calculated using Cohen's d and classified as follows: $d < 0.2$ (small effect size), $0.2 \leq d < 0.5$ (small to medium effect size), $0.5 \leq d < 0.8$ (medium effect size), and $d \geq 0.8$ (large effect size). This statistical approach effectively controlled for Type I error accumulation while ensuring the reliability of the results. Following Bonferroni correction, some comparisons that initially appeared significant no longer met the adjusted thresholds, reflecting the conservative and rigorous approach of this analysis. The presence of trends, such as higher deviations in denser bone types, was explored further through effect size evaluation, providing additional insights into the observed patterns.

Ethical considerations

This study was conducted in accordance with the ethical standards of the institutional review board (IRB) at Ruijin Hospital, Shanghai Jiao Tong University School of Medicine (Approval Number: 2023439) and the 1964 Helsinki Declaration and its later amendments. All patients provided written informed consent before participation. To ensure patient confidentiality, all data were anonymized during collection and analysis. No identifiable patient information was disclosed.

Results

Accuracy analysis between the maxilla and mandible

Implants placed in the mandible exhibited significantly greater deviations compared to the maxilla across all three metrics: coronal deviation (mandible: 1.01 mm ± 0.40mm, maxilla: 0.69 mm ± 0.38 mm, $p < 0.05$), apical deviation (mandible: 1.15 mm ± 0.41mm, maxilla: 0.82 mm ± 0.56mm, $p < 0.05$), and angular deviation (mandible: 1.34° ± 0.99°, maxilla: 2.46° ± 1.92°, $p < 0.05$). These findings suggest that the denser bone structure and reduced surgical accessibility of the mandible may contribute to increased inaccuracies (Table 2).

Regional accuracy within the maxilla and mandible

Significant regional variations were observed (Table 2). In the maxilla, the anterior region exhibited higher angular deviations (3.21° ± 2.22°) compared to the premolar and molar regions ($p < 0.05$). In the mandible, the anterior region showed the greatest overall positional deviations (1.19 mm ± 0.41 mm, $p < 0.05$), likely due to restricted access and variable anatomical constraints. These results underscore the importance of region-specific considerations during preoperative planning.

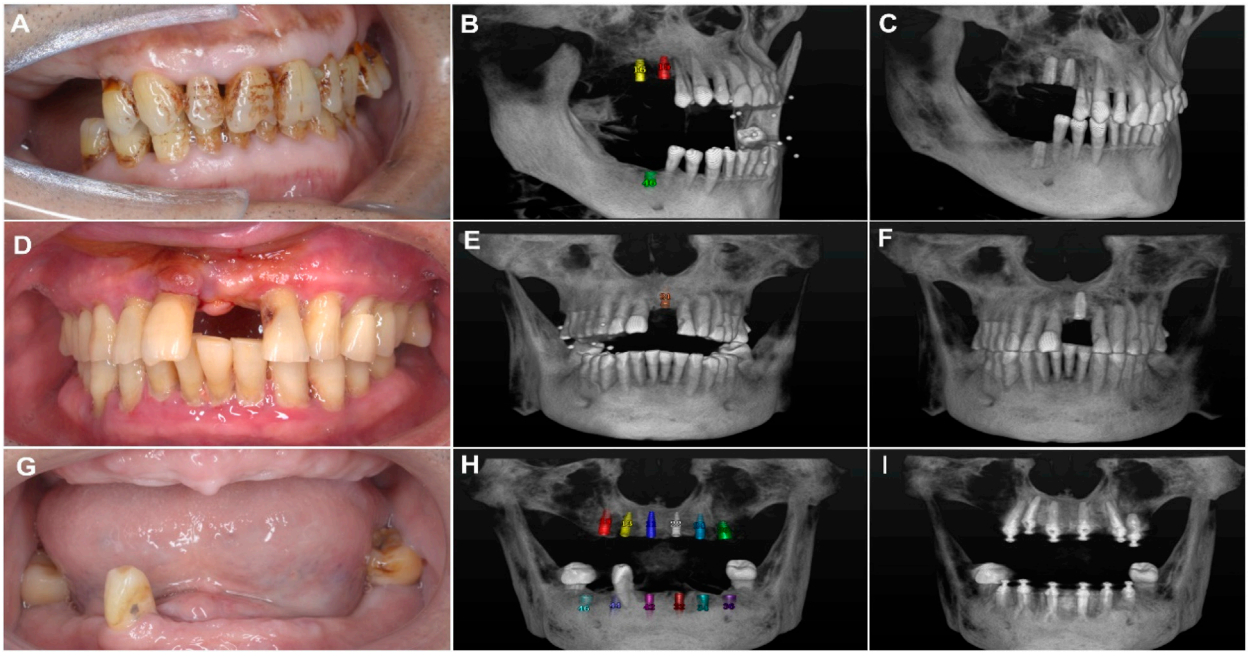

FIGURE 4
(A) Intraoral photo of the patient showing missing premolars and molars. **(B)** Three-dimensional imaging showing simulated implant placement at the edentulous sites with ceramic bead markers. **(C)** Postoperative 3D view showing the actual positions of the implants. **(D)** Intraoral photo of the patient showing missing maxillary anterior teeth. **(E)** 3D imaging illustrating the simulated implant placement at the edentulous sites in the maxillary anterior region with ceramic bead markers. **(F)** Postoperative view showing the actual implant positions. **(G)** Intraoral photo of the patient showing edentulism (complete tooth loss). **(H)** 3D imaging showing simulated implant placement, including the planned positions of multiple implants. **(I)** Postoperative 3D view showing the reconstructed dental arch.

Accuracy analysis of robotic-assisted implant placement in relation to implant diameter

The analysis of implant diameter revealed no statistically significant differences in accuracy metrics for implants of 3.3 mm, 4.1 mm, and 4.8 mm diameters in most parameters ($p > 0.05$) (Table 2). However, global deviation demonstrated a statistically significant difference, with a p-value of 0.019. Implants with larger diameters (4.8 mm) tended to exhibit slightly higher global deviations compared to smaller diameters. This finding may be attributable to the increased surgical complexity associated with larger implants, which require more extensive bone preparation and stabilization (Pérez-Pevida et al., 2020). Although the effect size is modest, these results suggest that implant diameter should be considered in relation to the patient's specific anatomical conditions to achieve optimal accuracy.

Influence of implant length on the accuracy of robotic-assisted implant placement

Implants of varying lengths (8 mm, 10 mm, and 12 mm) were analyzed to assess their impact on placement accuracy. Statistical analysis revealed no significant differences across all evaluated metrics ($p > 0.05$). These findings suggest that implant length, within the tested range, does not substantially affect precision (Table 2). A similar conclusion was reached in a related study, which demonstrated that the shape and length of implants did not influence the precision of implant positioning during robot-assisted immediate implant placement *in vitro* (Wang Y. et al., 2024). Future studies incorporating longer or shorter implants, as well as diverse bone densities, will be necessary to confirm these findings comprehensively.

Impact of jawbone density on the accuracy of implant placement

The impact of bone density, classified according to Misch's system (D1–D4), on implant accuracy was assessed. Results indicated no statistically significant differences in accuracy metrics across the four bone density categories ($p > 0.05$) (Table 2). However, a trend was observed where implants placed in D1 bone (the densest bone type) exhibited slightly higher overall deviations, potentially due to the increased resistance encountered during implant insertion, which could affect precision. In contrast, implants placed in D4 bone (the least dense bone type) showed lower vertical deviations, possibly attributed to the ease of achieving alignment in softer bone. Although these trends were not statistically significant, effect size analysis revealed clinically meaningful differences (Figure 5).

For coronal deviation (Table 3), the largest effect size (d = 5.19) was observed between the D1 (highest density) and D4 (lowest density) groups, indicating a significant impact of bone density on

10.3389/fbioe.2025.1536957

TABLE 2 Presents the deviation analysis of robot-assisted implant placement under various conditions, including coronal deviation, apical deviation, and angular deviation. The data is categorized into the following comparisons: jaw type, specific anato mical positions (position, including anterior, premolar, and molar regions of both the maxilla and mandible), implant dia meter, implant length, and bone density.

		Sample	Coronal deviation Mean ± SD			Apical deviation Mean ± SD			Angular deviation Mean ± SD (°)
			Global (mm)	Lateral (mm)	Vertical (mm)	Global (mm)	Lateral (mm)	Vertical (mm)	
Jaw	Upper	28	0.69 ± 0.38	0.45 ± 0.21	−0.38 ± 0.49	0.82 ± 0.56	0.57 ± 0.47	−0.39 ± 0.50	2.46 ± 1.92
	Lower	26	1.01 ± 0.40	0.31 ± 0.16	0.77 ± 0.58	1.15 ± 0.41	0.34 ± 0.19	−0.83 ± 0.65	1.34 ± 0.99
p-value			0.005**	0.012*	0.011*	0.018*	0.024*	0.008**	0.009**
Position	Upper anterior	10	0.90 ± 0.46	0.52 ± 0.26	−0.66 ± 0.50	1.06 ± 0.83	0.71 ± 0.74	−0.69 ± 0.53	3.21 ± 2.22
	Upper premolar	9	0.47 ± 0.13	0.37 ± 0.18	−0.83 ± 0.33	0.59 ± 0.32	0.49 ± 0.32	−0.09 ± 0.33	2.21 ± 1.72
	Upper molar	9	0.71 ± 0.38	0.45 ± 0.16	−0.41 ± 0.47	0.82 ± 0.32	0.53 ± 0.22	−0.40 ± 0.46	1.97 ± 1.78
	Lower anterior	9	1.05 ± 0.36☆	0.39 ± 0.15	−0.76 ± 0.76	1.19 ± 0.41	0.38 ± 0.23	−0.71 ± 0.75	1.57 ± 0.92
	Lower premolar	8	0.88 ± 0.34	0.25 ± 0.18	−0.87 ± 0.33☆	1.11 ± 1.16	0.27 ± 0.21	−1.18 ± 0.39☆	0.77 ± 0.52
	Lower molar	9	1.09 ± 0.51☆	0.30 ± 0.12	−0.69 ± 0.63	1.16 ± 0.59	0.38 ± 0.14	−0.69 ± 0.69	1.68 ± 1.22
p-value			0.014*	0.046*	0.035*	0.094	0.201	0.004**	0.039*
Implant diameter	3.3	24	0.84 ± 0.42	0.42 ± 0.20	−0.55 ± 0.62	1.00 ± 0.62	0.54 ± 0.51	−0.55 ± 0.62	2.49 ± 1.82
	4.1	18	0.78 ± 0.42	0.30 ± 0.18	−0.51 ± 0.56	0.89 ± 0.42	0.31 ± 0.17	−0.67 ± 0.70	1.01 ± 1.04★
	4.8	12	0.97 ± 0.41	0.41 ± 0.18	−0.72 ± 0.46	1.11 ± 0.40	0.53 ± 0.19	−0.66 ± 0.51	1.93 ± 1.49
p-value			0.506	0.125	0.606	0.529	0.118	0.816	0.019*
Implant length	8	7	0.64 ± 0.13	0.45 ± 0.19	−0.36 ± 0.37	0.72 ± 0.24	0.48 ± 0.28	−0.34 ± 0.36	2.15 ± 1.91
	10	19	0.88 ± 0.53	0.36 ± 0.19	−0.55 ± 0.59	0.94 ± 0.53	0.40 ± 0.14	−0.52 ± 0.61	1.67 ± 1.08
	12	28	0.88 ± 0.38	0.38 ± 0.20	−0.65 ± 0.59	1.08 ± 0.54	0.50 ± 0.49	−0.75 ± 0.65	1.99 ± 1.87
p-value			0.397	0.584	0.481	0.225	0.673	0.208	0.74
Bone density	D1	9	1.07 ± 0.38	0.51 ± 0.20	−0.89 ± 0.46	1.06 ± 0.50	0.31 ± 0.19	−0.85 ± 0.47	2.06 ± 1.07
	D2	23	0.88 ± 0.43	0.33 ± 0.21	−0.57 ± 0.62	1.11 ± 0.59	0.54 ± 0.49	−0.74 ± 0.71	1.77 ± 1.74
	D3	13	0.79 ± 0.45	0.39 ± 0.14	−0.84 ± 0.57	0.84 ± 0.43	0.35 ± 0.18	−0.38 ± 0.55	1.72 ± 1.12
	D4	9	0.62 ± 0.31	0.37 ± 0.19	−0.41 ± 0.45	0.81 ± 0.39	0.56 ± 0.33	−0.40 ± 0.44	2.34 ± 2.36
			0.154	0.16	0.274	0.322	0.253	0.169	0.798

* indicates statistically significant differences with ANOVA ($p < 0.05$), and ** indicates statistically significant differences with ANOVA ($p < 0.01$).
The Bonferroni correction results use ☆ to indicate a significant difference compared to the Upper premolar group, and ★ to indicate a significant difference compared to the Implant diameter 3.3 group.

coronal positioning precision and suggesting that higher bone density may increase the difficulty of controlling drilling deviations. A decreasing trend in effect size with lower bone density implies that deviations might be more controllable in less dense bone. For apical deviation, significant global effect sizes were noted between D2 and D4 (d = 3.02), and lateral deviations between D3 and D4 (d = 3.74), while vertical deviations in the D1-D3 groups showed notable effect sizes (d = 4.05), highlighting the multidimensional influence of bone density on apical positioning. For angular deviation, moderate to large effect sizes (d = 0.61–1.62) were observed across most groups, with the largest effect size between D2 and D4 (d = 1.62), emphasizing the role of bone density in angular control.

Discussion

The integration of robotic-assisted dental implantation into clinical practice has rapidly gained momentum in recent years, offering the potential to significantly enhance surgical precision, consistency, and predictability (van Riet et al., 2021). These systems provide unique advantages, including real-time feedback, precise control, and the reduction of human error, collectively leading to improved patient outcomes (Isufi et al., 2024). The findings from our study demonstrated remarkable implant placement accuracy, with a mean global platform deviation of 0.76 ± 0.36 mm, apex deviation of 0.85 ± 0.48 mm, and angular deviation of 2.05° ± 1.33°. Furthermore, vertical and horizontal deviations at the platform level were 0.39 ±

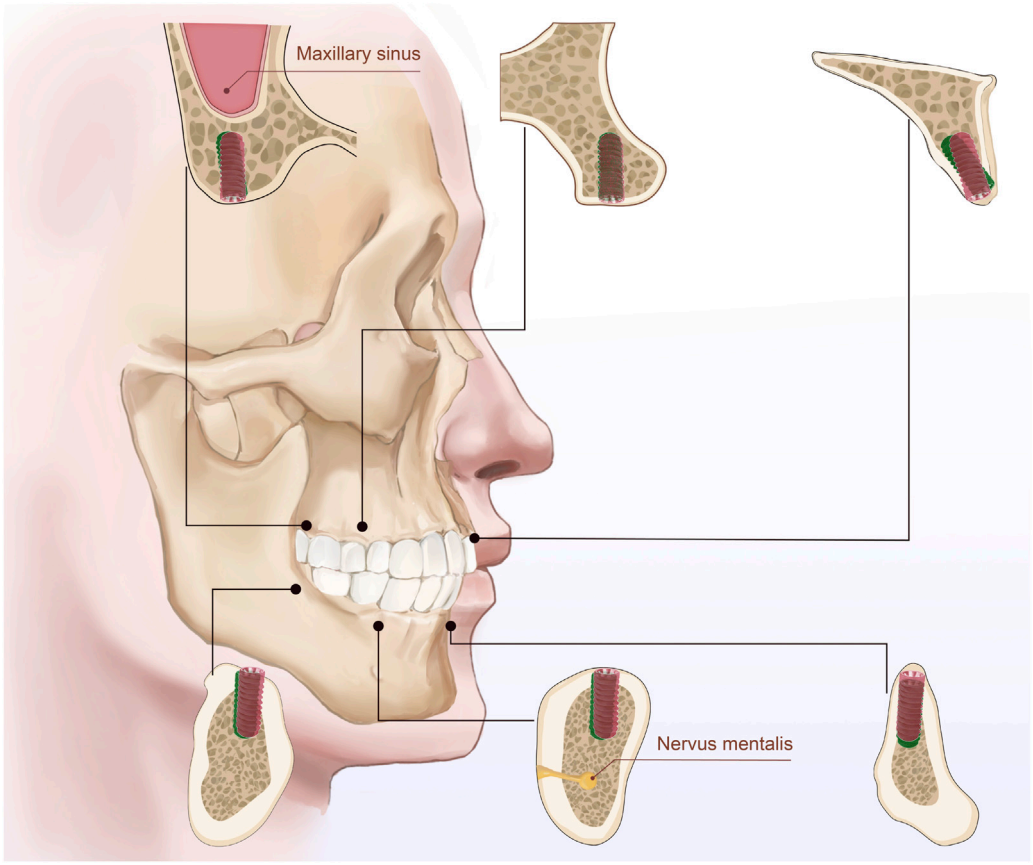

FIGURE 5
The illustration depicts the bone quality in six different regions of the maxilla and mandible (anterior, premolar, and molar regions) and bone density classified according to Misch's classification system (D1, D2, D3, and D4). Between the planned implant position (green) and the drilled position (red). The figure emphasizes the bone characteristics in each region and the relationship between implants and surrounding anatomical structures.

TABLE 3 Effect sizes were evaluated using Cohen's d, $d < 0.2$: Small effect size. $0.5 \leq d < 0.5$: Small to medium effect size. $0.5 \leq d < 0.8$: Medium effect size. $d \geq 0.8$: Large effect size.

	Coronal deviation			Apical deviation			Angular deviation
	Global	Lateral	Vertical	Global	Lateral	Vertical	
D1-D2	2.49	4.75	3.01	0.48	2.92	0.92	1.00
D1-D3	2.96	3.22	0.42	2.14	0.97	4.05	1.38
D1-D4	5.19	2.87	4.22	2.23	3.71	3.95	0.61
D2-D3	1.20	1.86	2.61	2.92	2.71	3.19	0.19
D2-D4	3.55	1.07	1.51	3.02	0.24	2.87	1.62
D3-D4	1.90	0.55	3.66	0.32	3.74	0.18	1.61

0.30 mm and 0.61 ± 0.39 mm, respectively, while the corresponding deviations at the apex level were 0.40 ± 0.36 mm and 0.71 ± 0.39 mm. These values align with or exceed those reported in previous studies (Bolding and Reebye, 2022) which described a passive robotic system achieving a global platform deviation of 1.04 mm, an apex deviation of 0.95 mm, and an angular deviation of 2.56°. Notably, even in edentulous cases, the robotic system maintained its precision despite the anatomical challenges, highlighting its potential for broader clinical applications in complex scenarios. Similarly, Yang et al. (2024), reported comparable accuracy metrics, confirming the exceptional precision of robotic systems in dental implantation. While the results underline the significant potential of robotic systems, the precision of implant placement across different anatomical regions remains underexplored. Complex areas, such as the maxillary anterior aesthetic zone and mandibular posterior region, pose unique challenges due to their intricate bone

morphology, high bone density, and proximity to critical anatomical structures (Huang et al., 2024). Our study found that larger-diameter implants exhibited slightly higher deviations, likely due to increased surgical complexity and the limitations of robotic systems in adapting to variations in implant diameter. Conical implants demonstrated greater deviations than cylindrical implants, potentially attributed to their self-tapping design, which requires additional downward force during placement, increasing the risk of misalignment (Ochi et al., 2013). In contrast, cylindrical implants, which lack self-tapping properties, exhibited greater stability. Additionally, larger-diameter implants faced higher resistance in cortical bone regions, and the robotic system's limited capacity to adapt to these mechanical variations likely contributed to increased deviations (Ozan et al., 2011).

Bone-related factors, such as density, width, and cortical bone thickness, also significantly influence implant placement accuracy. Previous studies (Putra et al., 2020) have demonstrated that poor bone conditions, including low bone density, narrow bone width, and thin cortical bone, increase the risk of deviations during implantation. In line with these findings, our study observed a significant association between bone density and implant accuracy. Denser bone regions, such as the posterior mandible, presented greater resistance during drilling, increasing angular deviations, while softer bone regions, such as the anterior maxilla, posed challenges for achieving primary stability and alignment (Huang et al., 2024). Although no statistically significant association was observed between bone density categories and implant deviation ($p > 0.05$), effect size analysis revealed clinically meaningful differences. For example, the largest coronal deviation effect size (d = 5.19) was observed between D1 (highest density) and D4 (lowest density) bone types, suggesting that higher bone density may increase drilling complexity and deviation risks. Similarly, significant apical and angular deviation effect sizes (d = 3.02–4.05) were observed between various bone density groups, highlighting the multidimensional impact of bone density on implant accuracy. These findings emphasize the need for optimized surgical protocols tailored to bone quality variations to minimize deviations.

These precision differences have profound clinical implications. Robotic-assisted systems have shown significant improvements in accuracy and consistency compared to traditional methods (Chen et al., 2024). However, their application in complex anatomical regions still requires optimization. For high-density cortical bone regions, specially designed pilot drills can be used to reduce slippage during initial positioning. Slowing the drilling speed in the mandibular molar region and incorporating real-time feedback mechanisms can further improve precision. Ensuring strict calibration and registration protocols is critical to maintain navigation accuracy, and systematic training for clinicians can maximize the effectiveness of robotic systems. Collectively, these measures help reduce deviations and improve the initial stability of implants. Despite their potential, robotic systems still face critical challenges. High-quality CBCT imaging and precise calibration remain essential for surgical accuracy, making them sensitive to imaging artifacts and errors during marker registration (Brief et al., 2005; Dong et al., 2012). Reference markers may occasionally become invisible during surgery due to interference from the surgeon or instruments, especially in systems with suboptimal camera designs. However, the robotic system in our study, with dual cameras positioned near the patient's head, demonstrated improved marker detection, reducing interruptions. Anatomically complex or hard-to-reach implant sites pose additional challenges, as robots may struggle with posture adjustment, increasing operational difficulty. Nevertheless, the system's follow-up functionality minimizes positional deviations caused by unintended head movements during the procedure.

Furthermore, robotic systems are still in their developmental stages and cannot independently perform complex procedures, such as sinus lifting or advanced bone grafting, which require precise manipulation in anatomically constrained environments. These procedures still rely heavily on the expertise of surgeons for optimal outcomes. While this study focused on implant placement accuracy, it did not address more complex surgical techniques. Future advancements should prioritize introducing tactile feedback, optimizing surgical path planning, and improving robotic posture adjustment for these procedures. Enhancing surgeon-robot interaction could further expand the system's applicability and safety in challenging scenarios.

This study has several limitations. This study excluded patients with systemic conditions such as diabetes and osteoporosis to ensure a homogeneous study population, thereby enhancing the internal validity of the findings and enabling a more precise assessment of the performance of robot-assisted systems in healthy individuals. However, this exclusion criterion limits the external validity and generalizability of the results, as it does not account for the system's performance in more complex clinical scenarios. For instance, diabetic patients may experience impaired wound healing, which could compromise the long-term stability of dental implants, while osteoporotic patients may present with reduced bone density, potentially affecting surgical accuracy. Future studies should incorporate a more diverse patient population, including individuals with systemic diseases, to comprehensively evaluate the efficacy and applicability of robotic systems across a broader range of clinical conditions. It was a single-center retrospective study with a limited sample size, necessitating large-scale, multicenter, randomized controlled trials to validate the system's accuracy and performance. The short-term evaluation of postoperative implant accuracy also leaves questions about long-term success and survival rates unanswered. We plan to conduct follow-up studies to assess long-term outcomes, including osseointegration, mechanical stability, and peri-implant biological changes, to comprehensively evaluate the clinical efficacy of robotic-assisted implantation.

In conclusion, robotic-assisted dental implantation represents a groundbreaking innovation with the potential to revolutionize implant dentistry. Our findings emphasize the system's ability to achieve exceptional precision across diverse scenarios. Addressing current limitations through technological advancements, standardized protocols, and long-term evaluations will pave the way for robotic systems to become a transformative tool in managing complex implant cases, ultimately setting new standards in dental care. Furthermore, regarding the integration of artificial intelligence (AI) predictive models into the robotic workflow, although this study did not address such technologies, we believe this direction holds great promise. AI predictive models can analyze patient-specific parameters, such as bone density, bone morphology, and other preoperative data, providing personalized assistance for complex case planning and improving procedural success rates. However, the practical integration of AI tools into

clinical workflows still faces significant challenges, including data standardization, model validation, and ensuring applicability across diverse clinical environments. Therefore, we recommend future research to explore the feasibility of integrating AI into real-world robotic workflows and to evaluate its potential impact on improving surgical planning efficiency and procedural accuracy. Optimizing AI applications within robotic systems could further advance personalized medicine and open new pathways for managing complex cases. Addressing these technical and clinical challenges will pave the way for the broader adoption of combined robotic and AI technologies in dental implant surgery, ultimately offering patients more precise and effective treatment options.

Data availability statement

The original contributions presented in the study are included in the article/supplementary material, further inquiries can be directed to the corresponding authors.

Ethics statement

The studies involving humans were approved by institutional review board (IRB) at Ruijin Hospital, Shanghai Jiao Tong University School of Medicine. The studies were conducted in accordance with the local legislation and institutional requirements. The participants provided their written informed consent to participate in this study.

Author contributions

MM: Writing–original draft, Writing–review and editing. XL: Data curation, Formal Analysis, Validation, Writing–review and editing. YZ: Data curation, Investigation, Writing–review and editing. DR: Writing–review and editing, Supervision, Investigation. WL: Writing–review and editing, Investigation. JZ: Writing–review and editing, Supervision. YG: Writing–review and editing, Supervision.

Funding

The author(s) declare that no financial support was received for the research, authorship, and/or publication of this article.

Conflict of interest

The authors declare that the research was conducted in the absence of any commercial or financial relationships that could be construed as a potential conflict of interest.

Generative AI statement

The author(s) declare that no Generative AI was used in the creation of this manuscript.

Publisher's note

References

Bahrami, R., Pourhajibagher, M., Nikparto, N., and Bahador, A. (2024). Robot-assisted dental implant surgery procedure: a literature review. *J. Dent. Sci.* 19 (3), 1359–1368. doi:10.1016/j.jds.2024.03.011

Block, M. S., and Emery, R. W. (2016). Static or dynamic navigation for implant placement-choosing the method of guidance. *J. Oral Maxillofac. Surg.* 74 (2), 269–277. doi:10.1016/j.joms.2015.09.022

Bolding, S. L., and Reebye, U. N. (2022). Accuracy of haptic robotic guidance of dental implant surgery for completely edentulous arches. *J. Prosthet. Dent.* 128 (4), 639–647. doi:10.1016/j.prosdent.2020.12.048

Brief, J., Edinger, D., Hassfeld, S., and Eggers, G. (2005). Accuracy of image-guided implantology. *Clin. Oral Implants Res.* 16 (4), 495–501. doi:10.1111/j.1600-0501.2005.01133.x

Chen, J., Zhuang, M., Tao, B., Wu, Y., Ye, L., and Wang, F. (2024). Accuracy of immediate dental implant placement with task-autonomous robotic system and navigation system: an *in vitro* study. *Clin. Oral Implants Res.* 35 (8), 973–983. doi:10.1111/clr.14104

de Almeida, E. O., Pellizzer, E. P., Goiatto, M. C., Margonar, R., Rocha, E. P., Freitas, A. C., Jr., et al. (2010). Computer-guided surgery in implantology: review of basic concepts. *J. Craniofac Surg.* 21 (6), 1917–1921. doi:10.1097/SCS.0b013e3181f4b1a0

D'Haese, J., Ackhurst, J., Wismeijer, D., De Bruyn, H., and Tahmaseb, A. (2017). Current state of the art of computer-guided implant surgery. *Periodontol* 73 (1), 121–133. doi:10.1111/prd.12175

Dong, X., Niu, T., Jia, X., and Zhu, L. (2012). Relationship between x-ray illumination field size and flat field intensity and its impacts on x-ray imaging. *Med. Phys.* 39 (10), 5901–5909. doi:10.1118/1.4750054

Howashi, M., Tsukiyama, Y., Ayukawa, Y., Isoda-Akizuki, K., Kihara, M., Imai, Y., et al. (2016). Relationship between the CT value and cortical bone thickness at implant recipient sites and primary implant stability with comparison of different implant types. *Clin. Implant Dent. Relat. Res.* 18 (1), 107–116. doi:10.1111/cid.12261

Hu, Y., Xu, S., Li, B., Inscoe, C. R., Tyndall, D. A., Lee, Y. Z., et al. (2024). Improving the accuracy of bone mineral density using a multisource CBCT. *Sci. Rep.* 14 (1), 3887. doi:10.1038/s41598-024-54529-4

Huang, J., Bao, J., Tan, Z., Shen, S., and Yu, H. (2024). Development and validation of a collaborative robotic platform based on monocular vision for oral surgery: an *in vitro* study. *Int. J. Comput. Assist. Radiol. Surg.* 19 (9), 1797–1808. doi:10.1007/s11548-024-03161-8

Isufi, A., Hsu, T. Y., and Chogle, S. (2024). Robot-assisted and haptic-guided endodontic surgery: a case report. *J. Endod.* 50 (4), 533–539.e1. doi:10.1016/j.joen.2024.01.012

Jorba-García, A., González-Barnadas, A., Camps-Font, O., Figueiredo, R., and Valmaseda-Castellón, E. (2021). Accuracy assessment of dynamic computer-aided implant placement: a systematic review and meta-analysis. *Clin. Oral Investig.* 25 (5), 2479–2494. doi:10.1007/s00784-021-03833-8

Misch, C. E. (1989). Bone classification, training keys to implant success. *Dent. Today* 8 (4), 39–44.

Misch, C. E. (1990). Density of bone: effect on treatment plans, surgical approach, healing, and progressive boen loading. *Int. J. Oral Implantol.* 6 (2), 23–31.

Ochi, M., Kanazawa, M., Sato, D., Kasugai, S., Hirano, S., and Minakuchi, S. (2013). Factors affecting accuracy of implant placement with mucosa-supported stereolithographic surgical guides in edentulous mandibles. *Comput. Biol. Med.* 43 (11), 1653–1660. doi:10.1016/j.compbiomed.2013.07.029

Ozan, O., Orhan, K., and Turkyilmaz, I. (2011). Correlation between bone density and angular deviation of implants placed using CT-generated surgical guides. *J. Craniofac Surg.* 22 (5), 1755–1761. doi:10.1097/SCS.0b013e31822e6305

Pérez-Pevida, E., Cherro, R., Camps-Font, O., and Piqué, N. (2020). Effects of drilling protocol and bone density on the stability of implants according to different macrogeometries of the implant used: results of an *in vitro* study. *Int. J. Oral Maxillofac. Implants* 35 (5), 955–964. doi:10.11607/jomi.8176

Putra, R. H., Yoda, N., Iikubo, M., Kataoka, Y., Yamauchi, K., Koyama, S., et al. (2020). Influence of bone condition on implant placement accuracy with computer-guided surgery. *Int. J. Implant Dent.* 6 (1), 62. doi:10.1186/s40729-020-00249-z

Shi, J. Y., Liu, B. L., Wu, X. Y., Liu, M., Zhang, Q., Lai, H. C., et al. (2024). Improved positional accuracy of dental implant placement using a haptic and machine-vision-controlled collaborative surgery robot: a pilot randomized controlled trial. *J. Clin. Periodontol.* 51 (1), 24–32. doi:10.1111/jcpe.13893

Takács, A., Hardi, E., Cavalcante, B. G. N., Szabó, B., Kispélyi, B., Joób-Fancsaly, Á., et al. (2023). Advancing accuracy in guided implant placement: a comprehensive meta-analysis. *J. Dent.* 139, 104748. doi:10.1016/j.jdent.2023.104748

van Riet, T. C. T., Chin Jen Sem, K. T. H., Ho, J. T. F., Spijker, R., Kober, J., and de Lange, J. (2021). Robot technology in dentistry, part one of a systematic review: literature characteristics. *Dent. Mater* 37 (8), 1217–1226. doi:10.1016/j.dental.2021.06.001

Visconti, M. A., Verner, F. S., Assis, N. M., and Devito, K. L. (2013). Influence of maxillomandibular positioning in cone beam computed tomography for implant planning. *Int. J. Oral Maxillofac. Surg.* 42 (7), 880–886. doi:10.1016/j.ijom.2013.03.001

Wang, M., Liu, F., Zhao, X., and Wu, Y. (2024a). Robot-assisted surgery for dental implant placement: a narrative review. *J. Dent.* 146, 105034. doi:10.1016/j.jdent.2024.105034

Wang, Y., Yu, S., Wang, Y., Feng, Y., Yan, Q., and Zhang, Y. (2024b). Effect of implant shape and length on the accuracy of robot-assisted immediate implant surgery: an *in vitro* study. *Clin. Oral Implants Res.* 35 (3), 350–357. doi:10.1111/clr.14232

Wu, X. Y., Shi, J. Y., Qiao, S. C., Tonetti, M. S., and Lai, H. C. (2024). Accuracy of robotic surgery for dental implant placement: a systematic review and meta-analysis. *Clin. Oral Implants Res.* 35 (6), 598–608. doi:10.1111/clr.14255

Yang, F., Chen, J., Cao, R., Tang, Q., Liu, H., Zheng, Y., et al. (2024). Comparative analysis of dental implant placement accuracy: semi-active robotic versus free-hand techniques: a randomized controlled clinical trial. *Clin. Implant Dent. Relat. Res.* 26 (6), 1149–1161. doi:10.1111/cid.13375

frontiers | Frontiers in Bioengineering and Biotechnology

TYPE Original Research
PUBLISHED 12 March 2025
DOI 10.3389/fbioe.2025.1554825

OPEN ACCESS

EDITED BY
Dan Lin,
Shanghai University of Medicine and Health Sciences, China

REVIEWED BY
Zhao Qin,
Syracuse University, United States
Yitong Wang,
Tongji University, China
Jinkai Zhang,
Shanghai Jiao Tong University School of Medicine, China

*CORRESPONDENCE
Chang Tan,
Tanchang@Joyinera.com
Zeyu Fu,
Fuzeyu@Joyinera.com

RECEIVED 03 January 2025
ACCEPTED 24 February 2025
PUBLISHED 12 March 2025

CITATION
Fu Z, Qu Y, Wu Y, Xu Y, Zhang H, Tang Y, Jin Z, Zhao J and Tan C (2025) Piezoelectric poly(3-hydroxybutyrate-co-3-hydroxyhexanoate) (PHBHHx) microspheres for collagen regeneration and skin rejuvenation. *Front. Bioeng. Biotechnol.* 13:1554825. doi: 10.3389/fbioe.2025.1554825

Piezoelectric poly(3-hydroxybutyrate-co-3-hydroxyhexanoate) (PHBHHx) microspheres for collagen regeneration and skin rejuvenation

Zeyu Fu*, Yingwei Qu, Yinghao Wu, Yuan Xu, Hengdi Zhang, Yaozong Tang, Ziying Jin, Jia Zhao and Chang Tan*

Beijing Joyinera Biomaterial Technology Co., Ltd., Beijing, China

Introduction: Skin aging is an inevitable physiological process driven by factors like cellular senescence, ultraviolet radiation (UV) radiation, and environmental pollutants. A key feature is the accelerated collagen degradation in the dermal extracellular matrix, leading to visible signs such as sagging, wrinkles, and hyperpigmentation. Traditional fillers, such as hyaluronic acid and collagen-based fillers, offer only temporary volume enhancement without stimulating collagen regeneration. Studies have shown that electrical signals generated by piezoelectric materials can promote tissue regeneration.

Methods: This study explored the potential of piezoelectric PHBHHx microspheres as an innovative skin filler for enhancing collagen regeneration and improving maxillofacial aesthetics, with the aid of low-intensity pulsed ultrasound (LIPUS) stimulation. A comprehensive characterizations of the piezoelectric PHBHHx microspheres were conducted, and their potential to stimulate collagen regeneration was assessed using a subcutaneous injection model in New Zealand white rabbits.

Results: The results indicated that PHBHHx microspheres exhibited stable degradation properties, great piezoelectric properties and excellent biocompatibility. Moreover, when stimulated by LIPUS, the collagen-regenerating effect of PHBHHx microspheres was further enhanced, histological analysis revealed a denser and more organized collagen structures in LIPUS-stimulated PHBHHx group.

Discussion: These findings highlight the potential of PHBHHx microspheres as an advanced biomaterial for applications in aesthetic medicine, particularly in promoting collagen regeneration and enhancing skin rejuvenation.

KEYWORDS

PHBHHx, LIPUS, piezoelectric, collagen regeneration, skin rejuvenation

1 Introduction

Skin aging, characterized by a decline in functional capacity, is a gradual and unavoidable physiological process influenced by a combination of internal and external factors (Wang et al., 2024). These include cellular senescence, chronic UV exposure, and environmental pollutants (Shin et al., 2023). The accelerated degradation of collagen, a vital structural protein within the dermal extracellular matrix (ECM) (Zhang et al., 2023) essential for maintaining skin strength, firmness, and resilience (Huang et al., 2022), is widely acknowledged as a key contributor to visible signs of aging, including sagging skin, deep wrinkles, and hyperpigmentation (David and Jennifer, 2021). Therefore, promoting collagen regeneration has become a key objective in the development of new skin fillers that not only address the cosmetic appearance but also improve the underlying skin architecture (Pu et al., 2080). Traditional dermal fillers, such as hyaluronic acid (HA) (Fanian et al., 2023) and collagen-based fillers (Yang et al., 2024), primarily focus on restoring facial volume (Burgess et al., 2024), reducing wrinkles (Kim, 2021), and addressing other signs of aging. While these fillers can provide short-term improvements in skin appearance, they can't offer long-term solutions, as their effects are transient and require repeated treatments (Narins et al., 2008). Furthermore, these fillers typically do not stimulate the body's natural regenerative processes, particularly the production of collagen (Li et al., 2023; Kim and Sykes, 2011). This underscores the need for innovative biomaterials that not only offer volumizing benefits but also promote endogenous collagen regeneration.

Piezoelectric materials can generate electrical signals in response to mechanical stimulation such as pressure, vibration, or deformation (Badali et al., 2024). Studies have confirmed that these electrical signals can mimic natural cellular cues, thereby enhancing tissue healing and regeneration (Rajabi et al., 2015; Donate et al., 2023; Panda and Basu, 2021). Zhang et al. (2025) prepared nanocomposite electrospun dressings using poly (L-lactic acid) (PLLA) and barium titanate ($BaTiO_3$) for scar-free wound recovery. The results demonstrated that ultrasound-induced activation of the piezoelectric effect reversed the fibrotic phenotype, resulting in scar-free healing and the regeneration of functional skin structures. Among the numerous piezoelectric materials, PHBHHx, a kind of intracellular polyhydroxyalkoxyfatty acid ester synthesized by many bacteria, has attracted wide attention due to its good biocompatibility, biodegradability and piezoelectricity (Bugnicourt et al., 2014). While PHBHHx has been extensively studied in various biomedical applications, including tissue engineering and drug delivery systems (Yang et al., 2022; Luo et al., 2024), its potential as a piezoelectric biomaterial for aesthetic applications remains largely unexplored. LIPUS is a type of pulsed ultrasound that uses a low intensity and output mode (Zheng et al., 2024). Due to its low intensity and pulsed output mode, LIPUS has minimal thermal effects while maintaining the transmission of acoustic energy to the target tissue. LIPUS has been shown to promote fresh, nonunion, or delayed union in animal models and clinical treatment (Donate et al., 2023). Studies have shown that LIPUS can effectively stimulate piezoelectric materials to generate electrical signals. Li et al. (2024) fabricated an ultrasound-responsive polyether ether ketone composite (PDA@BTO-SPEEK, PBSP) for repairing maxillofacial bone defects, utilizing the piezoelectric signal generated by barium titanate (BTO) under LIPUS stimulation, combined with the mediated effect of polydopamine (PDA). The results indicated that when PBSP is stimulated by LIPUS, it can generate stable electricity and effectively accelerate the osteogenic differentiation of osteoblasts.

In this context, we hypothesized that the combination of PHBHHx with LIPUS could generate localized electrical signals to enhance skin collagen regeneration and achieve maxillofacial esthetics (Figure 1). To test this, we developed a subcutaneous injection model in New Zealand white rabbits to assess the effectiveness of LIPUS-stimulated PHBHHx microspheres on collagen production. The results indicated that PHBHHx microspheres had a diameter of 20–60 μm, exhibited stable degradation properties both *in vitro* and *in vivo*, demonstrated great piezoelectric properties and excellent biocompatibility. Moreover, the LIPUS-stimulated PHBHHx group exhibited significantly enhanced collagen production compared to other groups. Histological analysis revealed a denser and more organized collagen structures in LIPUS-stimulated PHBHHx group. These findings suggested that PHBHHx microspheres have significant potential as a skin filler in aesthetic medicine, while also advancing the development of bioactive fillers that promote tissue regeneration at the cellular level.

2 Materials and methods

2.1 Materials

The PHBHHx microspheres used in this study were prepared by Beijing Joyinera biomaterial Technology Co., Ltd. (Beijing, China). For *in vitro* biological tests, L929 fibroblasts were acquired from Chinese Academy of Sciences (Shanghai, China). Fluorescein isothiocyanate (FITC)-phalloidin and DAPI were provided by Beyotime (Shanghai, China). Minimum Essential Medium (MEM), Fetal Bovine Serum (FBS), Phosphate-buffered saline (PBS), 0.25% trypsin-EDTA and penicillin-streptomycin (PS) were provided by Gibco (United States). Hematoxylin and eosin were provided by SIGMA (Shanghai, China), Masson's trichrome staining solution and Sirius Red staining Kit were provided by Solarbio (Beijing, China). Antibodies to Collagen I (Col-I) and Collagen III (Col-III) were provided by Bioss (Beijing, China). New Zealand white rabbits were supplied by Hangzhou Yuhang science union rabbit industry professional cooperatives (Hangzhou, China). SD rats were provide by Institute of Laboratory Animal Resources, Chinese Institute for Food and Drug Control (Beijing, China).

2.2 Preparation of PHBHHx microspheres and PHBHHx-CMC composite

The preparation of PHBHHx microspheres was conducted using an oil-in-water (O/W) emulsion solvent evaporation method (Tang et al., 2024). The process began with dissolving PHBHHx in dichloromethane to create the oil phase. This phase was then added dropwise to an aqueous solution of polyvinyl alcohol (PVA) under high-speed stirring, forming an emulsion. The emulsion was maintained under continuous stirring for several hours to allow the evaporation of the dichloromethane solvent,

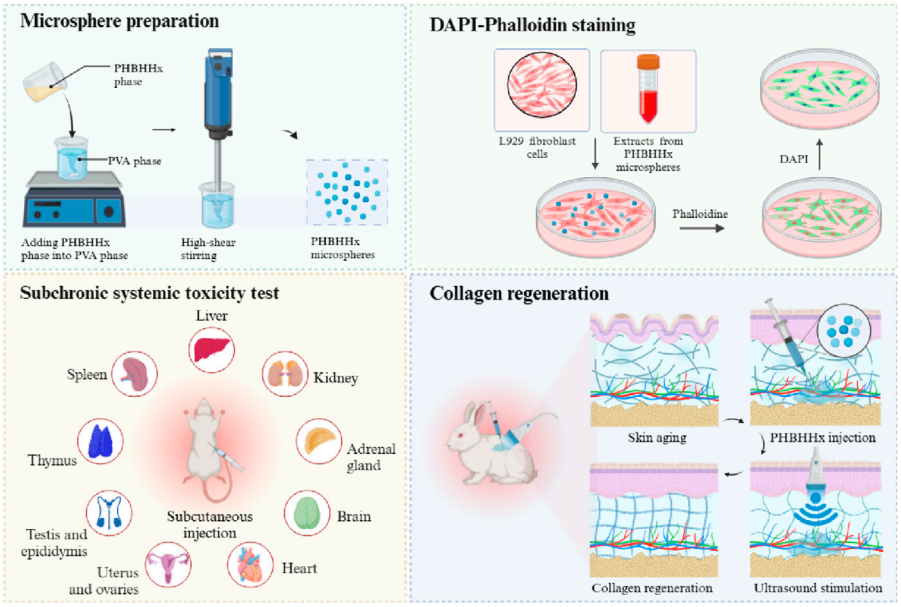

FIGURE 1
Schematic illustration of the preparation, *in vitro* and *in vivo* biocompatibility, and collagen regeneration properties of PHBHHx microspheres.

resulting in the formation of solid microspheres. The microspheres were then collected by filtration, followed by multiple washes with distilled water to remove any residual PVA. In addition, a vibrating sieving technique was employed to obtain microspheres with diameters ranging from 20 to 60 μm. In addition, to facilitate the subcutaneous injection of PHBHHx microspheres, a PHBHHx-carboxymethyl cellulose (CMC) composite was prepared by thoroughly stirring PHBHHx microspheres with CMC solution at a ratio of 300 mg of PHBHHx microspheres per 1 mL of CMC solution.

2.3 Preparation of porous and solid PHBHHx membranes

Porous and solid PHBHHx membranes were fabricated using electrospun technology by modulating the solution flow rate and electrode voltage. Prior to electrospun, 3 g PHBHHx was added into 10 mL of hexafluoroisopropanol and stirred overnight to obtain a homogeneous solution. For the preparation of porous membranes, a solution flow rate of 0.5 mL/h was utilized, along with a negative electrode voltage of 8Kv. In contrast, solid membranes were produced by increasing the flow rate to 2.5 mL/h while applying a negative electrode voltage of 14Kv, and maintaining a consistent positive electrode voltage of 12Kv for both membrane types. The collection drum was rotated at a speed of 30 r/min throughout the electrospun process.

2.4 Characterization of PHBHHx microspheres and PHBHHx-CMC composite

Scanning electron microscopy (SEM, Zeiss) was employed to examine the surface morphology of PHBHHx microspheres, as well as the structural characteristics of PHBHHx-CMC composite. For the PHBHHx-CMC composite, an oven drying treatment was required to remove water prior to detection. Samples were coated with a thin layer of gold before imaging. In addition, the particle size distribution of PHBHHx microspheres was measured using a laser diffraction particle size analyzer (Malvern Mastersizer 3000, UK). Fourier Transform Infrared Spectroscopy (FTIR, Thermo) was used to confirm the chemical structure of both the PHBHHx microspheres and the PHBHHx-CMC composite. The FTIR spectra were recorded in the range of 400–4000 cm^{-1}.

The piezoelectric properties of PHBHHx microspheres were characterized using piezoresponse force microscopy (PFM, Bruker Dimension Icon, Germany). Samples were prepared by dispersing PHBHHx microspheres in ethanol and then dropping onto silicon wafer. After drying, PFM measurements were conducted in contact mode, where an polarization voltage (-10-10V) was applied to a conductive AFM tip in contact with the sample surface.

To evaluate the mechanical properties and delivery efficacy of the PHBHHx-CMC composite as a potential filler for subcutaneous injection in aesthetic applications, the composite was loaded into a 1 mL syringe and injected with an 18-gauge needle (inner diameter: 1.2 mm) and secured in a specialized mold. A universal material testing machine was then employed to apply vertical load compression and pushing at a constant speed of 30 mm/min. The pushing force-displacement curve was recorded, with each sample tested in triplicate to ensure the reliability of the results.

The rheological property provided insight into the injectability of materials, which is critical for their application in skin filling. The rheological behavior of the PHBHHx-CMC composite was evaluated using a rotational rheometer (Haake Mars60, Germany). Measurements were performed at varying shear rates to determine the viscosity and flow properties of the composite. Briefly, a volume of 0.2 mL of the solution was carefully applied to

the test plate using a 1 mL syringe, ensuring a consistent test height of 1 mm. Following the positioning of the PP25 rotor at the designated test site, any excess solution was aspirated, and the test was initiated. The experiments were conducted at a controlled temperature of 25°C, with shear rates varying from 0.1 S^{-1} to 100 S^{-1}. The viscosity curve of the solution was recorded, with each sample evaluated in duplicate across three independent trials to ensure consistent reproducibility.

To determine the stability and longevity of PHBHHx as a biomaterial for potential applications in tissue engineering and aesthetic medicine, degradation studies were conducted both *in vitro* and *in vivo*. *In vitro* degradation was assessed by immersing the PHBHHx microspheres in phosphate-buffered saline (PBS) at temperature of 37°C and 60°C, with measurements of molecular weight (Mw) loss and morphological changes recorded at predetermined time points. For *in vivo* degradation, porous and solid PHBHHx electrospun membranes were subcutaneously implanted in the back of New Zealand white rabbits. After death was induced by intraperitoneal injection of Sutai ®50 (50 mg/kg body weight) at predetermined time points, the solid and porous membranes were removed and analyzed for morphological structure and molecular weight loss.

2.5 Biocompatibility of PHBHHx microspheres and PHBHHx-CMC composite

To assess the biocompatibility of PHBHHx microspheres, fibroblasts were cultured with extracts from microspheres for 24 and 48 h. After the incubation period, the cells were stained with DAPI and FITC-phalloidin to evaluate cell morphology and cytoskeletal structure. Additionally, a subchronic systemic toxicity test was conducted to further verify the biocompatibility of PHBHHx-CMC composite. After 1 week of breeding in the animal laboratory, rats were randomly divided into two groups based on body weight, with 20 SD rats in each group, half male and half female. In the experimental group, the PHBHHx-CMC composite was implanted subcutaneously on the back of the rats at a dosage of 0.4 mL/100 g body weight, with 4 injection sites per SD rat (sample group). In the control group, SD rats received 0.9% sodium chloride solution through the same injection method (control group). The injections were administered once a month for a total of 3 times, with a 90-day exposure period. Prior to dissection, SD rats were fasted for 16 h, and their body weight was measured after fasting. Anesthesia was induced by intraperitoneal injection of Sutai®50 at a dose of 50 mg/kg body weight, followed by blood collection from the abdominal aorta to measure hematological and biochemical parameters. After blood collection, euthanasia was performed under anesthesia, and organ abnormalities were observed. The wet weights of various organs were measured, and organ coefficients (g/100 g) were calculated. The tissues were then fixed in 4% formaldehyde solution for routine histopathological examination.

2.6 PHBHHx-CMC composite used for collagen regeneration

In this study, New Zealand white rabbits were used to assess the efficacy of PHBHHx-CMC composite as a skin filler. The rabbits were randomly assigned to four experimental groups: (1) group receiving 0.9% sodium chloride solution injection (Blank), (2) group receiving PHBHHx-CMC injection (PHBHHx), (3) group receiving PHBHHx-CMC composite injection and LIPUS stimulation (PHBHHx + US) and (4) group receiving 0.9% sodium chloride solution injection and LIPUS stimulation (US). After anesthetization, two injection sites were marked along the dorsal surface of each rabbit (n = 2), ensuring uniform placement and distance between injection points. In the LIPUS-stimulated groups, LIPUS was applied at a frequency of 1 MHz and an intensity of 0.3W/cm^2 for 20 min, 5 days per week, 1 week after injection. Tissue samples were harvested at 1, 2, 3, 5, and 13 weeks post-injection. Collected tissue samples were fixed in 4% formaldehyde solution, embedded in paraffin, and prepared into 4 μm sections for histopathological evaluation. Hematoxylin and eosin (H&E) staining was used to assess inflammatory response and overall tissue morphology. Masson's trichrome staining was performed to visualize collagen deposition and distribution, while Sirius red staining, under polarized light, was used to differentiate between type I and type III collagen fibers. In addition, the expression of type I and type III collagen was characterized by immunohistochemical staining. All stained sections were analyzed and quantitative measurements of collagen deposition and inflammatory markers were performed using ImageJ software.

2.7 Statistic analysis

The data was shown as mean ± standard deviation (SD). Data were analyzed by one-way analysis of variance (ANOVA). Differences at $P < 0.05$ were considered statistically significant. The data were statistically analyzed by GraphPad Prism 5.0.

3 Results and discussions

3.1 Characterization of PHBHHx microspheres and PHBHHx-CMC composite

SEM was used to characterize the microstructure of PHBHHx microspheres and PHBHHx-CMC composite. Images revealed that the PHBHHx microspheres exhibited a rough surface with microporous structure and uniform spherical shape (Figures 2A, B). This surface structure enhances the available surface area for interaction with surrounding tissues, which is beneficial for promoting cell adhesion (Ranella et al., 2010). The diameter distribution of PHBHHx microspheres ranged from 20 to 60μm, with an average diameter of 35.365 μm (Figure 2E). The PHBHHx-CMC composite, on the other hand, displayed smoother surfaces due to the encapsulating effect of the CMC layer, which provide additional mechanical support and improved injectability of the composite (Figure 2C). Additionally, membrane-like junctions formed by CMC can be observed between the PHBHHx microspheres (Figure 2D).

FTIR analysis confirmed the successful mixing of CMC and PHBHHx in PHBHHx-CMC composite, as evidenced by the appearance of characteristic absorption bands corresponding to CMC and PHBHHx (Figure 2F). In PHBHHx, the peak at

3445 cm^{-1} corresponds to O-H stretching vibration, while the peaks at 2,965 cm^{-1} and 2,935 cm^{-1} are attributed to C-H stretching vibrations. The peak at 1726 cm^{-1} indicates C=O stretching vibration, and the peaks at 1,464 cm^{-1} and 1,385 cm^{-1} are associated with C-H bending vibrations. The peak at 1,286 cm^{-1} corresponds to C-O stretching vibration, and the peaks at 1,185 cm^{-1}, 1,135 cm^{-1}, 1,096 cm^{-1}, and 1,055 cm^{-1} are attributed to C-O-C stretching vibrations. In PHBHHx-CMC composite, in addition to the absorption peaks characteristic of PHBHHx, a peak at 1,624 cm^{-1} corresponding to the C=O stretching vibration in CMC was also observed, confirming the successful integration of PHBHHx and CMC.

The piezoelectric properties of PHBHHx microspheres were evaluated using PFM. The piezoelectric response of PHBHHx microspheres was evaluated by phase-tip shift and amplitude-tip shift maps. The amplitude-tip bias mapping showed a linear increase in piezoresponse with increasing bias voltage, confirming the electromechanical coupling effect (Figure 2G). The phase-tip bias mapping revealed clear polarization behavior, indicating the presence of piezoelectric domains within the PHBHHx microspheres (Figure 2H). These results suggested that the PHBHHx microspheres exhibited stable piezoelectric characteristics.

The extrusion force of dermal fillers is a critical parameter that directly influences the ease of injection and patient comfort during aesthetic procedures (Pierre et al., 2015). It is determined by factors such as the viscosity (Bakrani Balani et al., 2023), cohesiveness (Alghamdi et al., 2019), and particle size of the filler material, as well as the gauge of the needle or cannula used. The extrusion force of PHBHHx-CMC composite was measured using an 18G needle. Initially, a rapid increase in force was observed as displacement began. As displacement continued to increase, the curve reaches a plateau at approximately 3.5N, indicating that a steady-state flow was achieved. The stabilization of force suggested that the filler material possesses consistent rheological properties once initial resistance was overcome. This behavior is critical for practical applications, as it implies that the filler can be injected with predictable and controlled force, minimizing patient discomfort and ensuring precise material delivery during aesthetic procedures (Figure 2I). The viscosity test results of PHBHHX-CMC indicated that the viscosity decreased sharply with the increase of shear rate, highlighting the non-Newtonian shear thinning property of the composite. Viscosity remained high at low shear rates but decreased significantly as shear rates approached 100 S^{-1}. These results indicated that the viscosity of the material can be controlled by the shear rate, which is more conducive to achieving controlled injection in clinical applications (Figure 2J).

The degradation behaviors of PHBHHx microspheres in PBS at 37°C and 60°C were systematically evaluated. The results indicated that PHBHHx microspheres retained their spherical structure without signs of cracking or collapse for up to 26 weeks at both 37°C and 60°C (Figures 3A, B), demonstrating high structural stability under these conditions. Unlike synthetic polymers such as polylactic acid (PLA) and polycaprolactone (PCL), PHAs primarily degrade through surface erosion (Pouton and Akhtar, 1996), this characteristic allows PHA materials to retain their structural integrity for a longer duration. Molecular weight analysis indicated that, at 37°C, the Mw of PHBHHx microspheres decreased to 65.54% of the initial value, dropping from 123,293 to 80,811 by week 26 (Figure 3C). In contrast, at 60°C, the Mw decreased more dramatically, falling to 9.41% of the initial value, from 123,293 to 11,605 (Figure 3D). Theses results highlight the temperature-dependent acceleration of degradation.

3.2 Biocompatibility of PHBHHx microspheres and PHBHHx-CMC composite

Biomaterials play a crucial role in biomedical applications, and their biological characteristics are essential in determining their suitability for clinical use. Among these, biocompatibility is a key property that directly influences the material's interaction with surrounding tissues and cells (Xu H. et al., 2024). Evaluating biocompatibility not only helps ensure minimal adverse reactions but also assesses the material's ability to support cellular activities such as adhesion, proliferation, and differentiation. To investigate this, an *in vitro* cytocompatibility assay of PHBHHx microspheres was conducted. The results showed that after 24 and 48 h of co-culture with extracts from PHBHHx microspheres, L929 fibroblasts displayed distinct nuclear and cytoskeletal staining, as evidenced by DAPI and FITC-phalloidin labeling, respectively. DAPI staining revealed intact, well-defined nuclei with no signs of significant nuclear condensation or fragmentation, indicating maintained cellular viability. Phalloidin staining demonstrated a well-organized actin cytoskeleton with distinct filamentous structures, suggesting normal cytoskeletal integrity. Additionally, a notable increase in cell proliferation was observed at 48 h compared to 24 h (Figures 4A, B). No significant differences were observed in the nuclear and cytoskeletal morphology between 24 and 48 h, highlighting the excellent biocompatibility of the PHBHHx microspheres. PHBHHx degrades via surface erosion, resulting in minimal immune response (Lizarraga Valderrama et al., 2018). Furthermore, its degradation product, 3HB, is a natural component of blood (Miyazaki et al., 2015), which further explains the excellent biocompatibility of PHBHHx.

To further assess the biocompatibility of the PHBHHx-CMC composite, its subcutaneous systemic toxicity was evaluated through a 90-day implantation study in SD rats. The results showed that during the experiment, the rats in the control group and the sample group had normal appearance and behavior, and moved freely. The weight gain of the sample and control groups was normal during the test period, and there was no significant difference between the two groups of the same sex (Supplementary Table S1; Supplementary Figure S1). There was no significant difference in the average 24-h feed consumption per 100 g body weight per week between the two groups of the same sex (Supplementary Table S2; Supplementary Figure S2). The absolute value of lymphocytes (LYMPH10^9/L) and the percentage of eosinophils (EO%) of male rats in the sample group were significantly different from those in the control group ($P < 0.01$). The percentages of neutrophil polymorphonuclear cell (NEUT%) and lymphocyte (LYMPH%) were significantly different between the two groups ($P < 0.05$). The activated partial thromboplastin time (APTT Sec) of female rats in the sample group was significantly different from that in the control group ($P < 0.05$), and there was no significant difference in the other indicators between the two groups of the same gender (Supplementary Table S3; Supplementary Figure S3). Alanine

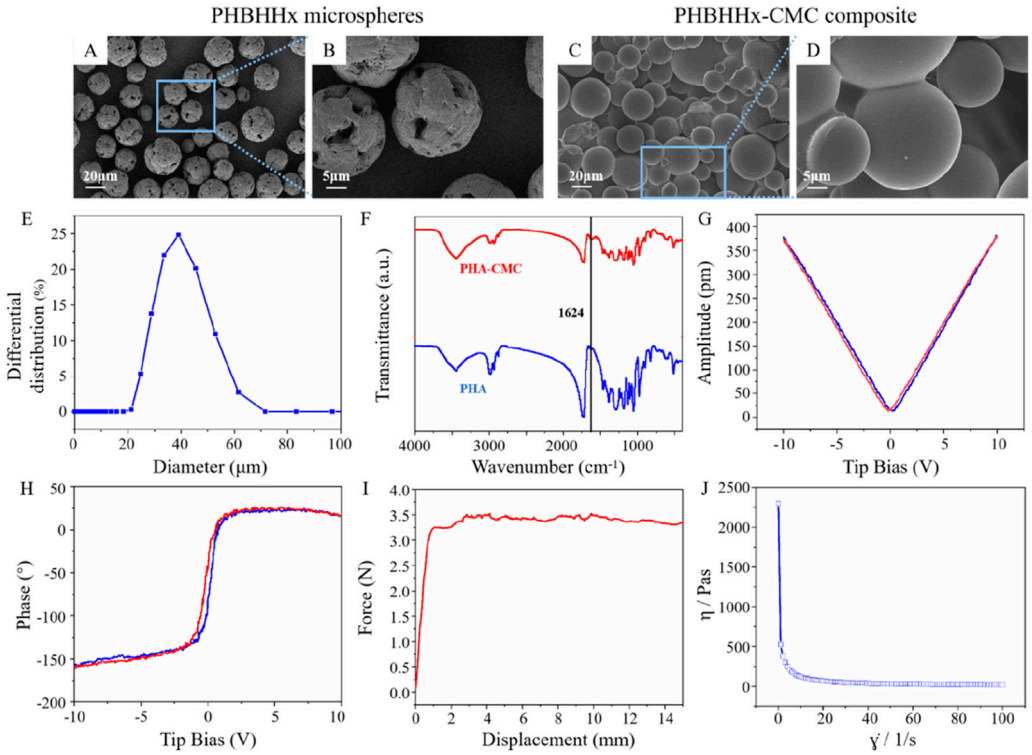

FIGURE 2
Characterization of PHBHHx microspheres and PHBHHx-CMC composite. SEM images of PHBHHx microspheres **(A, B)** and PHBHHx-CMC composite **(C, D)**. **(E)** Particle size distribution of PHBHHx microspheres. **(F)** FTIR spectrum of PHBHHx and PHBHHx-CMC composite. Piezoelectric properties of PHBHHx microspheres **(G, H)**. **(I)** The pushing force of PHBHHx-CMC composite. **(J)** The viscosity curve of PHBHHx-CMC composite.

aminotransferase (ALT) of female rats in the sample group was significantly different from that in the control group ($P < 0.01$). Aspartate aminotransferase (AST) in female rats was significantly different from that in the control group ($P < 0.05$). There was no significant difference in other indicators between the two groups of the same gender (Supplementary Table S4; Supplementary Figure S4). There was no significant difference in the wet weight of organs between the sample group of the same sex and the control group ($P > 0.05$) (Supplementary Table S5). There was no significant difference in organ coefficient between the sample group and the control group of the same gender ($P > 0.05$) (Supplementary Table S6). Hematological analysis revealed significant differences in male rats, with the absolute lymphocyte count (LYMPH10^9/L) and eosinophil percentage (EO%) being highly significant ($P < 0.01$), and neutrophil percentage (NEUT%) and lymphocyte percentage (LYMPH%) showing significant differences ($P < 0.05$) compared to controls. In female rats, activated partial thromboplastin time (APTT Sec) also differed significantly ($P < 0.05$). However, all values remained within the laboratory reference range, suggesting no biological significance. Biochemical analysis in female rats showed significantly higher alanine aminotransferase (ALT) ($P < 0.01$) and aspartate aminotransferase (AST) ($P < 0.05$) levels, yet these too were within the reference range, indicating no toxic effects. Histopathological examination revealed no tissue or organ damage associated with the composite. Overall, no signs of systemic toxicity, mortality, or adverse reactions were observed, and statistical analysis of all parameters, including organ weights and histopathology, indicated no clinically meaningful abnormalities or target organ toxicity related to the PHBHHx-CMC composite under the conditions of this study (Supplementary Table S7). No obvious toxic reaction or any signs of dying rats caused by PHBHHx-CMC composite were observed. After statistical analysis and comprehensive analysis of the results of hematology, blood biochemical indexes, organ wet weight, organ coefficient and histopathology, it was concluded that PHBHHx-CMC composite did not show clinically significant abnormal indicators or toxic target organs, indicating good biocompatibility.

In conclusion, both PHBHHx microspheres and the PHBHHx-CMC composite exhibited remarkable biocompatibility, as demonstrated by a comprehensive evaluation of their effects *in vitro* and *in vivo*. *In vitro* studies revealed no significant cytotoxicity, with fibroblasts maintaining normal morphology and viability when cultured with extracts from these materials. Similarly, *in vivo* assessments, including long-term implantation studies in SD rats, confirmed the absence of systemic toxicity or adverse local tissue reactions. These findings underscore the potential of PHBHHx microspheres as safe and effective biomaterials for biomedical applications.

3.3 *In vivo* degradation properties of PHBHHx porous and solid membranes

After demonstrating the biosafety of PHBHHx, the degradation properties of PHBHHX *in vivo* were investigated. The results

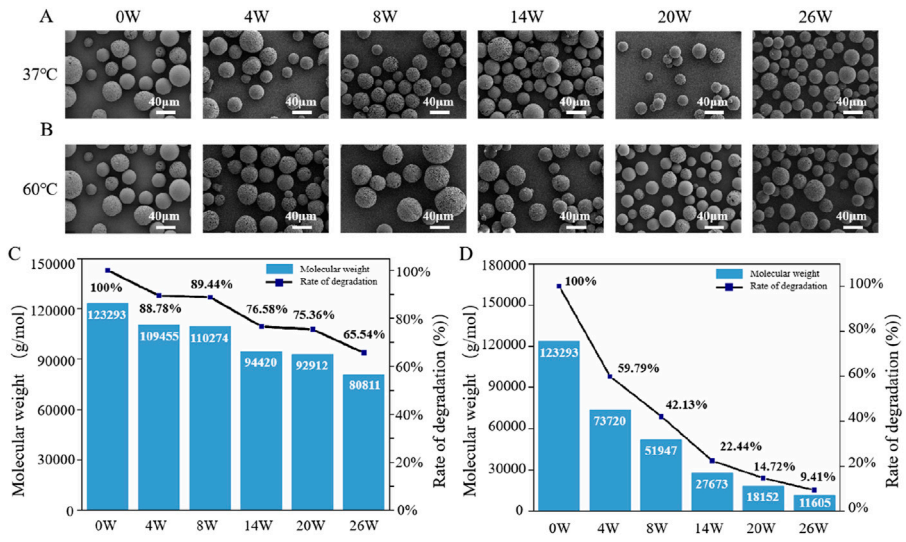

FIGURE 3
The *in vitro* degradation properties of PHBHHx microspheres. The morphological changes of PHBHHx microspheres in PBS at 37°C **(A)** and 60°C **(B)** The Mw changes of PHBHHx microspheres in PBS at 37°C **(C)** and 60°C **(D)**.

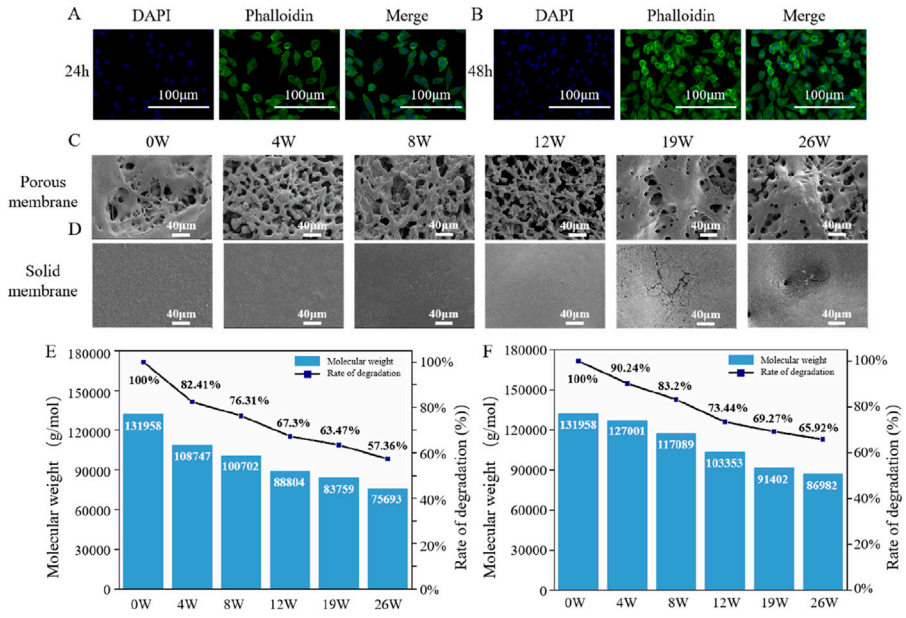

FIGURE 4
In vitro cytocompatibility and *in vivo* degradation properties of PHBHHx microspheres. DAPI-phalloidin staining of L929 cells *co*-cultured with extracts from PHBHHx microspheres for 24 h **(A)** and 48 h **(B)** The morphological changes of porous **(C)** and solid PHBHHx membranes **(D)** The Mw changes of porous **(E)** and solid **(F)** PHBHHx membranes.

indicated that electrospun porous PHBHHx membranes exhibited morphological changes as early as the fourth week, with an increasing number of broken fibers over time, characterized by smooth fracture surfaces (Figure 4C). Solid PHBHHx membranes underwent progressive surface smoothing, with surface cracks becoming evident by week 19 (Figure 4D). The primary reason for PHBHHx degradation *in vivo* is the presence of various enzymes in the body that can break its molecular chains, leading to gradual decomposition. *In vivo*, electrospun porous membranes demonstrated a faster reduction in molecular weight compared to solid membranes, by 26W, the Mw of electrospun porous membranes decreased to 57.36% of its initial value, from 131,958 to 75,693 (Figure 4E), while solid films decreased to 65.92% of its initial value, from 131,958 to 86,982 (Figure 4F), this is due to the fact that the porous structure increases the contact area with the environment, thereby accelerating degradation.

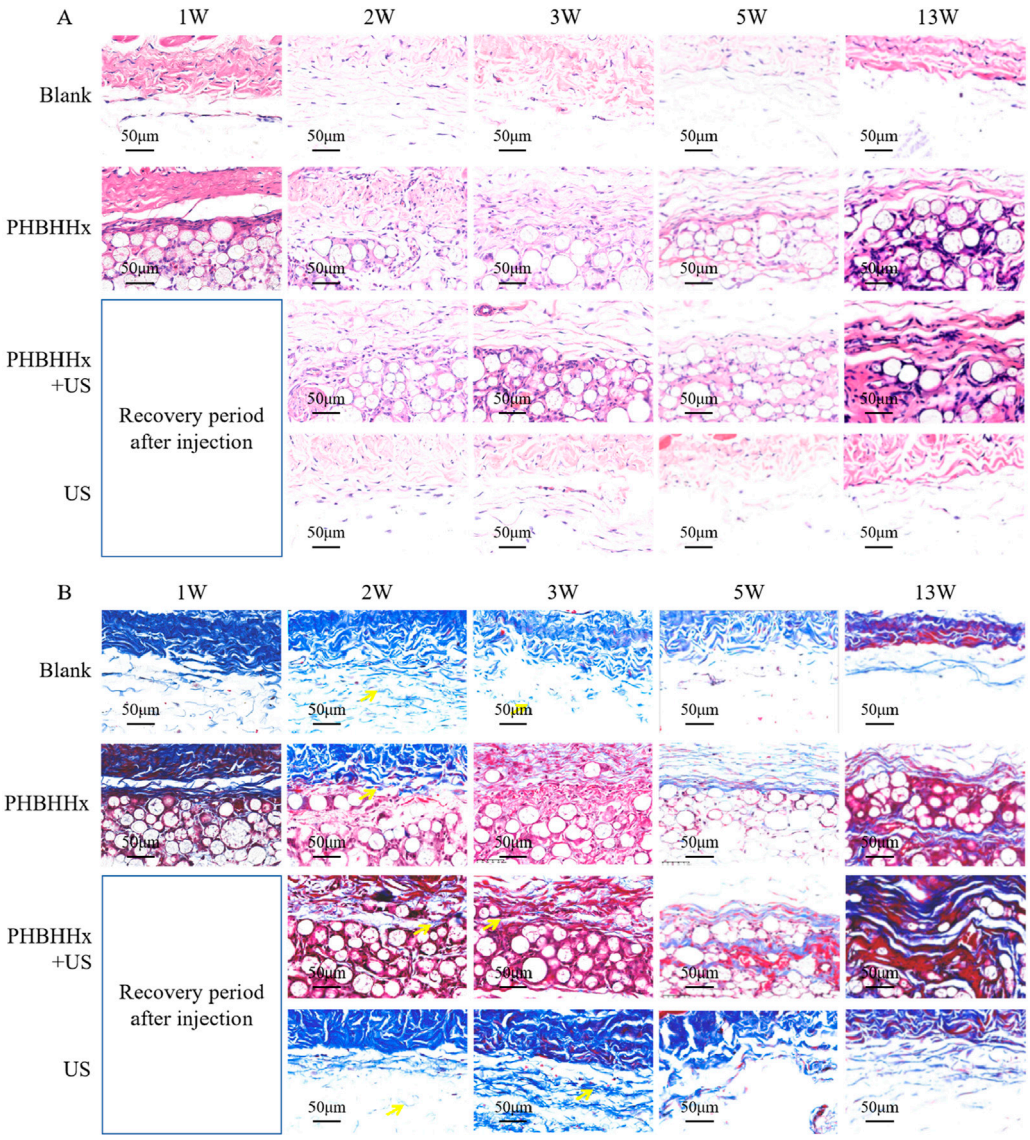

FIGURE 5
H&E staining **(A)** and Masson's trichrome staining **(B)** of skin tissue of blank, PHBHHx, PHBHHx + US and US groups.

3.4 PHBHHx-CMC composite used for collagen regeneration

To evaluate the potential of PHBHHx-CMC composite in promoting collagen regeneration, *in vivo* animal studies were conducted. Histopathological analysis of subcutaneous tissue samples collected at 1, 2, 3, 5, and 13 weeks post-injection revealed distinct differences in tissue response and collagen regeneration across the blank, PHBHHx, PHBHHx + US, and US groups (Figures 5–7). During the early stage (1–5 weeks), all groups exhibited a mild inflammatory response. Compared to the blank group and the US group, the inflammatory response was significantly higher in the PHBHHx and PHBHHx + US groups. However, the overall inflammatory level of PHBHHx and PHBHHx + US groups remained mild. These findings suggested that the PHBHHx-CMC composite demonstrates good biocompatibility with minimal tissue irritation and adverse reactions. By 13 weeks (Figure 5A), the blank group showed no pathological changes, inflammatory infiltration, or granulation tissue formation. The inflammatory response subsided as the saline solution was absorbed into the tissue, restoring it to its normal state. Similarly, no significant pathological changes or notable inflammatory responses were observed in the US group. In contrast, the PHBHHx and PHBHHx + US groups exhibited prominent fibrocystic structures surrounded by significant inflammatory cell infiltration, predominantly lymphocytes (Figure 5A). The heightened inflammatory response in the PHBHHx and PHBHHx + US groups may be attributed to the gradual absorption of CMC by the tissue, facilitating cellular infiltration into the microspheres and enhancing interactions between cells and the biomaterial. Additionally, the formation of fibrotic cystic structures around the implant material likely contributed to the recruitment of immune cells, thereby sustaining the inflammatory response. Compared to the PHBHHx group, the PHBHHx + US

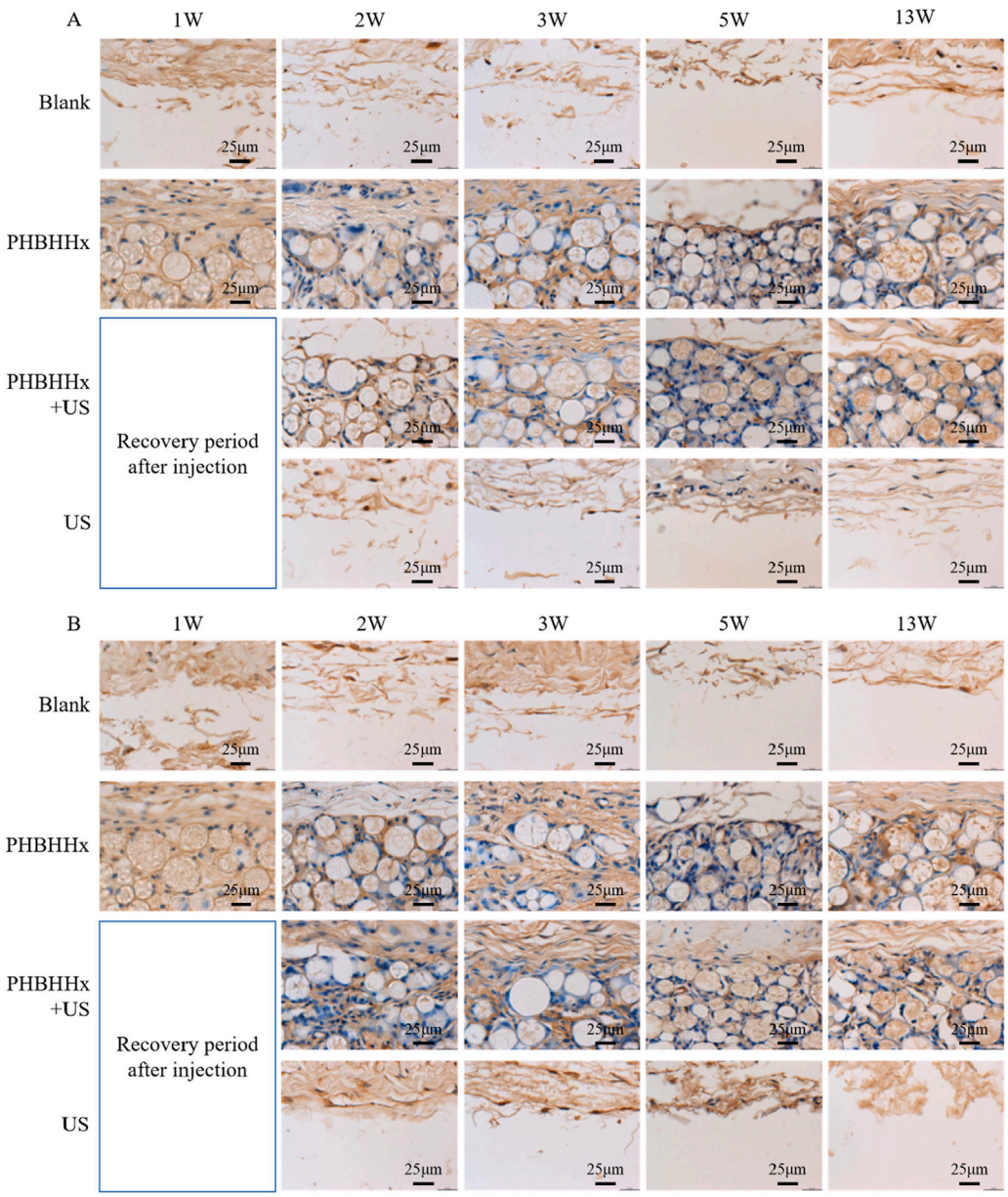

FIGURE 6
Immunohistochemical staining for Col-I **(A)** and Col-III **(B)** in skin tissues from the blank, PHBHHx, PHBHHx + US and US groups.

group exhibited a significantly reduced inflammatory response (Figure 7B), which may be attributed to the anti-inflammatory effect of LIPUS (Xu et al., 2021).

Masson's trichrome staining results showed that the collagen staining area in the blank group remained relatively low, indicating a mild tissue response. The collagen staining area in the US group was slightly larger compared to the blank group, which is related to the ability of LIPUS to promote the proliferation of subcutaneous fibroblasts and enhance collagen expression (Figure 5B). Over time, cells gradually infiltrated and penetrated into the material, resulting in a gradual increase in the collagen staining area in the PHBHHx and PHBHHx + US groups. Notably, at weeks 5 and 13, the PHBHHx + US group exhibited significantly deeper and larger collagen staining. In addition, the dermal thickness of the PHBHHx + US group also increased significantly by 13W (Figure 7C). These results indicated that the PHBHHx microspheres, which are the active component within the PHBHHx-CMC composite, significantly enhanced collagen synthesis and regeneration under the stimulation of LIPUS.

Immunohistochemical staining for type I and III collagen further supported these observations, compared to the blank and US groups, the PHBHHx and PHBHHx + US groups exhibited more intense brown staining in the subcutaneous tissue, indicating a more significant collagen synthesis in these groups (Figures 6A, B). Quantitative analysis of immunohistochemical staining revealed that the amount of newly synthesized collagen was significantly higher in the PHBHHx and PHBHHx + US groups compared to the

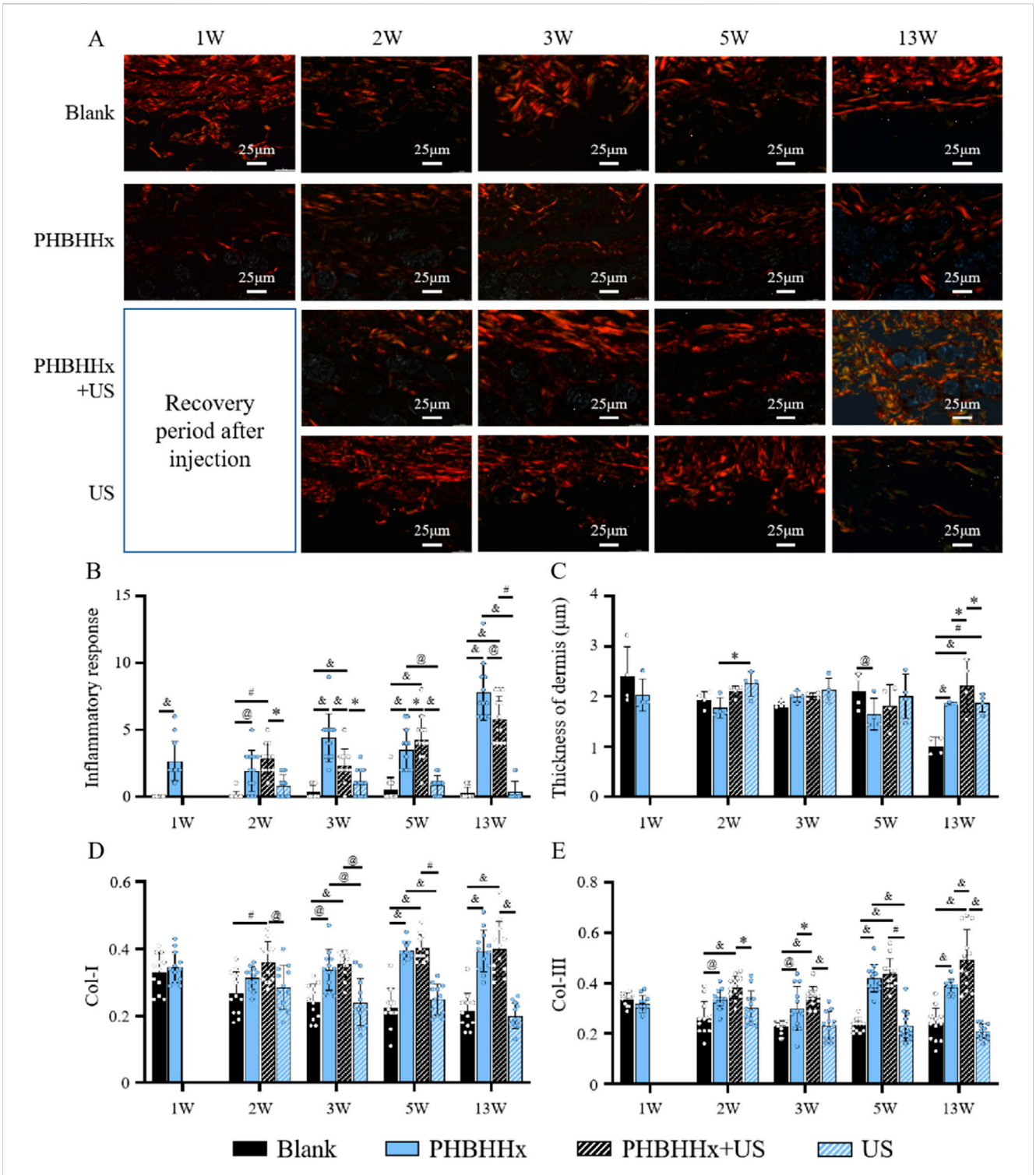

FIGURE 7
(A) Sirus red staining of skin tissue of blank, PHBHHx, PHBHHx + US and US groups. Quantitative evaluation of inflammatory response **(B)** thickness of dermal **(C)** and immunohistochemical [Col-I **(D)** and Col-III **(E)**] analysis of skin tissues from blank, PHBHHx, PHBHHx + US and US groups. The significance of the data was calculated by the one-way ANOVA (*$p < 0.05$, $^{@}p < 0.01$, $^{\#}p < 0.001$ and $^{\&}p < 0.0001$).

blank and US groups. Moreover, the PHBHHx + US group exhibited a significantly greater collagen content than the PHBHHx group ($p < 0.05$) (Figures 7D, E). Col-I, which is crucial for tissue strength and structural integrity, and Col-III, involved in early wound healing and tissue remodeling (Singh et al., 2023; Gao et al., 2023), were both substantially elevated in the PHBHHx + US group. These results indicated that LIPUS not only effectively alleviates the inflammatory response but also significantly promotes collagen synthesis induced by PHBHHx microspheres, thereby achieving better filling effects. Furthermore, Sirius Red staining confirmed these findings

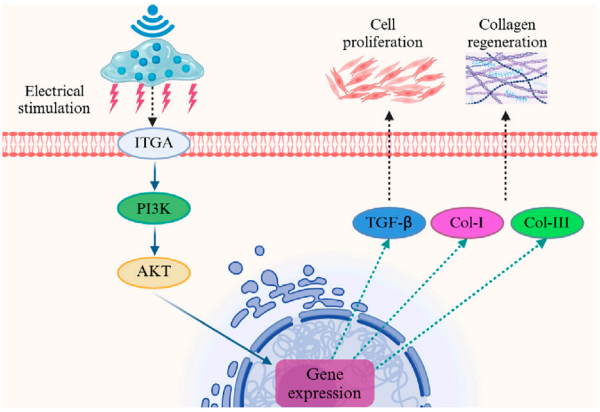

FIGURE 8
Potential mechanism of PHBHHx -CMC composite for promoting collagen regeneration.

(Figure 7A),more Col-I and Col-III were found in PHBHHx + US group. Over time, PHBHHx and PHBHHx + US microspheres exhibited prominent staining for type I (strong orange-yellow or bright red) and type III (green) collagen, with a marked increase in the staining of both collagen types in the PHBHHx + US group at week 13.

Overall, these results demonstrated that PHBHHx microspheres can effectively stimulated collagen formation, their ability to promote collagen regeneration can be significantly enhanced when stimulated by LIPUS. This suggested that the electrical signals generated by PHBHHx can further regulate cell activity to promote collagen production. Studies have shown that piezoelectric stimulation can promote fibroblast migration, proliferation, and collagen expression by modulating the PI3K/AKT serine/threonine kinase (AKT) pathway (Xu Q. et al., 2024; Dai et al., 2024). The mechanism by which PHBHHx enhances collagen regeneration under ultrasound stimulation may be that the electrical signal generated by PHBHHx under ultrasound stimulation is transmitted from the extracellular matrix (ECM) to intracellular components through the integrin-PI3K pathway. This process activates the PI3K/AKT pathway, which in turn affects the gene expression of downstream molecules such as Col-I, Col-III and TGF-β, thereby promoting cell proliferation and collagen regeneration (Figure 8). These findings highlight the potential of the piezoelectric PHBHHx to improve long-term outcomes in aesthetic applications.

4 Conclusion

This study demonstrated the potential of piezoelectric PHBHHx microspheres as a novel biomaterial for enhancing collagen regeneration under LIPUS stimulation. The PHBHHx microspheres, activated by mechanical deformation through external LIPUS, generated localized electrical signals that significantly enhance collagen production. Biocompatibility assessments confirmed that PHBHHx microspheres exhibited no significant cytotoxicity or systemic toxicity, both *in vitro* and *in vivo*. Histological analysis revealed that LIPUS-stimulated PHBHHx group exhibited notably increased collagen deposition, with more organized and denser collagen structures compared to other experimental groups. These findings suggest that the combination of PHBHHx microspheres and LIPUS offers a promising dual-functional strategy, not only enabling volumetric restoration but also actively promoting collagen regeneration through bioelectric cues, which may be linked to the PI3K/AKT pathway. In contrast to conventional dermal fillers that primarily offer temporary volumization, this method promotes endogenous tissue repair and remodeling at a deeper level. Additionally, the inflammatory response in the PHBHHx + US group was well-regulated, further supporting the safety and biocompatibility of the material. The combination of PHBHHx microspheres and LIPUS not only augments collagen production but also mitigates the risk of chronic inflammation, offering a comprehensive solution for soft tissue augmentation and regeneration.

Future research should focus on the scalability of this approach in clinical applications and examine the long-term effects of repeated LIPUS treatments on collagen production and tissue function. Also, the sample size of the animals used in this study is relatively small (n = 2). Hence, increasing the sample size is necessary in the next phase of this project. Such studies will help to further optimize therapeutic efficacy and advance the use of PHBHHx microspheres in aesthetic medicine and regenerative therapies. Overall, the combination of piezoelectric PHBHHx microspheres and LIPUS offers a versatile biomaterial platform with significant potential in soft tissue repair, aesthetic enhancement, and broader regenerative medicine applications. Furthermore, the translational pathway of PHBHHx microspheres from laboratory research to clinical application involves overcoming key challenges such as large-scale production, quality control, and individual variability. Ensuring scalable, cost-effective production while maintaining consistency and adherence to Good Manufacturing Practices (GMP). Rigorous quality control measures, including testing for size uniformity and purity, are essential for reproducibility. Additionally, factors like age, skin type, and immune response can influence treatment outcomes, highlighting the need for personalized treatment plans. Addressing these challenges will be crucial for the successful clinical application of PHBHHx microspheres.

Data availability statement

The original contributions presented in the study are included in the article/Supplementary Material, further inquiries can be directed to the corresponding authors.

Ethics statement

The animal study was approved by HangZhou Hibio Yunjing Tech Co., Ltd and Institute of Laboratory Animal Resources, Chinese Institute for Food and Drug Control. The study was conducted in accordance with the local legislation and institutional requirements.

Author contributions

ZF: Supervision, Writing–original draft, Writing–review and editing. YQ: Investigation, Writing–review and editing. YW: Investigation, Writing–review and editing. YX: Investigation, Writing–review and editing. HZ: Investigation, Writing–review and editing. YT: Investigation, Writing–review and editing. ZJ: Investigation, Writing–review and editing. JZ: Investigation, Writing–review and editing. CT: Supervision, Writing–review and editing.

Funding

The author(s) declare that financial support was received for the research, authorship, and/or publication of this article. This study was funded by Beijing Joyinera Biomaterial Technology Co., Ltd.

Conflict of interest

Authors ZF, YQ, YW, YX, HZ, YT, ZJ, JZ, and CT were employed by Beijing Joyinera Biomaterial Technology Co., Ltd.

The authors declare that this study received funding from Beijing Joyinera Biomaterial Technology Co., Ltd. The funder had the following involvement in the study: study design, data collection and analysis, decision to publish and preparation of the manuscript.

Generative AI statement

The author(s) declare that no Generative AI was used in the creation of this manuscript.

Publisher's note

Supplementary material

The Supplementary Material for this article can be found online at: https://www.frontiersin.org/articles/10.3389/fbioe.2025.1554825/full#supplementary-material

References

Alghamdi, H., Nair, S. A. O., and Neithalath, N. (2019). Insights into material design, extrusion rheology, and properties of 3D-printable alkali-activated fly ash-based binders. *Mat. Des.* 167, 107634. doi:10.1016/j.matdes.2019.107634

Badali, V., Checa, S., Zehn, M. M., Marinkovic, D., and Mohammadkhah, M. (2024). Computational design and evaluation of the mechanical and electrical behavior of a piezoelectric scaffold: a preclinical study. *Front. Bioeng. Biotech.* 11, 1261108. doi:10.3389/fbioe.2023.1261108

Bakrani Balani, S., Mokhtarian, H., Salmi, T., and Coatanéa, E. (2023). An investigation of the influence of viscosity and printing parameters on the extrudate geometry in the material extrusion process. *Polymers* 15, 2202. doi:10.3390/polym15092202

Bugnicourt, E., Cinelli, P., Lazzeri, A., and Alvarez, V. A. (2014). Polyhydroxyalkanoate (PHA): review of synthesis, characteristics, processing and potential applications in packaging, Express. *Polym. Lett.* 11, 791–808. doi:10.3144/expresspolymlett.2014.82

Burgess, C., Dayan, S., Bank, D., Weinkle, S., Sartor, M., Chawla, S., et al. (2024). Hyaluronic acid filler VYC-25L for jawline restoration yields high satisfaction, improved jawline measurements, and sustained effectiveness across skin types, age, and gender for up to 12 Months. *Aesthet. Surg. J. sjae172* 45, 98–107. doi:10.1093/asj/sjae172

Dai, J., Shao, J., Zhang, Y., Hang, R., Yao, X., Bai, L., et al. (2024). Piezoelectric dressings for advanced wound healing. *J. Mat. Chem. B* 12, 1973–1990. doi:10.1039/D3TB02492J

David, M. R., and Jennifer, L. (2021). Skin collagen through the lifestages: importance for skin health and beauty. *Plast. Aesthet. Res.* 8, 2. doi:10.20517/2347-9264.2020.153

Donate, R., Paz, R., Moriche, R., Sayagués, M. J., Alemán-Domínguez, M. E., and Monzón, M. (2023). An overview of polymeric composite scaffolds with piezoelectric properties for improved bone regeneration. *Mat. Des.* 231, 112085. doi:10.1016/j.matdes.2023.112085

Fanian, F., Deutsch, J.-J., Bousquet, M. T., Boisnic, S., Andre, P., Catoni, I., et al. (2023). A hyaluronic acid-based micro-filler improves superficial wrinkles and skin quality: a randomized prospective controlled multicenter study. *J. Dermatol. Treat.* 34, 2216323. doi:10.1080/09546634.2023.2216323

Gao, J., Guo, Z., Zhang, Y., Liu, Y., Xing, F., Wang, J., et al. (2023). Age-related changes in the ratio of Type I/III collagen and fibril diameter in mouse skin. *Regen. Biomater.* 10, rbac110. doi:10.1093/rb/rbac110

Huang, J., Heng, S., Zhang, W., Liu, Y., Xia, T., Ji, C., et al. (2022). Dermal extracellular matrix molecules in skin development, homeostasis, wound regeneration and diseases. *Semin. Cell. Dev. Biol.* 128, 137–144. doi:10.1016/j.semcdb.2022.02.027

Kim, J.-E., and Sykes, J. M. (2011). Hyaluronic acid fillers: history and overview. *Facial. Plast. Surg.* 27, 523–528. doi:10.1055/s-0031-1298785

Kim, J. S. (2021). Fine wrinkle treatment and hydration on the facial dermis using hydrotoxin mixture of microbotox and microhyaluronic acid. *Aesthet. Surg. J.* 4, 538–549. doi:10.1093/asj/sjaa231

Li, A. R., Taylor, B., Snyder, A. N., and Schlesinger, T. (2023). Algeness—what do we know about this filler. *Dermatol. Revs.* 4, 100–104. doi:10.1002/der2.184

Li, Y., Fan, Y., Zhao, S., and Cheng, B. (2024). Ultrasound-triggered piezoelectric polyetheretherketone with boosted osteogenesis via regulating Akt/GSK3β/β-catenin pathway. *J. Nanobiotechnol.* 22, 539. doi:10.1186/s12951-024-02814-9

Lizarraga Valderrama, L. R., Thomas, C., Cadiz Miranda, J. I., and Roy, I. (2018). *Tissue engineering: polyhydroxyalkanoate-based materials and composites, encyclopedia of polymer applications*. Boca Raton, FL, USA: Taylor and Francis Group, 2652–2675.

Luo, W., Li, Z., Ren, C., Xu, H., Zhang, H., Cao, Z., et al. (2024). Zn^{2+} driven H2S/Cu^{2+} sustained releasing nanofibers with immunoregulation for wound healing. *Mat. Des.* 238, 112626. doi:10.1016/j.matdes.2023.112626

Miyazaki, T., Honda, A., Ikegami, T., Iwamoto, J., Monma, T., Hirayama, T., et al. (2015). Simultaneous quantification of salivary 3-hydroxybutyrate, 3-hydroxyisobutyrate, 3-hydroxy-3-methylbutyrate, and 2-hydroxybutyrate as possible markers of amino acid and fatty acid catabolic pathways by LC-ESI-MS/MS. *SpringerPlus* 4, 494. doi:10.1186/s40064-015-1304-0

Narins, R. S., Dayan, S. H., Brandt, F. S., and Baldwin, E. K. (2008). Persistence and improvement of nasolabial fold correction with nonanimal-stabilized hyaluronic acid 100,000 gel particles/mL filler on two retreatment schedules: results up to 18 months on two retreatment schedules. *Dermatol. Surg.* 34, S2–S8. doi:10.1111/j.1524-4725.2008.34236.x

Panda, A. K., and Basu, B. (2021). Biomaterials-based bioengineering strategies for bioelectronic medicine. *Mat. Sci. Eng. R.* 146, 100630. doi:10.1016/j.mser.2021.100630

Pierre, S., Liew, S., and Bernardin, A. (2015). Basics of dermal filler rheology. *Dermatol. Surg.* 41, S120–S126. doi:10.1097/DSS.0000000000000334

Pouton, C. W., and Akhtar, S. (1996). Biosynthetic polyhydroxyalkanoates and their potential in drug delivery. *Rev* 18, 133–162. doi:10.1016/0169-409X(95)00092-L

Pu, S.-Y., Huang, Y.-L., Pu, C.-M., Kang, Y.-N., Hoang, K. D., Chen, K.-H., et al. (2080). Effects of oral collagen for skin anti-aging: a systematic review and meta-analysis. *Nutrients* 15, 2080. doi:10.3390/nu15092080

Rajabi, A. H., Jaffe, M., and Arinzeh, T. L. (2015). Piezoelectric materials for tissue regeneration: a review. *Biomater* 24, 12–23. doi:10.1016/j.actbio.2015.07.010

Ranella, A., Barberoglou, M., Bakogianni, S., Fotakis, C., and Stratakis, E. (2010). Tuning cell adhesion by controlling the roughness and wettability of 3D micro/nano silicon structures. *Biomater* 6, 2711–2720. doi:10.1016/j.actbio.2010.01.016

Shin, S. H., Lee, Y. H., Rho, N.-K., and Park, K. Y. (2023). Skin aging from mechanisms to interventions: focusing on dermal aging. *Front. Physiol.* 14, 1195272. doi:10.3389/fphys.2023.1195272

Singh, D., Rai, V., and Agrawal, D. K. (2023). Regulation of collagen I and collagen III in tissue injury and regeneration. *Cardiovasc. Med.* 7, 5–16. doi:10.26502/fccm.92920302

Tang, X., Duan, Q., Chen, Y., Yi, Z., Jiang, H., Ni, Y., et al. (2024). Encapsulated inorganic pigments in epoxy composite microspheres using emulsion synthesis. *Colloid. Surf. A* 701, 134963. doi:10.1016/j.colsurfa.2024.134963

Wang, Q., Yan, H., Yao, L., Li, W., and Xiao, J. (2024). A highly durable and biocompatible bionic collagen implant with exceptional anti-calcification and collagen regeneration capabilities for improved skin rejuvenation. *Mat. Des.* 244, 113177. doi:10.1016/j.matdes.2024.113177

Xu, H., Zhang, Y., Zhang, Y., Zhao, Z., Xue, T., Wang, J., et al. (2024a). 3D bioprinting advanced biomaterials for craniofacial and dental tissue engineering – a review. *Mat. Des.* 241, 112886. doi:10.1016/j.matdes.2024.112886

Xu, M., Wang, L., Wu, S., Dong, Y., Chen, X., Wang, S., et al. (2021). Review on experimental study and clinical application of low-intensity pulsed ultrasound in inflammation. *Imaging. Med. Surg.* 11, 443–462. doi:10.21037/qims-20-680

Xu, Q., Dai, W., Li, P., Li, Q., Gao, Z., Wu, X., et al. (2024b). Piezoelectric film promotes skin wound healing with enhanced collagen deposition and vessels regeneration via upregulation of PI3K/AKT. *Nano. Res.* 17, 7461–7478. doi:10.1007/s12274-024-6717-z

Yang, C.-Y., Chang, Y.-C., Tai, H.-C., Liao, Y.-H., Huang, Y.-H., Hui, R.C.-Y., et al. (2024). Evaluation of collagen dermal filler with lidocaine for the correction of nasolabial folds: a randomized, double-blind, multicenter clinical trial. *Clin. Cosmet. Inv. Derm.* 17, 1621–1631. doi:10.2147/CCID.S447760

Yang, L., Zhao, Y., Cui, D., Liu, Y., Zou, Q., Xu, S., et al. (2022). Coaxial bioelectrospinning of P34HB/PVA microfibers biomimetic scaffolds with simultaneity cell-laden for improving bone regeneration. *Mat. Des.* 213, 110349. doi:10.1016/j.matdes.2021.110349

Zhang, C., Song, W., Guo, X., Li, Z., Kong, Y., Du, J., et al. (2025). Piezoelectric nanocomposite electrospun dressings: tailoring mechanics for scar-free wound recovery. *Biomater. Adv.* 167, 214119. doi:10.1016/j.bioadv.2024.214119

Zhang, Q., An, Z.-Y., Jiang, W., Jin, W.-L., and He, X.-Y. (2023). Collagen code in tumor microenvironment: functions, molecular mechanisms, and therapeutic implications. *Biomed. Pharmacother.* 166, 115390. doi:10.1016/j.biopha.2023.115390

Zheng, F., Wu, T., Wang, F., Li, H., Tang, H., Cui, X., et al. (2024). Low-intensity pulsed ultrasound promotes the osteogenesis of mechanical force-treated periodontal ligament cells via Piezo1. *Front. Bioeng. Biotech.* 12, 1347406. doi:10.3389/fbioe.2024.1347406

frontiers | Frontiers in Bioengineering and Biotechnology

TYPE Systematic Review
PUBLISHED 09 April 2025
DOI 10.3389/fbioe.2025.1547158

OPEN ACCESS

EDITED BY
Dan Lin,
Shanghai University of Medicine and Health Sciences, China

REVIEWED BY
Sonu Saini,
Anand International College of Engineering, Jaipur, India
Giovanna Speranza Zabeu,
University of São Paulo, Brazil
Lam Le,
Can Thơ Medical University, Vietnam

*CORRESPONDENCE
Xiongqun Zeng,
xiongqunzeng@163.com

RECEIVED 19 December 2024
ACCEPTED 31 March 2025
PUBLISHED 09 April 2025

CITATION
Zhou W, Feng S, Chu X, Xu S and Zeng X (2025) Effect of collagen crosslinkers on sodium hypochlorite treated dentin bond strength: a systematic review and meta-analysis. *Front. Bioeng. Biotechnol.* 13:1547158. doi: 10.3389/fbioe.2025.1547158

Effect of collagen crosslinkers on sodium hypochlorite treated dentin bond strength: a systematic review and meta-analysis

Weiqing Zhou[1], Shuting Feng[1], Xiaojun Chu[2], Shuaimei Xu[1] and Xiongqun Zeng[1]*

[1]Department of Endodontics, Stomatological Hospital, School of Stomatology, Southern Medical University, Guangzhou, Guangdong, China, [2]Guangzhou Haizhu District Hospital of Stomatology, Guangzhou, Guangdong, China

Introduction: The bond strength (BS) between composite resin and dentin is a crucial factor determining the long-term success of restorations. Sodium hypochlorite (NaOCl), a frequently used root canal irrigating agent, has been demonstrated to notably influence the properties of dentin, thereby affecting the BS. Moreover, the application of collagen crosslinkers has become a potential approach to improve the stability of the resin-dentin bond. Nevertheless, the effect of collagen crosslinkers on the bond strength (BS) between sodium hypochlorite (NaOCl) treated dentin and composite resin remains a topic of contention, and there is a lack of in-depth understanding in the existing literature. The purpose of this systematic review and meta-analysis was to analyze the current literature on the effect of collagen crosslinkers on the BS between sodium hypochlorite treated dentin and composite resin.

Methods: Databases including PubMed, EMBASE, Cochrane library, Scopus, Web of Science and SinoMed were searched. *In vitro* studies reported the effect of crosslinking agents on NaOCl-treated dentin BS were included. The reference lists of studies included via databases were manually searched for more studies that fulfilled the inclusion criteria. The initial search yielded 1,538 studies, and subsequent screening resulted in the inclusion of 14 studies. Most of studies (78.6%, 11/14) were categorized as having a "low" risk of bias. The studies included in the meta-analysis employed a range of cross-linking agents, including ethylenediaminetetraacetic acid (EDTA), phytic acid (IP6), proanthocyanidin (PA), rosmarinic acid (RA) and sodium ascorbate (SA). Subgroup comparisons were performed according to NaOCl exposure duration. Studies treated with different concentration of NaOCl were analyzed separately.

Results: For dentin exposed less than 1 min or NaOCl at lower concentration, significant positive effect cannot be observed when using collagen crosslinkers. For dentin exposed more than 1 min in NaOCl at concentrations greater than 2.5%, EDTA, PA and SA were observed to significantly improve the BS. RA is proved effective in improving the BS of dentin exposed to high concentrations NaOCl within a shorter duration. Current evidence is insufficient to conclude that IP6 has a positive effect in NaOCl-treated dentin bonding performance.

Conclusion: The effect of collagen crosslinkers on the BS of NaOCl treated dentin was influenced by the concentration of NaOCl and the duration of exposure.

KEYWORDS

dental bonding, tensile strength, cross-linkers, sodium hypochlorite, meta-analysis, systematic review

1 Introduction

In modern dentistry, the long-term success of dental restorations highly depends on the bond strength (BS) between composite resins and dentin. A strong and stable bond not only ensures restoration functionality but also prevents complications like secondary caries and debonding. However, achieving and maintaining optimal BS is challenging due to multiple influencing factors. One such factor is sodium hypochlorite (NaOCl), a commonly used root canal irrigant in clinical practice.

Sodium hypochlorite (NaOCl) is renowned for its potent bactericidal properties, which enable it to effectively eliminate microorganisms colonizing the root canal system and its walls. Additionally, it can neutralize bacterial toxins and dissolve both live and necrotic pulp tissue. Nevertheless, mounting evidence indicates that NaOCl may have adverse effects on dentin. Research has shown that its application can lead to the decomposition of collagen within dentin, thereby disrupting the formation of the mixed layer. Consequently, the adhesive is unable to effectively penetrate the collagen fiber network or dentin tubules (Carrilho et al., 2009; Cai et al., 2023). Moreover, NaOCl chlorination generates oxidation radicals that react with the monomer radicals generated during the polymerization of methacrylate monomers, as well as the initiator and radicals in the bonding system. the concentration of free radicals in the growth chain is diminished, resulting in premature chain termination and subsequently influencing the polymerization reaction during the bonding process. It has been demonstrated in numerous studies that NaOCl markedly diminishes the BS of dentin (Morris et al., 2001; Farina et al., 2011; Dikmen, 2015; Pimentel Correa et al., 2016; Haralur et al., 2017; Li et al., 2022; Xu et al., 2022).

Collagen fibers are pivotal in anchoring the composite resin to the dentin surface. The bio-stability of both the underlying demineralized collagen and infiltrated resin is considered one of the most important factors for success of dental restorations (Breschi et al., 2008; Breschi et al., 2018). The enzymatic degradation of bare collagen and the hydrolytic precipitation of resin within the mixed layer are the primary factors influencing the durability of resin dentin bonding (Ricucci and Siqueira, 2011; Prasansuttiporn et al., 2012). The BS is mainly provided by the penetration of the resin into the demineralized dentin, which forms a mechanical inlay force. Incomplete resin monomer penetration results in the exposure of collagen fibers and subsequent degradation of these fibers under the influence of water, enzymes, bacteria, stress, temperature and other factors (Betancourt et al., 2019). This eventually leads to the failure of adhesive bonded restorations (Carvalho et al., 2005). To address these challenges and enhance the stability of collagen fibers in the bonding interface, the use of cross-linking agents has been proposed, which can promote the inter or intramolecular cross- linking of collagen molecules (Shafiei et al., 2023), thereby maintaining the integrity of the bonding interface.

This systematic review and meta-analysis aim to explore the effect of crosslinkers on BS between NaOCl-treated dentin and composite resins. Three types of crosslinkers are investigated. The synthetic chelating agent-based crosslinker, ethylenediaminetetraacetic acid (EDTA), chelates metal ions to form bridging complexes (Lanigan and Yamarik, 2002). Natural polyphenolic crosslinkers such as proanthocyanidin (PA), phytic acid (IP6), and rosmarinic acid (RA) form coordination or covalent bonds with the polar groups of metal ions or biomacromolecules via their phenolic hydroxyl groups or phosphoric acid groups (Choi et al., 2016; Ge et al., 2018; Visan and Angelescu, 2023). The organic acid salt crosslinker, sodium ascorbate (SA), generates active intermediates through redox reactions to facilitate covalent crosslinking (Boyera et al., 1998).

Despite it is widely recognized that cross-linking agents contribute to the bonding of composite resins to dentin, (Anumula et al., 2022; Hardan et al., 2022; Chen et al., 2023), their the impact on NaOCl-treated dentin remains a topic of contention. Given the lack of previous relevant meta-analyses, this study intends to fill this knowledge gap. The null hypothesis tested was that collagen crosslinkers have no effect on the BS of NaOCl-treated dentin during bonding procedures. Through a comprehensive search of relevant databases, strict inclusion and exclusion criteria, and data extraction and analysis, this study anticipates providing valuable insights into the role of crosslinkers in improving the bond strength between NaOCl-treated dentin and composite resins, which may ultimately contribute to more successful dental restorations.

2 Materials and methods

This systematic review was conducted following the Preferred Reporting Items for Systematic Reviews and Meta-Analysis (PRISMA) statement (Page et al., 2021) and has been registered in PROSPERO, number CRD42023451577. The research question of this review was: "Does crosslinking agents improve the BS of composite resin to NaOCl-treated dentin?" It is established on the PICOS framework: population (dentin substrate); intervention (use of crosslinking agents); control (adhesive application of NaOCl-treated dentin without the use of a crosslinking agents); outcome (BS); study design (*in vitro* studies).

2.1 Search strategy

The literature search was performed by two independent reviewers (ZW and FS) and six electronic databases (PubMed,

TABLE 1 PubMed search strategy.

Number	Search strategy	Results
#1	"cross linking reagents" [MeSH Terms] OR "cross linking reagents" [Title/Abstract] OR "crosslinking reagent" [Title/Abstract] OR "cross linking reagent" [Title/Abstract] OR "crosslinking reagents" [Title/Abstract] OR "cross linking" [Title/Abstract] OR "Cross-linkers" [Title/Abstract] OR "Crosslinking" [Title/Abstract] OR "Cross-links" [Title/Abstract] OR "cross linking" [Title/Abstract] OR "cross linking agents" [Title/Abstract] OR "dentin collagen" [Title/Abstract] OR "cross linking agent" [Title/Abstract] OR "Crosslink" [Title/Abstract] OR "cross linker" [Title/Abstract]	99,607
#2	"edetic acid" [MeSH Terms] OR "edetic acid" [Title/Abstract] OR "EDTA" [Title/Abstract] OR "ethylenedinitrilotetraacetic acid" [Title/Abstract] OR "Glutaral" [MeSH Terms] OR "Glutaral" [Title/Abstract] OR "Glutardialdehyde" [Title/Abstract] OR "Glutaraldehyde" [Title/Abstract] OR "carbodiimides" [MeSH Terms] OR "carbodiimides" [Title/Abstract] OR "Riboflavin" [MeSH Terms] OR "Riboflavin" [Title/Abstract] OR "vitamin g" [Title/Abstract] OR "vitamin b2" [Title/Abstract] OR "Proanthocyanidins" [MeSH Terms] OR "Proanthocyanidins" [Title/Abstract] OR "epigallocatechin gallate" [Title/Abstract] OR "epigallocatechin-3-gallate" [Title/Abstract] OR "epigallocatechin-3-O-gallate" [Title/Abstract] OR "EGCG" [Title/Abstract] OR "genipin" [Title/Abstract] OR "Curcumin" [MeSH Terms] OR "Curcumin" [Title/Abstract] OR "Tannins" [MeSH Terms] OR "Tannins" [Title/Abstract] OR "tannic acid" [Title/Abstract] OR "Hesperidin" [MeSH Terms] OR "Hesperidin" [Title/Abstract]	153,610
#3	#1 OR #2	244,241
#4	"dentin" [MeSH Terms] OR "dentin" [Title/Abstract] OR "Dentins" [Title/Abstract] OR "Dentine" [Title/Abstract] OR "Dentines" [Title/Abstract]	38,386
#5	"sodium hypochlorite" [MeSH Terms] OR "sodium hypochlorite" [Title/Abstract] OR "hypochlorite sodium" [Title/Abstract] OR "Clorox" [Title/Abstract] OR "Antiformin" [Title/Abstract] OR "NaOCl" [Title/Abstract] OR "NaClO" [Title/Abstract] OR "hypochlorite sodium" [Title/Abstract]	11,941
#6	"tensile strength" [MeSH Terms] OR "tensile strength" [Title/Abstract] OR "shear strength" [MeSH Terms] OR "shear strength" [Title/Abstract] OR "microtensile strength" [Title/Abstract] OR "microshear strength" [Title/Abstract] OR "shear bond strength" [Title/Abstract] OR "bond strength" [Title/Abstract] OR ("Bongding" [All Fields] AND "performance" [Title/Abstract]) OR "bonding effectiveness" [Title/Abstract] OR "Bond" [Title/Abstract] OR "dental bonding" [MeSH Terms] OR "dental bonding" [Title/Abstract] OR "adhesives" [MeSH Terms] OR "adhesives" [Title/Abstract] OR "adhesion" [Title/Abstract] OR "dentin bonding agents" [MeSH Terms] OR "dentin bonding agents" [Title/Abstract] OR "dentin bonding agent" [Title/Abstract] OR "dentin bonding agent" [Title/Abstract]	486,554
#7	(#3) AND (#4) AND (#5) AND (#6)	338

EMBASE, Cochrane library, Scopus, Web of Science and SinoMed) were screened to identify relevant manuscripts that could be included. Gray literature, encompassing theses, dissertations, and preprints, has been scrupulously searched as well. No publication year or language limit was used, and the database search was extended until 30th June 2024. Reference lists of the collected studies were also manually searched for additional relevant studies that met the inclusion criteria. Search strategy were detailed in Table 1.

2.2 Study selection

Studies were imported into NoteExpress (v4.0.0.9855). Two of the review authors (ZW and FS) independently assessed the titles and abstracts of all the studies. Full texts of potentially relevant studies were achieved after screening. A third reviewer (CX) was inquired for decision if an agreement could not be achieved. The inclusion criteria were as follows: (1) Evaluated the BS to NaOCl-treated dentin and composite resin; (2) Reported the effect on BS of the use of a crosslinking agent prior to the application of adhesive system (*in vitro*, *in vivo*, or both); (3) Included a control group where a crosslinking agent was not used; (4) Reported the micro tensile BS or shear bong strength in MPa.

The exclusion criteria were: (1) reviews; (2) case reports; (3) incomplete data reported (results presented solely in figures without specifying the exact mean values and standard deviations); (4) lacking comparison group. Details of the studies selection and elimination are shown in Figure 1.

2.3 Data extraction

Duplicate records were identified using NoteExpress software. Subsequently, these duplicates were cross - checked by the authors (ZW and FS) and then eliminated. Two reviewers (ZW and FS) carried out the data extraction independently. If there were any questions, the study authors were contacted. Inter-rater reliability testing was implemented to assess the consistency of reviewers' work. Conflicts were settled by consulting a third author (ZX). Relevant data were extracted and tabulated with Microsoft Office Excel. The following factors were taken into account when creating

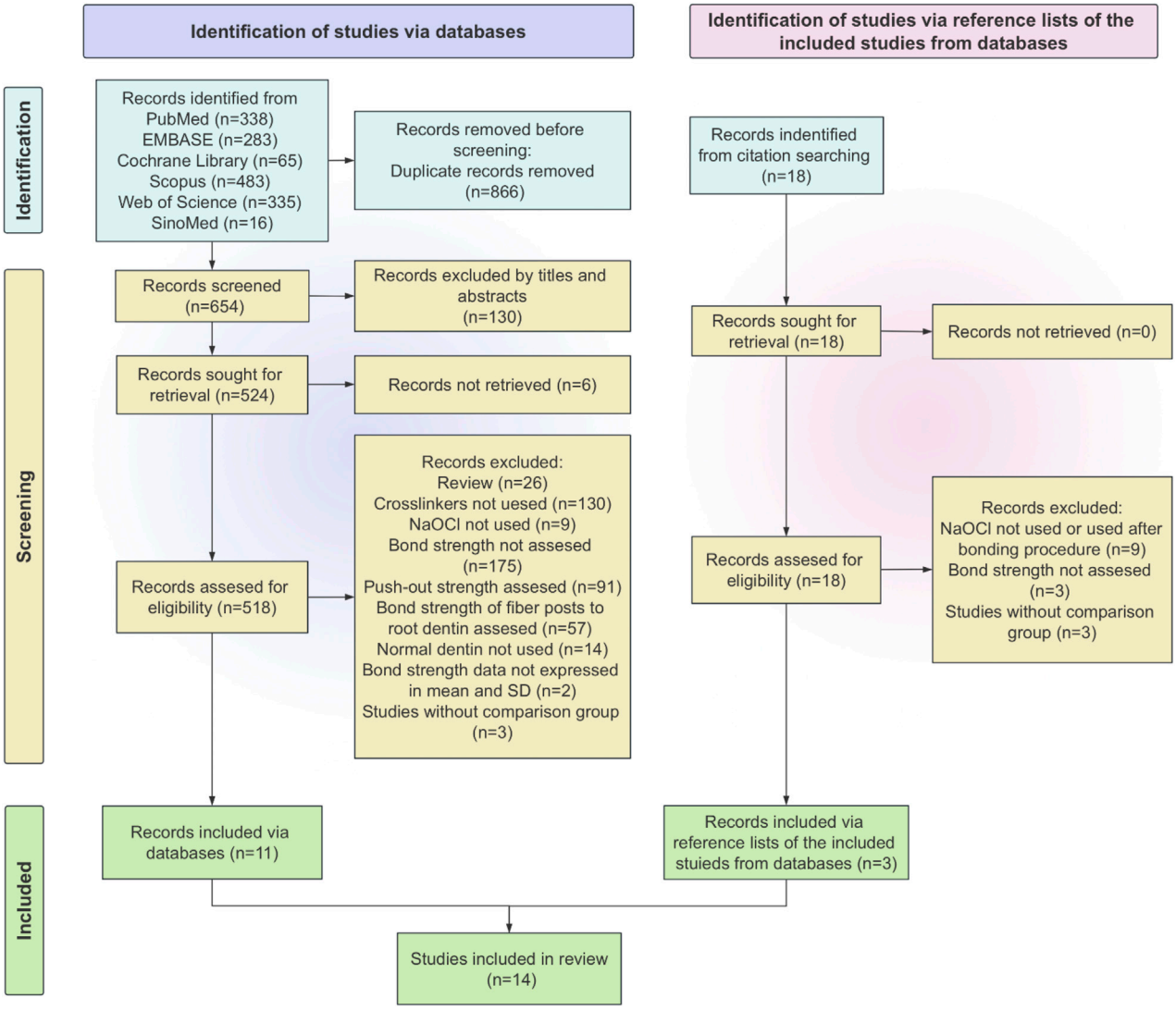

FIGURE 1
Flowchart of studies selection.

data extraction tables: author, year, tooth type, NaOCl concentration, NaOCl treated time, crosslinking agents, crosslinking agents' concentration, adhesive used, bond strength test, predominant failure mode and main results (Table 2).

2.4 Quality assessment

Based on and modified from previous study, (Hardan et al., 2022), risk of bias was assessed by two reviewers according to the following parameters: standardized specimens, specimen randomization, teeth free of caries/restoration, sample size calculation, blinding of sampling and assessment, manufacturer's instructions, control groups, failure mode and incomplete outcome data. If the parameter was included or carried out correctly, the study received a "Y," but if it was absent or carried out insufficiently, it received a "N." As shown in Table 3, of the characteristics that scored "Y," 1 to 3 denoted a high risk of bias, 4 to 6 a medium risk, and 7 to 9 a low risk. Interviewing the third reviewer (ZX) settled any disputes that arose between the two investigators. Inter-rater reliability testing was implemented to assess the consistency of reviewers' assessment.

2.5 Meta-analysis

The meta-analysis was performed separately for each crosslinking agents using RevMan 5.3 software. Subgroup comparisons were performed based on the duration of NaOCl exposure. Studies of EDTA group were analyzed separately according to the concentration of NaOCl (NaOCl greater than 2.5% or less than 2.5%). The level of significance for all tests was 5%. Statistical heterogeneity among studies was measured by the Chi^2 test and the I^2 test, with values greater than 50% were considered to indicate of substantial heterogeneity (Higgins, 2003). Depending on the value of heterogeneity, the meta-

TABLE 2 Characteristics of the studies included in the review.

Author, year	Tooth type	NaOCl concen-tration	NaOCl treated time	Cross-linking agents	Crosslink-ing agents' concen-tration	Collagen treatment time	Adhesive used	Bond Strength test	Major failure mode	Main results
Arslan, 2019 (Arslan et al., 2019)	Human molars 3 mm below the occlusal surface	2.5%	Not mentioned	EDTA	17%	Not mentioned	Clearfil SE Bond (Kuraray, Osaka, Japan)	SBS	Adhensive	There is no statistically significant difference in bond strength of NaOCl-treated dentin between EDTA group and control group
Barutcigil, 2014 (Barutcigil et al., 2014)	Human molars; pulp chamber roof	5%	5 min	EDTA	17%	5 min	Adper Scotchbond Multi-purpose (3M ESPE, St Paul, MN, United States); Adper SE Plus (3M ESPE); Clearfil S3 Bond (Kuraray Medical, Okayama, Japan); Silorane Bond (3M ESPE)	μTBS	Adhensive	NaOCl significantly reduced the bond strengths of all adhesives. The EDTA and NaOCl combination did not show a statistically significant reduction in bond strengths of the adhesives to pulpal dentin
Cecchin, 2010 (Cecchin et al., 2010)	Human molars 3 mm below the occlusal surface	1%	1 h	EDTA	17%	5 min	XENO III self-etching adhesive (Dentsply/DeTrey; Konstanz, Germany)	μTBS	—	The use of 1% NaOCl alone resulted in higher bond strength than the other treatments. The combination of 1% NaOCl and 17% EDTA produced similar bond strength to that of untreated dentin
Dikmen, 2015 (Dikmen, 2015)	Human molars 3 mm below the occlusal surface	5.25%	30 s	PA	5%	10 min	Single Bond Universal; Adhesive (3M ESPE; St Paul, MN, United States)	μTBS	Adhesive/Mix	The application of PA to NaOCl-treated dentin significantly improved the microtensile bond strength
Dikmen, 2018 (Dikmen and Tarim, 2018)	Human molars 3 mm below the occlusal surface	5.25%	30 s	EDTA SA	17% EDTA 10% SA	1 min 10 min	Adper Single Bond 2 (3M ESPE, St. Paul, MN, United States; Clearfil SE Bond (Kuraray Medical, Tokyo, Japan); Xeno 3 (Dentsply, DeTrey, Konstanz, Germany)	μTBS	Adhesive/Mix	Sodium ascorbate after NaOCl could restore compromised bond strengths
Farina, 2011 (Farina et al., 2011)	Human molars 3 mm below the occlusal surface	1%	40 min	EDTA	17%	5 min	Clearfil SE Bond self-etching adhesive (Kuraray; Okayama, Japan)	μTBS	Adhesive and mixed	The application of 2% CX followed by the application of 17% EDTA resulted in increasing the bond strength of the self-etching adhesive system to dentine, when compared with the results obtained for the other tested groups
Fawzi, 2010 (Fawzi, 2010)	Human molars; pulp chamber dentin flat	5.25%	10 min	EDTA	17%	1 min	Clearfil S3 Bond (Kuraray; Osaka, Japan); Adper Single Bond 2 (3M ESPE; St Paul, MN, United States)	SBS	—	The irrigant regimens examined could be used safely prior to bonding except for the NaOCl, which should be negated if it is to be followed by Adper Single Bond 2, and the etching step cannot be omitted if an etch-and-rinse adhesive system is the adhesive of choice
Kasraei, 2013 (Kasraei et al., 2013)	Human premolars 5 mm below the occlusal surface	2.5%	30 s	EDTA	0.5-M	30 s	I-Bond (heraeus Kulzer, hanau, Germany); Clearfil S3 Bond (Kuraray Co, Okayama, Japan)	μTBS	—	Application of EDTA or EDTA + NaOCl before one-step self-etch adhesives increased μTBS
Mohannad 2020 (Mohannad et al., 2020)	Human molars Not mentioned	5%	5 min	IP6 and EDTA	1%I P6 17% EDTA	IP6 1 min and 30 s EDTA 1 min	Scotchbond Universal adhesive (3M ESPE, St. Paul, MN, United States)	μTBS	Resin tags formed inside most of the dentinal tubules	IP6 reversed the adverse effects of NaOCl on resin-dentin adhesion without the chlorine-depleting effect of EDTA

(Continued on following page)

10.3389/fbioe.2025.1547158

TABLE 2 (*Continued*) Characteristics of the studies included in the review.

Author, year	Tooth type	NaOCl concen-tration	NaOCl treated time	Cross-linking agents	Crosslink-ing agents' concen-tration	Collagen treatment time	Adhesive used	Bond Strength test	Major failure mode	Main results
Prasansuttiporn, 2017 (Prasansuttiporn et al., 2017)	Human molars; pulp chamber dentin flat	Not mentioned	30 s	RA	100 μM	5s	Clearfil SE Bond (Kuraray Noritake; Tokyo, Japan)	μTBS	Mixed Failure	Rosmarinic acid restored the compromised initial bond strengths to smear-layer–deproteinized dentin
Prasansuttiporn 2011 (Prasansuttiporn et al., 2011)	Human molars; flat surfaces under the sound dentin	6%	30 s	SA RA	10% SA 100 μM RA	5 s 10 s	Clearfil Protect Bond (Kuraray Medical Inc., Tokyo, Japan)	μTBS	Mixed Failure	The application of sodium ascorbate solution for 5 or 10 s did not significantly increase the compromised bonding to NaOCl-treated dentin Applying rosmarinic acid for 5 or 10 s improved bond strengths to NaOCl-treated dentin
Santos, 2006 (Santos et al., 2006)	Bovine incisors pulp chamber dentin flat	5.25%	30 min	EDTA	17%	5 min	Clearfil SE Bond (Kuraray, Kurashiki, Japan)	μTBS	Mixed and interfacial	There was a significant decrease in bond strength associated to NaOCl, whereas chlorhexidine irrigation showed no effects on adhesion
Vongpha, 2005 (Vongphan et al., 2005)	Human molars; 3 mm below the occlusal surface	5.25%	10 min	SA	10$	10 min	Single bond (3M-ESPE, St Paul, MN, United States)	μTBS	Cohensive	Sodium hypochlorite significantly reduced the bond strengths of the adhesive when a total-etching was applied. The application of sodium ascorbate on sodium hypochlorite treated dentine significantly
Wang, 2019 (Wang et al., 2019)	Human molars Flat surfaces of sound dentin in the middle of the tooth	5.25%	20 min	PA	5% 10% 15%	1 min 5 min 10 min	Clearfil SE Bond (Kuraray Medical Inc., Tokyo, Japan)	μTBS	Adhesive and Mixed	Microtensile bond strength to NaOCl-treated dentine recovered after the application of either 5% PA for more than 5 min or 10% or 15% PA for more than 1 min. The application of PA before an adhesive procedure may immediately restore the compromised bond strength of NaOCl-treated dentine

SBS, shear bond strength test; μTBS, micro-tensile bond strength test.

10.3389/fbioe.2025.1547158

analysis used standardized mean difference (SMD), random effects model or fixed effects model. Leave-one-out sensitivity analysis was used to evaluate the reliability of the meta - analysis results (Deeks et al., 2008).

3 Results

From 1,538 potentially eligible studies obtained from six databases, 14 studies were selected for full-text analysis. Figure 1 is a flowchart that summarizes the studies selection process according to the PRISMA Statement. Characteristics of included studies.

All the studies were in English. EDTA (Santos et al., 2006; Cecchin et al., 2010; Fawzi, 2010; Farina et al., 2011; Kasraei et al., 2013; Barutcigil et al., 2014; Dikmen and Tarim, 2018; Arslan et al., 2019; Mohannad et al., 2020) was the most used crosslinking agent for nine studies. Three studies were conducted to investigate SA, (Vongphan et al., 2005; Prasansuttiporn et al., 2011; Dikmen and Tarim, 2018), while two studies were conducted for each of PA (Dikmen, 2015; Wang et al., 2019) and RA (Prasansuttiporn et al., 2011; Prasansuttiporn et al., 2017). A single study was conducted on IP6 (Mohannad et al., 2020). The characteristics of included studies are shown in Table 2. The results of the inter-reviewer agreement test revealed a high level of consistency (Kappa value = 0.883, CI 0.786–0.961), suggesting that the results are relatively reliable.

3.1 Meta-analysis

This review incorporates several substances that have been identified as crosslinking agents, including EDTA, IP6, PA, RA and SA. The crosslinking agents were applied to dentin after NaOCl for irrigation and prior to composite resin bonding. Different crosslinkers used as a pretreatment were analyzed separately. Furthermore, separate analysis of EDTA group were conducted for the concentration of NaOCl (NaOCl greater than 2.5% or less than 2.5%). Given the relatively high heterogeneity of the meta-analysis, after heterogeneity analysis and treatment, the data of EDTA, PA and SA meta-analysis were divided into two subgroups according to the duration of NaOCl exposure and analyzed using a random effects model. The results of meta-analysis are presented in the following Figures 2–7.

3.1.1 EDTA

The use of EDTA was statistically significant in weakening the bond strength of dentin to composite resin when dentin was exposed to a high concentration of NaOCl solution (concentration greater than 2.5%) for a short period of time (less than or equal to 1 min) (SMD:-0.80; CI:-1.56,-0.04; $P = 0.04$). Conversely, when dentin was exposed to high concentrations of NaOCl for more than 1 min, the use of EDTA had a statistically significant effect on enhancing the bond strength (SMD: 0.84; CI:0.06,1.62; $P = 0.04$). (Figure 2).

When dentin was exposed to low concentrations of NaOCl (concentrations less than or equal to 2.5%), the difference between the bond strength of dentin treated with EDTA and that of the control group was not statistically significant, regardless of the duration of exposure (Figure 3).

3.1.2 IP6

Two comparisons in Mohannand 2020, (Mohannad et al., 2020), was included in the meta-analysis of IP6. The concentration of NaOCl used in this study was 5% with a 5-min exposure. Mohanna, 2020 (b) was treated with IP6 for 1 min and Mohannad 2020 (c) was treated 30 s. The meta-analysis demonstrated that IP6 application on NaOCl-treated dentin BS exhibited no statistically significant differences (SMD: 0.75; CI: −0.17, 1.68; $P = 0.11$) (Figure 4).

3.1.3 PA

NaOCl solution at a concentration of 5.25% was used in all studies crosslinked with PA, and the difference in dentin bond strength between the PA experimental group and the control group was not statistically significant for exposure times of less than 1 min (SMD:0.86; CI: −0.85,2.18; $P = 0.21$); for exposure times of greater than 1 min, PA significantly increased bond strength (SMD: 2.60; CI: 1.61,3.59; $P < 0.001$) (Figure 5).

3.1.4 RA

NaOCl exposure time for each of the four comparisons using PA crosslinking was 30 s. The meta-analysis revealed that RA significantly increased the BS between NaOCl treated dentin and composite resin (SMD: 2.06; CI: 1.60, 2.53; $P < 0.001$) (Figure 6).

3.1.5 SA

The use of NaOCl at concentrations above or equal to 5.25% was a common feature of both studies utilizing SA cross-linking. The results demonstrated that SA exerted a weak effect on the bond strength of dentin when the exposure time was less than 1 min (SMD: 0.52; CI: −0.02, 1.07; $P = 0.06$). However, this difference was not statistically significant. When the exposure time to sodium hypochlorite was extended, a significant increase in the bond strength of dentin was observed in the presence of SA (SMD: 2.05; CI:0.92, 3.18; $P < 0.001$) (Figure 7).

3.2 Sensitivity analysis

A meta-analysis of studies utilizing different crosslinking agents were conducted separately, with leave- one-out sensitivity analyses performed. No significant alterations in the results were observed upon the exclusion of any of the articles, and the results of the meta-analysis were deemed to be robust.

3.3 Risk of bias

Most of the studies were categorized as having low risk of bias based on the standards set forth for the risk of bias assessment. Regarding the aforementioned criteria, approximately 25% of the studies did not report information about failure mode, the majority did not report blinding of sampling and assessment, and all did not perform sample size calculations (Figure 8). The result of the inter - reviewer agreement test manifested a high degree of consistency. The Kappa value was 0.897, with a 95% confidence interval ranging from 0.806 to 0.971, which implies that the results are relatively dependable.

4 Discussion

This is the first systematic review and meta-analysis to investigate the relationship between the BS of NaOCl-treated dentin and three variables: the cross-linker used, the concentration of NaOCl and the time of NaOCl exposure. The results of the meta-analysis indicated that the effect of collagen crosslinkers on the BS of NaOCl treated dentin was influenced by the concentration of NaOCl and the duration of exposure. When the NaOCl exposure time was extended to more than 1 min with concentrations greater than 2.5%, collagen crosslinkers including EDTA, PA and SA all demonstrated a significant positive effect on bond strength. Consequently, the hypothesis put forth in this review was found to be partially rejected.

EDTA, PA and SA are available for comparison between different exposure durations at high NaOCl concentration. The results showed that when higher concentrations of NaOCl were used and the exposure time was less than 1 min, none of the EDTA, PA, and SA had a statistically significant effect on dentin BS compared to the control group. When the exposure time was extended to more than 1 min with high concentrations of NaOCl, EDTA, PA and SA all demonstrated a significant positive effect on bond strength. It can be inferred that the effect of EDTA, PA and SA on the BS of NaOCl treated dentin was influenced by the concentration of NaOCl and the duration of exposure. This may be since the negative effect of NaOCl on dentin is only gradually apparent when higher concentrations act for a longer period. Taniguchi et al. (2009) treated dentin with 6% NaOCl for 15 s and did not observe a significant change in dentin adhesive strength, whereas in the case of Kambara et al. (2012), there was even a significant increase in dentin bond strength after treatment with 1% sodium hypochlorite solution for 15 s. However, dentin bond strengths treated with 2.5% and 5.25% NaOCl for 20 min were significantly lower than those of the negative control group, with a decrease of 46% and 50.2%, respectively (Wang and Liang, 2017).

Only the studies using EDTA crosslinking had an experimental group using a low concentration of sodium hypochlorite, and the studies using the other crosslinking agents used a high concentration of NaOCl. The meta-analysis showed that regardless of whether the duration of exposure of dentin to a low concentration of sodium hypochlorite was 1 h, 40 min, 30 s, or some other unmentioned period (Arslan et al., 2019), the application of EDTA had no statistically significant effect on BS. This may also be due to the fact that at lower concentrations, NaOCl does not cause significant changes in BS. Cecchin et al. (2010) treated dentin with 1% NaOCl during 1 h (reapplied every 5 min) and found that it lead to a higher BS of Xeno III system to dentin, they explain this outcome may be concerned with the superficial morphology of dentin treated with NaOCl was not significantly changed for that 1%NaOCl does not remove the smear layer and expose the dentinal tubules (Garberoglio and Becce, 1994).

4.1 EDTA & IP6

NaOCl and EDTA are the two most used irrigants in endodontic treatment. EDTA is an effective metal chelating compound with a high antioxidant potential (Let et al., 2007; Thbayh et al., 2023). It has been suggested that dentin treated with EDTA exhibits an increased resistance to degradation by NaOCl at the resin-dentin interface (Torii et al., 2003; Kim et al., 2011). Furthermore, EDTA exerts an inhibitory effect on matrix metalloproteinase (MMP), which contributes to the durability of resin-dentin bonding. Nevertheless, this effect is time-limited (Thompson et al., 2012; Toledano et al., 2012). EDTA is a less hazardous and more affordable cross-linking agent than traditional cross-linkers like epichlorohydrin (EPI) and 1-ethyl-3-(3-dimethylaminopropyl)-carbodiimide hydrochloride (EDC) (Zhao et al., 2017). From results above, it can be observed that the effect of EDTA on the BS is related to the exposure time of NaOCl at different concentrations. The interaction between the two may be related to the following reasons: First, the interaction of pH. Weak acidity of EDTA (pH 7.2) may neutralize the alkalinity of high-concentration NaOCl, reducing the effective chlorine concentration and weakening its antibacterial ability. However, this pH change has a relatively small impact during short - term exposure, while it may be more significant during long-term treatment. Second, high-concentration NaOCl rapidly dissolves the surface collagen, but does not completely remove the deeper layer organic residues within a short time. At this time, the demineralization effect of EDTA exposes more unmineralized collagen fibers, but these fibers are structurally loose due to the oxidative damage of NaOCl and cannot form an effective hybrid layer. Meanwhile, excessive demineralization leads to a decrease in the micro-hardness of the dentin surface, weakening the mechanical interlocking effect (Barón et al., 2013). Third, relatively long-time NaOCl exposure treatment thoroughly removes organic residues and the smear layer, forming a clean inorganic surface. EDTA further removes the hydroxyapatite debris after demineralization, opening the dentinal tubules, increasing the surface area and the resin penetration depth (De-Deus et al., 2006). Therefore, combined with the pretreatment of high concentration NaOCl for a relatively long time, the micromechanical retention between the resin and dentin is significantly enhanced.

IP6 is the primary phosphorus storage type found in plant seeds and bran (Raboy, 2003). It is extracted from natural plants that include six phosphate groups, making it a crosslinking agent that offers a large number of feasible crosslinking sites to help in the construction of three-dimensional macrostructures (Liu et al., 2024). In specific circumstances, IP6 can help form a ternary complex (Protein-CaPhytate) that has good chemical bond (Cheryan, 1980) and has been used in the construction of conductive hydrogels (Zhang et al., 2019; Liu et al., 2024). Similar to EDTA, with its remarkable capacity to chelate with multivalent cations including calcium, magnesium, and iron, IP6 is a highly negatively charged molecule (Luttrell, 1993; Torres et al., 2005). It functions ais an antioxidant, resisting oxidative reactions through the trapping of free radicals, reduction of their production and scavenging. Dentin surfaces treated with IP6 were free of smear layer and smear plugs, dentinal tubules opened and intertubular collagen was visible (Souparnika et al., 2023). IP6 has been identified as a potential etchant and chelating agent, given its acidic and chelating properties. It was reported can be used as a substitute for phosphoric acid and EDTA in clinical practice (Nassar et al., 2015; Kong et al., 2017; Gandhi et al., 2020).

In addition to considering the concentration of sodium hypochlorite and the duration, the fact that EDTA and IP6 not only function as antioxidants and crosslinking agents but also participate in the chemical reactions preceding bonding in the capacity of chelating agents. This may explain the outcome that EDTA declined the BS of NaOCl treated dentin in certain situation as well as IP6 exerts not significant positive effect on BS. Recognized as the most efficacious chelating agent with excellent lubricity, EDTA is commonly used in endodontic therapy (Calt and Serper, 2002; Barutcigil et al., 2014). It was reported that the demineralizing effect is pronounced, with the potential for dentin softening, dentinal tubules enlargement and collagen fibrils denaturation (Calt and Serper, 2002). Formation of the hybrid layer and the durability of bonding quality are consequently affected. Compare with EDTA, the application of IP6 for an equivalent period of time results in the removal of the smear layer in a more effective manner. According to Souparnmika et al., it was observed that although EDTA resulted in a nearly clean dentinal surface with open dentinal tubules while IP6 produced a dentinal surface free of debris with a higher number of open tubule, which both (Souparnika et al., 2023).

Although a notable elevation in BS was not observed in the meta-analysis of IP6, the BS of the experimental groups to which the IP6 treatment was applied was higher than that of the control group in all cases. This contrasts with the findings that EDTA exerts both beneficial and detrimental effects on BS. This may be explained by the fact that 1% IP6 (pH 1.3) has a higher acidity than 17% EDTA (pH 7.2), thereby has a superior capacity to neutralize the residual NaOCl on the dentin surface. Furthermore, Mohannad et al. (2020) reported that IP6 exhibited superior biocompatibility and smear layer removal capabilities on flat dentin surfaces in comparison to EDTA. Additionally, IP6 demonstrated better dentin tubules opening, which may facilitate enhanced penetration of the resin protrusion into the dentin tubules of the root canal. Moreover, IP6 had a noticeably stronger inhibitory effect on collagen breakdown than did PA and EDTA (Kong et al., 2017).

Based on the results of meta-analysis of the articles included in this study, it was concluded that the effect of IP6 on the BS of NaOCl-treated detin is not statistically significant. Despite the considerable efforts of many scholars to explore the use of IP6 in dentin bonding, (Muana et al., 2019; Yadav et al., 2021; Attia et al., 2022; Souparnika et al., 2023), here remains a paucity of research exploring the impact of IP6 on BS of NaOCl-treated dentin. Although our study provides some evidence for the effectiveness of IP6, current study has limitations in fully validating the effectiveness of IP6 as a crosslinking agent and that more studies are needed to provide robust evidence. Further validation is necessary before it can be widely recommended for use in clinical.

4.2 PA & RA

PA, RA are crosslinkers with excellent antioxidant properties (Huerta-Madroñal et al., 2021; Guan et al., 2022; Noor et al., 2022). In addition, they have been demonstrated to process the ability to inhibit MMP (Epasinghe et al., 2013). PA are natural crosslinkers extracted from polyphenolic compounds (Rauf et al., 2019). Regarded as one of the most active dentin tissue biomodifiers used in the dental bonding procedure, (Alkhazaleh et al., 2022), PA have the potential to enhance the mechanical properties of dentin, thereby improving the quality of the hybrid layer (Anovazzi et al., 2024).

The degree of heterogeneity observed in the meta-analysis of PA was considerable (I^2 = 96%), as illustrated in Figure 5. The source of the heterogeneity may be attributed to the three concentrations of 5%, 10%, and 15% and the three durations of PA treatment (1 min, 5 min, and 15 min, respectively) used in the study by Wang et al. (2019) Higher concentrations of PA can form a denser collagen matrix, which can impede the water leaching and reduce the vapor permeability of the proanthocyanidin–collagen film (Balalaie et al., 2018). It is therefore appropriate to conclude that the concentration and treatment time are also important for PA to reverse the adverse effect of NaOCl on dentin BS. Higher PA concentrations and longer durations will result in greater BS recovery.

Similar to PA, RA is a polyphenolic flavonoid extracted from rosemary, which has crosslinking and MMP-inhibitory abilities, as well as a high antioxidant capacity (Hawkins and Davies, 1999; Apak et al., 2008). The treatment times in the studies (Prasansuttiporn et al., 2011; Prasansuttiporn et al., 2017) were all within the interval of 5–10 s, which is the shortest for rosemarinic acid compared to other cross-linking agents. However, the results of the meta-analysis indicate that a statistically significant increase in the BS of NaOCl-treated dentin could still be observed after treatment with RA, suggesting that RA enhances the BS of NaOCl-treated dentin with a shorter treatment time. The efficient reversal of the reduction in BS of NaOCl-treated dentin by rosemarinic acid may be attributed to the fact that RA contains p-toluenesulfinic acid sodium salt. P-toluenesulfinic acid sodium salt is present in a product known as Accel (Sun Medical Co. Ltd.), which is used commercially as a pretreatment agent for adhesive root canal sealers to lessen or completely eliminate the oxidative effect of NaOCl (Khoroushi and Kachuei, 2014). In additionr, p-toluenesulfinic acid sodium salt can accelerate polymerization of composite resin (Apak et al., 2008). The polymerization of composite resin can be accelerated by the sodium salt of p-toluenesulfinic acid (Bowen, 1965; Taniguchi et al., 2009).

In addition, the solvent for RA was 5% ethanol in the two included studies that used RA as a cross-linking agent, and aqueous solutions of RA at different concentrations were used as cross-linking agents in other studies on RA. As a natural extract, the physiological activity of PA is influenced by a variety of factors including the extraction process and the solvent (Han et al., 2003; Ku et al., 2007). Aydi et al. (2016) found that the solubility of RA decreases with an increase in water content. Previous studies (Liu et al., 2011; Fang et al., 2012) found that the ultimate tensile strength of collagen in the PA-treated group was higher than that in the water-solvent group for the same treatment time in the ethanol-solvent group and the acetone-solvent group, suggesting that ethanol may be a more suitable solvent for PA pretreatment. This may be associated with the hydrogen bonding capacity of these solvents, as gauged by the Hansen solubility parameter for hydrogen bonding, δH (Chappelow et al., 2000). The δH values of ethanol and acetone were found to be lower than that of distilled water, indicating that the weaker bond-forming solvent would occupy fewer hydrogen bonding sites. The additional available hydrogen bonding sites, in conjunction with the collagen

TABLE 3 Risk of bias of the included studies.

Author year	Standardized specimens	Specimen randomization	Teeth free of caries/ restoration	Sample size calculation	Blinding of sampling and assessment	Manufacturer 's instructions	Control groups	Failure mode	Incomplete outcome data	Risk of bias
Arslan 2019	Y	Y	Y	N	N	Y	Y	Y	Y	low
Barutcigil 2014	Y	Y	Y	N	N	Y	Y	Y	Y	low
Cecchin 2010	Y	Y	Y	N	N	Y	Y	N	Y	medium
Dikmen 2015	Y	Y	Y	N	N	Y	Y	Y	Y	low
Dikmen 2018	Y	Y	Y	N	Y	Y	Y	Y	Y	low
Farina 2011	Y	Y	Y	N	N	Y	Y	Y	Y	low
Fawzi 2010	Y	Y	Y	N	N	Y	Y	N	Y	medium
Kasarei 2013	Y	Y	Y	N	N	Y	Y	N	Y	medium
Mohannad 2020	Y	Y	Y	N	N	Y	Y	Y	Y	low
Santos 2006	Y	Y	Y	N	N	Y	Y	Y	Y	low
Prasansuttiporn 2011	Y	Y	Y	N	N	Y	Y	Y	Y	low
Prasansuttiporn 2017	Y	Y	Y	N	N	Y	Y	Y	Y	low
Vongphan 2005	Y	Y	Y	N	N	Y	Y	Y	Y	low
Wang 2019	Y	Y	Y	N	N	Y	Y	Y	Y	low

10.3389/fbioe.2025.1547158

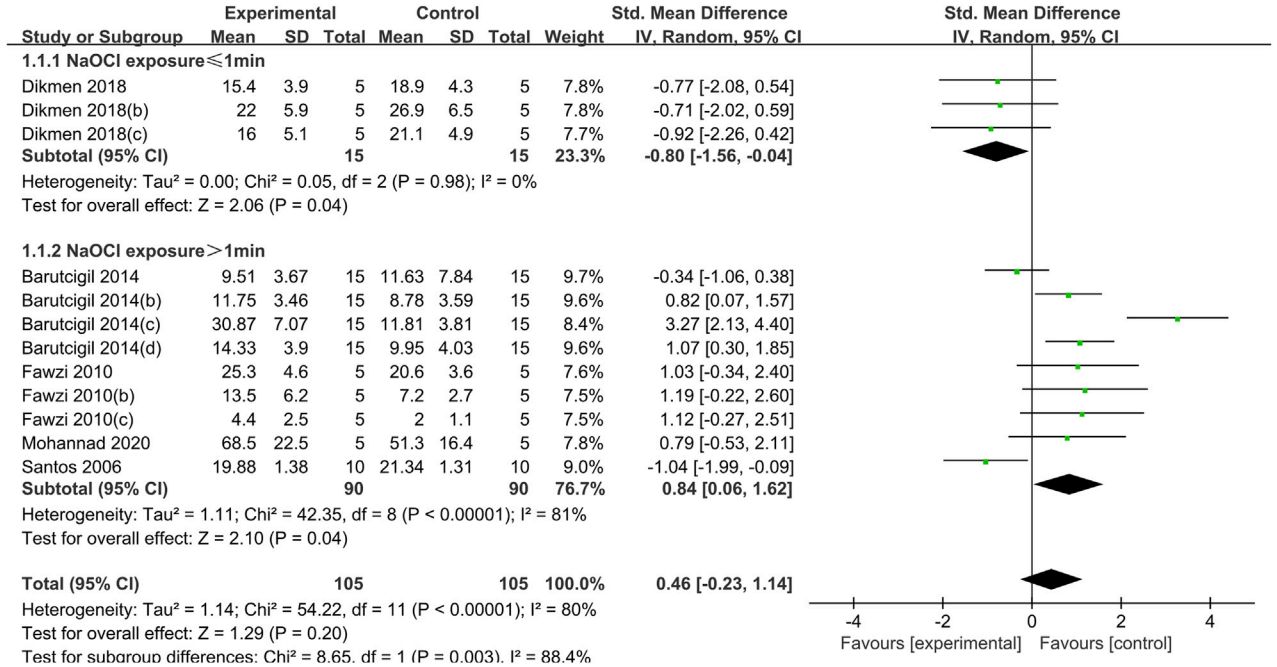

FIGURE 2
Forest plot of the BS comparison between the EDTA treated group and the control group according to the high concentration NaOCl exposure time.

structure, may facilitate the formation of new hydrogen bonds between PA collagen or collagen-collagen molecules, thereby inducing collagen cross-linking and resulting in enhanced mechanical properties (Nalla et al., 2005). Furthermore, Hagerman and Klucher (1986) have demonstrated that ethanol, rather than acetone, can reduce the dielectric constant of the medium and stimulate PA-collagen.

4.3 SA

The SA functions as a reducing agent, facilitating the interaction between oxygen and the NaOCl by-product (Vongphan et al., 2005). It has been reported that SA can reverse the negative effects of NaOCl on the polymerization of dentin bonding agent (Morris et al., 2001). Furthermore, by serving as an electron donor and scavenging free radicals, it can restore the BS (Weston et al., 2007) and permit full polymerization without prematurely stopping the process (Lai et al., 2001). Additionally, SA eliminates the vertical shag-carpet-like nanoleakage pattern created by NaOCl due to incomplete penetration of resin into demineralized dentin (Kewlani et al., 2020).

The studies using SA crosslinking employed high concentrations of NaOCl solutions. The subgroup with an exposure time of less than 1 min did not observe a significant increase in bond strength by SA. In addition to the previously mentioned reason for the short duration of the NaOCl application, the following factors may also be related to this outcome. In Prasansuttiporn, 2011 (a) (b), (Prasansuttiporn et al., 2011), 10% SA was applied for 5 and 10 s, which may not be sufficiently long to facilitate the formation of a strong bond between NaOCl-treated dentin and the self-etch adhesive agent. It is possible that an extended application period may have a significant impact on BS. Also, the location from which the dentin was sampled may be concerned. The majority of the studies included herein sampled the readily accessible extracted third molars for specimen preparation. The morphology and size of human third molars exhibit considerable variability, as do the shapes of their pulp chambers. Two principal methods are employed for the preparation of specimens. In Dikmen and Tarim (2018), for instance, the teeth were sectioned 3 mm below the occlusal surface, so do Kasarei et al. removed 5 mm of occlusal dentin to expose deeper superficial dentin without pulp exposure (Kasraei et al., 2013). An alternative approach was employed by Barutcigil et al. (2014) who sectioned the teeth through the pulp chamber. The orientation of dentin tubules is highly variable in different parts of the tooth (Liu et al., 2020). Some studies have shown that the structure of dentin tubules exerts a significant influence on the physical properties of dentin itself and their morphological distribution at the bonding interface affects the BS between the bonding system and dentin (Lin et al., 2017). The number of dentin tubules in the dentin on the side away (superficial dentin) from the pulp is fewer in number, with a correspondingly low density. The inter-dentin tubule matrix constitutes a large proportion of dentin tubules, and the distribution of collagen fibers is more concentrated than that observed in dentin on the side near the pulp (deeper dentin) (Guo et al., 2018). There are also more bonding sites with the resin bonding agent. Consequently, the resin adhesive has a higher penetration rate in the superficial dentin, which penetrates more rapidly than deeper dentin. In Dikmen's experiments, dentin specimens were taken from relatively shallow dentin, and the thickness of the mixed layer at the interface is thinner than that of the corresponding total-etch bonding mixed layer. The quality of this hybrid layer is a critical determinant of BS (Perdigão et al., 2013; Frassetto et al., 2016).

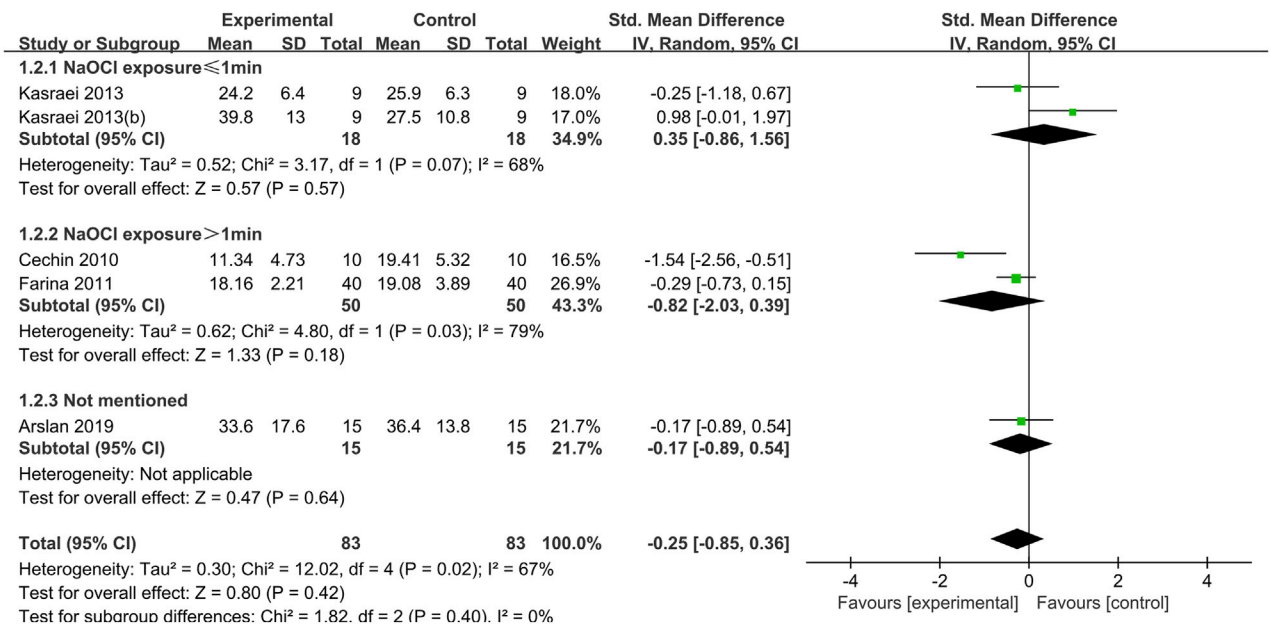

FIGURE 3
Forest plot of the BS comparison between the EDTA treated group and the control group according to the low concentration NaOCl exposure time.

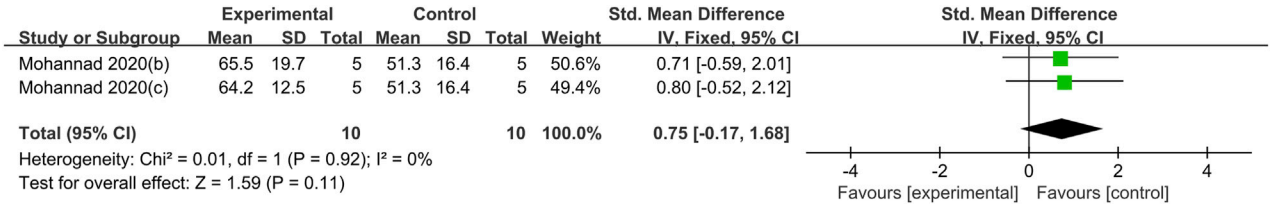

FIGURE 4
Forest plot of the BS comparison between the IP6 treated group and the control group.

4.4 Limitations and future direction

Researchers reported that the effect of NaOCl on dentin BS varies with chemistries of the bonding systems (Vargas et al., 1997; Prati et al., 1999; Frankenberger et al., 2000; Perdigão et al., 2000; Ishizuka et al., 2001; Stevens, 2014). As reported by Nikaido et al. (1999), the application of NaOCl in root canal treatment has been shown to have a detrimental effect on the adhesion of total-etch adhesive systems, with a comparatively minimal effect on self-etch primer systems. The technique sensitivity of total-etch adhesive system arises from the challenge of regulating the moisture content of etched dentin, which is essential to prevent collagen collapse and subsequent impediment of resin monomer infiltration (Spencer and Wang, 2002). The chemical products of the crosslinking agent and NaOCl can affect the dentin wetting of dentin prior to bonding, thus affecting the BS. This review did not impose restrictions on the types of adhesives in the included articles. Nevertheless, the majority of the studies included in this review used the Self-etch adhesive system, with only three studies using the total-etch adhesive system. Further studies using the total-etch adhesive system are required to elucidate the effect of crosslinking agents on the BS of NaOCl-treated dentin in the presence of different adhesive systems.

In addition, although the most commonly used clinical concentration of NaOCl is currently 5.25%, (Cai et al., 2023), and most of the NaOCl rinses used in the included articles were at a concentration of 5.25% and above, there is growing evidence that higher concentrations of NaOCl are more disruptive to the physicochemical properties and microstructure of dentin as well (Vargas et al., 1997; Boutsioukis and Arias-Moliz, 2022). This is evidenced by the fact that they are more likely to result in reduced BS as well as an elevated risk of root fracture (Erdemir et al., 2004; Pascon et al., 2009; Gu et al., 2017; Li et al., 2022; Xu et al., 2022). Some researchers have advocated the use of lower concentrations of NaOCl in clinical practice (Abuhaimed and Abou Neel, 2017; Boutsioukis and Arias-Moliz, 2022). However, it has also been suggested that irrigating with varying concentrations of NaOCl does not influence the compressive strength of dentin or the clinical outcome (Verma et al., 2019; Barakat et al., 2024). Further research into the effect of cross-linking agents on the BS of dentin treated with NaOCl at different concentrations is awaited.

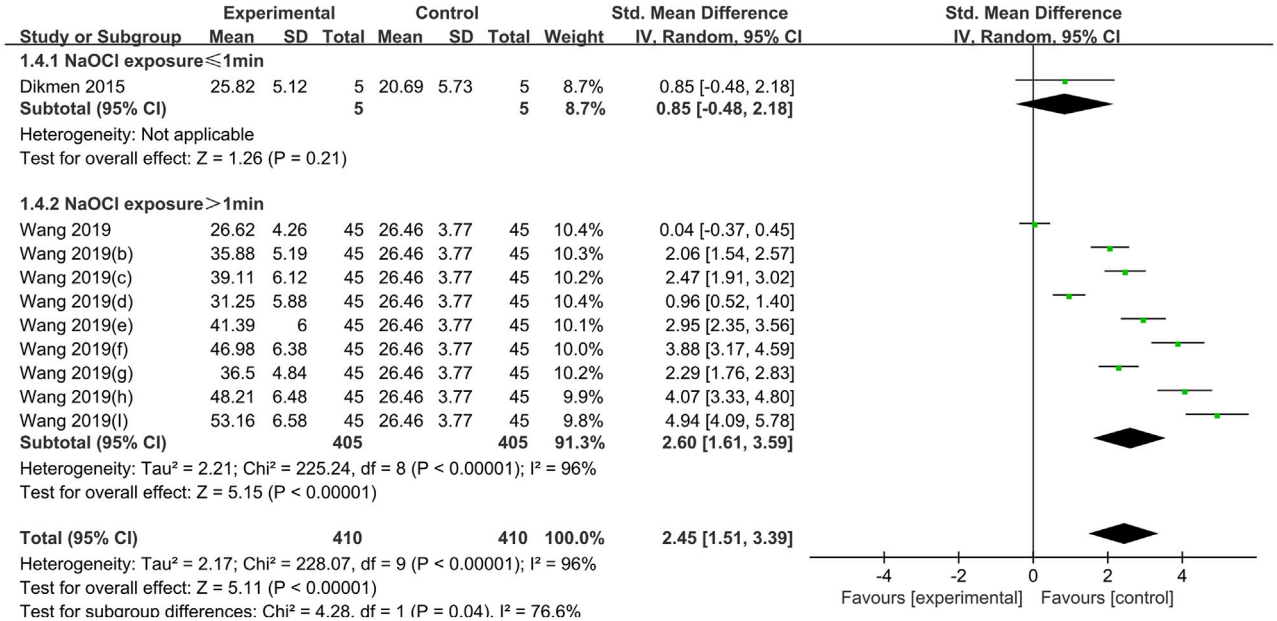

FIGURE 5
Forest plot of the BS comparison between the PA treated group and the control group according to the high concentration NaOCl exposure time.

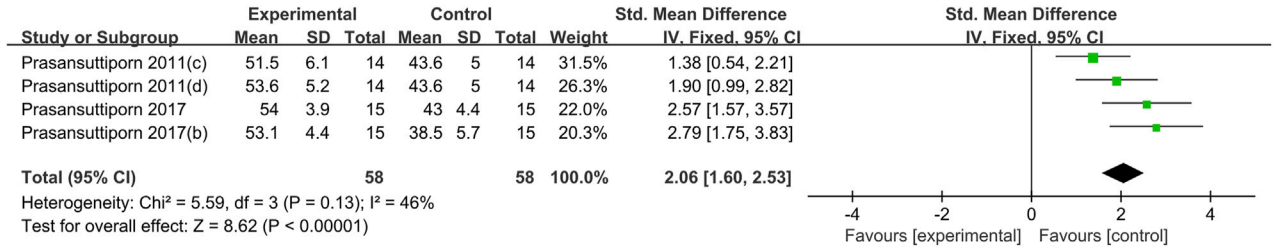

FIGURE 6
Forest plot of the BS comparison between the RA treated group and the control group.

It is also important to note that failure of a bonded restoration of a crown does not only occur in the immediate postoperative period. Rather, it is often observed after a certain period of use (Mokeem et al., 2023). The durability of hybrid layers has been demonstrated to be limited (Hashimoto et al., 2003; Pashley et al., 2004; Breschi et al., 2008). This outcome may be attributed to a multitude of factors, including inadequate resin monomer penetration into the demineralized dentin and unpolymerized monomer elution from the polymeric adhesive (Okuda et al., 2002; Breschi et al., 2008; Maravic et al., 2017). It is possible that these collagen fibers, which are exposed within the hybrid layer (incompletely infiltrated), may be affected by degradation. MMP are present in dentin in a dormant form and are triggered in low pH environments, which are similar to the conditions that occur during etching and caries processes (Mazzoni et al., 2015). Furthermore, all of the aforementioned changes require a certain amount of time to occur (Frassetto et al., 2016). However, with the exception of two of the included studies, which investigated long-term changes in BS, one of the limitations of the remaining studies was that they only evaluated the immediate recovery effect of crosslinking agents on BS to NaOCl-treated dentine. The durability of the improvement in bond strength of crosslinkers to NaOCl-treated dentin over time requires further investigation.

Finally, the studies included in this review generally lack the reporting of sample size calculation and the implementation of blinding. The calculation of sample size has a significant impact on the test power of a study and poses an obstacle to the assessment of heterogeneity. Inadequate implementation of blinding can lead to observational bias, affecting the generalizability of the meta-analysis results. This reflects the lack of experimental design in the research of this field or the omission of reporting such important information when writing articles. Therefore, special attention should be paid in future studies. In addition, all the included studies were all *in vitro* experiments using extracted human or bovine teeth, and the outcomes explored were limited to BS. *In vivo* studies are scarce.

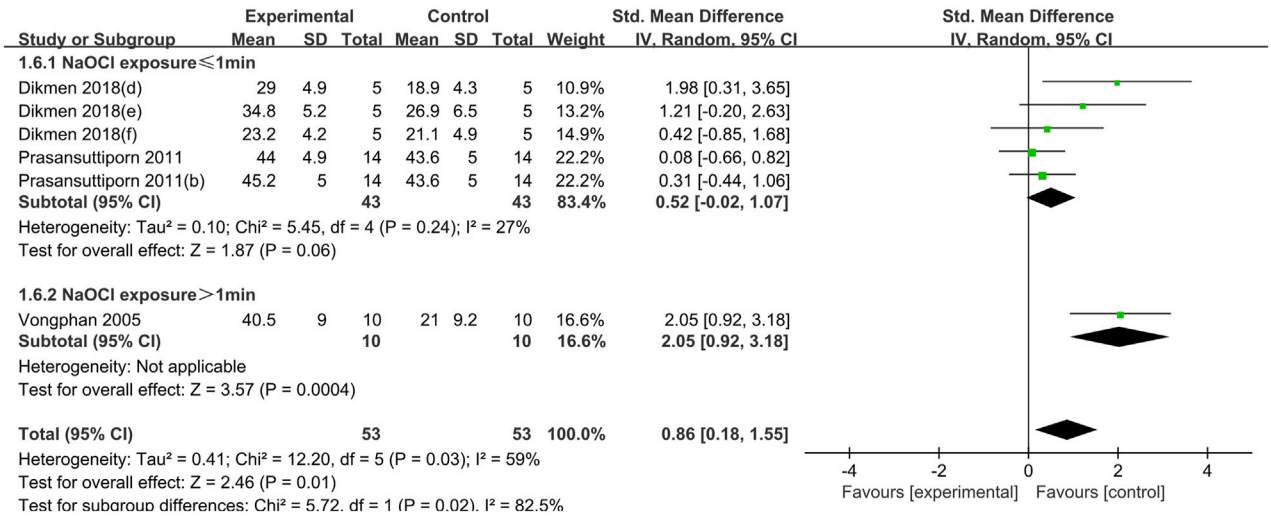

FIGURE 7
Forest plot of the BS comparison between the SA treated group and the control group according to the high concentration NaOCl exposure time.

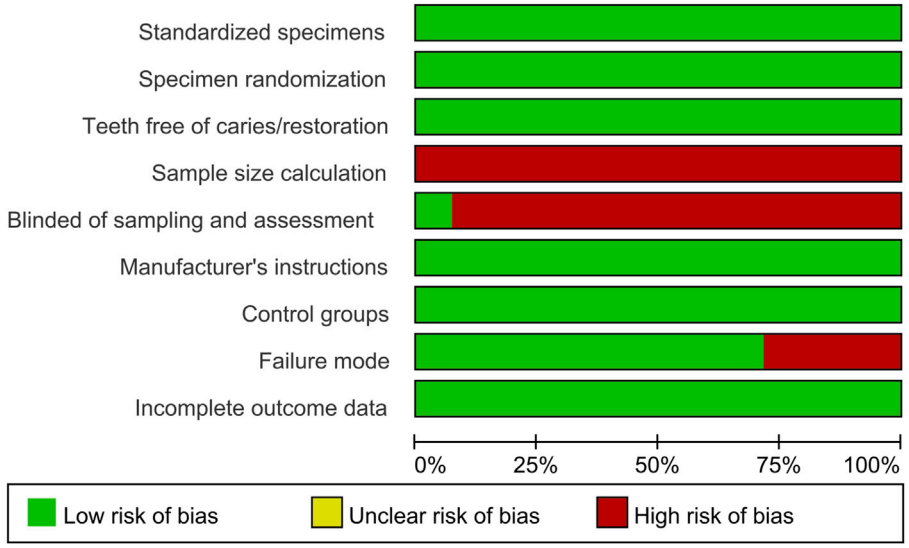

FIGURE 8
Summary of risk of bias.

There is a paucity of observations on the effects of crosslinking agents on microleakage, secondary caries, and filling loss. The role of crosslinking agents applied in NaOCl-treated dentin bonding has yet to be experimentally explored clinically.

5 Conclusion

Based on the results of this systematic review and meta-analysis, an overall advantage of using collagen crosslinkers in NaOCl treated dentin for enhancing the BS can be observed, which was influenced by the concentration of NaOCl and the duration of exposure. For dentin exposed more than 1 min in NaOCl at concentrations greater than 2.5%, EDTA, PA and SA were observed to significantly improve the bond strength. For dentin exposed less than 1 min or NaOCl at lower concentration, significant positive effect cannot be observed when using collagen crosslinkers. RA proved effective in improving the BS of NaOCl-treated dentin to composite resin at high NaOCl concentrations within a shorter duration. The evidence is insufficient to conclude that IP6 has a positive effect on the bond strength of NaOCl-treated dentin to composite resins.

Data availability statement

The original contributions presented in the study are included in the article/supplementary material, further inquiries can be directed to the corresponding author.

Author contributions

WZ: Conceptualization, Formal Analysis, Investigation, Methodology, Software, Writing – original draft, Writing – review and editing. SF: Investigation, Validation, Visualization, Writing – review and editing. XC: Data curation, Formal Analysis, Resources, Writing – review and editing. SX: Project administration, Writing – review and editing. XZ: Project administration, Supervision, Writing – review and editing.

Funding

The author(s) declare that no financial support was received for the research and/or publication of this article.

Conflict of interest

The authors declare that the research was conducted in the absence of any commercial or financial relationships that could be construed as a potential conflict of interest.

Generative AI statement

The author(s) declare that no Generative AI was used in the creation of this manuscript.

Publisher's note

All claims expressed in this article are solely those of the authors and do not necessarily represent those of their affiliated organizations, or those of the publisher, the editors and the reviewers. Any product that may be evaluated in this article, or claim that may be made by its manufacturer, is not guaranteed or endorsed by the publisher.

References

Abuhaimed, T. S., and Abou Neel, E. A. (2017). Sodium hypochlorite irrigation and its effect on bond strength to dentin. *Biomed. Res. Int.* 2017, 1–8. doi:10.1155/2017/1930360

Alkhazaleh, A., Elfagih, S., Chakka, L. R. J., Armstrong, S. R., Comnick, C. L., Qian, F., et al. (2022). Development of proanthocyanidin-loaded mesoporous silica nanoparticles for improving dental adhesion. *Mol. Pharm.* 19, 4675–4684. doi:10.1021/acs.molpharmaceut.2c00728

Anovazzi, G., Mendes Soares, I. P., Fernandes, L. de O., Gomes, L. N., Scheffel, D. L. S., Soares, D. G., et al. (2024). Water/ethanol and water/acetone proanthocyanidin solutions enhance the mechanical stability and sealing ability of resin-dentin bonds produced by the cross-linked dry bonding technique. *Int. J. Adhes. Adhes.* 132, 103736. doi:10.1016/j.ijadhadh.2024.103736

Anumula, L., Ramesh, S., Kolaparthi, V. S. K., Kirubakaran, R., Karobari, M. I., Arora, S., et al. (2022). Role of natural cross linkers in resin–dentin bond durability: a systematic review and meta-analysis. *Materials* 15, 5650. doi:10.3390/ma15165650

Apak, R., Güçlü, K., Ozyürek, M., Bektas Oğlu, B., and Bener, M. (2008). Cupric ion reducing antioxidant capacity assay for food antioxidants: vitamins, polyphenolics, and flavonoids in food extracts. *Methods Mol. Biol. Clifton N. J.* 477, 163–193. doi:10.1007/978-1-60327-517-0_14

Arslan, S., Balkaya, H., and Çakir, N. (2019). Efficacy of different endodontic irrigation protocols on shear bond strength to coronal dentin. *J. Conserv. Dent.* 22, 223. doi:10.4103/JCD.JCD_502_18

Attia, A. M., Abo-Elezz, A. F., and Safy, R. K. (2022). Effect of phytic acid on bond strength and interfacial integrity of universal adhesive to deep dentin. *Braz. Dent. J.* 33, 116–125. doi:10.1590/0103-6440202204810

Aydi, A., Claumann, C. A., Zibetti, A. W., and Abderrabba, M. (2016). Differential scanning calorimetry data and solubility of rosmarinic acid in different pure solvents and in binary mixtures (methyl acetate + water) and (ethyl acetate + water) from 293.2 to 313.2 K. *ACS Publ.* 61, 3718–3723. doi:10.1021/acs.jced.6b00008

Balalaie, A., Rezvani, M. B., and Mohammadi Basir, M. (2018). Dual function of proanthocyanidins as both MMP inhibitor and crosslinker in dentin biomodification: a literature review. *Dent. Mater. J.* 37, 173–182. doi:10.4012/dmj.2017-062

Barakat, R. M., Almohareb, R. A., Alsuwaidan, M., Faqehi, E., Alaidarous, E., and Algahtani, F. N. (2024). Effect of sodium hypochlorite temperature and concentration on the fracture resistance of root dentin. *BMC Oral Health* 24, 233. doi:10.1186/s12903-024-03954-y

Barón, M., Llena, C., Forner, L., Palomares, M., González-García, C., and Salmerón-Sánchez, M. (2013). Nanostructural changes in dentine caused by endodontic irrigants. *Med. Oral Patol. Oral Cirugia Bucal* 18, e733–e736. doi:10.4317/medoral.18713

Barutcigil, C., Harorli, O. T., Ozcan, E., Arslan, H., and Yildiz, M. (2014). Effects of ethylenediaminetetraacetic acid and sodium hypochlorite on the bond strength of bonding agents to pulp chamber lateral walls. *J. Dent. Sci.* 9, 229–234. doi:10.1016/j.jds.2012.10.007

Betancourt, D. E., Baldion, P. A., and Castellanos, J. E. (2019). Resin-dentin bonding interface: mechanisms of degradation and strategies for stabilization of the hybrid layer. *Int. J. Biomater.* 2019, 1–11. doi:10.1155/2019/5268342

Boutsioukis, C., and Arias-Moliz, M. T. (2022). Present status and future directions – irrigants and irrigation methods. *Int. Endod. J.* 55, 588–612. doi:10.1111/iej.13739

Bowen, R. L. (1965). Adhesive bonding of various materials to hard tooth tissues. IV. Bonding to dentin, enamel, and fluorapatite improved by the use of a surface-active comonomer. *J. Dent. Res.* 44, 906–911. doi:10.1177/00220345650440052601

Boyera, N., Galey, I., and Bernard, B. A. (1998). Effect of vitamin C and its derivatives on collagen synthesis and cross-linking by normal human fibroblasts. *Int. J. Cosmet. Sci.* 20, 151–158. doi:10.1046/j.1467-2494.1998.171747.x

Breschi, L., Maravic, T., Cunha, S. R., Comba, A., Cadenaro, M., Tjäderhane, L., et al. (2018). Dentin bonding systems: from dentin collagen structure to bond preservation and clinical applications. *Dent. Mater.* 34, 78–96. doi:10.1016/j.dental.2017.11.005

Breschi, L., Mazzoni, A., Ruggeri, A., Cadenaro, M., Di Lenarda, R., and De Stefano Dorigo, E. (2008). Dental adhesion review: aging and stability of the bonded interface. *Dent. Mater. Off. Publ. Acad. Dent. Mater.* 24, 90–101. doi:10.1016/j.dental.2007.02.009

Cai, C., Chen, X., Li, Y., and Jiang, Q. (2023). Advances in the role of sodium hypochlorite irrigant in chemical preparation of root canal treatment. *Biomed. Res. Int.* 2023, 8858283–8858317. doi:10.1155/2023/8858283

Calt, S., and Serper, A. (2002). Time-dependent effects of EDTA on dentin structures. *J. Endod.* 28, 17–19. doi:10.1097/00004770-200201000-00004

Carrilho, M. R., Tay, F. R., Donnelly, A. M., Agee, K. A., Carvalho, R. M., Hosaka, K., et al. (2009). Membrane permeability properties of dental adhesive films. *J. Biomed. Mater. Res. B Appl. Biomater.* 88, 312–320. doi:10.1002/jbm.b.30968

Carvalho, R. M., Chersoni, S., Frankenberger, R., Pashley, D. H., Prati, C., and Tay, F. R. (2005). A challenge to the conventional wisdom that simultaneous etching and resin infiltration always occurs in self-etch adhesives. *Biomaterials* 26, 1035–1042. doi:10.1016/j.biomaterials.2004.04.003

Cecchin, D., Farina, A. P., Galafassi, D., Baroni Barbizam, J. V., Milori Corona, S. A., and Carlini-Junior, B. (2010). Influence of sodium hypochlorite and EDTA on the microtensile bond strength of a self-etching adhesive system. *J. Appl. ORAL Sci.* 18, 385–389. doi:10.1590/S1678-77572010000400011

Chappelow, C. C., Power, M. D., Bowles, C. Q., Miller, R. G., Pinzino, C. S., and Eick, J. D. (2000). Novel priming and crosslinking systems for use with isocyanatomethacrylate dental adhesives. *Dent. Mater. Off. Publ. Acad. Dent. Mater.* 16, 396–405. doi:10.1016/s0109-5641(00)00034-8

Chen, H., Sun, G., Wang, H., Yu, S., Tian, Z., and Zhu, S. (2023). Effect of collagen cross-linkers on dentin bond strength: a systematic review and network meta-analysis. *Front. Bioeng. Biotechnol.* 10, 1100894. doi:10.3389/fbioe.2022.1100894

Cheryan, M., and Rackis, J. J. (1980). Phytic acid interactions in food systems. *Crit. Rev. Food Sci. Nutr.* 13, 297–335. doi:10.1080/10408398009527293

Choi, Y., Kim, H.-J., and Min, K.-S. (2016). Effects of proanthocyanidin, a crosslinking agent, on physical and biological properties of collagen hydrogel scaffold. *Restor. Dent. Endod.* 41, 296. doi:10.5395/rde.2016.41.4.296

De-Deus, G., Paciornik, S., and Mauricio, M. H. P. (2006). Evaluation of the effect of EDTA, EDTAC and citric acid on the microhardness of root dentine. *Int. Endod. J.* 39, 401–407. doi:10.1111/j.1365-2591.2006.01094.x

Deeks, J. J., Higgins, J. P., and Altman, D. G. (2008). "Analysing data and undertaking meta-analyses," in *Cochrane handbook for systematic reviews of interventions* (John Wiley & Sons, Ltd), 243–296. doi:10.1002/9780470712184.ch9

Dikmen, B., and Tarim, B. (2018). The effect of endodontic irrigants on the microtensile bond strength of different dentin adhesives. *Niger. J. Clin. Pract.*, 21, 280. doi:10.4103/njcp.njcp_282_17

Dikmen, Gurbuz, O., Ozsoy, A., Eren, M. M., Cilingir, A., and Yucel, T. (2015). Effect of different antioxidants on the microtensile bond strength of an adhesive system to sodium hypochlorite-treated dentin. *J. Adhes. Dent.* 17, 499–504. doi:10.3290/j.jad.a35257

Epasinghe, D. J., Yiu, C. K. Y., Burrow, M. F., Hiraishi, N., and Tay, F. R. (2013). The inhibitory effect of proanthocyanidin on soluble and collagen-bound proteases. *J. Dent.* 41, 832–839. doi:10.1016/j.jdent.2013.06.002

Erdemir, A., Ari, H., Güngüneş, H., and Belli, S. (2004). Effect of medications for root canal treatment on bonding to root canal dentin. *J. Endod.* 30, 113–116. doi:10.1097/00004770-200402000-00013

Fang, M., Liu, R., Xiao, Y., Li, F., Wang, D., Hou, R., et al. (2012). Biomodification to dentin by a natural crosslinker improved the resin-dentin bonds. *J. Dent.* 40, 458–466. doi:10.1016/j.jdent.2012.02.008

Farina, A. P., Cecchin, D., Barbizam, J. V. B., and Carlini-Junior, B. (2011). Influence of endodontic irrigants on bond strength of a self-etching adhesive. *Aust. Endod. J.* 37, 26–30. doi:10.1111/j.1747-4477.2010.00249.x

Fawzi, E. M., Elkassas, D. W., and Ghoneim, A. G. (2010). Bonding strategies to pulp chamber dentin treated with different endodontic irrigants: microshear bond strength testing and SEM analysis. *J. Adhes. Dent.* 12, 63–70. doi:10.3290/j.jad.a17594

Frankenberger, R., Krämer, N., Oberschachtsiek, H., and Petschelt, A. (2000). Dentin bond strength and marginal adaption after NaOCl pre-treatment. *Oper. Dent.* 25, 40–45.

Frassetto, A., Breschi, L., Turco, G., Marchesi, G., Di Lenarda, R., Tay, F. R., et al. (2016). Mechanisms of degradation of the hybrid layer in adhesive dentistry and therapeutic agents to improve bond durability--A literature review. *Dent. Mater. Off. Publ. Acad. Dent. Mater.* 32, e41–e53. doi:10.1016/j.dental.2015.11.007

Gandhi, S. A., Chandrasekar, P., Nachimuthu, J., Abraham, C. S., and Venkataraman, K. J. (2020). A comparative evaluation of phytic acid as final rinse solution with other chelating agents for elimination of intraradicular smear: a scanning electron microscope study. *J. Pharm. Bioallied Sci.* 12, S576–S582. doi:10.4103/jpbs.JPBS_186_20

Garberoglio, R., and Becce, C. (1994). Smear layer removal by root canal irrigants. *Oral Surg. Oral Med. Oral Pathol.* 78, 359–367. doi:10.1016/0030-4220(94)90069-8

Ge, L., Zhu, M., Li, X., Xu, Y., Ma, X., Shi, R., et al. (2018). Development of active rosmarinic acid-gelatin biodegradable films with antioxidant and long-term antibacterial activities. *Food Hydrocolloids.* 83, 308–316. doi:10.1016/j.foodhyd.2018.04.052

Gu, L.-S., Huang, X.-Q., Griffin, B., Bergeron, B. R., Pashley, D. H., Niu, L.-N., et al. (2017). Primum non nocere - the effects of sodium hypochlorite on dentin as used in endodontics. *Acta Biomater.* 61, 144–156. doi:10.1016/j.actbio.2017.08.008

Guan, H., Luo, W., Bao, B., Cao, Y., Cheng, F., Yu, S., et al. (2022). A comprehensive review of rosmarinic acid: from phytochemistry to pharmacology and its new insight. *Molecules* 27, 3292. doi:10.3390/molecules27103292

Guo, J., Wang, L.-P., Zhu, J., Yang, J., and Zhu, H.-S. (2018). Impact of dentinal tubule orientation on dentin bond strength. *Curr. Med. Sci.* 38, 721–726. doi:10.1007/s11596-018-1936-8

Hagerman, A. E., and Klucher, K. M. (1986). Tannin-protein interactions. *Prog. Clin. Biol. Res.* 213, 67–76.

Han, B., Jaurequi, J., Tang, B. W., and Nimni, M. E. (2003). Proanthocyanidin: a natural crosslinking reagent for stabilizing collagen matrices. *J. Biomed. Mater. Res. A* 65, 118–124. doi:10.1002/jbm.a.10460

Haralur, S. B., Alasabi, A. A., Al Qahtani, S. A. A., and Alqahtani, S. S. (2017). Influence of irrigating agents on fiber postpush-out bond strength to radicular dentin sections with the different adhesive system. *Eur. J. Dent.* 11, 380–384. doi:10.4103/ejd.ejd_280_16

Hardan, L., Daood, U., Bourgi, R., Cuevas-Suárez, C. E., Devoto, W., Zarow, M., et al. (2022). Effect of collagen crosslinkers on dentin bond strength of adhesive systems: a systematic review and meta-analysis. *Cells* 11, 2417. doi:10.3390/cells11152417

Hashimoto, M., Ohno, H., Sano, H., Kaga, M., and Oguchi, H. (2003). *In vitro* degradation of resin-dentin bonds analyzed by microtensile bond test, scanning and transmission electron microscopy. *Biomaterials* 24, 3795–3803. doi:10.1016/s0142-9612(03)00262-x

Hawkins, C. L., and Davies, M. J. (1999). Hypochlorite-induced oxidation of proteins in plasma: formation of chloramines and nitrogen-centred radicals and their role in protein fragmentation. *Biochem. J.* 340 (Pt 2), 539–548. doi:10.1042/bj3400539

Higgins, J. P. T. (2003). Measuring inconsistency in meta-analyses. *BMJ* 327, 557–560. doi:10.1136/bmj.327.7414.557

Huerta-Madroñal, M., Caro-León, J., Espinosa-Cano, E., Aguilar, M. R., and Vázquez-Lasa, B. (2021). Chitosan - rosmarinic acid conjugates with antioxidant, anti-inflammatory and photoprotective properties. *Carbohydr. Polym.* 273, 118619. doi:10.1016/j.carbpol.2021.118619

Ishizuka, T., Kataoka, H., Yoshioka, T., Suda, H., Iwasaki, N., Takahashi, H., et al. (2001). Effect of NaClO treatment on bonding to root canal dentin using a new evaluation method. *Dent. Mater. J.* 20, 24–33. doi:10.4012/dmj.20.24

Kambara, K., Nakajima, M., Hosaka, K., Takahashi, M., Thanatvarakorn, O., Ichinose, S., et al. (2012). Effect of smear layer treatment on dentin bond of self-adhesive cements. *Dent. Mater. J.* 31, 980–987. doi:10.4012/dmj.2012-031

Kasraei, S., Azarsina, M., and Khamverdi, Z. (2013). Effect of Ethylene diamine tetra acetic acid and sodium hypochlorite solution conditioning on microtensile bond strength of one-step self-etch adhesives. *J. Conserv. Dent.* 16, 243–246. doi:10.4103/0972-0707.111324

Kewlani, M., Saha, S. G., Bhardwaj, A., Saha, M. K., Vijaywargiya, P., Jain, S., et al. (2020). Comparative evaluation of the effect of decontamination protocol on the shear bond strength of eighth generation bonding agent to contaminated dentin: an *in vitro* study. *Med. Pharm. Rep.* 93, 287–291. doi:10.15386/mpr-1488

Khoroushi, M., and Kachuei, M. (2014). Pull-out bond strength of a self-adhesive resin cement to NaOCl-treated root dentin: effect of antioxidizing agents. *Restor. Dent. Endod.* 39, 95–103. doi:10.5395/rde.2014.39.2.95

Kim, D.-S., Park, S. H., Choi, G.-W., Choi, K.-K., and Kim, S.-Y. (2011). Effect of EDTA treatment on the hybrid layer durability in total-etch dentin adhesives. *Dent. Mater. J.* 30, 717–722. doi:10.4012/dmj.2011-056

Kong, K., Hiraishi, N., Nassar, M., Otsuki, M., Yiu, C. K. Y., and Tagami, J. (2017). Effect of phytic acid etchant on resin-dentin bonding: monomer penetration and stability of dentin collagen. *J. Prosthodont. Res.* 61, 251–258. doi:10.1016/j.jpor.2016.10.001

Ku, C. S., Sathishkumar, M., and Mun, S. P. (2007). Binding affinity of proanthocyanidin from waste Pinus radiata bark onto proline-rich bovine achilles tendon collagen type I. *Chemosphere* 67, 1618–1627. doi:10.1016/j.chemosphere.2006.11.037

Lai, S. C. N., Mak, Y. F., Cheung, G. S. P., Osorio, R., Toledano, M., Carvalho, R. M., et al. (2001). Reversal of compromised bonding to oxidized etched dentin. *J. Dent. Res.* 80, 1919–1924. doi:10.1177/00220345010800101101

Lanigan, R. S., and Yamarik, T. A. (2002). Final report on the safety assessment of EDTA, calcium disodium EDTA, diammonium EDTA, dipotassium EDTA, disodium EDTA, TEA-EDTA, tetrasodium EDTA, tripotassium EDTA, trisodium EDTA, HEDTA, and trisodium HEDTA. *Int. J. Toxicol.* 21 (Suppl. 2), 95–142. doi:10.1080/10915810290096522

Let, M. B., Jacobsen, C., and Meyer, A. S. (2007). Ascorbyl palmitate, gamma-tocopherol, and EDTA affect lipid oxidation in fish oil enriched salad dressing differently. *J. Agric. Food Chem.* 55, 2369–2375. doi:10.1021/jf062675c

Li, A. L. B., Markvart, M., and Abbott, P. V. (2022). Effect of different concentrations of sodium hypochlorite on the compressive strength of endodontically treated roots. *J. Endod.* 48, 370–374. doi:10.1016/j.joen.2021.12.006

Lin, X., Xie, F., Ma, X., Hao, Y., Qin, H., and Long, J. (2017). Fabrication and characterization of dendrimer-functionalized nano-hydroxyapatite and its application in dentin tubule occlusion. *J. Biomater. Sci. Polym. Ed.* 28, 846–863. doi:10.1080/09205063.2017.1308654

Liu, R., Fang, M., Xiao, Y., Li, F., Yu, L., Zhao, S., et al. (2011). The effect of transient proanthocyanidins preconditioning on the cross-linking and mechanical properties of demineralized dentin. *J. Mater Sci.* 22, 2403–2411. doi:10.1007/s10856-011-4430-4

Liu, X., Cao, Y., Wang, H., Hu, Y., Wang, Z., Li, Y., et al. (2024). Phytic acid cross-linked and Hofmeister effect strengthened polyvinyl alcohol hydrogels for zinc ion storage. *Chem. Commun.*, 60, 554, 557. doi:10.1039/D3CC05008D

Liu, Z., Zhang, Z., and Ritchie, R. O. (2020). Structural orientation and anisotropy in biological materials: functional designs and mechanics. *Adv. Funct. Mater.* 30, 1908121. doi:10.1002/adfm.201908121

Luttrell, B. M. (1993). The biological relevance of the binding of calcium ions by inositol phosphates. *J. Biol. Chem.* 268, 1521–1524. doi:10.1016/s0021-9258(18)53883-7

Maravic, T., Mazzoni, A., Comba, A., Scotti, N., Checchi, V., and Breschi, L. (2017). How stable is dentin as a substrate for bonding? *Curr. Oral Health Rep.* 4, 248–257. doi:10.1007/s40496-017-0149-8

Mazzoni, A., Tjäderhane, L., Checchi, V., Di Lenarda, R., Salo, T., Tay, F. R., et al. (2015). Role of dentin MMPs in caries progression and bond stability. *J. Dent. Res.* 94, 241–251. doi:10.1177/0022034514562833

Mohannad, N., Noriko, H., Sofiqul, I.Md., Jrh, R. M., Masayuki, O., and Junji, T. (2020). Effect of phytic acid as an endodontic chelator on resin adhesion to sodium hypochlorite-treated dentin. *Restor. Dent. Endod.* 45, 1–8. doi:10.5395/rde.2020.45.e44

Mokeem, L. S., Garcia, I. M., and Melo, M. A. (2023). Degradation and failure phenomena at the dentin bonding interface. *Biomedicines* 11, 1256. doi:10.3390/biomedicines11051256

Morris, M. D., Lee, K. W., Agee, K. A., Bouillaguet, S., and Pashley, D. H. (2001). Effects of sodium hypochlorite and RC-prep on bond strengths of resin cement to endodontic surfaces. *J. Endod.* 27, 753–757. doi:10.1097/00004770-200112000-00010

Muana, H. L., Hiraishi, N., Nakajima, M., Kong, K., and Tagami, J. (2019). Effect of the dentin chelating agents phytic acid and EDTA on degree of conversion, microhardness, and bond strength of chemical-curing self-adhesive cements. *J. Adhes. Dent.* 21, 299–306. doi:10.3290/j.jad.a42997

Nalla, R. K., Balooch, M., Ager, J. W., Kruzic, J. J., Kinney, J. H., and Ritchie, R. O. (2005). Effects of polar solvents on the fracture resistance of dentin: role of water hydration. *Acta Biomater.* 1, 31–43. doi:10.1016/j.actbio.2004.08.002

Nassar, M., Hiraishi, N., Tamura, Y., Otsuki, M., Aoki, K., and Tagami, J. (2015). Phytic acid: an alternative root canal chelating agent. *J. Endod.* 41, 242–247. doi:10.1016/j.joen.2014.09.029

Nikaido, T., Takano, Y., Sasafuchi, Y., Burrow, M. F., and Tagami, J. (1999). Bond strengths to endodontically-treated teeth. *Am. J. Dent.* 12, 177–180.

Noor, S., Mohammad, T., Rub, M. A., Raza, A., Azum, N., Yadav, D. K., et al. (2022). Biomedical features and therapeutic potential of rosmarinic acid. *Arch. Pharm. Res.* 45, 205–228. doi:10.1007/s12272-022-01378-2

Okuda, M., Pereira, P. N. R., Nakajima, M., Tagami, J., and Pashley, D. H. (2002). Long-term durability of resin dentin interface: nanoleakage vs. microtensile bond strength. *Oper. Dent.* 27, 289–296.

Page, M. J., McKenzie, J. E., Bossuyt, P. M., Boutron, I., Hoffmann, T. C., Mulrow, C. D., et al. (2021). The PRISMA 2020 statement: an updated guideline for reporting systematic reviews. *BMJ* 372, n71. doi:10.1136/bmj.n71

Pascon, F. M., Kantovitz, K. R., Sacramento, P. A., Nobre-dos-Santos, M., and Puppin-Rontani, R. M. (2009). Effect of sodium hypochlorite on dentine mechanical properties. A review. *J. Dent.* 37, 903–908. doi:10.1016/j.jdent.2009.07.004

Pashley, D. H., Tay, F. R., Yiu, C., Hashimoto, M., Breschi, L., Carvalho, R. M., et al. (2004). Collagen degradation by host-derived enzymes during aging. *J. Dent. Res.* 83, 216–221. doi:10.1177/154405910408300306

Perdigão, J., Lopes, M., Geraldeli, S., Lopes, G. C., and García-Godoy, F. (2000). Effect of a sodium hypochlorite gel on dentin bonding. *Dent. Mater. Off. Publ. Acad. Dent. Mater.* 16, 311–323. doi:10.1016/s0109-5641(00)00021-x

Perdigão, J., Reis, A., and Loguercio, A. D. (2013). Dentin adhesion and MMPs: a comprehensive review. *J. Esthet. Restor. Dent. Off. Publ. Am. Acad. Esthet. Dent. Al* 25, 219–241. doi:10.1111/jerd.12016

Pimentel Correa, A. C., Cecchin, D., Affonso De Almeida, J. F., Figueiredo De Almeida Gomes, B. P., Zaia, A. A., and Randi Ferraz, C. C. (2016). Sodium thiosulfate for recovery of bond strength to dentin treated with sodium hypochlorite. *J. Endod.* 42, 284–288. doi:10.1016/j.joen.2015.11.010

Prasansuttiporn, T., Nakajima, M., Foxton, R. M., and Tagami, J. (2012). Scrubbing effect of self-etching adhesives on bond strength to NaOCl-treated dentin. *J. Adhes. Dent.* 14, 121–127. doi:10.3290/j.jad.a22340

Prasansuttiporn, T., Nakajima, M., Kunawarote, S., Foxton, R. M., and Tagami, J. (2011). Effect of reducing agents on bond strength to NaOCl-treated dentin. *Dent. Mater. Off. Publ. Acad. Dent. Mater.* 27, 229–234. doi:10.1016/j.dental.2010.10.007

Prasansuttiporn, T., Thanatvarakorn, O., Tagami, J., Foxton, R. M., and Nakajima, M. (2017). Bonding durability of a self-etch adhesive to normal versus smear-layer deproteinized dentin: effect of a reducing agent and plant-extract antioxidant. *J. Adhes. Dent.* 19, 253–258. doi:10.3290/j.jad.a38409

Prati, C., Chersoni, S., and Pashley, D. H. (1999). Effect of removal of surface collagen fibrils on resin-dentin bonding. *Dent. Mater. Off. Publ. Acad. Dent. Mater.* 15, 323–331. doi:10.1016/s0109-5641(99)00052-4

Raboy, V. (2003). myo-Inositol-1,2,3,4,5,6-hexakisphosphate. *Phytochemistry* 64, 1033–1043. doi:10.1016/s0031-9422(03)00446-1

Rauf, A., Imran, M., Abu-Izneid, T., Iahtisham-Ul-Haq, Patel, S., Pan, X., et al. (2019). Proanthocyanidins: a comprehensive review. *Biomed. Pharmacother. Biomedecine Pharmacother.* 116, 108999. doi:10.1016/j.biopha.2019.108999

Ricucci, D., and Siqueira, J. F. (2011). Recurrent apical periodontitis and late endodontic treatment failure related to coronal leakage: a case report. *J. Endod.* 37, 1171–1175. doi:10.1016/j.joen.2011.05.025

Santos, J., de Oliveira Carrilho, M. R., Fernando De Goes, M., Augusto Zaia, A., de Almeida Gomes, B. P. F., de Souza-Filho, F. J., et al. (2006). Effect of chemical irrigants on the bond strength of a self-etching adhesive to pulp chamber dentin. *J. Endod.* 32, 1088–1090. doi:10.1016/j.joen.2006.07.001

Shafiei, F., Dehghani, Z., and Tavangar, M. S. (2023). Effect of natural antioxidants on bond strength recovery of resin-modified glass ionomers to the NaOCl-affected pulp chamber dentin. *Clin. Exp. Dent. Res.* 9, 258–262. doi:10.1002/cre2.697

Souparnika, D. P., Babu, B. S., Shetty, N., Imteyaz, F., Parthiban, G., and Kumar, G. V. (2023). Phytic acid: a novel dentine conditioning agent for glass ionomer cement restorations: an *in vitro* scanning electron microscopic study. *J. Pharm. Bioallied Sci.* 15, S391–S395. doi:10.4103/jpbs.jpbs_411_22

Spencer, P., and Wang, Y. (2002). Adhesive phase separation at the dentin interface under wet bonding conditions. *J. Biomed. Mater. Res.* 62, 447–456. doi:10.1002/jbm.10364

Stevens, C. D. (2014). Immediate shear bond strength of resin cements to sodium hypochlorite-treated dentin. *J. Endod.* 40, 1459–1462. doi:10.1016/j.joen.2014.02.022

Taniguchi, G., Nakajima, M., Hosaka, K., Iwamoto, N., Ikeda, M., Foxton, R. M., et al. (2009). Improving the effect of NaOCl pretreatment on bonding to caries-affected dentin using self-etch adhesives. *J. Dent.* 37, 769–775. doi:10.1016/j.jdent.2009.06.005

Thbayh, D. K., Palusiak, M., Viskolcz, B., and Fiser, B. (2023). Comparative study of the antioxidant capability of EDTA and Irganox. *Heliyon* 9, e16064. doi:10.1016/j.heliyon.2023.e16064

Thompson, J. M., Agee, K., Sidow, S. J., McNally, K., Lindsey, K., Borke, J., et al. (2012). Inhibition of endogenous dentin matrix metalloproteinases by ethylenediaminetetraacetic acid. *J. Endod.* 38, 62–65. doi:10.1016/j.joen.2011.09.005

Toledano, M., Yamauti, M., Osorio, E., and Osorio, R. (2012). Zinc-inhibited MMP-mediated collagen degradation after different dentine demineralization procedures. *Caries Res.* 46, 201–207. doi:10.1159/000337315

Torii, Y., Hikasa, R., Iwate, S., Oyama, F., Itou, K., and Yoshiyama, M. (2003). Effect of EDTA conditioning on bond strength to bovine dentin promoted by four current adhesives. *Am. J. Dent.* 16, 395–400.

Torres, J., Domínguez, S., Cerdá, M. F., Obal, G., Mederos, A., Irvine, R. F., et al. (2005). Solution behaviour of myo-inositol hexakisphosphate in the presence of multivalent cations. Prediction of a neutral pentamagnesium species under cytosolic/nuclear conditions. *J. Inorg. Biochem.* 99, 828–840. doi:10.1016/j.jinorgbio.2004.12.011

Vargas, M. A., Cobb, D. S., and Armstrong, S. R. (1997). Resin-dentin shear bond strength and interfacial ultrastructure with and without a hybrid layer. *Oper. Dent.* 22, 159–166.

Verma, N., Sangwan, P., Tewari, S., and Duhan, J. (2019). Effect of different concentrations of sodium hypochlorite on outcome of primary root canal treatment: a randomized controlled trial. *J. Endod.* 45, 357–363. doi:10.1016/j.joen.2019.01.003

Visan, R. M., and Angelescu, D. G. (2023). Coarse-grained model of phytic acid for predicting the supramolecular architecture of ionically cross-linked chitosan hydrogels. *J. Phys. Chem. B* 127, 5718–5729. doi:10.1021/acs.jpcb.3c02115

Vongphan, N., Senawongse, P., Somsiri, W., and Harnirattisai, C. (2005). Effects of sodium ascorbate on microtensile bond strength of total-etching adhesive system to NaOCl treated dentine. *J. Dent.* 33, 689–695. doi:10.1016/j.jdent.2005.01.008

Wang, Y., Chen, C., Zang, H. L., and Liang, Y. H. (2019). The recovery effect of proanthocyanidin on microtensile bond strength to sodium hypochlorite-treated dentine. *Int. Endod. J.* 52, 371–376. doi:10.1111/iej.13005

Wang, Y., and Liang, Y. H. (2017). Influence of surface treatment with sodium hypochlorite solution on dentin bond strength. *J. Peking. Univ. Health Sci.* 49, 105–109.

Weston, C., Ito, S., Wadgaonkar, B., and Pashley, D. (2007). Effects of time and concentration of sodium ascorbate on reversal of NaOCl-induced reduction in bond strengths. *J. Endod.* 33, 879–881. doi:10.1016/j.joen.2007.04.004

Xu, H., Ye, Z., Zhang, A., Lin, F., Fu, J., and Fok, A. S. L. (2022). Effects of concentration of sodium hypochlorite as an endodontic irrigant on the mechanical and structural properties of root dentine: a laboratory study. *Int. Endod. J.* 55, 1091–1102. doi:10.1111/iej.13800

Yadav, P. C., Raghu, R., Shetty, A., and Rajasekhara, S. (2021). Postspace pretreatment with 17% ethylenediamine tetraacetic acid, 7% maleic acid, and 1% phytic acid on bond strength of fiber posts luted with a self-adhesive resin cement. *J. Conserv. Dent.* 24, 558–562. doi:10.4103/jcd.jcd_489_21

Zhang, S., Zhang, Y., Li, B., Zhang, P., Kan, L., Wang, G., et al. (2019). One-Step preparation of a highly stretchable, conductive, and transparent poly(vinyl alcohol)–phytic acid hydrogel for casual writing circuits. *ACS Appl. Mater. Interfaces* 11, 32441–32448. doi:10.1021/acsami.9b12626

Zhao, F., Repo, E., Yin, D., Chen, L., Kalliola, S., Tang, J., et al. (2017). One-pot synthesis of trifunctional chitosan-EDTA-β-cyclodextrin polymer for simultaneous removal of metals and organic micropollutants. *Sci. Rep.* 7, 15811. doi:10.1038/s41598-017-16222-7

frontiers | Frontiers in Bioengineering and Biotechnology

TYPE Original Research
PUBLISHED 08 May 2025
DOI 10.3389/fbioe.2025.1580502

OPEN ACCESS

EDITED BY
Dan Lin,
Shanghai University of Medicine and Health Sciences, China

REVIEWED BY
Congyu Yu,
Harvard University, United States
Ziqi Wang,
Harbin Institute of Technology, China
Yifan Zhang,
Hangzhou Dental Hospital, China

*CORRESPONDENCE
Hongbo Yu,
yhb3508@163.com

†These authors have contributed equally to this work

‡These authors have contributed equally to this work and share senior last authorship

RECEIVED 20 February 2025
ACCEPTED 25 April 2025
PUBLISHED 08 May 2025

CITATION
Bao J, Tan Z, Sun Y, Xu X, Liu H, Cui W, Yang Y, Cheng M, Wang Y, Ku C, Ho YK, Zhu J, Fan L, Qian D, Shen S, Wen Y and Yu H (2025) Deep ensemble learning-driven fully automated multi-structure segmentation for precision craniomaxillofacial surgery.
Front. Bioeng. Biotechnol. 13:1580502.
doi: 10.3389/fbioe.2025.1580502

Deep ensemble learning-driven fully automated multi-structure segmentation for precision craniomaxillofacial surgery

Jiahao Bao[1†], Zongcai Tan[2†], Yifeng Sun[3†], Xinyu Xu[4†], Huazhen Liu[4], Weiyi Cui[1], Yang Yang[5], Mengjia Cheng[6], Yiming Wang[1], Congshuang Ku[1], Yuen Ka Ho[1], Jiayi Zhu[1], Linfeng Fan[7‡], Dahong Qian[8‡], Shunyao Shen[1‡], Yaofeng Wen[8‡] and Hongbo Yu[1‡*]

[1]Department of Oral and Craniomaxillofacial Surgery, Shanghai Ninth People's Hospital, Shanghai Jiao Tong University School of Medicine, College of Stomatology, Shanghai Jiao Tong University, National Center for Stomatology, National Clinical Research Center for Oral Diseases, Shanghai Research Institute of Stomatology, Shanghai Key Laboratory of Stomatology, Shanghai, China, [2]Hamlyn Centre for Robotic Surgery, Institute of Global Health Innovation, Imperial College London, London, United Kingdom, [3]School of Mechanical Engineering, Shanghai Dianji University, Shanghai, China, [4]School of Electronic Information and Electrical Engineering, Shanghai Jiao Tong University, Shanghai, China, [5]Shanghai Lanhui Medical Technology Co., Ltd., Shanghai, China, [6]Faculty of Dentistry, The University of Hong Kong, Hong Kong, Hong Kong SAR, China, [7]Department of Radiology, Shanghai Ninth People's Hospital, College of Stomatology, Shanghai Jiao Tong University School of Medicine, Shanghai, China, [8]School of Biomedical Engineering, Shanghai Jiao Tong University, Shanghai, China

Objectives: Accurate segmentation of craniomaxillofacial (CMF) structures and individual teeth is essential for advancing computer-assisted CMF surgery. This study developed CMF-ELSeg, a novel fully automatic multi-structure segmentation model based on deep ensemble learning.

Methods: A total of 143 CMF computed tomography (CT) scans were retrospectively collected and manually annotated by experts for model training and validation. Three 3D U-Net–based deep learning models (V-Net, nnU-Net, and 3D UX-Net) were benchmarked. CMF-ELSeg employed a coarse-to-fine cascaded architecture and an ensemble approach to integrate the strengths of these models. Segmentation performance was evaluated using Dice score and Intersection over Union (IoU) by comparing model predictions to ground truth annotations. Clinical feasibility was assessed through qualitative and quantitative analyses.

Results: In coarse segmentation of the upper skull, mandible, cervical vertebra, and pharyngeal cavity, 3D UX-Net and nnU-Net achieved Dice scores above 0.96 and IoU above 0.93. For fine segmentation and classification of individual teeth, the cascaded 3D UX-Net performed best. CMF-ELSeg improved Dice scores by 3%–5% over individual models for facial soft tissue, upper skull, mandible, cervical vertebra, and pharyngeal cavity segmentation, and maintained high accuracy Dice > 0.94 for most teeth. Clinical evaluation confirmed that CMF-ELSeg performed reliably in patients with skeletal malocclusion, fractures, and fibrous dysplasia.

Conclusion: CMF-ELSeg provides high-precision segmentation of CMF structures and teeth by leveraging multiple models, serving as a practical tool for clinical applications and enhancing patient-specific treatment planning in CMF surgery.

KEYWORDS

deep learning, craniomaxillofacial surgery, virtual surgical planning, computed tomography, segmentation

1 Introduction

Craniomaxillofacial (CMF) deformities include congenital and acquired malformations such as dentofacial, post-traumatic, post-tumor resection–related, and temporomandibular joint deformities, which significantly compromise the facial aesthetics and stomatognathic functions of patients (Xia et al., 2009). Surgical correction of CMF deformities is challenging due to their complex characteristics. To achieve favorable surgical outcomes, personalized and precise surgical plans are necessary (Alkhayer et al., 2020; On et al., 2024). Recently, virtual surgical planning (VSP) based on three-dimensional (3D) imaging technologies, including 3D preoperative treatment planning and simulation of surgical outcome, has been increasingly utilized in CMF surgery, facilitating deformity diagnosis, cephalometric analysis, surgical simulation, and the fabrication of cutting guides and splints (Naran et al., 2018). The initial step of the VSP workflows involves the segmentation of CMF structures, followed by 3D reconstruction of the composite dental-maxillofacial model from computed tomography (CT) scans (Bao et al., 2024). Overall, efficient and accurate segmentation approaches provide a robust basis for advancing computer-assisted CMF surgery.

Manual segmentation by experienced clinicians acts as the gold standard, but it is widely acknowledged that this process is considerably time-consuming, labor-intensive, and error-prone with segmentation performance varying among experts. In current clinical applications, semi-automatic approaches like threshold-based, region-growing or template-fitting methods (e.g., GrowCut, Canny Segmentation and Robust Statistics Segmenter algorithms) integrate automated segmentation with manual label annotation by experts, which have been applied in digital planning software and alleviate the workload of clinicians (Wallner et al., 2019; Zhang L. et al., 2023). However, instance segmentation, which involves distinguishing and delineating each unique structure within the CMF region, remains challenging due to substantial interindividual morphological variations, intricate structural connections, poor contrast in joints and tooth apices, and frequent presence of artifacts (Priya et al., 2024; Xiang et al., 2024). Traditional approaches still cannot achieve favorable segmentation results and need manual adjustment for clinical use. Therefore, establishing a fully automated, high-precision segmentation system holds considerable clinical significance for CMF surgery.

With the rising clinical needs and the development of artificial intelligence, deep learning has been applied across various aspects of healthcare, including medical diagnosis, treatment planning, surgical assistance, postoperative monitoring and rehabilitation training (Jiang et al., 2017; Chen et al., 2022; Huang et al., 2024; Wang et al., 2024). In the field of dentistry, deep learning has significantly improved digital dentistry workflows such as caries detection, prosthetic evaluation, orthodontic analysis, periodontitis diagnosis and treatment planning (Graves and Uribe, 2024; Nordblom et al., 2024; Setzer et al., 2024). Fully automated medical image segmentation approaches based on deep learning have been proposed to overcome previous limitations and enhance the precision and efficiency of CMF surgery due to its ability to learn features associated with target tasks from large-scale data (Liu et al., 2023; Nogueira-Reis et al., 2023; Xiang et al., 2024). Inspired by its remarkable advancements, many studies have developed and evaluated specific algorithms for CMF CT or Cone-beam CT (CBCT) segmentation (Zhang et al., 2020; Liu et al., 2024). Notably, U-Net-based framework demonstrated excellent performance for medical image segmentation, which has an encoder-decoder framework with skip connections (Ronneberger et al., 2015). Liu et al. proposed a 3D U-Net-based model to segment midface and mandible from CBCT for computer-aided CMF surgical simulation (Liu et al., 2021; Deng et al., 2023). Dot et al. evaluated the performance of the nnU-Net for automatic segmentation of the upper skull, mandible, upper teeth, lower teeth and mandibular canal from CT scans for orthognathic surgery (Dot et al., 2022). However, some limitations restrict their clinical applicability. First, most existing algorithms were dedicated to coarse segmentation considering few structures (e.g., less than 30 structures), and only a few studies have attempted to segment all the structures of interest (facial soft tissue, upper skull, mandible bone, cervical vertebra, hyoid bone, pharyngeal cavity, inferior alveolar nerve, upper teeth, lower teeth and individual teeth), which limits models' clinical application (Dot et al., 2022; Liu et al., 2024). Second, due to the diverse sizes and shapes of different structures, direct cross-scale training leads to the deficiency of semantic information in multiple segmentation tasks and the capability of the individual model for cross-scale information extraction is limited. The segmentation accuracy and robustness require improvement. To date, no studies have investigated the use of ensemble learning strategies to improve the potential of fully automated segmentation algorithms for application in CMF surgery. Meanwhile, although current studies focusing on segmentation algorithms are promising, the reliability and accessibility of different methods for multi-structure segmentation and classification in the CMF region have not been systematically and comprehensively benchmarked (Schneider et al., 2022). Most published studies were conducted based on small-size hold out dataset (Dot et al., 2024). Hence, it is of great significance to systematically evaluate the segmentation performance of existing models and to develop a novel multi-objective segmentation model capable of automatically extracting information across different scales.

Based on previous studies and the identified deficiencies, the current study aims to comprehensively benchmark the performance of three 3D U-Net-based deep learning models (V-Net, nnU-Net,

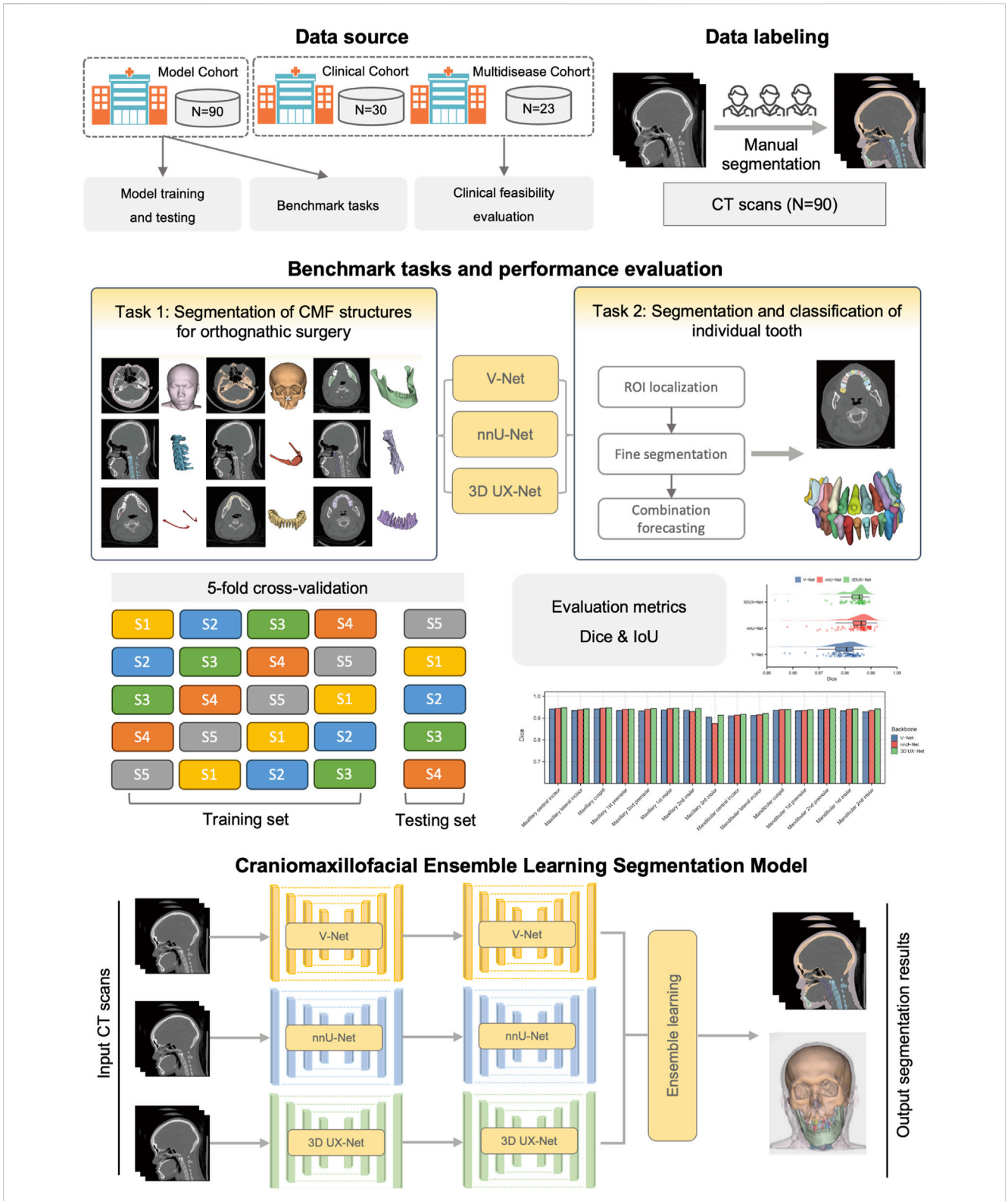

FIGURE 1
Overview of the study design.

3D UX-Net) for multi-structure segmentation and classification using an identical CMF CT dataset. In addition, we propose a novel fully automated framework, named CMF-ELSeg, that utilizes deep ensemble learning methodologies specifically tailored for multi-class segmentation in CMF surgery. By integrating the strengths of each individual model, CMF-ELSeg achieves accurate segmentation of CMF structures and teeth, and can identify each tooth according to the Fédération Dentaire Internationale (FDI)

classification. Our framework serves as a powerful tool for surgical planning, significantly enhancing the decision-making and design processes in CMF surgery.

2 Materials and methods

The overview of the study design is shown in Figure 1. Our study follows the Checklist for Artificial Intelligence in Dental Research (Schwendicke et al., 2021). This study was ethically approved by the ethics committee of Shanghai Ninth People's Hospital, Shanghai Jiao Tong University School of Medicine (IRB No. SH9H-2022-TK12-1).

2.1 Participants and dataset

Three cohorts were formed in our study to train and validate the segmentation model. CMF CT scans were collected from the Department of Oral and Cranio-Maxillofacial Surgery, Shanghai Ninth People's Hospital. Cohort 1 (Model cohort) and Cohort 2 (Clinical cohort) were employed for model training and clinical feasibility evaluation. The inclusion criteria for Cohort 1 and Cohort 2 were as follows: (1) patients diagnosed with skeletal malocclusion; (2) patients who required orthodontic and orthognathic joint treatment; (3) patients who received CMF CT scans covering the entire maxillofacial region. Participants were excluded if they met any of the following conditions: (1) refusal to participate ($n = 4$); (2) inadequate image quality that did not meet the requirements for surgical planning ($n = 8$); (3) diagnosis of congenital dentofacial deformities, such as CMF syndromes, cleft lips, and cleft palates ($n = 18$). Preoperative CT scans were taken during the VSP phase following the completion of preoperative orthodontic treatment, while postoperative CT scans were obtained 6 months after surgery. The parameters of CT images are as follows: a pixel size ranging from 0.40 mm × 0.40 mm to 0.53 mm × 0.53 mm; a slice interval between 0.625 mm and 1.250 mm; and a resolution of 512 × 512 pixels. The details of patient characteristics are shown in the Supplementary Material (Supplementary Figures S1, S2). In addition, the Cohort 3 (Multi-disease cohort), including samples from patients with maxillofacial fractures, fibrous dysplasia, and congenital syndromes, was used to validate the generalizability of the model.

2.2 Data annotations

In total, 90 CT scans in Cohort 1 were obtained in Digital Imaging and Communications in Medicine (DICOM) format and imported into 3D Slicer software (version 4.2.0). Manual segmentation for each CT scan was completed by two experienced radiologists and verified by one oral and maxillofacial doctor with rich experience in CMF surgery. The ground truth of each segmentation label was generated, including facial soft tissue, upper skull, mandible bone, cervical vertebra, hyoid bone, pharyngeal cavity, inferior alveolar nerve, upper teeth, lower teeth and individual teeth (Supplementary Figure S3). All ground truth annotations were carefully reviewed to meet the high standards required for clinical use. The details of data annotations and preprocessing were shown in the Supplementary Material.

2.3 Benchmark tasks and construction of cascaded segmentation networks

Our benchmark includes two tasks: (1) comparing the performance of different backbones in CMF structures segmentation; and (2) comparing the performance of fine segmentation networks in teeth instance segmentation. Considering the deficiency of semantic information details in direct cross-scale training, and the difficulty in simultaneously achieving effective recognition of segmentation tasks at different granularities, the cascaded segmentation network illustrated in Figure 2 was developed, which is composed of the coarse segmentation network for CMF structures segmentation and the fine segmentation network for teeth segmentation and ID classification. Three widely used U-Net models including V-Net, nnU-Net, and 3D UX-Net were selected as backbones for training and benchmark evaluation (Milletari et al., 2016; Isensee et al., 2021; Lee et al., 2023). The descriptions of the backbone models are included in the Supplementary Material (Supplementary Figure S4).

In the coarse stage, the CMF anatomical structures of interest (facial soft tissue, upper skull, mandible bone, cervical vertebra, hyoid bone, pharyngeal cavity, inferior alveolar nerves) were first segmented. The teeth are roughly categorized into upper and lower classes according to the position of the teeth in the maxilla and mandible. Then, the CT images and labels were synchronously scaled and cropped using nearest neighbor interpolation based on the foreground region of the upper and lower teeth to obtain the regions of interest (ROI). In the fine stage, the framework of fine segmentation networks shared the same basic architecture as the model from the first stage. A combination forecasting approach based on the features of adjacent teeth to reduce misidentification was applied to achieve fine segmentation of individual teeth. The final layer of the decoder includes two output layers corresponding to the segmentation of teeth into 33 classes (32 individual teeth and the background) and five classes (odd and even-numbered upper and lower teeth, along with the background), respectively. This improvement utilizes a Dice loss function for the five-class segmentation to correct the 33-class segmentation. The loss function for the fine segmentation network is defined as follows:

$$L = \lambda_1 L_{dice}\left(\widehat{p_{33}}, G_{33}\right) + \lambda_2 L_{dice}\left(\widehat{p_5}, G_5\right)$$

Where $\widehat{p_{33}}$ and G_{33} represent the predicted results and ground truth for 33-class tooth segmentation, respectively, and $\widehat{p_5}$ and G_5 represent the predicted results and ground truth for five-class tooth segmentation, respectively. The accuracy of individual cascaded network with different backbones was compared in the task of teeth segmentation.

2.4 Framework of CMF-ELSeg

Based on the performance of the coarse-to-fine cascaded segmentation networks, we proposed an ensemble learning segmentation model for CMF surgery, named CMF-ELSeg, to

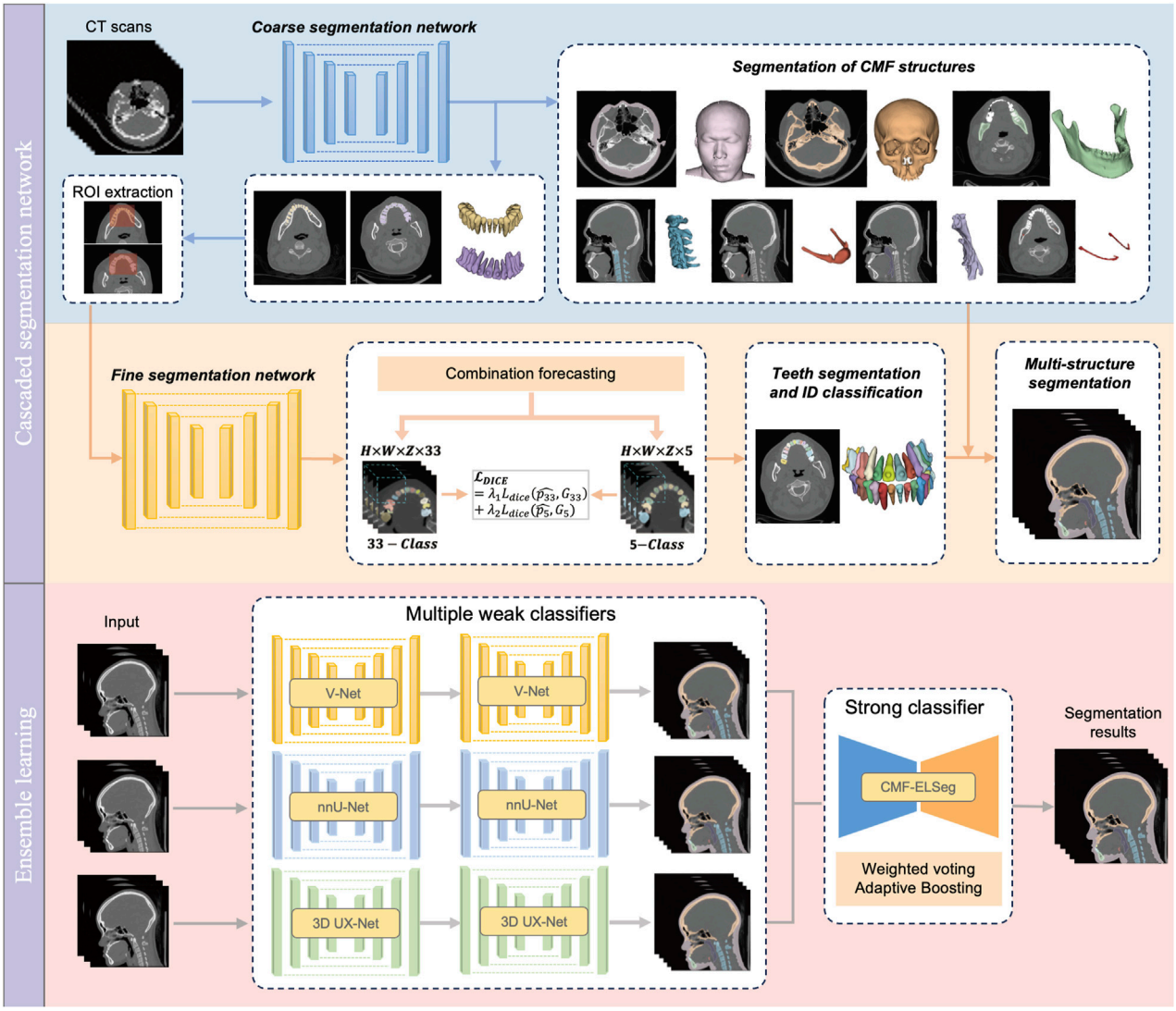

FIGURE 2
Architecture of our proposed deep learning model.

enhance overall segmentation ability (Figure 2). Three cascaded segmentation networks, employing V-Net, nnU-Net, and 3D UX-Net as backbones, were integrated for the development of the ensemble model. Each backbone was chosen for its distinct advantages in voxel recognition. Each individual cascaded segmentation network was trained separately and the CMF-ELSeg was developed leveraging the diversity of different models through a weighted voting strategy to produce a fused segmentation result. To avoid overfitting and poor robustness, we employed ensemble learning to learn the trainable voting weights. Specifically, the Adaptive Boosting (AdaBoost) method was utilized for adaptively assigning appropriate weights to the classifiers during the training process, which is advantageous in effectively reducing bias and variance, thereby improving overall generalization and accuracy (Freund and Schapire, 1997; Schapire, 2013). By combining multiple weak classifiers and iteratively adjusting the weights of the dataset to focus on previously misclassified samples, AdaBoost enhanced the performance of the segmentation task. The weights of weak classifiers were calculated by evaluating the accuracy of three individual cascaded segmentation networks according to the following formula:

$$\alpha_t = \frac{1}{2} ln\left(\frac{1-\epsilon_t}{\epsilon_t}\right), \ t = 1, 2, 3$$

where t represents the number of three individual cascaded segmentation network, and ϵ_t represents the error rate of the different model. Subsequently, we integrated multiple weak classifiers to construct a strong classifier, thereby enhancing the accuracy of segmentation tasks.

2.5 Evaluation of model performance

Both qualitative and quantitative assessments were conducted. By inputting the original CT images into the deep learning models, we obtained the segmentation results (predictions) for each target.

For visualization, individual CMF 3D models were reconstructed employing 3D Slicer software. The segmentation performance of the deep learning models for each CMF structure and individual tooth was assessed by comparing the predictions with manually delineated ground truth. Quantitative evaluation metrics including the Dice and Intersection over Union (IoU) were utilized for this evaluation. The specific definitions of these metrics are listed in the Supplementary Material.

2.6 Evaluation of clinical feasibility

Cohort 2 and Cohort 3 were used to validate the clinical feasibility and generalizability of CMF-ELSeg. Specifically, Cohort 2 comprised 30 patients with skeletal malocclusion, while Cohort 3 included 23 patients with a variety of CMF conditions. A four-point categorical scale was used to evaluate the segmentation quality of each category as well as the overall segmentation performance: "Grade A" = optimal automatic segmentation, indicating that the results can be directly used for VSP (The overall grade can only be rated as "A" if all individual categories are also graded as "A"); "Grade B" = minor visual errors in the automatic segmentation, with results still deemed suitable for direct use in surgical planning; "Grade C" = segmentation errors that could impact surgical planning but are easily correctable, such as defects in the anterior wall of the maxillary sinus, misidentification of individual teeth, or discontinuities in the nerve canal; and "Grade D" = significant errors that are difficult to manually correct and adversely affect surgical planning, requiring re-segmentation, such as misidentification of multiple teeth or incorrect classification of the maxilla and mandible (Deng et al., 2023). The segmentation and reconstruction results were evaluated by three experienced surgeons, who collaboratively determined the grade for each label and the overall performance.

Following the qualitative evaluation, the experts responsible for the initial manual annotations refined the preliminary segmentation results rated as B, C, or D. Manual corrections were performed using the 3D Slicer to modify and correct mislabeled regions slice by slice. The revision continued until the segmentation quality for each anatomical structure and individual tooth fully satisfied the criteria of Grade A, indicating that the corrected results could be directly employed for VSP. Dice coefficients were subsequently calculated to compare the automatic segmentation results with the manually corrected outcomes. The corresponding modification times were also recorded throughout this process.

2.7 Statistical analysis

All these models underwent training using a 5-fold cross-validation strategy. The analysis and visualization of all data were conducted using Python (v.3.7) and R software (v.4.1.2). For statistical analysis, categorical variables were presented as numbers and percentages, and continuous variables were presented as means ± standard deviations (mean ± Std). We employed the *T*-test for normally distributed continuous variables, and the Mann-Whitney U test for non-normally distributed continuous variables to compare continuous variables between two groups. $P < 0.05$ was considered as the statistical significance.

3 Results

3.1 Performance evaluation of cascaded segmentation networks for CMF structures and individual teeth segmentation

Figure 3 and Supplementary Table S2 show the performance (Dice and IoU) of V-Net, nnU-Net, and 3D UX-Net for CMF structures segmentation. The segmentation performance of 3D UX-Net and nnU-Net was comparable and significantly better than that of V-Net (Figure 3A; Supplementary Figure S5A). In the segmentation task for the upper skull, mandible, cervical vertebra and pharyngeal cavity, both 3D UX-Net and nnU-Net achieved average Dice scores exceeding 0.96 and average IoU exceeding 0.93. The nnU-Net generally has the highest mean value on all metrics, particularly excelling in the segmentation of the hyoid bone, inferior alveolar nerve, upper teeth, and lower teeth.

The performance of fine segmentation for individual teeth was evaluated and the quantitative analysis results were presented in Figure 3B and Supplementary Figure S5B. The cascaded segmentation network based on 3D UX-Net demonstrated optimal performance across all evaluation metrics, maintaining high accuracy and stability even when segmenting the maxillary 3rd molar (Dice = 0.9133 ± 0.0778; IoU = 0.8514 ± 0.1153) (Supplementary Table S3). nnU-Net based model's Dice and IoU scores were slightly lower than those of 3D UX-Net but higher than those of V-Net except for the maxillary 3rd molars. Additionally, the most notable segmentation error made by the model based on nnU-Net was the mislabeling of individual teeth, which occurs less frequently in the model developed based on 3D UX-Net.

3.2 Performance evaluation of CMF-ELSeg

The mean results of Dice and IoU for each segmentation label are shown in Figure 4A and Supplementary Table S4. Two cases were randomly selected from our dataset to illustrate our results (Case 1: a patient with dentofacial deformity before orthognathic surgery; Case 2: a patient who has undergone orthognathic surgery). It can be observed that apart from suboptimal segmentation performance for the hyoid bone and inferior alveolar nerves (Dice coefficient less than 0.9), CMF-ELSeg consistently achieves high segmentation levels across other categories. Compared to individual models, CMF-ELSeg demonstrated approximately a 3%–5% improvement in Dice coefficient scores in the segmentation of CMF structures including facial soft tissue, upper skull, mandible bone, cervical vertebra, and pharyngeal cavity (Figure 4B). Figures 5A–D and Supplementary Figure S6 showed the results of 2D segmentation and 3D reconstruction for each label. Additionally, the results of 2D segmentation, 3D reconstruction and surface deviations of all teeth were presented

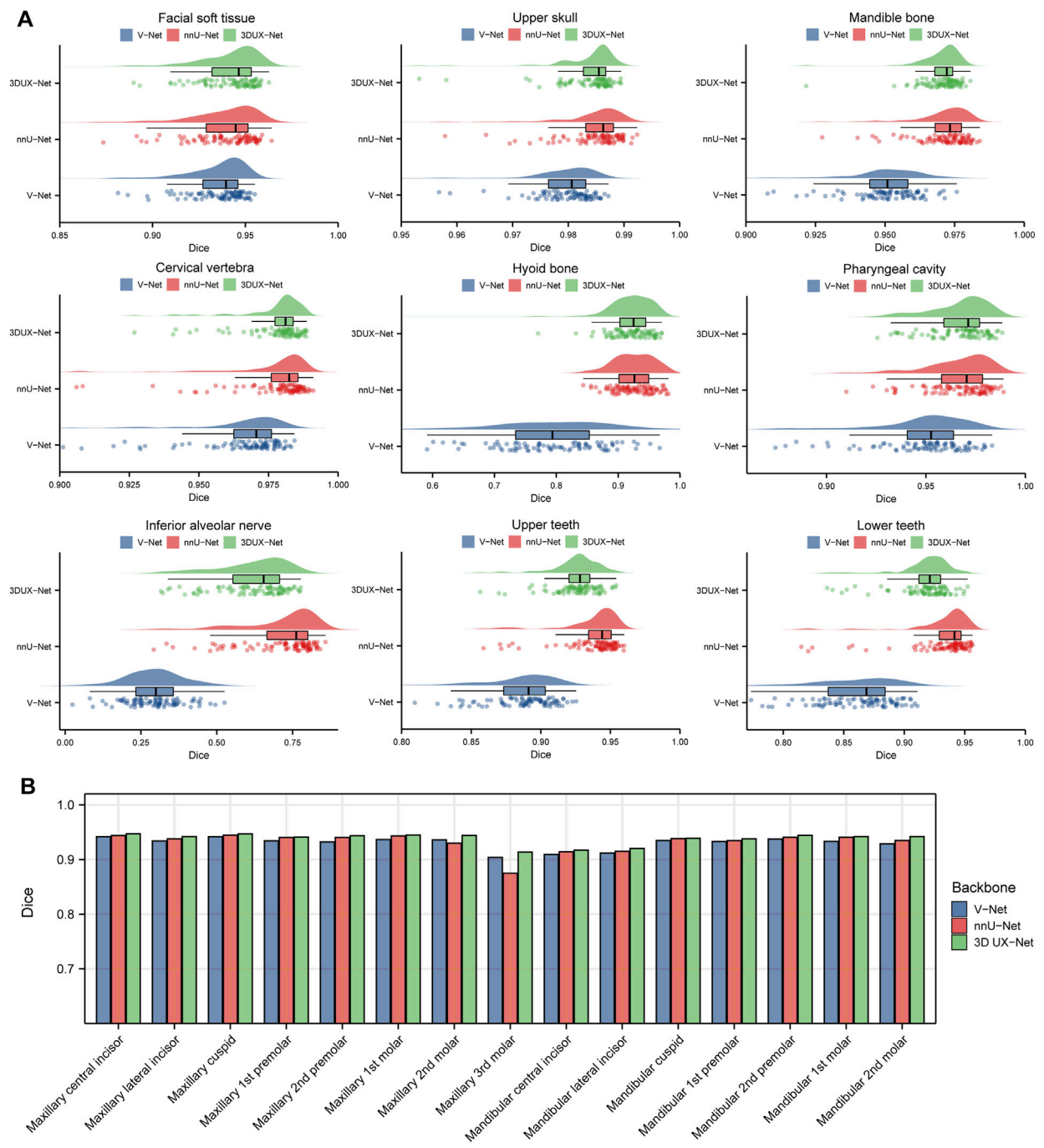

FIGURE 3
Quantitative analysis results for segmentation performance. **(A)** Dice scores for segmentation performance of CMF structures using V-Net, nnU-Net, and 3D UX-Net. **(B)** Dice scores for segmentation performance of individual teeth using cascaded segmentation networks based on V-Net, nnU-Net, and 3D UX-Net.

in Figures 6, 7. It showed consistently high segmentation accuracy in the segmentation and classification of individual teeth, where CMF-ELSeg achieved Dice exceeding 0.94 for most teeth segmentation tasks, with slightly lower Dice scores observed for Maxillary 3rd molar (0.9282 ± 0.0515), Mandibular central incisor (0.9180 ± 0.0425), Mandibular lateral incisor (0.9204 ± 0.0577), Mandibular 1st premolar (0.9397 ± 0.0332), and Mandibular 2nd molar (0.9307 ± 0.1053) (Supplementary Tables S4, S5).

3.3 Clinical feasibility evaluation of CMF-ELSeg

Cohort 2 included 30 patients with skeletal malocclusion. The example of segmentation and the results of the qualitative evaluation of CMF-ELSeg are shown in Figures 8A,B. Among 30 cases, 90% were ranked "Grade A" or "Grade B," indicating that these results could be directly used for VSP without the need for manual revision.

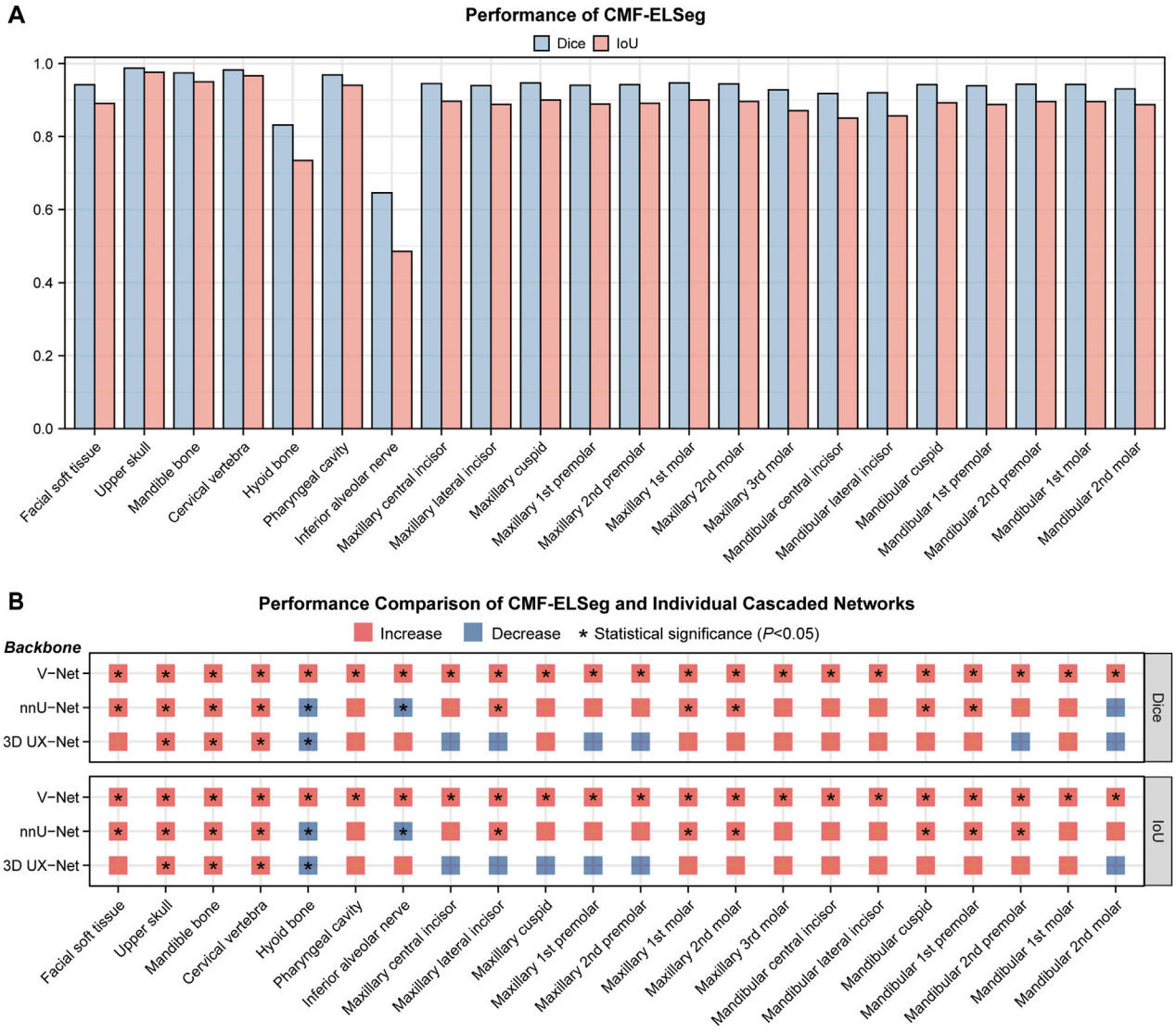

FIGURE 4
Segmentation performance of CMF-ELSeg. **(A)** Quantitative analysis results for segmentation performance of CMF structures and individual teeth. **(B)** Comparison of segmentation performance between CMF-ELSeg and the baseline models. *$P < 0.05$.

Only 10% of the cases were rated as "Grade C," with no segmentation results rated as "Grade D." The quantitative analysis results showed that, except for the segmentation of the hyoid bone (0.943 ± 0.148) and inferior alveolar nerve (0.882 ± 0.153), the average Dice scores for the other structures exceeded 0.975 (Supplementary Table S6; Figure 8C). The revision times were recorded in Supplementary Table S6 and Figure 8C, where the overall revision time was 15.119 ± 10.155 min. Cohort 3 consisted of 23 patients with various craniofacial disorders, including 10 cases of maxillofacial fractures, eight cases of fibrous dysplasia, and five cases of complex craniofacial conditions (cleidocranial dysplasia, secondary deformities from cleft lip and palate) (Figure 8D). CMF-ELSeg demonstrated strong performance in the segmentation and reconstruction of maxillofacial fractures and fibrous dysplasia, with the evaluation of Grade B and above reaching 100% for facial fractures and 87.5% for fibrous dysplasia (Figure 8E). However, the model's performance significantly decreased when applied to complex craniofacial conditions, with 40% of cases rated as C and D (Figure 8E). The automatic segmentation results are shown in Figure 8F.

4 Discussion

Segmentation and reconstruction of CMF structures and individual teeth are essential steps for orthodontics and orthognathic treatment planning. Developing and validating fully automatic segmentation algorithms and selecting the optimal model are of great significance (Zhang R. et al., 2023; Chen et al., 2024). In this study, we designed a novel coarse-to-fine cascaded segmentation network and employed a combination forecasting method to enhance the accuracy of individual teeth segmentation. By comparing three network backbones and utilizing ensemble learning, CMF-ELSeg achieved a 3%–5%

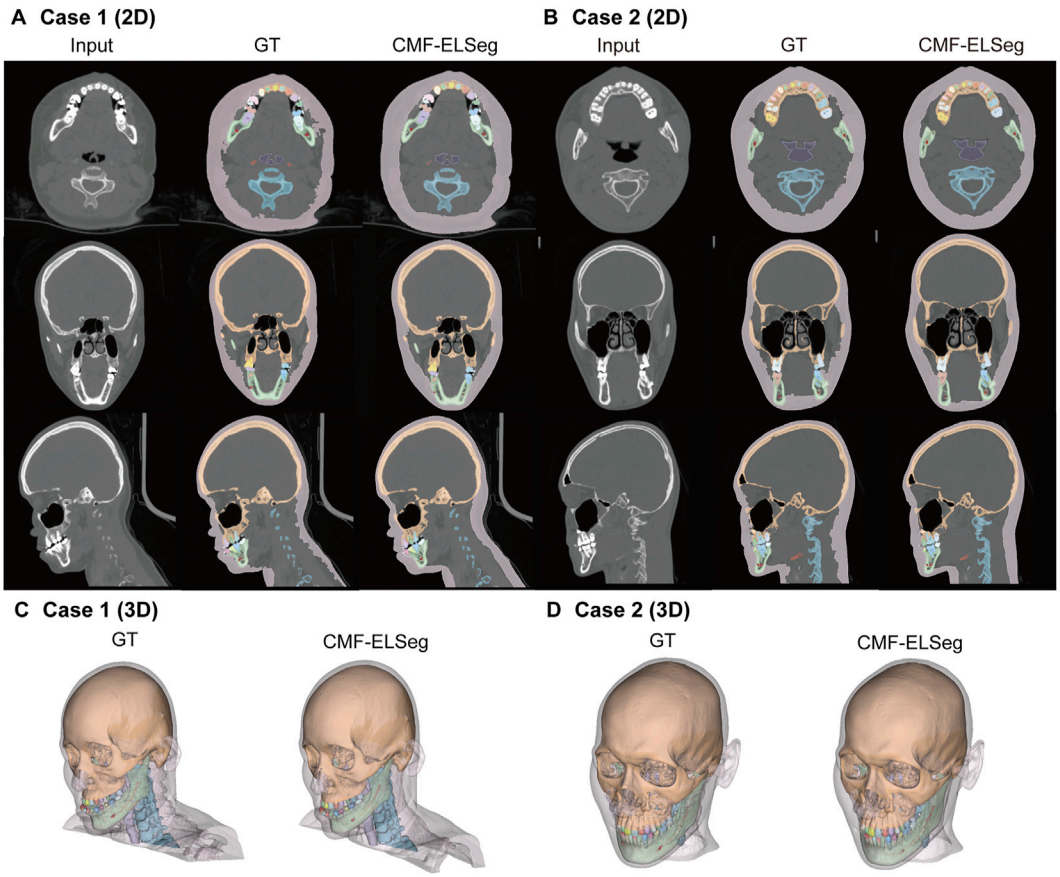

FIGURE 5
Segmentation and 3D reconstruction results of CMF structures and individual teeth using CMF-ELSeg. **(A,B)** Segmentation results illustrated for two representative cases. **(C,D)** 3D reconstruction results illustrated for two representative cases. Case 1: a skeletal class III malocclusion patient with orthodontic brackets. Case 2: a patient who has undergone orthognathic surgery.

improvement in segmentation performance for CMF structures and individual teeth compared to individual models.

To our knowledge, this is the first study to simultaneously segment multiple CMF structures and individual teeth (Cui et al., 2022; Xiang et al., 2024). First, we evaluated the segmentation performance of the three models on nine CMF structures, which are commonly involved in surgical planning. We selected V-Net, nnU-Net, and 3D UX-Net for their complementary strengths in handling complex CMF segmentation needs. Specifically, V-Net's residual convolutional architecture allows for enhanced feature extraction in volumetric data, while nnU-Net's self-configuring capabilities make it particularly effective across variable anatomical regions. Meanwhile, 3D UX-Net's transformer-based architecture captures both global and local features, contributing to high-precision segmentation of individual teeth and other small structures. The ensemble approach leverages these unique strengths, optimizing the performance of CMF-ELSeg in the context of intricate CMF anatomy. The use of Dice and IoU scores across CMF and dental structures provides a robust, multifaceted evaluation of CMF-ELSeg's segmentation performance. However, the segmentation of the inferior alveolar nerve yielded lower Dice scores, due to its small size and complex trajectory (Ntovas et al., 2024). nnU-Net significantly outperformed the other two models in segmenting elongated anatomical structures, including inferior alveolar nerves and the hyoid bone, making it the preferred choice for its user-friendly features (Isensee et al., 2021). Our findings are consistent with those from Dot et al., who employed the nnU-Net to segment CMF structures from CT scans and demonstrated its reliable performance in accomplishing fully automated segmentation for skeletal malocclusion patients before orthognathic surgery (Dot et al., 2022).

Specifically, due to the lack of semantic detail in direct cross-scale training and the challenge of recognizing segmentation tasks at varying granularities, we constructed a coarse-to-fine cascaded framework for individual tooth segmentation and identification (ID) classification. Among the three backbones, the 3D UX-Net-based model demonstrated the best tooth segmentation capability. By extracting the ROI during the coarse segmentation stage, the model could capture relevant spatial features and attenuate background noise (Jing et al., 2018; Lee et al., 2022). Meanwhile, the feature combination approach effectively addressed the issue of misidentification caused by tooth contact. As our training data were obtained from the VSP stage either before orthognathic surgery or 6 months post-surgery, premolars were often absent. Our experimental results also demonstrated the robust performance of the proposed model when dealing with samples that had missing

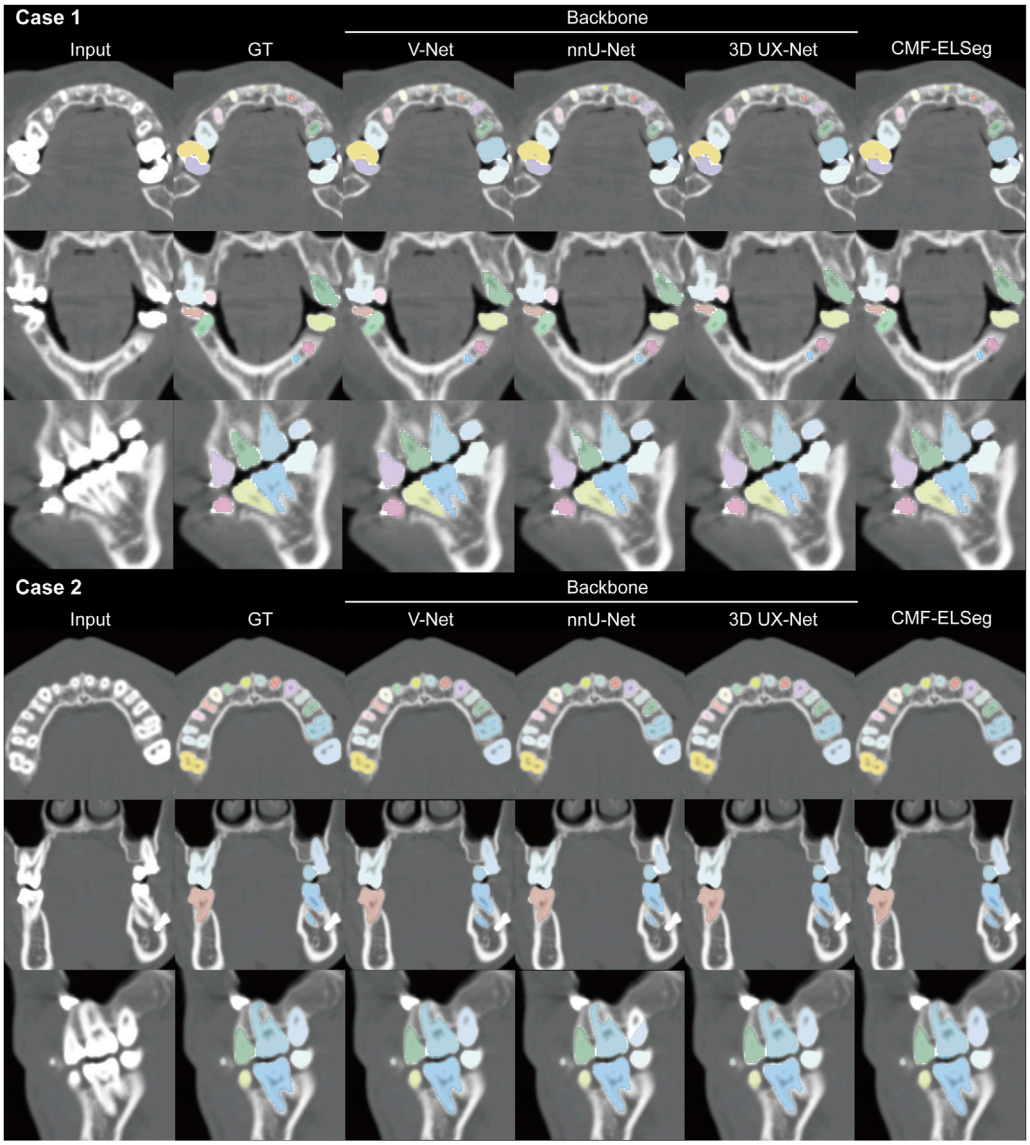

FIGURE 6
Segmentation results of individual teeth using CMF-ELSeg and individual cascaded segmentation network. Case 1: a skeletal class III malocclusion patient with orthodontic brackets. Case 2: a patient who has undergone orthognathic surgery.

teeth or significant anatomical and positional variations in wisdom teeth (Zhou et al., 2024). By integrating the multiple CMF structures and individual teeth, the reconstructed 3D models can meet the needs of orthognathic surgery and orthodontic treatment planning.

Another key contribution of our study is the introduction of ensemble learning to CMF surgery, a paradigm in machine learning that enhances methodological performance. Recently, several new segmentation algorithms based on the U-Net architecture have been developed. We selected three U-shaped models as backbones. V-Net extends U-Net from 2D to 3D, enhancing local feature extraction through its residual architecture in each convolutional stage (Milletari et al., 2016). Chen et al. proposed a multi-task method based on the V-Net that can segment different kinds of teeth and deal with non-open bite regions and metal artifacts from CBCT (Chen et al., 2020). nnU-Net integrates multiple U-Net methods such as 2D U-Net and 3D U-Net (Isensee et al., 2021). As a publicly available and user-friendly tool, it can automatically configure itself and adapt to any new dataset without manual intervention. The Vision Transformer (ViT) excels in medical imaging tasks, with some researchers combining it with U-Net to enhance segmentation performance (Berroukham et al., 2023). Jin et al. proposed a novel Swin Transformer–U-Net model to segment and classify nasal and pharyngeal airway subregions (Jin et al., 2023). Compared to CNNs, which focus solely on local image structures, ViT captures global features by analyzing connections between localized regions but has limitations in feature localization. Therefore, some hybrid frameworks combine the complementary strengths of ViT and CNNs. 3D UX-Net, developed by Lee et al., is a U-shaped network combining convolution with Swin Transformer for volumetric segmentation, effectively reducing parameters through its lightweight volumetric ConvNet (Lee et al., 2023). While it has demonstrated state-of-the-art performance in various datasets, its

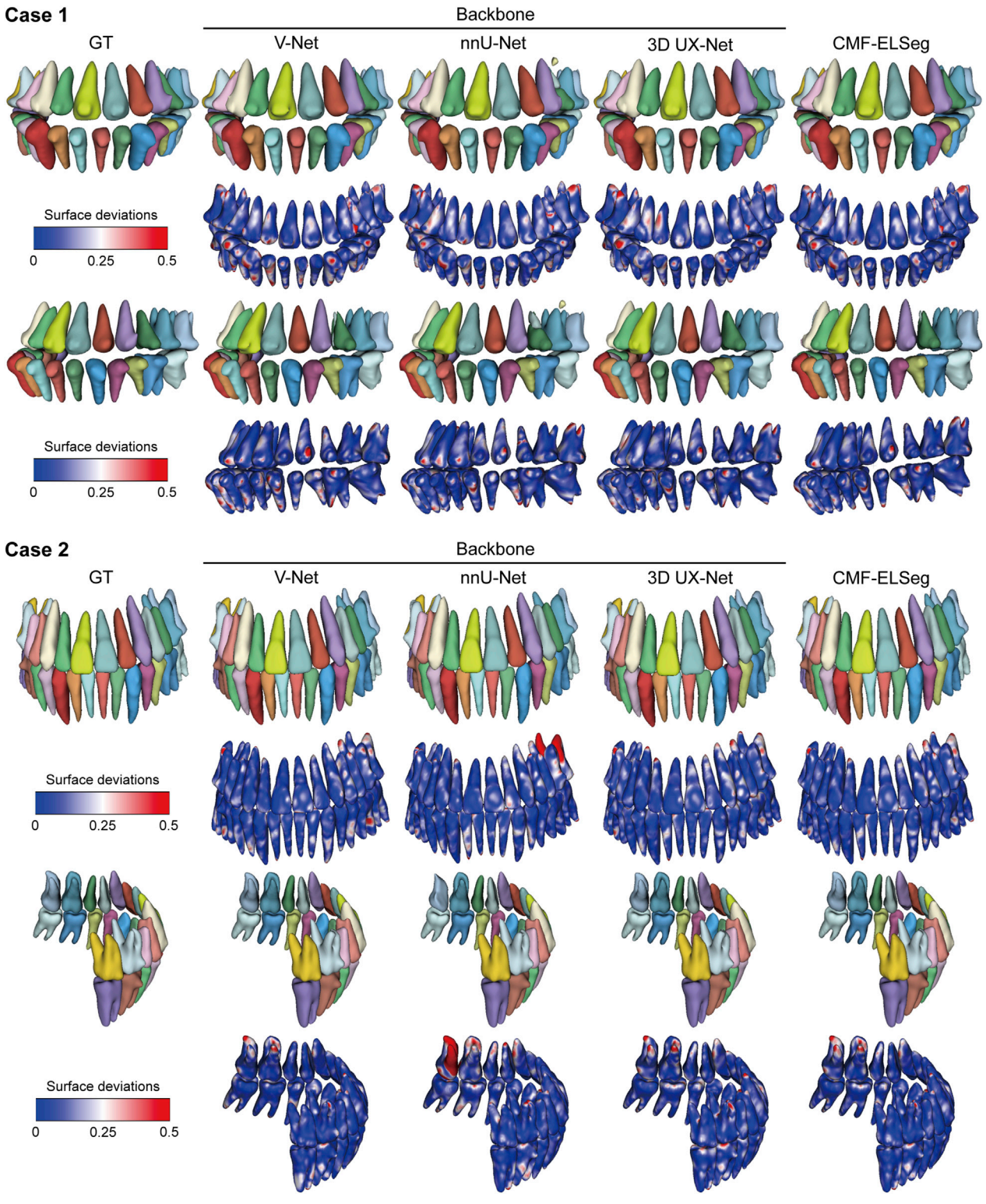

FIGURE 7
3D reconstruction results and surface deviations of individual teeth using CMF-ELSeg and individual cascaded segmentation network. Case 1: a skeletal class III malocclusion patient with orthodontic brackets. Case 2: a patient who has undergone orthognathic surgery.

application in CMF structure and tooth segmentation remains unexplored. Here, the proposed ensemble model (CMF-ELSeg) combines multiple cascaded segmentation networks, leveraging their diversity to enhance overall performance (Wang et al., 2023; Roshan et al., 2024). The AdaBoost method effectively reduces bias and variance, improving generalization and accuracy. Experimental results show that CMF-ELSeg significantly outperformed individual cascaded segmentation models. Additionally, our model's

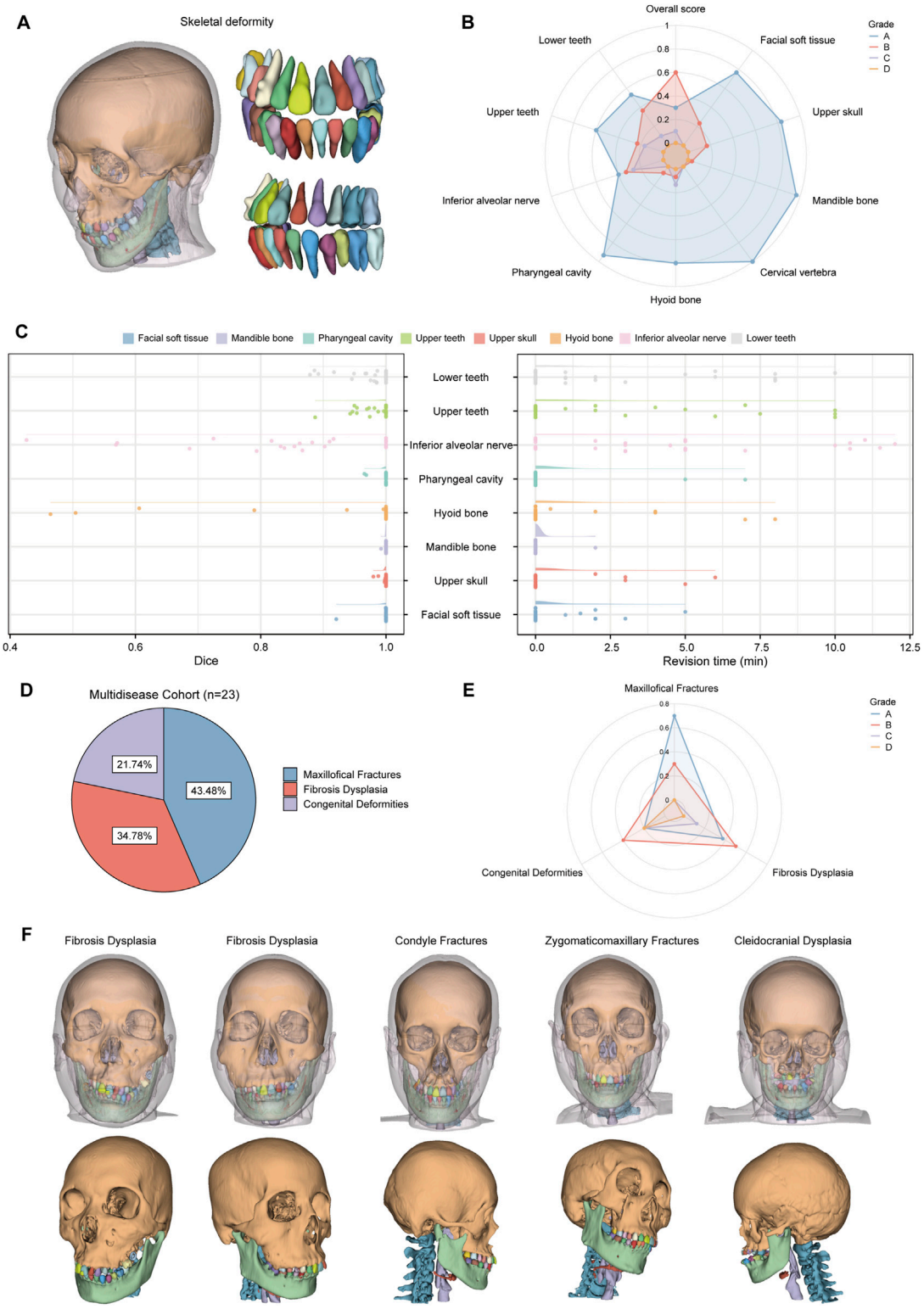

FIGURE 8
Clinical feasibility evaluation of CMF-ELSeg. **(A)** An example of the segmentation and reconstruction results using CMF-ELSeg for patients with skeletal malocclusion. **(B)** The qualitative analysis results of CMF-ELSeg in Cohort 2. **(C)** Quantitative analysis results of CMF-ELSeg in Cohort 2. **(D)** The composition of patients in Cohort 3. **(E)** The qualitative analysis results of CMF-ELSeg in Cohort 3. **(F)** Segmentation and reconstruction cases of CMF-ELSeg in Cohort 3.

performance in tooth segmentation can be extended to various clinical scenarios, such as orthodontic treatment planning, management of periodontitis patients, and implant restoration design (Polizzi et al., 2023; Polizzi et al., 2024).

This study has several limitations that should be addressed in future work. First, model development and evaluation were conducted using a single-center dataset, necessitating validation through large-sample, multicenter studies. The CT scans were primarily from patients with CMF deformities requiring combined orthodontic and orthognathic treatment. To enhance the model's applicability and robustness, future research will include a broader patient population, encompassing individuals with complex craniofacial conditions such as fractures, jaw defects, craniofacial syndromes, and cleft lip and palate. Second, our results indicated relatively lower segmentation accuracy for tubular and thin anatomical structures, such as the hyoid bone, inferior alveolar nerve, orbital walls and maxillary sinuses. Addressing these challenges might involve integrating higher-resolution sub-volume inputs specifically focused on these fine structures to enhance spatial resolution. Specialized segmentation architectures, potentially incorporating attention mechanisms or transformer-based modules optimized for thin and tubular structures, could further improve performance. Third, clinical validation revealed poor performance in complex craniofacial conditions like cleft lip and palate and congenital syndromes, where segmentation was compromised. Calcified lesions, such as those in fibrous dysplasia, impacted precision due to varying degrees of calcification. To address these issues, we plan to refine the model by developing specialized algorithms tailored to complex craniofacial conditions and calcified tissues. This will enhance the model's robustness and applicability across a broader range of clinical cases. In addition, while the cascaded architecture and ensemble inference of CMF-ELSeg significantly enhance segmentation accuracy and robustness, these strategies inherently increase computational complexity and inference time. Although our current inference speed remains clinically acceptable for routine preoperative surgical planning, real-time deployment or integration into interactive clinical workflows may necessitate further optimization. We have developed the VSP-AI platform and integrated our segmentation algorithm into it (Supplementary Figure S7). This platform streamlines the VSP design process, optimizing workflow and improving efficiency. In the future, we plan to conduct clinical validation studies to evaluate the model's accuracy and efficiency in real-world trials, providing valuable insights into its practical applicability.

5 Conclusion

In conclusion, our study introduced CMF-ELSeg, a fully multi-structure segmentation model designed to simultaneously segment multiple CMF structures and individual teeth for orthognathic surgical planning. Built on a coarse-to-fine cascaded segmentation network architecture, CMF-ELSeg leverages an ensemble learning approach that combines the strengths of V-Net, nnU-Net, and 3D UX-Net. This multi-model approach led to a 3%–5% improvement in Dice coefficients for segmentation of facial soft tissue, upper skull, mandible bone, cervical vertebra, and pharyngeal cavity compared to individual models. Additionally, CMF-ELSeg consistently achieved high accuracy for individual teeth segmentation, with Dice coefficients exceeding 0.94 for most teeth. These results underscore CMF-ELSeg's high precision and its potential as a practical tool for clinical practice, significantly enhancing the efficacy of patient-specific treatment planning for CMF surgery.

Data availability statement

The raw data supporting the conclusions of this article will be made available by the authors, without undue reservation.

Ethics statement

The studies involving humans were approved by the ethics committee of Shanghai Ninth People's Hospital, Shanghai Jiao Tong University School of Medicine (IRB No. SH9H-2022-TK12-1). The studies were conducted in accordance with the local legislation and institutional requirements. Written informed consent for participation was not required from the participants or the participants' legal guardians/next of kin in accordance with the national legislation and institutional requirements.

Author contributions

JB: Conceptualization, Data curation, Formal Analysis, Investigation, Validation, Writing – original draft. ZT: Data curation, Methodology, Software, Validation, Writing – review and editing. YS: Data curation, Methodology, Software, Validation, Writing – review and editing. XX: Data curation, Methodology, Software, Validation, Writing – review and editing. HL: Data curation, Visualization, Writing – review and editing. WC: Data curation, Visualization, Writing – review and editing. YY: Data curation, Visualization, Writing – review and editing. MC: Writing – review and editing, Data curation, Investigation, Validation. YW: Writing – review and editing, Data curation, Investigation, Validation. CK: Writing – review and editing, Investigation, Validation, Visualization. YH: Writing – review and editing, Investigation, Validation, Visualization. JZ: Writing – review and editing, Investigation, Validation, Visualization. LF: Writing – review and editing, Conceptualization, Funding acquisition, Resources, Supervision. DQ: Writing – review and editing, Conceptualization, Funding acquisition, Resources, Supervision. SS: Writing – review and editing, Conceptualization, Funding acquisition, Resources, Supervision. YW: Writing – review and editing, Conceptualization, Funding acquisition, Resources, Supervision. HY: Writing – review and editing, Conceptualization, Funding acquisition, Resources, Supervision.

Funding

The author(s) declare that financial support was received for the research and/or publication of this article. This work was supported by National Natural Science Foundation of China (81571022), Multicenter clinical research project of Shanghai Jiao Tong University School of Medicine (DLY201808), and Shanghai Natural Science Foundation (23ZR1438100).

Conflict of interest

Author YY was employed by Shanghai Lanhui Medical Technology Co., Ltd.

The remaining authors declare that the research was conducted in the absence of any commercial or financial relationships that could be construed as a potential conflict of interest.

Generative AI statement

The author(s) declare that no Generative AI was used in the creation of this manuscript.

Publisher's note

Supplementary material

The Supplementary Material for this article can be found online at: https://www.frontiersin.org/articles/10.3389/fbioe.2025.1580502/full#supplementary-material

References

Alkhayer, A., Piffkó, J., Lippold, C., and Segatto, E. (2020). Accuracy of virtual planning in orthognathic surgery: a systematic review. *Head and Face Med.* 16, 34. doi:10.1186/s13005-020-00250-2

Bao, J., Zhang, X., Xiang, S., Liu, H., Cheng, M., Yang, Y., et al. (2024). Deep learning-based facial and skeletal transformations for surgical planning. *J. Dent. Res.* 103, 809–819. doi:10.1177/00220345241253186

Berroukham, A., Housni, K., and Lahraichi, M. (2023). "Vision transformers: a review of architecture, applications, and future directions," in *2023 7th IEEE congress on information science and Technology (CiSt)*, 205–210. doi:10.1109/CiSt56084.2023.10410015

Chen, X., Liu, Q., Deng, H. H., Kuang, T., Lin, H. H.-Y., Xiao, D., et al. (2024). Improving image segmentation with contextual and structural similarity. *Pattern Recognit.* 152, 110489. doi:10.1016/j.patcog.2024.110489

Chen, X., Wang, X., Zhang, K., Fung, K.-M., Thai, T. C., Moore, K., et al. (2022). Recent advances and clinical applications of deep learning in medical image analysis. *Med. Image Anal.* 79, 102444. doi:10.1016/j.media.2022.102444

Chen, Y., Du, H., Yun, Z., Yang, S., Dai, Z., Zhong, L., et al. (2020). Automatic segmentation of individual tooth in dental CBCT images from tooth surface map by a multi-task FCN. *IEEE Access* 8, 97296–97309. doi:10.1109/ACCESS.2020.2991799

Cui, Z., Fang, Y., Mei, L., Zhang, B., Yu, B., Liu, J., et al. (2022). A fully automatic AI system for tooth and alveolar bone segmentation from cone-beam CT images. *Nat. Commun.* 13, 2096. doi:10.1038/s41467-022-29637-2

Deng, H. H., Liu, Q., Chen, A., Kuang, T., Yuan, P., Gateno, J., et al. (2023). Clinical feasibility of deep learning-based automatic head CBCT image segmentation and landmark detection in computer-aided surgical simulation for orthognathic surgery. *Int. J. Oral Maxillofac. Surg.* 52, 793–800. doi:10.1016/j.ijom.2022.10.010

Dot, G., Chaurasia, A., Dubois, G., Savoldelli, C., Haghighat, S., Azimian, S., et al. (2024). DentalSegmentator: robust open source deep learning-based CT and CBCT image segmentation. *J. Dent.* 147, 105130. doi:10.1016/j.jdent.2024.105130

Dot, G., Schouman, T., Dubois, G., Rouch, P., and Gajny, L. (2022). Fully automatic segmentation of craniomaxillofacial CT scans for computer-assisted orthognathic surgery planning using the nnU-Net framework. *Eur. Radiol.* 32, 3639–3648. doi:10.1007/s00330-021-08455-y

Freund, Y., and Schapire, R. E. (1997). A decision-theoretic generalization of on-line learning and an application to boosting. *J. Comput. Syst. Sci.* 55, 119–139. doi:10.1006/jcss.1997.1504

Graves, D. T., and Uribe, S. E. (2024). Advanced imaging in dental research: from gene mapping to AI global data. *J. Dent. Res.* 103, 1329–1330. doi:10.1177/00220345241293040

Huang, J., Bao, J., Tan, Z., Shen, S., and Yu, H. (2024). Development and validation of a collaborative robotic platform based on monocular vision for oral surgery: an *in vitro* study. *Int. J. Comput. Assist. Radiol. Surg.* 19, 1797–1808. doi:10.1007/s11548-024-03161-8

Isensee, F., Jaeger, P. F., Kohl, S. A. A., Petersen, J., and Maier-Hein, K. H. (2021). nnU-Net: a self-configuring method for deep learning-based biomedical image segmentation. *Nat. Methods* 18, 203–211. doi:10.1038/s41592-020-01008-z

Jiang, F., Jiang, Y., Zhi, H., Dong, Y., Li, H., Ma, S., et al. (2017). Artificial intelligence in healthcare: past, present and future. *Stroke Vasc. Neurol.* 2, 230–243. doi:10.1136/svn-2017-000101

Jin, S., Han, H., Huang, Z., Xiang, Y., Du, M., Hua, F., et al. (2023). Automatic three-dimensional nasal and pharyngeal airway subregions identification via vision transformer. *J. Dent.* 136, 104595. doi:10.1016/j.jdent.2023.104595

Jing, L., Chen, Y., and Tian, Y. (2018). Coarse-to-fine semantic segmentation from image-level labels. doi:10.48550/arXiv.1812.10885

Lee, H. H., Bao, S., Huo, Y., and Landman, B. A. (2023). 3D UX-net: a large Kernel volumetric ConvNet modernizing hierarchical transformer for medical image segmentation. doi:10.48550/arXiv.2209.15076

Lee, J., Ilyas, T., Jin, H., Lee, J., Won, O., Kim, H., et al. (2022). A pixel-level coarse-to-fine image segmentation labelling algorithm. *Sci. Rep.* 12, 8672. doi:10.1038/s41598-022-12532-7

Liu, J., Hao, J., Lin, H., Pan, W., Yang, J., Feng, Y., et al. (2023). Deep learning-enabled 3D multimodal fusion of cone-beam CT and intraoral mesh scans for clinically applicable tooth-bone reconstruction. *Patterns (N Y)* 4, 100825. doi:10.1016/j.patter.2023.100825

Liu, Q., Deng, H., Lian, C., Chen, X., Xiao, D., Ma, L., et al. (2021). SkullEngine: a multi-stage CNN framework for collaborative CBCT image segmentation and landmark detection. *Mach. Learn Med. Imaging* 12966, 606–614. doi:10.1007/978-3-030-87589-3_62

Liu, Y., Xie, R., Wang, L., Liu, H., Liu, C., Zhao, Y., et al. (2024). Fully automatic AI segmentation of oral surgery-related tissues based on cone beam computed tomography images. *Int. J. Oral Sci.* 16, 34. doi:10.1038/s41368-024-00294-z

Milletari, F., Navab, N., and Ahmadi, S.-A. (2016). V-net: fully convolutional neural networks for volumetric medical image segmentation. 565–571. doi:10.1109/3dv.2016.79

Naran, S., Steinbacher, D. M., and Taylor, J. A. (2018). Current concepts in orthognathic surgery. *Plast. Reconstr. Surg.* 141, 925e–936e. doi:10.1097/PRS.0000000000004438

Nogueira-Reis, F., Morgan, N., Nomidis, S., Van Gerven, A., Oliveira-Santos, N., Jacobs, R., et al. (2023). Three-dimensional maxillary virtual patient creation by convolutional neural network-based segmentation on cone-beam computed tomography images. *Clin. Oral Investig.* 27, 1133–1141. doi:10.1007/s00784-022-04708-2

Nordblom, N. F., Büttner, M., and Schwendicke, F. (2024). Artificial intelligence in orthodontics: critical review. *J. Dent. Res.* 103, 577–584. doi:10.1177/00220345241235606

Ntovas, P., Marchand, L., Finkelman, M., Revilla-León, M., and Att, W. (2024). Accuracy of artificial intelligence-based segmentation of the mandibular canal in CBCT. *Clin. Oral Implants Res.* 35, 1163–1171. doi:10.1111/clr.14307

On, S.-W., Cho, S.-W., Park, S.-Y., Yi, S.-M., Park, I.-Y., Byun, S.-H., et al. (2024). Advancements in computer-assisted orthognathic surgery: a comprehensive review and clinical application in South Korea. *J. Dent.* 146, 105061. doi:10.1016/j.jdent.2024.105061

Polizzi, A., Quinzi, V., Lo Giudice, A., Marzo, G., Leonardi, R., and Isola, G. (2024). Accuracy of artificial intelligence models in the prediction of periodontitis: a systematic review. *JDR Clin. Trans. Res.* 9, 312–324. doi:10.1177/23800844241232318

Polizzi, A., Quinzi, V., Ronsivalle, V., Venezia, P., Santonocito, S., Lo Giudice, A., et al. (2023). Tooth automatic segmentation from CBCT images: a systematic review. *Clin. Oral Invest.* 27, 3363–3378. doi:10.1007/s00784-023-05048-5

Priya, J., Raja, S. K. S., and Kiruthika, S. U. (2024). State-of-art technologies, challenges, and emerging trends of computer vision in dental images. *Comput. Biol. Med.* 178, 108800. doi:10.1016/j.compbiomed.2024.108800

Ronneberger, O., Fischer, P., and Brox, T. (2015). "U-net: convolutional networks for biomedical image segmentation," in *Medical image computing and computer-assisted intervention – MICCAI 2015*. Editors N. Navab, J. Hornegger, W. M. Wells, and

A. F. Frangi (Cham: Springer International Publishing), 234–241. doi:10.1007/978-3-319-24574-4_28

Roshan, S., Tanha, J., Zarrin, M., Babaei, A. F., Nikkhah, H., and Jafari, Z. (2024). A deep ensemble medical image segmentation with novel sampling method and loss function. *Comput. Biol. Med.* 172, 108305. doi:10.1016/j.compbiomed.2024.108305

Schapire, R. E. (2013). "Explaining AdaBoost," in *Empirical inference: festschrift in honor of Vladimir N. Vapnik*. Editors B. Schölkopf, Z. Luo, and V. Vovk (Berlin, Heidelberg: Springer), 37–52. doi:10.1007/978-3-642-41136-6_5

Schneider, L., Arsiwala-Scheppach, L., Krois, J., Meyer-Lueckel, H., Bressem, K. K., Niehues, S. M., et al. (2022). Benchmarking deep learning models for tooth structure segmentation. *J. Dent. Res.* 101, 1343–1349. doi:10.1177/00220345221100169

Schwendicke, F., Singh, T., Lee, J.-H., Gaudin, R., Chaurasia, A., Wiegand, T., et al. (2021). Artificial intelligence in dental research: checklist for authors, reviewers, readers. *J. Dent.* 107, 103610. doi:10.1016/j.jdent.2021.103610

Setzer, F. C., Li, J., and Khan, A. A. (2024). The use of artificial intelligence in endodontics. *J. Dent. Res.* 103, 853–862. doi:10.1177/00220345241255593

Wallner, J., Schwaiger, M., Hochegger, K., Gsaxner, C., Zemann, W., and Egger, J. (2019). A review on multiplatform evaluations of semi-automatic open-source based image segmentation for cranio-maxillofacial surgery. *Comput. Methods Programs Biomed.* 182, 105102. doi:10.1016/j.cmpb.2019.105102

Wang, C., Cui, Z., Yang, J., Han, M., Carneiro, G., and Shen, D. (2023). BowelNet: joint semantic-geometric ensemble learning for bowel segmentation from both partially and fully labeled CT images. *IEEE Trans. Med. Imaging* 42, 1225–1236. doi:10.1109/TMI.2022.3225667

Wang, Z., Liu, J., Li, H., Zhang, Q., Li, X., Huang, Y., et al. (2024). "Using hip assisted running exoskeleton with impact isolation mechanism to improve energy efficiency," in *2024 IEEE/RSJ international conference on intelligent robots and systems (IROS)*, 214–220. doi:10.1109/IROS58592.2024.10802632

Xia, J. J., Gateno, J., and Teichgraeber, J. F. (2009). New clinical protocol to evaluate craniomaxillofacial deformity and plan surgical correction. *J. Oral Maxillofac. Surg.* 67, 2093–2106. doi:10.1016/j.joms.2009.04.057

Xiang, B., Lu, J., and Yu, J. (2024). Evaluating tooth segmentation accuracy and time efficiency in CBCT images using artificial intelligence: a systematic review and Meta-analysis. *J. Dent.* 146, 105064. doi:10.1016/j.jdent.2024.105064

Zhang, J., Liu, M., Wang, L., Chen, S., Yuan, P., Li, J., et al. (2020). Context-guided fully convolutional networks for joint craniomaxillofacial bone segmentation and landmark digitization. *Med. Image Anal.* 60, 101621. doi:10.1016/j.media.2019.101621

Zhang, L., Li, W., Lv, J., Xu, J., Zhou, H., Li, G., et al. (2023a). Advancements in oral and maxillofacial surgery medical images segmentation techniques: an overview. *J. Dent.* 138, 104727. doi:10.1016/j.jdent.2023.104727

Zhang, R., Jie, B., He, Y., Zhu, L., Xie, Z., Liu, Z., et al. (2023b). Craniomaxillofacial bone segmentation and landmark detection using semantic segmentation networks and an unbiased heatmap. *IEEE J. Biomed. Health Inf.* PP, 427–437. doi:10.1109/JBHI.2023.3337546

Zhou, Z., Chen, Y., He, A., Que, X., Wang, K., Yao, R., et al. (2024). NKUT: dataset and benchmark for pediatric mandibular wisdom teeth segmentation. *IEEE J. Biomed. Health Inf.* 28, 3523–3533. doi:10.1109/JBHI.2024.3383222

frontiers | Frontiers in Bioengineering and Biotechnology

TYPE Original Research
PUBLISHED 13 May 2025
DOI 10.3389/fbioe.2025.1577321

OPEN ACCESS

EDITED BY
Dan Lin,
Shanghai University of Medicine and Health Sciences, China

REVIEWED BY
Uriel Zapata,
EAFIT University, Colombia
Xin Ma,
Beihang University, China
Paweł Turek,
Rzeszów University of Technology, Poland

*CORRESPONDENCE
Xiaoyan Gao,
yanluo_214@hotmail.com
Xiaofeng Xu,
xuxiaofeng110@163.com
Shilei Zhang,
leinnymd@hotmail.com

†These authors have contributed equally to this work and share first authorship

RECEIVED 15 February 2025
ACCEPTED 23 April 2025
PUBLISHED 13 May 2025

CITATION
Wu J, Jiang L, Cheng Y, Zhang W, Zhang J, Gao X, Xu X and Zhang S (2025) Patient-specific dynamic reference frame for navigation-assisted surgery in mandible: a novel noninvasive technical method.
Front. Bioeng. Biotechnol. 13:1577321.
doi: 10.3389/fbioe.2025.1577321

Patient-specific dynamic reference frame for navigation-assisted surgery in mandible: a novel noninvasive technical method

Jinyang Wu[1†], Lai Jiang[1†], Yingqi Cheng[1†], Wenbin Zhang[1], Jianfei Zhang[1], Xiaoyan Gao[2*], Xiaofeng Xu[1*] and Shilei Zhang[1*]

[1]Department of Oral and Cranio-maxillofacial Surgery, Shanghai Ninth People's Hospital, Shanghai Jiao Tong University School of Medicine, College of Stomatology, Shanghai Jiao Tong University, National Center for Stomatology, National Clinical Research Center for Oral Diseases, Shanghai Key Laboratory of Stomatology, Shanghai, China, [2]International Medical Department, Shanghai Ninth People's Hospital, Shanghai Jiao Tong University School of Medicine, College of Stomatology, Shanghai Jiao Tong University, National Center for Stomatology, National Clinical Research Center for Oral Diseases, Shanghai Key Laboratory of Stomatology, Shanghai, China

Objectives: Computer-assisted navigation has been established as a valuable tool in oral and craniomaxillofacial surgery. However, the steep learning curve associated with mandibular navigation surgery has hindered its widespread adoption. This study introduces a non-invasive, convenient, and accurate navigation method for mandibular surgery and evaluates its clinical effectiveness.

Methods: A modified patient-specific dynamic reference frame (PS-DRF) was designed and fabricated based on the patient's lower jaw dental cast, integrating navigation technology with 3D printing. During surgery, the PS-DRF was securely affixed to the lower dentition, enabling automatic pair-point registration through fiducial localization via a navigation probe. The surgical procedure was conducted under real-time navigation guidance.

Results: Preoperative registration and intraoperative navigation were successfully achieved in this case. The navigation-guided mandibular surgery was completed without complications. Postoperative superimposition of the simulated virtual model and the actual surgical outcome demonstrated high accuracy, with a deviation of less than 2 mm.

Conclusion: The PS-DRF system offers a convenient, effective, and adaptable approach by integrating navigation technology with 3D printing. This method has the potential to simplify navigation-assisted mandibular surgery and facilitate the broader clinical implementation of computer-assisted navigation in maxillofacial procedures.

KEYWORDS

computer-assisted navigation, 3D printing, dynamic reference frame, patient specific, mandible

1 Introduction

Computer-assisted navigation (CAN) is an integrated method that combines computer vision, medical image processing, and real-time localization (Lin et al., 2023). It has been widely applied in oral and maxillofacial surgery, including in areas such as fractures reduction (Pierrefeu et al., 2015), orthognathic surgery (Badiali et al., 2015; Lin et al., 2015), resection and reconstruction of maxillofacial tumors (Palla and Callahan, 2021; Wilkat et al., 2021), and foreign body removal (Gröbe et al., 2009; Gui et al., 2013). The application of CAN in oral and maxillofacial surgery typically includes the following steps. First, preoperative 3D modeling. MRI, CT, and other medical imaging data are used to reconstruct a three-dimensional virtual model, creating a digital anatomical model of the patient, which serves as the key data foundation for the surgical navigation system. Second, preoperative virtual surgical planning and simulation. Using the 3D model, the anatomical features of the surgical area and their relationships with surrounding critical structures are analyzed, establishing a surgical approach and formulating a surgical plan for intraoperative guidance. Third, intraoperative registration and localization. The anatomical data of the patient are aligned with the actual surgical site using a system-compatible spatial locator and probe. Fourth, intraoperative real-time tracking. Using preoperative medical images, spatial localization technologies such as optical or electromagnetic systems (Berger et al., 2015; Brouwer de Koning et al., 2021) are used to measure the spatial position and orientation of the tissues and surgical instruments in the surgical area. This data is then accurately displayed in the surgical navigation system, assisting the surgeon in following the preoperative surgical plan. Compared to traditional surgical methods, navigation systems significantly enhance the visibility of surgical operations and allow for comparison with preoperative planning, helping surgeons adjust their approach to ensure high surgical precision. In confined operative spaces, the system helps avoid damage to critical anatomical structures, making the operation more minimally invasive and safer (Alkhayatt et al., 2024).

Despite the significant advantages of navigation technology in oral and maxillofacial surgery, certain limitations still exist. On one hand, the precision of navigation-assisted surgery is largely dependent on registration accuracy. The selection of registration points primarily involves the localization of titanium screws implanted in maxillofacial bone (Novelli et al., 2014), the placement of surface markers attached on facial skin (Schramm et al., 2009), or the use of anatomical landmarks (Mekuria et al., 2016). Implanting multiple titanium screws in the alveolar bone often results in additional pain for the patient. Surface markers tend to detach easily, which may compromise sterile procedures and increase the risk of unnecessary infections. Furthermore, both of these marker types require the patient to undergo a repeat CT scan to visualize the markers in the imaging data, exposing the patient to secondary radiation. The use of anatomical landmarks, such as dental cusp structures or facial soft tissues, is a commonly applied method. However, it still cannot achieve satisfactory accuracy and stability. Factors such as scanning resolution, the patient's individual anatomical characteristics, and the surgeon's subjective judgment and experience can all affect registration accuracy to varying degrees. On the other hand, maxillofacial surgeries typically involve intraoral or minimally invasive small incisions, which require frequent intraoperative adjustments to the patient's head position and orientation. To achieve synchronous spatial transformations, it is often necessary to make an additional incision in the skull to install a spatial reference frame (Collyer, 2010). This process is cumbersome, has a steep learning curve, increases surgical trauma, and extends operative time.

Furthermore, the mandible, as an independent moving structure in the craniomaxillofacial skeleton, poses challenges for synchronization between the navigation system and CT scans, due to the mobility of the temporomandibular joint (Casap et al., 2008; Bettschart et al., 2012). In multifaceted surgical procedures involving both the upper and lower jaw, such as arthroplasty or double-jaw osteotomy, the use of a navigation system requires intermaxillary fixation (Lübbers et al., 2011), which further limits the surgeon's field of view and operational flexibility in dynamic clinical settings.

Therefore, there is a significant need for advancements and new technologies to develop a navigation system that is better suited for oral and maxillofacial surgery. Ideally, such a system should enhance accessibility and facilitate clinical adoption by updating compatible hardware that is easy to obtain and implement, while avoiding major alterations to existing surgical workflows. This paper introduces a modified patient-specific dynamic reference frame (PS-DRF) designed to reduce the complexity of navigation-assisted surgical procedures involving the mandible, while improving the minimally invasive nature, stability, and precision of surgery.

2 Materials and methods

2.1 Materials

A 29-year-old female patient developed severe mandibular deviation within 1 year due to a right-sided condylar osteochondroma. The patient required a precise right condylectomy to achieve complete tumor removal, restore optimal occlusal alignment, and reconstruct a symmetrical lower third of the face. Optical navigation assisted by the PS-DRF was employed to facilitate the surgical procedure. The patient's authorized consent was signed. This study was approved by the institutional review board and the ethics committees of Shanghai Ninth People's Hospital, Shanghai Jiao Tong University School of Medicine (SH9H-2021-T66-3).

2.2 Methods

2.2.1 Preoperative design and fabrication of the PS-DRF

Following the patient's initial consultation, dental impressions and plaster models were fabricated in the outpatient clinic. The obtained dental casts of upper and lower jaws were scanned using the Activity 880 laser scanner (SmartOptics, Oslo, Norway), generating virtual dental models in STL format. Based on the dental model of lower jaw, a patient-specific occlusal splint was designed in software Geomagic Studio 2013 (Geomagic Inc.,

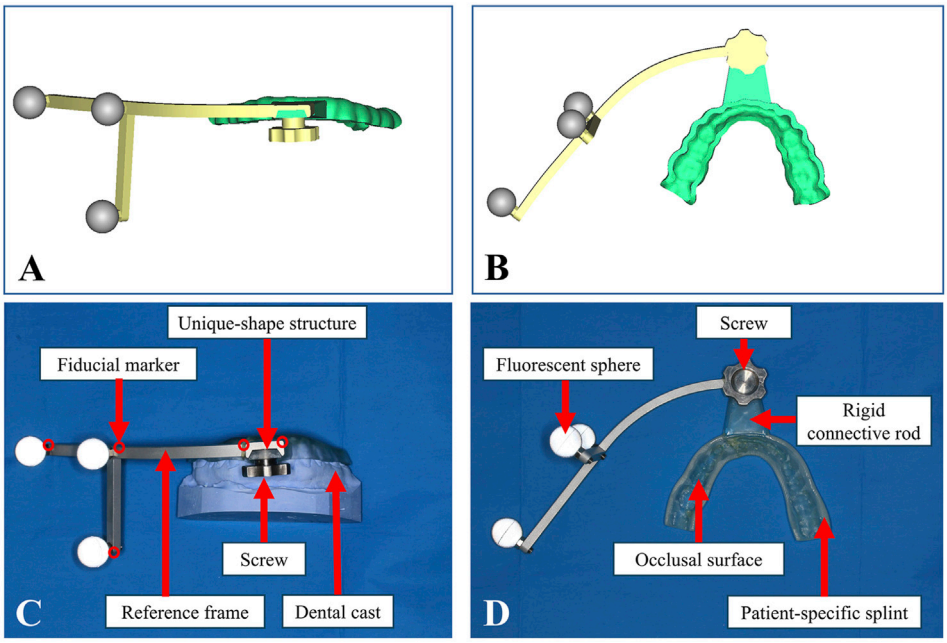

FIGURE 1
Design and fabrication of the PS-DRF. **(A)** Positive view of virtual PS-DRF. **(B)** Elevation view of virtual PS-DRF. **(C)** Positive view of real PS-DRF showed the structures. **(D)** Elevation view of real PS-DRF showed the structures.

Morrisville, NC, United States). The occlusal splint was equipped with a rigid connecting rod. Fiducial markers for registration were incorporated into the splint and rod or set into the reference frame. These markers, represented as 1 mm in diameter and 1 mm in depth conical indentations, enable precise collection of fiducial data during navigation. Due to their rigid structure and distinctive shape, these markers provide greater stability than other maxillofacial anatomical landmarks, such as skin or teeth. The end of the connecting rod contains a unique-shape structure that matches the attachment mechanism of the reference frame. The designed occlusal splint was then fabricated using 3D printing technology via an Objet260 Connex3 3D printer (Stratasys Ltd., MN, United States) whose printing accuracy was up to 200 microns and the MED620 resin material (Stratasys Ltd., MN, United States). A metal reference frame equipped with three infrared-reflective spheres was secured to the occlusal splint via the unique-shape connecting rod and screw at designated positions, as shown in Figure 1. In the virtual environment of Geomagic Studio 2013, the complete assembly of the structure was simulated and integrated with the dental model, followed by export and storage in STL format.

2.2.2 Virtual surgical planning (VSP)

Preoperative CT data was obtained by a 64-slice CT unit (LightSpeed VCT 64-slice Scanner, GE Inc., Fairfield, United States), with slices width and height 512*512 pxl, pixel size 0.488 mm and increment 0.625 mm. Then the CT data from the patient was processed for VSP by experienced surgeons from the Department of Oral and Cranio-Maxillofacial Surgery at Shanghai Ninth People's Hospital, Shanghai Jiao Tong University School of Medicine. Three-dimensional reconstruction was performed using software ProPlan CMF 3.0 (Materialise, Leuven, Belgium), with structure segmentation based on thresholding and anatomical features, followed by standardized noise reduction and artifact removal. The final STL model of the PS-DRF and dental casts, stored via Geomagic Studio 2013 during the design phase, was then imported into ProPlan CMF 3.0 to enhance the precision of the mandibular dental surface structure. The mandibular dentition reconstructed from CT data was replaced with the dental model of lower jaw via "Create Mandibular Composite Model" tool. The PS-DRF was subsequently registered to its intended position on the mandible via "Alignment tool". Finally, occlusal alignment complied with the occlusion which was obtained by matching the upper and lower dental casts and recorded by Activity 880 laser scanner. Simulated osteotomy was conducted to remove the tumor and achieve facial symmetry by means of keeping the height of remained ramus same as the health side. If the mandible was still asymmetric, genioplasty or gonioplasty should be simulated. Those ensured that the reconstructive outcome met the preoperative expectations. The detailed workflow is illustrated in Figure 2.

2.2.3 Surgical procedure assisted by optical navigation system

The segmented models from the VSP were exported in STL format and, along with the preoperative CT dataset, were imported into the AccuNavi-A optical navigation system (UEG MEDICAL, Shanghai, China).

After induction of general anesthesia in the operating room, the sterilized and disinfected dynamic reference frame (DRF) was securely fixed to the patient's mandibular dentition via the patient-specific splint, as illustrated in Figure 3. Therefore, PS-DRF was rigid with the mandible, even mandible was moveable, the navigation system could track the surgical targets in real-time. A

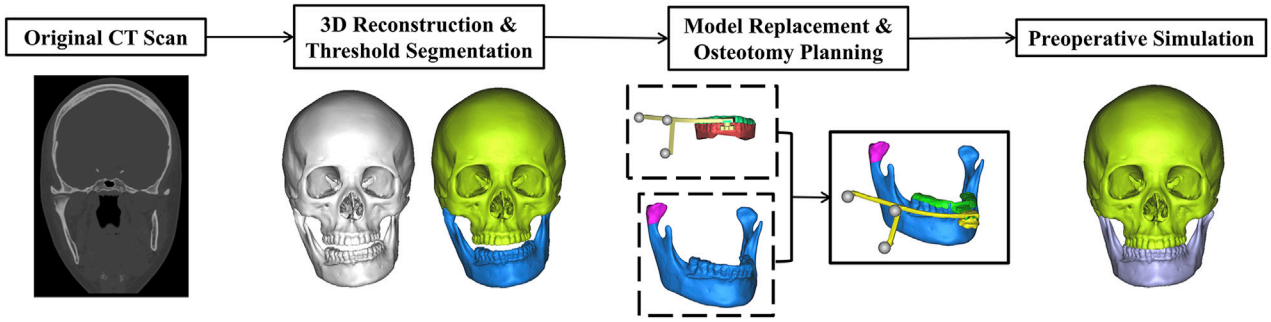

FIGURE 2
Workflow of virtual surgical planning.

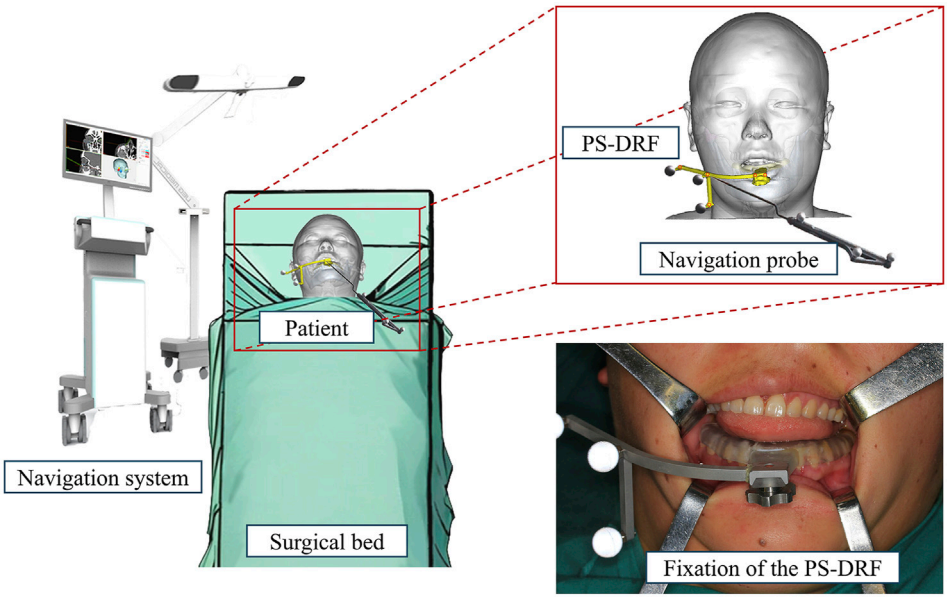

FIGURE 3
PS- DRF was fixed to the patient's mandibular dentition.

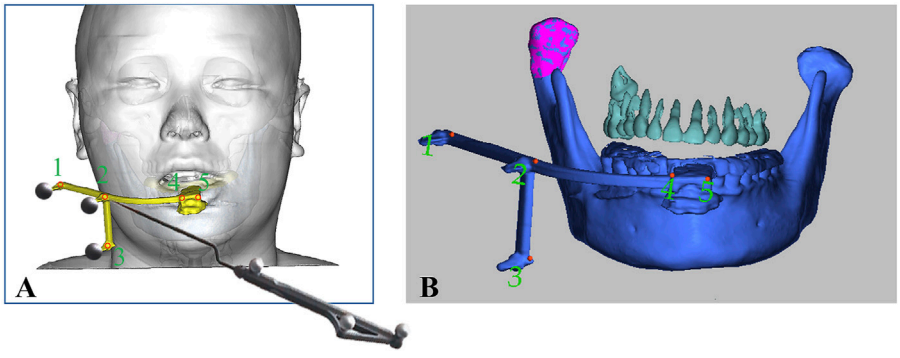

FIGURE 4
Registration was performed via predesigned fiducial points in the PS- DRF. **(A)** Schema of registration procedure via PS-DRF. **(B)** Screenshot of navigation system showed the registration points in PS-DRF.

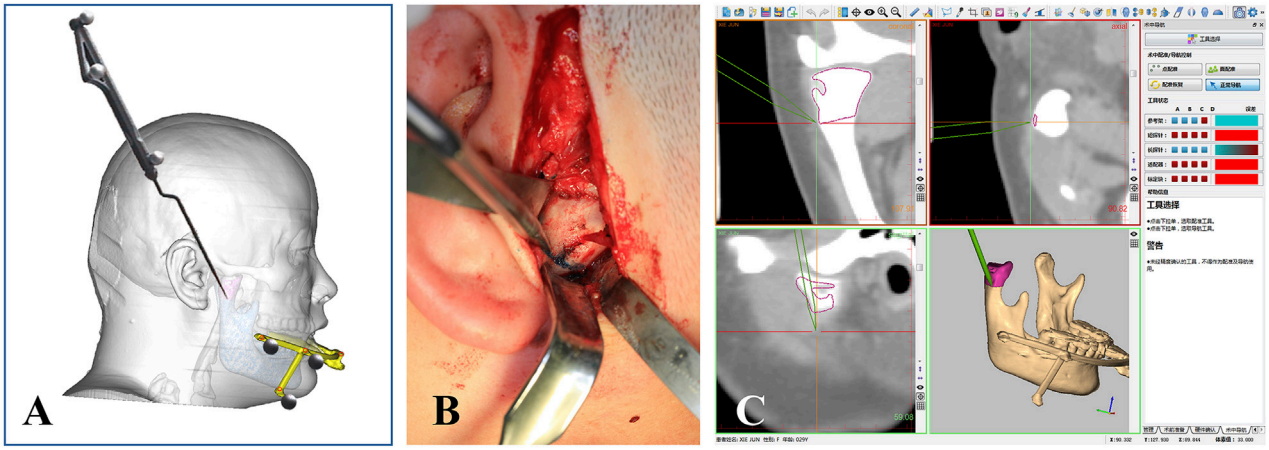

FIGURE 5
Intraoperative real-time 3D tracking. **(A)** Schema of confirming the osteotomy line via navigation prove. **(B)** Osteotomy line was located by the probe at the surgical area. **(C)** Screenshot of navigation system showed the osteotomy line was being tracked in real-time.

passive tracking device emitted infrared light toward the surgical field, and once all reflective spheres were confirmed to be within the detection range, a navigation probe was used to sequentially register five predesigned fiducial points, as shown in Figure 4.

The infrared reflections from the spheres were captured by the tracking device, enabling the spatial localization of each fiducial marker. The system recognized the fixed-array tracker and calculated the spatial position and displacement of the navigation probe relative to the patient, thereby completing the coordinate transformation between the patient's surgical site and the image-guided navigation space.

A 3.5 cm incision was designed anterior to the right ear, and dissection was performed to expose the surgical area and reveal the right condylar osteochondroma, as shown in Figure 5B. Next, the osteotomy line was confirmed using the navigation probe, as shown in Figures 5A,C, and condylectomy was performed under navigation guidance. During the osteotomy and tumor removal, the depth of surgical instrument was continuously monitored through the navigation system to avoid damage to critical anatomical structures, such as the cranial base. In the navigation stage, the surgical assistant should keep the PS-DRF fixed rigidly with mandible, or it might cause greater errors or make navigation failed.

3 Results and discussion

In this study, the placement and registration of the PS-DRF took approximately 5 min. While there is currently no large-scale systematic study in the literature on the time required for different registration methods in oral and maxillofacial surgery, based on the findings of Badiali et al. (2015), traditional cranial-fixed reference frames add an additional 10–20 min of installation and registration time during surgery. The installation process of the PS-DRF was significantly simplified, effectively reducing the time cost of the registration procedure. Furthermore, traditional optical navigation systems typically require the surgeon to repeatedly adjust the probe position to complete multi-point registration, which can be time-consuming. In contrast, the fixed position design of the PS-DRF's registration points ensures stability during registration procedure, reducing intraoperative adjustment time, improving overall surgical efficiency, and lowering the technical threshold for the operator.

Image fusion is one of the key steps in assessing surgical accuracy. During the fitting process, ProPlan CMF 3.0 was used to reconstruct and segment the mandibular models, employing voxel and point cloud computation methods to achieve spatial superimposition and error analysis between the preoperative VSP model and the postoperative actual model. The results of this study showed that the error between the preoperative and postoperative models was less than 2 mm (as shown in Figure 6), confirming the performance of the PS-DRF in surgical navigation could match the clinical demand. Compared to the traditional optical navigation system used by Lin et al. (2015), this method demonstrated comparable accuracy, with the added advantage of clinical safety and stability.

Although this study demonstrated the clinical feasibility and advantages of the PS-DRF, certain limitations still exist. For example, this method may not be applicable in cases where the patient cannot undergo impression taking due to limited mouth opening. Additionally, the dental fixation method may have some limitations in certain special patient populations, such as those with severe dental defects or edentulous patients, and those who cannot cooperate with impression-taking. Future research should focus on designing corresponding solutions for patients with different dental conditions.

In recent years, the application of digital technologies in oral and maxillofacial surgery has significantly advanced the development of precise surgical planning and implementation. Virtual surgical planning (VSP) is one of the key applications of digital technologies. It establishes a patient-specific 3D model using high-resolution medical imaging, enabling comprehensive preoperative assessment and surgical simulation. Many important neurovascular structures in the oral and maxillofacial region, such as the internal maxillary artery, pterygoid plexus, facial nerve, and

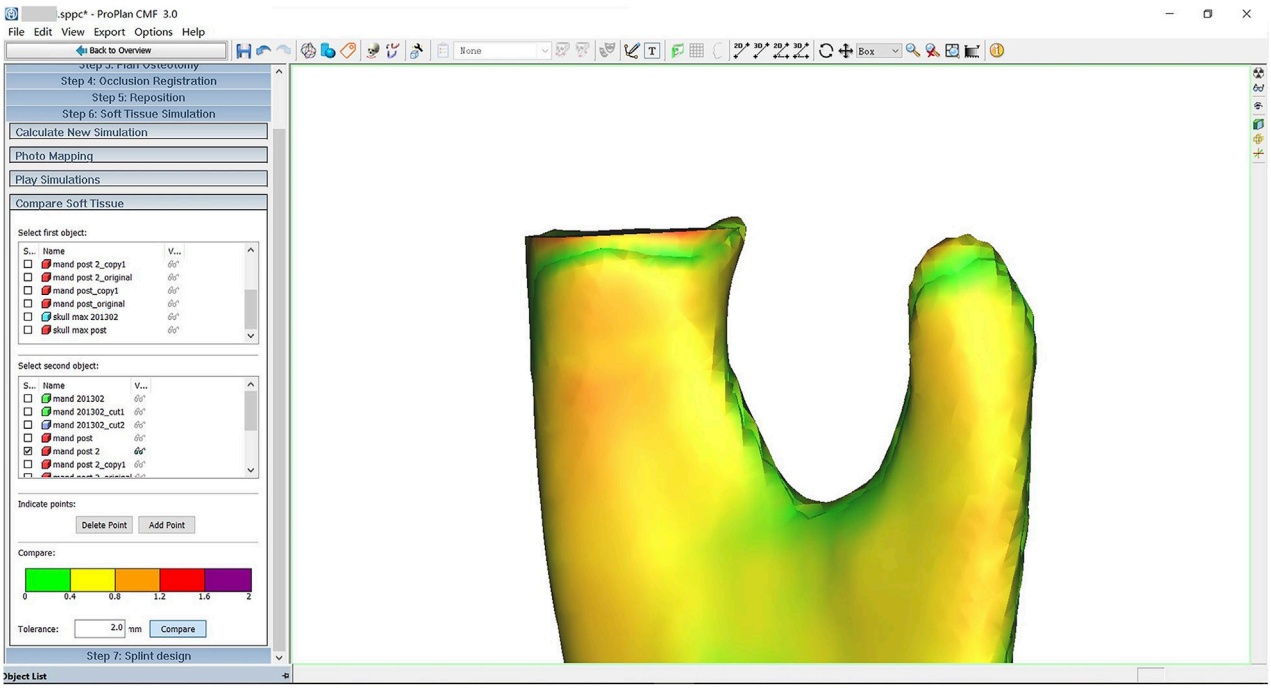

FIGURE 6
Image fusion showed surgical errors.

trigeminal nerve, pass through the soft and hard tissues in deep space. Surgeons typically take great care to avoid injuries caused by these anatomical structures during the operation procedure. Additionally, the surgical approach must consider preserving the function of the oral and maxillofacial system and maintaining facial aesthetics postoperatively, with minimally invasive, precise operations being particularly challenging. Therefore, the precise implementation of VSP relies on the use of subsequent 3D-printed guides or surgical navigation systems. The PS-DRF proposed in this paper integrates VSP, computer-assisted navigation, and 3D printing technology, demonstrating significant clinical value and promising application prospects based on clinical applications.

Traditional surgical guides are typically designed and printed based on preoperative CT imaging data using CAD/CAM technology. The designer can perform repeated simulations and comparisons on the reconstructed rigid 3D model to ensure that the guide fits the anatomical structures of the surgical area and is aligned with the surgical procedure and the patient's specific needs. Extensive clinical applications have demonstrated that 3D-printed surgical guides significantly enhance the intuitiveness and stability of the operation, thereby greatly reducing the difficulty of surgical procedures. However, due to the variability in patients' anatomical structures, positional errors may occur during surgery. For example, studies have shown that when dealing with short or thin bone walls in the surgical area, insufficient contact surface area often results in instability (Li et al., 2013). Additionally, the placement of the surgical guide requires adequate space, which often necessitates larger incisions to expose a sufficient surface for guide placement. In cases with narrow surgical access and deep anatomical structures, more time is required for the guide placement. Therefore, the application range of surgical guides in complex maxillofacial surgeries has certain limitations.

The accuracy of computer-assisted navigation has been thoroughly validated, with its core principles lying in comprehensive preoperative planning and spatial registration, followed by the real-time collection and tracking of spatial information to monitor the positions of patient's anatomical structures and surgical instruments, thus guiding the surgeon to perform precise operations. The registration structures relied upon by traditional navigation systems can be classified into two types: invasive and non-invasive, both of which are highly dependent on the surgeon's subjective judgment and experience. During long surgical procedures, distraction and physical fatigue present potential risks for human error. Compared to traditional methods, Abbate et al. introduced a method of directly fixing the reference frame to the mandibular ramus to track mandibular movement and assist in segmental mandibular resection and reconstruction (Abbate et al., 2017). Lee et al. proposed a 3D-printed personalized registration framework fixed to the external auditory canal and upper anterior teeth to improve the navigation accuracy in orbital floor reconstruction surgeries (Lee et al., 2019). Yamamoto et al. developed a maxillomandibular support-based reference frame designed to maintain mouth opening during the procedure (Yamamoto et al., 2020), which is used for navigation-assisted curettage of mandibular cyst. These three improvements simplified the registration process without causing additional trauma, making them more acceptable to patients.

The PS-DRF also belongs to the non-invasive registration methods but features a design better suited for oral and maxillofacial surgery. First, registration structures relying on fixation to the external auditory canal perform well when the

patient is in the supine position. However, when frequent intraoperative adjustments of head position are required, positional deviations are often unavoidable. In contrast, a registration splint fixed solely to the dental arch overcomes this limitation. Second, the PS-DRF does not come into direct contact with the mandible, preventing potential obstruction of the surgical field, thus offering greater versatility. Additionally, its compact and lightweight design eliminates the need for additional surgical instrument channels. Instead, a new splint can be custom-designed based on the patient's dental cast, while the reference frame itself can be repeatedly sterilized and reused, optimizing medical resource utilization and cost-effectiveness.

4 Conclusion

In summary, based on existing research, the modified PS-DRF offers four key advantages. (1) Stable positioning without additional surgical trauma, while also eliminating the need for a second preoperative CT scan, thereby avoiding redundant radiation exposure. (2) The navigation splint, designed based on specific cusp anatomical structures, moves synchronously with the mandible, ensuring that no significant deviation occurs between the spatial coordinates of the navigation system and the actual surgical space. (3) The conical fiducial marker design facilitates the operators to recognize and locate the markers easily, reduces reliance on both the surgeon's clinical experience and manual dexterity during registration, and provides high reproducibility. (4) Only a thin occlusal splint needs to be 3D printed for each patient, making the method easily scalable and cost-effective.

In the future, systematic clinical research on the PS-DRF will be a primary focus to further validate its effectiveness and safety. The integration of multimodal data with AI-driven technologies may further optimize the data processing workflow, such as automatic anatomical structure recognition and intelligent planning based on deep learning algorithms. Enhancing the degree of automation will significantly reduce the design and fabrication time of PS-DRF, thereby improving the efficiency of surgical navigation technology in oral and maxillofacial surgery.

Data availability statement

The raw data supporting the conclusions of this article will be made available by the authors, without undue reservation.

Ethics statement

The studies involving humans were approved by Institutional review board and the ethics committees of Shanghai Ninth People's Hospital, Shanghai Jiao Tong University School of Medicine. The studies were conducted in accordance with the local legislation and institutional requirements. The participants provided their written informed consent to participate in this study. Written informed consent was obtained from the individual(s) for the publication of any potentially identifiable images or data included in this article.

Author contributions

JW: Conceptualization, Methodology, Software, Writing – original draft, Writing – review and editing. LJ: Data curation, Writing – review and editing, Writing – original draft, Formal Analysis. YC: Visualization, Writing – review and editing, Writing – original draft, Data curation. WZ: Conceptualization, Supervision, Writing – review and editing. JZ: Supervision, Writing – review and editing, Conceptualization. XG: Supervision, Writing – review and editing, Investigation. XX: Supervision, Writing – review and editing, Formal Analysis. SZ: Funding acquisition, Project administration, Supervision, Writing – review and editing.

Funding

The author(s) declare that financial support was received for the research and/or publication of this article. This work was supported by the Natural Science Foundation of Shanghai, Shanghai Action Plan for Science, Technology and Innovation (24ZR1443700), Fundamental Research Funds for the Central Universities (YG2023LC05), SJTU Trans-med Awards Research (20230104), the National Clinical Research Center for Oral Diseases (NCRCO202307 and NCRCO202106), Shanghai Ninth People's Hospital, Shanghai Jiao Tong University School of Medicine (Research Doctor, XKQJS202401, JS22A03), Shanghai's Top Priority Research Center (2022ZZ01017), CAMS Innovation Fund for Medical Sciences(CIFMS) (2019-I2M-5-037), and Project 21DZ2271700-1 from Shanghai Key Laboratory of Medical Imaging Computing and Computer Assisted Intervention.

Conflict of interest

The authors declare that the research was conducted in the absence of any commercial or financial relationships that could be construed as a potential conflict of interest.

Generative AI statement

The author(s) declare that no Generative AI was used in the creation of this manuscript.

Publisher's note

References

Abbate, V., Orabona, G. D. A., Solari, D., Bonavolontà, P., Iaconetta, G., and Califano, L. (2017). Mandibular surgical navigation: an innovative guiding method. *J. Craniofac Surg.* 28 (8), 2122–2126. doi:10.1097/scs.0000000000003816

Alkhayatt, N. M., Alzahrani, H. H., Ahmed, S., Alotaibi, B. M., Alsaggaf, R. M., Am, A. L., et al. (2024). Computer-assisted navigation in oral and maxillofacial surgery: a systematic review. *Saudi Dent. J.* 36 (3), 387–394. doi:10.1016/j.sdentj.2023.12.002

Badiali, G., Roncari, A., Bianchi, A., Taddei, F., Marchetti, C., and Schileo, E. (2015). Navigation in orthognathic surgery: 3D accuracy. *Facial Plast. Surg.* 31 (5), 463–473. doi:10.1055/s-0035-1564716

Berger, M., Kallus, S., Nova, I., Ristow, O., Eisenmann, U., Dickhaus, H., et al. (2015). Approach to intraoperative electromagnetic navigation in orthognathic surgery: a phantom skull based trial. *J. Craniomaxillofac Surg.* 43 (9), 1731–1736. doi:10.1016/j.jcms.2015.08.022

Bettschart, C., Kruse, A., Matthews, F., Zemann, W., Obwegeser, J. A., Grätz, K. W., et al. (2012). Point-to-point registration with mandibulo-maxillary splint in open and closed jaw position. Evaluation of registration accuracy for computer-aided surgery of the mandible. *J. Craniomaxillofac Surg.* 40 (7), 592–598. doi:10.1016/j.jcms.2011.10.016

Brouwer de Koning, S. G., Geldof, F., van Veen, R. L. P., van Alphen, M. J. A., Karssemakers, L. H. E., Nijkamp, J., et al. (2021). Electromagnetic surgical navigation in patients undergoing mandibular surgery. *Sci. Rep.* 11 (1), 4657. doi:10.1038/s41598-021-84129-5

Casap, N., Wexler, A., and Eliashar, R. (2008). Computerized navigation for surgery of the lower jaw: comparison of 2 navigation systems. *J. Oral Maxillofac. Surg.* 66 (7), 1467–1475. doi:10.1016/j.joms.2006.06.272

Collyer, J. (2010). Stereotactic navigation in oral and maxillofacial surgery. *Br. J. Oral Maxillofac. Surg.* 48 (2), 79–83. doi:10.1016/j.bjoms.2009.04.037

Gröbe, A., Weber, C., Schmelzle, R., Heiland, M., Klatt, J., and Pohlenz, P. (2009). The use of navigation (BrainLAB Vector vision(2)) and intraoperative 3D imaging system (Siemens Arcadis Orbic 3D) in the treatment of gunshot wounds of the maxillofacial region. *Oral Maxillofac. Surg.* 13 (3), 153–158. doi:10.1007/s10006-009-0166-4

Gui, H., Yang, H., Shen, S. G., Xu, B., Zhang, S., and Bautista, J. S. (2013). Image-guided surgical navigation for removal of foreign bodies in the deep maxillofacial region. *J. Oral Maxillofac. Surg.* 71 (9), 1563–1571. doi:10.1016/j.joms.2013.04.001

Lee, J., Mekuria, K., Son, T. G., Jeong, W. S., Choi, J. W., and Kim, Y. (2019). A novel noninvasive patient-specific navigation method for orbital reconstructive surgery: a phantom study using patient data. *Plast. Reconstr. Surg.* 143 (3), 602e–612e. doi:10.1097/prs.0000000000005381

Li, B., Zhang, L., Sun, H., Yuan, J., Shen, S. G., and Wang, X. (2013). A novel method of computer aided orthognathic surgery using individual CAD/CAM templates: a combination of osteotomy and repositioning guides. *Br. J. Oral Maxillofac. Surg.* 51 (8), e239–e244. doi:10.1016/j.bjoms.2013.03.007

Lin, H. H., Chang, H. W., Wang, C. H., Kim, S. G., and Lo, L. J. (2015). Three-dimensional computer-assisted orthognathic surgery: experience of 37 patients. *Ann. Plast. Surg.* 74 (Suppl. 2), S118–S126. doi:10.1097/sap.0000000000000455

Lin, Z., Lei, C., and Yang, L. (2023). Modern image-guided surgery: a narrative review of medical image processing and visualization. *Sensors (Basel)* 23 (24), 9872. doi:10.3390/s23249872

Lübbers, H. T., Obwegeser, J. A., Matthews, F., Eyrich, G., Grätz, K. W., and Kruse, A. (2011). A simple and flexible concept for computer-navigated surgery of the mandible. *J. Oral Maxillofac. Surg.* 69 (3), 924–930. doi:10.1016/j.joms.2010.01.009

Mekuria, K., Kim, Y., Cho, H., Lee, D., Park, S., Lee, B. H., et al. (2016). The effect of optical marker configuration on tracking accuracy in image guided surgery. *Stud. Health Technol. Inf.* 220, 227–232. doi:10.3233/978-1-61499-625-5-227

Novelli, G., Tonellini, G., Mazzoleni, F., Bozzetti, A., and Sozzi, D. (2014). Virtual surgery simulation in orbital wall reconstruction: integration of surgical navigation and stereolithographic models. *J. Craniomaxillofac Surg.* 42 (8), 2025–2034. doi:10.1016/j.jcms.2014.09.009

Palla, B., and Callahan, N. (2021). Does the use of computer-assisted surgery affect the margin status in resections of ameloblastoma? *J. Oral Maxillofac. Surg.* 79 (7), 1467–1473. doi:10.1016/j.joms.2020.09.007

Pierrefeu, A., Terzic, A., Volz, A., Courvoisier, D., and Scolozzi, P. (2015). How accurate is the treatment of midfacial fractures by a specific navigation system integrating "mirroring" computational planning? Beyond mere average difference analysis. *J. Oral Maxillofac. Surg.* 73 (2), 315.e1–315.e10. doi:10.1016/j.joms.2014.09.022

Schramm, A., Suarez-Cunqueiro, M. M., Rücker, M., Kokemueller, H., Bormann, K. H., Metzger, M. C., et al. (2009). Computer-assisted therapy in orbital and mid-facial reconstructions. *Int. J. Med. Robot.* 5 (2), 111–124. doi:10.1002/rcs.245

Wilkat, M., Kübler, N., and Rana, M. (2021). Advances in the resection and reconstruction of midfacial tumors through computer assisted surgery. *Front. Oncol.* 11, 719528. doi:10.3389/fonc.2021.719528

Yamamoto, S., Taniike, N., and Takenobu, T. (2020). Application of an open position splint integrated with a reference frame and registration markers for mandibular navigation surgery. *Int. J. Oral Maxillofac. Surg.* 49 (5), 686–690. doi:10.1016/j.ijom.2019.09.015

frontiers | Frontiers in Bioengineering and Biotechnology

TYPE Original Research
PUBLISHED 02 June 2025
DOI 10.3389/fbioe.2025.1590348

OPEN ACCESS

EDITED BY
Guicai Li,
Nantong University, China

REVIEWED BY
Pietro Mandracci,
Polytechnic University of Turin, Italy
Ravinder Saini,
King Khalid University, Saudi Arabia

*CORRESPONDENCE
Yaqin Zhu,
zyq1590@163.com
Dan Lin,
lind@sumhs.edu.cn
Tiantian Wu,
wutiantian_happy@126.com

RECEIVED 09 March 2025
ACCEPTED 23 May 2025
PUBLISHED 02 June 2025

CITATION
Han Y, Zhang X, Weng J, Tian S, Dong X, Cai Z, Zhang Y, Wu T, Lin D and Zhu Y (2025) Optimization of a novel dental self-healing resin composite by bacteria-induced biomineralization.
Front. Bioeng. Biotechnol. 13:1590348.
doi: 10.3389/fbioe.2025.1590348

Optimization of a novel dental self-healing resin composite by bacteria-induced biomineralization

Yanyan Han[1,2], Xiaoxuan Zhang[3], Jianing Weng[3], Shiqi Tian[3], Xian Dong[4], Zhiheng Cai[1,2], Yi Zhang[4], Tiantian Wu[1,2]*, Dan Lin[4]* and Yaqin Zhu[1,2]*

[1]Department of General Dentistry, Shanghai Ninth People's Hospital, Shanghai Jiao Tong University School of Medicine, Shanghai, China, [2]College of Stomatology, Shanghai Jiao Tong University, National Center for Stomatology, National Clinical Research Center for Oral Diseases, Shanghai Key Laboratory of Stomatology, Shanghai Research Institute of Stomatology, Shanghai, China, [3]Shanghai Jiao Tong University School of Medicine, Shanghai, China, [4]Shanghai University of Medicine and Health Sciences, College of of Medical Technology, Shanghai, China

Introduction: Dental resin restorations often fail due to microcrack expansion, causing fractures and secondary caries. Self-healing resin composites based on Microbially Induced Calcium Carbonate Precipitation (MICP) offer a solution. In these composites, moisture and air activate bacteria to precipitate calcium carbonate ($CaCO_3$) and repair microcracks. When a crack seals, bacteria become dormant or form spores until the next crack forms, triggering repeated self-healing.

Methods: This study involved the optimization of nutrients to enhance biocompatibility, the preparation of dental resin composites incorporating eight different bacterial strains, the investigation of Mn^{2+} to enhance self-healing properties, and the utilization of a method to evaluate self-healing efficiency tailored for the oral environment. This method took a microscopic view of the healing process in artificial saliva, and the self-healing efficiency was determined by quantifying the scratch area.

Results: In the final results, *Bacillus* sphaericus (ATCC 4525) cultured with Mn^{2+} exhibited the most impressive self-healing effect, while *Bacillus* pasteurii (B80469) had the weakest self-healing effect in the study. Otherwise, Bifidobacterium longum showed no significant difference between its initial and secondary healing effects.

Discussion: This dental self-healing resin composite can undergo multiple rounds of self-repair and boasts high biocompatibility, leading to a significant reduction in the failure rate of dental resin restorations.

KEYWORDS

self-healing, bacteria, biomineralization, MICP, CaCO3

1 Introduction

Dental caries, the most common oral disease affecting individuals of all ages (Organization, 2022), poses a significant challenge in maintaining oral health. Traditional dental resin composites are widely used for cavity fillings due to their ease of application and aesthetic appeal, however, they have limitations, including being susceptible to microcracking from the pressure of chewing and thermal stress (Deligeorgi et al., 2001), these microscopic cracks are difficult to detect and repair, leading to issues such as damage to the restoration and fractures, and the formation of secondary caries. To address these challenges, current research efforts were focused on improving the inorganic fillers and incorporating reinforcements in composites to prevent cracking (Nitta et al., 2017; Münchow et al., 2018; Wang et al., 2024), however, despite these efforts, resin restorations continue to face challenges with persistent fractures.

As a response to this issue, self-healing dental resin composites have been developed and studied by Wertzberger et al. (2010), which showed promise results in extending the lifespan of dental resin restorations, providing both social and economic benefits. Research on self-healing dental resin composites has mainly focused on utilizing PUF microcapsules for self-repair. When microcracks or damage occur in resin composites, the microcapsules rupture and release a healing agent to repair the cracks. The self-healing performances of this system have been demonstrated to restore between 25% and 80% of the original fracture toughness (Wertzberger et al., 2010; Huyang et al., 2016; Wu et al., 2016; Yue et al., 2018; Menikheim et al., 2022; Yao et al., 2022). While the microcapsule self-healing system has shown promising results in self-repair and crack suppression, it has limited self-healing ability and some degree of biological toxicity.

Calcium carbonate ($CaCO_3$) is a naturally mineral byproduct of microbial metabolism, its application for crack repair of building structure was first proposed by Gollapudi et al. (1995) in 1995, and later expanded upon by Ramachandran et al. (2001) in 2001 with the concept of Microbially Induced Calcium Carbonate Precipitation (MICP) for crack repair in concrete. MICP involves microbial metabolism forming CO_3^{2-}, which combined with Ca^{2+} in the environment, leads to the precipitation of $CaCO_3$ crystals for biomineralization. Microbial self-healing concrete, which uses microbes activated by moisture or oxygen to form biogenic $CaCO_3$ and fill cracks, reduces permeability and enhances durability, and it is widely used for its effectiveness, sustainability, and low toxicity (Jonkers et al., 2010; Van Tittelboom et al., 2010; Wiktor and Jonkers, 2011; Wang J. et al., 2012; Seifan et al., 2016a; Van Tittelboom et al., 2016), with ongoing research focusing on optimizing factors like bacterial strains, nutrients, and aeration (Okwadha and Li, 2010; Achal et al., 2011; Khaliq and Ehsan, 2016; Xu and Wang, 2018; Xu et al., 2018). The primary process of MICP occurs through the nitrogen cycle, with bacteria capable of producing essential protein enzymes with mineralizing properties through metabolic processes, such as urease, which aids in the formation of $CaCO_3$, such as *Bacillus pasteurella*, *Bacillus* sphaericus, *Bacillus* licheniformis, and *Bacillus subtilis*, playing crucial roles in inducing carbonate precipitation. Seifan et al. (2020) incorporated Generally Recognized As Safe (GRAS) bacteria into dental resin composites to enable self-healing of microcracks through $CaCO_3$ formation, activated by moisture and air, with bacteria cycling between active and dormant states for repeated repairs. Their study demonstrated that Bifidobacterium longum and *Bacillus* licheniformis could effectively induce biomineralization in Z250 dental resin composites. However, to address cytotoxicity associated with the nutritional components including urea and calcium chloride utilized in the study, biocompatible calcium lactate and glucose were introduced as alternative nutrients, showing great potential for enhancing dental materials (Figure 1).

This study investigated the first and secondary self-healing abilities of eight different strains of bacteria in dental resin composites by creating microcracks on resin samples and observing the healing progress of these microcracks at different time intervals in a simulated oral environment, to assess accurate self-healing efficiency which was measured quantitatively through crack area measurements, and the strains that demonstrated the highest self-healing efficiency in dental resin composite were

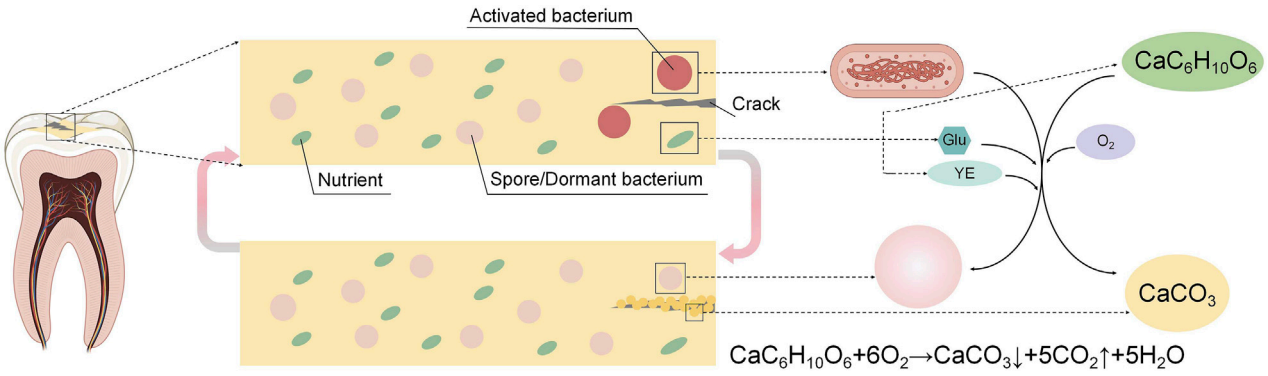

FIGURE 1
Self-healing mechanism of dental microorganism self-healing resin composites: As a microcrack occurs, moisture and air infiltration trigger the bacteria to produce calcium carbonate ($CaCO_3$), facilitating the natural healing process of the microcracks. Once the cracks are sealed, the bacteria become inactive due to the lack of water and oxygen until the microcracks reoccur. At that point, the bacteria are reactivated and restart repairing the microcracks.

TABLE 1 Cultivation conditions of different strains.

Stain	Stain abbreviation	Serial number	Aerobic style	Temperature (°C)	PH	Culture medium
Lactobacillus reuteri	LaR	BMZ140479 (from ATCC55739)	Anaerobe	37	7.0	MRS
Bifidobacterium longum	BiL	B81617 (from ATCC15702)	Anaerobe	37	7.0	BHI
Bacillus licheniforms	BaL	ATCC9859 /ATCC9789	Facultative anaerobe	37	8	BHI
Bacillus sphaericus	BaSph	ATCC4525 /LMG22257	Aerobic	37	7.0	NA
Lysinibacillus sphaericus	BaLy	BMZ008183	Aerobic	37	7.2	NA
Bacillus pasteurii	BaP	B80469 (from NCIM2477)	Aerobic	30	7.0	CASO+ 20 g/L urea

identified, providing valuable insights and data for the advancement of self-healing dental resin composites, which aims to reduce the occurrence of fracture and the incidence of secondary caries, thereby extending the service life of the dental resin composites.

2 Materials and methods

2.1 Strains and materials

Bacterial strains which were GRAS including ATCC4525 *Bacillus* sphaericus (BaSph-A) and ATCC9789 *Bacillus* licheniformis (BaL-B) were acquired from Shanghai Rongmin Biotechnology Center, BMZ008183 Lysinibacillus sphaericus (BaLy), ATCC9859 *Bacillus* licheniformis (BaL-A), B80469 (sourced from NCIM2477) *Bacillus pasteurella* (BaP), B81617 (sourced from ATCC15702), Bifidobacterium longum (BiL), BMZ140479 (sourced from ATCC55739) *Lactobacillus* reuteri (LaR) and LMG22257 *Bacillus* sphaericus (BaSph-B) were obtained from Ningbo Mingzhou Biotechnology Co., Ltd additionally.

Calcium chloride, urea, yeast extract, CASO medium (soy peptone casein digest), De Man, Rogosa and Sharpe Medium (MRS) medium, Brain-Heart Infusion Broth (BHI) and Nutrient Agar (NA) medium were all sourced from Beijing Pufei Biotechnology Co., Ltd. $MnSO_4.H_2O$ (99%) was purchased from Macklin Biochemical Technology Co., Ltd. (Shanghai, China). Barium Aluminosilicate Glass (NF180nm, BAS Glass) was produced by Schott AG Co., Ltd (LandShut, Germany). Bisphenol A glycidyl methacrylate (Bis-GMA), tri(ethylene glycol) dimethacrylate (TEGDMA, 95%), camphorquinone (CQ, 97%), ethyl 4-dimethylaminobenzoate (4-EDMAB, 99%) were all purchased from Sigma-Aldrich Reagent (Shanghai, China). The artificial saliva (pH 6.8) was obtained from Phygene Life Sciences Company (Fuzhou, China). Ethanol (75%) was purchased by Dongyi Chemical Co. Ltd (Shanghai, China). Pure water (H_2O) was prepared by an ultrapure water system (Direct-Pure UP With Dispenser UP 10 UV), purchased from Rephile Corporation (Shanghai, China). All chemicals reagents were utilized without further purification.

2.2 Cultivation of strains

The strains were inoculated at a volume fraction of 1‰ into various culture media that had been sterilized using high pressure, then incubated for 48 h in a shaking incubator set at 150 rpm (specific culture conditions in Table 1). After incubation, the culture medium was transferred onto nutrient agar plates containing 15 g/L agar, and spread evenly across the entire surface, then left to cultivate for an additional 48 h, finally the bacteria that grew on the agar plates were used as the initial strains. These initial strains were then inoculated at a volume fraction of 1‰ into the corresponding culture media that had been sterilized by high pressure. They were incubated for 48 h again in a shaking incubator set at 150 rpm, resulting in liquid cultures of either *Bacillus* or non-Bacillus strains. To further boost spore production referring to previous studies (Xu et al., 2018), 10 mg/L of $MnSO_4.H_2O$ was added to the final culture medium containing BaSph-A, referred to as BaSph-Mn, in addition to the strains cultured separately.

2.3 Identification of spores

The bacterial liquid of *bacillus* was undergone sterilization process through pasteurization, which involves heating to 80°C for 20 min followed by rapid cooling in ice water for 5 min. This step was crucial in reducing the number of vegetative cells present in the bacterial liquid, then the liquid was centrifuged (BIORIDGRE TGL-18M, Shanghai, China) at 7,000 rpm, 4°C for 7 min to separate and harvest the spores. A portion of these spores were stained for further analysis, which were placed on slides using malachite green dye and safranin counterstaining, subsequently, they were examined under confocal laser scanning microscope (Leica TCS-SP8, Germany) to observe their characteristics and morphology.

2.4 Preparation of dental self-healing resin composites

The collected spores from *Bacillus* and Bacterial liquid from non-Bacillus were washed, then centrifuged to remove excess liquid,

FIGURE 2
The resin disc samples with six artificial scratches.

resulting in a paste-like substance, which was subjected to freeze drying (BiLon, Bilang, Shanghai, China) for a period of 3 days, ultimately grinded to yield the lyophilized bacterial/spores.

The basic resin consisted of 49wt% BisGMA, 49wt% TEGDMA, 0.4wt% CQ, and 1.6wt% EDMAB, which is mixed magnetically at room temperature for 24 h, then combined with barium glass powder, nutrient powder (consisting of calcium lactate:yeast extract:glucose = 5:8:20) and bacterial powder (basic resin: barium glass powder: nutrient powder: bacterial powder = 45wt %:45wt%: 5wt%:5wt%) using a dual-center dispersion mixer known as the SpeedMixer (DAC150.1 FVZ-K, FlackTek, Inc., Germany) and a three-roll milling machine (EXAKT 80E, Exakt, Germany) for thorough homogenization.

2.5 Preparation of self-healing resin samples

Resin composites were injected into the silicone rubber mold of the disc and light-cured with a light-curing lamp (blue light, 470 nm, SLC-VIII B, Sifang, Hangzhou, China) for 60 s on each side. The samples were then polished with silicon carbide paper (P1500). Finally, they were formed into disc samples with a thickness of 1 mm (Φ = 10 mm), with two samples prepared for each group. After being placed for 1 day, a surgical blade was used to carve six artificial cracks of identical length (2 mm) onto the surface of each resin disc (Figure 2).

2.6 Evaluation of self-healing capabilities

The resin disks were placed in artificial saliva and stored at 37°C. They were photographed under a stereo-microscope on days 0, 1, 3, 5, 7, 14, 21, 30, 45, and 60. The area of the cracks was calculated using ImageJ image processing software, and differences at different time points were compared to obtain the initial self-healing data. On day 60, one resin disk sample was taken and dried overnight in an oven at 60°C. The morphology and microstructure of the healing surface were further observed using SEM (FE-SEM, S-4800, HITACHI, Japan). Another resin disk was re-carved along the original line, and the above steps were repeated to obtain the secondary self-healing data. The healing efficiency ($\eta 1$) was calculated according to Formulas 1.

$$\eta 1 = \frac{HA}{SA} \times 100\% \quad (1)$$

Where HA = healing area, SA = scratch area.

2.7 Statistical analysis

Statistical analysis was conducted using SPSS 27.0 software. Healing areas at different time were expressed as mean ± standard deviation. One-way analysis of variance (ANOVA) was employed for statistical comparisons, followed by the LSD method for datasets exhibiting homogeneous variance and Tamhane's T2 method for those with heterogeneous variance. The significance level was set at $p < 0.05$ (*: $p < 0.05$, **: $p < 0.01$, ***: $p < 0.001$, ****: $p < 0.0001$).

3 Results

3.1 Characterization of bacteria/spores

Upon observation of the microscope photos, it is apparent that the stained spores standed out as green distinctly. The removal of red bacteria during centrifugation allowed a clear visualization of spores for *Bacillus*, different strains of which exhibited variability in size and shape, underscoring the diversity within this bacterial species. Identifying non-spore-forming bacteria was simplified by their absence of spores (Figure 3). It has also been demonstrated that the vegetative cells were effectively eradicated.

3.2 Initial self-healing process

Figure 4 showed the progression of initial self-healing cracks in nine groups of dental self-healing resin discs and a control group, as observed under an *in vivo* stereomicroscope. The control group displayed minimal changes in scratches through 60 days, in contrast, the cracks in the other groups exhibited varying degrees of reduction and partial healing, with BaSph-A + Mn and BiL demonstrating the most significant reduction.

Figure 5A presents a comparison of the healing status over the first 60 days among the nine groups of dental self-healing resin discs and the control group. Figure 5B depicts the cumulative healing rate of the nine groups of dental self-healing resin discs and the control group over the initial 60-day period. Furthermore, Figure 5C illustrates the healing rates on the 60th day of the first 60 days, highlighting the self-healing efficiency of BaP resin discs as the lowest at 41.4%, followed by BaLy at 53.6% and BaL-A at 54.8%, however, all three were significantly more effective than the control group at 16.2% ($P < 0.00001$); the highest healing efficiency was observed in the resin discs prepared with BaSph-A + Mn, BiL and BaL-B, all of which exceeded 70%. Among these three groups, the

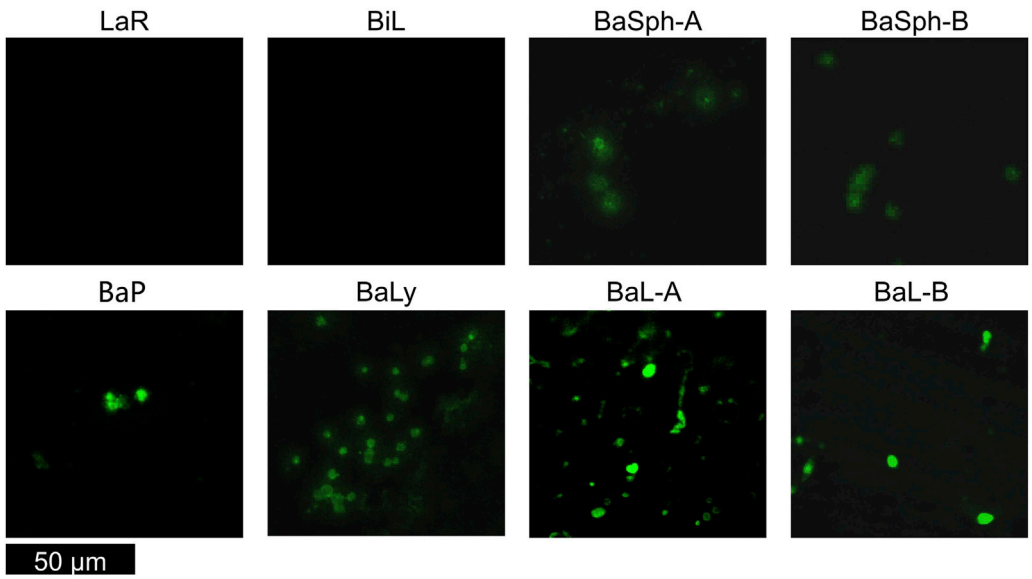

FIGURE 3
Confocal laser scanning microscope images of various non-spore-forming bacteria and *Bacillus* spores. Non-spore-forming bacteria was simplified by their absence of spores, the stained spores of *Bacillus* standed out as green.

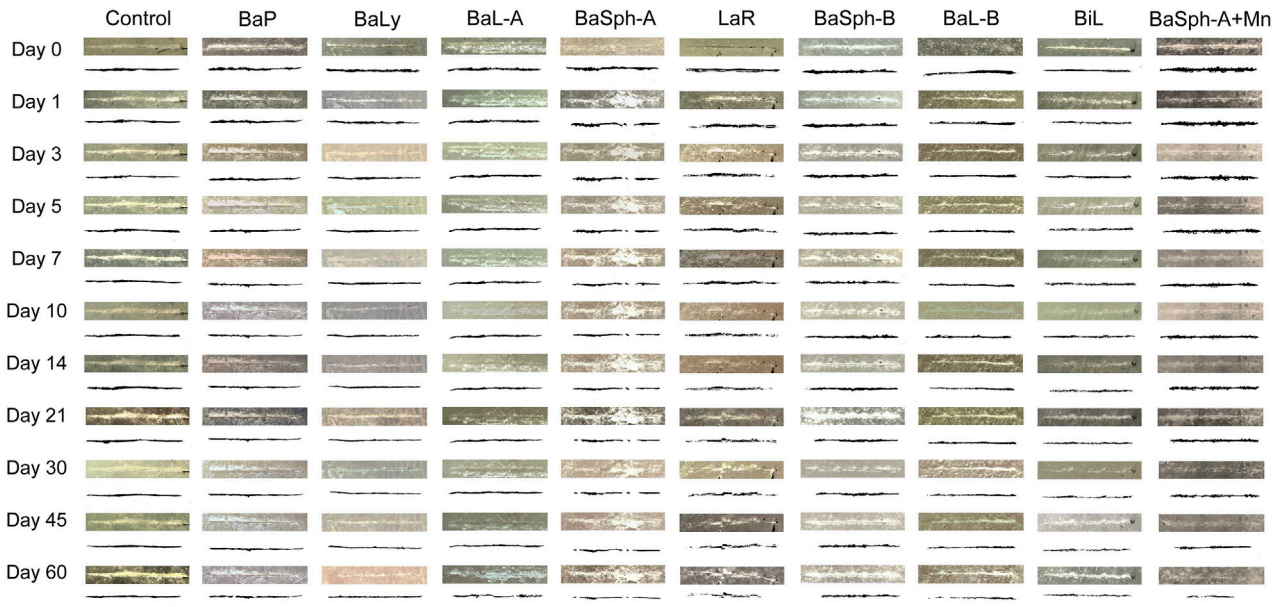

FIGURE 4
Observation and measurement of the initial self-healing of scratches of resin splines (0–60 days) under stereomicroscope (3.2x). The control group displayed minimal changes in scratches through 60 days, in contrast, the cracks in the other groups exhibited varying degrees of reduction and partial healing.

healing efficiency of BaSph-A + Mn was particularly impressive at 85.8%, although there was no significant difference between the three groups ($P > 0.05$). Following closely behind were BaSph-A, BaSph-B and LaR, all of which were effective in inducing $CaCO_3$ precipitation with healing rates around 63%. The initial healing rates (mean ± standard deviation) of each group at different time points are shown in Table 2.

Figure 6 offers a more detailed view of the healing process observed in the scratches through SEM images, the results aligned with the previous assessments of healing efficiency. In the magnified images, a white substance can be observed within the scratches of the bacterial groups, with BaSph-A + Mn exhibiting the most pronounced crack healing which can be attributed to the effective induction of spore formation by Mn^{2+}, which significantly boosts $CaCO_3$ production.

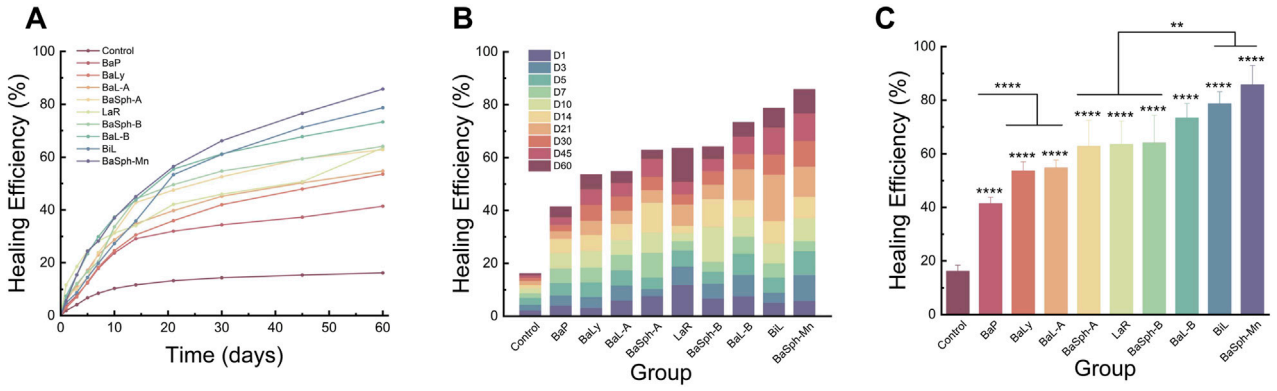

FIGURE 5
(A) Line chart and **(B)** stacked bar chart of comparation of initial-healing rate in different groups in 60 days. **(C)** Bar chart of comparation of initial-healing rate in different groups at day 60. *P < 0.05, **P < 0.01, ***P < 0.001, ****P < 0.0001.

TABLE 2 Initial-healing rate (means±standard deviations, %) (n = 12) in different groups.

Time	Control	BaP	BaLy	BaL-A	BaSph-A	LaR	BaSph-B	BaL-B	BiL	BaSph-Mn
Day 0	0	0	0	0	0	0	0	0	0	0
Day 1	1.9 ± 0.8	3.8 ± 0.8	3.0 ± 0.6	5.8 ± 2.8	7.4 ± 4.3	11.6 ± 4.4	6.5 ± 4.6	7.4 ± 3.4	4.8 ± 4.1	5.6 ± 4.0
Day 3	4.2 ± 0.9	7.7 ± 2.0	7.1 ± 1.9	11.4 ± 3.7	10.1 ± 3.6	18.6 ± 4.0	12.1 ± 5.9	15.5 ± 4.1	8.7 ± 5.8	15.5 ± 1.0
Day 5	6.8 ± 1.3	12.4 ± 3.4	12.7 ± 2.8	17.2 ± 3.7	14.5 ± 4.7	24.7 ± 5.4	16.7 ± 6.7	23.4 ± 4.7	14.5 ± 6.7	24.4 ± 2.9
Day 7	8.5 ± 1.6	17.9 ± 4.3	18.3 ± 3.2	23.0 ± 2.8	23.9 ± 8.6	28.2 ± 5.8	20.4 ± 7.7	29.9 ± 5.4	19.8 ± 7.5	28.2 ± 3.8
Day 10	10.3 ± 2.0	23.8 ± 5.1	24.6 ± 3.0	28.7 ± 3.1	31.5 ± 8.1	31.3 ± 6.3	33.6 ± 8.2	37.3 ± 6.5	27.3 ± 9.7	37.0 ± 7.5
Day 14	11.7 ± 2.1	29.12 ± 5.5	30.6 ± 2.7	34.8 ± 3.8	42.8 ± 8.6	34.1 ± 6.7	44.2 ± 9.1	43.8 ± 6.5	35.8 ± 8.9	45.1 ± 9.2
Day 21	13.3 ± 2.1	32.0 ± 5.6	35.9 ± 2.9	39.8 ± 3.3	47.5 ± 8.5	42.1 ± 7.8	49.6 ± 12.6	55.5 ± 7.7	53.4 ± 4.9	56.4 ± 7.8
Day 30	14.4 ± 2.1	34.4 ± 5.2	42.0 ± 3.7	45.2 ± 3.0	52.6 ± 8.7	45.9 ± 6.2	54.8 ± 8.5	61.3 ± 5.3	61.1 ± 5.7	66.2 ± 10.1
Day 45	15.4 ± 2.2	37.3 ± 3.5	47.9 ± 3.5	50.3 ± 2.7	59.4 ± 8.7	50.7 ± 5.8	59.4 ± 8.4	67.7 ± 4.6	71.2 ± 7.4	76.6 ± 9.8
Day 60	16.2 ± 2.1	41.4 ± 2.2	53.6 ± 3.1	54.8 ± 2.8	62.8 ± 9.0	63.5 ± 8.2	64.1 ± 9.8	73.3 ± 5.2	78.7 ± 4.2	85.8 ± 6.5

Furthermore, BaSph-A, BaSph-B, BaL-A, BaL-B, LaR and BiL demonstrated varying degrees of healing, while the control group along with BaP and BaLy groups showed no significant healing effect.

3.3 Secondary self-healing process

Figure 7 compared the healing progress of resin discs in eight different groups of dental self-healing resin discs and the control group over repeated healing experiment. The results indicated that the control group's scratches remained relatively unchanged from day 1 to day 60, while the experimental groups displayed varying degrees of shallow, resembling the initial healing situations.

Figures 8A,B provided representation of the healing process for the eight groups of dental self-healing resin discs and the control group. Additionally, Figure 8C highlights the healing progress on day 60, revealing that BaP had the lowest self-healing efficiency at 40.1%, consistent with the initial healing results. The BaLy group followed closely behind with an efficiency of 45.5%, both significantly better than the control group's efficiency of 16.2% ($P < 0.001$). The resin disc with BiL was demonstrated with the highest healing efficiency at 68.2%, while the remaining experimental groups showed similar healing rates around 50%, indicating effective promotion of $CaCO_3$ precipitation. The secondary healing rates (mean ± standard deviation) of each group at different time points are shown in Table 3.

Furthermore, SEM images of the secondary healing phase (Figure 9) supported these findings, showing varying degrees of healing in the BaL-A, BaL-B, BaLy, BaSph-A, BaSph-B, BiL and LaR groups, while the control and BaP groups displayed less significant improvements.

3.4 Comparative analysis of two self-healing processes

Figure 10 illustrated a comparison of the healing rates of different strains of bacteria during initial and secondary healing. It is evident that the control group had the lowest healing rate during secondary healing

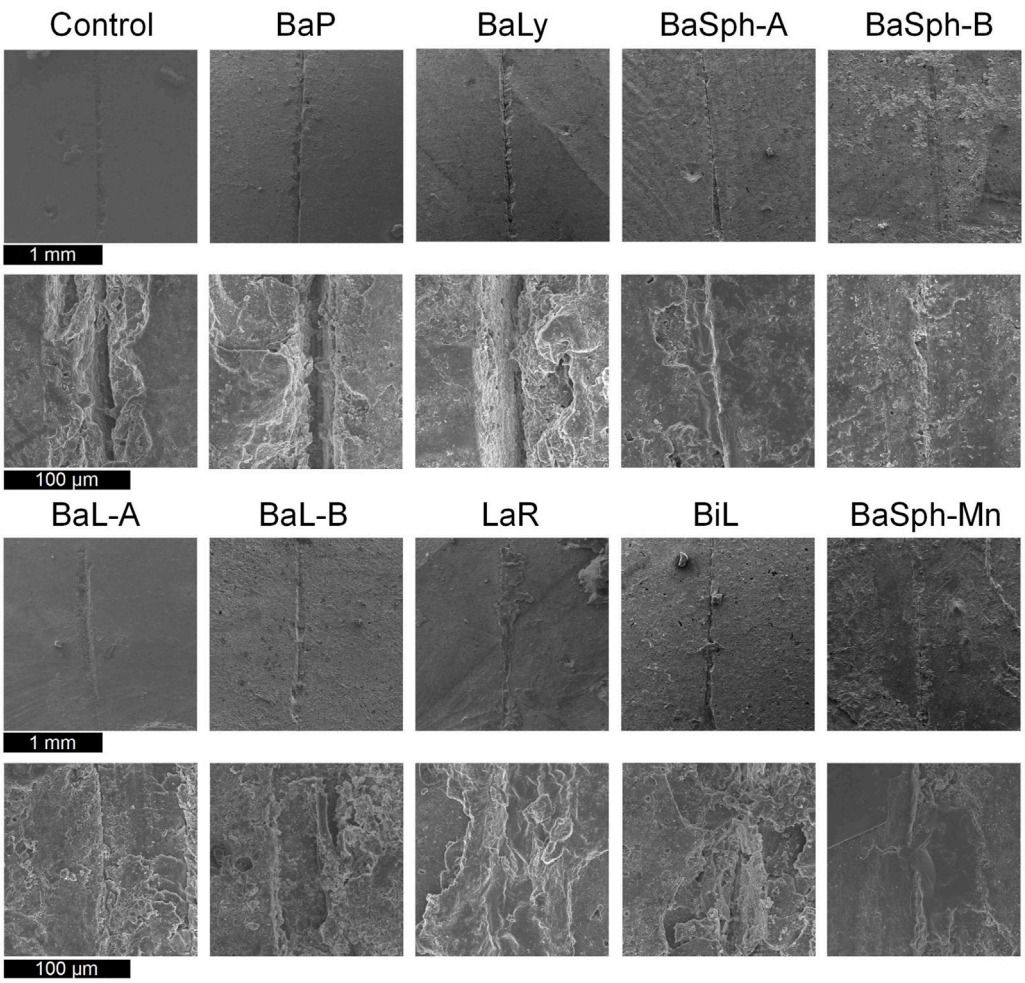

FIGURE 6
SEM images of the initial healing of cracks of resin samples (day 60), a white substance can be observed within the scratches of the bacterial groups.

and showed no significant difference compared with initial healing group. The healing rates of other strains of bacteria during secondary healing were lower compared to initial healing groups, with strains BaP, BiL, BaL-A and BaSph-A showing no significant difference ($P > 0.05$). The secondary healing rates of BaL-B, BaSph-B and BaLy significantly decreased ($P < 0.05$), but still maintain a self-healing efficiency of around 50%. This decrease in healing efficiency may be attributed to a slight loss of nutrients, suggesting the need to consider increasing the proportion of nutrients in future studies.

In conclusion, the most effective strain for inducing $CaCO_3$ precipitation and displaying significant self-healing abilities is BiL, followed by BaL-B, BaSph-A, BaSph-B, BaL-A and LaR exhibit comparable levels of self-healing efficiency. BaP and BaLy, on the other hand, show less effectiveness in self-healing. The inclusion of Mn^{2+} has been found to enhance spore yield and improve self-healing capability.

4 Discussion

Over time, microcracks gradually develop in resin restorations, eventually causing fractures. Previous studies on self-healing dental resin composites have focused mainly on re-bonding close to complete fracture. However, in the oral environment, resin restorations are constantly subjected to biting forces, making it impractical for them to re-bond statically after fracturing. In fact, cracks and excessive pressure can lead to the direct fracture and detachment of dental restorations at any time. Therefore, assessing self-healing properties solely based on re-bonding close to complete fracture is inaccurate. Microcracks typically form before complete fracture, and if they can be continuously self-healed, the likelihood of resin fracture would be significantly reduced. Early self-healing of microcracks can prevent further damage. Hence, prioritizing the evaluation of early self-healing performance is essential.

Given the continuous use of restorations, the ability of self-healing materials to repair themselves repeatedly is crucial. MICP was emerged as an innovative approach for repeated self-healing of microcracks in dental resin composites. This study investigated the initial and secondary self-healing processes of cracks in resin restorations under simulated oral conditions, in which the area changes of microcracks were observed and quantitatively analyzed a microscopic level, providing a more accurate evaluation of the initial and secondary self-healing efficiencies of self-healing resin composites of eight bacterial stain groups, covering the majority of the bacterial species studied in self-healing concrete.

10.3389/fbioe.2025.1590348

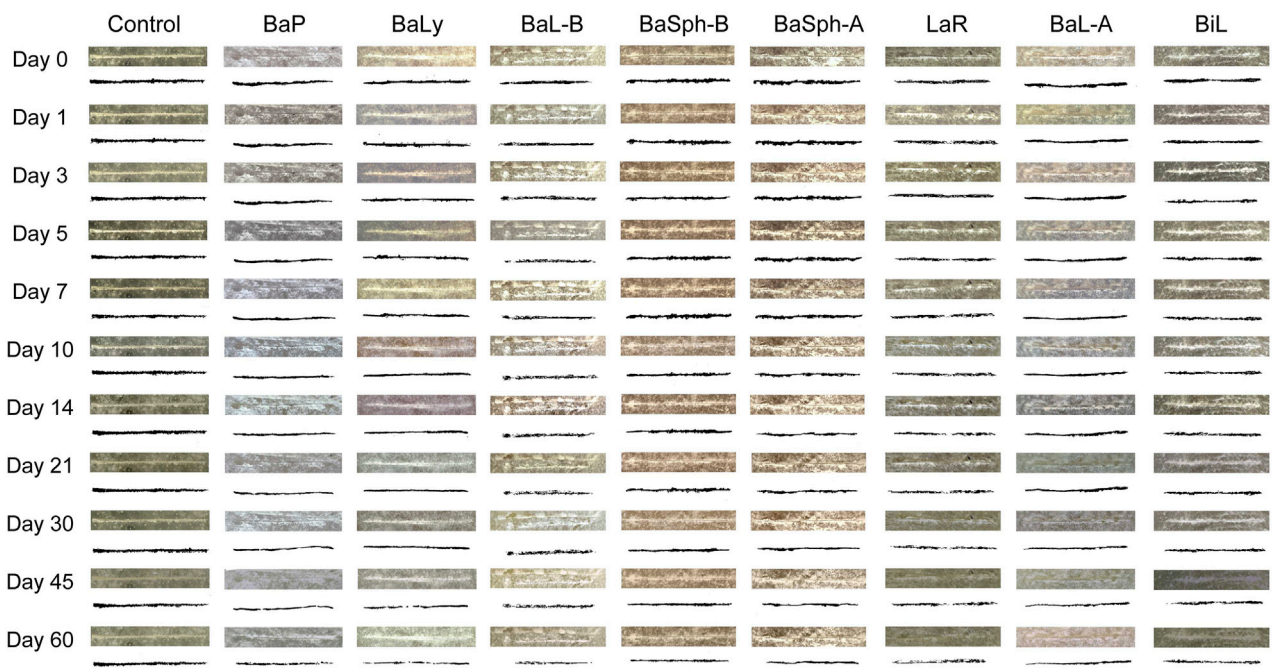

FIGURE 7
Observation and measurement of the secondary self-healing of scratches of resin splines (0–60 days) under stereomicroscope (3.2x). The control group's scratches remained relatively unchanged from day 1 to day 60, while the experimental groups displayed varying degrees of shallow, resembling the initial healing situations.

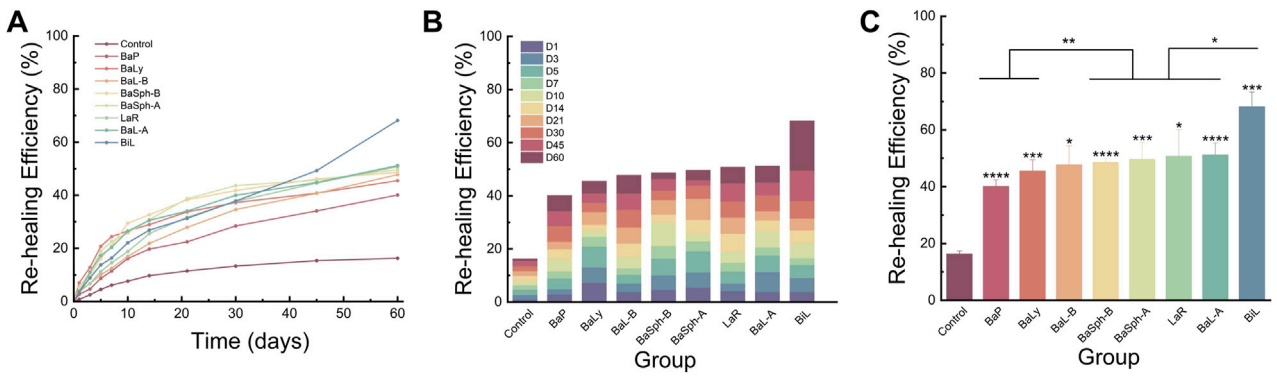

FIGURE 8
(A) Line chart and **(B)** stacked bar chart of comparation of secondary-healing rate in different groups in 60 days. **(C)** Bar chart of comparation of secondary-healing rate in different groups at day 60. *P < 0.05, **P < 0.01, ***P < 0.001, ****P < 0.0001.

In our study, each group consisted of either 6 or 12 samples. This sample size was determined by aligning with common practices in the field, considering the effect size and variability, and taking into account resource constraints. However, the relatively small sample size may limit the generalizability of our findings. Future research will explore larger sample sizes and more advanced techniques. Additionally, the 60-day observation period was selected because prior research on self-healing concrete has varied significantly in duration, with many studies spanning only 30 days. Given that bacterial-induced calcium carbonate formation generally requires a longer timeframe, we extended the observation period to 60 days to obtain more comprehensive and reliable data. Moreover, the present quantitative method employing stereomicroscopy for image acquisition exhibits certain limitations, primarily due to the involvement of subjective judgment. Future research endeavors will focus on exploring more objective techniques and tools to enhance the quantification of self-healing effects. Lastly, our study did not pursue qualitative analysis of the substance, as fundamental analytical tools such as EDS cannot provide a definitive confirmation, which is partly due to the semi-

TABLE 3 Secondary-healing rate (means±standard deviations, %) (n = 6) in different groups.

Time	Control	BaP	BaLy	BaL-B	BaSph-B	BaSph-A	LaR	BaL-A	BiL
Day 0	0	0	0	0	0	0	0	0	0
Day 1	0.8 ± 0.5	2.7 ± 0.4	7.0 ± 5.7	3.6 ± 0.7	4.3 ± 0.2	5.3 ± 2.2	4.0 ± 1.5	3.6 ± 1.3	3.6 ± 1.0
Day 3	2.5 ± 1.0	4.7 ± 1.5	12.9 ± 7.4	6.8 ± 0.7	9.8 ± 0.4	10.9 ± 2.9	6.8 ± 2.0	11.1 ± 3.5	8.9 ± 1.6
Day 5	4.5 ± 1.0	8.7 ± 3.5	20.8 ± 10.3	10.1 ± 1.7	16.2 ± 1.0	18.9 ± 4.1	11.3 ± 1.8	17.3 ± 2.8	13.7 ± 1.6
Day 7	6.1 ± 1.8	11.4 ± 4.9	24.4 ± 9.3	12.5 ± 1.8	20.9 ± 0.6	22.7 ± 2.6	14.6 ± 1.5	20.4 ± 2.7	16.4 ± 2.9
Day 10	7.7 ± 1.3	16.2 ± 5.6	26.6 ± 8.6	17.0 ± 2.3	29.5 ± 1.2	25.8 ± 4.4	18.8 ± 2.2	26.5 ± 6.6	22.1 ± 2.8
Day 14	9.7 ± 1.3	19.7 ± 4.9	28.9 ± 8.4	21.8 ± 3.6	32.7 ± 1.2	30.8 ± 4.2	25.6 ± 4.4	30.6 ± 5.8	26.9 ± 2.3
Day 21	11.5 ± 2.1	22.5 ± 5.1	33.7 ± 7.9	27.9 ± 4.0	38.3 ± 1.4	38.7 ± 3.9	31.7 ± 5.5	34.0 ± 4.4	31.3 ± 3.6
Day 30	13.3 ± 2.0	28.4 ± 4.7	37.2 ± 7.0	34.6 ± 5.6	41.8 ± 1.9	43.7 ± 3.9	37.7 ± 7.1	40.0 ± 5.1	37.8 ± 1.7
Day 45	15.4 ± 1.2	34.1 ± 3.2	40.8 ± 6.0	40.7 ± 6.1	46.2 ± 1.0	45.7 ± 3.8	44.6 ± 8.5	44.8 ± 5.2	49.3 ± 5.6
Day 60	16.3 ± 1.0	40.1 ± 2.1	45.5 ± 3.6	47.7 ± 6.0	48.6 ± 1.1	49.6 ± 4.8	50.8 ± 8.3	51.2 ± 3.8	68.2 ± 4.6

quantitative nature of EDS and the fact that our filler composition also contains Ca^{2+}, while the substance in question has been consistently identified as $CaCO_3$ in prior investigations of self-healing concrete (Wang J.-Y. et al., 2012; Wang J. et al., 2012; Achal et al., 2013; Wang et al., 2014a; Wang et al., 2014b; Wang et al., 2014c). Certainly, some studies have mentioned that X-ray Diffraction (XRD) (Wang J.-Y. et al., 2012; Wang J. et al., 2012) and Fourier Transform Infrared Spectroscopy (FTIR) (Achal et al., 2013) can be used to analyze crystalline materials and confirm the formation of calcium carbonate. We will address this gap in our future research by providing the relevant data.

The microorganisms and nutrients employed in this study are essential active ingredients in self-healing materials. *Bacillus* sphaericus and *Bacillus* licheniformis demonstrated high calcium carbonate production in specific condition (Seifan et al., 2016b), and self-healing concrete containing these bacteria, calcium lactate, and yeast extract can effectively repair cracks up to 0.46 mm in width (Wiktor and Jonkers, 2011). In this study, spores of *bacillus* were incorporated into resin composites instead of bacteria in the previous study (Seifan et al., 2020). The polymerization shrinkage of dental resin composites and changes in the oral environment can hinder bacterial biomineralization. However, *Bacillus* licheniformis, known for its resilient spores, can survive in challenging conditions, it is a promising candidate for dental materials, especially in the oral cavity's fluctuating temperatures.

Using a protective carrier to immobilize bacteria could offer a more effective solution, but additional research is required to further explore this possibility. Furthermore, this study demonstrated that the addition of Mn^{2+} to *Bacillus* culture significantly improved its self-healing abilities, resulting in superior performance compared to other strains, which is attributed to the ability of Mn^{2+} to enhance spore production per unit time (Xu et al., 2018). Therefore, future research efforts could concentrate on selected strains that effectively induce $CaCO_3$ precipitation and incorporating Mn^{2+} into *Bacillus* incubation to enhance self-healing properties.

Since Metchnikoff's pioneering work in 1907 (Metchnikoff, 2004), the definition of probiotics has significantly evolved. They are now defined as safe, beneficial, living microorganisms, primarily bacteria, that improve human health (Fuller, 1989) by regulating intestinal flora and enhancing immune function (Suez et al., 2019). Recent studies also highlight their potential benefits in oral health, including reducing harmful bacteria and preventing dental caries, periapical inflammation, and periodontal disease (Kumar et al., 2021; Homayouni Rad et al., 2023; Shi et al., 2023; Luo et al., 2024). The findings of this study highlighted the significant potential of Bifidobacterium longum and *Bacillus* licheniforms as powerful microorganisms with inherent self-healing properties, which were consistent with the results of previous study (Seifan et al., 2020), meanwhile, they are valuable probiotics which have been shown to be benign to the human body, which can actually assist in maintaining a healthy balance within both the gastrointestinal and oral microbiomes when incorporated into dental materials. Meanwhile, *Bacillus pasteurella* (B80469) had the weakest self-healing effect in the study, it referred that it may due to the inappropriate temperature of the oral environment, because *Bacillus pasteurella* should be cultivated at 30°C.

In addition to microorganisms, essential nutrients for their survival are crucial. Previous study (Seifan et al., 2020) on self-healing dental composites used urea (which can raise oral pH, harming cells and flora) and calcium chloride (which releases heat, risking burns and absorbing into the mucosa), which have toxic effects on organs and can corrode oral prostheses (Seifan et al., 2016a). Thus, they are unsuitable for dental materials. In contrast, this study used calcium lactate and yeast extract, which are common in oral care products. Calcium lactate forms $CaCO_3$ to heal dental resin composites safely, while yeast extract nourishes oral cells and maintains microbiota balance. However, it is important to investigate if dietary nutrients like calcium and glucose can compensate for oral nutrient losses. Moreover, microbial self-healing agents with poor compatibility can weaken dental resin composites. Future goals include using biocompatible and mechanically superior alternatives like polylactic acid. The study found that nutrient content decreases over time, reducing self-healing efficacy. The samples in this study were immersed in an artificial saliva solution composed of NaCl, KCl, $CaCl_2$, NaH_2PO_4, urea and Na_2S, which mimics the composition and concentration of

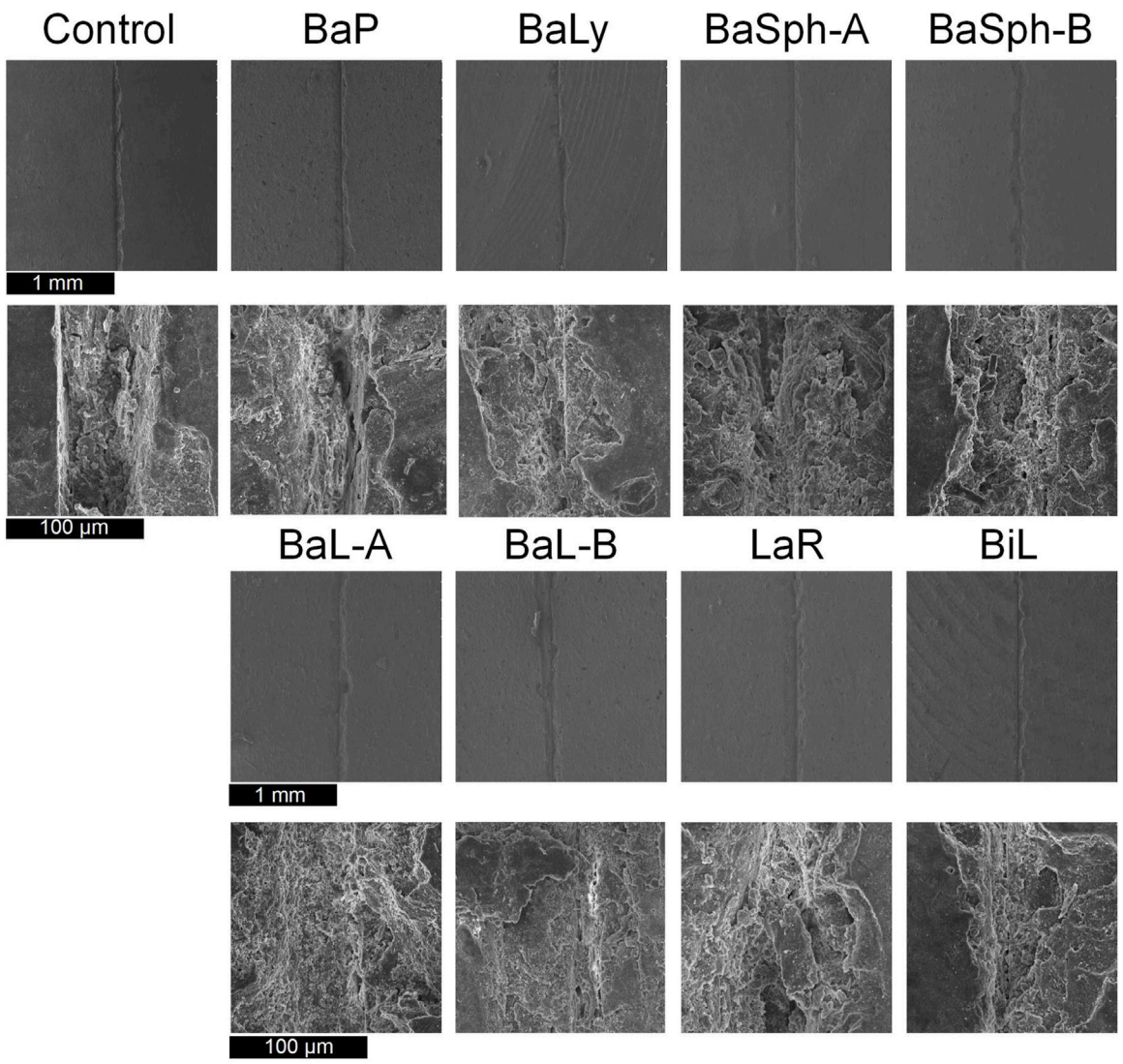

FIGURE 9
SEM images of the secondary healing of cracks of resin samples (day 60), a white substance can be observed within the scratches of the bacterial groups.

human saliva, thereby simulating the compensation of nutrients. While higher nutrient concentrations improve healing, they may increase costs and compromise mechanical properties. The proportion of the self-healing component in this study was set at 5% based on prior research (Huyang et al., 2016; Yahyazadehfar et al., 2018), which ensures high self-healing efficacy without compromising mechanical properties. However, determining the optimal dosage and ratio of probiotics and nutrients is vital for cost management and minimizing loss. In this study, microorganisms and nutrients were meticulously integrated into the fundamental components of the dental resin, this methodological approach aligns with the current best practices within the dental materials community, thereby ensuring both safety and efficacy. A series of comprehensive compatibility assessments will be conducted to ensure that this integration does not conflict with existing materials.

Moreover, resin composites commonly face issues with developing secondary caries due to polymerization shrinkage. Through the utilization of microbial self-healing technique, bacteria present within resin restoration may be activated during polymerization shrinkage and gap formation, which triggers biomineralization, leading to the creation of $CaCO_3$ or hydroxyapatite (HAP), thereby reducing the occurrence of secondary caries. Future research will focus on determining the effectiveness of this innovative self-healing dental resin composite that relies on biomineralization, in repairing microcracks and preventing secondary caries simultaneously, which aims to improve the overall success rate of resin restorations. Additionally, in environments rich in phosphates, $CaCO_3$ has the potential to convert into HAP (Wang et al., 2021). Further exploration may involve investigating ways to facilitate the conversion of $CaCO_3$ surrounding cracks into HAP, which would contribute to the enhanced restoration of tooth tissue and reinforcement of the mechanical properties of resin restorations.

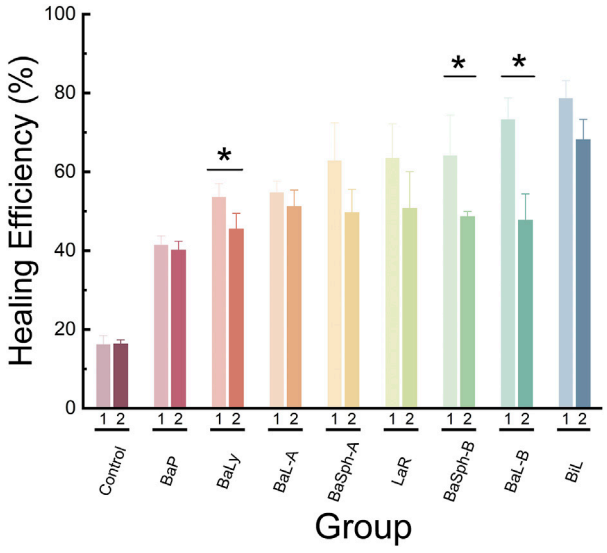

FIGURE 10
Comparation of healing rate and re-healing rate in different groups at day 60. *P < 0.05, **P < 0.01, ***P < 0.001, ****P < 0.0001.

5 Conclusion

This study is dedicated to the utilization of bacteria-mediated biomineralization technique in developing an innovative, biocompatible dental self-healing resin composite, capable of autonomously detecting and repairing cracks in simulated oral environments, which has demonstrated remarkable long-term self-healing abilities, including the capacity to repair the same crack twice. The bacteria, including beneficial probiotics, such as B81617 Bifidobacterium longum and ATCC9789 *Bacillus* licheniformis were selected based on their exceptional repeated self-healing properties. These strains have consistently demonstrated a remarkable healing efficiency that exceeds 70%, positioning them as exceptionally effective candidates for applications where consistent and reliable self-healing properties are essential. Meanwhile, the self-healing effect of *Bacillus* was significantly enhanced by the addition of Mn^{2+} during sporulation culture, which in turn increased the spore yield. These findings represent a significant advancement in the field of dental self-healing resin composites and offer a promising solution to the widespread issue of resin restoration fractures.

Data availability statement

The original contributions presented in the study are included in the article/supplementary material, further inquiries can be directed to the corresponding authors.

Author contributions

YH: Conceptualization, Data curation, Formal Analysis, Investigation, Methodology, Project administration, Software, Supervision, Validation, Visualization, Writing – original draft, Writing – review and editing. XZ: Data curation, Investigation, Software, Visualization, Writing – review and editing. JW: Data curation, Investigation, Software, Visualization, Writing – review and editing. ST: Data curation, Investigation, Software, Visualization, Writing – review and editing. XD: Resources, Writing – review and editing. ZC: Resources, Writing – review and editing. YiZ: Resources, Writing – review and editing. TW: Supervision, Writing – review and editing. DL: Methodology, Supervision, Writing – review and editing. YaZ: Funding acquisition, Project administration, Supervision, Writing – review and editing.

Funding

The author(s) declare that financial support was received for the research and/or publication of this article. The authors gratefully acknowledge the support of the National Natural Science Foundation of China (No. 82370953, 32201104), and the Science and Technology Commission of Shanghai Municipality (24QA2708100, 22010502600). The authors gratefully acknowledge the support of Shanghai Jiao Tong University School of Medicine and Shanghai University of Medicine and Health Sciences for supplying facilities and equipment.

Conflict of interest

The authors declare that the research was conducted in the absence of any commercial or financial relationships that could be construed as a potential conflict of interest.

Generative AI statement

The author(s) declare that no Generative AI was used in the creation of this manuscript.

Publisher's note

References

Achal, V., Mukerjee, A., and Reddy, M. S. (2013). Biogenic treatment improves the durability and remediates the cracks of concrete structures. *Constr. Build. Mater.* 48, 1–5. doi:10.1016/j.conbuildmat.2013.06.061

Achal, V., Mukherjee, A., and Reddy, M. S. (2011). Microbial concrete: way to enhance the durability of building structures. *J. Mater. Civ. Eng.* 23 (6), 730–734. doi:10.1061/(asce)mt.1943-5533.0000159

Deligeorgi, V., Mjör, I. A., and Wilson, N. H. H. (2001). An overview of reasons for the placement and replacement of restorations. *Prim. Dent. Care* 8 (1), 5–11. doi:10.1308/135576101771799335

Fuller, R. (1989). Probiotics in man and animals. *J. Appl. Bacteriol.* 66 (5), 365–378. doi:10.1111/j.1365-2672.1989.tb05105.x

Gollapudi, U., Knutson, C., Bang, S., and Islam, M. (1995). A new method for controlling leaching through permeable channels. *Chemosphere* 30 (4), 695–705. doi:10.1016/0045-6535(94)00435-w

Homayouni Rad, A., Pourjafar, H., and Mirzakhani, E. (2023). A comprehensive review of the application of probiotics and postbiotics in oral health. *Front. Cell. Infect. Microbiol.* 13, 1120995. doi:10.3389/fcimb.2023.1120995

Huyang, G., Debertin, A. E., and Sun, J. (2016). Design and development of self-healing dental composites. *Mater. and Des.* 94, 295–302. doi:10.1016/j.matdes.2016.01.046

Jonkers, H. M., Thijssen, A., Muyzer, G., Copuroglu, O., and Schlangen, E. (2010). Application of bacteria as self-healing agent for the development of sustainable concrete. *Ecol. Eng.* 36 (2), 230–235. doi:10.1016/j.ecoleng.2008.12.036

Khaliq, W., and Ehsan, M. B. (2016). Crack healing in concrete using various bio influenced self-healing techniques. *Constr. Build. Mater.* 102, 349–357. doi:10.1016/j.conbuildmat.2015.11.006

Kumar, G., Tewari, S., Tagg, J., Chikindas, M. L., Popov, I. V., and Tiwari, S. K. (2021). Can probiotics emerge as effective therapeutic agents in apical periodontitis? a review. *Probiotics Antimicrob. proteins* 13 (2), 299–314. doi:10.1007/s12602-021-09750-2

Luo, S.-C., Wei, S.-M., Luo, X.-T., Yang, Q.-Q., Wong, K.-H., Cheung, P. C., et al. (2024). How probiotics, prebiotics, synbiotics, and postbiotics prevent dental caries: an oral microbiota perspective. *npj Biofilms Microbiomes* 10 (1), 14. doi:10.1038/s41522-024-00488-7

Menikheim, S., Leckron, J., Duffy, M., Zupan, M., Mallory, A., Lien, W., et al. (2022). Biocompatible nanocapsules for self-healing dental resins and bone cements. *ACS omega* 7 (36), 31726–31735. doi:10.1021/acsomega.2c02080

Metchnikoff, I. I. (2004). *The prolongation of life: optimistic studies*. Springer Publishing Company.

Münchow, E. A., Meereis, C. T. W., da Rosa, W. L. d.O., da Silva, A. F., and Piva, E. (2018). Polymerization shrinkage stress of resin-based dental materials: a systematic review and meta-analyses of technique protocol and photo-activation strategies. *J. Mech. Behav. Biomed. Mater.* 82, 77–86. doi:10.1016/j.jmbbm.2018.03.004

Nitta, K., Nomoto, R., Tsubota, Y., Tsuchikawa, M., and Hayakawa, T. (2017). Characteristics of low polymerization shrinkage flowable resin composites in newly-developed cavity base materials for bulk filling technique. *Dent. Mater. J.* 36 (6), 740–746. doi:10.4012/dmj.2016-394

Okwadha, G. D., and Li, J. (2010). Optimum conditions for microbial carbonate precipitation. *Chemosphere* 81 (9), 1143–1148. doi:10.1016/j.chemosphere.2010.09.066

Organization, W. H. (2022). *Global oral health status report: towards universal health coverage for oral health by 2030*. Geneva: World Health Organization., Licensing: CC BY-NC-SA 3.0 IGO.

Ramachandran, S. K., Ramakrishnan, V., and Bang, S. S. (2001). Remediation of concrete using micro-organisms. *ACI Mater. Journal-American Concr. Inst.* 98 (1), 3–9. doi:10.14359/10154

Seifan, M., Samani, A. K., and Berenjian, A. (2016a). Bioconcrete: next generation of self-healing concrete. *Appl. Microbiol. Biotechnol.* 100, 2591–2602. doi:10.1007/s00253-016-7316-z

Seifan, M., Samani, A. K., and Berenjian, A. (2016b). Induced calcium carbonate precipitation using Bacillus species. *Appl. Microbiol. Biotechnol.* 100, 9895–9906. doi:10.1007/s00253-016-7701-7

Seifan, M., Sarabadani, Z., and Berenjian, A. (2020). Microbially induced calcium carbonate precipitation to design a new type of bio self-healing dental composite. *Appl. Microbiol. Biotechnol.* 104 (5), 2029–2037. doi:10.1007/s00253-019-10345-9

Shi, J., Wang, Q., Ruan, G., Chen, Y., Zhao, M., Shi, D., et al. (2023). Efficacy of probiotics against dental caries in children: a systematic review and meta-analysis. *Crit. Rev. Food Sci. Nutr.* 63 (29), 9977–9994. doi:10.1080/10408398.2022.2077693

Suez, J., Zmora, N., Segal, E., and Elinav, E. (2019). The pros, cons, and many unknowns of probiotics. *Nat. Med.* 25 (5), 716–729. doi:10.1038/s41591-019-0439-x

Van Tittelboom, K., De Belie, N., De Muynck, W., and Verstraete, W. (2010). Use of bacteria to repair cracks in concrete. *Cem. Concr. Res.* 40 (1), 157–166. doi:10.1016/j.cemconres.2009.08.025

Van Tittelboom, K., Wang, J., Araújo, M., Snoeck, D., Gruyaert, E., Debbaut, B., et al. (2016). Comparison of different approaches for self-healing concrete in a large-scale lab test. *Constr. Build. Mater.* 107, 125–137. doi:10.1016/j.conbuildmat.2015.12.186

Wang, J., Chen, H., Liu, H., Wang, R., Qin, Z., and Zhu, M. (2024). Surface modifications of short quartz fibers and their influence on the physicochemical properties and *in vitro* cell viability of dental composites. *Dent. Mater.* 40, e1–e10. doi:10.1016/j.dental.2024.05.023

Wang, J., Dewanckele, J., Cnudde, V., Van Vlierberghe, S., Verstraete, W., and De Belie, N. (2014a). X-ray computed tomography proof of bacterial-based self-healing in concrete. *Cem. Concr. Compos.* 53, 289–304. doi:10.1016/j.cemconcomp.2014.07.014

Wang, J., Snoeck, D., Van Vlierberghe, S., Verstraete, W., and De Belie, N. (2014b). Application of hydrogel encapsulated carbonate precipitating bacteria for approaching a realistic self-healing in concrete. *Constr. Build. Mater.* 68, 110–119. doi:10.1016/j.conbuildmat.2014.06.018

Wang, J., Soens, H., Verstraete, W., and De Belie, N. (2014c). Self-healing concrete by use of microencapsulated bacterial spores. *Cem. Concr. Res.* 56, 139–152. doi:10.1016/j.cemconres.2013.11.009

Wang, J., Van Tittelboom, K., De Belie, N., and Verstraete, W. (2012b). Use of silica gel or polyurethane immobilized bacteria for self-healing concrete. *Constr. Build. Mater.* 26 (1), 532–540. doi:10.1016/j.conbuildmat.2011.06.054

Wang, J.-Y., De Belie, N., and Verstraete, W. (2012a). Diatomaceous earth as a protective vehicle for bacteria applied for self-healing concrete. *J. industrial Microbiol. Biotechnol.* 39 (4), 567–577. doi:10.1007/s10295-011-1037-1

Wang, M., Wu, S., Guo, J., Liao, Z., Yang, Y., Chen, F., et al. (2021). Immobilization and migration of arsenic during the conversion of microbially induced calcium carbonate to hydroxylapatite. *J. Hazard. Mater.* 412, 125261. doi:10.1016/j.jhazmat.2021.125261

Wertzberger, B. E., Steere, J. T., Pfeifer, R. M., Nensel, M. A., Latta, M. A., and Gross, S. M. (2010). Physical characterization of a self-healing dental restorative material. *J. Appl. Polym. Sci.* 118 (1), 428–434. doi:10.1002/app.31542

Wiktor, V., and Jonkers, H. M. (2011). Quantification of crack-healing in novel bacteria-based self-healing concrete. *Cem. Concr. Compos.* 33 (7), 763–770. doi:10.1016/j.cemconcomp.2011.03.012

Wu, J., Weir, M. D., Zhang, Q., Zhou, C., Melo, M. A. S., and Xu, H. H. (2016). Novel self-healing dental resin with microcapsules of polymerizable triethylene glycol dimethacrylate and N, N-dihydroxyethyl-p-toluidine. *Dent. Mater.* 32 (2), 294–304. doi:10.1016/j.dental.2015.11.014

Xu, J., and Wang, X. (2018). Self-healing of concrete cracks by use of bacteria-containing low alkali cementitious material. *Constr. Build. Mater.* 167, 1–14. doi:10.1016/j.conbuildmat.2018.02.020

Xu, J., Wang, X., and Wang, B. (2018). Biochemical process of ureolysis-based microbial CaCO 3 precipitation and its application in self-healing concrete. *Appl. Microbiol. Biotechnol.* 102, 3121–3132. doi:10.1007/s00253-018-8779-x

Yahyazadehfar, M., Huyang, G., Wang, X., Fan, Y., Arola, D., and Sun, J. (2018). Durability of self-healing dental composites: a comparison of performance under monotonic and cyclic loading. *Mater. Sci. Eng. C* 93, 1020–1026. doi:10.1016/j.msec.2018.08.057

Yao, S., Qin, L., Wang, Z., Zhu, L., Zhou, C., and Wu, J. (2022). Novel nanoparticle-modified multifunctional microcapsules with self-healing and antibacterial activities for dental applications. *Dent. Mater.* 38 (8), 1301–1315. doi:10.1016/j.dental.2022.06.012

Yue, S., Wu, J., Zhang, Q., Zhang, K., Weir, M. D., Imazato, S., et al. (2018). Novel dental adhesive resin with crack self-healing, antimicrobial and remineralization properties. *J. Dent.* 75, 48–57. doi:10.1016/j.jdent.2018.05.009

frontiers | Frontiers in Bioengineering and Biotechnology

TYPE Systematic Review
PUBLISHED 25 June 2025
DOI 10.3389/fbioe.2025.1630495

OPEN ACCESS

EDITED BY
Nicholas G Fischer,
University of Minnesota Twin Cities,
United States

REVIEWED BY
Mahmoud Ebrahimi,
University of Maragheh, Iran
Roberta Gasparro,
University of Naples Federico II, Italy
Soodad Alhiloh,
phd in oral and maxillofacial
prosthodontics, Iraq

*CORRESPONDENCE
Antonio López-Valverde,
alopezvalverde@usal.es

RECEIVED 17 May 2025
ACCEPTED 16 June 2025
PUBLISHED 25 June 2025

CITATION
López-Valverde N, López-Valverde A and Blanco JA (2025) Effectiveness of bone expansion, compacting and densification in narrow alveolar crests: a systematic review and a meta-analysis.
Front. Bioeng. Biotechnol. 13:1630495.
doi: 10.3389/fbioe.2025.1630495

Effectiveness of bone expansion, compacting and densification in narrow alveolar crests: a systematic review and a meta-analysis

Nansi López-Valverde, Antonio López-Valverde* and José Antonio Blanco

Department of Surgery, Faculty of Medicine, University of Salamanca, Salamanca, Spain

Background: The treatment of edentulism with dental implants is a common and reliable procedure with high medium- and long-term survival rates. Primary stability in the bone is vitally important to prevent micro-movements at the beginning of healing. However, the main drawback of dental implantology is bone deficiency. To alleviate this situation, clinicians' resort to surgical techniques that increase bone volume and allow the devices to be placed. Bone expansion, compaction, and densification are used to compact the bone trabeculae, densifying the bone and improving the primary stability and osseointegration of implants. The aim of the study was to evaluate the role of these surgical techniques in deficient alveolar ridges in order to prepare them to receive durable dental implants.

Methods: Searches were made of the PubMed/Medline, Embase, Cochrane Central, Dentistry and Oral Sciences Source and Web of Science (WOS) databases and GreyNet International, to identify RCTs, prospective studies, retrospective studies and case series published in English in the last 15 years, which evaluated the efficacy of bone expansion, bone compaction and densification in narrow alveolar ridges and their impact on bone density (BD), alveolar ridge expansion (CE) and implant stability quotient (ISQ). Methodological quality was evaluated using the Joanna Briggs Institute for RCTs (JBI MAStARI) tool and risk of bias using the Cochrane Risk of Bias Tool (RoB2), and meta-analyses were performed using Review Manager 5.4.1 software to calculate effect size and integrate the results of the included studies.

Results: Ten of the 2,464 studies examined met the inclusion criteria. The meta-analysis of the parameters analyzed was favorable for the experimental group, indicating that bone expansion, compaction and densification techniques significantly increase DB (−0.71, 95% CI (Confidence Interval) [-1.15 to −0.27], p = 0.002), EC (−1.12, 95% CI [-2.21 to −0.03], p = 0.04) and ISQ (−8.88, 95% CI [-13.85 to −3.91], p = 0.0005), with a high publication bias for CE and ISQ.

Conclusion: The techniques of bone expansion, compaction and densification demonstrated their effectiveness in narrow alveolar ridges, although studies are needed to validate the results found.

Systematic Review Registration: Identifier CRD42025646738.

KEYWORDS

narrow alveolar ridge, crestal expansion, threaded expanders, osteotomes, bone compaction, bone densification

1 Introduction

The treatment of total or partial edentulism using dental implants has become common practice in dental surgeries and is currently considered a reliable and long-lasting surgical-prosthetic treatment, with survival rates estimated at over 90% over the first 10 years (Lekholm et al., 1999). The world market for dental implants is growing at a dizzying pace, with estimated figures in recent years exceeding 23 billion dollars (Alghamdi and Jansen, 2020).

The need for implant treatments due to edentulism increases exponentially with age and, in this sense, it has been estimated that the aging of the population during the third decade of this century will reach figures of more than 20% of the total European population and 30% of the US population (Höpflinger, 2015). However, despite all the advantages they offer, according to longitudinal studies, a certain number of implants, which the scientific literature estimates at percentages of around 15%–19% for the maxilla and 1.2% for the anterior mandibular area, fail (el Askary et al., 1999a; el Askary et al., 1999b), despite the fact that Espósito et al. reported that biology-related implant failures, out of a sample of 2,812 implants, did not reach 8% in a 5-year follow-up period (Esposito et al., 1998). For the implant to be successful, there needs to be adequate bone compression around the device and immediate fixation at the moment of insertion (primary stability), as well as long-term fixation (secondary stability) (Misch et al., 2008). Primary stability is vitally important for long-term success, as it prevents micromovements of the implant during the early stages of the healing process. The degree of primary stability can be influenced by a series of factors, such as the design of the implant, the size of the osteotomy, bone density and/or the patient's comorbidities (Heimes et al., 2023). It has been shown that high levels of primary stability at the time of implant insertion result in rapid secondary stability. Therefore, it is necessary to take maximum care of primary stability at the moment of insertion of the endosseous implant, to increase the chances of long-term permanence (Ivanova et al., 2021). It has been reported that the peri-implant bone must have a minimum thickness of 1.5 mm for the implant to support the loads (Chiapasco et al., 2009), however, bone deficit is the main drawback faced by dental implantology, and although 3D-printed scaffold-based technologies show promise for bone regeneration (Hao et al., 2024), failure rates in bone grafts are high due to insufficient blood supply necessary for integration and regeneration. When the alveolar crests lack adequate bone volume, additional surgical procedures are necessary to reconstruct and increase the bone deficit and, in this respect, several systematic reviews have identified the most appropriate techniques to provide the quality and quantity of alveolar bone necessary to allow the placement of a dental implant and, in addition, ensure its survival over time (Aghaloo and Moy, 2007; Aghaloo et al., 2016; Chiapasco et al., 2006). These reviews conclude that there is a certain discrepancy in the results of successes and failures of implants placed in surgically modified deficient ridges, with some indicating a higher failure rate (Crespi et al., 2021), others no significant differences (Elnayef et al., 2015) and others even reporting high success rates (Waechter et al., 2017; Anitua et al., 2013). This leads to a certain degree of confusion among clinicians, which means that making decisions based on scientific evidence when it comes to gaining bone volume in atrophic alveolar ridges is a complex task that is difficult to assess and predict. Furthermore, the variables change continuously, due, above all, to technological developments, the macro and micro design of the implants and the sophisticated diagnostic (Wang et al., 2025) and surgical techniques used. On the other hand, the avalanche and the large increase in publications in recent years on bone gain in atrophic edentulous ridges make it almost impossible to keep up to date with the latest techniques and appropriate instruments (Figure 1) and for all these reasons, the clinician must have the appropriate knowledge and criteria to put into practice the necessary surgical procedures that will provide the best results.

Horizontally deficient alveolar ridges are a common clinical situation, for which various procedures are performed to increase the crestal width: guided bone regeneration (GBR), division and expansion of the alveolar ridge, block bone grafts, etc. The division of the alveolar ridge was described by Tatum (1986), although it was Simion et al. (1992) who perfected it and published it in great detail in 1992. In 1994, Scipioni described the crestal expansion technique (CET) in edentulous jaws in a 5-year retrospective study on a large sample of 170 subjects and 329 implants (Scipioni et al., 1994). Subsequently, in 1999, he published a histological study on hard tissue repair in edentulous sites treated with the CET in 20 humans, suggesting that osteoblasts differentiate from pre-existing mesenchymal cells located in the original walls of the fissure, with the consequent deposition of new bone in the surgically created intraosseous defect (Scipioni et al., 1999).

"Bone compaction" (BC) and "bone densification" or "osteodensification" (ODT) are terms used to define a series of techniques that, through the use of certain surgical instruments, such as osteotomes, expanders, or specially designed surgical drills, generate compaction of the bone trabeculae. This produces tension from the osteotomy of the bone bed towards the outside, elastically deforming the bone through the tension produced by the osteodensifying surgical device, which, unlike perforating devices, does not cause bone loss. The elastic deformation of the bone would tend to return to its original shape when the tension disappears, increasing the original bone density. (Tricio et al., 1995).

All this, together with the incorporation of new techniques and equipment into clinical practice, would mean optimal use of alveolar ridges with bone deficiency, transforming them into useful sites for implant placement.

The aim of this systematic review and meta-analysis was to evaluate the effectiveness of bone expansion, compaction, and densification methods in narrow alveolar ridges to determine

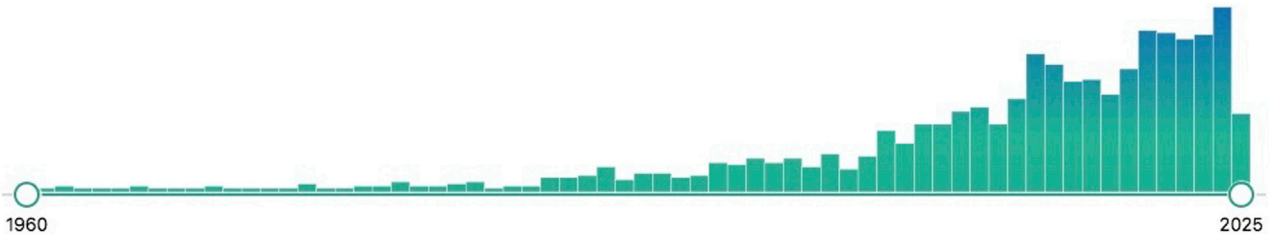

FIGURE 1
Graph of the increase in publications in recent years in PubMed using the term "ridge expansion".

TABLE 1 PICOs format.

Population (P)	Patients with horizontal atrophy of the maxillary or mandibular ridges
Intervention (I)	Expansive treatments, bone compaction or densification
Comparison (C)	Between different techniques or expansive treatments for bone compaction or densification
Outcomes (O)	Clinical parameters: Δ Bone density (BD); Δ Alveolar ridge expansion (ARE); Δ ISQ (Implant Stability Quotient)
Type of studies (s)	Randomized clinical trials (RCTs), case series, prospective studies and retrospective studies

Δ, variable increase; BD, bone density; ARE, alveolar ridge expansion; ISQ, implant stability quotient.

their usefulness in placing long-lasting dental implants, focusing on their impact on bone density (BD), alveolar crest expansion (ACE), and implant stability quotient (ISQ).

2 Methods

2.1 Presentation of the study

This systematic review has been carried out in accordance with the PRISMA (Preferred Reporting Items for Systematic Review and Meta-Analysis) criteria (Page et al., 2021) and the guidelines of the Clinical Practice Guidelines (Cumpston et al., 2019). The protocol for this systematic review has been registered in the PROSPERO database (International Prospective Register of Ongoing Systematic Reviews) with the registration number CRD42025646738.

2.2 Question of interest; PICOs format

The research question was approached according to the PICOs format: "Are methods of bone expansion, compaction or densification in narrow alveolar ridges, with horizontal atrophy, effective in promoting the long-term stability and durability of dental implants?"

To address the research question, intervention studies in adult patients with narrow maxillary and mandibular ridges were included (P), that evaluated or compared expansive treatment of bone compaction or densification (I), either with each other or with other surgical treatments (C), to observe the effects on the clinical parameters studied (O), considering only randomized clinical trials, case series, prospective studies and retrospective studies (s) (Table 1).

2.3 Data sources and bibliographic search method

An electronic search was carried out in the PubMed/Medline, Embase, Cochrane Central, Dentistry and Oral Sciences Source databases and in the Web of Science (WOS) scientific information service to identify RCTs, prospective studies, retrospective studies and case series published in English in the last 15 years, using the EndNote bibliographic reference manager (Clarivate Analytics). We also searched the gray literature to obtain as much information as possible and avoid publication bias (GreyNet International). The Boolean operators AND and OR were used. The search strategy was designed using the terms described in Table 2.

2.4 Inclusion and exclusion criteria

The research studies were selected according to the following inclusion criteria: (1) randomized clinical trials (single or double blind), case series and prospective and retrospective studies that included more than 5 adult subjects (≥18 years of age) in the study; (2) with alveolar ridges with horizontal atrophy (dimension ≤2.5 mm); (3) that provided data on clinical parameters indicative of this anatomical limitation; (4) with statistical methods that included means and standard deviation, together with units with which to quantify bone surfaces or volumes; (5) published in English. Studies that did not follow all the criteria defined above were excluded, as were clinical cases, studies lacking data on crestal anatomical limitation, *in vitro* or animal experimental studies, literature reviews and irrelevant studies, such as editorials, conference contributions, etc.

2.5 Data extraction

Data from each included study were extracted and tabulated by two reviewers (NL-V and AL-V) using the standardized JBI-MAStARI data extraction tools. The titles and abstracts of the

TABLE 2 Search strategy.

Databases	Search terms
PubMed/Medline	Alveolar Process/surgery [MeSH term] OR Alveolar Ridge Augmentation/methods [MeSH term] OR Bone regeneration [MeSH term] AND Alveolar Ridge Augmentation [MeSH term] Jaw, Edentulous/surgery [MeSH term] OR Alveolar Bone Loss/pathology OR Alveolar Bone Loss/surgery OR Bone Resorption OR Bone Resorption AND Bone Remodeling/physiology AND Dental implants [MeSH term] AND Dental implantation AND Dental Implantation, Endosseous AND Mouth, Edentulous/surgery AND Osseointegration AND Osteotomes AND Osteodensification AND Bone densification AND Humans [MeSH term]
Embase	Narrow maxilla AND Alveolar Ridge Augmentation/methods [MeSH term] OR Bone regeneration [MeSH term]
Cochrane Central	Narrow maxilla AND Alveolar Ridge Augmentation/methods [MeSH term] OR Bone regeneration [MeSH term] OR Osteodensification OR Bone densification AND Humans [MeSH term]
Dentistry and Oral Sciences	Alveolar Ridge Augmentation AND Alveolar Ridge Augmentation OR Osteodensification OR Bone densification
Web of Science	Narrow maxilla AND Alveolar Ridge Augmentation/methods OR Osteodensification OR Bone densification AND Humans
Boolean operators	AND y OR

MeSH, Medical Subject Headings (MEDLINE, thesaurus).

selected studies were reviewed by both reviewers. Those that met the inclusion criteria were read and the data extracted. The extracted data included specific details of the interventions, methods of delivery, populations, specific objectives, and significant results, in order to formulate the question of interest. Disagreements between reviewers were resolved through discussion and mediation by a third reviewer (JABR).

2.6 Evaluation of the quality of the results of the studies included

The studies included in this systematic review and meta-analysis were methodologically evaluated using the tool developed by the Joanna Briggs Institute for RCTs (JBI MAStARI), which adopts a particular point of view of the scientific evidence and the methods used to synthesize the different types of this evidence. The checklist consists of thirteen items and the responses to the items are either "yes", "no", "unclear" or "not applicable". A "yes" response scores one point. To be considered a methodologically sound study, it must score at least seven points (Jordan et al., 2019).

2.7 Risk of bias

The Cochrane Risk of Bias Tool (RoB2) (Sterne et al., 2019), which assesses 7 domains of bias: random sequence generation (selection bias), allocation concealment (selection bias), blinding of participants and staff (performance bias), blinding of outcome assessment (detection bias), and incomplete outcome data (attrition bias), was used for their assessment. Studies were assessed with "high," "low," and "borderline" risk of bias; "borderline" risk of bias applied to those with a lack of information about possible bias.

2.8 Meta-analysis

The data were analyzed using Review Manager software (RevMan Software. Version 5.4.1, The Cochrane Collaboration, Copenhagen, Denmark; 2020). The efficacy of methods of bone expansion, compaction and densification in narrow alveolar ridges to assess their usefulness when installing dental implants in a lasting way was evaluated by means of a meta-analysis for each of the clinical parameters analyzed. Due to the heterogeneity of the results in the ISQ and CE variables, a meta-analysis of random effects and fixed effects was performed for the BD variable, given its homogeneity. All were based on the standardized mean difference (SMD) and the confidence interval (95% CI). Heterogeneity was considered low with $I^2 = 0–30\%$; moderate with $I^2 = 40–50\%$; substantial with $I^2 = 60–75\%$; and high with $I^2 \geq 75\%$. The threshold for statistical significance was set at $p < 0.05$. No meta-analysis of adverse effects was performed due to the scarcity of reports on this topic.

3 Results

A total of 2,464 records were originally identified (981 in PubMed/MEDLINE, 1,382 in WOS, 26 in EMBASE, 11 in Cochrane Central and 64 in Dentistry and Oral Sciences), and 2,116 duplicate records relating to clinical case reports, animal studies and *in vitro* studies were eliminated in an initial screening. In a second screening, a further 306 records were eliminated because they were considered irrelevant or because they reported data that was of no interest for the objectives set out in our study, leaving 47 studies to be evaluated and their eligibility determined. Of these, 37 were eliminated because they either did not provide data, or the data they did provide was in the form of graphs or figures that could not be analyzed mathematically/statistically, leaving 10 studies (Vaddamanu et al., 2024; Rizk et al., 2024; Tofan et al., 2024; Tushar et al., 2024; Ahmed et al., 2022; Salman and Bede, 2022; Yadav et al., 2022; Bergamo et al., 2021; Koutouzis et al., 2019; Anitua and Alkhraisat, 2016) to include in our systematic review and meta-analysis in synthesis, qualitative and quantitative (Figure 2).

3.1 General characteristics of the studies included

A total of 241 subjects were included in the 10 selected studies. Five studies were RCTs (Vaddamanu et al., 2024; Rizk et al., 2024;

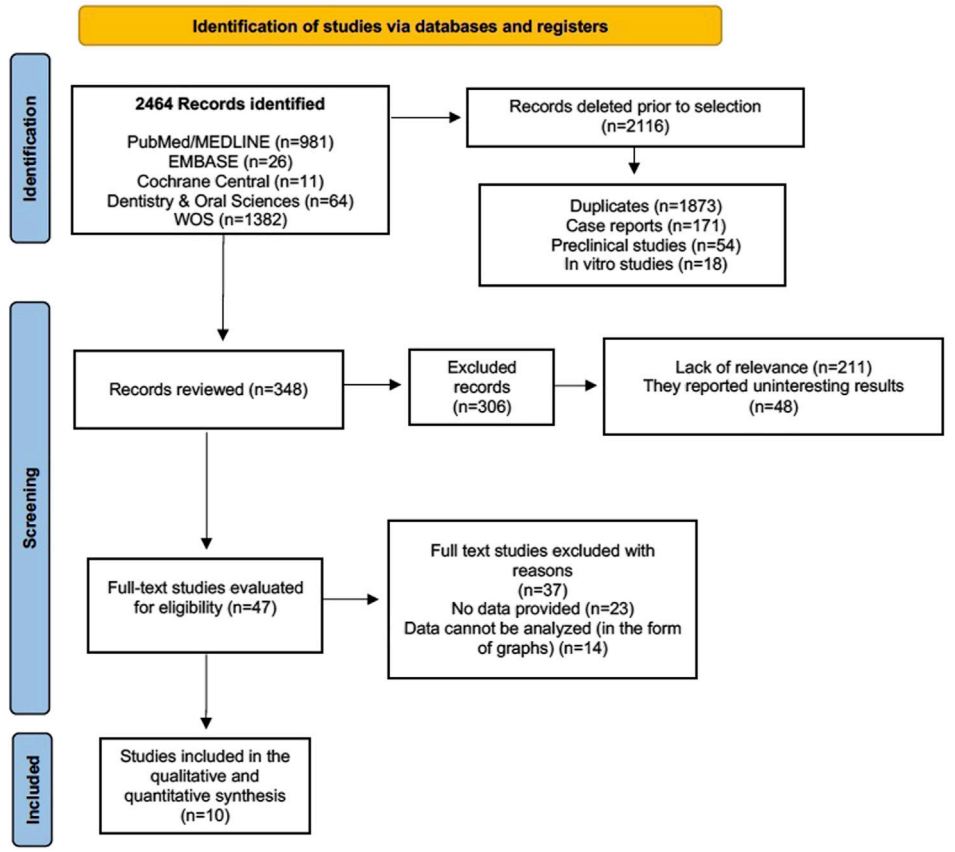

FIGURE 2
Flow chart.

Tofan et al., 2024; Tushar et al., 2024; Ahmed et al., 2022), two were prospective studies (Salman and Bede, 2022; Yadav et al., 2022) and three were retrospective studies (Bergamo et al., 2021; Koutouzis et al., 2019; Anitua and Alkhraisat, 2016). Two studies assessed the bone density (BD in HU) (Vaddamanu et al., 2024; Ahmed et al., 2022), eight the CE (in mm) (Rizk et al., 2024; Tofan et al., 2024; Tushar et al., 2024; Ahmed et al., 2022; Salman and Bede, 2022; Yadav et al., 2022; Koutouzis et al., 2019; Anitua and Alkhraisat, 2016) and three recorded the ISQ values (Tushar et al., 2024; Ahmed et al., 2022; Bergamo et al., 2021). The follow-up periods ranged from the immediate assessment after the surgical technique to 6 months post-intervention. Only three studies were registered on the ClinicalTrials.gov RCT platform. The general characteristics of the included studies are shown in Table 3.

3.2 Specific characteristics and sociodemographic data of the studies included

Two of the studies included were carried out in Egyptian centers (Rizk et al., 2024; Ahmed et al., 2022), two in Indian universities (Tushar et al., 2024; Yadav et al., 2022), two in Iraqi centers (Tofan et al., 2024; Salman and Bede, 2022) and the rest in Saudi Arabia, Brazil, United States and Spain [Vaddamanu et al., 2024; Bergamo et al., 2021; Koutouzis et al., 2019; Anitua and Alkhraisat, 2016, respectively]. The studies by Vaddamanu et al. (Vaddamanu et al., 2024) and Salman and Bede (2022) assessed the DO obtained using osteodensifying drills at the time of surgery and 6 months post-surgery. Five studies compared the DO obtained with osteodensifying drills and manual or motorized threaded expanders (Rizk et al., 2024; Tofan et al., 2024; Tushar et al., 2024; Ahmed et al., 2022). Bergamo et al. (2021) compared osteoconductive drills and conventional sequential drills in terms of DO. Yadav et al. (202)) assessed CE using manual threaded expanders and Anitua and Alkhraisat (2016) used motorized expanders to assess CE. Three studies evaluated the ISQ (Salman and Bede, 2022; Bergamo et al., 2021; Koutouzis et al., 2019) and most of the studies used CBCT as a radiological diagnostic tool (Rizk et al., 2024; Tofan et al., 2024; Tushar et al., 2024; Ahmed et al., 2022; Salman and Bede, 2022; Yadav et al., 2022; Koutouzis et al., 2019; Anitua and Alkhraisat, 2016). The specific characteristics of the studies are reflected in table 4.

TABLE 3 General characteristics of the studies included.

Study and year	Type of study and registration	Number of participants	Clinical parameters analyzed	Follow-up period	Results
Vaddamanu et al. (2024)	RCT. ClinicalTrials.gov N°: NCT06268639	32	BD (in HU)	Assessment was immediate pre- and post-operatively	The observed increases in ODT, evidenced by the substantial changes in HU, demonstrate the effectiveness of ODT as a valuable technique in dental implantology. By promoting a more favorable bone environment for implant integration, ODT could lead to better outcomes for dental implants, especially in situations of low BD in HU (pre-operative 821.3 ± 485.5; post-operative 1,126.7 ± 373.6)
Rizk et al. (2024)	Comparative RCT. Not registered Ethics committee: Department of Oral and Maxillofacial Surgery of the Faculty of Dentistry at Ain Shams University	14	CE (in mm)	6 months	The change in bone width when comparing osteodensifying drills and implant expanders, immediately after the intervention, was greater with osteodensifying drills ($p = 0.018$ and $p = 0.022$, respectively). After 6 months, the difference between the two groups was also significant ($p = 0.025$ vs. $p = 0.040$)
Tofan et al. (2024)	Comparative RCT. Not registered. Approval of the institutional research ethics committee (reference number 410121). Implantology Unit/ Department of Oral and Maxillofacial Surgery, Dental College Teaching Hospital, University of Baghdad, Iraq	19	CE (in mm)	Assessment was immediate pre- and post-operatively	There were no significant differences in the width of the alveolar ridge between the groups using osteodensifying drills and those using threaded expanders (5.48 ± 0.57 vs. 5.53 ± 0.71). However, the ODT technique using osteodensifying drills was much quicker to perform
Tushar et al. (2024)	Comparative study. Not registered. Institutional Ethics Committee of the Institute of Technology and Sciences. Dental College, Hospital and Research Center in Greater Noida, India. Approval number: ITSDCGN/ 2018/001	15	CE (in mm) Implant stability quotient (ISQ) BD (in HU)	6 months	The results for BD and ISQ were not significant. For bone measurements, the p-value was highly significant ($p < 0.01$)
Ahmed et al. (2022)	RCT. Not registered. Department of Oral and Maxillofacial Surgery of the Faculty of Dental Medicine of Al-Azhar University (Egypt)	20	Implant stability quotient (ISQ) and CE (in mm) BD (in HU)	6 months	The ODT zones showed a significantly higher insertion torque than the crestal split zones, however, the ODT showed a shorter duration than the crestal split. The horizontal bone gain in the postoperative period, at 6 months, did not show a significant difference (1.99 ± 0.68 vs. 2.63 ± 0.74)

(Continued on following page)

TABLE 3 (*Continued*) General characteristics of the studies included.

Study and year	Type of study and registration	Number of participants	Clinical parameters analyzed	Follow-up period	Results
Salman and Bede (2022)	Prospective study. Department of Oral and Maxillofacial Surgery, Faculty of Dentistry, University of Baghdad. Research Ethics Committee (protocol number: 207120). Registered at ClinicalTrials.gov (identification number: NCT04748952)	23	CE (in mm)	Assessment was immediate pre- and post-operatively	The average width of the bone before expansion was 4.04 ± 0.7 mm, while after expansion it was 5.3 ± 0.51 mm. The difference was statistically significant ($p < 0.001$)
Yadav et al. (2022)	Prospective study. No ethics committee appointment. Not registered	22	CE (in mm)	Assessment was immediate pre- and post-operatively	The preoperative bone width had an average value of 3.64 ± 0.41. After the operation, the bone width increased to an average value of 5.62 ± 0.45 mm. This postoperative increase was statistically significant ($p < 0.001$)
Bergamo et al. (2021)	Multicenter retrospective study. Ethics committees (protocol numbers #10295719.1.0000.5417 and #SH004 Integ Review). Clinical Trial Register (NCT04779203)	56	Implant stability quotient (ISQ)	6 months	The general ISQ data showed higher values for the experimental group (osteodensifying drills) compared to the control group (threaded osteotomes), regardless of the period evaluated (74 ± 1.5 vs. 66 ± 1.5). There were no significant differences in the mean expansion value in the apical zone between the groups; however, there was a difference in the crestal zone
Koutouzis et al. (2019)	Multicenter retrospective study. Not registered World Medical Association Declaration of Helsinki. All patients signed a consent form	21	CE (in mm)	Assessment was immediate pre- and post-operatively	The expansion did not show significant differences between the groups in the apical area (7.66 ± 1.41 vs. 8.66 ± 1.11). However, there was a significant difference in the crestal area. In group 1 (3–4 mm ridge) 75% expansion
Anitua and Alkhraisat (2016)	Retrospective study in accordance with the Declaration of Helsinki for research on human beings. Not registered	20	CE (in mm)	6 months	The preoperative width of the alveolar ridge was 3.1 mm (range, 2–6 mm) as measured on CBCT images. The surgical technique using osteotomes and transitional implants increased this width to 5.1 mm (range, 3.7–7.4 mm)

BD, bone density; HU, hounsfield unit; CE, crestal expansion; ISQ, implant stability quotient; ODT, osteodensification technique; CBCT, cone beam computed tomography.

3.3 Methodological rigor (JBI MAStARI)

The methodological quality of the studies ranged from those that exceeded the 7 basic points considered to be of high/adequate methodological rigor (Vaddamanu et al., 2024; Rizk et al., 2024; Tofan et al., 2024; Tushar et al., 2024; Ahmed et al., 2022) to those that obtained a lower score (Salman and Bede, 2022; Yadav et al., 2022; Bergamo et al., 2021; Koutouzis et al., 2019; Anitua and Alkhraisat, 2016). However, the latter were prospective and retrospective studies and as such, lacked a control group; furthermore, they did not follow the criteria of randomization and blinding (Figure 3).

3.4 Overall meta-analysis

A meta-analysis of continuous variables was proposed that included means and standard deviations. Three individual meta-analyses were carried out according to the parameter analyzed: one for BD, a second for horizontal CE and a third for implant stability (ISQ), according to the surgical techniques proposed in the different studies. Heterogeneity ranged from 0% for the BD meta-analysis to 96% for the CE and ISQ meta-analyses, so a fixed-effect meta-analysis was performed for the BD variable and a random-effects meta-analysis for the ISQ and CE. No analysis of adverse effects was performed due to lack of data.

TABLE 4 Specific characteristics of the studies included.

Study	Center and country	Anatomical characteristics of the subjects included	Surgical technique; equipment	Radiological analysis	Implant stability measurement
Vaddamanu et al. (2024)	King Khalid University. Saudi Arabia	People with partial or complete edentulous ridges in the maxilla or mandible	Osteodensifying drills (Huwais Technique)	Dentascan (CT) (DICOM software)	
Rizk et al. (2024)	Department of Oral and Maxillofacial Surgery at the Faculty of Dentistry, Ain Shams University. Egypt	Patients >18 years of age with totally or partially edentulous maxillary ridges, with horizontal bone defects, in which the bucco-palatal dimension >4 mm, with a minimum of 2 mm of trabecular bone core between the cortical plates and a height >10 mm	Osteodensifying drills (Huwais Technique) Manual threaded expanders	CBCT scan. (DICOM software)	
Tofan et al. (2024)	The Implantology Unit/ Department of Oral and Maxillofacial Surgery, Dental College Teaching Hospital, University of Baghdad. Irak	Trabecular bone core ≥2 mm and trabecular/cortical bone ratio ≥1/1	Osteodensifying drills (Huwais Technique) Motorized threaded expanders	CBCT scan	
Tushar et al. (2024)	Institute of Technology and Sciences Dental College, Hospital and Research Center in Greater Noida. India	Absence of maxillary anterior teeth in the first and second quadrants with a horizontal width of bone >3–4 mm	Osteodensifying drills (Huwais Technique) Motorized threaded expanders	CBCT scan	
Ahmed et al. (2022)	Faculty of Dental medicine, Al-Azhar University. Egypt	Patients ≥18 years of age of both sexes with a long-standing edentulous area in the mandible that has healed for at least 6 months after extraction and an alveolar crest with horizontal dimensions of 3–6 mm width in the buccolingual direction and vertical dimensions >10 mm in height	Piezoelectric surgery with horizontal crestal incision. Osteodensifying drills (Huwais technique). Manual expanders	CBCT scan	
Salman and Bede (2022)	Department of Oral and Maxillofacial Surgery, College of Dentistry, University of Baghdad. Irak	Patients aged 18 years or over, with an alveolar crest width of 3–5 mm, with a trabecular bone core of ≥2 mm and a trabecular/ cortical bone ratio of ≥1/1, as well as sufficient vertical dimensions	Osteodensifying drills (Huwais technique)	CBCT scan	ISQ. (Osstell Beacon®)
Yadav et al. (2022)	University of Medical Sciences, Saifai, Etawah, Uttar Pradesh. India	Patients aged between 20 and 60 with sufficient residual alveolar ridge height and width >3 mm	Threaded expanders	CBCT scan	
Bergamo et al. (2021)	Department of Prosthodontics and Periodontology, University of Sao Paulo, School of Dentistry. Brazil	It does not provide anatomical details of bone crests	Osteodensifying drills (Huwais technique) Conventional sequential drilling		ISQ (Osstell Mentor®)
Koutouzis et al. (2019)	Department of Periodontology, College of Dental Medicine, Nova Southeastern University, Florida. United States	It does not provide anatomical details of bone crests	Osteodensifying drills (Huwais technique)	CBCT scan	ISQ (Ostell, Gothenburg, Sweden®)
Anitua and Alkhraisat (2016)	Department Head, Eduardo Anitua Foundation, Vitoria, Spain	Horizontal bone atrophy in the jaw	Ultrasonic sagittal osteotomy. Motorized expanders (BTI Biotechnology Institute, Vitoria, Spain)	CBCT scan	

CBCT, cone beam computed tomography; DICOM, digital imaging and communications in medicine; ISQ, implant stability quotient.

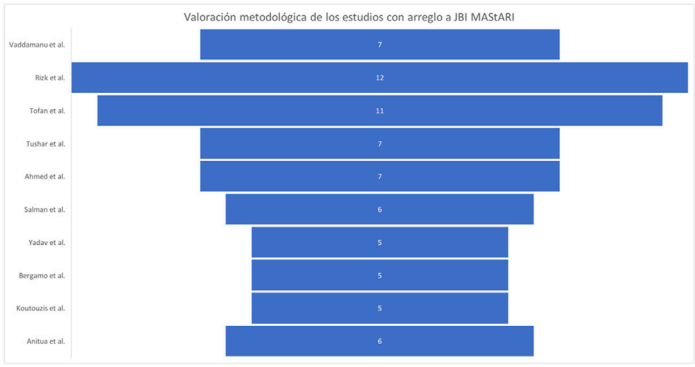

Questions:

Q1. Was true randomisation used for assigning participants to treatment groups?; **Q2.** Was allocation to treatment groups concealed?; **Q3.** Were treatment groups similar at the baseline?; **Q4.** Were participants blind to treatment assignment?; **Q5.** Were those delivering treatment blind to treatment assignment?; **Q6.** Were outcomes assessors blind to treatment assignment?; **Q7.** Were treatment groups treated identically other than the intervention of interest?; **Q8.** Was follow-up complete and if not, were differences between groups in terms of their follow- up adequately described and analysed?; **Q9.** Were participants analysed in the groups to which they were randomized?; **Q10.** Were outcomes measured in the same way for treatment groups?; **Q11.** Were outcomes measured in a reliable way?; **Q12.** Was appropriate statistical analysis used**?; Q13.** Was the trial design appropriate, and any deviation from the standard RCT design accounted for in the conduct and analysis of the trial?.

FIGURE 3
Methodological evaluation graph according to the Joanna Briggs Institute tool.

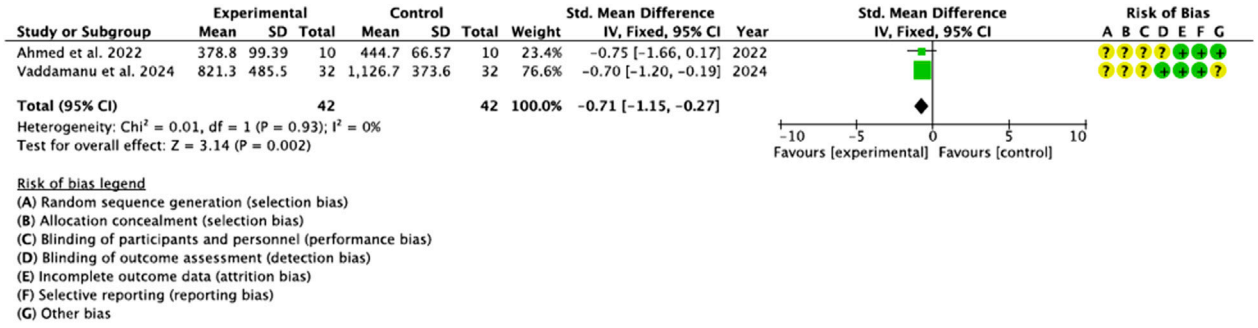

FIGURE 4
Forest plot for BD.

3.4.1 BD

Two studies (Vaddamanu et al., 2024; Ahmed et al., 2022) provided data on the increases through osteodensification observed in BD. We identified no heterogeneity in the included studies (I^2 = 0%). The meta-analysis showed a significant trend towards the experimental group compared to the control group (−0.71, 95% CI [-1.15 to −0.27], p = 0.002). (Figure 4).

3.4.2 CE

Eight studies (Vaddamanu et al., 2024; Rizk et al., 2024; Tofan et al., 2024; Tushar et al., 2024; Ahmed et al., 2022; Salman and Bede, 2022; Koutouzis et al., 2019; Anitua and Alkhraisat, 2016) provided data on the gain in crestal width using different expansion techniques. Heterogeneity was high before and after the sensitivity test ($I^2 \geq 75\%$). The meta-analysis before the sensitivity test was not significant (0.41, 95% CI [-1.02 to 0.84], p = 0.58); however, after the sensitivity test, once the studies by Yadav et al., Koutouzis et al. and Anitua and Alkhraisat (Yadav et al., 2022; Anitua and Alkhraisat, 2016) had been eliminated, it showed statistical significance in favor of the experimental group (−1.12, 95% CI [-2.21 to −0.03], p = 0.04). (Figure 5).

3.4.3 ISQ

Three of the studies included (Tushar et al., 2024; Ahmed et al., 2022; Bergamo et al., 2021) provided available data on the parameter of implant stability following expansion and ODT. Heterogeneity was high (I^2 = 96%) and the meta-analysis showed a significant trend towards the experimental group compared to the control group (−8.88, 95% CI [-13.85 to −3.91], p = 0.0005). (Figure 6).

3.5 Risk of bias

One of the pillars of evidence-based medicine is risk of bias and, therefore, the quality of the included studies was analyzed using the Cochrane Risk of Bias tool (Sterne et al., 2019). The studies were evaluated in 5 areas: (1) the randomization process; (2) deviations from planned interventions; (3) scarce or non-existent results data; (4) measurement of these results; (5) selection of the reported result and a sixth bias (6) which is related to the other biases. According to the Cochrane Handbook for Systematic Reviews of Interventions, a rating of "high" was given to studies considered to have a high risk of bias, "low" to those with a low risk of bias, and "borderline" to those with an unclear risk of bias or lack of information on possible bias. However, some studies included randomization software, and it was

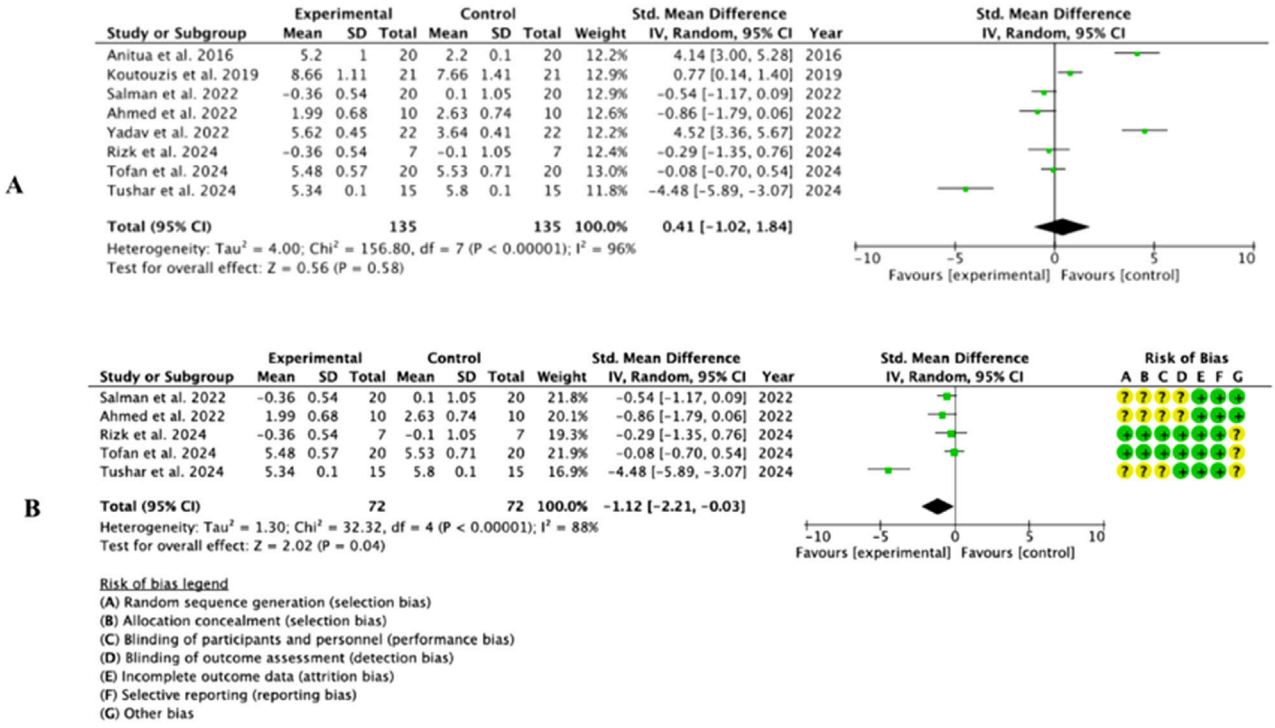

FIGURE 5
Forest Plot before **(A)** and after **(B)** the sensitivity analysis of the CE parameter.

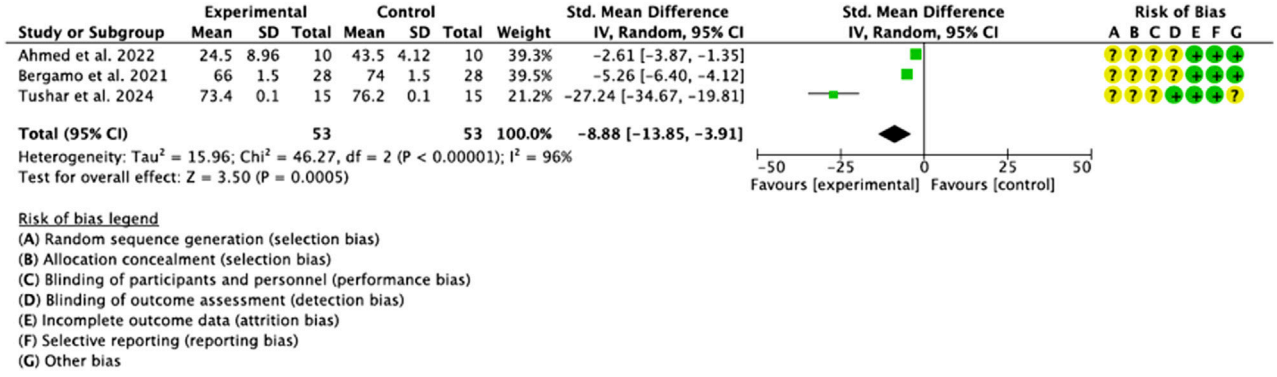

FIGURE 6
Forest Plot of the ISQ parameter.

difficult to assess which domains they referred to and which they did not. The domains "random sequence generation" (selection bias), "allocation concealment" (selection bias), "blinding of participants and personnel" (performance bias) and "blinding of outcome assessment" (detection bias) were the ones with the greatest uncertainty. The study by Anitua and Alkhraisat (2016) was the one that presented the greatest risk, especially in domains 1 and 2 (selection biases) "random sequence generation" and "allocation concealment", despite the authors recognizing among the limitations that, being a study with a retrospective design, it lacked a control group, and there was no randomization or blinding. The studies with the lowest risk of bias were those of Rizk et al. (2024) and Tofan et al. (2024) (Figure 7).

3.6 Publication bias

The x-axis represents the observed results, and the y-axis represents the standard error. No dispersion was found in the funnel plot for BD (A), however, the plots for the variables CE and ISQ (B and C) showed a marked dispersion, which is evidence of a significant publication bias (Figure 8).

FIGURE 7
Graphic indicating risk of bias.

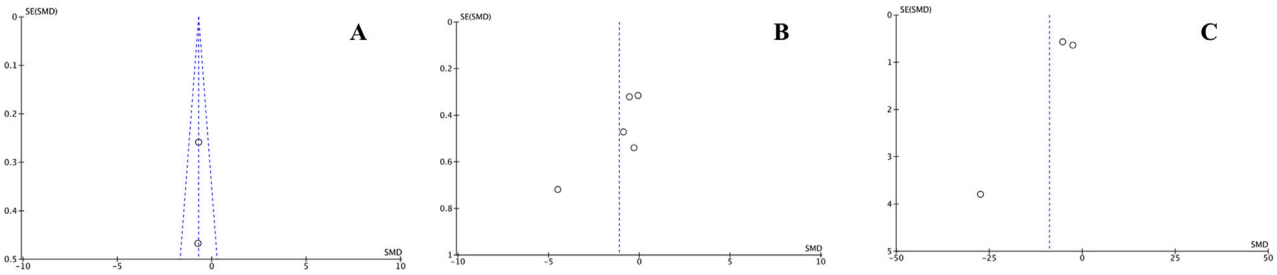

FIGURE 8
Publication biases expressed in funnel plots for the variables DO **(A)**, CE **(B)** and ISQ **(C)**.

4 Discussion

In addition to systematically reviewing the current scientific literature, our study used a meta-analysis to evaluate the effectiveness of methods of bone expansion, compaction and densification in deficient alveolar ridges, in order to predict their usefulness when installing long-lasting dental implants. To increase the power of this systematic review, several types of studies were combined: RCTs, case series and prospective and retrospective studies. However, this particularity skews and limits the results. In fact, the studies with the worst evaluation were the prospective and retrospective ones that were not guided by randomization criteria; however, when the sample sizes of the primary studies are small, the combination of studies increases the statistical power.

The main result of our meta-analysis was that bone expansion, compaction, and densification methods in narrow alveolar ridges increase BD, ACE, and ISQ, making them useful for receiving dental implants.

A meta-analysis consists of conducting systematic reviews of quantitative and mathematical-statistical data from individual studies, using the data provided by the included studies, and calculating a statistical mean and an effect size for the event or treatment studied. Meta-analysis evaluates the need for future research (Sterne et al., 2019; Bown and Sutton, 2010), depending on the quality of the individual studies included (Straus and McAlister, 2000; Scheidt et al., 2019). Muka et al. (2020) proposed guidelines on how to conduct a systematic review and meta-analysis of observational studies and pooled RCTs, which served as a guide for our study.

Five RCTs (Vaddamanu et al., 2024; Rizk et al., 2024; Tofan et al., 2024; Tushar et al., 2024; Ahmed et al., 2022) and five observational studies (Salman and Bede, 2022; Yadav et al., 2022;

Bergamo et al., 2021; Koutouzis et al., 2019; Anitua and Alkhraisat, 2016) met the inclusion criteria. The study by Tushar et al. (2024) found no differences in the ISQ between the groups comparing the motorized expanders and the osteodensifying drills; however, the motorized ridge expanders proved to be more effective in expanding the ridge, with a highly significant value ($p < 0.01$) and achieved, after 6 months, better primary stability than the ODT. These results would be contrary to those reported in the literature (Gaikwad et al., 2022; Lima Monteiro et al., 2024; Inchingolo et al., 2021).

The BD was evaluated by two RCTs (Vaddamanu et al., 2024; Ahmed et al., 2022) highlighting the benefits of ODT on BD and the primary stability of the implant, with the distal region of the osteotomy presenting the greatest BD (Vaddamanu et al., 2024). Ahmed et al. (2022) attribute the advantages of ODT to the autograft bone particles that would function as a nucleus for faster bone development around the implant, which could reduce healing time. However, Inchingolo et al. (2021) in a recent meta-analysis highlighted what we have emphasized about the existing contradictions in this regard in the literature. Some studies provide solid results that confirm the benefits of ODT, backed up by some statistically relevant values (Padhye et al., 2020; Hindi and Bede, 2020; Pai et al., 2018) and others, on the contrary, do not provide data that demonstrate differences in relation to the conventional technique. Koutouzis et al. in a retrospective multicenter study (Koutouzis et al., 2019) found no significant differences in the mean expansion value between the groups treated with and without ODT. Two preclinical studies in experimental sheep models (Lahens et al., 2019; Trisi et al., 2016) also found no differences in the osseointegration of implants placed with or without ODT. In this respect, the conclusions of a preclinical study published in the Journal of Dental Research (Wa et al., 2017) in a murine model are striking, providing evidence that condensation can increase the density of the peri-implant bone, although it does not guarantee greater bone-implant contact, nor does it improve implant stability. Compacted bone is denser, in the sense that it has a higher bone volume/total volume (BV/TV), however, this compacted bone would be structurally damaged and weakened (Zhang et al., 2021).

Tushar et al. (2024), Ahmed et al. (2022) compared variations in implant stability (ISQ index) in expanded bones in two RCTs; the first study using motorized expanders and the ODT, and the second using manual expanders and the ODT. Tushar et al. (2024) support the use of motorized expanders over bone densification, since, according to the authors, it limits CE. These conclusions would contradict certain reviews of the scientific literature that give greater popularity to the use of osteotomes, especially in the maxillary bone, due to the lower possibility of generating heat and the greater initial stability of the implant, due to lateral bone condensation (González-García et al., 2011; Jha et al., 2017). For their part, Ahmed et al. (2022) resorted to crestal corticotomy, combined either with manual expanders or osteodensifying drills, granting the latter technique greater implant stability, with results coinciding with those of Huwais and Meyer (2017). Bergamo et al. (2021) carried out a prospective multicenter study on 56 patients and 150 implants in several institutions, with a follow-up period of 6 months, and found that the ISQ values were higher for the experimental group (osteodensifying drills) compared to the control group (threaded osteotomes). However, despite the fact that implant insertion torque is the most common criterion for assessing adequate primary stability (Gallucci et al., 2018) and that low insertion torque (≤35 N force) is a controversial factor in the survival rate of dental implants, a recent systematic review with meta-analysis by Darriba et al. (2023) who evaluated the success rates at 24 months in 326 implants with immediate loading, concluded that a low insertion torque does not have a significant effect on implant survival rates. In this respect, another systematic review and meta-analysis carried out by Be et al. (2016) which included four studies in humans and six in animals, highlighted the lack of evidence in favor of high or low torque implants for our outcomes of interest: bone resorption, implant failure and BIC.

All these conclusions from the different studies lead us to consider the discrepancies that exist in the scientific literature on insertion torque values, from those who recommend low or moderate values, which allow the formation of considerable amounts of new bone that recovers around the implant (BIC, bone to implant contact) during the first stage of osseointegration (Duyck et al., 2015), to those who propose high insertion torques (>80 N) on the grounds that these high ISQ values would not cause bone resorption or implant failure (Consolo et al., 2013; Trisi et al., 2011). An example of this is the study by Khayat et al. (2013) who reported, in a prospective controlled clinical trial in humans, that the use of a high insertion torque of up to 176 N did not prevent osseointegration of the implant and did not cause marginal bone loss. Another recent comparative study (Arpudaswamy et al., 2024) that evaluated insertion torque and ISQ at the time of implant placement, and secondary stability metrics such as ISQ 3 months after insertion, between implants inserted into osteotomy sites prepared with conventional drills and osteosynthesis drills in the femoral condyles of New Zealand white rabbits, with low-density bone (type D4), showed that implants placed using ODT exhibited superior initial stability and superior stability progression, compared to those placed using conventional drilling techniques. Clinically, this would mean that ODT shows a higher insertion torque and a higher ISQ, by improving the bone density and volume surrounding the implants. This increased stability can lead to better osseointegration and a reduction in healing times, which ultimately benefits patients with compromised bone quality. On the other hand, Schierano et al., in a preclinical study published at the beginning of 2025 (Schierano et al., 2025), highlight the advantages of piezoelectric surgery in biological and clinical responses, especially in the increase of certain osteogenic factors and the formation of new bone, as well as a possible association with an increase in the ISQ.

CE was a clinical parameter evaluated in eight studies (Rizk et al., 2024; Tofan et al., 2024; Tushar et al., 2024; Ahmed et al., 2022; Salman and Bede, 2022; Yadav et al., 2022; Koutouzis et al., 2019; Anitua and Alkhraisat, 2016), resulting in the most highly valued of the three analyzed. Four of them were RCTs (Rizk et al., 2024; Tofan et al., 2024; Tushar et al., 2024; Ahmed et al., 2022) and four more (Salman and Bede, 2022; Yadav et al., 2022; Koutouzis et al., 2019; Anitua and Alkhraisat, 2016) were observational studies. Within the context of RCTs, Rizk et al. (2024), Tushar et al. (2024) and Ahmed et al. (2022) compared ODT with CE techniques, such as threaded expanders, either manual (Rizk et al., 2024), motorized (Tushar et al., 2024) or crestal corticotomy ("split") (Ahmed et al., 2022). The results reported by these studies are completely contradictory. Rizk

et al. (2024) analyzed fourteen implants placed in eight patients, seven using the osteodensifying drill technique and seven using expansion with manual threaded expanders. The analysis was carried out at three points: point 0 (below the implant cover screw), point A (1 mm below the level of the cover screw) and point B (2 mm below the level of the cover screw), in the immediate postoperative period and 6 months after placement. In the immediate postoperative period, they found a statistically significant difference between the two groups at points 0 and A in the experimental group (ODT) with the control group (manual expansion); however, the difference at point B was not statistically significant. Six months after insertion they found that the crest was undergoing continuous remodeling and, in some implants, the width of the alveolar crest was slightly less than the width of the preoperative alveolar crest. They even attribute the failure of three implants (despite the normal radiographic image of the surrounding bone) to the increase in bone density in the narrow alveolar crest, which could have caused a decrease in blood supply and an increase in temperature during surgery, for which reason they recommend using expansion techniques only in cases where other more predictable methods for horizontal bone augmentation are not feasible, such as GBR, bone blocks and crestal splitting. The conclusions of Rizk et al. (2024) are contradicted by those of Tushar et al. (2024), Ahmed et al. (2022) who propose expansion techniques (motorized expanders, ODT and split techniques) as effective methods for the expansion of narrow ridges. A systematic review carried out by Padhye et al. (2020) concluded by stating that, through ODT, bone expansion is achieved at the osteotomy site, although they recognize the need for well-designed prospective cohorts and randomized controlled trials to definitively establish the credibility of these techniques, both in the biological aspect and in clinical success. Similar conclusions are proposed by Inchingolo et al. (2021) who recommend thorough training of professionals before resorting to these techniques, considering them, from a practical point of view, complex to perform in inexperienced hands, describing the studies carried out to date as" modest and immature", something we do not agree with, since the three studies discussed (Rizk et al., 2024; Tushar et al., 2024; Ahmed et al., 2022) achieved an adequate score on the JBI MAStARI scale of methodological quality, especially the study by Rizk et al. (2024) which achieved almost the maximum score.

The observational studies included (Salman and Bede, 2022; Yadav et al., 2022; Koutouzis et al., 2019; Anitua and Alkhraisat, 2016) evaluated 86 patients who received 119 implants with different conclusions that are presented and discussed below: Salman and Bede (2022) in a prospective study of 23 subjects, evaluated CE in narrow alveolar ridges, with low BD, before and after the use of osteodensifying drills, reaching the conclusion that the use of this type of device produced bone expansion without dehiscence or fenestration, increasing the width of the alveolar crest between 4 and 5.3 mm and allowing the simultaneous placement of implants with high primary and secondary stability. These results would be consistent with those obtained by Koutouzis et al. (2019) who, in a retrospective multicenter study of 21 subjects, also concluded that ODT allowed for an expansion of the alveolar crests in the coronal area of 3–8 mm (average 5.2 mm). Other studies (Tricio et al., 1995) also coincided in their results with the previous ones, reporting, through these expansion techniques, increases in crestal width ranging from 1.1 to 2.4 mm. Jarikian et al. (2021) in a non-randomized clinical study of 11 patients who had received 28 implants, compared ODT with bone densifying drills in narrow alveolar ridges (4–5 mm), obtaining similar results with an average of 2.36 mm of expansion, compared to the 1.5 mm achieved with threaded expanders. However, some preclinical studies have reported different results with regard to bone expansion, using ODT. Yeh et al. (2021) found that the ODT increased bone mineral density and primary contact between bone and implant in bovine rib segments; they also suggested that implant placement using ODT, compared to conventional drilling, can increase ridge dimensions in narrow alveolar ridges. Similarly, Li et al. (2023) demonstrated *ex vivo* that ODT increases the primary stability of cylindrical implants without overheating the bone and significantly increases the width of the crest. However, Tian et al. (2019), in atrophic mandibular ridges, in a porcine model, compared the ODT with the conventional osteotome technique, finding no significant differences between the two with regard to the degree of crestal CE. Yadav et al. (2022) assessed the stability of twenty-two implants placed in the maxilla and mandible of as many subjects after narrow ridge augmentation (assessed by CBCT), using the crestal split corticotomy technique. The preoperative bone width had an average value of 3.64 ± 0.41. After the operation, the bone width increased to an average value of 5.62 ± 0.45 mm, with a statistically significant postoperative period ($p < 0.001$). In this respect, a recent systematic review (Manekar et al., 2023) that analyzed twenty-two cohort studies and two randomized controlled trials, with 634 patients and 1,287 implants placed after alveolar ridge splitting and expansion, found an overall survival rate of 98.07% at 3 months of follow-up. They also showed that motorized expanders, as well as being a minimally invasive procedure, reduce the number of surgical procedures and the total duration of treatment and are recommended for osteocondensation. It should be noted, however, that the study by Yadav et al. (2022), together with Bergamo et al. (2021), Koutouzis et al. (2019) were the lowest rated in terms of methodology (5 points), as they did not report or left unclear issues of great relevance such as the randomization and blinding of participants and personnel involved in the study, which greatly limits the analysis of their results.

In a retrospective cohort study involving 20 patients and 31 implants (26 of which were placed in the posterior mandibular area), Anitua and Alkhraisat (2016) proposed the placement of transitional implants with a diameter of 2.5 and 3 mm, following CE with motorized threaded expanders, in crests with horizontal bone atrophy. In the second surgery, the transitional implant was removed, and the definitive dental implant was placed. Using CBCT, they verified that the preoperative width of the alveolar crest was originally 3.1 mm and the "guided bone augmentation" increased this width to 5.1 mm. This study reinforces the indication of crestal split in the treatment of horizontally atrophic jaws. Recently, a meta-analysis evaluated alveolar ridge splitting in implant surgery. This study by Lin et al. (2023) included twenty-four observational studies and one RCT; fourteen of the included studies investigated horizontal bone gain and seventeen examined implant survival. This meta-analysis found that the width obtained by crestal division was 3.633 mm within the range of 2.0–5.3 mm, which is consistent with what was reported by Anitua and Alkhraisat (2016). In addition, they found that the implant

survival rate exceeded 98%, similar to the rate obtained with standard implant placement procedures. However, Crespi et al. (2021) in a retrospective study of thirty-eight patients, reported significantly lower incremental crestal values in the mandible than in the maxilla; nevertheless, the survival rates of the implants placed were 100% for the mandibles and 95.5% for the maxillas. The different expansion achieved in the mandible and maxilla could be explained by the fact that the buccal bone in the maxilla is highly viscoelastic and flexible, and this minimizes bone trauma. In contrast, the buccal wall of the mandible is made of harder, corticalized bone, which makes crestal division difficult. On the other hand, Altiparmak et al. (2017) had already reported that crestal splitting had a higher survival rate than onlay bone grafting (100% and 92%, respectively) and Mahmoud et al. (2020) had previously reported that there were no significant differences in the increase in crestal width between autologous bone block grafting and ridge splitting with flapless piezoelectric surgery. All of this would mean that the ridge splitting technique could shorten the treatment period, reduce postoperative inflammation and pain, eliminate the need for second surgeries, shorten treatment times and reduce costs. These considerations are at odds with the technique proposed by Anitua and Alkhraisat (2016) which, in addition to being complex and unsuitable for professionals without a certain level of experience, since the removal of the transitional devices can lead to bone fractures, lengthens the treatments and raises their cost, not exactly facilitating patient collaboration. Studies on new drilling techniques will help to alleviate many of these drawbacks (Fan et al., 2023).

Our study revealed a number of limitations that are worth highlighting: In terms of methodology, the heterogeneity of the studies included (RCTs and observational studies), together with publication and selection biases. Regarding the clinical aspect, the different surgical techniques and instruments used, the different methods of measuring the parameters analyzed, the different anatomical locations for expansion, and the follow-up periods.

All of this makes it hard to do a proper evaluation and means that the conclusions we present should be taken with some caution.

5 Conclusion

i) The two studies that evaluated BD were homogeneous, with a significant trend toward the intervention group.
ii) The three studies that evaluated ISQ, despite their heterogeneity, showed statistical significance toward the experimental group.
iii) The eight studies that evaluated CE, after sensitivity analysis, showed moderate statistical significance for the experimental group.

Despite the limitations, all this would mean that expansion, compaction and ODT in narrow alveolar ridges could be useful and reliable for clinicians when placing long-lasting dental implants, but more well-designed studies are needed to corroborate these results.

Data availability statement

The original contributions presented in the study are included in the article/supplementary material, further inquiries can be directed to the corresponding author.

Author contributions

NL-V: Data curation, Conceptualization, Validation, Methodology, Supervision, Investigation, Writing – review and editing, Formal Analysis, Project administration, Writing – original draft. AL-V: Writing – review and editing, Writing – original draft, Formal Analysis, Methodology, Conceptualization, Project administration, Supervision, Investigation, Validation, Data curation. JB: Writing – original draft, Methodology, Investigation, Data curation, Conceptualization, Supervision, Formal Analysis, Validation, Project administration, Writing – review and editing.

Funding

The author(s) declare that no financial support was received for the research and/or publication of this article.

Conflict of interest

The authors declare that the research was conducted in the absence of any commercial or financial relationships that could be construed as a potential conflict of interest.

Generative AI statement

The author(s) declare that no Generative AI was used in the creation of this manuscript.

Publisher's note

References

Aghaloo, T. L., Misch, C., Lin, G. H., Iacono, V. J., and Wang, H. L. (2016). Bone augmentation of the edentulous maxilla for implant placement: a systematic review. *Int. J. Oral Maxillofac. Implants* 31 (Suppl. l), s19–s30. doi:10.11607/jomi.16suppl.g1

Aghaloo, T. L., and Moy, P. K. (2007). Which hard tissue augmentation techniques are the most successful in furnishing bony support for implant placement? *Int. J. Oral Maxillofac. Implants* 22 (Suppl. l), 49–70.

Ahmed, OEFMS, Mahmoud, A. A. F., Ali, H. E. M., AlAshmawy, M. M., Abdullah, A. B., Fattah, M. A. B., et al. (2022). Assessment of narrow alveolar ridge expansion by ossiodensification vs. Ridge splitting technique for dental implant placement: clinical and radiographic study. *Int. J. Health Sci.* 6, 392–403. doi:10.53730/ijhs.v6nS9.12291

Alghamdi, H. S., and Jansen, J. A. (2020). The development and future of dental implants. *Dent. Mater J.* 39, 167–172. doi:10.4012/dmj.2019-140

Altiparmak, N., Akdeniz, S. S., Bayram, B., Gulsever, S., and Uckan, S. (2017). Alveolar ridge splitting *versus* autogenous onlay bone grafting: complications and implant survival rates. *Implant Dent.* 26, 284–287. doi:10.1097/ID.0000000000000541

Anitua, E., and Alkhraisat, M. H. (2016). Is alveolar ridge split a risk factor for implant survival? *J. Oral Maxillofac. Surg.* 74, 2182–2191. doi:10.1016/j.joms.2016.06.182

Anitua, E., Begoña, L., and Orive, G. (2013). Clinical evaluation of split-crest technique with ultrasonic bone surgery for narrow ridge expansion: status of soft and hard tissues and implant success. *Clin. Implant Dent. Relat. Res.* 5, 176–187. doi:10.1111/j.1708-8208.2011.00340.x

Arpudaswamy, S., Ali, S. S. A., Karthigeyan, S., Appanna, P. A., Kumar, K. V., and Shetty, R. M. (2024). Comparative evaluation of osseodensification vs conventional osteotomy technique on primary and secondary implant stability in rabbit model split body RCT. *J. Contemp. Dent. Pract.* 25, 1052–1059. doi:10.5005/jp-journals-10024-3751

Berardini, M., Trisi, P., Sinjari, B., Rutjes, A. W., and Caputi, S. (2016). The effects of high insertion torque Versus low insertion torque on marginal bone resorption and implant failure rates: a systematic review with meta-analyses. *Implant Dent.* 25, 532–540. doi:10.1097/ID.0000000000000422

Bergamo, E. T. P., Zahoui, A., Barrera, R. B., Huwais, S., Coelho, P. G., Karateew, E. D., et al. (2021). Osseodensification effect on implants primary and secondary stability: Multicenter controlled clinical trial. *Clin. Implant Dent. Relat. Res.* 23, 317–328. doi:10.1111/cid.13007

Bown, M. J., and Sutton, A. J. (2010). Quality control in systematic reviews and meta-analyses. *Eur. J. Vasc. Endovasc. Surg.* 40, 669–677. doi:10.1016/j.ejvs.2010.07.011

Chiapasco, M., Casentini, P., and Zaniboni, M. (2009). Bone augmentation procedures in implant dentistry. *Int. J. Oral Maxillofac. Implants* 24 (Suppl. l), 237–259.

Chiapasco, M., Zaniboni, M., and Boisco, M. (2006). Augmentation procedures for the rehabilitation of deficient edentulous ridges with oral implants. *Clin. Oral Implants Res.* 17 (Suppl. 2), 136–159. doi:10.1111/j.1600-0501.2006.01357.x

Consolo, U., Travaglini, D., Todisco, M., Trisi, P., and Galli, S. (2013). Histologic and biomechanical evaluation of the effects of implant insertion torque on peri-implant bone healing. *J. Craniofac Surg.* 24, 860–865. doi:10.1097/SCS.0b013e31827ca3cf

Crespi, R., Toti, P., Covani, U., Crespi, G., and Menchini-Fabris, G. B. (2021). Maxillary and mandibular split crest technique with immediate implant placement: a 5-Year cone beam retrospective study. *Int. J. Oral Maxillofac. Implants* 36, 999–1007. doi:10.11607/jomi.8572

Cumpston, M., Li, T., Page, M. J., Chandler, J., Welch, V. A., Higgins, J. P., et al. (2019). Updated guidance for trusted systematic reviews: a new edition of the cochrane handbook for systematic reviews of interventions. *Cochrane Database Syst. Rev.* 10, ED000142. doi:10.1002/14651858.ED000142

Darriba, I., Seidel, A., Moreno, F., Botelho, J., Machado, V., Mendes, J. J., et al. (2023). Influence of low insertion torque values on survival rate of immediately loaded dental implants: a systematic review and meta-analysis. *J. Clin. Periodontol.* 50, 158–169. doi:10.1111/jcpe.13733

Duyck, J., Roesems, R., Cardoso, M. V., Ogawa, T., De Villa Camargos, G., and Vandamme, K. (2015). Effect of insertion torque on titanium implant osseointegration: an animal experimental study. *Clin. Oral Implants Res.* 26, 191–196. doi:10.1111/clr.12316

el Askary, A. S., Meffert, R. M., and Griffin, T. (1999a). Why do dental implants fail? Part II. *Implant Dent.* 8, 265–278. doi:10.1097/00008505-199903000-00008

el Askary, A. S., Meffert, R. M., and Griffin, T. (1999b). Why do dental implants fail? Part I. *Implant Dent.* 8, 173–185. doi:10.1097/00008505-199908020-00011

Elnayef, B., Monje, A., Lin, G. H., Gargallo-Albiol, J., Chan, H. L., Wang, H. L., et al. (2015). Alveolar ridge split on horizontal bone augmentation: a systematic review. *Int. J. Oral Maxillofac. Implants* 30 (0), 596–606. doi:10.11607/jomi.4051

Esposito, M., Hirsch, J. M., Lekholm, U., and Thomsen, P. (1998). Biological factors contributing to failures of osseointegrated oral implants. (I). Success criteria and epidemiology. *Eur. J. Oral Sci.* 106, 527–551. doi:10.1046/j.0909-8836.t01-2-.x

Fan, R. Z., Mei, X. S., and Cui, J. (2023). Process in laser drilling of deep microholes without taper on metal materials. *Sci. China Technol. Sci.* 67, 37–59. doi:10.1007/s11431-023-2557-x

Gaikwad, A. M., Joshi, A. A., and Nadgere, J. B. (2022). Biomechanical and histomorphometric analysis of endosteal implants placed by using the osseodensification technique in animal models: a systematic review and meta-analysis. *J. Prosthet. Dent.* 127, 61–70. doi:10.1016/j.prosdent.2020.07.004

Gallucci, G. O., Hamilton, A., Zhou, W., Buser, D., and Chen, S. (2018). Implant placement and loading protocols in partially edentulous patients: a systematic review. *Clin. Oral Implants Res.* 29, 106–134. doi:10.1111/clr.13276

González-García, R., Monje, F., and Moreno, C. (2011). Alveolar split osteotomy for the treatment of the severe narrow ridge maxillary atrophy: a modified technique. *Int. J. Oral Maxillofac. Surg.* 40, 57–64. doi:10.1016/j.ijom.2010.03.030

Hao, X., Jiang, B., Wu, J., Xiang, D., Xiong, Z., Li, C., et al. (2024). Nanomaterials for bone metastasis. *J. Control Release* 373, 640–651. doi:10.1016/j.jconrel.2024.07.067

Heimes, D., Becker, P., Pabst, A., Smeets, R., Kraus, A., Hartmann, A., et al. (2023). How does dental implant macrogeometry affect primary implant stability? A narrative review. *Int. J. Implant Dent.* 9, 20. doi:10.1186/s40729-023-00485-z

Hindi, A. R., and Bede, S. Y. (2020). The effect of osseodensification on implant stability and bone density: a prospective observational study. *J. Clin. Exp. Dent.* 12, e474–e478. doi:10.4317/jced.56727

Höpflinger, F. (2015). Wandel des Alterns hin zu einer dynamischen Altersgesellschaft [Changes in ageing towards a dynamic elderly society]. *Urol. A* 5, 1747–1752. doi:10.1007/s00120-015-4012-z

Huwais, S., and Meyer, E. G. (2017). A novel osseous densification approach in implant osteotomy preparation to increase biomechanical primary stability, bone mineral density, and bone-to-implant contact. *Int. J. Oral Maxillofac. Implants* 32, 27–36. doi:10.11607/jomi.4817

Inchingolo, A. D., Inchingolo, A. M., Bordea, I. R., Xhajanka, E., Romeo, D. M., Romeo, M., et al. (2021). The effectiveness of osseodensification drilling protocol for implant site osteotomy: a systematic review of the literature and meta-analysis. *Mater. (Basel)* 14, 1147. doi:10.3390/ma14051147

Ivanova, V., Chenchev, I., Zlatev, S., and Mijiritsky, E. (2021). Correlation between primary, secondary stability, bone density, percentage of vital bone formation and implant size. *Int. J. Environ. Res. Public Health* 18, 6994. doi:10.3390/ijerph18136994

Jarikian, S., Jaafo, M. H., and Al-Nerabieah, Z. (2021). Clinical evaluation of two techniques for narrow alveolar ridge expansion: clinical study. *Int. J. Dent. Oral Sci.* 8, 1047–1052. doi:10.19070/2377-8075-21000264

Jha, N., Choi, E. H., Kaushik, N. K., and Ryu, J. J. (2017). Types of devices used in ridge split procedure for alveolar bone expansion: a systematic review. *PLoS One* 12, e0180342. doi:10.1371/journal.pone.0180342

Jordan, Z., Lockwood, C., Munn, Z., and Aromataris, E. (2019). The updated joanna briggs institute model of evidence-based healthcare. *Int. J. Evid. Based Healthc.* 17, 58–71. doi:10.1097/XEB.0000000000000155

Khayat, P. G., Arnal, H. M., Tourbah, B. I., and Sennerby, L. (2013). Clinical outcome of dental implants placed with high insertion torques (up to 176 ncm). *Clin. Implant Dent. Relat. Res.* 15, 227–233. doi:10.1111/j.1708-8208.2011.00351.x

Koutouzis, T., Huwais, S., Hasan, F., Trahan, W., Waldrop, T., and Neiva, R. (2019). Alveolar ridge expansion by osseodensification-mediated plastic deformation and compaction autografting: a multicenter retrospective study. *Implant Dent.* 28, 349–355. doi:10.1097/ID.0000000000000898

Lahens, B., Lopez, C. D., Neiva, R. F., Bowers, M. M., Jimbo, R., Bonfante, E. A., et al. (2019). The effect of osseodensification drilling for endosteal implants with different surface treatments: a study in sheep. *J. Biomed. Mater. Res. B Appl. Biomater.* 107, 615–623. doi:10.1002/jbm.b.34154

Lekholm, U., Gunne, J., Henry, P., Higuchi, K., Lindén, U., Bergström, C., et al. (1999). Survival of the brånemark implant in partially edentulous jaws: a 10-year prospective multicenter study. *Int. J. Oral Maxillofac. Implants* 14, 639–645.

Li, S., Tan, S. Y., Lee, E. Y., Miranda, L. A., and Matsubara, V. H. (2023). The effect of osseodensification on ridge expansion, intraosseous temperature, and primary implant stability: a pilot study on bovine ribs. *J. Oral Implantol.* 49, 179–186. doi:10.1563/aaid-joi-D-21-00259

Lima Monteiro, F., Moreira, C. L., Galego Arias Pecorari, V., Cardona Orth, C., Joly, J. C., and Peruzzo, D. (2024). Biomechanical and histomorphometric analysis of osseodensification drilling *versus* conventional technique: a systematic review and meta-analysis. *Quintessence Int.* 55, 212–222. doi:10.3290/j.qi.b4656937

Lin, Y., Li, G., Xu, T., Zhou, X., and Luo, F. (2023). The efficacy of alveolar ridge split on implants: a systematic review and meta-analysis. *BMC Oral Health* 23, 894. doi:10.1186/s12903-023-03643-2

Mahmoud, Z. T., Wainwright, M., and Troedhan, A. (2020). Flapless piezotome crest split achieves comparable outcomes to autologous onlay grafts with significant less patient morbidity and Complications-A randomized clinical study. *J. Oral Maxillofac. Surg.* 78, 1953–1964. doi:10.1016/j.joms.2020.06.008

Manekar, V. S., Shenoi, R. S., Manekar, S. M., and Morey, S. (2023). The effect of modern devices of alveolar ridge split and expansion in the management of horizontally deficient alveolar ridge for dental implant: a systematic review. *Natl. J. Maxillofac. Surg.* 14, 369–382. doi:10.4103/njms.njms_423_21

Misch, C. E., Perel, M. L., Wang, H. L., Sammartino, G., Galindo-Moreno, P., Trisi, P., et al. (2008). Implant success, survival, and failure: the international congress of oral implantologists (ICOI) Pisa consensus conference. *Implant Dent.* 17, 5–15. doi:10.1097/ID.0b013e3181676059

Muka, T., Glisic, M., Milic, J., Verhoog, S., Bohlius, J., Bramer, W., et al. (2020). A 24-step guide on how to design, conduct, and successfully publish a systematic review and meta-analysis in medical research. *Eur. J. Epidemiol.* 35, 49–60. doi:10.1007/s10654-019-00576-5

Padhye, N. M., Padhye, A. M., and Bhatavadekar, N. B. (2020). Osseodensification -- A systematic review and qualitative analysis of published literature. *J. Oral Biol. Craniofac Res.* 10, 375–380. doi:10.1016/j.jobcr.2019.10.002

Page, M. J., McKenzie, J. E., Bossuyt, P. M., Boutron, I., Hoffmann, T. C., Mulrow, C. D., et al. (2021). The PRISMA 2020 statement: an updated guideline for reporting systematic reviews. *BMJ* 372, n71. doi:10.1136/bmj.n71

Pai, U. Y., Rodrigues, S. J., Talreja, K. S., and Mundathaje, M. (2018). Osseodensification - a novel approach in implant dentistry. *J. Indian Prosthodont Soc.* 18, 196–200. doi:10.4103/jips.jips_292_17

Rizk, O., Ashraf, S., Zaki, A. H., and AbdelMohsen, K. M. (2024). Are bone expansion techniques effective for implant placement in narrow alveolar ridges? *J. Craniofac Surg.* 36 (Dec 19), e441–e446. doi:10.1097/SCS.0000000000011013

Salman, R. D., and Bede, S. Y. (2022). The use of osseodensification for ridge expansion and dental implant placement in narrow alveolar ridges: a prospective observational clinical study. *J. Craniofac Surg.* 33, 2114–2117. doi:10.1097/SCS.0000000000008624

Scheidt, S., Vavken, P., Jacobs, C., Koob, S., Cucchi, D., Kaup, E., et al. (2019). Systematic reviews and meta-analyses. *Z Orthop. Unf.* 157, 392–399. doi:10.1055/a-0751-3156

Schierano, G., Baldi, D., Peirone, B., von Degerfeld, M. M., Modica, F., Notaro, V., et al. (2025)). Implant stability quotient and osteogenic process in dental implant sites prepared using piezoelectric technique: a study in minipigs. *J. Prosthodont.* doi:10.1111/jopr.14025

Scipioni, A., Bruschi, G. B., and Calesini, G. (1994). The edentulous ridge expansion technique: a five-year study. *Int. J. Periodontics Restor. Dent.* 14, 451–459.

Scipioni, A., Bruschi, G. B., Calesini, G., Bruschi, E., and De Martino, C. (1999). Bone regeneration in the edentulous ridge expansion technique: histologic and ultrastructural study of 20 clinical cases. *Int. J. Periodontics Restor. Dent.* 19, 269–277.

Simion, M., Baldoni, M., and Zaffe, D. (1992). Jawbone enlargement using immediate implant placement associated with a split-crest technique and guided tissue regeneration. *Int. J. Periodontics Restor. Dent.* 12, 462–473.

Sterne, J. A. C., Savović, J., Page, M. J., Elbers, R. G., Blencowe, N. S., Boutron, I., et al. (2019). RoB 2: a revised tool for assessing risk of bias in randomised trials. *BMJ* 366, l4898. doi:10.1136/bmj.l4898

Straus, S. E., and McAlister, F. A. (2000). Evidence-based medicine: a commentary on common criticisms. *CMAJ* 163, 837–841.

Tatum, H., Jr (1986). Maxillary and sinus implant reconstructions. *Dent. Clin. North Am.* 30, 207–229. doi:10.1016/s0011-8532(22)02107-3

Tian, J. H., Neiva, R., Coelho, P. G., Witek, L., Tovar, N. M., Lo, I. C., et al. (2019). Alveolar ridge expansion: comparison of osseodensification and conventional osteotome techniques. *J. Craniofac Surg.* 30, 607–610. doi:10.1097/SCS.0000000000004956

Tofan, N. H., Al-Hussaini, A. H., and Mustafa, N. S. (2024). Efficiency of osseodensification *versus* screw expansion technique for augmentation of narrow alveolar ridges: a comparative clinical study. *J. Bagh. Coll. Dent.* 36 34–43. doi:10.26477/jbcd.v36i1.3589

Tricio, J., van Steenberghe, D., Rosenberg, D., and Duchateau, L. (1995). Implant stability related to insertion torque force and bone density: an *in vitro* study. *J. Prosthet. Dent.* 74, 608–612. doi:10.1016/s0022-3913(05)80313-0

Trisi, P., Berardini, M., Falco, A., and Podaliri, V. M. (2016). New osseodensification implant site preparation method to increase bone density in low-density bone: *in vivo* evaluation in sheep. *Implant Dent.* 25, 24–31. doi:10.1097/ID.0000000000000358

Trisi, P., Todisco, M., Consolo, U., and Travaglini, D. (2011). High *versus* low implant insertion torque: a histologic, histomorphometric, and biomechanical study in the sheep mandible. *Int. J. Oral Maxillofac. Implants* 26, 837–849.

Tushar, P., Prakash, J. M., Kumari, P., B, J. M., and Kumari Jayaprakash, P. (2024). Horizontal ridge expansion: a comparative study of motorized ridge expanders Versus osseodensification techniques. *Cureus* 16, e73875. doi:10.7759/cureus.73875

Vaddamanu, S. K., Saini, R. S., Vyas, R., Kanji, M. A., Alshadidi, A. A. F., Hafedh, S., et al. (2024). A comparative study on bone density before and after implant placement using osseodensification technique: a clinical evaluation. *Int. J. Implant Dent.* 10, 56. doi:10.1186/s40729-024-00565-8

Waechter, J., Leite, F. R., Nascimento, G. G., Carmo Filho, L. C., and Faot, F. (2017). The split crest technique and dental implants: a systematic review and meta-analysis. *Int. J. Oral Maxillofac. Surg.* 46, 116–128. doi:10.1016/j.ijom.2016.08.017

Wang, H., He, Y., Wan, L., Li, C., Li, Z., Li, Z., et al. (2025). Deep learning models in classifying primary bone tumors and bone infections based on radiographs. *NPJ Precis. Oncol.* 9, 72. doi:10.1038/s41698-025-00855-3

Wang, L., Wu, Y., Perez, K. C., Hyman, S., Brunski, J. B., Tulu, U., et al. (2017). Effects of condensation on peri-implant bone density and remodeling. *J. Dent. Res.* 96, 413–420. doi:10.1177/0022034516683932

Yadav, B. K., Himabindu, L., Thakur, R. K., Alqahtani, A. S., Gufran, K., and Tiwary, A. (2022). Clinical assessment of the bone width following lateral ridge expansion in augmentation of narrow alveolar ridges for placing immediate dental implants. *J. Pharm. Bioallied Sci.* 14, S986–S990. doi:10.4103/jpbs.jpbs_816_21

Yeh, Y. T., Chu, T. G., Blanchard, S. B., and Hamada, Y. (2021). Effects on ridge dimensions, bone density, and implant primary stability with osseodensification approach in implant osteotomy preparation. *Int. J. Oral Maxillofac. Implants* 36, 474–484. doi:10.11607/jomi.8540

Zhang, Z., Gan, Y., Guo, Y., Lu, X., and Li, X. (2021). Animal models of vertical bone augmentation (review). *Exp. Ther. Med.* 22, 919. doi:10.3892/etm.2021.10351

frontiers | Frontiers in Bioengineering and Biotechnology

TYPE Original Research
PUBLISHED 27 June 2025
DOI 10.3389/fbioe.2025.1611948

OPEN ACCESS

EDITED BY
Dan Lin,
Shanghai University of Medicine and Health Sciences, China

REVIEWED BY
Yuanzhang Jiang,
Sichuan University, China
Marco Friuli,
National Research Council (CNR), Italy

*CORRESPONDENCE
Weili Xie,
xiewl@hrbmu.edu.cn

RECEIVED 15 April 2025
ACCEPTED 13 June 2025
PUBLISHED 27 June 2025

CITATION
Wang T, Xie Q, Liang H, Sun Y and Xie W (2025) Multifunctional PLGA/collagen/zeolitic imidazolate framework-8 composite nanofibrous membranes for guided bone regeneration.
Front. Bioeng. Biotechnol. 13:1611948.
doi: 10.3389/fbioe.2025.1611948

Multifunctional PLGA/collagen/zeolitic imidazolate framework-8 composite nanofibrous membranes for guided bone regeneration

Tianqi Wang[1], Qi Xie[1], Hongbo Liang[2], Yu Sun[1] and Weili Xie[1]*

[1]The First Affiliated Hospital of Harbin Medical University, School of Stomatology, Harbin Medical University, Harbin, China, [2]School of Materials Science and Engineering, Harbin Institute of Technology, Harbin, China

Introduction: Guided bone regeneration (GBR) is widely used for maxillofacial defects, but fabricating membranes that enhance osteoinduction and antimicrobial resistance remains challenging. This study addresses critical bone defect therapy by developing collagen (Col) and zeolitic imidazolate framework-8 (ZIF-8) reinforced poly(lactide-co-glycolide) (PLGA) nanofibrous membranes.

Methods: Material characterization analyzed the composite nanofibrous membranes' morphology, structure, wettability, tensile strength, *in vitro* degradation, and ion release. Biocompatibility and osteogenesis were evaluated using live/dead staining, cytoskeleton staining, CCK-8 assay, alkaline phosphatase (ALP) activity quantification, ALP staining, alizarin red S (ARS) staining and ARS quantification. Antibacterial efficacy was assessed via agar plate counting and bacterial growth kinetics. *In vivo* bone regeneration was examined in a rat cranial critical defect model treated with the membrane; bone formation was evaluated by Micro-CT and hematoxylin-eosin staining after 4 weeks.

Results: Optimization of the PLGA/Col weight ratio (100:3) yielded composite membranes demonstrating superior tensile strength. The PLGA/Col/ZIF-8 nanofibrous composite incorporating 1 wt% ZIF-8 nanoparticles exhibited optimal biocompatibility with sustained Zn^{2+} release kinetics. *In vitro* experiments demonstrated that sustained release of Zn^{2+} has the dual effects of stimulating osteogenic differentiation and effectively preventing early bacterial infection. *In vivo* a rat calvarial defect model further confirmed the positive bone regeneration effect of the PLGA/Col/ZIF-8 composite nanofibrous membrane.

Discussion: PLGA/Col/ZIF-8 composite nanofibrous membranes have great potential for application in guiding bone tissue regeneration.

KEYWORDS

electrospinning, nanofibrous membrane, ZIF-8, tensile strength, guided bone regeneration

1 Introduction

The incidence of alveolar and maxillofacial bone defects caused by trauma, tumor and inflammation is high, and such pathological bone defects often lead to biomechanical stability and functional reconstruction of conventional restorations and implant-supported prosthetic solutions (Visscher et al., 2016; Yang et al., 2022). In this context, revolutionary advances in bone tissue engineering technologies are providing breakthrough solutions for the regenerative repair of bone defects. Guided bone regeneration (GBR) biomaterials can significantly improve the effectiveness of structural and functional reconstruction of critical-sized bone defects (Urban and Monje, 2019). The core principle of GBR is to create a physical barrier between the bone defect area and the soft tissue by using a biological barrier membrane that selectively inhibits the infiltration of fibrous connective tissue and epithelial cells based on a spatial competition mechanism, while creating a preferential microenvironment for the proliferation of osteogenic progenitor cells. The barrier membrane maintains the stability of the clot and the morphology of the defect area through mechanical isolation and relieves pressure on the soft tissues, thereby supporting the process of directed migration, differentiation and mineralization of osteoblasts (Laney, 2017; Sheikh et al., 2017).

Currently, GBR membranes are mainly divided into non-resorbable and resorbable materials. Although polytetrafluoroethylene (PTFE) is clinically effective as a non-resorbable membrane, its non-resorbability requires secondary surgical removal, which significantly increases the risk of postoperative infection and limits its clinical use (Carbonell et al., 2014; Garcia et al., 2018; Trobos et al., 2018). In contrast, resorbable collagen (Col) membranes, with their excellent biocompatibility, biodegradability and natural bioactivity, have become an important alternative in bone augmentation therapy, promoting bone repair through tissue regeneration mechanisms while avoiding secondary surgery (Dimitriou et al., 2012; Liu and Kerns, 2014). However, the poor mechanical properties and rapid degradation behavior of collagen membranes have hindered their development, as they are unable to maintain their spatial configuration (Garcia et al., 2017; Rothamel et al., 2005). Micro- and nanoscale fiber structures produced by electrospinning technology have been widely used in the development of GBR membranes due to their highly biomimetic properties. These structures can mimic the topological characteristics of the natural extracellular matrix (ECM) and effectively promote cell adhesion, proliferation and metabolic exchange, while the micro-barrier formed by the nanofiber network can selectively block the invasion of fibrous connective tissue and ensure the stability of the osteogenic microenvironment in the bone defect region. However, these electrostatically spun GBR membranes have not yet been clinically translated (Martins et al., 2020; Wang et al., 2019; Wang et al., 2013). Therefore, the development of GBR membranes with good mechanical properties, degradation rate, osteoinductive activity and antimicrobial functionality required to withstand the multidimensional effects of mechanical stress, microbial colonization and biomolecular metabolism in the dynamic oral cavity bioenvironment is a core research direction.

Col, a core component of connective tissue, is widely used in biomaterial design due to its low immunogenicity, biodegradability and structural support function (Ren et al., 2022). Poly (lactide-co-glycolide) (PLGA), an FDA-approved biodegradable polyester, has proven to be the preferred substrate for bone tissue engineering scaffolds due to its combination of excellent mechanical strength and histocompatibility (Brown et al., 2018). Based on this, this study aims to improve the interfacial compatibility and mechanical stability of electrostatically spun fiber membranes through intermolecular interactions by the composite of Col and PLGA (Ahi et al., 2020; Kwak et al., 2016; Yang et al., 2018). Prior research shows that PLGA/Col composite systems have been validated in the field of nerve axon guidance scaffolds, brain injury repair carriers and bone defect filling materials (Park et al., 2018). However, the composite system still suffers from significant functional deficiencies in terms of osteoinductive differentiation efficiency and antimicrobial activity in guided bone regeneration membrane applications.

The dual role of bioactive ions in tissue repair and bacterial resistance modulation is gradually becoming a research focus. Zinc, an essential trace element, plays a key biological function by regulating osteoblast differentiation, matrix mineralization and maintenance of bone homeostasis (Yamaguchi and Weitzmann, 2011). In addition, its antimicrobial activity has been widely demonstrated (Nagata and Lonnerdal, 2011). However, excessive zinc ions have the potential to cause toxicity and to inhibit the expression of bone-related genes. Therefore, a controlled slow-release system is required to achieve zinc ion delivery (Giliopoulos et al., 2020; Yang and Yang, 2020). Metal-organic frameworks (MOFs) are a class of porous materials self-assembled by coordination between organic ligands and metal ions, among which zeolite imidazolate framework-8 (ZIF-8) is composed of zinc ions coordinated with dimethylimidazole, which combines excellent biocompatibility and osteoinductive properties (Pan et al., 2011). The material exhibits stability in neutral environments, yet rapidly dissociates under acidic conditions, thereby facilitating the prompt release of Zn^{2+} in bacterial infection microenvironments (Sun et al., 2012). It has been demonstrated that nano ZIF-8 activates the MAPK signaling pathway in bone marrow mesenchymal stem cells through the process of endocytosis, thereby significantly promoting osteogenic differentiation (Gao et al., 2021; Wang et al., 2016). Therefore, ZIF-8 nanoparticles can be introduced into GBR membranes as antimicrobial-osteogenic functional modification materials to achieve the membrane material to play a precise regulatory role of antimicrobial and osteogenic in the process of bone repair.

In this study, a novel PLGA/Col/ZIF-8 composite nanofibrous membrane was fabricated by electrospinning technology for bone defect repair. Initially, a mechanically adapted substrate was constructed by means of gradient doping Col in a PLGA matrix, followed by the subsequent integration of ZIF-8 into PLGA/Col to achieve a microenvironment-triggered release mechanism of zinc ions, thereby resulting in both antimicrobial and osteogenic effects. Furthermore, a rat cranial defect model was utilized to confirm its capacity to repair bone tissue defects *in vivo*, thereby assessing the potential of this composite fibrous membrane in bone regeneration strategies.

2 Materials and methods

2.1 Materials and reagents

Poly (lactic-co-glycolic acid) (PLGA; LA/GA = 75:25, Mw = 66–107 kDa) was procured from Sigma Aldrich. Type I collagen (Col I) was obtained from Macklin, while 1,1,1,3,3,3-hexafluoro-2-propanol (HFIP) and 2-methylimidazole (2-MIM) were sourced from Aladdin. Zinc nitrate hexahydrate was procured from Innochem. All of the aforementioned chemical reagents were of analytical grade and did not undergo any further purification.

2.2 Fabrication of PLGA/col/ZIF-8 electrospun membrane

The synthesis and characterization of the ZIF-8 nanoparticles were conducted in accordance with the following procedure (Supplementary Figures S1, S2). The electrospun solution was prepared by dissolving PLGA in HFIP (20% w/v) under magnetic stirring at room temperature. To prepare the PLGA/Col electrospun solution, 1 g of PLGA was dissolved in 5 mL of HFIP. Subsequently, the different weight ratios of Col/PLGA (1:100, 3:100, 5:100 and 10:100; abbreviated as PC1, PC3, PC5 and PC10, respectively) were added under stirring until complete dissolution. The electrospun solution of PLGA/Col/ZIF-8 was prepared in the following manner: ZIF-8 at varying weight ratios (0.5 wt%, 1 wt%, 1.5 wt% and 2 wt%; designated as PC3Z0.5, PC3Z1, PC3Z1.5 and PC3Z2, respectively) was subjected to sonication and dispersion in 5 mL HFIP. Subsequently, 1 g of PLGA and 0.03 g of Col I were added to the solution, which was then magnetically stirred until complete dissolution of the PLGA and Col I had occurred. The solution was then sonicated for a further 0.5 h to ensure uniform dispersion of the nano-ZIF-8 within the spinning solution. The electrospun solutions were introduced into the system via a 23 G flat-tipped needle at a constant injection rate of 0.5 mL/h, using a plastic syringe. The distance between the needle and the flat collector was 15 cm, the applied positive voltage was 10–15 kV, and the humidity was approximately 21%–31%.

2.3 Characterization

The microscopic morphology of the membranes was examined using a scanning electron microscope (SEM, Gemini 560, ZEISS, Germany). The chemical compositions of the membranes were established through the use of a Fourier transform infrared spectrometer (FTIR, Nicolet iS5, Thermo, United States). Moreover, Nano Measurer was employed to quantify the diameter and distribution of the membranes from the acquired SEM image. The presence of ZIF-8 crystals in the membranes was confirmed through X-ray diffraction (XRD, X'PERT, Panalytical, Holland). Thermogravimetric analysis (TG, STA449F3, NETZSCH, Germany) was employed to ascertain the thermal stability of the membranes. All samples were subjected to a heating process, increasing the temperature from 30°C to 500°C at a rate of 10°C/min, in a nitrogen-enriched environment. The wettability of the membranes (n = 3) was evaluated using a contact angle meter (SDC 350, SINDIN, China). In order to evaluate the impact of Col and ZIF-8 NPs incorporation on the mechanical properties of the membranes (n = 3), an electronic universal testing machine (Model 6103, MTS, China) with a 50 N load cell was employed to conduct a series of tests on the membranes under dry and wet condition (soaking in deionized water for 24 h), which had overall dimensions of 50 mm × 10 mm × 0.2 mm. The crosshead speed was set at 15 mm/min. For degradation test, membrane samples (n = 3) were precisely sectioned into 10 mm × 10 mm squares. Initial dry mass (W_0) was determined using an analytical balance. Specimens were subsequently immersed in 10 mL of phosphate-buffered saline (PBS, pH 7.4) and incubated at 37°C. The PBS was replenished weekly to maintain ionic stability. The samples were removed at each predetermined time point, at days 1, 3, 7, 14, 21, 28 and 56, and then placed in a vacuum drying oven until completely dry and weighed (W_t). Weight loss (%) = $(W_0 - W_t)/W_0 \times 100$. The release of zinc ions from the composite membranes (n = 3) was quantified using inductively coupled plasma emission spectroscopy (ICP-OES, iCAP 7,400, Thermo, United States). The membranes were immersed in PBS with a specified pH value (pH 7.4) for 1, 3, 5, and 7 days at 37°C without agitation, the extracts were collected at various time points and the amount of released Zn^{2+} ions was measured.

2.4 Biocompatibility *in vitro*

2.4.1 Cell culture

The mouse bone marrow mesenchymal stem cells (BMSCs) were procured from Immocell Biotechnology. The BMSCs were cultured in Dulbecco's Modified Eagle Medium: F-12 (DMEM/F12, Pricella, China) supplemented with 10% Fetal Bovine Serum (FBS, Gibco, United States) and 1% mixture of penicillin-streptomycin (Gibco, United States), and passaged every 2 days. The osteogenic differentiation of BMSCs was induced using an osteogenic induction medium (OriCell, China). All cells were cultured in accordance with standard conditions (37°C, 5% CO_2, 95% relative humidity). The fiber membranes employed in all cell experiments were subjected to a pre-processing step involving immersion in a 75% ethanol solution for 1 hour. Thereafter, the prepared membranes underwent a sterilization procedure involving exposure to ultraviolet light.

2.4.2 Cell proliferation

BMSCs were seeded on the fiber membranes (n = 4) in 96-well plates at a cell density of 2.5×10^3 cells per well. Following a period of cultivation lasting for 1, 3, and 5 days, the extent of cellular proliferation was gauged through the utilization of the cell counting kit-8(CCK-8, MedChemExpress, China). At the designated time point, the cells were rinsed with PBS and cultured in a medium containing 10% CCK-8 solution at 37°C for 2 h. Subsequently, the optical density (OD) value at 450 nm was determined using a microplate reader.

2.4.3 Cell live/dead staining

The cells were seeded on the fiber membranes (n = 4) in 24-well plates at a density of 2×10^4 cells per well. Following a 24 h incubation period, the working solution was prepared at a ratio of 1:1:1,000, comprising Calcein AM, PI and detection buffer.

Subsequently, the solution was added to each well and incubated at 37°C for 30 min in the dark. The presence of live (green) and dead (red) cells were observed using fluorescence microscopy.

2.4.4 Cell morphology

The cells were seeded on the membranes (n = 4) in 24-well plates at a density of 2×10^4 cells per well for a 24 h culture period. Subsequently, the cells were fixed with 4% paraformaldehyde and rinsed with PBS. They were then permeabilized with 0.5% Triton X-100 and rinsed with PBS. Subsequently, F-actin (red) and nuclei (blue) were stained with TRITC-phalloidin and 4, 6-diamidino-2-phenylindole dihydrochloride (DAPI) in the dark, respectively, and observed using fluorescence microscopy.

2.5 Osteogenic ability *in vitro*

2.5.1 ALP activity

BMSCs were seeded at a density of 2×10^4 cells per well on the membranes (n = 4) in 24-well plates. The osteogenic induction medium was replenished every 2 days. Following a 7-day and 14-day cultivation period, a quantitative evaluation of ALP activity was conducted in accordance with the instructions provided in the ALP detection kit (Beyotime, China). For qualitative analysis of ALP, BMSCs were fixed with 4% paraformaldehyde for 15 min at room temperature and subsequently stained with the BCIP/NBT ALP kit for 30 min in the absence of light.

2.5.2 Alizarin red S staining

BMSCs were seeded at a density of 2×10^4 cells per well on the membranes (n = 4) in 24-well plates. Following a 21-day period of cultivation in an osteogenic induction medium, the extracellular matrix mineralization capacity was evaluated through the use of ARS staining. The BMSCs were fixed with 4% paraformaldehyde for a period of 30 min, after which they were stained with alizarin red S (OriCell, China) for a further 10 min at 37°C. The stained samples were thoroughly washed with PBS to remove any residual dye, and images were acquired under a stereomicroscope. 10% cetylpyridinium chloride was added to each well, and the stained mineralized nodules were solubilized by shaking the bed for 30 min. The absorbance at 630 nm was then detected by a microplate reader.

2.6 Antibacterial assay

2.6.1 Bacterial culture

Escherichia coli (*E. coli*) and *Staphylococcus aureus* (*S. aureus*) were retrieved from the −80°C refrigerator, with individual colonies selected and dispersed in medium. The suspension was then shaken and cultured at 37°C with 130 rpm agitation, resulting in a bacterial concentration of 1×10^6 CFU/mL, which was subsequently utilized in subsequent experiments.

2.6.2 Agar plate count

At 37°C, samples (n = 3) were cocultured with *E. coli* and *S. aureus* for 24 h. Thereafter, 60 μL of broth was aspirated and diluted to specific concentrations as needed. Subsequently, 100 μL of the diluted broth was spread evenly on solid agar plates. After 12 h of continuous incubation at 37°C, the number of colonies on the plates was counted and photographed.

2.6.3 Bacterial growth curve

The three groups of nanofiber membranes (n = 3) were co-cultured with *E. coli* or *S. aureus* and placed in a bacterial shaking incubator at 37°C. At specific time points (0, 2, 4, 6, 8, 10, and 12 h), an appropriate volume of bacterial suspension was aspirated, transferred to a 96-well plate, and the OD at 600 nm was measured using a microplate reader. Bacterial growth curves were then plotted based on the OD values.

2.7 Animal experiments

2.7.1 Animal grouping and surgery

All animal procedures were approved by the Ethical Committee on Animal Experiments of Harbin Medical University. Twenty male Sprague-Dawley rats were randomly divided into four groups (n = 5): blank control group, P, PC, and PCZ. Under general anesthesia, the dorsal area was shaved and disinfected, followed by the creation of a 2 cm skin incision to form a subcutaneous pocket. After implantation of the corresponding materials, the wound was closed using non-absorbable monofilament sutures. Peripheral blood samples were collected 3 days post-surgery for biochemical analysis.

Twenty Sprague Dawley rats were anaesthetized, the surgical site on the top of the head was prepared and disinfected, and a longitudinal incision was made in the middle of the skull, with the periosteum elevated to expose the cranial surface. A circular bone defect measuring 5 mm in diameter was created on the side of the middle cranial suture using a ring bone extraction drill. The bone defect was full-length and did not damage the dura mater. During the procedure, saline rinsing of the ring drill was ensured for cooling protection. Twenty Sprague-Dawley rats were randomized into four groups (Blank; P; PC; PCZ). Calvarial defects in three treatment groups (n = 5) received membrane implantation, while the blank control group remained non-interventional. Following the implantation of the membrane material, the subcutaneous tissue was closed and the skin layer incision was sutured. The rats were euthanized 4 weeks after the surgical procedure. The removal and fixation of the cranial tissues, as well as the heart, liver, spleen, lung and kidney organs, was conducted using 4% paraformaldehyde for subsequent analysis.

2.7.2 Blood biochemistry assay

Blood samples were collected for the purpose of quantifying various hematological parameters, including white blood cells (WBC), red blood cells (RBC), hemoglobin (HGB), platelets (PLT), aspartate aminotransferase (AST), alanine aminotransferase (ALT), blood urea nitrogen (UREA) and creatinine (CREA).

2.7.3 Micro-CT analysis

Micro-CT was utilised to scan the fixed cranial tissue blocks, thus facilitating analysis of bone regeneration at the defect site in each group. The cranial scanning parameters comprised a voltage of 70 kV, a current of 114 μA, a voxel of 10 μm and a 0.5 mm aluminium filter. The 3D images were reconstructed by software, after which the bone volume fraction (bone volume/total volume, BV/TV) was measured and analysed.

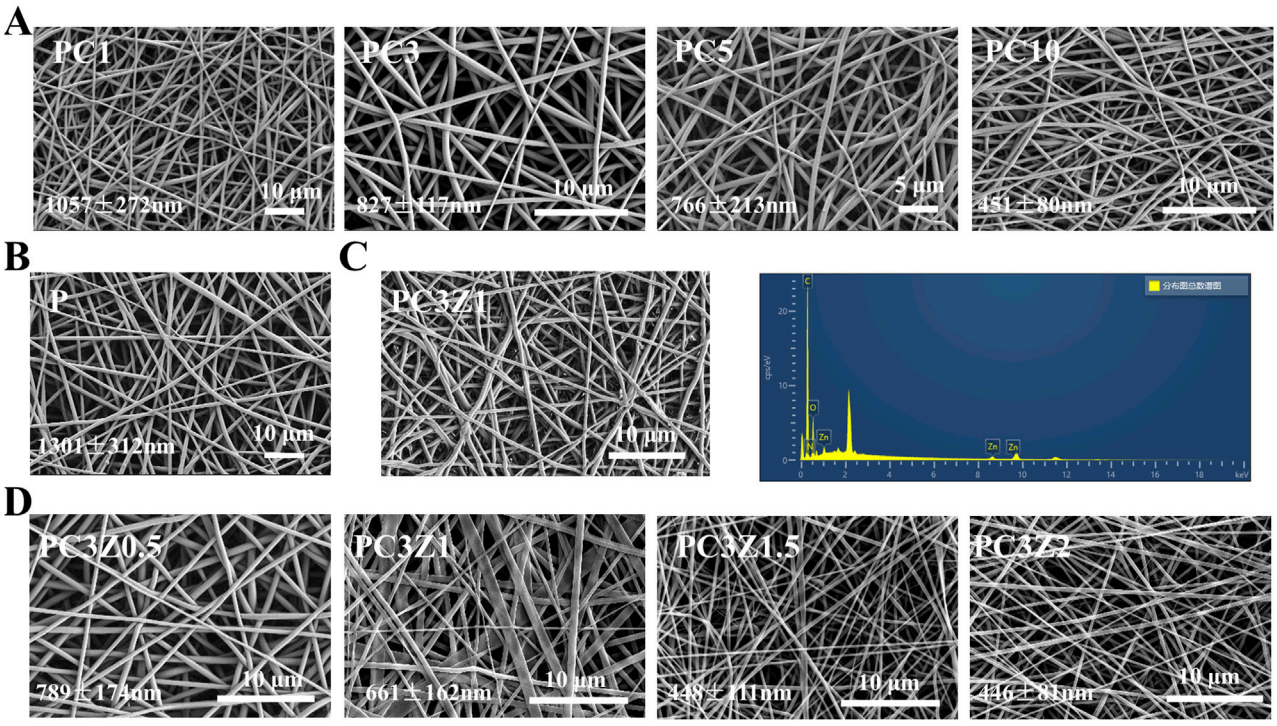

FIGURE 1
SEM images and corresponding diameter of membranes with different Col contents **(A,B)** and different ZIF-8 contents **(D)**. **(C)** Corresponding EDS spectrogram of PC3Z1 fibers.

2.7.4 Histology staining

Following micro-CT scanning, the samples were subjected to decalcification using a 10% EDTA solution. Thereafter, they underwent a process of gradient dehydration, followed by paraffin embedding, sectioning (4 μm thickness), staining with hematoxylin and eosin (H&E), and imaging under a light microscope. For the purpose of visceral histological assessment, heart, liver, spleen, lung and kidney tissues were collected from each group and fixed in 4% paraformaldehyde. The tissues were then dehydrated in ethanol and embedded in paraffin. The tissues were sectioned into 4 μm and stained for H&E.

2.8 Statistical analysis

All experiments were repeated at least three times, and the data were calculated as the mean ± standard deviation. Statistical analysis of the date was performed using one-way ANOVA (GraphPad Prism 8, United States). The level of statistical significance of differences was set $P < 0.05$.

3 Results and discussion

3.1 Optimization of col and ZIF-8 content

In order to prepare PCZ composite fibrous membranes with both excellent mechanical properties and good cytocompatibility, different contents of Col and ZIF-8 were added to the PLGA fibrous membranes (the optimization process is illustrated in Supplementary Figures S3, S4, and the PCZ composite fibrous membranes with the optimal performance were selected for subsequent analysis.

The morphology of the membrane is illustrated in Figures 1A,B,D, where the fiber exhibit random orientation and form an interconnected porous structure. The P membranes exhibited an average fiber diameter of 1,301 ± 312 nm, demonstrating homogeneous morphological characteristics with smooth surfaces devoid of bead-like or spindle-shaped structural defects. Increasing Col content from 1% to 15% induced a progressive fiber diameter reduction from 1,057 ± 272 nm to 451 ± 80 nm in PC membranes. This inverse correlation originated from collagen's viscosity-lowering effect on the electrospinning solution, thereby decreasing the mean fiber dimensions (Lee et al., 2009). Supplementary Figure S3 demonstrates a biphasic tensile strength response to elevated Col concentrations in the membranes. The PC3 formulation, corresponding to the tensile strength maximum, was subjected to subsequent ZIF-8 parametric analysis to optimize mechanical performance. A moderate increase in Col content can enhance the tensile properties of the material by optimizing the fiber network structure through intermolecular cross-linking; beyond the critical concentration, excess collagen triggers phase separation or crystallization defects, leading to stress concentration and reduced mechanical strength.

To determine the optimal ZIF-8 NPs loading, PC3 fibers were modified with four ZIF-8 NPs weight fractions (0.5-2 wt%). Supplementary Figure S4 demonstrated maximal proliferative activity at 1 wt% ZIF-8 on days 3/5, establishing this

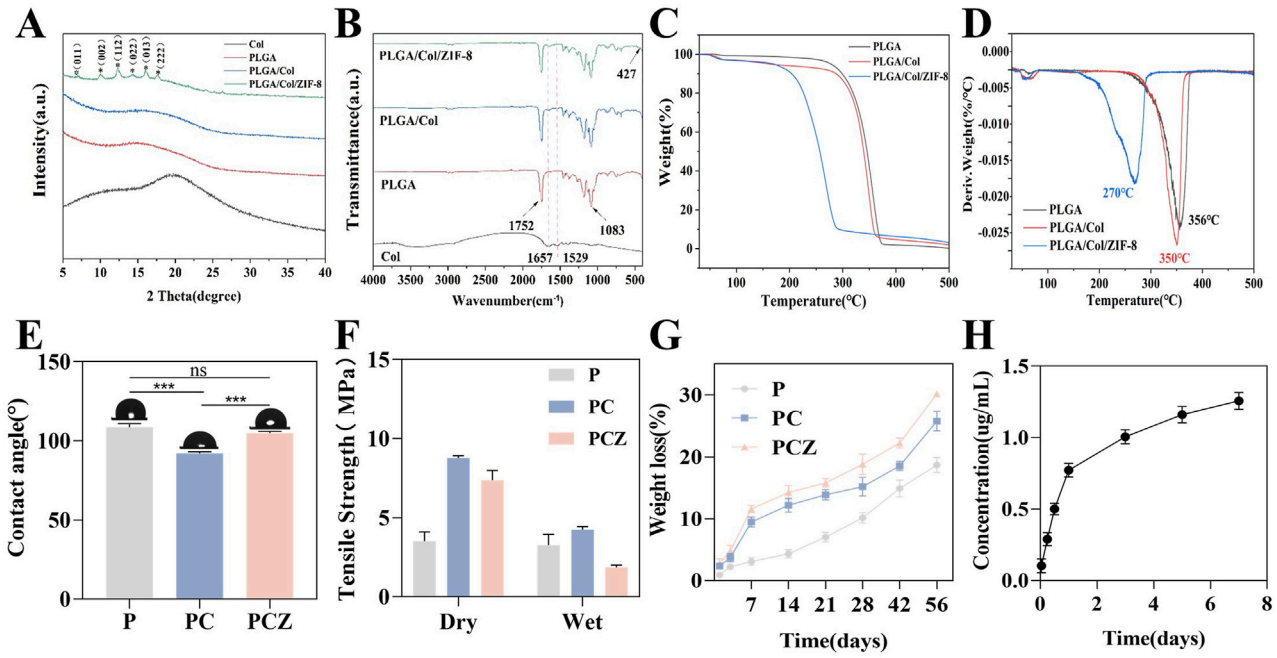

FIGURE 2
Characterization of fibrous membrane. **(A)** XRD patterns of the nanofibers. **(B)** FTIR spectra of the nanofibers. **(C)** TG analysis of the nanofibers. **(D)** DTG curve of the nanofibers. **(E)** Water contact angles of the nanofibers. **(F)** Tensile strength of the nanofibers in the dry and wet conditions. **(G)** Degradation behavior of the nanofibers after soaking in PBS solution. **(H)** Cumulative Zn^{2+} release from the PCZ nanofibers. Data are presented as mean ± SD (n = 3, $*P < 0.05$, $**P < 0.01$, $***P < 0.001$).

concentration for PCZ membrane fabrication. As shown in Figure 1D, the doping of ZIF-8 NPs led to a further decrease in the average diameter of fibers in the PCZ membrane. This originated from ZIF-8-induced viscosity reduction in the spinning solution. The initial 10 kV voltage insufficiently countered surface tension, causing droplet ejection, necessitating voltage elevation to 15 kV for stabilized fiber formation. Furthermore, EDS analysis demonstrated the presence of C, N, O and Zn, thereby further indicating the presence of ZIF-8 NPs in the nanofibers (Figure 1C). Therefore, Pure PLGA (P), PC3 (PC), and PC3Z1 (PCZ) membranes were prioritized for detailed investigation in this study.

3.2 Characterizations of the composite fibrous membranes

As shown in Figure 2A, the XRD analysis of the fibrous membrane revealed that pure PLGA and Col belong to the amorphous structure, presenting only one broad peak. The incorporation of Col resulted in the diffusion and broadening of the peaks corresponding to PC and PCZ. This phenomenon may be attributed to the interaction between PLGA and Col molecules, which impedes the arrangement of PLGA chains. The XRD pattern of PCZ exhibited distinctive peaks at 7.07°, 10.03°, 12.30°, 14.32°, 16.01° and 17.64°. These peaks correspond to the ZIF-8 crystal face at (011), (002), (112), (022), (013) and (222), which indicates the presence of ZIF-8 dispersion within the nanofibers. The FTIR spectra (Figure 2B) revealed that the PLGA, PLGA/Col, and PLGA/Col/ZIF-8 exhibited stretching bands of C=O and C-O at 1752 cm^{-1} and 1,083 cm^{-1}, respectively, which corresponded to the characteristic peaks of PLGA. The absorption peaks of am-ide I and amide II in Col were observed at 1,657 cm^{-1} and 1,529 cm^{-1}, respectively. The absorption peaks of PLGA/Col and PLGA/Col/ZIF-8 exhibited slight shifts towards lower wavelengths, appearing at 1,644 cm^{-1} and 1,526 cm^{-1}, respectively. This suggests that the amino group in Col most likely formed hydrogen bonds with the PLGA molecular chain. Additionally, PLGA/Col/ZIF-8 displayed a Zn-N stretching vibration at 427 cm^{-1}.

The thermal analysis of the fibrous membrane is illustrated in Figures 2C,D. The TG curve with a first-order derivative demonstrates that the fastest thermal decomposition temperature of PLGA is 356°C, while the fastest thermal decomposition temperatures of Col and ZIF-8 are 350°C and 270°C, respectively. It can be concluded that the introduction of Col and ZIF-8 resulted in a reduction of the fastest thermal decomposition temperature of the membranes, while still meeting the thermal stability requirements of GBR membranes. The initial stage of mass loss can be attributed to the evaporation of physically adsorbed water, while the subsequent stage may be attributed to the collapse of the molecular chain structure and thermal decomposition. As displayed in Figure 2E, the PLGA membrane exhibited hydrophobic behavior, with a water contact angle of 100.43°. The incorporation of Col markedly enhanced the hydrophilicity of the membrane, reducing the surface contact angle of the material to 90.97°. This was predominantly attributed to the hydrophilic nature of the amino and carboxyl functional groups of Col. The contact angle of PCZ was 104.27°.

The mechanical strength of a material is also an important performance indicator. Accordingly, the objective of this experiment was to evaluate the mechanical properties of various membranes through a tensile strength test. As demonstrated in Figure 2F, the tensile strength of the pure P membrane in the dry state was found to be 3.52 ± 0.58 MPa. In contrast, the tensile strength of the PC composite membrane and the PCZ composite membrane was significantly higher, reaching approximately 2.5 and 2 times that of the pure P membrane, respectively. It is important to acknowledge the considerable impact of ambient humidity on the mechanical properties of materials. While the pure P membrane exhibited only 7% strength attenuation under wet conditions, the tensile strength of the PC and PCZ composite membrane decreased sharply by 52% and 75%, respectively. Specifically, the tensile strength of the PCZ membrane was measured at 7.37 ± 0.63 MPa in the dry condition, which decreased to 1.87 ± 0.14 MPa after 24 h of water immersion. A comparison with commercially available products demonstrated that the tensile strength of the Bio-Gide resorbable barrier membrane in the dry/wet state was 4.6 ± 0.94 MPa versus 1.68 ± 0.54 MPa, respectively (Raz et al., 2019). This comparison demonstrates that the mechanical properties of PCZ membranes in the wet state are still superior to those of clinically available products, which is crucial for guided bone regeneration applications.

Studies have indicated that the diameter of electrospun fibers critically influences their mechanical properties, with reduced diameters typically accompanied by enhanced strength and reduced ductility (Stachewicz et al., 2012; Tan et al., 2005). The introduction of col significantly decreased fiber diameter (Figure 1), thereby enhancing the mechanical strength of the composites. This improvement stems from two aspects. Firstly, active groups such as amino/carboxyl groups in col molecules form intermolecular hydrogen-bonding networks with PLGA, which stabilize molecular conformations and enhance macroscopic mechanical performance. As previously mentioned, XRD and FTIR results partially support this perspective. Secondly, the incorporation of ZIF-8 nanoparticles may cause disordering of polymer chain arrangements and particle agglomeration phenomena, resulting in slightly lower tensile strength in the PCZ group compared to the PC group. Nevertheless, the overall tensile performance of PCZ membranes remains significantly superior to that of pure PLGA membranes and fully meets the mechanical strength requirements for GBR applications.

In order to evaluate the *in vitro* degradability of the prepared membranes, the mass loss during their immersion was detected. As demonstrated in Figure 2G, the mass loss rate of PCZ was marginally higher than that of PC. However, the degradation kinetic curves of these two samples exhibited analogous trends. The experimental data demonstrated that the degradation rate of the pure PLGA material was significantly lower than that of the other fibrous membranes at all the detected time nodes, thereby confirming that the addition of Col changes the material properties and significantly accelerates the degradation process of the composite fibers. This phenomenon can be attributed to the formation of continuous structural defects within the composite material due to the rapid degradation of Col. This, in turn, facilitates the penetration of hydrolysis media by increasing the contact surface between the fibrous membrane and the soaking solution. Furthermore, the progressive dissolution and release of ZIF-8 NPs from the PCZ fiber membrane occurred with the extension of the degradation time, which further led to a slightly faster degradation rate of the PCZ than that of the PC membrane. Subsequently, the release behavior of Zn^{2+} from PCZ nanofibrous membranes was evaluated. As shown in Figure 2H, under simulated physiological conditions (pH 7.4, 37°C), the Zn^{2+} release profile exhibits a typical two-stage pattern: an initial burst release occurs within the first 24 h (cumulative release: 0.77 ± 0.05 μg/mL), followed by a sustained-release phase, reaching a cumulative concentration of 1.26 ± 0.06 μg/mL by day 7. Notably, this release amount is significantly lower than the internationally recognized safe threshold range for zinc ions (0.65–16.25 ppm) (Nagata and Lönnerdal, 2011). Studies have shown that zinc-based sustained-release materials generally exhibit an initial rapid release (1–7 days) followed by exponential decay, rather than a linear accumulation trend (Xue et al., 2021). With regard to the toxicity threshold, it has been confirmed *in vitro* that ZIF-8 concentrations less than 50 μg/mL possess anti-apoptotic properties and improve cell survival (Gao et al., 2021). Importantly, the peak release level of this system at 7 days was only 2.5% of that safety threshold, further corroborating its safety advantage.

3.3 *In vitro* biocompatibility

Cell-material interactions initiate with attachment, potentially progressing to adhesion, followed by proliferation and spreading phases (Anselme, 2000). BMSCs cultured on the surface of fibrous membranes exhibited proliferation behaviors quantified via CCK-8 assay. Enhanced proliferative capacity, a cornerstone of cellular physiology, directly supports differentiation potential in biomaterial interfaces. Figure 3A indicated that the proliferation of cells on the fibrous membranes exhibited an overall increasing trend over time. There was no statistically significant difference in cell proliferation between the groups on days 1 and 3, indicating that the fibrous membranes exhibited good biocompatibility. The proliferation of BMSCs was significantly enhanced by PCZ nanofiber membranes compared to the P and PC groups on day 5. The enhanced cell proliferation capacity may be attributed to the release of zinc ions at optimal concentrations, which facilitated the proliferation of BMSCs (Yusa et al., 2011). Furthermore, cell adhesion and nutrient exchange on membranes is found to be highly correlated with fiber diameter, morphology and pore size (Zhou et al., 2015). Previous studies have shown that the number of cells adhering to nanofibers is greater than that adhering to microfibers.

Live/dead staining revealed cell viability on fibrous membranes (Figure 3B). Following 24 h culture, all groups exhibited predominantly viable cells (green) with minimal red fluorescence (dead cells), confirming the material was not significantly toxic to the cells. Given the critical role of cell adhesion in proliferation and differentiation, this study assessed the impact of fibrous membranes on the adhesion behavior and morphological spreading of BMSCs by means of a cytoskeleton-specific staining technique. Dual-channel fluorescent labeling (phalloidin for F-actin, red; DAPI for nuclei, blue) was employed (Figure 3C). After 24 h incubation, a certain number of BMSCs were observed to be adhered to the surface of the P, PC and PCZ membranes. It was evident that the incorporation of ZIF-8 NPs had a significant impact

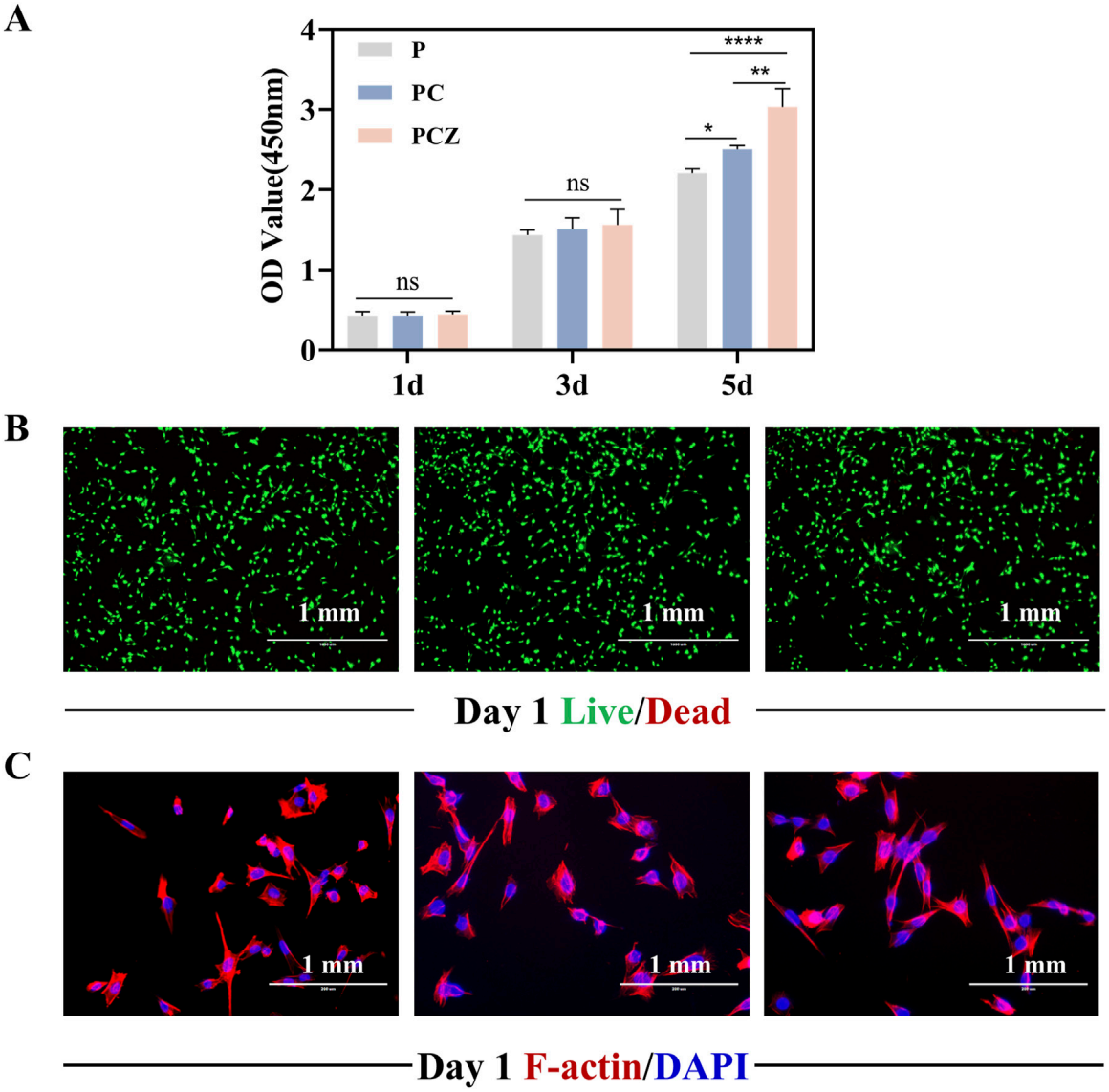

FIGURE 3
Biocompatibility of BMSCs cultured on the nanofibers *in vitro*. **(A)** Proliferation of BMSCs on the surface of the nanofibers measured by CCK-8 assay on day 1, 3, and 5. **(B)** Fluorescent staining of live/dead of BMSCs on the nanofibers at day 1. **(C)** Fluorescent staining of the cytoskeleton and nuclei of BMSCs on the nanofibers at day 1. Data are presented as mean ± SD (n = 4, $^{*}P < 0.05$, $^{**}P < 0.01$, $^{***}P < 0.001$).

on the spreading area of the cells within the material. The cells exhibited a characteristic polygonal morphology, accompanied by filamentous pseudopod extension features, suggesting that the cells had established stable extracellular matrix interactions. It was further demonstrated that PCZ fibrous membranes would construct a growth-promoting microenvironment via strengthened cell-matrix interactions.

3.4 *In vitro* osteogenic differentiation

As a characteristic biomarker of early stages of osteogenic differentiation, ALP expression levels were used to systematically assess the effect of nanofibrous membranes on the efficacy of early osteogenic induction in BMSCs (Ren et al., 2021). ALP staining (Figures 4A,B) and quantitative analysis of ALP activity (Figures 4D,E) demonstrated that following a 7-day and 14-day culture period, cells in all groups showed the phenomenon of violet-blue precipitate deposition, with the PCZ group showing the densest staining areas and the deepest staining intensity due to synergistic effect of ZIF-8 NPs. The PC group demonstrated significantly higher staining intensity and activity at 14 days ($P < 0.01$) in comparison to the P group. However, no statistical difference was observed between the two groups at 7 days ($P > 0.05$). Quantitative analysis further demonstrated that ALP activity in the PCZ group increased in a time-dependent manner, and its 14-day activity value was elevated approximately 1.6-fold in comparison with that of the P group ($P < 0.001$). The results indicated that ZIF-8 NPs significantly

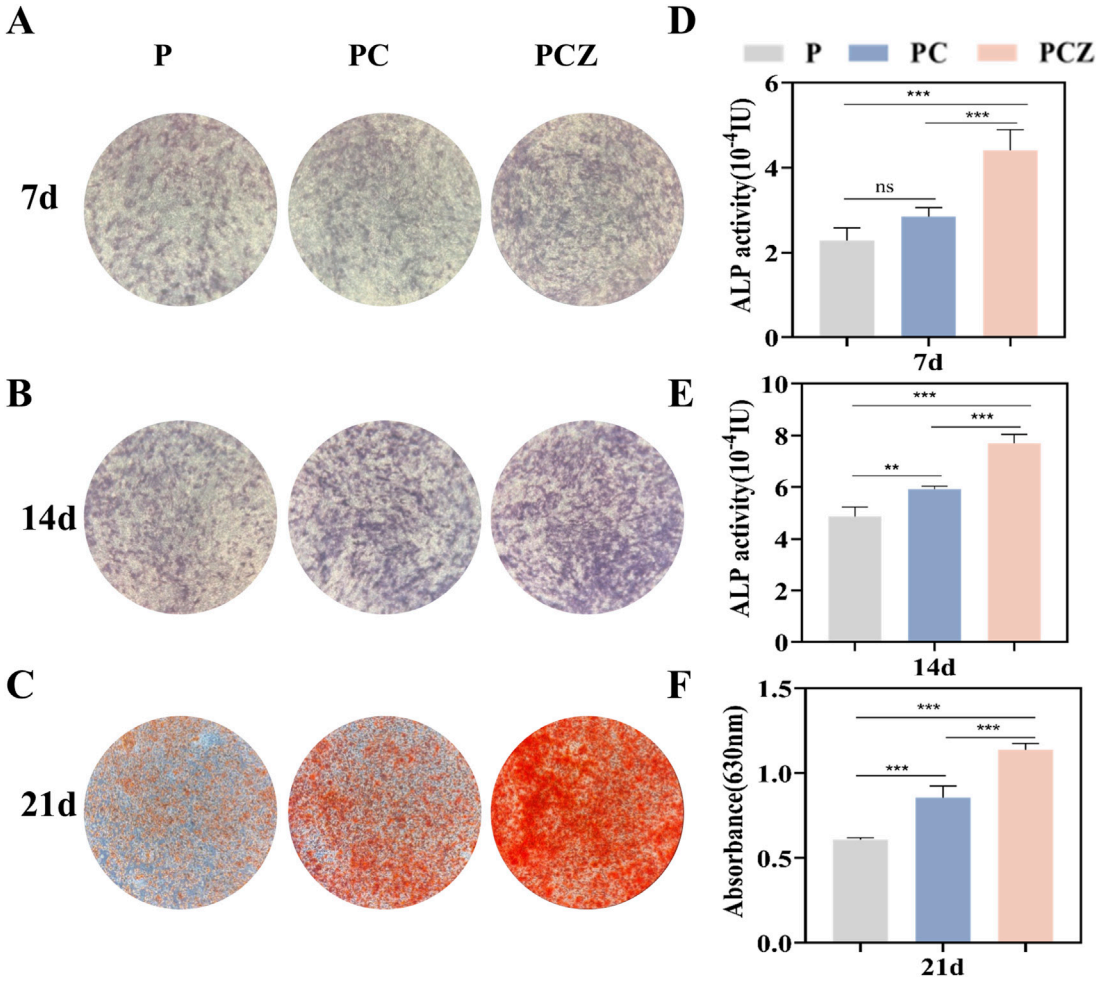

FIGURE 4
Osteogenic differentiation of BMSCs cultured on the nanofibers *in vitro*. **(A,B)** ALP staining of BMSCs cultured on the nanofibers at day 7 and 14 after osteogenic differentiation stimulation, and **(D,E)** the determination of ALP activity. **(C)** Qualitative and **(F)** quantitative characterization of Alizarin Red S staining of BMSCs cultured on different membranes at day 21. Data are presented as mean ± SD (n = 4, $^{*}P < 0.05$, $^{**}P < 0.01$, $^{***}P < 0.001$).

strengthened the early osteogenic differentiation ability of PCZ composite fibrous membranes by regulating osteogenesis-related signaling pathways.

The capacity of the extracellular matrix to mineralize was systematically assessed by means of ARS calcium nodule staining. This is a key morphological marker of advanced osteogenic differentiation (Sculean et al., 2008). Following a 21-day incubation period, the presence of orange mineralized nodule deposition was observed in all groups (Figure 4C). The PCZ group demonstrated the highest mineralization density and strongest staining intensity, followed by the PC group. In contrast, the P group exhibited the lightest staining and the lowest number of calcium nodules. The results of the semi-quantitative analysis conducted by ARS (Figure 4F) demonstrated a consistent trend with staining, with significantly higher OD values observed in the PCZ group compared to the PC group ($P < 0.01$) and the P group ($P < 0.001$). The results obtained above demonstrate that the prepared PCZ composite fiber membrane has the capacity to promote extracellular matrix mineralization and calcium deposition.

3.5 *In vitro* antibacterial ability

In the aftermath of GBR, the regenerative outcome of hard and soft tissues is subject to the influence of bacterial colonization and infection (Wang et al., 2020). The introduction of antimicrobial components has been demonstrated to be efficacious in the prevention of infection, as well as in the reduction of inflammation (Brown et al., 2018). In the context of bacterial research, *E. coli* (Gram-negative bacteria) and *S. aureus* (Gram-positive bacteria) have been selected as models to assess the antimicrobial capacity of PCZ nanofiber membranes.

As demonstrated in Figure 5A, the antibacterial properties of distinct fiber membranes were examined through agar plate counting. In comparison to P and PC, PCZ nanofiber membrane exhibited substantial bacterial inhibition, evidenced by a substantial decrease in the number of bacterial colonies following 12 h of inoculation with *E. coli* and *S. aureus* (Figure 5B). Moreover, OD values of bacterial strains co-cultured with the fiber membranes were investigated. As depicted in Figures 5C,D, after 12 h of co-incubation, the OD value of the P showed no significant

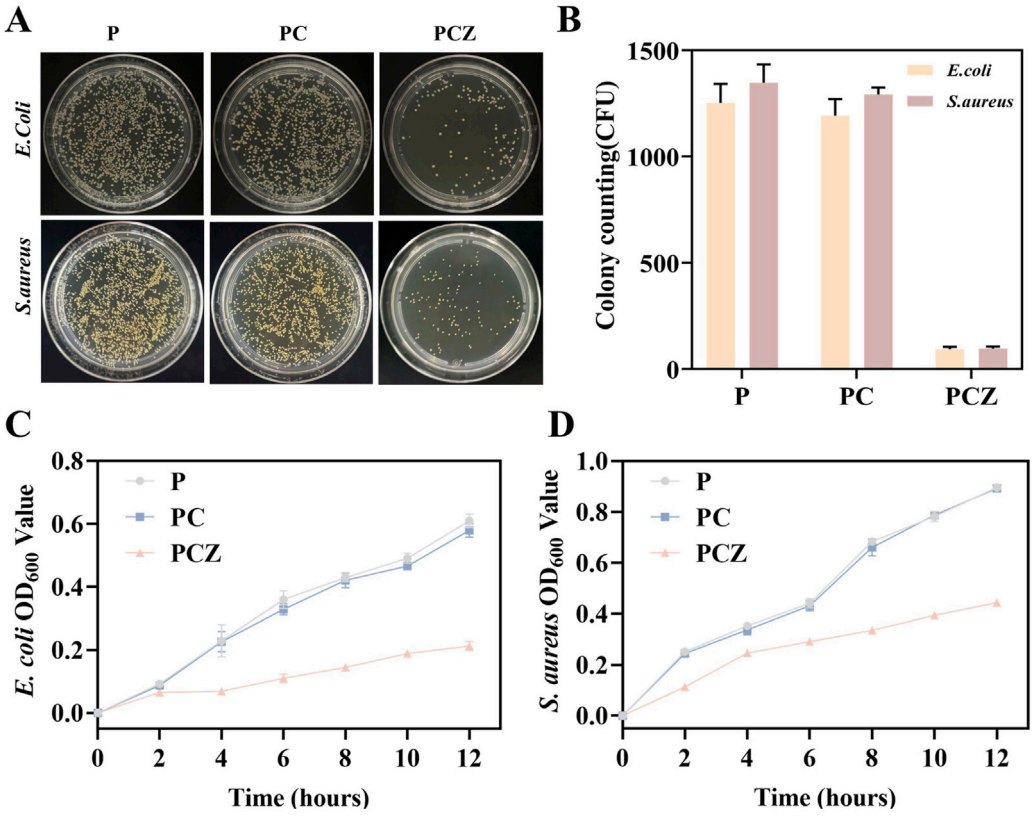

FIGURE 5
Antibacterial ability of the nanofibers *in vitro*. **(A)** Agar plate images for *E. coli* and *S. aureus* treated with the different membranes. **(B)** Colony counts for *E. coli* and *S. aureus*. OD values of bacterial solution for **(C)** *E. coli* and **(D)** *S. aureus* cocultured with different membranes. Data are presented as mean ± SD (n = 3, $*P < 0.05$, $**P < 0.01$, $***P < 0.001$).

difference compared to that of the PC, indicating that Col contributes minimally to the antibacterial activity of the PC membrane. In contrast, the OD values for *E. coli* and *S. aureus* in the PCZ were substantially lower than those in the P and PC. This demonstrates a significantly enhanced antibacterial effect, further confirming that the Zn^{2+} released from the PCZ fiber membrane demonstrates certain inhibitory activity against *E. coli* and *S. aureus*.

Membrane materials have been shown to carry a high risk of infection during the initial week following implantation. To prevent further bacterial colonization, it is essential to ensure a sustained release of Zn^{2+} (Xue et al., 2014). ZIF-8 nanoparticles, derived from PCZ nanofiber membranes, have been demonstrated to be effective in preventing bacterial colonization, with a sustained release capacity of at least 7 days (Figure 2F). This property is crucial in the early stages of bacterial colonization, where it can play a pivotal role in preventing the establishment of bacterial communities (Wu, B. et al., 2019).

3.6 *In vivo* bone regeneration

The study evaluated the efficacy of PCZ nanofiber membranes on bone tissue regeneration in a rat cranial defect model (diameter: 5 mm). Three types of membrane materials, P, PC and PCZ membranes, were tested in parallel and the results were compared with a "no membrane control" group (Figure 6A). The rats were euthanized 4 weeks after surgery, and the cranial defects were collected and assessed for bone regeneration by Micro-CT and histological analysis.

A reconstructed Micro-CT scan image is presented in Figure 6A, showing newly formed bone within the defect at 4 weeks postoperatively. The 3D reconstructed image demonstrated a significant increase in bone regeneration in the defect treated with PCZ fibrous membrane. Specifically, a significant increase in bone volume to tissue volume (BV/TV) was observed in the PCZ fiber membrane treated site compared to the untreated site and the other fiber membrane treated sites ($P < 0.01$) (Figure 6B).

Moreover, the results of H&E staining further validated the results of the Micro-CT analysis. As demonstrated in Figure 6C, in the blank control group, connective tissue occupied the majority of the bone defect area, with only a minimal amount of new bone formation observable at the edges. Observations revealed the presence of new bone formation on the inner face of the fibrous membrane material in all three groups (P, PC and PCZ). The study demonstrated that the osteoconductive ability of the membrane was indicated by the growth of new bone from the edge of the defect. A significant number of osteoblasts could be seen surrounding the bone defect area in the PCZ group, indicating a promising bone regeneration ability. Furthermore, new bone was discovered beneath the membrane, predominantly originating from its base. This phenomenon can be attributed to the

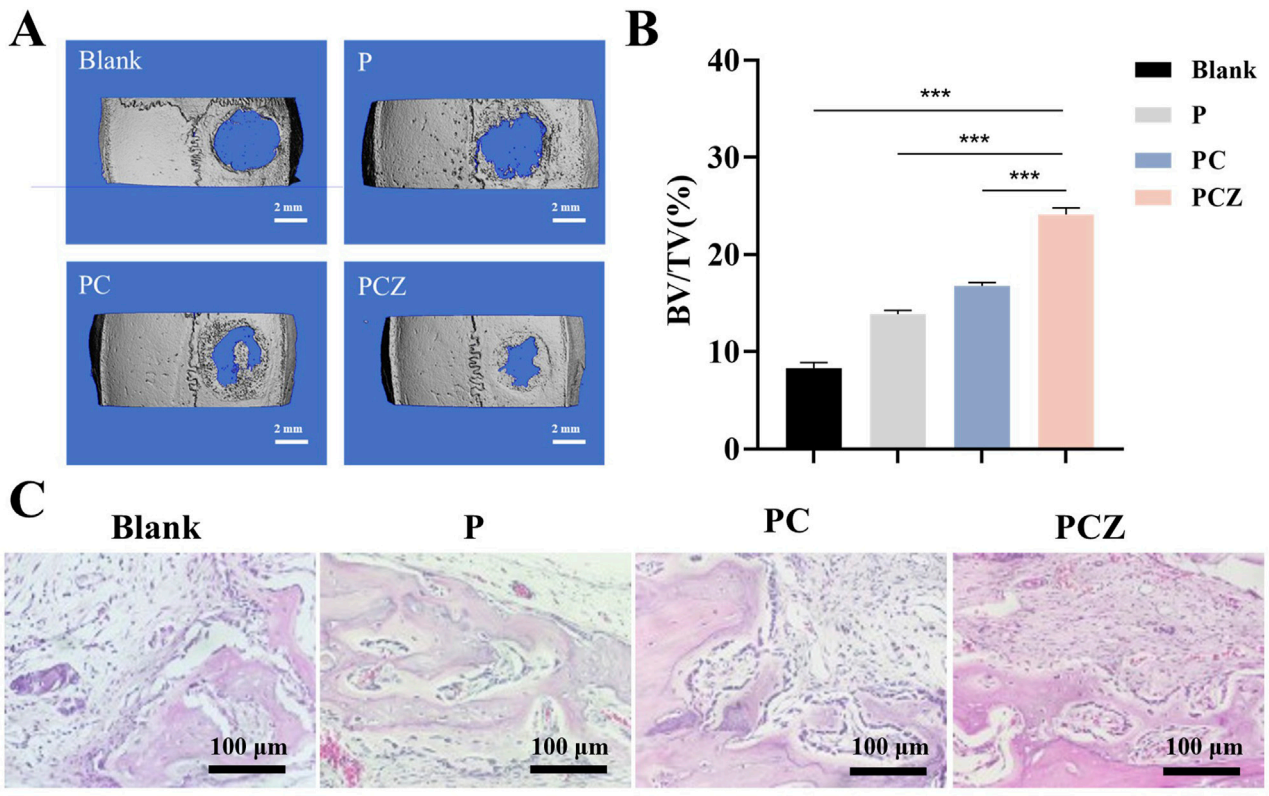

FIGURE 6
New bone formation in a rat cranial defect model after implantation of the nanofibers. **(A)** Micro-CT reconstructions of the defects after 4 weeks post-surgery in different groups (Blank, P, PC, and PCZ). **(B)** Bone volume to tissue volume (BV/TV) in the calvarial defect determined by micro-CT. **(C)** H&E staining images of sections of different groups after 4 weeks post-surgery. Data are presented as mean ± SD (n = 5, $*P < 0.05$, $**P < 0.01$, $***P < 0.001$).

presence of stem cells beneath the dura matter, a characteristic commonly observed in models of cranial defects. For histological assessment of visceral organs, examination of critical organs (heart, liver, spleen, lungs, and kidneys) via H&E staining revealed no significant toxicity or injury (Supplementary Figure S5A). Additionally, in the blood biochemical tests, no abnormalities were detected in WBC, RBC, HGB, PLT, AST, ALT, UREA, or CREA at day 3 (Supplementary Figure S5B). The implanted membranes demonstrated neither hematological nor organ toxicity, providing critical evidence supporting their biological applications. This study has limitations in detecting inflammatory indicators; future research must further examine the pathological manifestations of inflammatory responses.

While this study confirms the macroscopic efficacy of composite materials in promoting bone regeneration through multi-scale characterization, the following limitations must be acknowledged. First, the molecular regulatory mechanisms by which the material mediates bone repair remain incompletely elucidated. Second, although electrospinning technology successfully constructed a biomimetic nanofiber scaffold, scalable production remains constrained by the low throughput of single-nozzle spinning and its sensitivity to processing parameters. Furthermore, this study focused on the early stage of bone repair, primarily monitoring the 7-day Zn^{2+} release kinetics, but the risk of Zn^{2+} accumulation during the later degradation phase and its coupling effect with new bone remodeling rates require further validation through long-term experiments. To address these issues, subsequent investigations will build upon previous signal transduction pathway research to examine whether canonical osteogenic signaling pathways participate in PCZ-induced BMSCs osteogenic differentiation. Simultaneously, the *in vivo* observation period will be prolonged to 12 weeks to further evaluate the spatiotemporal matching between material degradation and bone functional reconstruction, thereby facilitating the material's advancement toward clinical translation.

4 Conclusion

In this study, a novel Col and ZIF-8 reinforced PLGA fiber-guided bone regeneration membrane was successfully prepared by electrospinning. The incorporation of Col into the PLGA-based membranes resulted in a substantial enhancement of their mechanical strength, while the addition of ZIF-8 nanoparticles facilitated the sustained release of zinc ions from the fibrous membranes. The incorporation of ZIF-8 and Col enhanced the cytocompatibility of PLGA membranes to BMSCs; notably, doped ZIF-8 considerably promoted osteogenic differentiation of BMSCs. PCZ fibrous membranes have been demonstrated to provide a basic microenvironment for osteoblasts and have been shown to promote bone defect repair in a rat cranial defect model. Therefore, it is

considered that electrostatically spun PCZ fiber membranes are potential candidates for guided bone tissue regeneration applications.

Data availability statement

The raw data supporting the conclusions of this article will be made available by the authors, without undue reservation.

Ethics statement

The animal study was approved by the Ethical Committee on Animal Experiments of Harbin Medical University (Approval No. 2024007). The study was conducted in accordance with the local legislation and institutional requirements.

Author contributions

TW: Conceptualization, Writing – original draft, Methodology, Formal Analysis. QX: Formal Analysis, Supervision, Writing – review and editing, Validation. HL: Methodology, Writing – review and editing, Software, Resources. YS: Writing – review and editing, Validation, Supervision, Resources. WX: Funding acquisition, Project administration, Conceptualization, Writing – review and editing.

Funding

The author(s) declare that financial support was received for the research and/or publication of this article. This research was funded by the Construction of Oral Experimental Teaching Base (Grant No. 31993190299).

Conflict of interest

The authors declare that the research was conducted in the absence of any commercial or financial relationships that could be construed as a potential conflict of interest.

Generative AI statement

The author(s) declare that no Generative AI was used in the creation of this manuscript.

Publisher's note

All claims expressed in this article are solely those of the authors and do not necessarily represent those of their affiliated organizations, or those of the publisher, the editors and the reviewers. Any product that may be evaluated in this article, or claim that may be made by its manufacturer, is not guaranteed or endorsed by the publisher.

Supplementary material

The Supplementary Material for this article can be found online at: https://www.frontiersin.org/articles/10.3389/fbioe.2025.1611948/full#supplementary-material

References

Ahi, Z. B., Assunçao-Silva, R. C., Salgado, A. J., and Tuzlakoglu, K. (2020). A combinatorial approach for spinal cord injury repair using multifunctional collagen-based matrices: development, characterization and impact on cell adhesion and axonal growth. *Biomed. Mat.* 15 (5), 055024. doi:10.1088/1748-605X/ab924d

Anselme, K. (2000). Osteoblast adhesion on biomaterials. *Biomaterials* 21 (7), 667–681. doi:10.1016/S0142-9612(99)00242-2

Brown, J. H., Das, P., DiVito, M. D., Ivancic, D., Tan, L. P., and Wertheim, J. A. (2018). Nanofibrous plga electrospun scaffolds modified with type I collagen influence hepatocyte function and support viability *in vitro*. *Acta. Biomater.* 73, 217–227. doi:10.1016/j.actbio.2018.02.009

Carbonell, J. M., Martín, I. S., Santos, A., Pujol, A., Sanz-Moliner, J. D., and Nart, J. (2014). High-density polytetrafluoroethylene membranes in guided bone and tissue regeneration procedures: a literature review. *Int. J. Oral. Maxillofac. Surg.* 43 (1), 75–84. doi:10.1016/j.ijom.2013.05.017

Dimitriou, R., Mataliotakis, G. I., Calori, G. M., and Giannoudis, P. V. (2012). The role of barrier membranes for guided bone regeneration and restoration of large bone defects: current experimental and clinical evidence. *BMC Med.* 10, 81. doi:10.1186/1741-7015-10-81

Gao, X. M., Xue, Y. Y., Zhu, Z., Chen, J. Y., Liu, Y. H., Cheng, X. T., et al. (2021). Nanoscale zeolitic imidazolate Framework-8 activator of canonical mapk signaling for bone repair. *ACS Appl. Mat. Interfaces.* 13 (1), 97–111. doi:10.1021/acsami.0c15945

Garcia, J., Dodge, A., Luepke, P., Wang, H. L., Kapila, Y., and Lin, G. H. (2018). Effect of membrane exposure on guided bone regeneration: a systematic review and meta-analysis. *Clin. Oral. Implants. Res.* 29 (3), 328–338. doi:10.1111/clr.13121

Garcia, J. J., Berghezan, S., Caramês, J. M. M., Dard, M. M., and Marques, D. N. S. (2017). Effect of cross-linked Vs non-cross-linked collagen membranes on bone: a systematic review. *J. Periodontal. Res.* 52 (6), 955–964. doi:10.1111/jre.12470

Giliopoulos, D., Zamboulis, A., Giannakoudakis, D., Bikiaris, D., and Triantafyllidis, K. (2020). Polymer/metal organic framework (MOF) nanocomposites for biomedical applications. *Molecules* 25 (1), 185. doi:10.3390/molecules25010185

Kwak, S., Haider, A., Gupta, K. C., Kim, S., and Kang, I. K. (2016). Micro/nano multilayered scaffolds of plga and collagen by alternately electrospinning for bone tissue engineering. *Nanoscale Res. Lett.* 11, 323–16. doi:10.1186/s11671-016-1532-4

Laney, W. R. (2017). Glossary of oral and maxillofacial implants. *Int. J. Oral Maxillofac. Implants.* 32 (4), G200–G200. doi:10.11607/jomi.2017.4.gomi

Lee, J. J., Yu, H. S., Hong, S. J., Jeong, I., Jang, J. H., and Kim, H. W. (2009). Nanofibrous membrane of collagen-polycaprolactone for cell growth and tissue regeneration. *J. Mat. Sci. Mat. Med.* 20 (9), 1927–1935. doi:10.1007/s10856-009-3743-z

Liu, J., and Kerns, D. G. (2014). Mechanisms of guided bone regeneration: a review. *Open Dent. J.* 8, 56–65. doi:10.2174/1874210601408010056

Martins, A., Reis, R. L., and Neves, N. M. (2020). Biofunctional nanostructured systems for regenerative medicine. *Nanomedicne* 15 (16), 1545–1549. doi:10.2217/nnm-2020-0147

Nagata, M., and Lönnerdal, B. (2011). Role of zinc in cellular zinc trafficking and mineralization in a murine osteoblast-like cell line. *J. Nutr. Biochem.* 22 (2), 172–178. doi:10.1016/j.jnutbio.2010.01.003

Pan, Y. C., Liu, Y. Y., Zeng, G. F., Zhao, L., and Lai, Z. P. (2011). Rapid synthesis of zeolitic imidazolate Framework-8 (Zif-8) nanocrystals in an aqueous system. *Chem. Commun.* 47 (7), 2071–2073. doi:10.1039/c0cc05002d

Park, H. K., Joo, W., Gu, B. K., Ha, M. Y., You, S. J., and Chun, H. J. (2018). Collagen/Poly(D,L-Lactic-Co-Glycolic acid) composite fibrous scaffold prepared by independent nozzle control multi-electrospinning apparatus for dura repair. *J. Ind. Eng. Chem.* 66, 430–437. doi:10.1016/j.jiec.2018.06.010

Raz, P., Brosh, T., Ronen, G., and Tal, H. (2019). Tensile properties of three selected collagen membranes. *Biomed. Res. Int.* 2019, 1–8. doi:10.1155/2019/5163603

Ren, C. X., Hao, X. Q., Wang, L., Hu, Y., Meng, L., Zheng, S. Z., et al. (2021). Metformin carbon dots for promoting periodontal bone regeneration Via activation of erk/ampk pathway. *Adv. Healthc. Mat.* 10 (12), e2100196. doi:10.1002/adhm.202100196

Ren, Y. R., Fan, L., Alkildani, S., Liu, L., Emmert, S., Najman, S., et al. (2022). Barrier membranes for guided bone regeneration (GBR): a focus on recent advances in collagen membranes. *Int. J. Mol. Sci.* 23 (23), 14987. doi:10.3390/ijms232314987

Rothamel, D., Schwarz, F., Sager, M., Herten, M., Sculean, A., and Becker, J. (2005). Biodegradation of differently cross-linked collagen membranes: an experimental study in the rat. *Clin. Oral. Implants. Res.* 16 (3), 369–378. doi:10.1111/j.1600-0501.2005.01108.x

Sculean, A., Nikolidakis, D., and Schwarz, F. (2008). Regeneration of periodontal tissues: combinations of barrier membranes and grafting materials - biological foundation and preclinical evidence: a systematic review. *J. Clin. Periodontol.* 35, 106–116. doi:10.1111/j.1600-051X.2008.01263.x

Sheikh, Z., Qureshi, J., Alshahrani, A. M., Nassar, H., Ikeda, Y., Glogauer, M., et al. (2017). Collagen based barrier membranes for periodontal guided bone regeneration applications. *Odontology* 105 (1), 1–12. doi:10.1007/s10266-016-0267-0

Stachewicz, U., Bailey, R. J., Wang, W., and Barber, A. H. (2012). Size dependent mechanical properties of electrospun polymer fibers from a composite structure. *Polymer* 53 (22), 5132–5137. doi:10.1016/j.polymer.2012.08.064

Sun, C. Y., Qin, C., Wang, X. L., Yang, G. S., Shao, K. Z., Lan, Y. Q., et al. (2012). Zeolitic imidazolate Framework-8 as efficient Ph-Sensitive drug delivery vehicle. *Dalton Trans.* 41 (23), 6906–6909. doi:10.1039/c2dt30357d

Tan, E. P. S., Ng, S. Y., and Lim, C. T. (2005). Tensile testing of a single ultrafine polymeric fiber. *Biomaterials* 26 (13), 1453–1456. doi:10.1016/j.biomaterials.2004.05.021

Trobos, M., Juhlin, A., Shah, F. A., Hoffman, M., Sahlin, H., and Dahlin, C. (2018). *in vitro* evaluation of barrier function against oral bacteria of dense and expanded polytetrafluoroethylene (ptfe) membranes for guided bone regeneration. *Clin. Implant. Dent. Relat. Res.* 20 (5), 738–748. doi:10.1111/cid.12629

Urban, I. A., and Monje, A. (2019). Guided bone regeneration in alveolar bone reconstruction. *Oral Maxillofac. Surg. Clin. North Am.* 31 (2), 331–338. doi:10.1016/j.coms.2019.01.003

Visscher, D. O., Farré-Guasch, E., Helder, M. N., Gibbs, S., Forouzanfar, T., van Zuijlen, P. P., et al. (2016). Advances in bioprinting technologies for craniofacial reconstruction. *Trends Biotechnol.* 34 (9), 700–710. doi:10.1016/j.tibtech.2016.04.001

Wang, C. Y., Wang, J., Zeng, L. D., Qiao, Z. W., Liu, X. C., Liu, H., et al. (2019). Fabrication of electrospun polymer nanofibers with diverse morphologies. *Molecules* 24 (5), 834. doi:10.3390/molecules24050834

Wang, J., Wang, Y. M., Zhang, Y. T., Uliana, A., Zhu, J. Y., Liu, J. D., et al. (2016). Zeolitic imidazolate framework/graphene oxide hybrid nanosheets functionalized thin film nanocomposite membrane for enhanced antimicrobial performance. *ACS Appl. Mat. Interfaces.* 8 (38), 25508–25519. doi:10.1021/acsami.6b06992

Wang, J. L., Zhan, L. L., Zhang, X. H., Wu, R. F., Liao, L., and Wei, J. C. (2020). Silver nanoparticles coated Poly(L-Lactide) electrospun membrane for implant associated infections prevention. *Front. Pharmacol.* 11, 431. doi:10.3389/fphar.2020.00431

Wang, X. F., Ding, B., and Li, B. Y. (2013). Biomimetic electrospun nanofibrous structures for tissue engineering. *Mat. Today.* 16 (6), 229–241. doi:10.1016/j.mattod.2013.06.005

Wu, B., Fu, J., Zhou, Y., Shi, Y., Wang, J., Feng, X., et al. (2019). Metal-organic framework-based chemo-photothermal combinational system for precise, rapid, and efficient antibacterial therapeutics. *Pharmaceutics* 11, 463. doi:10.3390/pharmaceutics12020148

Xue, J., He, M., Liu, H., Niu, Y., Crawford, A., Coates, P. D., et al. (2014). Drug loaded homogeneous electrospun PCL/Gelatin hybrid nanofiber structures for anti-infective tissue regeneration membranes. *Biomaterials* 35 (34), 9395–9405. doi:10.1016/j.biomaterials.2014.07.060

Xue, Y., Zhu, Z., Zhang, X., Chen, J., Yang, X., Gao, X., et al. (2021). Accelerated bone regeneration by MOF modified multifunctional membranes through enhancement of osteogenic and angiogenic performance. *Adv. Healthc. Mat.* 10 (6), e2001369. doi:10.1002/adhm.202001369

Yamaguchi, M., and Weitzmann, M. N. (2011). Zinc stimulates osteoblastogenesis and suppresses osteoclastogenesis by antagonizing Nf-Kb activation. *Mol. Cell. Biochem.* 355 (1-2), 179–186. doi:10.1007/s11010-011-0852-z

Yang, J., and Yang, Y. W. (2020). Metal-organic frameworks for biomedical applications. *Small* 16 (10), e1906846. doi:10.1002/smll.201906846

Yang, X., Li, Y. Y., He, W., Huang, Q. L., Zhang, R. R., and Feng, Q. L. (2018). Hydroxyapatite/collagen coating on plga electrospun fibers for osteogenic differentiation of bone marrow mesenchymal stem cells. *J. Biomed. Mat. Res. A* 106 (11), 2863–2870. doi:10.1002/jbm.a.36475

Yang, Z., Wu, C., Shi, H. X., Luo, X. Y., Sun, H., Wang, Q., et al. (2022). Advances in barrier membranes for guided bone regeneration techniques. *Front. Bioeng. Biotechnol.* 10, 921576. doi:10.3389/fbioe.2022.921576

Yusa, K., Yamamoto, O., Fukuda, M., Koyota, S., Koizumi, Y., and Sugiyama, T. (2011). *In vitro* prominent bone regeneration by release zinc ion from Zn-Modified implant. *Biochem. Biophys. Res. Commun.* 412 (2), 273–278. doi:10.1016/j.bbrc.2011.07.082

Zhou, T., Wang, N. P., Xue, Y., Ding, T. T., Liu, X., Mo, X. M., et al. (2015). Retraction: development of biomimetic tilapia collagen nanofibers for skin regeneration through inducing keratinocytes differentiation and collagen synthesis of dermal fibroblasts. *ACS Appl. Mat. Interfaces.* 7 (35), 19863. doi:10.1021/acsami.5b07490

frontiers | Frontiers in Bioengineering and Biotechnology

TYPE Original Research
PUBLISHED 03 October 2025
DOI 10.3389/fbioe.2025.1673758

OPEN ACCESS

EDITED BY
Bolei Cai,
The Fourth Military Medical University, China

REVIEWED BY
Hongyang Ma,
Peking University Hospital of Stomatology, China
Taufik Abdullah Mappa,
Taipei Medical University, Taiwan

*CORRESPONDENCE
Jianjun Yang,
yjjqd@qdu.edu.cn
Zexian Xu,
kqxuzx@163.com

RECEIVED 26 July 2025
ACCEPTED 24 September 2025
PUBLISHED 03 October 2025

CITATION
Li H, Luo D, Gao Y, Wang D, Yang J and Xu Z (2025) Animal experiment on osseointegration of porous titanium root analogue implants with composite CSn-TAK242 coating.
Front. Bioeng. Biotechnol. 13:1673758.
doi: 10.3389/fbioe.2025.1673758

Animal experiment on osseointegration of porous titanium root analogue implants with composite CSn-TAK242 coating

Hui Li[1,2], Dan Luo[1,2], Yudong Gao[1], Dashan Wang[1,2], Jianjun Yang[1,2]* and Zexian Xu[1,2,3]*

[1]The Affiliated Hospital of Qingdao University, Qingdao, China, [2]School of Stomatology, Qingdao University, Qingdao, China, [3]Dental Digital Medicine and 3D Printing Engineering Laboratory of Qingdao, Qingdao, China

Objective: Chitosan nanoparticles loaded with TLR4 inhibitors (TAK242) were coated on porous titanium root analogue implants and placeded into beagles to investigate the role of TLR4 inhibitors in inhibiting inflammatory reactions and promoting osseointegration *in vivo*.
Methods: The control group consisted of porous titanium root analogue implants fabricated via digital medical technology and 3D printing, while the experimental group included porous titanium root analogue implants with CSn and CSn-TAK242 bioactive coatings. Three groups of implants were inserted into the jaws of dogs, with their stability coefficients immediately measured upon implantation. After 3 months, samples were collected, and the bone integration and gingival attachment of the three groups were assessed using X-rays, Micro-CT, and histological section staining.
Results: All groups of porous titanium root analogue implants were correctly placed within the alveolar sockets. The stability coefficients of the implants immediately post-implantation in the control group, CSn group, and CSn-TAK242 group were (64.29 ± 4.01), (62.55 ± 1.98), and (64.59 ± 3.28), respectively, with no significant statistical difference ($P>0.05$). Three months post-surgery, imaging and histological examinations revealed bone integration with the surrounding bone tissue for all implant groups. BIC results showed: control group (68.11 ± 3.63)%, CSn group (71.07 ± 2.83)%, and Csn-TAK242 group (78.6 ± 4.52)%, with the BIC being highest in the CSn-TAK242 group, followed by the CSn group, and lowest in the control group ($P<0.05$). More importantly, compared with the control group, the BV/TV of the CSn-TAK242 group was significantly higher. In addition, the Tb.Th of the CSn-TAK242 group was significantly higher than that of the control group and CSn group ($P<0.05$). The smooth structures at the upper ends of the implants had tight gingival tissue attachment.
Conclusion: Porous titanium root analogue implants consistent with the target root morphology were successfully fabricated using digital medical technology and 3D printing. The composite CSn-TAK242 coating further enhanced the osseointegration effects of these implants.

KEYWORDS

3D printing, porous titanium, root analogue implants, osseointegration, chitosan

1 Introduction

Implant-supported dental prostheses are preferred for their aesthetic appeal, comfort, and high success rates, making them the optimal restoration method for patients with missing teeth (Wu et al., 2021). However, the standard cylindrical or conical shapes commonly used for implants in oral clinics differ significantly from the natural form of tooth roots, especially in the molar region, leading to compromised initial stability (Croitoru and Ință, 2019; Zhao et al., 2025). Additionally, traditional titanium implants often face challenges related to their high elastic modulus, which can cause stress shielding and low bioactivity, thereby increasing the risk of surgical failure (Dallago et al., 2018; Li et al., 2020).

To address these limitations, researchers have designed and manufactured personalized titanium root analogue implants (RAI) that mimic the natural root morphology. RAI adapts better to the shape of the extraction socket, minimizes damage to surrounding bone and soft tissues, and simplifies the surgical process as it does not require the implantation of bone substitutes and allows for immediate placement (Dantas et al., 2021; Aldesoki et al., 2024). With the rapid advancement of 3D printing and computer-aided design/manufacturing (CAD/CAM) technologies, some scholars have created porous RAI with a bone-like trabecular structure (Aldesoki et al., 2023). Studies indicate that the porous design of these implants facilitates metabolic waste exchange. Additionally, implants with a porosity of 60%–75% have an elastic modulus similar to bone, which enhances osteoblast adhesion and promotes osseointegration (Schubert et al., 2018; Böse et al., 2020).

The integration of the implant with surrounding bone tissues is crucial for the success of oral implantation (Bohara and Suthakorn, 2022). In the initial phase of osseointegration, mild inflammatory responses induced by tissue damage and cellular debris are essential for activating bone resorption and new bone formation. However, excessive inflammation and microbial infection can impair normal bone healing. DAMPs, such as cell debris and necrotic tissue products, can be recognized by Toll-like receptor 4 (TLR4), leading to the translocation of NF-kB and the release of cytokines, further exacerbating the inflammatory response and inhibiting tissue repair (Al-Rikabi et al., 2020; Xu et al., 2020). An abundance of inflammatory cytokines stimulates the proliferation and differentiation of osteoclasts, accelerating bone resorption, which may eventually lead to implant failure (Gao et al., 2015). Thus, reducing inflammation early in bone healing is beneficial for implant osseointegration.

According to recent studies, TLR4 is essential in mediating inflammatory responses and regulating bone metabolism (Jin et al., 2023). Activation of TLR4 stimulates the Medullary Differentiation Factor 88 (MyD88) signaling pathway, regulating osteoclast differentiation. Inhibiting TLR4 expression can promote cell proliferation and inhibit apoptosis, thereby accelerating the bone healing process (Kong et al., 2024; Tominari et al., 2024; Park et al., 2025). A study on cranial defect repair in mice genetically modified to lack TLR2 and TLR4 demonstrated superior bone healing performance compared to normal mice, further confirming the critical role of TLR4 in bone regeneration (Chukkapalli et al., 2018).

Our previous research found that chitosan nanoparticles (CSn) can serve as an effective drug delivery system (Zhou et al., 2021). CSn loaded with the TLR4 inhibitor TAK242 (CSn-anti-TLR4) has been shown to suppress inflammatory responses and promote cell proliferation and osteogenesis, offering a new therapeutic strategy to enhance alveolar bone healing and, consequently, implant osseointegration (Bhattacharyya et al., 2018). However, studies exploring the role of TLR4 inhibitors in enhancing implant osseointegration in animal models are currently lacking.

Therefore, this study employs digital medicine and 3D printing technology to fabricate personalized titanium RAIs that match the target tooth roots of Beagle dogs. The surface of these implants is coated with CSn and CSn loaded with the TLR4 inhibitor TAK242 (CSn-TAK242), to observe the osseointegration of RAIs in Beagle dogs. This research aims to provide evidence for the clinical application of composite-coated porous titanium RAIs and offer new insights into improving clinical implant success rates and lifespan.

2 Materials and methods

2.1 Experimental animals

The experimental animals were provided by Qingdao bolong Beagle Dog Breeding Co.,Ltd. Six healthy adult male Beagle dogs aged between 1 and 1.5 years, with an average weight of (15.2 ± 0.6) kg, were selected. All animal experiments were conducted in accordance with the guidelines for animal laboratory use and the operating regulations of the Animal Ethics Committee of Qingdao University Affiliated Hospital (NO. QYFYKYLL 958311920).

2.2 Main instruments and materials

Materials and equipment used included Ti_6Al_4V powder with a purity of 99.7% and particle size of 20–50 μm (Beijing Zhonghang Maite Powder Metallurgy Technology Co., Ltd., China), chitosan powder (Shandong Hengtai Jinhu Biological Products Co., Ltd., China), TAK-242 (Apoptosis and Epigenetics Company, United States), I-CAT CBCT tomography system (CAVA, United States), Mimics 17.0 (Materialise, Belgium), Geomagic Studio modeling software (Materialise, Belgium), MLAB R metal 3D laser printer (Concept laser, Germany), scanning electron microscope (SEM, JEOL, Japan), X ray diffraction (XRD, X'Pert Pro MPD, PANalytical), Fourier transform infrared spectrometer (FTIR, Nicolet 380 IR, Thermo Scientic), Micro-CT scanner (SCANCO Medical AG, Switzerland), among others.

2.3 Preparation and grouping of the composite coating on the 3D printed porous titanium RAIs

2.3.1 Data acquisition and modeling

The six Beagle dogs were sequentially numbered from D1 to D6. After anesthesia, they were fixed in the CBCT scanning chamber for sequential scanning (Figure 1A), and the original image data in DICOM format was exported. The data was imported into Mimics 17.0 software, where the bilateral third and fourth premolar roots of the six Beagle dogs (a total of 24 teeth, 48 roots) were selected as target roots and numbered (Figure 1B). Appropriate thresholds were set to extract three-dimensional images of the target roots. The upper part of the tooth

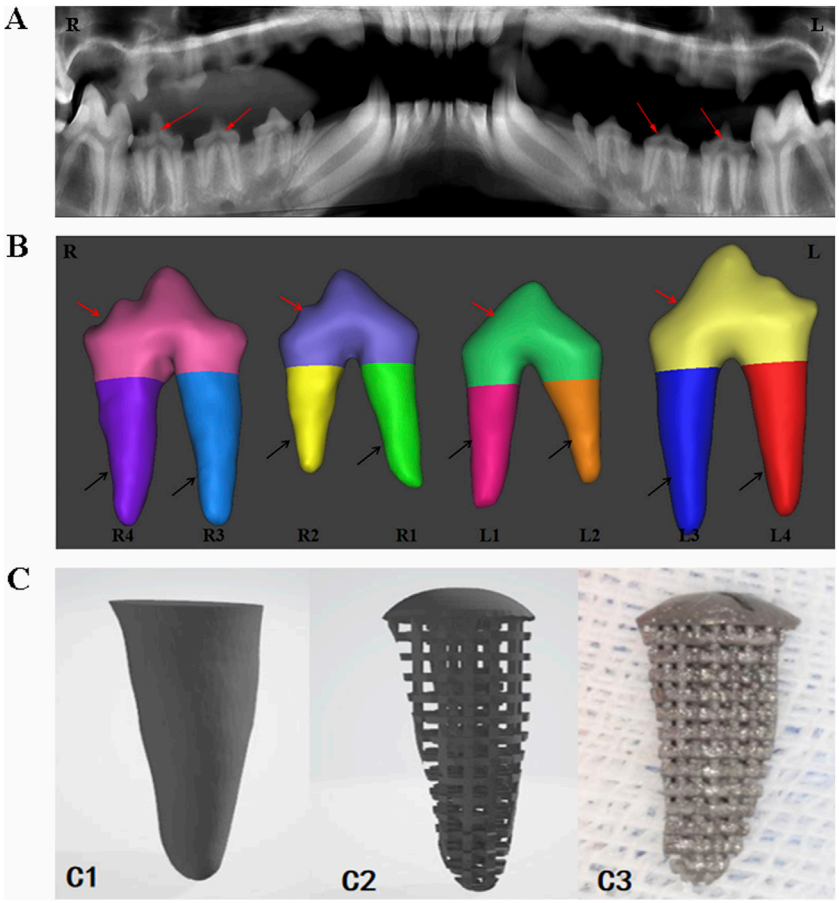

FIGURE 1
Digital model acquisition, design, and printing of RAIs. **(A)** CBCT data acquisition. **(B)** 3D model of target tooth, the red arrow indicates the crown part, and the black arrow indicates the root part. **(C1)** Extract the target tooth root image. **(C2)** Constructing a three-dimensional digital model of porous structures. **(C3)** 3D printing of porous titanium RAIs that match the shape of the target tooth root.

crown was removed at the alveolar ridge crest, and the extracted three-dimensional images were imported into Geomagic Studio software for designing the porous structure of the RAIs and the rounded structure at the upper end of the roots (Figure 1C_1C_2).

2.3.2 Preparation of porous titanium RAIs

The digital model data in STL format was imported into the MLAB R metal 3D laser printer, which used Ti_6Al_4V powder with a particle size of 20–50 μm to perform melting and sintering in an argon environment. The laser spot diameter was 70 μm, the powder layer thickness was 50 μm, and the production speed was 80 cm^3/h. Forty-eight porous titanium RAIs matching the morphology of the target roots were manufactured based on the modeling design (Figure 1C_3).

2.3.3 Preparation and grouping of the composite coating on the surface of the porous titanium porous titanium RAIs

This experiment employed the coating preparation methods for CSn and CSn-TAK242 previously established in earlier *in vitro* studies. Specifically,100 mg of CS powder was dissolved in 0.1 mol/L acetic acid solution, which was then brought to a final volume of 100 mL. The mixture was stirred continuously for 1 h using a magnetic stirrer to obtain a 1 mg/mL chitosan solution. An appropriate amount of this chitosan–acetic acid solution was taken, and a 5% (w/v) sodium tripolyphosphate solution was added dropwise under continuous magnetic stirring until the solution turned turbid. Stirring was continued for another 30 min, followed by standing for 15 min. The supernatant was collected and subjected to sonication for 5 min to obtain a well-dispersed CSn suspension. For the preparation of CSn-TAK242, an appropriate volume of the 1 mg/mL chitosan–acetic acid solution was mixed with TAK242 dilution to achieve a final drug concentration of 2 μM. To this chitosan–TAK242–acetic acid mixture, a 5% sodium tripolyphosphate solution was added dropwise under magnetic stirring until turbidity appeared. The mixture was stirred for another 30 min, allowed to stand for 15 min, and then the supernatant was collected and sonicated for 5 min to yield a uniformly dispersed CSn-TAK242 solution. By the ion crosslinking method, CSn and CSn-TAK242 solutions were prepared, and the porous titanium RAIs (n = 16) were immersed in CSn and CSn-TAK242 solutions for 10 min, air-dried naturally, and this step was repeated three times to obtain a uniform coating density. These were respectively labeled as the CSn group and the CSn-TAK242 group. Implants without surface coating treatment were designated as the Control group.

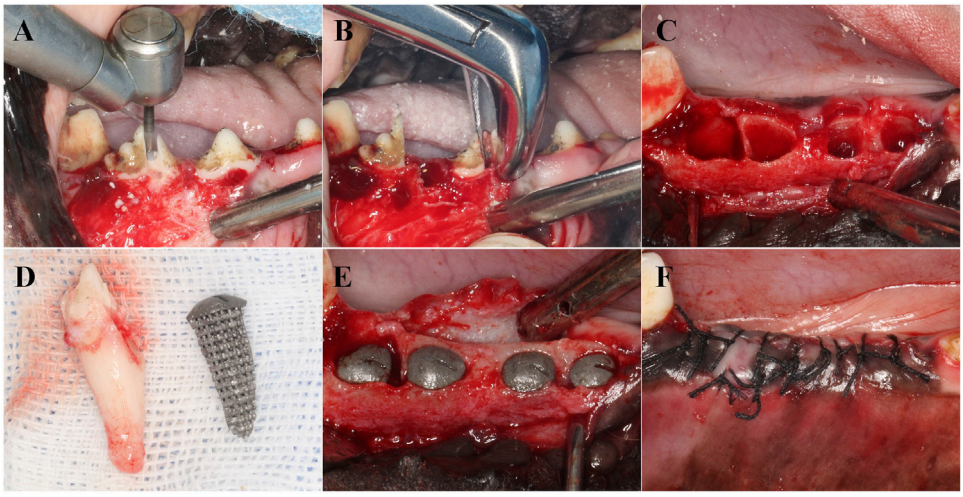

FIGURE 2
Implantation process of RAIs. **(A)** Separate dental crowns. **(B)** Remove the root of the teeth. **(C)** Scratching and cleaning the alveolar cavity. **(D)** RAIs consistent with the target teeth. **(E)** Place the RAIs in the corresponding position. **(F)** Suture.

2.4 Characterization

The surface morphology of the three groups of implants was observed using SEM. The elemental composition of the implants was detected using XPS. Phase analysis of the samples was conducted using XRD at a scanning speed of 10°/min and a scanning range of 10°–80°. The structural analysis was performed using FTIR within the testing range of 4,000–400 cm^{-1}.

2.5 Animal experiment

The entire surgical procedure was performed under general anesthesia induced using intravenous propofol (2–5 mg/kg/i.v.) and maintained with isoflurane (1%–3%). The dogs were first premedicated with medetomidine (30 μg/kg/i.m.). Local anesthesia at the surgical sites was induced by injecting 2% lidocaine hydrochloride with 1:100,000 epinephrine. The Beagle dogs were secured on the operating table, and after disinfection, the third and fourth premolars were minimally extracted. The sterilized RAIs from the three groups were implanted into the corresponding alveolar sockets according to their numbers. A Summers bone chisel was used to position the implants along the longitudinal axis of the tooth root, and a bone hammer was lightly tapped to position them. The immediate implant stability quotient (ISQ) was measured using the ID 5 implant stability measurement device. The surgical site was sutured tightly to achieve submerged healing (Figure 2). The retention and growth of the implants within the Beagle dogs were observed periodically.

2.6 Radiographic observation

Three months post-surgery, the dogs were sedated with medetomidin and anesthetized with isoflurane and propofol. Pentobarbital overdose (40–60 mg/kg/i.v., Dolethal, Vetoquinol) was used to euthanize the dogs. Mandibular bone tissue blocks containing a single RAI and surrounding bone tissue of approximately 5 mm were excised. The tissue blocks were immersed in 4% polyformaldehyde solution and fixed for 24 h before taking X-ray images to observe the status of the RAIs within the tissue blocks. The bone density of the internal and external 1 mm thick regions of the simulated RAIs were measured, and the average value was calculated. The bone density measurement results were expressed in Hounsfield units (HU). Concurrently, Micro-CT scanning was performed, and the new bone formation volume/total volume ratio (BV/TV), trabecular thickness (Tb.Th) and the bone-to-implant contact (BIC) for the three groups of RAIs were analyzed.

2.7 RT-qPCR detection

Three months post-surgery, under general anesthesia, the Beagle dogs were euthanized, and bone tissue around the implants from each group was excised. RNA from the bone tissue near the implants was extracted, and the expression of cytokines in the alveolar bone around the implants was measured using RT-qPCR (n = 3). The extracted RNA was reverse-transcribed into cDNA using the HiScript II Q RT SuperMix for RT-qPCR (gDNA wiper) kit. The expression levels of MyD88 mRNA, TRIF mRNA, TLR2 mRNA, and TLR4 mRNA in the bone were detected using an RT-qPCR instrument. The primer sequences are shown in Table 1, with the β-actin gene serving as an internal reference.

2.8 Histomorphological analysis

The fixed tissue blocks were rinsed with saline and dehydrated using a gradient of alcohol concentrations at 50%, 75%, 85%, 95%, and 100%. The blocks were then infiltrated and embedded with light-curing resin. Slices were cut along the buccolingual

TABLE 1 RT-qPCR primer sequence.

Primer	Sequence
MyD88	CCAGGGGGTCTGTATGCTTG CCCCAGACCCTGAGAAAAGG
TRIF	TGCACTGAAATGTTGGCAGC AACTGGGAAGCGGTGTCTTC
TLR2	AGCCTTGACCTCTCCAACAA TGAGGTTCACACAATCCCGA
TLR4	GTTTGAAGCAGGCCAGTGAT GGCTGACCAAGCCATCAAAA
β-actin	TGTGTTATGTGGCCCTGGAC TTCCATGCCCAGGAAGGAAG

MyD88, myeloid differentiation primary response gene 88; TRIF, TIR-domain-containing adaptor inducing interferon-β; TLR2, Toll-like receptor 2; TLR4:Toll-like receptor 2.

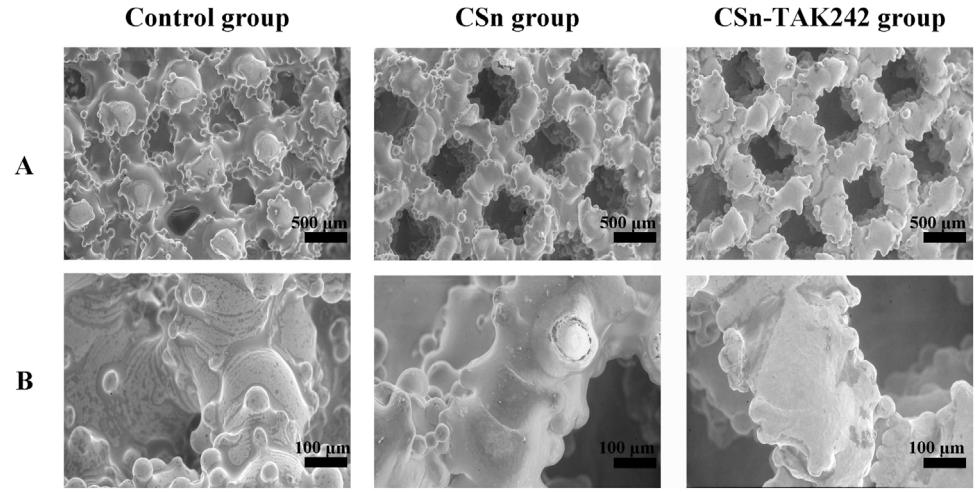

FIGURE 3
SEM images of three groups of RAIs. **(A)** Low magnification. **(B)** High magnification.

longitudinal axis of the tissue blocks using an EXAKT hard tissue cutting machine, with a slice thickness of 50 μm. The slices were then ground using the EXAKT grinding system and subsequently stained with Ladewig and encapsulated to produce histological sections, which were observed under an optical microscope to examine the bone tissue growth into the pores of the porous titanium RAIs and the attachment of the smooth rounded structures at the upper end of the implants to the gingival tissues.

2.9 Statistical analysis

Data analysis was performed using SPSS 22.0 statistical software. The normality of the data was confirmed by the Shapiro-Wilk test, and homogeneity of variances was verified using Levene's test. Continuous data are presented as X ± S deviation. An independent samples t-test was employed to compare the data between the three groups, with $P<0.05$ considered statistically significant.

3 Results

3.1 Characterization

The surfaces of the three groups of implants were observed using scanning electron microscopy after fixation. Under low magnification (Figure 3A), the implants appeared as layers of mesh structures accumulated with some titanium particles fused and protruding in a semi-spherical shape, creating a rough surface. The different meshes intertwined and connected with each other. The surface porosity of the three groups was similar, each featuring pores ranging from 300 to 500 μm in size, with good interconnectivity. Under high magnification (Figure 3B), the surface of the control group was smooth and rounded, while the experimental groups exhibited a uniformly distributed and dense coating.

XPS results (Figure 4A) showed that the Control group contained only titanium alloy elements Ti and Al, the CSn group included the addition of N, and the CSn-TAK242 group also showed

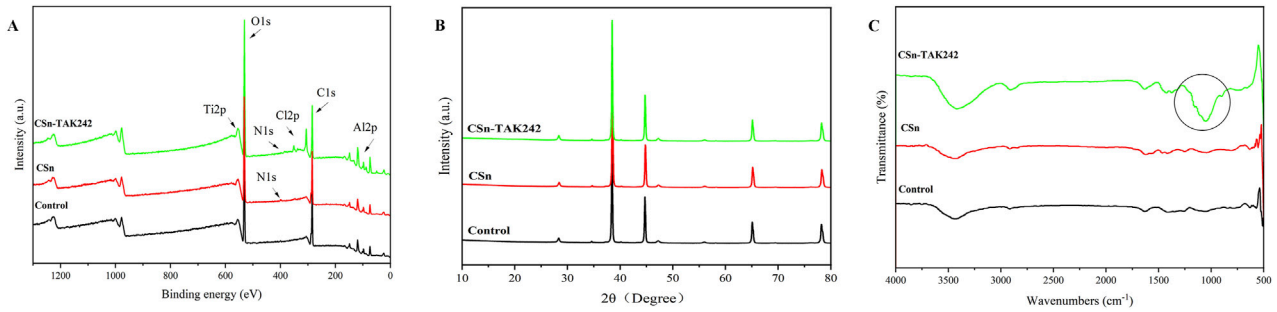

FIGURE 4
Characterization of three groups of RAIs. **(A)** XPS, **(B)** XRD and **(C)** FTIR.

TABLE 2 ISQ, Survival rate, HU values, BV/TV, Tb.Th, BIC of three groups of RAIs.

Project	Control group	CSn group	CSn-TAK242 group
ISQ values	64.29 ± 4.01	62.55 ± 1.98	64.59 ± 3.28
Survival rate (%)	81.25%	87.5%[a]	87.5%[a]
HU values	276 ± 11.43	293 ± 7.92	423 ± 15.74[a,b]
BV/TV (%)	53.62 ± 2.74	60.97 ± 2.68[a]	68.58 ± 3.14[a,b]
Tb.Th (mm)	0.3435 ± 0.0018	0.3709 ± 0.0026[a]	0.4406 ± 0.0032[a,b]
BIC (%)	68.11 ± 3.63	71.07 ± 2.83	78.69 ± 4.52[a,b]

Statistical differences are represented as.
[a]P < 0.05 (vs. Control group).
[b]P < 0.05 (vs. CSn, group).

traces of Cl, an element from the TAK242 drug. XRD patterns (Figure 4B) demonstrated that, compared with the Control group, no additional peaks emerged in the XRD profiles of the CSn group and the CSn-TAK242 group. The FTIR results (Figure 4C) revealed a distinct peak at 1,054 cm^{-1} in the CSn-TAK242 group, which corresponds to the characteristic peak of the TAK242 drug, while the other peaks exhibited similarity among the three groups. Through the analysis of the above results, it can be confirmed that CSn-TAK242 has successfully polymerized on the surface of the RAIs.

3.2 Postoperative observations

All 48 porous titanium RAIs prepared using 3D printing technology were successfully placed in the alveolar sockets. As shown in Table 2, the ISQ results were as follows: Control group (64.29 ± 4.01), CSn group (62.55 ± 1.98), and CSn-TAK242 group (64.59 ± 3.28), with no significant statistical difference in implant stability quotient among the three groups (P>0.05). The gingival flaps were able to completely cover the top of the implants and were tightly sutured closed. Ten days after surgery, some sites showed suture loss, wound dehiscence, and gingival swelling with the structure of the top of the porous titanium RAIs exposed but stable. All other wounds healed primarily with no signs of gingival swelling or infection. Three months post-implantation, CBCT imaging showed that 7 implants were lost, with 14 remaining in the CSn-TAK242 group, 14 in the CSn group, and 13 in the Control group. The remaining 41 porous titanium RAIs were analyzed.

3.3 Radiographic observation

As shown in Figure 5, X-rays indicated that all three groups of porous titanium RAIs were within the alveolar bone and tightly integrated with it, with no transmission shadow between the implant and bone, and no significant bone resorption. As shown in Table 2, HU values for the CSn-TAK242 and CSn groups were higher than those for the Control group, with the CSn-TAK242 group showing higher values than the CSn group (P<0.05). Micro-CT scans demonstrated that the pores of the porous titanium RAIs were filled with substantial bone tissue and closely integrated with the implants (Figure 6). BIC results showed: Control group (68.11 ± 3.63), CSn group (71.07 ± 2.83), and Csn-TAK242 group (78.69 ± 4.52), with the BIC being highest in the CSn-TAK242 group, followed by the CSn group, and lowest in the Control group (P<0.05). More importantly, compared with the Control group, the BV/TV of the CSn-TAK242 group was significantly higher. In addition, the Tb.Th of the CSn-TAK242 group was significantly higher than that of the Control group and CSn group, indicating that the CSn-TAK242 group had more thickness and quantity of new bone trabeculae, which demonstrated that the CSn-TAK242 group has a better effect on implant osseointegration (Table 2).

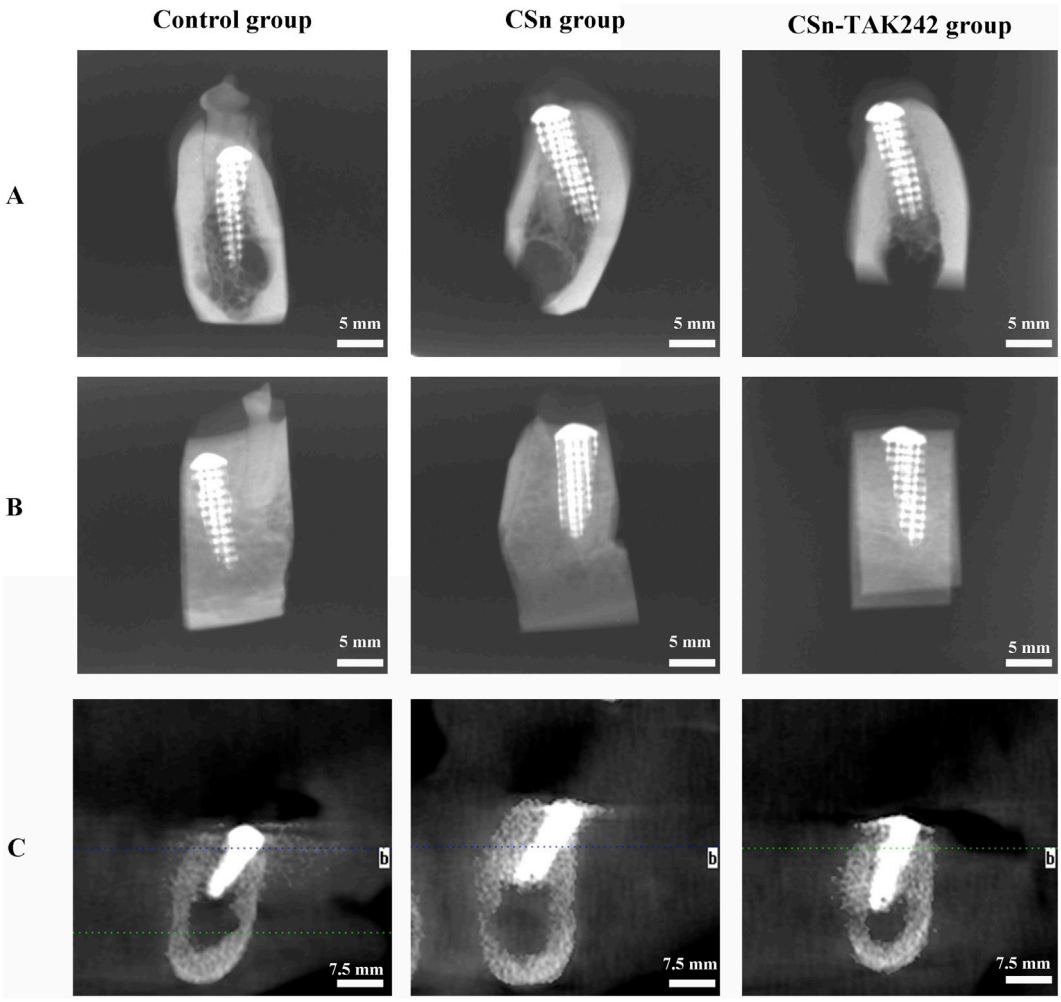

FIGURE 5
Radiographic observation of three groups of RAIs. **(A)** Buccal and lingual diameters of X-rays. **(B)** Mesial and distal diameters of X-rays. **(C)** CBCT.

3.4 Cytokine mRNA expression in bone tissue

mRNA was extracted from bone tissue, and the expression of cytokines in peri implant alveolar bone was detected by RT-qPCR. Compared to the CSn and Control groups (Figures 7A,B), the CSn-TAK242 group showed significantly reduced expression of MyD88 mRNA and TRIF mRNA ($P<0.05$). The CSn-TAK242 group exhibited significantly increased expression of TLR2 mRNA and TLR4 mRNA compared to the Control and CSn groups, with no significant differences between the Control and CSn groups (Figures 7C,D).

3.5 Histological slice observations

The histological sections observed under a microscope 3 months after the implantation of group 3 porous titanium RAIs are shown in Figure 8. Bone tissue is present in the pores inside the implants of the CSn-TAK242 group, CSn group, and Control group, forming a good bone integration tightly connected to the implants. The bone formation in the pores of the CSn-TAK242 group implants is superior to that of the CSn and Control groups. The smooth, rounded structures at the top ends of the implants in all three groups are closely adhered to by gingival tissue.

4 Discussion

Currently, the crowns of implant-supported dentures are crafted to replicate the appearance and function of natural teeth, meeting both aesthetic and practical requirements. However, the underlying support structures (typically cylindrical or conical implants) differ markedly from the natural root forms of molars, failing to emulate the biomechanical properties of natural tooth roots. With recent advancements in digital medicine and 3D printing technologies, researchers have started to explore the creation of RAIs, custom-designed to mirror natural tooth roots (Guo et al., 2020). This biomimetic approach aims to harmonize form and function in implant-supported denture restoration, offering a more integrated solution in dental prosthetics.

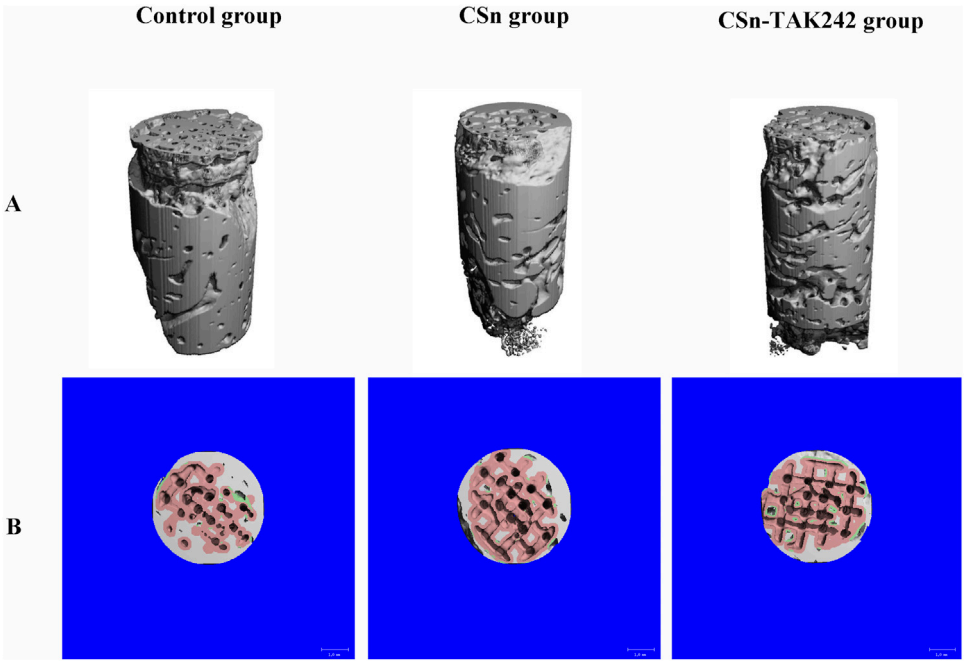

FIGURE 6
Micro CT image of three groups of RAIs at 3 months post-surgery. **(A)** 3D image. **(B)** Cross section plane image.

Compared to the standardized production of traditional cylindrical or conical implants, the advantages of RAIs are primarily: 1) The shape is consistent with the alveolar socket, allowing for extensive contact with the bone walls of the socket to generate friction and thus achieve good initial stability; 2) Often, there is no need for complex preparation of the alveolar socket, avoiding the heat damage to alveolar bone caused by mechanical cutting in traditional implant surgeries; 3) Immediate implantation of RAIs post-extraction can preserve the alveolar bone to the greatest extent, slowing the resorption of the bone walls of the socket, which is crucial for maintaining the morphology of soft and hard tissues in the implant area and reshaping aesthetic outcomes; 4) Reducing the difficulty of immediate implant surgeries and simplifying the surgical procedures, thus shortening the treatment period and alleviating patient discomfort. Customized RAIs effectively address the surgical challenges associated with immediate placement of traditional implants (Xu et al., 2022; Yang et al., 2023). Therefore, this study fabricated porous titanium RAIs consistent with natural tooth roots, coated with CSn and CSn-TAK242 coatings, and verified their osteogenic effects *in vivo* through animal experiments, providing experimental evidence for clinical applications.

Initial stability and the rate of osseointegration are crucial factors determining the success of dental implants. Good initial stability forms the foundation for implant survival, while an excellent rate of osseointegration ensures long-term stability within the alveolar bone. Research has shown that resonance frequency analysis can measure the stability of implants, providing an ISQ ranging from 0 to 100 (Huang et al., 2020). Higher ISQ values indicate better stability, with implants exhibiting ISQ values above 60 having a very low failure rate. In this study, three groups of porous titanium RAIs, consistent with the morphology of the alveolar socket, were immediately implanted, achieving high average ISQ values due to extensive frictional contact with the bone walls of the socket, thus facilitating ideal osseointegration.

Furthermore, studies suggest that the BIC rate should be no less than 50% to ensure the implant can withstand functional loads (Jiang et al., 2015). Micro-CT scans from our study revealed that all three groups of porous titanium RAIs achieved satisfactory osseointegration 3 months post-implantation: the Control group had a BIC of (68.11 ± 3.63)%, the CSn group had (71.07 ± 2.83)%, and the CSn-TAK242 group (78.69 ± 4.52)%. The BIC value of the CSn-TAK242 group was significantly higher than that of the control group, which meant that the coating accelerated the formation of local bone tissue and improved the osseointegration of RAIs. In comparison, similar studies found a BIC of (41.2 ± 20.6)% for pure titanium RAIs after 6 months. Our porous titanium RAIs showed superior osseointegration compared to similar titanium implants. Many scholars have reported on the BIC of standardized production implants; for instance, Freilich and others implanted Straumann implants into rabbit mandibles with DBM osteogenic scaffolds, resulting in a BIC of 58.1% at 8 weeks, and Kim and others reported a BIC ranging from 60.9% to 65.5% 10 weeks after implanting Osstem implants in dogs post-extraction (Kim et al., 2008; Freilich et al., 2009). Compared to these studies, our porous titanium RAIs achieved better osseointegration within a shorter healing period and outperformed standardized production implants. This improvement is due to the suitable porosity of our implants, which enhances the osseointegration rate by increasing the contact area between the implant and bone tissue, thereby facilitating the localization, adhesion, proliferation, and differentiation of bone cells. Bone cells grow into the porous structure, forming micromechanical interlocks with the implant, which increases the strength of osseointegration. Additionally, the interconnected network structure of the pores provides an advantageous environment for the exchange of bodily fluids, promoting bone tissue reconstruction and regeneration, and accelerating the process of osseointegration (Yu et al., 2020). Histological sections observed under the microscope showed that

10.3389/fbioe.2025.1673758

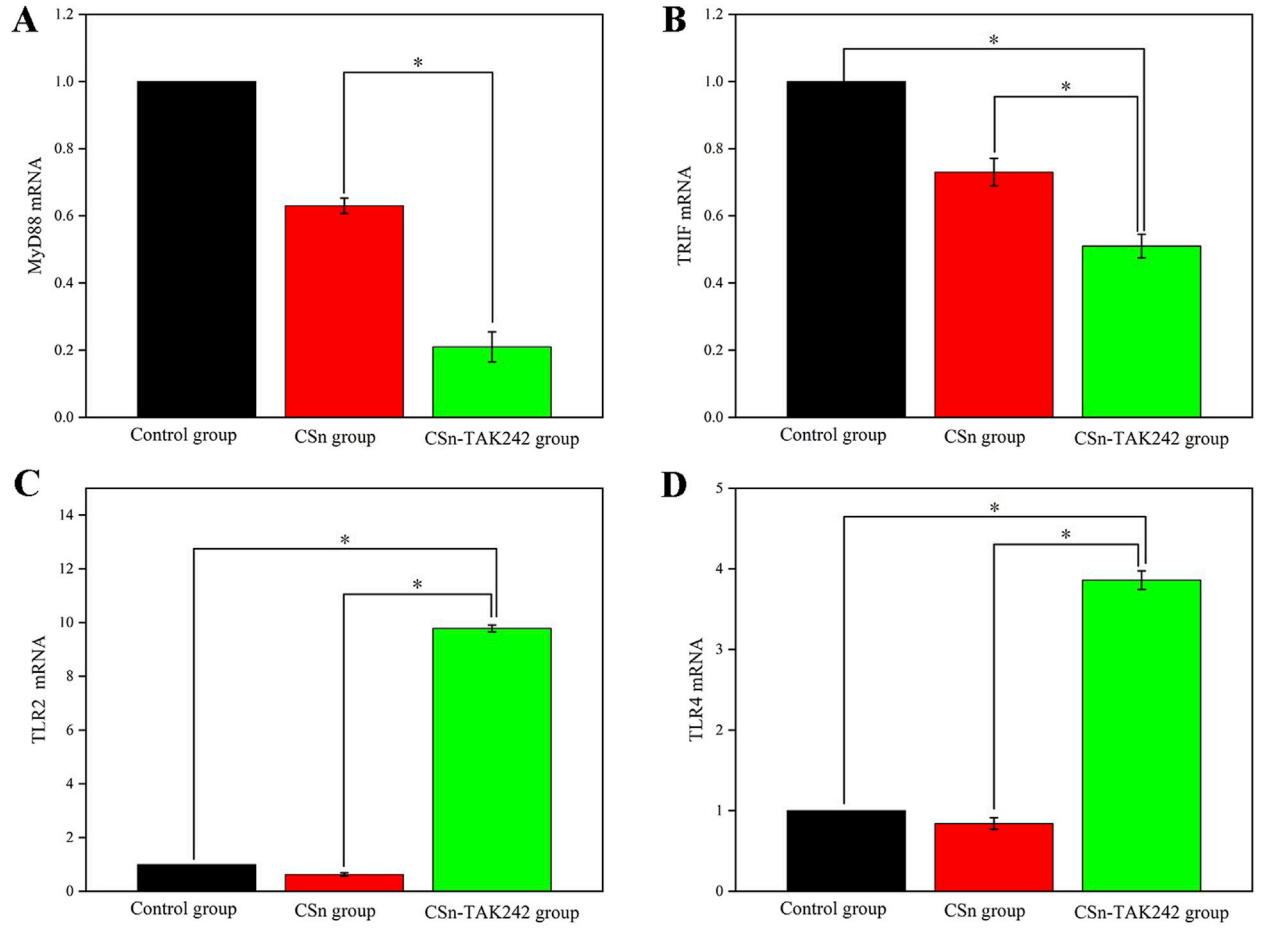

FIGURE 7
Cytokine mRNA expression in bone tissue (*p < 0.05). **(A)** MyD88 mRNA. **(B)** TRIF mRNA. **(C)** TLR2 mRNA. **(D)** TLR4 mRNA.

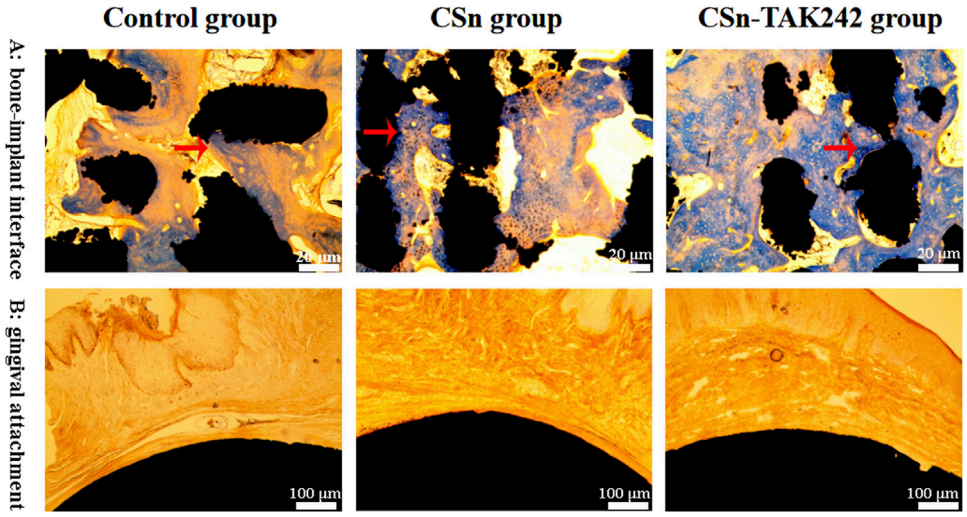

FIGURE 8
Histological slice observations. **(A)** Observation of osseointegration of implants. **(B)** The adhesion between the smooth arc-shaped structure on the upper part of the implant and the gingival tissue.

bone integration occurred not only on the outer surface of the porous titanium RAIs but also within the internal pores, confirming that these implants can achieve ideal osseointegration with the alveolar bone in a shorter healing period, thus ensuring their long-term stability.

To enhance the osseointegration between porous titanium RAIs and alveolar bone, this study applied composite CSn coatings and CSn-TAK242 coatings to the implant surfaces. Chitosan, a natural, non-toxic alkaline polysaccharide with excellent biocompatibility, degradability, and antibacterial properties, is widely used in the biomedical field. Chitosan-based drug delivery systems are favored for their targeting, sustained release, improved drug stability, and extended duration of action, often carrying bone metabolic drugs, growth factors, and exogenous regulatory genes to promote bone cell growth and tissue healing (Li et al., 2019; Liu et al., 2024). TAK242, an effective inhibitor of TLR4, reduces the expression of TLR4 and decreases the destructive impact of inflammatory factors on periodontal tissues, while also minimizing their negative effects on osteogenesis, thereby indirectly promoting osseointegration. The CSn-TAK242 coating demonstrated superior osteogenic effects compared to both the CSn coating and uncoated porous RAIs. The TLR4/MyD88 signaling pathway plays a significant role in bone metabolism and immune response regulation in osteolytic diseases. Although studies confirm TLR4's involvement in the healing of soft and hard tissue injuries, its role in implant osseointegration remains unclear. This study, by inhibiting the TLR4 signaling pathway, aimed to mitigate the inflammatory response and promote implant osseointegration (Zhong et al., 2019). The experimental results validated our hypothesis that inhibiting TLR4 could reduce inflammatory reactions during implantation, decrease alveolar bone resorption, and enhance implant osseointegration. Additionally, applying CSn and CSn-TAK242 coatings on porous titanium RAIs validated their role in enhancing osseointegration in animal experiments, aligning with the preliminary *in vitro* findings. Therefore, this study concludes that chitosan, as an effective bone-inducing material, can be applied as a surface coating on porous titanium RAIs to enhance osseointegration. Moreover, as an efficient drug carrier, chitosan can deliver TAK242 and release it slowly in the osseointegration area, offering superior enhancement of bone integration for porous titanium RAIs. While promising, the clinical translation of this strategy must consider potential limitations, including the immunogenic risk associated with animal-derived chitosan.

TLR4 is a sensitive transmembrane receptor protein that recognizes bacterial products and cellular debris, transducing downstream signals to initiate inflammatory responses. MyD88 and TRIF are two major adaptor proteins mediating TLR4 signal transduction and downstream pathways. The MyD88-dependent pathway serves as the primary signaling route for most Toll-like receptors; however, TLR4 can also indirectly recruit TRIF via the TRAM adaptor molecule. The signaling cascade dependent on TRIF is referred to as the MyD88-independent pathway. Studies have shown that MyD88-knockout mice exhibit accelerated bone healing accompanied by attenuated inflammatory responses compared to wild-type mice. In this model, enhanced bone regeneration may be mediated through the MyD88 pathway. Research also indicates that TRIF mediates multiple signaling cascades, not only triggering the release of various inflammatory factors but also participating in processes such as cell proliferation and apoptosis. Tsutsui et al. (2010) demonstrated that LPS activates the TRIF pathway via TLR4 and upregulates TNF-α expression. Additionally, LPS can stimulate immune cells or organs through the MyD88 pathway to promote TNF-α release, modulate the expression of macrophage colony-stimulating factor and osteoclast differentiation factor, and thereby regulate osteoclast differentiation. The present experimental results revealed that both the CSn and CSn-TAK242 groups exhibited reduced expression levels of MyD88 mRNA and TRIF mRNA. Furthermore, these groups demonstrated significantly improved bone union and milder inflammatory responses compared to the control group. Thus, this study confirms that inhibition of TLR4 function exerts a positive influence on downstream signaling pathways and the process of bone healing.

It is noteworthy that the TLR4 mRNA expression level in the CSn-TAK242 group was significantly higher than that in the CSn group. This phenomenon may be attributed to the specific blockade of the TLR4 intracellular signaling pathway by TAK242, which prevents its interaction with adaptor molecules. However, TLR4 itself is not eliminated; instead, its expression may be upregulated due to negative feedback regulation. Furthermore, the TLR2 mRNA level in the CSn-TAK242 group was higher than those in both the CSn group and the control group, suggesting potential crosstalk between Toll-like receptors. This observation is supported by the findings of Wang et al. (2012), who reported that TLR2 knockout mice exhibited reduced TLR4 mRNA levels compared to wild-type mice, demonstrating that the effects of TLR2 deficiency may be partly mediated through downregulation of TLR4 expression. The results of this experiment are consistent with it.

A total of 48 porous titanium RAIs were placed in this experiment, all of which demonstrated good primary stability and were subjected to submerged healing. However, only seven implants were ultimately retained, indicating a relatively high failure rate. The authors suggest that the loss of porous titanium RAIs may be attributed to multiple factors, potentially related to experimental design, surgical procedures, and postoperative animal care. Furthermore, the missing RAIs will be analyzed and discussed in detail in the follow-up study.

5 Conclusion

In summary, the use of 3D-printed porous titanium RAIs has effectively replaced compromised dental structures, achieving a seamless unity of form and function. Meanwhile, CSn-TAK242 coatings on porous titanium RAIs also exhibiting superior osseointegration. However, issues such as the connection methods between porous titanium RAIs and the upper dental crowns, as well as the placement techniques for the implants, will require further exploration and research.

Data availability statement

The raw data supporting the conclusions of this article will be made available by the authors, without undue reservation.

Ethics statement

The animal study was approved by Animal Ethics Committee of Qingdao University Affiliated Hospital. The study was conducted in accordance with the local legislation and institutional requirements.

Author contributions

HL: Methodology, Investigation, Writing – original draft. DL: Data curation, Writing – original draft, Investigation. YG: Investigation, Writing – original draft, Methodology, Validation. DW: Writing – original draft, Methodology, Visualization. JY: Formal Analysis, Writing – review and editing. ZX: Resources, Writing – review and editing, Supervision.

Funding

The author(s) declare that financial support was received for the research and/or publication of this article. This research was funded by the funding for the "Clinical Medicine + X Project" of Qingdao University Hospital (grant number: QDFY+X2023207), the Shandong Provincial Medical and Health Science and Technology Development Project (grant number:202308020875), the Qingdao Science and Technology Benefit People Project (No. 21-1-4-rkjk-20-nsh), and the Qingdao City South District Science and Technology Project (grant number: 2023-2-005-YY). This research was also supported by Young Talent of Lifting engineering for Science and Technology in Shandong, China (grant number: SDAST2024QTB030).

Acknowledgments

This study was approved by the Animal Ethics Committee of Qingdao University Affiliated Hospital (QYFYKYLL 958311920). The dog is the most loyal friend of mankind. We pay tribute to the Beagle dog in the experiment.

Conflict of interest

The authors declare that the research was conducted in the absence of any commercial or financial relationships that could be construed as a potential conflict of interest.

Generative AI statement

The author(s) declare that no Generative AI was used in the creation of this manuscript.

Any alternative text (alt text) provided alongside figures in this article has been generated by Frontiers with the support of artificial intelligence and reasonable efforts have been made to ensure accuracy, including review by the authors wherever possible. If you identify any issues, please contact us.

Publisher's note

References

Al-Rikabi, R., Al-Shmgani, H., Dewir, Y. H., and El-Hendawy, S. (2020). *In vivo* and *in vitro* evaluation of the protective effects of hesperidin in lipopolysaccharide-induced inflammation and cytotoxicity of cell. *Molecules* 25, 478. doi:10.3390/molecules25030478

Aldesoki, M., Keilig, L., Dörsam, I., Evers-Dietze, B., Elshazly, T. M., and Bourauel, C. (2023). Trueness and precision of milled and 3D printed root-analogue implants: a comparative *in vitro* study. *J. Dent.* 130, 104425. doi:10.1016/j.jdent.2023.104425

Aldesoki, M., Bourauel, C., Elshazly, T. M., Schkommodau, E., and Keilig, L. (2024). Evaluation of micromotion in multirooted root analogue implants embedded in synthetic bone blocks: an *in vitro* study. *BMC Oral Health* 24, 99–9. doi:10.1186/s12903-024-03854-1

Bhattacharyya, S., Wang, W., Tamaki, Z., Shi, B., Yeldandi, A., Tsukimi, Y., et al. (2018). Pharmacological inhibition of tolllike receptor-4 signaling by TAK242 prevents and induces regression of experimental organ fibrosis. *Front. Immunol.* 9, 2434–10. doi:10.3389/fimmu.2018.02434

Bohara, S., and Suthakorn, J. (2022). Surface coating of orthopedic implant to enhance the osseointegration and reduction of bacterial colonization: a review. *Biomater. Res.* 26, 26–17. doi:10.1186/s40824-022-00269-3

Böse, M., Hildebrand, D., Beuer, F., Wesemann, C., Schwerdtner, P., Pieralli, S., et al. (2020). Root-analogue implants for immediate implant placement: a retrospective case series. *Clin. Oral Implants Res.* 31, 275. doi:10.1111/clr.213_13644

Chukkapalli, S. S., Ambadapadi, S., Varkoly, K., Jiron, J., Aguirre, J. I., Bhattacharyya, I., et al. (2018). Impaired innate immune signaling due to combined Toll-like receptor 2 and 4 deficiency affects both periodontitis and atherosclerosis in response to polybacterial infection. *Pathog. Dis.* 76, fty076–11. doi:10.1093/femspd/fty076

Croitoru, S. M., and Inţă, M. (2019). Study on shape of dental implants. *Adv. Eng. Forum* 34, 183–188. doi:10.4028/www.scientific.net/aef.34.183

Dallago, M., Fontanari, V., Torresani, E., Leoni, M., Pederzolli, C., Potrich, C., et al. (2018). Fatigue and biological properties of Ti-6Al-4V ELI cellular structures with variously arranged cubic cells made by selective laser melting. *J. Mech. Behav. Biomed. Mater* 78, 381–394. doi:10.1016/j.jmbbm.2017.11.044

Dantas, T., Madeira, S., Gasik, M., Vaz, P., and Silva, F. (2021). Customized root-analogue implants: a review on outcomes from clinical trials and case reports. *Mater. (Basel)* 14, 2296–14. doi:10.3390/ma14092296

Freilich, M., Shafer, D., Wei, M., Kompalli, R., Adams, D., and Kuhn, L. (2009). Implant system for guiding a new layer of bone. Computed microtomography and histomorphometric analysis in the rabbit mandible. *Clin. Oral Implants Res.* 20, 201–207. doi:10.1111/j.1600-0501.2008.01615.x

Gao, H., Li, B., Zhao, L., and Jin, Y. (2015). Influence of nanotopography on periodontal ligament stem cell functions and cell sheet based periodontal regeneration. *Int. J. Nanomedicine* 10, 4009–4027. doi:10.2147/IJN.S83357

Guo, F., Hu, M., Wang, C., Huang, S., Lou, M., and Liu, C. (2020). Studies on the performance of molar porous root-analogue implant by finite element model simulation and verification of a case report. *J. Oral Maxillofac. Surg.* 78, 1965.e1–1965.e9. doi:10.1016/j.joms.2020.06.002

Huang, H., Wu, G., and Hunzier, E. (2020). The clinical significance of implant stability quotient (ISQ) measurements: a literature review. *J. Oral Biol. Craniofacial Res.* 10, 629–638. doi:10.1016/j.jobcr.2020.07.004

Jiang, G., Li, Q., Wang, C., Dong, J., and He, G. (2015). Fabrication of graded porous titanium-magnesium composite for load-bearing biomedical applications. *Mater. Des.* 67, 354–359. doi:10.1016/j.matdes.2014.12.001

Jin, X., Yu, Y., Lin, Y., Yang, J., and Chen, Z. (2023). Tendon-regulating and bone-setting manipulation promotes the recovery of synovial inflammation in rabbits with knee osteoarthritis via the TLR4–MyD88–NF-κB signaling pathway. *Ann. Transl. Med.* 11, 245. doi:10.21037/atm-22-3039

Kim, S. H., Choi, B. H., Li, J., Kim, H. S., Ko, C. Y., Jeong, S. M., et al. (2008). Peri-implant bone reactions at delayed and immediately loaded implants: an experimental study. *Oral Surg. Oral Med. Oral Pathol. Oral Radiol. Endodontology* 105, 144–148. doi:10.1016/j.tripleo.2007.04.016

Kong, J., Cheng, W., Chang, L., Yu, J., Wang, R., and Xie, J. (2024). Effects of HMGB1/TLR4 on secretion IL-10 and VEGF in human jaw bone-marrow mesenchymal stem cells. *J. Appl. Oral Sci.* 32, e20230304–e20230309. doi:10.1590/1678-7757-2023-0304

Li, W., Yang, Y., Zhang, H., Xu, Z., Zhao, L., Wang, J., et al. (2019). Improvements on biological and antimicrobial properties of titanium modified by AgNPs-loaded chitosan-heparin polyelectrolyte multilayers. *J. Mater. Sci. Mater. Med.* 30, 52. doi:10.1007/s10856-019-6250-x

Li, X., Wang, M., Zhang, W., Bai, Y., Liu, Y., Meng, J., et al. (2020). A magnesium-incorporated nanoporous titanium coating for rapid osseointegration. *Int. J. Nanomedicine* 15, 6593–6603. doi:10.2147/IJN.S255486

Liu, Z., Li, S., Xu, Z., Li, L., Liu, Y., Gao, X., et al. (2024). Preparation and characterization of carboxymethyl chitosan/sodium alginate composite hydrogel scaffolds carrying chlorhexidine and strontium-doped hydroxyapatite. *ACS Omega* 9, 22230–22239. doi:10.1021/acsomega.4c01237

Park, S., Yoon, K., Hong, E., Kim, M. W., Kang, M. G., Mizuno, S., et al. (2025). Tm4sf19 inhibition ameliorates inflammation and bone destruction in collagen-induced arthritis by suppressing TLR4-mediated inflammatory signaling and abnormal osteoclast activation. *Bone Res.* 13, 40. doi:10.1038/s41413-025-00419-y

Schubert, O., Beuer, F., Nold, E., Edelhoff, D., and Metz, I. (2018). Two digital strategies in modern implantology-root-analogue implants and the digital one-abutment/one-time concept. *Int. J. Comput. Dent.* 21, 115–131.

Tominari, T., Matsumoto, C., Tanaka, Y., Shimizu, K., Takatoya, M., Sugasaki, M., et al. (2024). Roles of toll-like receptor signaling in inflammatory bone resorption. *Biology* 13, 692–15. doi:10.3390/biology13090692

Tsutsui, H., Imamura, M., Fujimoto, J., and Nakanishi, K. (2010). The TLR4/TRIF-mediated activation of NLRP3 inflammasome underlies endotoxin-induced liver injury in mice. *Gastroenterol. Res. Pract.* 2010, 1–11. doi:10.1155/2010/641865

Wang, D., Gilbert, J. R., Cray, J. J., Kubala, A. A., Shaw, M. A., Billiar, T. R., et al. (2012). Accelerated calvarial healing in mice lacking toll-like receptor 4. *PLoS One* 7, e46945–11. doi:10.1371/journal.pone.0046945

Wu, S., Xu, J., Zou, L., Luo, S., Yao, R., Zheng, B., et al. (2021). Long-lasting renewable antibacterial porous polymeric coatings enable titanium biomaterials to prevent and treat peri-implant infection. *Nat. Commun.* 12, 3303–3314. doi:10.1038/s41467-021-23069-0

Xu, S., Zhou, Q., Jiang, Z., Wang, Y., Yang, K., Qiu, X., et al. (2020). The effect of doxycycline-containing chitosan/carboxymethyl chitosan nanoparticles on NLRP3 inflammasome in periodontal disease. *Carbohydr. Polym.* 237, 116163. doi:10.1016/j.carbpol.2020.116163

Xu, Z., Yang, Z., and Yang, J. (2022). Digital workflow for the design, manufacture, and application of custom-made short implants with wing retention device. *Front. Bioeng. Biotechnol.* 10, 885746–885747. doi:10.3389/fbioe.2022.885746

Yang, Z., Zhang, J., Xu, Z., Liu, X., Yang, J., and Tan, J. (2023). Biomechanical evaluation of custom-made short implants with wing retention applied in severe atrophic maxillary posterior region restoration: a three-dimensional finite element analysis. *Front. Bioeng. Biotechnol.* 11, 1137779–8. doi:10.3389/fbioe.2023.1137779

Yu, T., Gao, H., Liu, T., Huang, Y., and Wang, C. (2020). Effects of immediately static loading on osteointegration and osteogenesis around 3D-printed porous implant: a histological and biomechanical study. *Mater. Sci. Eng. C* 108, 110406. doi:10.1016/j.msec.2019.110406

Zhao, B., Liu, J., Li, X., Liu, C., Gao, J., and Hu, M. (2025). Comparison of residual stress distribution between root-analogue implant and threaded cylindrical implant. *BMC Oral Health* 25, 1080. doi:10.1186/s12903-025-06412-5

Zhong, X., Xiao, Q., Liu, Z., Wang, W., Lai, C. H., Yang, W., et al. (2019). TAK242 suppresses the TLR4 signaling pathway and ameliorates DCD liver IRI in rats. *Mol. Med. Rep.* 20, 2101–2110. doi:10.3892/mmr.2019.10439

Zhou, D., Xu, Z., Li, Y., Chen, L., Liu, Y., Xu, Y., et al. (2021). Preparation and characterization of thermosensitive hydrogel system for dual sustained-release of chlorhexidine and bovine serum albumin. *Mater. Lett.* 300, 130121. doi:10.1016/j.matlet.2021.130121

frontiers | Frontiers in Bioengineering and Biotechnology

TYPE Review
PUBLISHED 12 November 2025
DOI 10.3389/fbioe.2025.1637941

OPEN ACCESS

EDITED BY
Bolei Cai,
The Fourth Military Medical University, China

REVIEWED BY
Dan Lin,
Shanghai University of Medicine and Health Sciences, China
Kunal Sharma,
Swiss Federal Institute of Technology Lausanne, Switzerland

*CORRESPONDENCE
Pei Wang,
ndfskqyy620@ncu.edu.cn
Fen Liu,
ndfskqyy347@ncu.edu.cn

†These authors have contributed equally to this work and share first authorship

RECEIVED 30 May 2025
REVISED 14 October 2025
ACCEPTED 29 October 2025
PUBLISHED 12 November 2025

CITATION
Wang P, Liang J and Liu F (2025) Beyond antibiotics: advances in photothermal strategies for oral infections.
Front. Bioeng. Biotechnol. 13:1637941.
doi: 10.3389/fbioe.2025.1637941

Beyond antibiotics: advances in photothermal strategies for oral infections

Pei Wang[1,2,3*†], Jian Liang[1,2,3†] and Fen Liu[1,2,3*]

[1]School of Stomatology, Jiangxi Medical College, Nanchang University, Nanchang, Jiangxi, China, [2]Jiangxi Provincial Key Laboratory of Oral Diseases, Nanchang, Jiangxi, China, [3]Jiangxi Provincial Clinical Research Center for Oral Diseases, Nanchang, Jiangxi, China

The rising prevalence of antibiotic resistance necessitates innovative alternatives for managing polymicrobial oral infections. Photothermal therapy (PTT) emerges as a revolutionary approach that transcends conventional antimicrobial limitations by leveraging near-infrared (NIR)-activated photothermal agents to generate localized hyperthermia, enabling precise biofilm eradication while circumventing systemic drug resistance. The modality capitalizes on the anatomical accessibility of oral tissues and the optical transparency of dental structures, allowing spatiotemporal control over pathogenic niches from superficial caries biofilms to deep periodontal pockets. Recent advances in nanoplatform engineering have unlocked multifunctional PTT systems capable of synergizing thermal ablation with immunomodulation, biofilm matrix penetration, and even tissue regeneration, addressing the dual challenges of microbial persistence and host inflammatory damage. However, clinical translation remains hindered by unresolved technical barriers, including optimal thermal dosage calibration, lesion-specific material design, and long-term biosafety assessment. This review systematically dissects cutting-edge photothermal strategies across the oral infectious spectrum (dental caries, endodontic infections, periodontitis, and peri-implantitis) while critically evaluating their mechanistic innovations in overcoming antibiotic limitations. We further propose a roadmap for next-generation smart PTT systems integrating stimulus-responsive materials and microbiome-aware therapeutic paradigms to achieve personalized oral infection management.

KEYWORDS

photothermal nanoparticles, biofilm disruption, antibiotic-free strategies, localized hyperthermia, oral immunotherapy

1 Introduction

As one of the most critical anatomical regions in the body, the oral cavity constitutes the initial segment of the digestive tract and maintains direct exposure to the external environment (Madani et al., 2014; Kunath et al., 2024). This unique anatomical and physiological positioning renders it highly susceptible to colonization by a diverse array of microorganisms. Structures such as teeth, gingival sulci, and mucosal surfaces provide a nutrient-rich ecological niche for these microbial communities to colonize, flourish, and thrive (Deo and Deshmukh, 2019; Brookes et al., 2023). The oral microbiome, recognized as the second most complex microbial ecosystem in the human body, predominantly colonizes the surface of oral mucosa and dentition (Kilian et al., 2016; Xiao et al., 2020; Baker et al., 2024). The maintenance of oral microbial homeostasis is critical for preserving both oral

and systemic health. Multiple exogenous and endogenous factors—including dietary patterns, tobacco use, suboptimal oral hygiene practices, systemic comorbidities, and pharmacological interventions—can perturb the equilibrium of the oral microbiota, predisposing to pathogenic shifts (Sedghi et al., 2021; Gupta et al., 2024). Such dysbiosis states enable the proliferation of opportunistic pathogens, precipitating polymicrobial infections exemplified by periodontitis (Lamont et al., 2018; Jiang et al., 2021; Sedghi et al., 2021; Belibasakis et al., 2024). As a global health priority, oral infections rank among the most prevalent human infections, imposing significant socioeconomic burdens on healthcare infrastructure and international economies (Peres et al., 2019; Bernabe et al., 2020; Collaborators, 2025; Zheng et al., 2025). Clinically, these diseases often present with symptoms such as toothache and gingival inflammation, which can significantly impair mastication, communication, and aesthetic function, ultimately diminishing people's quality of life (Spanemberg et al., 2019; Popescu et al., 2024). Moreover, emerging evidence underscores a compelling association between oral infections and an elevated risk of systemic disorders, including diabetes mellitus, atherosclerosis, and Alzheimer's disease (Scannapieco and Cantos, 2016; Altamura et al., 2024; Popescu et al., 2024; Villoria et al., 2024). Consequently, the prevention, management, and therapeutic intervention of oral infections have garnered considerable scientific and clinical attention, underscoring the imperative for interdisciplinary research and innovative strategies to mitigate their global impact.

Oral infections comprise a diverse group of highly prevalent conditions, including dental caries, endodontics, periodontitis, and peri-implantitis, etc (Gondivkar et al., 2019; Peres et al., 2019). The management and treatment of these diseases are characterized by three distinct features: First, the affected organs (such as the pulp chamber, root canal, and periodontal tissues) are small in volume yet anatomically complex, making it difficult to completely eradicate infections, which often results in suboptimal treatment outcomes or even failure. Second, most of the oral infections are oral biofilm infection-associated diseases (Muras et al., 2022; Pan et al., 2025). Extracellular polymeric substances (EPS) in microbial biofilms offer adhesion and protection, rendering innate immune cells and conventional antimicrobials ineffective at breaking down oral biofilms and eradicating the microbes they contain (Bowen et al., 2018; Chen et al., 2023a). Third, the oral and maxillofacial region, being crucial for speech, mastication, respiration, and aesthetics, possesses complex physiological and psychological functions, necessitating minimally invasive treatment approaches that preserve function. Oral infections typically necessitate the removal of pathogenic bacteria and their biofilms (Ertem et al., 2017; Pitts and Mayne, 2021; Alawaji et al., 2022). Current clinical approaches are based on mechanical removal supplemented by antibiotics, such as scaling and root planning (SRP) therapy combined with minocycline for periodontitis (Mombelli, 2018; Sanz et al., 2020; Laforgia et al., 2024). However, the effectiveness of the traditional mechanical bacteria and biofilms removal method is primarily compromised by the intricate and small anatomical structures of the organs (Li et al., 2021; Lin et al., 2024). Meanwhile, inappropriate antibiotic use has led to bacterial resistance, including multidrug-resistant bacteria (Hernando-Amado et al., 2019; Rams et al., 2020). Oral biofilms significantly contribute to drug resistance, as their matrix effectively bars the penetration and activation of antibiotics. Moreover, as bacteria expand and metabolic residues accumulate, the resulting acidic shift within the biofilm environment not only inactivates antibiotics but also compromises their overall effect. Therefore, alternative non-antibiotic-dependent antimicrobial strategies are required to address these issues.

Widely utilized across various fields, including antimicrobial applications, photothermal therapy (PTT) represents a promising strategy for the treatment of oral infections (He et al., 2023; Wang et al., 2024; Liang et al., 2025; Zhang and Chen, 2025). PTT operates by exposing photothermal agents (PTAs) to light at a specific wavelength (e.g., visible or near-infrared, NIR), which facilitates the interaction of photons with the PTAs' surface (Overchuk et al., 2023). This interaction induces molecular vibrations and rotations, converting the absorbed energy into heat and elevating the local temperature (Fang et al., 2025; Zhang et al., 2025). Elevated temperatures disrupt bacterial cell membranes, compromising their structural integrity and increasing permeability, which leads to the leakage of essential intracellular components (Cao et al., 2024; Mondal et al., 2024). Concurrently, crucial bacterial proteins involved in replication, metabolic processes, and survival are denatured, ultimately leading to bacterial demise (Yin et al., 2019). Unlike antibiotics, PTT's physical antibacterial mechanism offers broad-spectrum capabilities, a low likelihood of inducing drug resistance, and the ability to circumvent pre-existing drug-resistant bacterial strains (Cao et al., 2024). PTT has also demonstrated significant advantages in combating biofilms. PTAs, especially in nanoparticle form, can readily traverse the EPS to access the embedded microbial cells (Pinto et al., 2020). Moreover, hyperthermia exhibits significant potential to disrupt the intrinsic physiological microenvironment of biofilms by inactivating their inherently bioactive substrates, such as nucleic acids and proteins, which contribute to the degradation of oral biofilms (Liu et al., 2021; Chen et al., 2023b; Mammari and Duval, 2023). It has also been reported that PTT can disrupt pathogen co-aggregation via the Cbe-Ltp1-Ptk1-fimA signaling pathway, thereby preventing biofilm development (Lin et al., 2024). While high temperatures (>50 °C) inhibit bacterial growth, mild PTT (mPTT; <45 °C) can modulate host immune responses and promote tissue regeneration (Sheng et al., 2021; Zhang et al., 2021; Huang et al., 2022; Li et al., 2022; Xue et al., 2022; Xue et al., 2023). Extensive studies have demonstrated that periodic mild PTT, by maintaining local temperatures at approximately 40 °C–43 °C for short durations (e.g., 3–5 min) repeated several times, can substantially mitigate inflammation and accelerate both angiogenesis and osteogenesis (Zhang et al., 2019; Li et al., 2022; Wu et al., 2022; Zeng et al., 2023; You et al., 2024). Thermal stimulation could regulate macrophage polarization by activating the PI3K-AKT1 signaling pathway, which promotes the phenotypic transition of pro-inflammatory M1 macrophages towards an anti-inflammatory and pro-reparative M2 state. Angiogenesis might be fostered through the vascular endothelial growth factor (VEGF), heat shock protein 90 (HSP90)/endothelial nitric oxide synthase (eNOS) pathways, while osteogenesis might be promoted by enhancing bone morphogenetic protein-2 (BMP-2) expression and activating the Wnt signaling pathway (Zhang et al., 2019; Sheng et al., 2021). Therefore, PTT offers a powerful and versatile approach, integrating potent antimicrobial activity with desirable anti-inflammatory and pro-regenerative functions, making

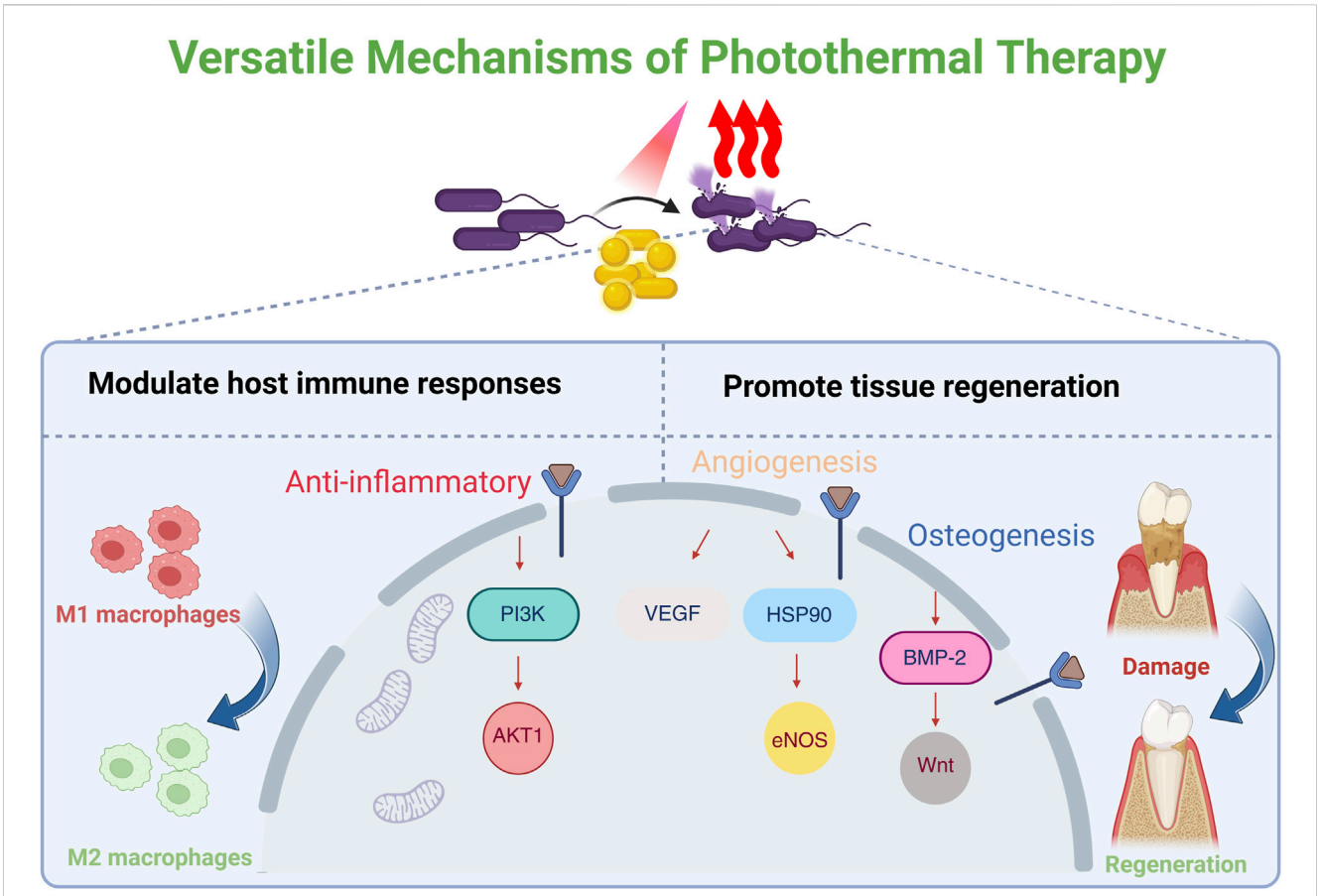

FIGURE 1
Schematic illustration of the versatile mechanisms of photothermal therapy (PTT). PTT could modulate the host's biological response. This includes promoting the polarization of pro-inflammatory M1 macrophages towards an anti-inflammatory M2 phenotype via the PI3K-AKT1 signaling pathway. The resulting pro-regenerative microenvironment enhances angiogenesis through the VEGF/HSP90/eNOS pathway and promotes osteogenesis by activating the BMP-2 and Wnt signaling pathways. Created in BioRender. Liang, J. (2025) https://BioRender.com/6vgs15f.

it a valuable strategy when combined with other antimicrobial and regenerative strategies (Chen et al., 2023b). As a non-antibiotic-dependent antimicrobial strategy, PTT offers antibacterial performance superior to that of antibiotics. This advantage stems from its non-invasive, spatiotemporal, and site-selective characteristics, strong tissue penetration, low side effects, broad-spectrum antibacterial properties, inherent resistance to the development of drug resistance, and versatile nature as a therapeutic platform (Wu J. et al., 2019) (Figure 1).

The efficacy of PTT for oral infections hinges on two factors: the PTAs and the light sources. While the superficial anatomical location of oral tissue mitigates concerns regarding penetration depth, PTT's overall effectiveness is primarily limited by the photothermal conversion efficiency (PCE) of PTAs and the risk of collateral thermal damage to healthy tissues from overheating (Liu et al., 2019; Yu S. et al., 2024). Over the past few decades, advancements in nanomaterials have significantly improved the PCE of PTAs (Zhao et al., 2024). Research has gradually shifted from focusing solely on the photothermal properties of individual materials to strategically designing and synthesizing multifunctional platforms. These platforms integrate features like targeted drug delivery, synergistic antibacterial action, and combinational immune modulation, thereby enhancing therapeutic efficacy while minimizing adverse effects. This field has rapidly progressed, yielding encouraging results. While existing reviews primarily focus on specific materials [e.g., gold-based nanomaterials (Zhang S. et al., 2024; Qi et al., 2025)] or single diseases [e.g., dental caries (Xu et al., 2025) and periodontitis (Li J. et al., 2024)], a comprehensive, interdisciplinary overview of the broader spectrum of major oral infections is still missing. Here, we summarize the advances of PTT in oral infections with a focus on dental caries, endodontics, periodontics, and peri-implantitis, highlight the design concepts and mechanisms, address the challenges PTT faces, and suggest future directions (Figure 2). We aim to provide a foundational framework for advancing PTT research for the treatment of oral infections and to catalyze the development of precise, efficient, and clinically viable therapeutic strategies (Table 1).

2 PTT for dental caries

Dental caries is a chronic condition precipitated by the accumulation of dental plaque, metabolic acid production, and subsequent localized demineralization of hard tissues, which can lead to severe tooth defects (Pitts et al., 2017; Shen et al., 2024; Zhao

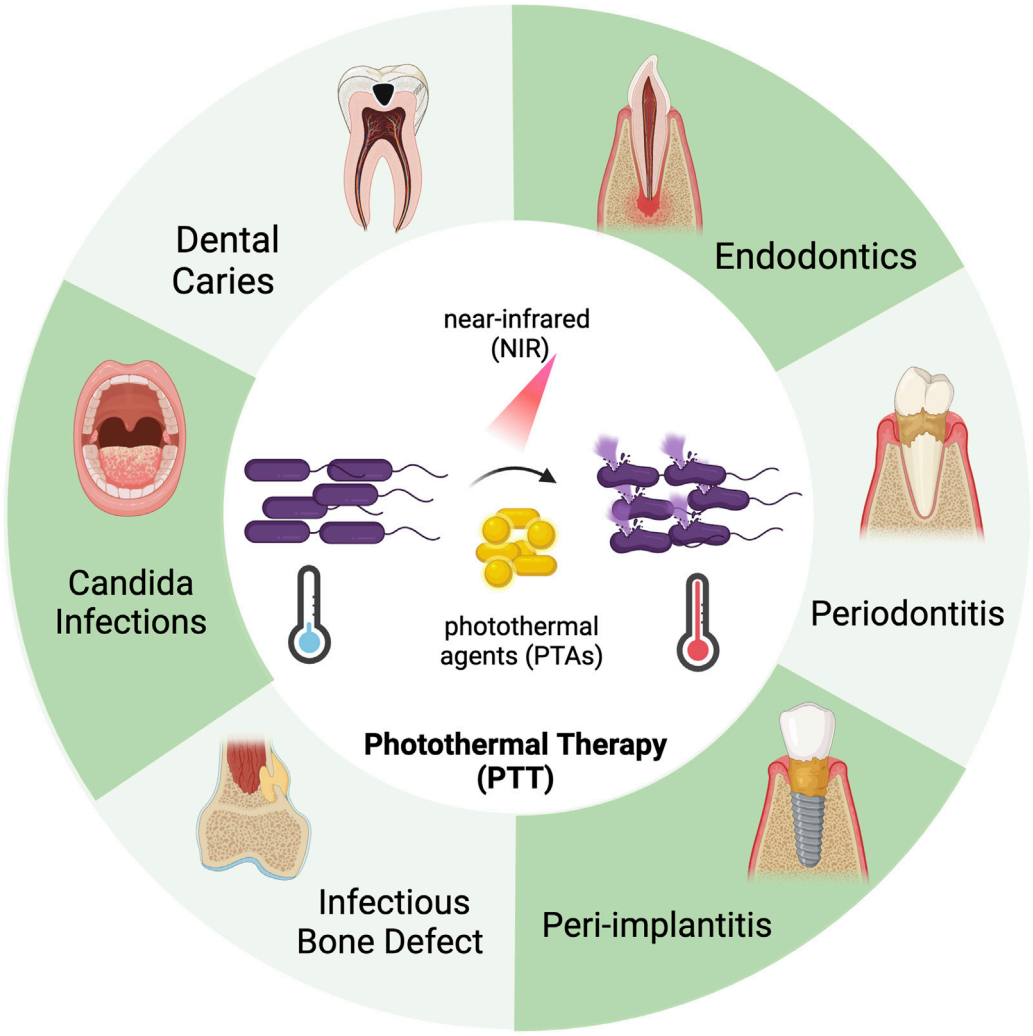

FIGURE 2
Schematic illustration of photothermal therapy (PTT) for oral infectious diseases. By leveraging photothermal agents (PTAs), PTT converts near-infrared (NIR) laser into localized hyperthermia to induce pathogen mortality. The application of PTT to oral infectious diseases has predominantly seen progress in the areas of dental caries, endodontics, periodontics, and peri-implantitis, but also holds significant promise for treating other infections like infectious bone defects and *candida* infections. Created in BioRender. Liang, J. (2025) https://BioRender.com/6vgs15f.

et al., 2024). Dental plaque, composed of cariogenic microbial biofilms, serves as a critical etiological driver in dental caries development, with *Streptococcus mutans* (*S. mutans*) being the primary cariogenic pathogen (Li et al., 2024d; Mazurel et al., 2025). The primary approach to preventing and treating caries involves using antimicrobial drugs combined with mechanical removal of decayed tissue (Akindele et al., 2025; Song et al., 2025). However, biofilms impede the penetration of antimicrobial drugs and enable bacteria to adapt their metabolic states to the biofilm microenvironment, thereby fostering antibiotic resistance (Jakubovics et al., 2021; Hajishengallis et al., 2023). Moreover, mechanical removal often damages healthy tooth structures and is prone to caries recurrence (AlSahafi et al., 2022). There have been innovative approaches for caries prevention and treatment, including therapeutics to prevent the demineralization caused by dental biofilm (Li et al., 2024d) (novel chemoprophylactic agents, antimicrobial peptides, probiotics and replacement therapy, etc.) as well as therapeutics to promote the remineralization process (fluoride and casein phosphopeptides, etc.) (Chen and Wang, 2010). However, the implementation of these methods is limited by factors such as mucosal irritation, systemic toxicity, the development of drug-resistant microbes, and the inability to maintain adequate drug concentrations in the oral cavity.

The unique properties of PTT, such as its ability to deliver localized and controlled thermal energy, make it a promising alternative to conventional methods for managing dental caries. By leveraging the photothermal effect, PTT can selectively target cariogenic biofilms without causing significant damage to surrounding healthy tissues (Zhu et al., 2014; Tan et al., 2018; Yang et al., 2018). Since cariogenic bacteria generate an acidic

TABLE 1 Summaries of photothermal therapy (PTT) for oral infectious diseases. This section comprehensively summarizes the details of recent research reported in the literature, emphasizing the functionalization of photothermal agents (PTAs), their therapeutic highlights, and the underlying design concepts and mechanisms.

Disease type	Therapy model	Photothermal agents	Functionalization	Exposure condition	Bacterial species	Research phase	Therapeutic highlights	Ref.
Dental Caries	PTT	PDA	Fe_3O_4 NPs loaded with Ag via PDA reduction and grafted with glycol chitosan post-PDA coating	808 nm, 0.75 W cm^{-2}, 10 min	*S. mutans*	Planktonic bacteria, biofilms	Ag-enhanced PTT, pH-responsive release of Ag^+, magnetically retrievable nano agents	Xu et al. (2020a)
	PTT, drug therapy		ZIF-8 coated with PDA	808 nm, 1.5 W cm^{-2}, 10 min	*S. mutans*	Planktonic bacteria, biofilms, animal model	Synergistic oral biofilm eradication using pH-responsive Zn^{2+} release and photothermal effect	Pan et al. (2025)
	PTT, PDT, drug therapy	IR780	Poly (ethylene glycol)-b-poly(3-acrylamide phenylboronic acid)-b-poly(2-(5,5-dimethyl-1,3-dioxan-2-yloxy) ethyl acrylate) dual block copolymers co-encapsulating ciprofloxacin and IR780	808 nm, 1.5 W cm^{-2}, 5 min	*S. mutans*	Planktonic bacteria, biofilms, isolated dental model, animal model	Integrating biofilm penetration and bacterial anchoring for targeted drug delivery	Yu et al. (2022)
	PTT, Drug Therapy	GO	Amino-functionalized	808 nm, 0.88 W cm^{-2}, 5 min	*S. mutans*	Planktonic bacteria	Amino-GO with integrated positive charge, strong photothermal effect, and inherent cutting effect	Lu et al. (2021)
	PTT	PB NPs	Ag^+-doped Prussian blue nanoparticles encased in cationic guar gum	808 nm, 0.4 W cm^{-2}, 3 min	*S. mutans*, *S. sobrinus*, *S. sanguinis*	Planktonic bacteria, biofilms, animal model	Combined PTT with Ag^+ release for enhanced and safer caries treatment	Li et al. (2024b)
	PTT, PDT	Zinc phthalocyanine tetrasulfonate ($ZnPcS_4$)	$ZnPcS_4$ with surface modification by guanidinium-functionalized, fluorocarbon-grafted calix [5]arene	660 nm, 1 W cm^{-2}, 5 min	*S. mutans*	Planktonic bacteria, biofilms, *in vitro* human biofilms model, animal model	Adaptive PTT and PDT enhancement enabling on-demand modality switching	Zhang et al. (2024b)
	PTT	BP NSs	Encapsulated in chitosan and PLGA-PEG-PLGA hydrogel matrices	808 nm, 1 W cm^{-2}, 5 min	*S. mutans*, *S. sanguinis*	Planktonic bacteria, animal model	Highly efficient bactericidal and remineralization-promoting effects	Ran et al. (2024)
Endodontics	PTT	AuNRs	—	810 nm, 0.2 W, 20 min	*E. faecalis*	*In vitro* biofilms	Mature *E. faecalis* biofilm developed in roots using a Modified Drip Flow Reactor (MDFR) and a Static Method	Galdámez-Falla et al. (2022)
	PTT, PCT	AuNPs	AuNPs integrated onto $Cu_{2-x}S$	808 nm, 0.5 W cm^{-2}, 10 min	*E. faecalis*, *F. nucleatum*	Isolated dental models, animal model	Combining PTT and peroxidase-like catalytic therapy (PCT) to enhance biofilm bacteria eradication in root canals	Cao et al. (2021)
	PTT	AuAg core-shell	—	808 nm, 1 W cm^{-2}, 10 min	*E. faecalis*	Planktonic bacteria, biofilms	Effective antibacterial agents against Ag^+-resistant *E. faecalis*	Feng et al. (2024)
	PTT, PDT	BP NSs	BP NSs decorated with monodisperse AuNPs	808 nm, 1 W cm^{-2}, 5 min	*E. faecalis*	Planktonic bacteria, biofilms	First study on antibacterial and antibiofilm activity of BP/Au nanocomposites via NIR light-mediated photothermal process	Aksoy et al. (2020)
	PTT, chemotherapy	Two isoindigo (DIID)-based semiconducting conjugated polymer (PBDT-DIID)	PBDT-DIID NP core incorporating polylactide	808 nm, 0.8 W cm^{-2}, 2.5 min	*E. faecalis*	Isolated dental model	Photothermal enhancement of root canal treatment outcome by heating 1% NaClO solution	Duan et al. (2022)
Periodontitis	PTT, CDT	PDA	Cu_2O NPs and PDA-coated titanium dioxide loaded within a hydrogel composite	NIR, 1.00 W cm^{-2}, 18 min 452 nm, 5.52 W m^{-2}, 5 min	*S. aureus*, *E. coli*, *S. mutans*	Planktonic bacteria, animal model	ROS generation boosts antibacterial efficacy and facilitates Cu^+ oxidation to Cu^{2+}, synergistically promoting osteogenesis with the photothermal effect	Xu et al. (2020b)

(Continued on following page)

10.3389/fbioe.2025.1637941

TABLE 1 (*Continued*) Summaries of photothermal therapy (PTT) for oral infectious diseases. This section comprehensively summarizes the details of recent research reported in the literature, emphasizing the functionalization of photothermal agents (PTAs), their therapeutic highlights, and the underlying design concepts and mechanisms.

Disease type	Therapy model	Photothermal agents	Functionalization	Exposure condition	Bacterial species	Research phase	Therapeutic highlights	Ref.
	PTT, immunotherapy	AuAg NPs	Branched AuAg NPs with a procyanidin-Fe network surface loading	808 nm, 2.5 W cm^{-2}, 3 min	*P. gingivalis*, *F. nucleatum*	Planktonic bacteria, animal model	ROS scavenging and promotion of M2 macrophage polarization via the PI3K/AKT pathway, leading to immunity regulation	Wang et al. (2022a2)
	PTT, immunotherapy		AuAg NPs loaded with procyanidins	808 nm, 2.5 W cm^{-2}, 5 min	*P. gingivalis*	Planktonic bacteria, animal model	Ag^{+} enhanced PTT provides antibacterial effect, while procyanidins regulate host immunity by scavenging ROS, inhibiting inflammation, and modulating macrophage polarization	Wang et al. (2023a)
	PTT, CDT	CuS NPs	CuS and MnS co-crystallized into nanosheets, enabling MnO_2 layer-assisted synthesis of CuS/MnS@MnO_2	808 nm, 1 W cm^{-2}, 5 min	*P. gingivalis*, *F. nucleatum*	Planktonic bacteria, biofilms, animal model	Single nanocrystalline material achieving PTT and CDT for maximized nanomedicine synergy	Chen et al. (2023c)
	PTT		CuS NPs precipitated with chitosan, then methacrylated and photo-crosslinked with GelMA to form hybrid hydrogels	808 nm, 1 W cm^{-2}, 5 min	*E. coli*, *S. aureus*, MRSA	Planktonic bacteria, animal model	Injectable hybrid hydrogels achieved both enhanced osteogenesis and NIR-triggered sterilization	Yang et al. (2025)
	PTT, PDT		CuS loaded with serine endopeptidase	980 nm, 1.5 W cm^{-2}, 3 min	*F. nucleatum*	Planktonic bacteria, biofilms, animal model	Enzymatic degradation of the biofilm by introducing a protease	Gao et al. (2023)
	PTT, drug therapy	GNC	GNR filled with phase-change materials (PCM) and tetracycline (TC), with a surface modification of poly(N-isopropylacrylamide-co-diethylaminoethyl methacrylate) (PND)	808 nm, 1.0 W cm^{-2}, 3 min	*S. aureus*	Planktonic bacteria, animal model	Precise NIR light-controlled release of encapsulated drugs via dual thermosensitive transitions of PCM (liquid-solid) and PND (coil-granule)	Zhang et al. (2020)
	PTT, drug therapy	Au nano bipyramids	Mesoporous silica-coated Au nano bipyramids mixed with gelatin methacrylate	808 nm, 1.2 W cm^{-2}, 5 min	*P. gingivalis*	Planktonic bacteria	Antibiotic drug release and photothermal treatment triggered by NIR irradiation	Lin et al. (2020)
	PTT, PDT	ICG	ICG complexed with sPDMA, a poly(2-(dimethylamino)ethyl methacrylate) brush synthesized by ATRP using bromo-β-cyclodextrin (CD-Br) initiator	808 nm, 2 W cm^{-2}, 5 min	*P. gingivalis*	Planktonic bacteria, animal model	Polycationic brushes as a novel carrier material for antibacterial agents	Shi et al. (2021)
	PTT, SRP		—	810 nm, 0.5 W, 1.5 min	-	Clinical randomized controlled trial	Evaluation of ICG-diode laser effects on periodontal cells with regenerative capacity	Chiang et al. (2020)
	PTT, immunotherapy	MPB NPs	MPB NPs loaded with baicalein	808 nm, 1 W cm^{-2}, 15 min	*P. gingivalis*, *F. nucleatum*	Planktonic bacteria, animal model	ROS-scavenging nanoplatform promotes M2 macrophage polarization via photothermal bioplatform-assisted immunotherapy	Tian et al. (2022)
	PTT, PDT, immunotherapy	AuNRs	S-nitrosothiols and ICG loaded into mesoporous silica-coated AuNRs	808 nm, 1 W cm^{-2}, 5 min	*P. gingivalis*, *F. nucleatum*	Planktonic bacteria, biofilms, animal model	NIR light triggers antibacterial effects (AuNR, PTT), anti-inflammatory action (ICG, PDT), and modulation of inflammatory immunity (generated NO)	Qi et al. (2022)
	PTT, Drug therapy, immunotherapy	PB NPs	PB NPs coated with PDA and subsequently loaded with minocycline	808 nm, 1 W cm^{-2}, 5 min	*S. sanguinis*, *P. gingivalis*, *F. nucleatum*	Planktonic bacteria, biofilms, animal model	Mild temperature anti-plaque activity and ROS scavenging attributed to PB nanozymes (enzyme-like activity) and PDA (catechol reducibility)	Wang et al. (2023b)
	PTT, PDT	IR820	IR820 complexed with oxyhemoglobin	808 nm, 2 W cm^{-2}, 5 min	*P. gingivalis*	*In vitro* biofilms, animal model	Hemoglobin as a carrier for targeted delivery of therapeutics to *P. gingivalis*	Bai et al. (2022)

(Continued on following page)

10.3389/fbioe.2025.1637941

TABLE 1 (*Continued*) Summaries of photothermal therapy (PTT) for oral infectious diseases. This section comprehensively summarizes the details of recent research reported in the literature, emphasizing the functionalization of photothermal agents (PTAs), their therapeutic highlights, and the underlying design concepts and mechanisms.

Disease type	Therapy model	Photothermal agents	Functionalization	Exposure condition	Bacterial species	Research phase	Therapeutic highlights	Ref.
	PTT, CDT	Cu_3P	Cu_3P modified with poly (allylamine hydrochloride) and lactate oxidase	1064 nm, 0.75 W cm^{-2}, 5 min	*S. gordonii*, *P. gingivalis*	*In vitro* biofilms, animal model	Single-material system with PTT and CDT functionalities exhibiting synergistic therapeutic efficiency through a dynamic positive feedback loop	Lin et al. (2024)
	PTT, PDT	T8IC NPs	Hydrogel with 3D network architecture as a carrier for BMP-2 and T8IC	808 nm, 1.5 W cm^{-2}, 5 min	*P. gingivalis*	Planktonic bacteria, biofilms, animal model	Enhanced PDT and sustained BMP-2 release achieved with mild PTT (45 °C) in a Hydrogel + T8IC + Laser + BMP-2 + H_2O_2 system, demonstrating excellent bactericidal effect, osteogenic induction, and biosafety	Wang et al. (2023c)
	PTT, PDT, CDT	Bi_2S_3 NPs	Bi_2S_3 NPs anchored on Cu-tetrakis(4-carboxyphenyl)porphyrin nanosheets to create a novel Z-scheme heterostructured nanocomposite	635 nm,1 W cm^{-2}, 10 min	*P. gingivalis*, *F. nucleatum*, *S. gordonii*	Planktonic bacteria, biofilms, animal model	Heterostructure facilitates highly efficient light absorption and electron-hole separation, leading to synergistic PDT/PTT/CDT with potent antibacterial activity against periodontal pathogens	Kong et al. (2023)
	PTT, drug therapy	Fe_3O_4	Fe_3O_4 wrapped ZnO with an outer layer of epsilon-polylysine (EPL)	808 nm, 1 W cm^{-2}, 5 min	*P. gingivalis*	Planktonic bacteria, biofilms, animal model	Anti-inflammatory effects and enhanced antibiofilm efficacy via mild-temperature antibacterial PTT	Li et al. (2025)
	PTT, CDT	Bi_2Te_3 NSs	Lu-Bi_2Te_3 decorated with Fe_3O_4 and poly(ethylene glycol)-b-poly(l-arginine) (PEG-b-PArg)	1064 nm, 1 W cm^{-2}, 5 min	*P. gingivalis*, *F. nucleatum*, *S. aureus*, *E. coli*	Planktonic bacteria, biofilms, animal model	Synergistic generation of ROS and RNS via photothermal/thermocatalytic effects under NIR-II laser irradiation leads to biofilm damage	Dai et al. (2023)
	PTT, gas therapy	PB nanozymes	Ruthenium (Ru)-doped PB nanozymes integrated with sodium nitroprusside (SNP)	808 nm, 1 W cm^{-2}, 5 min	*P. gingivalis*, *F. nucleatum*	Planktonic bacteria, biofilms, animal model	NO-releasing nanozyme therapy using mild-temperature photothermal activation	Li et al. (2024e)
	PTT, PDT, gas therapy	Ag_2S	Ag_2S NPs loaded with ZIF-90, ICG, and L-arg molecule	808 nm, 1 W cm^{-2}, 5 min	*P. gingivalis*, *F. nucleatum*	Planktonic bacteria, biofilms, animal model	NO-synergized PTT and PDT using a nanocomposite platform	Wu et al. (2023)
	PTT, immunotherapy	AuNPs	Yolk–Shell structure composed of Au and CeO_2 loaded with dimethyl fumarate	635 nm, 0.8 W cm^{-2}, 5 min	*E. coli*, *S. aureus*	Planktonic bacteria, animal model	Triple-combination therapy for periodontitis enabled through antioxidant, mitochondrial maintenance, and immunomodulation	Li et al. (2024d)
Peri-implantitis	PTT	TiO_2	(Si/P/F) multi-doped porous TiO2 matrix	808 nm, 0.6 W cm^{-2}, 5 min	*S. aureus*	Planktonic bacteria, biofilms, animal model	Endowing dental implants with superior bactericidal ability, accelerated epithelial sealing and osseointegration, and reduced alveolar resorption	Xue et al. (2023)
	PTT	ICG	—	810 nm, 0.67 W cm^{-2}, Not mentioned	*S. gordonii*	*In vitro* biofilms	First evaluation of the antimicrobial effect of PTT on zirconia surfaces	Shim et al. (2022)
	PTT, PDT		ICG and rapamycin encapsulated within liposomes	808 nm, 1.5 W cm^{-2}, 5 min	*S. aureus*, *S. oralis*	Planktonic bacteria, biofilms, animal model	Increases bacterial motility by elevating intracellular ATP, inhibits bacterial adhesion and biofilm formation, thus preventing disease recurrence	Xiao et al. (2024)
	PTT	GO	Reduced GO (rGO)	940 nm, 4 W cm^{-2}, 2 min	*S. mutans*, *P. gingivalis*	Planktonic bacteria	Zirconia coated with rGO via atmospheric plasma to eliminate implant surface plaque	Park et al. (2023)

(Continued on following page)

10.3389/fbioe.2025.1637941

TABLE 1 (*Continued*) Summaries of photothermal therapy (PTT) for oral infectious diseases. This section comprehensively summarizes the details of recent research reported in the literature, emphasizing the functionalization of photothermal agents (PTAs), their therapeutic highlights, and the underlying design concepts and mechanisms.

Disease type	Therapy model	Photothermal agents	Functionalization	Exposure condition	Bacterial species	Research phase	Therapeutic highlights	Ref.
	PTT	PDA	—	808 nm, 1 W cm^{-2}, 5 min	*S. aureus*	Planktonic bacteria, *In vitro* 3D peri-implantitis model	First report of collateral thermal damage to tissues overlying an implant surface coated with photothermal NPs	Ren et al. (2020)
	PTT		Simvastatin-loaded ZIF-8 nanoparticles coated with PDA and subsequently incorporated into a Chitosan (CS)/β-glycerophosphate (β-GP) system	808 nm, 0.5 W cm^{-2}, 10 min	*S. aureus*, *P. gingivalis*	Planktonic bacteria, biofilms, animal model	Demonstrated attenuation of infection and inflammation in peri-implantitis lesions	Liu et al. (2025)
	PTT, PDT		Ce6-loaded ZIF-8 nanoparticles coated with PDA/UBI	660 nm, 1.3 W cm^{-2}, 5 min	*S. aureus*, *E. coli*	Planktonic bacteria, biofilms, animal model	Precise targeting of bacteria and enhanced oral biofilm penetration	Wang et al. (2025)
Infectious bone defect	PTT	MXene	MXene (Ti_3C_2) incorporated into a 3D bioprinted composite hydrogel scaffold composed of GelMA, β-TCP, and Sodium alginate (Sr^{2+})	808 nm, 1.5 W cm^{-2}, 5 min	*S. aureus*, *E. coli*	Planktonic bacteria, animal model	Personalized bone tissue engineering scaffolds exhibiting synergistic antibacterial and osteogenic effects	Nie et al. (2022)
	PTT	MgMps	MgMps combined with PLLA to form a lamellar heterostructured Mg/PLLA composite membrane via accumulative rolling	808 nm, 0.7 W cm^{-2}, 1 min	*E. coli*, *S. aureus*	Planktonic bacteria, animal model	Programmed degradation to release Mg^{2+}, antibacterial efficacy and endogenous vascularized bone regeneration ability	Wang et al. (2023d)
Candida infections	PTT	MPN-Pd	Metal-phenolic networks with Pd nanoparticle nodes (MPN-Pd)	808 nm, 1 W cm^{-2}, 45 min	*C. albicans*	Planktonic bacteria, biofilms, animal model	Demonstrated PTT's potential against oral fungus infection	Chen et al. (2023a)

Abbreviation. 3D, three-dimensional; ATP, adenosine-triphosphate; ATRP, atom transfer radical polymerization; AuNPs, gold nanoparticles; AuNRs, gold nanorods; BMP-2, bone morphogenetic protein-2; BP, black phosphorus; *C. albicans, Candida albicans*; CDT, chemical dynamic therapy; *E. coli, Escherichia coli*; *E. faecalis: Enterococcus faecalis*; EPL: epsilon-polylysine; *F. nucleatum: Fusobacterium nucleatum*; GelMA, gelatin methacrylate; GNC, gold nanocages; GO, graphene oxide; ICG, indocyanine green; MgMps, Mg microparticles; MPB, mesoporous Prussian blue; MPN, metal-phenolic networks; MRSA, Methicillin-resistant *Staphylococcus aureus*; NIR, near-infrared; NPs, nanoparticles; NSs: nanosheets; *P. gingivalis: Porphyromonas gingivalis*; PB, prussian blue; PCM, phase-change materials; PCT, peroxidase-like catalytic therapy; PDA, polydopamine; PDT, photodynamic therapy; PEG, polyethylene glycol; PLLA, polylactic acid; PLGA, poly lactic acid-co-glycolic acid; PTT, photothermal therapy; rGO, reduced graphene oxide; RNS, reactive nitrogen species; ROS: reactive oxygen species; *S. aureus, Staphylococcus aureus*; *S. gordonii: Streptococcus gordonii; S. mutans, Streptococcus mutans;* SNP, sodium nitroprusside; *S. oralis, Streptococcus oralis; S. sanguinis, Streptococcus sanguinis; S. sobrinus, Streptococcus sobrinus*; SRP, scaling and root planning; TC, tetracycline; UBI, ubiquicidine; ZIF, zinc imidazolate framework.

10.3389/fbioe.2025.1637941

microenvironment through biofilm formation and acid production on tooth surfaces, pH-responsive targeting strategies have been developed for PTAs (Xu H. et al., 2022; Yu et al., 2022). A photothermal antibacterial "warm paste" was fabricated by loading Ag onto the surface of Fe_3O_4 nanoparticles by polydopamine (PDA) reduction, followed by a second PDA coating and subsequent grafting with glycol chitosan. Under normal physiological conditions, the PDA layer inhibits the excessive release of Ag^+ and reduces its damage to normal tissues. However, within a cariogenic acidic environment, the protonation of amine groups on glycol chitosan leads to a positive charge on the nanoparticles, which enhances their strong adhesion to negatively charged cariogenic bacteria at the intended site. When irradiated by NIR, the increased temperature promotes Ag + release, leading to a high local concentration in the cavitated dental tissue. This thereby achieves effective targeted antimicrobial action through an Ag-assisted PTT strategy (Figure 3A) (Xu H. et al., 2022). Other pH-responsive agents tailored for acidic oral niches include zinc imidazolate framework-8 (ZIF-8) and Poly (ethylene glycol) (PEG) etc (Yu et al., 2022; Pan et al., 2025). The positive charge of some modified PTAs like amino-functionalized graphene oxide (GO) ensures their strong interaction with the negatively charged bacterial cells, which can also be helpful for the target of cariogenic bacteria (Lu et al., 2021). This precision is particularly advantageous in the complex and delicate environment of the oral cavity, where preserving tooth structure and minimizing collateral damage is critical. Furthermore, PTT's ability to generate heat at specific depths reduces the production of exopolysaccharides—the main component endowing biofilm architecture and stability (Yao W. et al., 2025). This mechanism aids in the disintegration of biofilms and ensures effective penetration, addressing a major limitation of traditional antimicrobial therapies. Emerging studies have also highlighted the potential of PTT to synergize with other therapeutic modalities (Xu X. et al., 2022; Li et al., 2024c). One key feature of PTT, its efficient thermal generation at desired locations, can enhance combination therapies in various ways. For instance, PTT can be combined with photodynamic therapy (PDT) or antimicrobial agents, where the photothermal effect promotes the controlled release of these agents (Xu H. et al., 2022; Pan et al., 2025) or enables on-demand modality switching between PTT and PDT (Zhang Y. et al., 2024), thereby boosting their efficacy in eradicating biofilms. An adaptive supramolecular nanoformulation (ZnPcS4@GC5AF5, GFZ) switchable from PTT to PDT under the trigger of adenosine triphosphate (ATP) was reported. The activation of the photothermal properties of GFZ through visible irradiation led to bacterial cell membrane rupture and intracellular ATP release. Subsequently, ATP reduced the photothermal activity (low state) and restored the photodynamic activity (ON state). A large number of reactive oxygen species (ROS)were generated while avoiding high local temperatures, which not only resulted in eradicating pathogenic bacteria biofilms but also minimized heat damage to normal pulp tissues (Figure 3B) (Zhang Y. et al., 2024).

Despite these promising advances, several challenges remain in translating PTT into clinical practice for caries treatment. Key issues include optimizing the parameters of light irradiation (e.g., wavelength, intensity, and duration) to achieve effective biofilm eradication without causing thermal damage to oral tissues. Additionally, PTAs' long-term safety and biocompatibility must be rigorously evaluated to confirm their suitability in the oral cavity. The prevention and management of dental caries represent a protracted process, so further research is also needed to investigate the potential of PTT in preventing caries' recurrence and addressing the complex microbial ecology of dental biofilms. Developing composite materials capable of inhibiting the proliferation of cariogenic bacteria and facilitating the remineralization of early-stage demineralized dental tissues constitutes a promising research trajectory for the future (Zhu et al., 2022). In conclusion, PTT represents a groundbreaking approach to combating dental caries, offering a combination of precision, efficacy, and minimal invasiveness that addresses the limitations of current therapies. As research in this field continues to advance, PTT holds the potential to revolutionize the prevention and treatment of dental caries, ultimately improving oral health outcomes and alleviating the global burden of this pervasive disease.

3 PTT for endodontics

The dental pulp comprises sterile connective tissue and is protected by the surrounding enamel, dentin, and cementum (Pohl et al., 2024). Exposure resulting from factors including trauma, dental caries, or tooth wear can precipitate endodontics, characterized by symptoms such as pain, sinus tracts, and swelling (Karamifar et al., 2020). The elimination of bacteria and their biofilms assumes a pivotal role in the treatment of endodontics (Neelakantan et al., 2017). In clinical practices, root canal therapy (RCT) represents a commonly employed approach for removing microorganisms that instigate or exacerbate this ailment (Burns et al., 2022; Huang et al., 2024). Although biomechanical root canal preparation and chemical sterilization of irrigants could effectively eradicate the microbes, achieving thorough debridement and eradicating tenacious infections persist as formidable challenges in root canal treatment (Moradi Eslami et al., 2019). Additionally, High concentrations of chemical irrigants may cause serious damage by irritating periodontal soft and periapical tissues (Xu H. et al., 2022). *Enterococcus faecalis* (*E. faecalis*) is a key bacterial species frequently isolated from root canals afflicted with refractory endodontic infections, contributing to 20%–70% of RCT failures (Manoil et al., 2023). This is attributed to its capacity to form biofilms which can adapt to external alterations as an integrated entity (Pourhajibagher et al., 2018; Cao et al., 2021). Consequently, various studies aim to explore novel materials, encompassing irrigants and intracanal dressings, to eliminate *E. faecalis* in the biofilm phase (Aksoy et al., 2020; Cao et al., 2021; Duan et al., 2022; Galdámez-Falla et al., 2022; Feng et al., 2024). During PTT, hyperthermia aids in biofilm disintegration and induces bacterial demise (Mei et al., 2023; Zhou et al., 2024). Crucially, it remains confined within the root canal, as tooth hard tissues impede the complete transfer of heat to the periodontal tissues, thereby reducing potential damage to these tissues (Duan et al., 2022). Studies have demonstrated that PTT exhibits remarkable efficacy against *E. faecalis* and its biofilms without compromising dentin strength, supporting its potential as a prospective antibacterial therapy during RCT (Castillo-Martínez et al., 2015; Khantamat et al., 2015; Bermúdez-Jiménez et al., 2020; Galdámez-Falla et al., 2022).

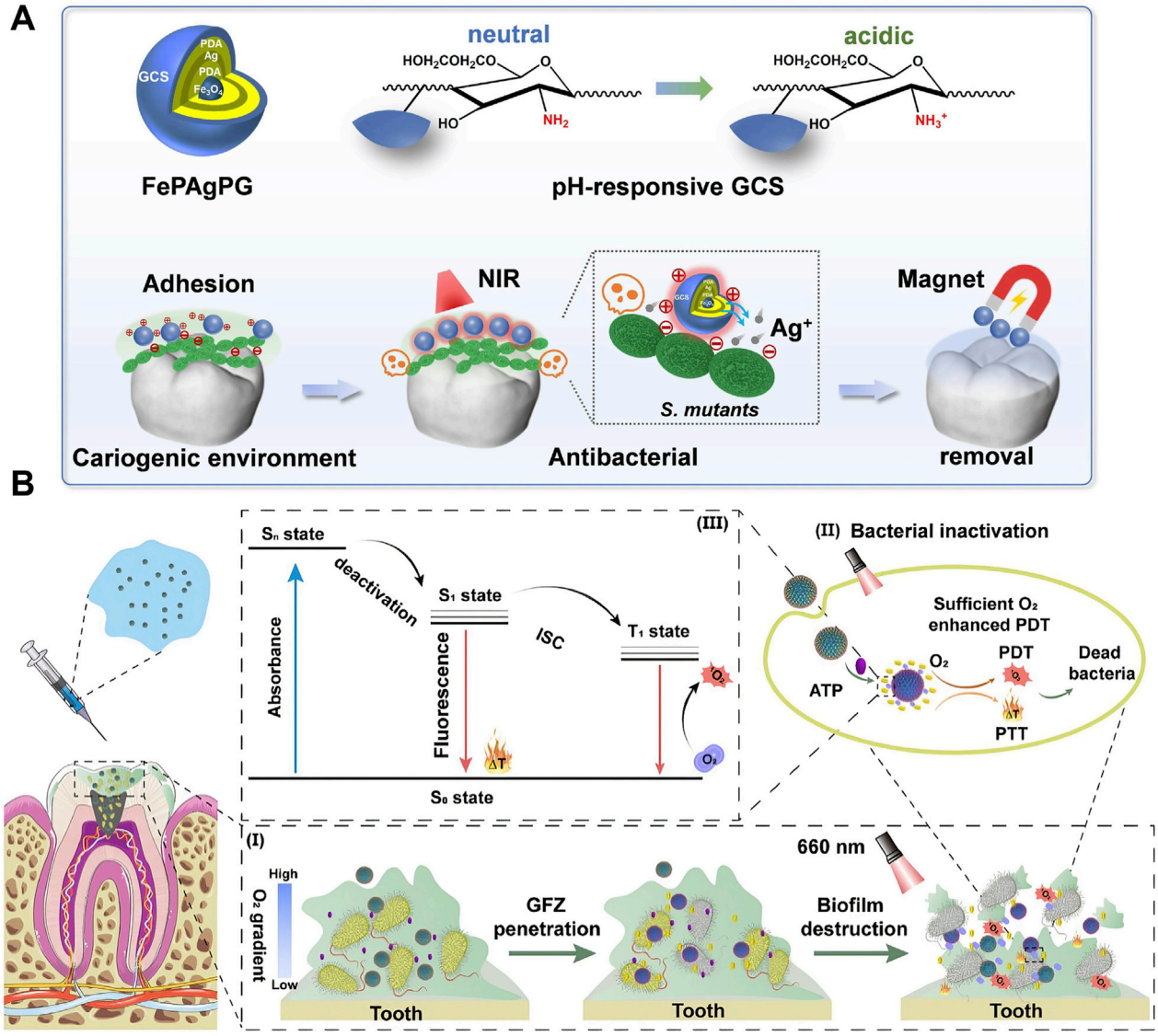

FIGURE 3
Photothermal therapy (PTT) for dental caries. **(A)** Schematic illustration depicting a removable photothermal antibacterial "warm paste" designed to target cariogenic bacteria. Reproduced with permission (Xu H. et al., 2022). Copyright 2021, Elsevier Group. **(B)** Schematic illustration of effective biofilm removal using a supramolecular nanoformulation featuring adaptive photothermal/photodynamic conversion. Reproduced with permission (Zhang Y. et al., 2024). Copyright 2024, American Chemical Society.

The thermal generation of PTT not only directly inhibits *E. faecalis* and its biofilms, but can also be combined with root canal conventional irrigants, such as sodium hypochlorite (NaClO) and hydrogen peroxide (H_2O_2), to augment the overall efficacy of root canal disinfection. Cao et al. (2021) constructed Au@$Cu_{2-x}S$ NPs by integrating $Cu_{2-x}S$ with peroxidase-like activity and Au NPs with photothermal effect to augment the capacity to eliminate biofilms. It not only exhibits strong photothermal activity but also catalyzes H_2O_2 to generate hydroxyl radicals (·OH), which are more effective for biofilm degradation. Mechanistic studies demonstrated that the treatment effectively degrades proteins and polysaccharides—the primary components of biofilm EPS. The synergistic strategy combining PTT and peroxidase-like catalytic treatment with H_2O_2 holds significant potential for eradicating bacteria and biofilms within root canals (Figure 4A). Heating 1% NaClO—another irrigant extensively used clinically—within the root canal during PTT also significantly enhances its antibacterial efficacy (Abou-Rass and Oglesby, 1981; Tosić et al., 2016). A temperature increase of <10 °C on the external root surface achieved 99.7% antimicrobial efficacy against *E. faecalis* using heated 1% NaClO solution (Figure 4B) (Duan et al., 2022). Additionally, scanning electron microscopy (SEM) reveals that the teeth treated in the experimental group exhibit regular exposure of dentinal tubules. Conversely, the dentin in the control groups exhibited a rough surface, characterized by a profusion of bacteria and smear layers, with the majority of dentinal tubules remaining occluded (Figure 4C) (Duan et al., 2022). These studies manifested the potential of safely

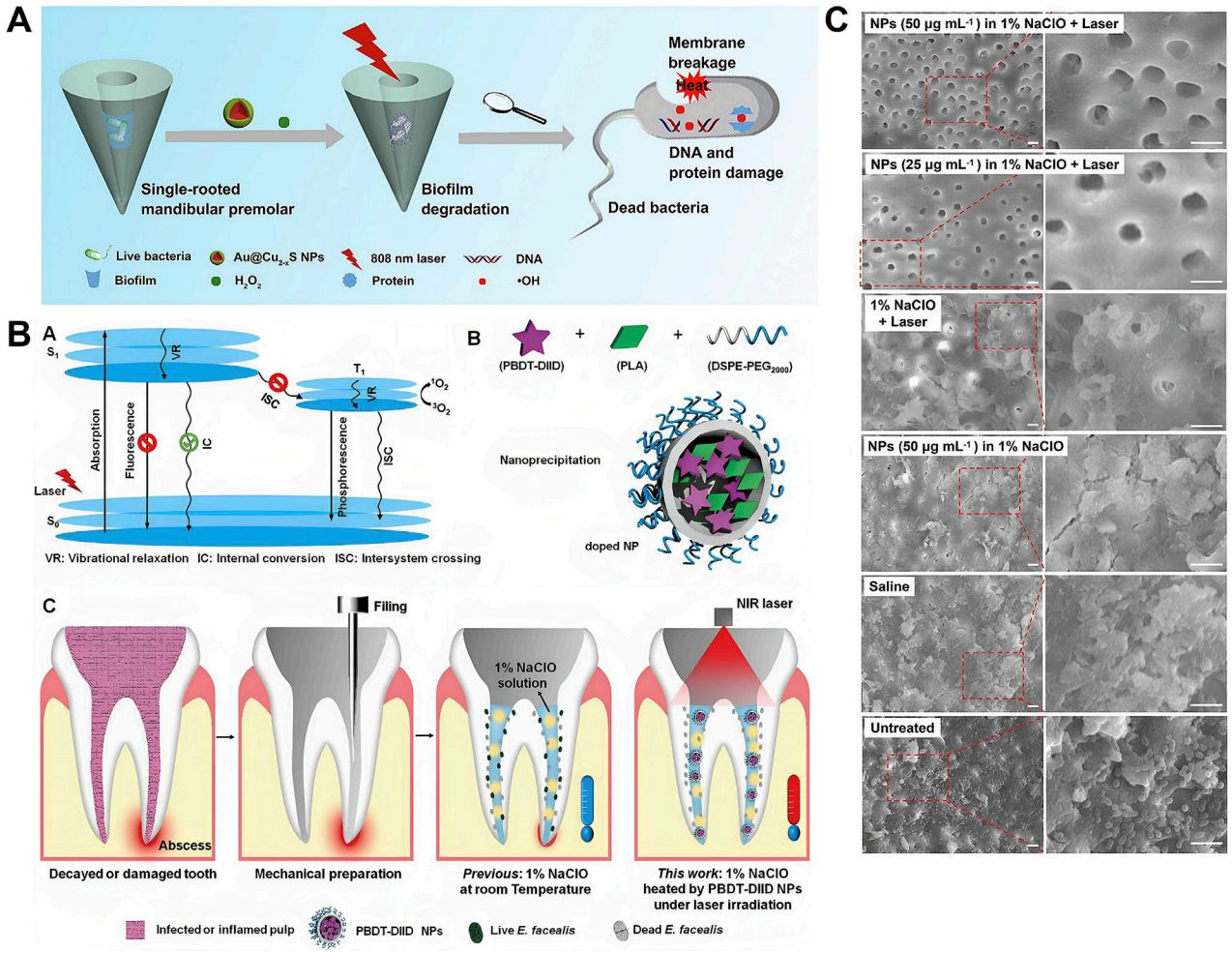

FIGURE 4
Photothermal therapy (PTT) for endodontics. **(A)** Schematic illustration of Au@Cu2-xS nanoparticles with NIR photothermal and peroxidase (POD) catalytic activities for antibiofilm-oriented root canal therapy. Reproduced with permission (Cao et al., 2021). Copyright 2021, Elsevier Group. **(B)** Schematic diagram illustrating the heating of a 1% NaClO solution under 808 nm laser irradiation in the presence of PBDT-DIID nanoparticles to enhance intracanal sterilization. **(C)** Representative SEM images of the middle of the sample tooth in different groups. Reproduced with permission (Duan et al., 2022). Copyright 2022, John Wiley and Sons Group.

and efficaciously improve the RCT outcome by heating the irrigants.

Current research on PTT for endodontic diseases focuses primarily on its antibacterial role as an adjunct to root canal therapy, predominantly targeting *E. faecalis*. As effective treatments for refractory and recurrent root canal infections remain lacking, PTT offers a promising therapeutic approach. Nevertheless, the tooth root canal is complex and contains many small branching canals. The root canal biofilm is a very complex, organized entity (Neelakantan et al., 2017). Single-rooted mandibular premolar models and monospecies biofilms used in previous studies may oversimplify the root canals and the ecological phenomenon of biofilms. They may not truly reflect the results achievable in the clinical scenario. After the photothermal material is injected into the root canal and exerts its function, the challenge of effectively removing it without impeding subsequent root canal filling represents major hurdle confronting research in this field.

4 PTT for periodontitis

Among all oral infectious diseases, the PTT for periodontitis has garnered the most extensive attention. Periodontitis represents a chronic inflammatory disorder instigated by bacteria (Kwon et al., 2021). The establishment of pathogenic bacteria within subgingival dental plaque provokes the host immune response, resulting in the generation of a significant amount of ROS and subsequent oxidative stress (Sczepanik et al., 2020; Kwon et al., 2021; Iniesta et al., 2023). Consequently, this process leads to the degradation of tooth-supporting tissues, eventually resulting in the development of periodontal pockets, alveolar bone resorption, and subsequent tooth loosening (Kuboniwa et al., 2017; Tóthová and Celec, 2017; Heitz-Mayfield, 2024). Currently, in clinical practice, mechanical debridement and antibiotics are commonly employed (Mombelli, 2018; Cobb and Sottosanti, 2021). Nevertheless, in most cases, mechanical debridement proves arduous to comprehensively eliminate periodontitis infections within deep-seated periodontal

pockets, furcation, and irregular root surface regions (Umeda et al., 2004). Additionally, the protracted administration of antibiotics engenders numerous issues, such as the development of drug-resistant bacteria, bacillary dysentery, and gastrointestinal disorders (Rams et al., 2020). Beyond bacterial factors, biofilm-induced immune dysregulation constitutes another major contributor to impaired bacterial clearance and disease persistence in periodontitis. Consequently, periodontitis treatment represents a key research focus in dentistry, with current strategies targeting not only antibacterial action but also anti-inflammatory effects and periodontal regeneration (Kong et al., 2023; Wang F. et al., 2023; Li T. et al., 2024; Li Z. et al., 2024; Yang et al., 2025). PTT offers distinct advantages for periodontitis treatment, as it not only enables efficient and safe bacterial elimination but also promotes cell proliferation, angiogenesis, wound healing, and bone regeneration—key factors in periodontal recovery (Zhang et al., 2021). More significantly, it can be integrated with PDT, chemical dynamic therapy (CDT), antibacterial agents, and bioactive materials to construct a material system featuring multi-functional synergy in antibacterial, anti-inflammatory, and tissue-regeneration functions (Shi et al., 2021; Bai et al., 2022; Wang H. et al., 2023; Lin et al., 2024; Wu et al., 2025).

Unlike dental caries or endodontic treatments—which involve heat-tolerant hard tissues—periodontitis affects the thermally sensitive periodontium. Combination therapy—a well-established paradigm in antimicrobial treatment—enhances therapeutic efficacy by integrating distinct therapeutic mechanisms beyond the capabilities of individual monotherapies (Wang N. et al., 2022). This approach enables superior outcomes at reduced thermal dosages. Mild hyperthermia (<45 °C) enhances the bactericidal efficacy of antibiotics by inhibiting enzyme activity, while preserving surrounding tissue integrity. tissues (Gao et al., 2019). The synergy between PTT and antibiotics such as tetracycline (TC) (Zhang et al., 2020) and minocycline (Lin et al., 2020; Wang X. et al., 2023) represents a strategic approach for an efficacious periodontal antibacterial therapy. To enhance drug delivery efficiency and curtail systemic harm, drug delivery systems (DDS) are frequently utilized to administer antibiotics (Lin et al., 2020; Zhang et al., 2020; Shi et al., 2021). Hydrogels, widely employed in DDS, can conform to the irregular morphology of periodontal pockets and enhance the retention rate of the released drugs at the local infection site. The heat of PTT can stimulate and trigger the controlled release of drugs within the DDS, thereby achieving synergistic sterilization through the combined action of antibiotics and photothermal effects (Lin et al., 2020; Zhang et al., 2020). Beyond antibiotics, PTT could synergize with alternative antibacterial strategies—including Ag^+ (Wang F. et al., 2023),. PDT (Bai et al., 2022; Gao et al., 2023; Wu et al., 2023), CDT (Chen Q. et al., 2023; Dai et al., 2023; Lin et al., 2024), and gas therapy (Dai et al., 2023; Li Z. et al., 2024)—to enhance periodontal biofilm eradication. The synergistic integration of PDT and PTT, activated by a single 808 nm NIR source, amplifies antibacterial efficacy while reducing both drug dosage and laser energy requirements (Qi et al., 2022). This dual-modal approach enhances bacterial elimination beyond monotherapies: PTT-induced hyperthermia disrupts membrane integrity, facilitating deeper penetration of ROS generated through PDT to inflict lethal oxidative damage (Wang R. et al., 2022; Wu et al., 2023). Highly toxic ·OH generated by CDT exhibits potent destructive effects on bacterial biofilms and cell membranes, demonstrating significant efficacy against bacterial infections (Guo et al., 2020). Notably, these ·OH radicals critically deplete ATP levels, inhibiting heat shock proteins and reducing bacterial heat resistance (Chen et al., 2020; Wang F. et al., 2023). This thereby enhances the efficiency of PTT, highlighting a promising single-material solution for concurrent CDT and PTT. Gas therapy represents a novel, promising strategy for targeting deep infections in periodontal tissues. Nitric oxide (NO) has demonstrated outstanding antimicrobial efficacy and the ability to combat resistance linked to bacterial biofilms (Li Z. et al., 2024). It could increase the sensitivity of the bacteria to heat and promote tissue healing by stimulating angiogenesis and alleviating the damage caused by periodontitis (Yuan et al., 2020; Dai et al., 2023). When combined with PTT, this approach demonstrates significant synergistic efficacy in the treatment of periodontitis (Dai et al., 2023; Li T. et al., 2024).

Bacterial infection might be the primary cause of inflammation's initial stages, but the host's immune inflammatory response is responsible for promoting periodontitis (Hajishengallis, 2014). To treat periodontitis thoroughly, regulating host immunity is also crucial in addition to clearing the biofilm in the disease area (Qi et al., 2022; Wang N. et al., 2022; Chen Q. et al., 2023). Proanthocyanidins (PCs), a class of natural phenolic compounds, demonstrate efficacy in impeding the elevation of ROS inhibiting inflammatory factors, and regulating macrophage polarisation in periodontal disease sites (Gil-Cardoso et al., 2019; Kim et al., 2019; Wang H. et al., 2022; Zhang et al., 2023). A nanocomposite named AuAg-PC NPs was synthesized with PCs as a reducing agent. Biofilms can be eradicated through Ag^+-synergistic PTT, whereas PCs demonstrate the capacity to eliminate ROS and modulate tissue self-healing via the PI3K/Akt signaling pathway. Hence, the nanocomposites can eradicate periodontal pathogens and restore the immune regulation environment (Figure 5A) (Wang F. et al., 2023). Additionally, baicalein (BA) (Tian et al., 2022), nitric oxide (NO) (Qi et al., 2022), PB nanozymes (Wang P. et al., 2023; Li Z. et al., 2024), ceria (CeO_2) (Li T. et al., 2024), rapamycin Xiao et al., 2024) and dimethyl fumarate (DMF) (Li T. et al., 2024) have been employed to modulate the detrimental innate inflammatory responses triggered during persistent infections. Considering that the destruction of periodontal soft tissues and the resorption of alveolar bone induced by periodontitis are irreversible processes, periodontal tissue regeneration is crucial for treating periodontitis (Yao H. et al., 2025). Although PTT can promote osteogenesis, monotherapies are often insufficient to elicit an adequate therapeutic response—and PTT is no exception. Recently, tissue engineering has proffered new prospects for repairing periodontal tissue defects in patients with periodontitis (Hussain et al., 2022; Wang P. et al., 2023). A thermosensitive and injectable hydrogel with a three-dimensional (3D) network architecture was employed as a delivery system for the controlled release of osteoinductive agents (BMP-2) and phototherapy agents (T8IC and H_2O_2). PTT combined with PDT exhibited excellent bactericidal effects while sustained release of BMP-2 and mild temperature (45 °C) induced osteogenesis (Figure 5B) (Wang P. et al., 2023). An appropriate concentration of Cu^{2+} promotes the proliferation and osteogenic differentiation of bone marrow mesenchymal stem cells (BMSCs) (Burghardt et al., 2015). Nanomaterials such as copper sulfide (CuS)

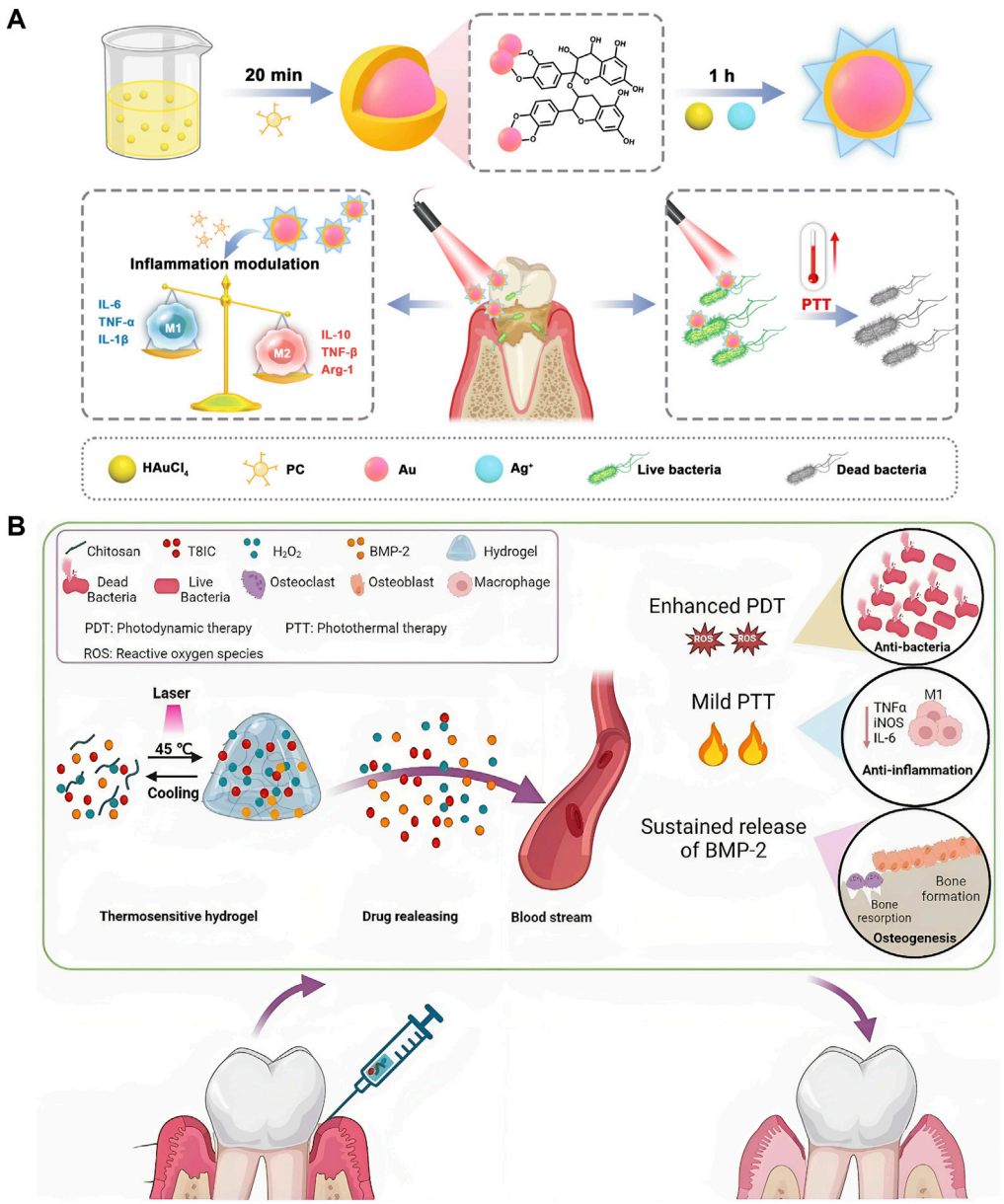

FIGURE 5
Photothermal therapy (PTT) for periodontitis. **(A)** Schematic illustration depicting the synthesis principle and therapeutic mechanism of AuAg-PC nanoparticles in treating periodontitis. Reproduced with permission (Wang F. et al., 2023). Copyright 2023, Royal Society of Chemistry. **(B)** Schematic illustration of thermosensitive and injectable hydrogel with T8IC, H_2O_2, and bone morphogenetic protein-2 (BMP-2). Reproduced under Creative Commons CC BY license (Wang P. et al., 2023). Copyright 2023, The Author(s), Published by Springer Nature Group.

nanoparticles leverage this biological activity while exhibiting strong NIR absorption and exceptional PCE, enabling their use as potent PTAs (Yang et al., 2025). This dual functionality facilitates simultaneous spatiotemporal antibacterial action and alveolar bone regeneration.

Notable progress has been achieved in the research on PTT for periodontitis. The research spans three key aspects: antibacterial, anti-inflammatory, and tissue-regeneration. Each function can synergize with the others, yielding favorable outcomes. However, we have not yet seen a multifunctional material or system integrating all of them, and the development of triple-functional materials or systems represents a future research trajectory. Although current photothermal conversion materials, such as gold nanorods, exhibit excellent biocompatibility, their long-term retention in the body may hinder periodontal tissue regeneration and affect overall health. Future research should focus on developing photothermal materials that can be metabolized and cleared by the body to avoid potential adverse effects. Additionally, previous studies predominantly utilize near-infrared region I (NIR-I, 650–1000 nm) lasers; near-infrared region II (NIR-II, 1000–1700 nm) which offers deeper tissue penetration into the periodontal pocket and improved precision in targeting periodontal lesions is a promising direction for future research (Luo et al., 2025).

5 PTT for peri-implantitis

Peri-implantitis constitutes a pathological condition associated with dental plaque that occurs in the tissues surrounding dental implants (Giok et al., 2024). The hallmark of this condition includes inflammation of the peri-implant mucosa and concomitant supporting bone loss (Berglundh et al., 2018; Schwarz et al., 2018). Inflammatory manifestations, bleeding or hyperemia upon probing, an augmentation in probing depth, and radiographic indications of bone resorption constitute the typical clinical features of peri-implantitis (Diaz et al., 2022). Unlike natural teeth, implants lack a periodontal ligament to separate the inflammatory cell infiltrate from the crestal bone (Carcuac et al., 2013). Therefore, peri-implantitis progresses faster than periodontitis around teeth. In the absence of effective intervention, the inflammatory process progressively damages osseointegration and ultimately causing implant mobility and loss (Daubert et al., 2015; Derks et al., 2016). Furthermore, the peri-implant microbiome and biofilm composition differ from those around natural teeth, making peri-implantitis management more challenging and less predictable than periodontitis treatment (Koyanagi et al., 2013; Wu L. et al., 2019). Clinically, the management of peri-implantitis bears resemblance to that of periodontitis, predominantly relying on the mechanical elimination of biofilms and the administration of antibiotics (Giok et al., 2024). However, due to the inaccessibility of infected implant surfaces and the potential for mechanical debridement to damage implant topography, effective biofilm eradication and re-osseointegration remain clinically challenging (Wang et al., 2020; Munakata et al., 2022; Ichioka et al., 2023). Therefore, preventing peri-implantitis is clinically paramount—significantly more critical than treatment.

The development of peri-implantitis begins with planktonic bacterial adhesion to implant surfaces (Osman et al., 2022). While titanium alloys and zirconia are common dental implant materials, neither exhibits inherent antibacterial activity (Pieralli et al., 2017; W. Nicholson, 2020; Chen et al., 2021). Consequently, enhancing the antimicrobial functionality of implants is critical to mitigate peri-implantitis. Surface modifications can profoundly alter the micro/nanotopography and chemical composition of titanium implants, enhancing hydrophilicity, mechanical stability, osseointegration capacity, and antibacterial efficacy (Sun et al., 2023; Gkioka and Rausch-Fan, 2024; Yu Y. M. et al., 2024). When irradiated with NIR light, dental implants coated with graphene oxide (GO) (Park et al., 2023) or PDA nanoparticles (Ren et al., 2020) demonstrate reduced adhesion of *S. mutans* and *Porphyromonas gingivalis* (*P. gingivalis*). Despite their antibacterial efficacy, photothermal coatings risk collateral tissue damage through heat dissipation near infection sites, potentially compromising healthy peri-implant tissue integration (Werner et al., 2009). Ren et al. (2020) devised a model wherein keratinocytes were cultured on a membrane filter within a transwell system while fibroblasts adhered to a titanium surface beneath the membrane. This model could be used to investigate the previously uninvestigated risk of collateral tissue damage from photothermal coatings on implant surfaces (Figure 6A). The use of novel biomaterials represents another strategy. Similar to periodontal therapy, this approach targets bacterial elimination and reduces inflammatory responses through immunoregulation (Xue et al., 2023; Liu et al., 2025). A critical distinction, however, is the requirement for a firm biological seal between the abutment and the gingival epithelium (Mahmoud et al., 2019). This seal is essential to prevent bacterial invasion and subsequent marginal bone loss (Fischer et al., 2022). Additionally, dental implants must achieve osseointegration with alveolar bone post-implantation (Chen et al., 2024). Xue et al. (2023) proposed a multipurpose photothermal strategy that uses Si/P/F-doped TiO_2 to address these challenges through dual functionality: exhibiting strong photothermal response and NIR-triggered F^- release. The resulting hyperthermia-F^- synergy disrupts *Staphylococcus aureus* (*S. aureus*) by reducing ATP synthesis, increasing membrane permeability, and generating ROS that oxidize cellular components to cause bacterial death. Concurrently, mild hyperthermia with released ions enhances gingival epithelial hemidesmosome formation and osteoblast activity. Another critical distinction in the field of peri-implantitis is the complexity of establishing animal models. Several *in vivo* studies of dental peri-implantitis have employed mouse femoral peri-implantitis models (Xiao et al., 2024; Wang et al., 2025); however, these models fail to accurately replicate the clinical condition of dental peri-implantitis within the alveolar bone (Zhang J. et al., 2024). The "ligature model" in alveolar bone mimics naturally occurring peri-implantitis and is suitable for studying the disease (Carcuac et al., 2013). The optimal timing for implant placement in mouse alveolar bone to establish a murine peri-implantitis model remains a contentious issue due to the limited understanding of the anatomical structure and physiological state of the alveolar bone after implant placement (Tzach-Nahman et al., 2017; Wong et al., 2018). Micro-CT and histological sectioning techniques suggested 6 weeks after the extraction of the maxillary first molar might be the appropriate time for implant placement (Figure 6B) (Liu et al., 2025). This finding offers significant data supporting the development of the murine peri-implantitis model.

Given the escalating prevalence of dental implants in dental prosthodontics clinical practice, it is anticipated that peri-implantitis will garner increasing attention. As a non-invasive and non-antibiotic-resistant antibacterial strategy, PTT holds great promise in preventing and treating peri-implantitis. Notably, when integrated with bone regeneration strategies, it can substantially promote the osseointegration process while preventing postoperative infection and enhancing the success rate of implant surgery. The current research bottleneck lies in determining how to minimize or eliminate collateral photothermal damage to healthy tissue cells in the peri-implant region while effectively eradicating bacteria through photothermal action. With the establishment of suitable animal models, future research in this field will accelerate, leading to significant advances.

6 PTT for other oral infectious diseases

Infectious bone defects (IBD) collectively refer to a class of diseases characterized by tenacious infection, persistent inflammation, bone destruction, impaired blood supply, and a protracted course of diseases, making them particularly challenging to manage (Han et al., 2024). It can be caused by jaw osteomyelitis, trauma, postoperative infection of tumors, etc

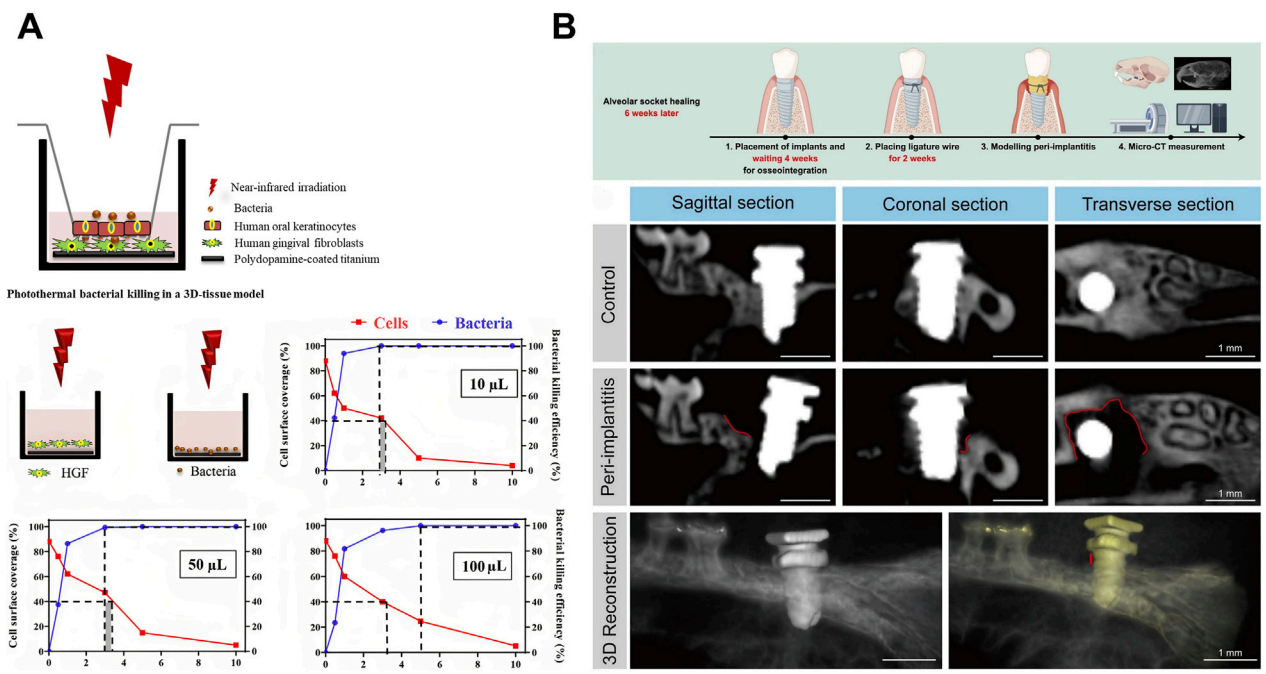

FIGURE 6
Photothermal therapy (PTT) for peri-implantitis. **(A)** Schematic illustration demonstrating photothermal bacterial killing in a 3D tissue model and surface coverage of human gingival fibroblasts (HGFs) and the eradication of *Staphylococcus aureus* (*S. aureus*) upon NIR irradiation of PDA nanoparticle coated titanium surfaces in monocultures. Samples were immersed in varying volumes of DMEM-HG medium (for HGFs) and PBS (for staphylococci), as illustrated in the schematics. The dotted lines demarcate NIR irradiation times considered acceptable for preserving tissue integration (>40% cell surface coverage; red data) and ensuring significant bacterial killing (>99.9%; blue data). The gray shading indicates the range of acceptable irradiation times that satisfy both criteria. Reproduced under Creative Commons CC BY-NC-ND 4.0 license (Ren et al., 2020). Copyright 2020, American Chemical Society. **(B)** Schematic diagram, Micro-CT, Hematoxylin-Eosin (HE) staining, and tartrate-resistant acid phosphatase (TRAP) staining of *in vivo* modeling of peri-implantitis in mice. Reproduced with permission (Liu et al., 2025). Copyright 2025, Elsevier Group.

(Dong et al., 2017). Clinical treatment strategies typically encompass antibiotic administration, excision of necrotic bone fragments, debridement procedures, and transplantation of bone grafts (Qian et al., 2023; Han et al., 2024). Nevertheless, antimicrobial overuse drives the evolution of drug-resistant strains (Hu et al., 2024). Moreover, requiring bone graft implantation post-infection eradication significantly prolongs treatment duration. Therefore, developing biomaterials that simultaneously deliver antibacterial functionality and personalized osteogenic capabilities is imperative. The photothermal effect delivers dual benefits: conferring antibacterial activity while using moderate local heating to upregulate key genes (e.g., osteogenesis-related genes) that promote tissue regeneration (Avci et al., 2013; Ma et al., 2020). Wang W. et al. (2023) developed a lamellar heterostructured Mg/PLLA composite periosteum membrane via an accumulative rolling method for application at bone defect sites. A consistent supply of Mg^{2+} activates key extracellular matrix proteins and transcription factors implicated in bone regeneration and angiogenesis. The photothermal effect of Mg microparticles can eliminate bacteria while further enhancing bone marrow-derived mesenchymal stromal cells (BMSCs) differentiation. Although overheating risks inducing apoptosis in both bacteria and healthy cells, longitudinal analysis revealed converging cell densities between composite membrane treated and control groups over time. This demonstrates that strategically controlled PTT ultimately favors tissue repair over thermal damage. Consequently, the PTT-enhanced composite periosteum achieved on-demand antibacterial efficacy and exceptional endogenous vascularized bone regeneration (Figure 7A). Beyond artificial periosteum, research has extended to 3D-printed hydrogels for tissue regeneration (Nie et al., 2022). These studies indicate that the application of PTT in the field of biomedical engineering holds great promise.

Beyond its efficacy against oral bacterial infections, PTT has demonstrated effectiveness against other microbial infections, including fungal infections. *Candida albicans* (*C. albicans*) is a primary etiological agent for most nosocomial infections affecting immunocompromised patients, and emerging multidrug resistance has made it an urgent threat (Arendrup and Patterson, 2017). Oropharyngeal candidiasis represents a form of oral candidal infection with a higher prevalence in individuals with conditions such as diabetes mellitus, immunodeficiency, and xerostomia (Stoopler et al., 2024). Similarly, it is associated with *C. albicans* biofilms on the oral mucosa. The intrinsic resistance of biofilms to antifungal agents has augmented the challenges associated with effective antifungal treatment. Chen et al. (2023a) developed a metal-phenolic network with Pd nanoparticle nodes (MPN-Pd) and found that *C. albicans* is more sensitive to hyperthermia than bacteria like *E. faecalis* and *S. mutans* which might be attributed to the fungal membrane containing dipalmitoylphosphatidylcholine phospholipid molecules that are more sensitive to temperature. The histological evaluation of

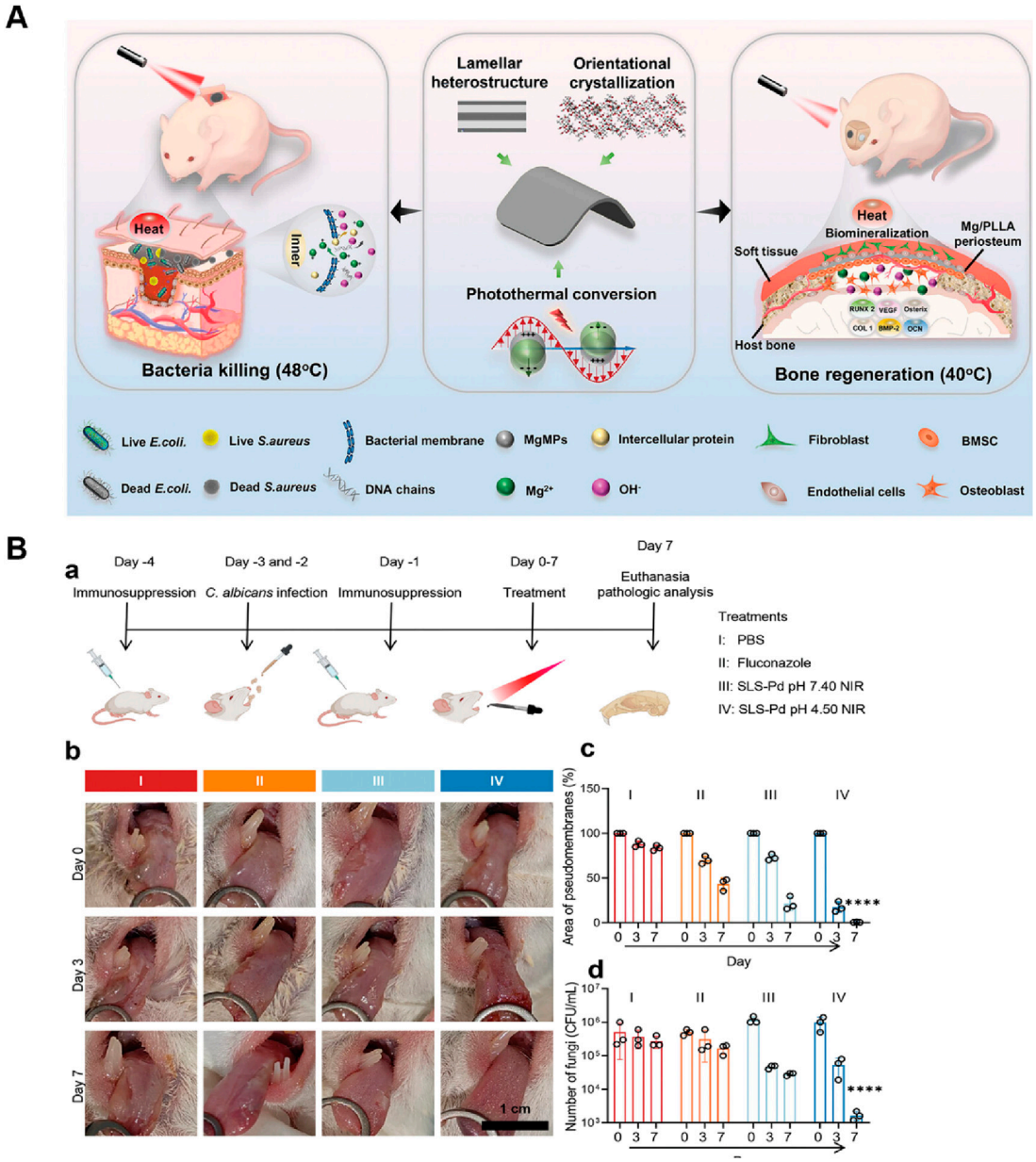

FIGURE 7
PTT for infectious bone defect and *candida* infection. **(A)** Schematic illustration of the self-reinforced Mg/PLLA composite membrane with lamellar heterostructure working as a periosteum for on-demand bacteria inhibition and rapid bone reconstruction. Reproduced with permission (Wang F. et al., 2023). Copyright 2022, John Wiley and Sons Group. **(B)** MPN-Pd-mediated system for the treatment of oral candidiasis. (a) Workflow of the *in vivo* experiment. (b) Digital images of oral candidiasis models under different treatments. (c) Quantitative analysis of the pseudomembrane area. (d) Viability of *Candida albicans* (*C. albicans*) evaluation. Reproduced with permission (Chen et al., 2023a). Copyright 2023, John Wiley and Sons Group.

mouse oral *candida* infection model indicates that the PTT is effective in the therapeutic goal of treating oropharyngeal candidiasis by eradicating *C. albicans* in the oral cavity, while showing no sign of collateral damage (Figure 7B). However, the current research on the antifungal application of PTT remains in its nascent stages, with limited experimental and clinical data currently available. Viral infections cause oral infectious like herpetic stomatitis. Theoretically, PTT also has the potential to be used for antiviral therapy, as viral structures and proteins are also prone to denaturation and inactivation at high temperatures (Bai et al., 2023; Li B. et al., 2024). Given PTT's remarkable antibacterial prowess and compatibility with other treatment modalities or bioactive materials, it is expected to be used to treat a broader spectrum of oral infections.

7 Summary and outlook

PTT heralds a paradigm shift in the prophylaxis and therapeutic strategies for oral infections. It proffers an efficacious, precise, and minimally invasive alternative to antibiotics. By capitalizing on the potency of light and heat, PTT surmounts the limitations inherent in

extant therapies, such as the burgeoning issue of antibiotic resistance and the propensity for tissue damage. Simultaneously, it furnishes a platform conducive to innovative and multifarious applications. As research within this domain continues to burgeon, PTT offers significant potential to revolutionize the management of oral infections charting a course towards more efficacious and sustainable solutions in oral healthcare. Critically, PTT demonstrates not only potent antibacterial efficacy but also significant potential for promoting tissue regeneration. Its compatibility with other therapeutic modalities enables synergistic treatment outcomes—particularly valuable for managing periodontitis and infectious bone defects where restoring biological function extends beyond mere antibacterial control.

Despite its considerable potential, PTT's clinical translation markedly lags behind that of its counterpart, PDT, with scarce clinical trials, and a range of challenges must be surmounted to fully actualize its clinical implementation for treating oral infections. The dual objectives of potent bactericidal effects and minimal collateral tissue damage pose an inherent trade-off, which may be addressed by improving targeting specificity. This underscores the need for advanced intelligent drug delivery systems and highly precise laser irradiation with deep-tissue penetration capability. Furthermore, combining PTT with adjuvant therapies to enhance bacterial photosensitization offers an alternative viable approach. Moreover, long-term biocompatibility and safety of PTAs necessitate comprehensive assessment to attenuate potential risks, such as tissue inflammation or systemic toxicity. The clinical translation of PTAs hinges on their long-term biosafety and effective clearance to mitigate the toxicity risk from bioaccumulation. To address this, key strategies focus on either biodegradability or renal clearance. For metallic PTAs like gold, which are poorly biodegradable, engineering ultrasmall, renally-clearable (<5 nm) nanoparticles offers a promising solution (Hwang et al., 2014; Tang et al., 2014). Alternatively, designing for biodegradability is a major focus. This includes inherently biodegradable inorganic materials like black phosphorus, which degrades into harmless phosphates, and carbon-based materials (e.g., GO) that can be broken down by enzymes (Lalwani et al., 2014). Organic materials often show superior biocompatibility; the FDA-approved dye indocyanine green (ICG) provides a clinical benchmark with its rapid hepatobiliary clearance, while engineered polymers (semiconducting polymer nanoparticles, SPNPs) can be designed with cleavable bonds (Lyu et al., 2018; Della Pelle et al., 2021). Ultimately, this focus on creating intentionally degradable or clearable nanoparticles is the critical step toward bringing PTT from preclinical studies to clinical reality. Finally, a significant barrier to the clinical translation of PTT is the lack of standardized parameters across preclinical studies. This challenge is formidable, extending beyond just light exposure conditions. A review of the literature reveals considerable variability in irradiation, with typical parameters involving an 808 nm laser at a power density of 0.5-3 Wcm^{-2} for 5–10 min, aiming for temperatures of 55 °C–60 °C for conventional PTT or a milder ~41 °C–43 °C for mild PTT. Furthermore, given that this research is still largely in the preclinical stage, different laboratories employ unique nanoparticle platforms and diverse infection models. This heterogeneity makes it exceedingly difficult to directly compare the therapeutic efficacy of different photothermal systems. Therefore, establishing standardized protocols that encompass not only irradiation parameters but also the class of nanomaterial and the type of infection being modeled is imperative to accelerate the clinical translation of this promising therapeutic modality.

In light of this, future research endeavors regarding the application of PTT in oral infections, encompassing dental caries, endodontics, periodontitis, and peri-implantitis, should center on the following aspects: i. Establish experimental models that can duplicate the complexity of biofilms to evaluate the antibacterial efficacy of PTT comprehensively. The mechanism of PTT against dental plaque biofilms also needs to be further studied. ii. Develop photothermal materials that are smart-responsive, degradable, or can be cleared by body metabolism to improve the biosafety of PTT. iii. Probe into applying NIR-II lasers in deep-seated oral tissues to augment the precision of treatment. iv. Fortify interdisciplinary integration, promote the combinatorial utilization of PTT with traditional antibacterial, immunomodulatory, and tissue-regeneration strategies, and engineer multifunctional materials. v. Facilitate large-scale clinical trials, standardize treatment parameters, evaluate long-term biosafety, and ultimately propel its clinical translation. Future research should also be directed towards elucidating the interplay between PTT and the oral microbiota, especially its implications for non-pathogenic commensal bacteria. Preserving the eco-logical equilibrium of the oral microbiota is pivotal for upholding overall oral health and forestalling diseases associated with dysbiosis. Additionally, developing cost-effective and scalable PTT systems is imperative for its widespread clinical deployment, particularly in resource-constrained settings. In summary, PTT presents a highly promising approach to the treatment of oral infections, replete with substantial potential for clinical translational applications. With the evolution of multi-disciplinary convergence, it may emerge as a novel approach for combating oral-related infections, thereby conferring greater benefits to humanity.

Author contributions

PW: Writing – review and editing, Writing – original draft, Funding acquisition, Conceptualization. JL: Writing – original draft. FL: Writing – original draft, Writing – review and editing, Conceptualization.

Funding

The author(s) declare that financial support was received for the research and/or publication of this article. This research was funded by the Technological Plan of Traditional Chinese Medicine Administration of Jiangxi Province of China (2022A329), the Jiangxi Provincial Natural Science Foundation (20212BAB206072, 20224BAB216078), the Jiangxi Province Chinese Medicine Science and Technology Program (2021A385).

Acknowledgements

The authors thank Yanfang Lin, Ao Jia, Yifan Liu, Yuyao Li, Rong Li, Junping Fan, and Dongping Li for their review of this manuscript.

Conflict of interest

The authors declare that the research was conducted in the absence of any commercial or financial relationships that could be construed as a potential conflict of interest.

Generative AI statement

The author(s) declare that Generative AI was used in the creation of this manuscript. AI help us polish manuscript.

Any alternative text (alt text) provided alongside figures in this article has been generated by Frontiers with the support of artificial intelligence and reasonable efforts have been made to ensure accuracy, including review by the authors wherever possible. If you identify any issues, please contact us.

Publisher's note

All claims expressed in this article are solely those of the authors and do not necessarily represent those of their affiliated organizations, or those of the publisher, the editors and the reviewers. Any product that may be evaluated in this article, or claim that may be made by its manufacturer, is not guaranteed or endorsed by the publisher.

References

Abou-Rass, M., and Oglesby, S. W. (1981). The effects of temperature, concentration, and tissue type on the solvent ability of sodium hypochlorite. *J. Endod.* 7 (8), 376–377. doi:10.1016/s0099-2399(81)80059-3

Akindele, B. O., Orenuga, O. O., Olatosi, O. O., and Oladele, R. O. (2025). Comparative evaluation of the clinical effectiveness of chemomechanical (papacarie) and conventional mechanical caries removal methods in treatment of carious primary molars: a randomized controlled clinical study. *BMC Oral Health* 25 (1), 290. doi:10.1186/s12903-025-05654-7

Aksoy, İ., Küçükkeçeci, H., Sevgi, F., Metin, Ö., and Hatay Patir, I. (2020). Photothermal antibacterial and antibiofilm activity of black phosphorus/gold nanocomposites against pathogenic bacteria. *ACS Appl. Mat. Interfaces* 12 (24), 26822–26831. doi:10.1021/acsami.0c02524

Alawaji, Y. N., Alshammari, A., Mostafa, N., Carvalho, R. M., and Aleksejuniene, J. (2022). Periodontal disease prevalence, extent, and risk associations in untreated individuals. *Clin. Exp. Dent. Res.* 8 (1), 380–394. doi:10.1002/cre2.526

AlSahafi, R., Wang, X., Mitwalli, H., Alhussein, A., Balhaddad, A. A., Melo, M. A. S., et al. (2022). Novel antibacterial low-shrinkage-stress resin-based cement. *Dent. Mat.* 38 (11), 1689–1702. doi:10.1016/j.dental.2022.08.005

Altamura, S., Del Pinto, R., Pietropaoli, D., and Ferri, C. (2024). Oral health as a modifiable risk factor for cardiovascular diseases. *Trends cardiovasc. Med.* 34 (4), 267–275. doi:10.1016/j.tcm.2023.03.003

Arendrup, M. C., and Patterson, T. F. (2017). Multidrug-resistant candida: epidemiology, molecular mechanisms, and treatment. *J. Infect. Dis.* 216 (Suppl. l_3), S445–S451. doi:10.1093/infdis/jix131

Avci, P., Gupta, A., Sadasivam, M., Vecchio, D., Pam, Z., Pam, N., et al. (2013). Low-level laser (light) therapy (LLLT) in skin: stimulating, healing, restoring. *Semin. Cutan. Med. Surg.* 32 (1), 41–52. Available online at: https://pubmed.ncbi.nlm.nih.gov/24049929/

Bai, L., Shi, E., Li, Y., Yang, M., Li, C., Li, C., et al. (2022). Oxyhemoglobin-based nanophotosensitizer for specific and synergistic photothermal and photodynamic therapies against *Porphyromonas gingivalis* oral infection. *ACS Biomater. Sci. Eng.* 9 (1), 485–497. doi:10.1021/acsbiomaterials.2c01034

Bai, Y., Huang, P., Feng, N., Li, Y., Huang, J., Jin, H., et al. (2023). Treat the "untreatable" by a photothermal agent: triggering heat and immunological responses for rabies virus inactivation. *Adv. Sci.* 10 (2), 2205461. doi:10.1002/advs.202205461

Baker, J. L., Mark Welch, J. L., Kauffman, K. M., McLean, J. S., and He, X. (2024). The oral microbiome: diversity, biogeography and human health. *Nat. Rev. Microbiol.* 22 (2), 89–104. doi:10.1038/s41579-023-00963-6

Belibasakis, G. N., Seneviratne, C. J., Jayasinghe, R. D., Vo, P.T.-D., Bostanci, N., and Choi, Y. (2024). Bacteriome and mycobiome dysbiosis in oral mucosal dysplasia and oral cancer. *Periodontol* 96 (1), 95–111. doi:10.1111/prd.12558

Berglundh, T., Armitage, G., Araujo, M. G., Avila-Ortiz, G., Blanco, J., Camargo, P. M., et al. (2018). Peri-implant diseases and conditions: consensus report of workgroup 4 of the 2017 world workshop on the classification of periodontal and peri-implant diseases and conditions. *J. Clin. Periodontol.* 45 (S20), S286-S291–S291. doi:10.1111/jcpe.12957

Bermúdez-Jiménez, C., Niño-Martínez, N., Patiño-Marín, N., Martínez-Gutiérrez, F., Ruiz, F., Bach, H., et al. (2020). Effective control of biofilms by photothermal therapy using a gold nanorod hydrogel. *J. Biomed. Mat. Res. Part B Appl. Biomater.* 108 (2), 333–342. doi:10.1002/jbm.b.34392

Bernabe, E., Marcenes, W., Hernandez, C. R., Bailey, J., Abreu, L. G., Alipour, V., et al. (2020). Global, regional, and national levels and trends in burden of oral conditions from 1990 to 2017: a systematic analysis for the global burden of disease 2017 study. *J. Dent. Res.* 99 (4), 362–373. doi:10.1177/0022034520908533

Bowen, W. H., Burne, R. A., Wu, H., and Koo, H. (2018). Oral biofilms: Pathogens, matrix, and polymicrobial interactions in microenvironments. *Trends Microbiol.* 26 (3), 229–242. doi:10.1016/j.tim.2017.09.008

Brookes, Z., Teoh, L., Cieplik, F., and Kumar, P. (2023). Mouthwash effects on the oral microbiome: are they good, bad, or balanced? *Int. Dent. J.* 73 (Suppl. 2), S74–S81. doi:10.1016/j.identj.2023.08.010

Burghardt, I., Luthen, F., Prinz, C., Kreikemeyer, B., Zietz, C., Neumann, H. G., et al. (2015). A dual function of copper in designing regenerative implants. *Biomaterials* 44, 36–44. doi:10.1016/j.biomaterials.2014.12.022

Burns, L. E., Kim, J., Wu, Y., Alzwaideh, R., McGowan, R., and Sigurdsson, A. (2022). Outcomes of primary root canal therapy: an updated systematic review of longitudinal clinical studies published between 2003 and 2020. *Int. Endod. J.* 55 (7), 714–731. doi:10.1111/iej.13736

Cao, J., Sun, Q., Shen, A.-G., Fan, B., and Hu, J.-M. (2021). Nano au@ $Cu_{2-x}S$ with near-infrared photothermal and peroxidase catalytic activities redefines efficient antibiofilm-oriented root canal therapy. *Chem. Eng. J.* 422, 130090. doi:10.1016/j.cej.2021.130090

Cao, J., Song, Z., Du, T., and Du, X. (2024). Antimicrobial materials based on photothermal action and their application in wound treatment. *Burns Trauma* 12, tkae046. doi:10.1093/burnst/tkae046

Carcuac, O., Abrahamsson, I., Albouy, J. P., Linder, E., Larsson, L., and Berglundh, T. (2013). Experimental periodontitis and peri-implantitis in dogs. *Clin. Oral Implant. Res.* 24 (4), 363–371. doi:10.1111/clr.12067

Castillo-Martínez, J. C., Martínez-Castañón, G. A., Martínez-Gutierrez, F., Zavala-Alonso, N. V., Patiño-Marín, N., Niño-Martinez, N., et al. (2015). Antibacterial and antibiofilm activities of the photothermal therapy using gold nanorods against seven different bacterial strains. *J. Nanomater.* 2015, 783671. doi:10.1155/2015/783671

Chen, F., and Wang, D. (2010). Novel technologies for the prevention and treatment of dental caries: a patent survey. *Expert. Opin. Ther. Pat.* 20 (5), 681–694. doi:10.1517/13543771003720491

Chen, Q. W., Liu, X. H., Fan, J. X., Peng, S. Y., Wang, J. W., Wang, X. N., et al. (2020). Self-mineralized photothermal bacteria hybridizing with mitochondria-targeted metal–organic frameworks for augmenting photothermal tumor therapy. *Adv. Funct. Mat.* 30 (14), 1909806. doi:10.1002/adfm.201909806

Chen, Z., Wang, Z., Qiu, W., and Fang, F. (2021). Overview of antibacterial strategies of dental implant materials for the prevention of peri-implantitis. *Bioconjug. Chem.* 32 (4), 627–638. doi:10.1021/acs.bioconjchem.1c00129

Chen, L., Peng, M., Li, H., Zhou, J., He, W., Hu, R., et al. (2023a). Metal-phenolic network with Pd nanoparticle nodes synergizes oxidase-like and photothermal properties to eradicate oral polymicrobial biofilm-associated infections. *Adv. Mat.* 36 (7), 2306376. doi:10.1002/adma.202306376

Chen, L., Peng, M., Zhou, J., Hu, X., Piao, Y., Li, H., et al. (2023b). Supramolecular photothermal Cascade nano-reactor enables photothermal effect, Cascade reaction, and *in situ* hydrogelation for biofilm-associated tooth-extraction wound healing. *Adv. Mat.* 35 (31), 2301664. doi:10.1002/adma.202301664

Chen, Q., Qi, M., Shi, F., Liu, C., Shi, Y., Sun, Y., et al. (2023c). Novel twin-crystal nanosheets with MnO_2 modification to combat bacterial biofilm against periodontal infections *via* multipattern strategies. *Adv. Healthc. Mat.* 12 (19), 2300313. doi:10.1002/adhm.202300313

Chen, B., Wang, W., Hu, M., Liang, Y., Wang, N., Li, C., et al. (2024). Photo-thermo-electric dental implant for anti-infection and enhanced osteoimmunomodulation. *ACS Nano* 18 (36), 24968–24983. doi:10.1021/acsnano.4c05859

Chiang, C.-P., Hsieh, O., Tai, W.-C., Chen, Y.-J., and Chang, P.-C. (2020). Clinical outcomes of adjunctive indocyanine green-diode lasers therapy for treating refractory

periodontitis: a randomized controlled trial with *in vitro* assessment. *J. Formos. Med. Assoc.* 119 (2), 652–659. doi:10.1016/j.jfma.2019.08.021

Cobb, C. M., and Sottosanti, J. S. (2021). A re-evaluation of scaling and root planing. *J. Periodontol.* 92 (10), 1370–1378. doi:10.1002/jper.20-0839

Collaborators, G. B. D. O. D., Marcenes, W., Abdulkader, R. S., Abreu, L. G., Afzal, S., Alhalaiqa, F. N., et al. (2025). Trends in the global, regional, and national burden of oral conditions from 1990 to 2021: a systematic analysis for the global burden of disease study 2021. *Lancet* 405 (10482), 897–910. doi:10.1016/S0140-6736(24)02811-3

Dai, X., Liu, Y., Meng, F., Li, Q., Wu, F., Yuan, J., et al. (2023). Amplification of oxidative damage using near-infrared II-mediated photothermal/thermocatalytic effects for periodontitis treatment. *Acta Biomater.* 171, 519–531. doi:10.1016/j.actbio.2023.09.014

Daubert, D. M., Weinstein, B. F., Bordin, S., Leroux, B. G., and Flemming, T. F. (2015). Prevalence and predictive factors for peri-implant disease and implant failure: a cross-sectional analysis. *J. Periodontol.* 86 (3), 337–347. doi:10.1902/jop.2014.140438

Della Pelle, G., Delgado Lopez, A., Salord Fiol, M., and Kostevsek, N. (2021). Cyanine dyes for photo-thermal therapy: a comparison of synthetic liposomes and natural erythrocyte-based carriers. *Int. J. Mol. Sci.* 22 (13), 6914. doi:10.3390/ijms22136914

Deo, P. N., and Deshmukh, R. (2019). Oral microbiome: unveiling the fundamentals. *J. Oral Maxillofac. Pathol.* 23 (1), 122–128. doi:10.4103/jomfp.JOMFP_304_18

Derks, J., Schaller, D., Håkansson, J., Wennström, J. L., Tomasi, C., and Berglundh, T. (2016). Peri-implantitis - onset and pattern of progression. *J. Clin. Periodontol.* 43 (4), 383–388. doi:10.1111/jcpe.12535

Diaz, P., Gonzalo, E., Villagra, L. J. G., Miegimolle, B., and Suarez, M. J. (2022). What is the prevalence of peri-implantitis? A systematic review and meta-analysis. *BMC Oral Health* 22 (1), 449. doi:10.1186/s12903-022-02493-8

Dong, Y., Liu, W., Lei, Y., Wu, T., Zhang, S., Guo, Y., et al. (2017). Effect of gelatin sponge with colloid silver on bone healing in infected cranial defects. *Mat. Sci. Eng. c-mater. Biol. Appl.* 70 (Pt 1), 371–377. doi:10.1016/j.msec.2016.09.015

Duan, X., Zhang, Q., Jiang, Y., Wu, X., Yue, X., Geng, Y., et al. (2022). Semiconducting polymer nanoparticles with intramolecular motion-induced photothermy for tumor phototheranostics and tooth root canal therapy. *Adv. Mat.* 34 (17), 2200179. doi:10.1002/adma.202200179

Ertem, E., Gutt, B., Zuber, F., Allegri, S., Le Ouay, B., Mefti, S., et al. (2017). Core-shell silver nanoparticles in endodontic disinfection solutions enable long-term antimicrobial effect on oral biofilms. *ACS Appl. Mat. Interfaces* 9 (40), 34762–34772. doi:10.1021/acsami.7b13929

Fang, Z., Zhang, S., Wang, W., Xu, Y., Lu, M., Qian, Y., et al. (2025). Aggregation-induced emission-based phototheranostics to combat bacterial infection at wound sites: a review. *Biomaterials* 315, 122950. doi:10.1016/j.biomaterials.2024.122950

Feng, Y., Sun, Q., Liu, P., Fan, W., and Fan, B. (2024). Antibacterial property and mechanisms of au@ag core-shell nanoparticles with near-infrared absorption against *E. faecalis* infection of dentin. *Int. J. Nanomed.* 19, 6981–6997. doi:10.2147/ijn.S468649

Fischer, N. G., Kobe, A. C., Dai, J., He, J., Wang, H., Pizarek, J. A., et al. (2022). Tapping basement membrane motifs: oral junctional epithelium for surface-mediated soft tissue attachment to prevent failure of percutaneous devices. *Acta Biomater.* 141, 70–88. doi:10.1016/j.actbio.2021.12.030

Fulaz, S., Hiebner, D., Barros, C. H. N., Devlin, H., Vitale, S., Quinn, L., et al. (2019). Ratiometric imaging of the *in situ* pH distribution of biofilms by use of fluorescent mesoporous silica nanosensors. *ACS Appl. Mat. Interfaces* 11 (36), 32679–32688. doi:10.1021/acsami.9b09978

Galdámez-Falla, V.-M., Castillo-Martínez, J.-C., de Alba-Montero, I., Patiño-Marín, N., Niño-Martínez, N., Ruiz, F., et al. (2022). Formation of a mature biofilm of Enterococcus faecalis in root canal and its treatment using gold nanorods. *J. Mat. Sci. Res. Rev.* 5 (1), 31–43. Available online at: https://journaljmsrr.com/index.php/JMSRR/article/view/200.

Gao, G., Jiang, Y. W., Jia, H. R., and Wu, F. G. (2019). Near-infrared light-controllable on-demand antibiotics release using thermo-sensitive hydrogel-based drug reservoir for combating bacterial infection. *Biomaterials* 188, 83–95. doi:10.1016/j.biomaterials.2018.09.045

Gao, P., Li, G., Wang, Z., Zhang, H., Shan, Y., Yuan, X., et al. (2023). Protease-loaded CuS nanoparticles with synergistic photothermal/dynamic therapy against *F. Nucleatum*-induced periodontitis. *ACS Appl. Mat. Interfaces* 15 (27), 32215–32225. doi:10.1021/acsami.3c04534

Gil-Cardoso, K., Comitato, R., Ginés, I., Ardévol, A., Pinent, M., Virgili, F., et al. (2019). Protective effect of proanthocyanidins in a rat model of mild intestinal inflammation and impaired intestinal permeability induced by LPS. *Mol. Nutr. Food. Res.* 63 (8), 1800720. doi:10.1002/mnfr.201800720

Giok, K. C., Veettil, S. K., and Menon, R. K. (2024). Comparative effectiveness of interventions for the treatment of peri-implantitis: a systematic review with network meta-analysis. *J. Prosthet. Dent.* doi:10.1016/j.prosdent.2024.03.024

Gkioka, M., and Rausch-Fan, X. (2024). Antimicrobial effects of metal coatings or physical, chemical modifications of titanium dental implant surfaces for prevention of peri-implantitis: a systematic review of *in vivo* studies. *Antibiotics-Basel* 13 (9), 908. doi:10.3390/antibiotics13090908

Gondivkar, S., Gadbail, A., Sarode, G. S., Sarode, S. C., Patil, S., and Awan, K. H. (2019). Infectious diseases of oral cavity. *Dis. Mon.* 65 (6), 164–184. doi:10.1016/j.disamonth.2018.09.008

Guo, G., Zhang, H., Shen, H., Zhu, C., He, R., Tang, J., et al. (2020). Space-selective chemodynamic therapy of $CuFe_5O_8$ nanocubes for implant-related infections. *ACS Nano* 14 (10), 13391–13405. doi:10.1021/acsnano.0c05255

Gupta, A., Saleena, L. M., Kannan, P., and Shivachandran, A. (2024). The impact of oral diseases on respiratory health and the influence of respiratory infections on the oral microbiome. *J. Dent.* 148, 105213. doi:10.1016/j.jdent.2024.105213

Hajishengallis, G. (2014). Immunomicrobial pathogenesis of periodontitis: keystones, pathobionts, and host response. *Trends Immunol.* 35 (1), 3–11. doi:10.1016/j.it.2013.09.001

Hajishengallis, G., Lamont, R. J., and Koo, H. (2023). Oral polymicrobial communities: assembly, function, and impact on diseases. *Cell Host Microbe* 31 (4), 528–538. doi:10.1016/j.chom.2023.02.009

Han, Z., Xiong, J., Jin, X., Dai, Q., Han, M., Wu, H., et al. (2024). Advances in reparative materials for infectious bone defects and their applications in maxillofacial regions. *J. Mat. Chem. B* 12 (4), 842–871. doi:10.1039/d3tb02069j

He, L., Di, D., Chu, X., Liu, X., Wang, Z., Lu, J., et al. (2023). Photothermal antibacterial materials to promote wound healing. *J. Control. Release* 363, 180–200. doi:10.1016/j.jconrel.2023.09.035

Heitz-Mayfield, L. J. A. (2024). Conventional diagnostic criteria for periodontal diseases (plaque-induced gingivitis and periodontitis). *Periodontol* 95 (1), 10–19. doi:10.1111/prd.12579

Hernando-Amado, S., Coque, T. M., Baquero, F., and Martínez, J. L. (2019). Defining and combating antibiotic resistance from one health and global health perspectives. *Nat. Microbiol.* 4 (9), 1432–1442. doi:10.1038/s41564-019-0503-9

Hu, X., Chen, J., Yang, S., Zhang, Z., Wu, H., He, J., et al. (2024). 3D printed multifunctional biomimetic bone scaffold combined with TP-Mg nanoparticles for the infectious bone defects repair. *Small* 20 (40), 2403681. doi:10.1002/smll.202403681

Huang, K., Liu, W., Wei, W., Zhao, Y., Zhuang, P., Wang, X., et al. (2022). Photothermal hydrogel encapsulating intelligently bacteria-capturing Bio-MOF for infectious wound healing. *ACS Nano* 16 (11), 19491–19508. doi:10.1021/acsnano.2c09593

Huang, D., Wang, X., Liang, J., Ling, J., Bian, Z., Yu, Q., et al. (2024). Expert consensus on difficulty assessment of endodontic therapy. *Int. J. Oral Sci.* 16 (1), 22. doi:10.1038/s41368-024-00285-0

Hussain, A., Tebyaniyan, H., and Khayatan, D. (2022). The role of epigenetic in dental and oral regenerative medicine by different types of dental stem cells: a comprehensive overview. *Stem Cells Int.* 2022, 1–15. doi:10.1155/2022/5304860

Hwang, S., Nam, J., Jung, S., Song, J., Doh, H., and Kim, S. (2014). Gold nanoparticle-mediated photothermal therapy: current status and future perspective. *Nanomedicine* 9 (13), 2003–2022. doi:10.2217/nnm.14.147

Ichioka, Y., Derks, J., Larsson, L., and Berglundh, T. (2023). Surface decontamination of explanted peri-implantitis-affected implants. *J. Clin. Periodontol.* 50 (8), 1113–1122. doi:10.1111/jcpe.13836

Iniesta, M., Chamorro, C., Ambrosio, N., Marín, M. J., Sanz, M., and Herrera, D. (2023). Subgingival microbiome in periodontal health, gingivitis and different stages of periodontitis. *J. Clin. Periodontol.* 50 (7), 905–920. doi:10.1111/jcpe.13793

Jakubovics, N. S., Goodman, S. D., Mashburn-Warren, L., Stafford, G. P., and Cieplik, F. (2021). The dental plaque biofilm matrix. *Periodontol. 2000* 86 (1), 32–56. doi:10.1111/prd.12361

Jiang, W., Deng, Z., Dai, X., and Zhao, W. (2021). PANoptosis: a new insight into oral infectious diseases. *Front. Immunol.* 12, 789610. doi:10.3389/fimmu.2021.789610

Karamifar, K., Tondari, A., and Saghiri, M. A. (2020). Endodontic periapical lesion: an overview on the etiology, diagnosis and current treatment modalities. *Eur. Endod. J.* 5 (2), 54–67. doi:10.14744/eej.2020.42714

Khantamat, O., Li, C.-H., Yu, F., Jamison, A. C., Shih, W.-C., Cai, C., et al. (2015). Gold nanoshell-decorated silicone surfaces for the near-infrared (NIR) photothermal destruction of the pathogenic bacterium *E. faecalis*. *ACS Appl. Mat. Interfaces* 7 (7), 3981–3993. doi:10.1021/am506516r

Kilian, M., Chapple, I. L., Hannig, M., Marsh, P. D., Meuric, V., Pedersen, A. M., et al. (2016). The oral microbiome - an update for oral healthcare professionals. *Br. Dent. J.* 221 (10), 657–666. doi:10.1038/sj.bdj.2016.865

Kim, J., Kim, H. Y., Song, S. Y., Go, S. H., Sohn, H. S., Baik, S., et al. (2019). Synergistic oxygen generation and reactive oxygen species scavenging by manganese ferrite/ceria Co-decorated nanoparticles for rheumatoid arthritis treatment. *ACS Nano* 13 (3), 3206–3217. doi:10.1021/acsnano.8b08785

Kong, Q., Qi, M., Li, W., Shi, Y., Su, J., Xiao, S., et al. (2023). A novel Z-Scheme heterostructured Bi_2S_3/Cu-TCPP nanocomposite with synergistically enhanced therapeutics against bacterial biofilm infections in periodontitis. *Small* 19 (43), 2302547. doi:10.1002/smll.202302547

Koyanagi, T., Sakamoto, M., Takeuchi, Y., Maruyama, N., Ohkuma, M., and Izumi, Y. (2013). Comprehensive microbiological findings in peri-implantitis and periodontitis. *J. Clin. Periodontol.* 40 (3), 218–226. doi:10.1111/jcpe.12047

Kuboniwa, M., Houser, J. R., Hendrickson, E. L., Wang, Q., Alghamdi, S. A., Sakanaka, A., et al. (2017). Metabolic crosstalk regulates Porphyromonas gingivalis colonization and virulence during oral polymicrobial infection. *Nat. Microbiol.* 2 (11), 1493–1499. doi:10.1038/s41564-017-0021-6

Kunath, B. J., De Rudder, C., Laczny, C. C., Letellier, E., and Wilmes, P. (2024). The oral-gut microbiome axis in health and disease. *Nat. Rev. Microbiol.* 22 (12), 791–805. doi:10.1038/s41579-024-01075-5

Kwon, T., Lamster, I. B., and Levin, L. (2021). Current concepts in the management of periodontitis. *Int. Dent. J.* 71 (6), 462–476. doi:10.1111/idj.12630

Laforgia, A., Inchingolo, A. D., Piras, F., Colonna, V., Giorgio, R. V., Carone, C., et al. (2024). Therapeutic strategies and genetic implications for periodontal disease management: a systematic review. *Int. J. Mol. Sci.* 25 (13), 7217. doi:10.3390/ijms25137217

Lalwani, G., Xing, W., and Sitharaman, B. (2014). Enzymatic degradation of oxidized and reduced graphene nanoribbons by lignin peroxidase. *J. Mat. Chem. B* 2 (37), 6354–6362. doi:10.1039/C4TB00976B

Lamont, R. J., Koo, H., and Hajishengallis, G. (2018). The oral microbiota: dynamic communities and host interactions. *Nat. Rev. Microbiol.* 16 (12), 745–759. doi:10.1038/s41579-018-0089-x

Li, S. S., Wu, C. Z., and Li, L. J. (2021). Progress on photodynamic therapy in oral diseases. *West China J. Stomatol.* 39 (2), 215–220. doi:10.7518/hxkq.2021.02.014

Li, B., Liu, F., Ye, J., Cai, X., Qian, R., Zhang, K., et al. (2022). Regulation of macrophage polarization through periodic photo-thermal treatment to facilitate osteogenesis. *Small* 18 (38), 2202691. doi:10.1002/smll.202202691

Li, B., Wang, W., Zhao, L., Li, M., Yan, D., Li, X., et al. (2024a). Aggregation-induced emission-based macrophage-like nanoparticles for targeted photothermal therapy and virus transmission blockage in monkeypox. *Adv. Mat.* 36 (9), 2305378. doi:10.1002/adma.202305378

Li, J., Wang, Y., Tang, M., Zhang, C., Fei, Y., Li, M., et al. (2024b). New insights into nanotherapeutics for periodontitis: a triple concerto of antimicrobial activity, immunomodulation and periodontium regeneration. *J. Nanobiotechnol.* 22 (1), 19. doi:10.1186/s12951-023-02261-y

Li, S., Li, Q., Zhang, H., Li, F., Hu, J., Qian, J., et al. (2024c). Dental caries management with antibacterial silver-doped prussian blue hydrogel by the combined effects of photothermal response and ion discharge. *ACS Appl. Mat. Interfaces* 16 (22), 28172–28183. doi:10.1021/acsami.4c04302

Li, S., Wang, F., Chen, Y., Shi, W., Liu, D., Lv, M., et al. (2024d). Lysine aggregates-based nanostructured antimicrobial peptides for cariogenic biofilm microenvironment-activated caries treatment. *Aggregate* 5 (5), e578. doi:10.1002/agt2.578

Li, T., Shu, M., Zhu, C., Liu, Q., Li, Y., Wang, R., et al. (2024e). Triple-combination therapy with a multifunctional yolk-shell nanozyme Au@CeO_2 loaded with dimethyl fumarate for periodontitis. *Adv. Sci.* 12 (7), 2413891. doi:10.1002/advs.202413891

Li, Z., Fan, X., Liu, Y., Yue, M., Wu, T., Wang, X., et al. (2024f). Engineering mild-photothermal responsive and NO donor prussian blue nanozymes using mild synthesis for inflammation regulation and bacterial eradication in periodontal disease. *Adv. Mat.* 37 (6), 2409840. doi:10.1002/adma.202409840

Li, Y., Wang, P., Liu, Y., Wu, X., Long, G., Chen, Y., et al. (2025). Fe_3O_4-Based nanospheres with high photothermal conversion efficiency for dual-effect and mild biofilm eradication against periodontitis. *ACS Appl. Mat. Interfaces* 17 (10), 14832–14845. doi:10.1021/acsami.4c17966

Liang, J., Wang, P., Lin, Y., Jia, A., Tong, F., and Li, Z. (2025). Advances in photothermal therapy for oral cancer. *Int. J. Mol. Sci.* 26 (9), 4344. doi:10.3390/ijms26094344

Lin, J., He, Z., Liu, F., Feng, J., Huang, C., Sun, X., et al. (2020). Hybrid hydrogels for synergistic periodontal antibacterial treatment with sustained drug release and NIR-Responsive photothermal effect. *Int. J. Nanomed.* 15, 5377–5387. doi:10.2147/IJN.S248538

Lin, J., Fang, J., Zhou, J., Qi, M., Shi, Y., Li, C., et al. (2024). NIR-II triggered Cu(I) phosphide for chemodynamic and photothermal periodontitis treatment: efficient reduction of bacterial co-aggregation. *Acta Biomater.* 187, 396–408. doi:10.1016/j.actbio.2024.08.013

Liu, Y., Bhattarai, P., Dai, Z., and Chen, X. (2019). Photothermal therapy and photoacoustic imaging *via* nanotheranostics in fighting cancer. *Chem. Soc. Rev.* 48 (7), 2053–2108. doi:10.1039/C8CS00618K

Liu, Z., Zhao, X., Yu, B., Zhao, N., Zhang, C., and Xu, F. J. (2021). Rough carbon-iron oxide nanohybrids for Near-Infrared-II light-responsive synergistic antibacterial therapy. *ACS Nano* 15 (4), 7482–7490. doi:10.1021/acsnano.1c00894

Liu, D., Chen, J., Gao, L., Chen, X., Lin, L., Liu, Y., et al. (2025). Nano Sim@ZIF8@PDA modified injectable temperature sensitive nanocomposite hydrogel for photothermal/drug therapy for peri-implantitis. *Carbohydr. Polym.* 354, 123327. doi:10.1016/j.carbpol.2025.123327

Lu, B.-Y., Zhu, G.-Y., Yu, C.-H., Chen, G.-Y., Zhang, C.-L., Zeng, X., et al. (2021). Functionalized graphene oxide nanosheets with unique three-in-one properties for efficient and tunable antibacterial applications. *Nano Res.* 14 (1), 185–190. doi:10.1007/s12274-020-3064-6

Luo, R., Zhang, C., Zhang, Z., Ren, P., Xu, Z., and Liu, Y. (2025). NIR-II upconversion nanomaterials for biomedical applications. *Nanoscale* 17 (6), 2985–3002. doi:10.1039/d4nr04445b

Lyu, Y., Zeng, J., Jiang, Y., Zhen, X., Wang, T., Qiu, S., et al. (2018). Enhancing both biodegradability and efficacy of semiconducting polymer nanoparticles for photoacoustic imaging and photothermal therapy. *ACS Nano* 12 (2), 1801–1810. doi:10.1021/acsnano.7b08616

Ma, L., Feng, X., Liang, H., Wang, K., Song, Y., Tan, L., et al. (2020). A novel photothermally controlled multifunctional scaffold for clinical treatment of osteosarcoma and tissue regeneration. *Mat. Today* 36, 48–62. doi:10.1016/j.mattod.2019.12.005

Madani, M., Berardi, T., and Stoopler, E. T. (2014). Anatomic and examination considerations of the oral cavity. *Med. Clin. North Am.* 98 (6), 1225–1238. doi:10.1016/j.mcna.2014.08.001

Mahmoud, M. Y., Steinbach-Rankins, J. M., and Demuth, D. R. (2019). Functional assessment of peptide-modified PLGA nanoparticles against oral biofilms in a murine model of periodontitis. *J. Control. Release* 297, 3–13. doi:10.1016/j.jconrel.2019.01.036

Mammari, N., and Duval, R. E. (2023). Photothermal/photoacoustic therapy combined with metal-based nanomaterials for the treatment of microbial infections. *Microorganisms* 11 (8), 2084. doi:10.3390/microorganisms11082084

Manoil, D., Cerit, E. E., Fang, H., Durual, S., Brundin, M., and Belibasakis, G. N. (2023). Profiling antibiotic susceptibility among distinct *Enterococcus faecalis* isolates from dental root canals. *Antibiotics-Basel* 13 (1), 18. doi:10.3390/antibiotics13010018

Mazurel, D., Brandt, B. W., Boomsma, M., Crielaard, W., Lagerweij, M., Exterkate, R. A. M., et al. (2025). *Streptococcus mutans* and caries: a systematic review and meta-analysis. *J. Dent. Res.* 104, 594–603. doi:10.1177/00220345241303880

Mei, J., Xu, D., Wang, L., Kong, L., Liu, Q., Li, Q., et al. (2023). Biofilm microenvironment-responsive self-assembly nanoreactors for all-stage biofilm associated infection through bacterial cuproptosis-like death and macrophage Re-Rousing. *Adv. Mat.* 35 (36), e2303432. doi:10.1002/adma.202303432

Mombelli, A. (2018). Microbial colonization of the periodontal pocket and its significance for periodontal therapy. *Periodontol. 2000* 76 (1), 85–96. doi:10.1111/prd.12147

Mondal, S. K., Chakraborty, S., Manna, S., and Mandal, S. M. (2024). Antimicrobial nanoparticles: current landscape and future challenges. *RSC Pharm.* 1 (3), 388–402. doi:10.1039/d4pm00032c

Moradi Eslami, L., Vatanpour, M., Aminzadeh, N., Mehrvarzfar, P., and Taheri, S. (2019). The comparison of intracanal medicaments, diode laser and photodynamic therapy on removing the biofilm of *Enterococcus faecalis* and *Candida albicans* in the root canal system (*ex-vivo* study). *Photodiagn. Photodyn. Ther.* 26, 157–161. doi:10.1016/j.pdpdt.2019.01.033

Munakata, M., Suzuki, A., Yamaguchi, K., Kataoka, Y., and Sanda, M. (2022). Effects of implant surface mechanical instrumentation methods on peri-implantitis: an *in vitro* study using a circumferential bone defect model. *J. Dent. Sci.* 17 (2), 891–896. doi:10.1016/j.jds.2021.08.018

Muras, A., Mallo, N., Otero-Casal, P., Pose-Rodríguez, J. M., and Otero, A. (2022). Quorum sensing systems as a new target to prevent biofilm-related oral diseases. *Oral Dis.* 28 (2), 307–313. doi:10.1111/odi.13689

Neelakantan, P., Romero, M., Vera, J., Daood, U., Khan, A. U., Yan, A., et al. (2017). Biofilms in endodontics-current status and future directions. *Int. J. Mol. Sci.* 18 (8), 1748. doi:10.3390/ijms18081748

Nicholson, W. (2020). Titanium alloys for dental implants: a review. *Prosthesis* 2 (2), 100–116. doi:10.3390/prosthesis2020011

Nie, R., Sun, Y., Lv, H., Lu, M., Huangfu, H., Li, Y., et al. (2022). 3D printing of MXene composite hydrogel scaffolds for photothermal antibacterial activity and bone regeneration in infected bone defect models. *Nanoscale* 14 (22), 8112–8129. doi:10.1039/d2nr02176e

Osman, M. A., Kushnerev, E., Alamoush, R. A., Seymour, K. G., and Yates, J. M. (2022). Two gingival cell lines response to different dental implant abutment materials: an *in vitro* study. *Dent. J.* 10 (10), 192. doi:10.3390/dj10100192

Overchuk, M., Weersink, R. A., Wilson, B. C., and Zheng, G. (2023). Photodynamic and photothermal therapies: synergy opportunities for nanomedicine. *ACS Nano* 17 (9), 7979–8003. doi:10.1021/acsnano.3c00891

Pan, G., Zheng, J., Li, Z., Duan, Q., Zhang, M., and Wang, D. (2025). Dual-responsive polydopamine-embellished Zn-MOFs enabling synergistic photothermal and antibacterial metal ion therapy for oral biofilm eradication. *J. Mat. Chem. B* 13 (11), 3730–3743. doi:10.1039/d4tb02427c

Park, L., Kim, H.-S., Jang, W., Ji, M.-K., Ryu, J.-H., Cho, H., et al. (2023). Antibacterial evaluation of zirconia coated with plasma-based graphene oxide with photothermal properties. *Int. J. Mol. Sci.* 24 (10), 8888. doi:10.3390/ijms24108888

Peres, M. A., Macpherson, L. M. D., Weyant, R. J., Daly, B., Venturelli, R., Mathur, M. R., et al. (2019). Oral diseases: a global public health challenge. *Lancet* 394 (10194), 249–260. doi:10.1016/s0140-6736(19)31146-8

Pieralli, S., Kohal, R. J., Jung, R. E., Vach, K., and Spies, B. C. (2017). Clinical outcomes of zirconia dental implants: a systematic review. *J. Dent. Res.* 96 (1), 38–46. doi:10.1177/0022034516664043

Pinto, R. M., Soares, F. A., Reis, S., Nunes, C., and Van Dijck, P. (2020). Innovative strategies toward the disassembly of the EPS matrix in bacterial biofilms. *Front. Microbiol.* 11, 952. doi:10.3389/fmicb.2020.00952

Pitts, N. B., and Mayne, C. (2021). Making cavities history: a global policy consensus for achieving a dental cavity–free future. *JDR Clin. Transl. Res.* 6 (3), 264–267. doi:10.1177/23800844211020298

Pitts, N. B., Zero, D. T., Marsh, P. D., Ekstrand, K., Weintraub, J. A., Ramos-Gomez, F., et al. (2017). Dental caries. *Nat. Rev. Dis. Prim.* 3, 17030. doi:10.1038/nrdp.2017.30

Pohl, S., Akamp, T., Smeda, M., Uderhardt, S., Besold, D., Krastl, G., et al. (2024). Understanding dental pulp inflammation: from signaling to structure. *Front. Immunol.* 15, 1474466. doi:10.3389/fimmu.2024.1474466

Popescu, C., Munteanu, C., Anghelescu, A., Ciobanu, V., Spînu, A., Andone, I., et al. (2024). Novelties on neuroinflammation in alzheimer's disease-focus on gut and oral microbiota involvement. *Int. J. Mol. Sci.* 25 (20), 11272. doi:10.3390/ijms252011272

Pourhajibagher, M., Kazemian, H., Chiniforush, N., Hosseini, N., Pourakbari, B., Azizollahi, A., et al. (2018). Exploring different photosensitizers to optimize elimination of planktonic and biofilm forms of *Enterococcus faecalis* from infected root canal during antimicrobial photodynamic therapy. *Photodiagn. Photodyn. Ther.* 24, 206–211. doi:10.1016/j.pdpdt.2018.09.014

Qi, M., Ren, X., Li, W., Sun, Y., Sun, X., Li, C., et al. (2022). NIR responsive nitric oxide nanogenerator for enhanced biofilm eradication and inflammation immunotherapy against periodontal diseases. *Nano Today* 43, 101447. doi:10.1016/j.nantod.2022.101447

Qi, J., Si, C., Liu, H., Li, H., Kong, C., Wang, Y., et al. (2025). Advances of metal-based nanomaterials in the prevention and treatment of oral infections. *Adv. Healthc. Mat.* 14 (15), 2500416. doi:10.1002/adhm.202500416

Qian, H., Lei, T., Hua, L., Zhang, Y., Wang, D., Nan, J., et al. (2023). Fabrication, bacteriostasis and osteointegration properties researches of the additively-manufactured porous tantalum scaffolds loading vancomycin. *Bioact. Mat.* 24, 450–462. doi:10.1016/j.bioactmat.2022.12.013

Rams, T. E., Sautter, J. D., and van Winkelhoff, A. J. (2020). Comparative *in vitro* resistance of human periodontal bacterial pathogens to tinidazole and four other antibiotics. *Antibiotics-Basel* 9 (2), 68. doi:10.3390/antibiotics9020068

Ran, Y., Shi, J., Ding, Y., Li, L., Lu, D., Zeng, Y., et al. (2024). Black phosphorus nanosheets-loaded mussel-inspired hydrogel with wet adhesion, photothermal antimicrobial, and *in situ* remineralization capabilities for caries prevention. *Adv. Sci.* 11 (45), 2409155. doi:10.1002/advs.202409155

Ren, X., Gao, R., van der Mei, H. C., Ren, Y., Peterson, B. W., and Busscher, H. J. (2020). Eradicating infecting bacteria while maintaining tissue integration on photothermal nanoparticle-coated titanium surfaces. *ACS Appl. Mat. Interfaces* 12 (31), 34610–34619. doi:10.1021/acsami.0c08592

Sanz, M., Herrera, D., Kebschull, M., Chapple, I., Jepsen, S., Beglundh, T., et al. (2020). Treatment of stage I-III periodontitis-the EFP S3 level clinical practice guideline. *J. Clin. Periodontol.* 47 (22), 4–60. doi:10.1111/jcpe.13290

Scannapieco, F. A., and Cantos, A. (2016). Oral inflammation and infection, and chronic medical diseases: implications for the elderly. *Periodontol* 72 (1), 153–175. doi:10.1111/prd.12129

Schwarz, F., Derks, J., Monje, A., and Wang, H.-L. (2018). Peri-implantitis. *J. Clin. Periodontol.* 45 (S20), S246-S266–S266. doi:10.1111/jcpe.12954

Sczepanik, F. S. C., Grossi, M. L., Casati, M., Goldberg, M., Glogauer, M., Fine, N., et al. (2020). Periodontitis is an inflammatory disease of oxidative stress: we should treat it that way. *Periodontol. 2000* 84 (1), 45–68. doi:10.1111/prd.12342

Sedghi, L., DiMassa, V., Harrington, A., Lynch, S. V., and Kapila, Y. L. (2021). The oral microbiome: role of key organisms and complex networks in oral health and disease. *Periodontol* 87 (1), 107–131. doi:10.1111/prd.12393

Shen, L., Sun, F., Wang, Y., Liu, Y., Xin, Q., Zhu, Z., et al. (2024). Caries-prone primary teeth: a hidden reason and prophylactic treatment in the viewpoint of materials science. *ACS Appl. Mat. Interfaces* 16 (32), 41881–41891. doi:10.1021/acsami.4c07388

Sheng, L., Zhang, Z., Zhang, Y., Wang, E., Ma, B., Xu, Q., et al. (2021). A novel "hot spring"-mimetic hydrogel with excellent angiogenic properties for chronic wound healing. *Biomaterials* 264, 120414. doi:10.1016/j.biomaterials.2020.120414

Shi, E., Bai, L., Mao, L., Wang, H., Yang, X., Wang, Y., et al. (2021). Self-assembled nanoparticles containing photosensitizer and polycationic brush for synergistic photothermal and photodynamic therapy against periodontitis. *J. Nanobiotechnol.* 19, 413–415. doi:10.1186/s12951-021-01114-w

Shim, S. H., Lee, S. Y., Lee, J.-B., Chang, B.-S., Lee, J.-K., and Um, H.-S. (2022). Antimicrobial photothermal therapy using diode laser with indocyanine green on *Streptococcus gordonii* biofilm attached to zirconia surface. *Photodiagn. Photodyn. Ther.* 38, 102767. doi:10.1016/j.pdpdt.2022.102767

Song, X., Ji, M., Shu, X., and Zou, L. (2025). Drug delivery systems loaded with plant-derived natural products for dental caries prevention and treatment. *J. Mat. Chem. B* 13 (6), 1920–1934. doi:10.1039/d4tb01924e

Spanemberg, J. C., Cardoso, J. A., Slob, E., and López-López, J. (2019). Quality of life related to oral health and its impact in adults. *J. Stomatol. Oral Maxillofac. Surg.* 120 (3), 234–239. doi:10.1016/j.jormas.2019.02.004

Stoopler, E. T., Villa, A., Bindakhil, M., Díaz, D. L. O., and Sollecito, T. P. (2024). Common oral conditions: a review. *JAMA* 331 (12), 1045–1054. doi:10.1001/jama.2024.0953

Sun, X. D., Liu, T. T., Wang, Q. Q., Zhang, J., and Cao, M. S. (2023). Surface modification and functionalities for titanium dental implants. *ACS Biomater. Sci. Eng.* 9 (8), 4442–4461. doi:10.1021/acsbiomaterials.3c00183

Tan, L., Li, J., Liu, X., Cui, Z., Yang, X., Zhu, S., et al. (2018). Rapid biofilm eradication on bone implants using red phosphorus and near-infrared light. *Adv. Mat.* 30 (31), e1801808. doi:10.1002/adma.201801808

Tang, S., Chen, M., and Zheng, N. (2014). Sub-10-nm Pd nanosheets with renal clearance for efficient near-infrared photothermal cancer therapy. *Small* 10 (15), 3139–3144. doi:10.1002/smll.201303631

Tian, Y., Li, Y., Liu, J., Lin, Y., Jiao, J., Chen, B., et al. (2022). Photothermal therapy with regulated Nrf2/NF-κB signaling pathway for treating bacteria-induced periodontitis. *Bioact. Mat.* 9, 428–445. doi:10.1016/j.bioactmat.2021.07.033

Tosić, G., Miladinović, M., Kovaević, M., and Stojanović, M. (2016). Choice of root canal irrigants by Serbian dental practitioners. *Vojnosanit. Pregl.* 73 (1), 47–52. doi:10.2298/vsp140909034t

Tóthová, L., and Celec, P. (2017). Oxidative stress and antioxidants in the diagnosis and therapy of periodontitis. *Front. Physiol.* 8, 1055. doi:10.3389/fphys.2017.01055

Tzach-Nahman, R., Mizraji, G., Shapira, L., Nussbaum, G., and Wilensky, A. (2017). Oral infection with Porphyromonas gingivalis induces peri-implantitis in a murine model: evaluation of bone loss and the local inflammatory response. *J. Clin. Periodontol.* 44 (7), 739–748. doi:10.1111/jcpe.12735

Umeda, M., Takeuchi, Y., Noguchi, K., Huang, Y., Koshy, G., and Ishikawa, I. (2004). Effects of nonsurgical periodontal therapy on the microbiota. *Periodontol* 36, 98–120. doi:10.1111/j.1600-0757.2004.03675.x

Villoria, G. E. M., Fischer, R. G., Tinoco, E. M. B., Meyle, J., and Loos, B. G. (2024). Periodontal disease: a systemic condition. *Periodontol* 96 (1), 7–19. doi:10.1111/prd.12616

Wang, C.-Y., Yang, Y.-H., Li, H., Lin, P.-Y., Su, Y.-T., Kuo, M.Y.-P., et al. (2020). Adjunctive local treatments for patients with residual pockets during supportive periodontal care: a systematic review and network meta-analysis. *J. Clin. Periodontol.* 47 (12), 1496–1510. doi:10.1111/jcpe.13379

Wang, H., Wang, D., Huangfu, H., Lv, H., Qin, Q., Ren, S., et al. (2022a). Branched AuAg nanoparticles coated by metal–phenolic networks for treating bacteria-induced periodontitis *via* photothermal antibacterial and immunotherapy. *Mat. Des.* 224, 111401. doi:10.1016/j.matdes.2022.111401

Wang, N., Luo, J., Deng, F., Huang, Y., and Zhou, H. (2022b). Antibiotic combination therapy: a strategy to overcome bacterial resistance to aminoglycoside antibiotics. *Front. Pharmacol.* 13, 839808. doi:10.3389/fphar.2022.839808

Wang, R., Kim, D., Yang, M., Li, X., and Yoon, J. (2022c). Phthalocyanine-assembled "one-for-two" nanoparticles for combined photodynamic-photothermal therapy of multidrug-resistant bacteria. *ACS Appl. Mat. Interfaces* 14 (6), 7609–7616. doi:10.1021/acsami.1c21891

Wang, F., Wu, Q., Jia, G., Kong, L., Zuo, R., Feng, K., et al. (2023a). Black Phosphorus/MnO_2 nanocomposite disrupting bacterial thermotolerance for efficient mild-temperature photothermal therapy. *Adv. Sci.* 10 (30), e2303911. doi:10.1002/advs.202303911

Wang, H., Wang, D., Huangfu, H., Chen, S., Qin, Q., Ren, S., et al. (2023b). Highly efficient photothermal branched Au–Ag nanoparticles containing procyanidins for synergistic antibacterial and anti-inflammatory immunotherapy. *Biomater. Sci.* 11 (4), 1335–1349. doi:10.1039/D2BM01212J

Wang, P., Wang, L., Zhan, Y., Liu, Y., Chen, Z., Xu, J., et al. (2023c). Versatile hybrid nanoplatforms for treating periodontitis with chemical/photothermal therapy and reactive oxygen species scavenging. *Chem. Eng. J.* 463, 142293. doi:10.1016/j.cej.2023.142293

Wang, W., Zhang, G., Wang, Y., Ran, J., Chen, L., Wei, Z., et al. (2023d). An injectable and thermosensitive hydrogel with nano-aided NIR-II phototherapeutic and chemical effects for periodontal antibacteria and bone regeneration. *J. Nanobiotechnol.* 21 (1), 367. doi:10.1186/s12951-023-02124-6

Wang, X., Qian, Y., Wang, S., Wang, M., Sun, K., Cheng, Z., et al. (2023e). Accumulative rolling Mg/PLLA composite membrane with lamellar heterostructure for enhanced bacteria inhibition and rapid bone regeneration. *Small* 19 (42), 2301638. doi:10.1002/smll.202301638

Wang, Y., Chang, L., Gao, H., Yu, C., Gao, Y., and Peng, Q. (2024). Nanomaterials-based advanced systems for photothermal/photodynamic therapy of oral cancer. *Eur. J. Med. Chem.* 272, 116508. doi:10.1016/j.ejmech.2024.116508

Wang, X., Shi, W., Jin, Y., Li, Z., Deng, T., Su, T., et al. (2025). Photodynamic and photothermal bacteria targeting nanosystems for synergistically combating bacteria and biofilms. *J. Nanobiotechnol.* 23 (1), 40. doi:10.1186/s12951-025-03126-2

Werner, S., Huck, O., Frisch, B., Vautier, D., Elkaim, R., Voegel, J.-C., et al. (2009). The effect of microstructured surfaces and laminin-derived peptide coatings on soft tissue interactions with titanium dental implants. *Biomaterials* 30 (12), 2291–2301. doi:10.1016/j.biomaterials.2009.01.004

Wong, R. L., Hiyari, S., Yaghsezian, A., Davar, M., Casarin, M., Lin, Y. L., et al. (2018). Early intervention of peri-implantitis and periodontitis using a mouse model. *J. Periodontol.* 89 (6), 669–679. doi:10.1002/jper.17-0541

Wu, D., Duan, X., Guan, Q., Liu, J., Yang, X., Zhang, F., et al. (2019a). Mesoporous polydopamine carrying manganese carbonyl responds to tumor microenvironment for multimodal imaging-guided cancer therapy. *Adv. Funct. Mat.* 29 (16), 1900095. doi:10.1002/adfm.201900095

Wu, J., Li, F., Hu, X., Lu, J., Sun, X., Gao, J., et al. (2019b). Responsive assembly of silver nanoclusters with a biofilm locally amplified bactericidal effect to enhance treatments against multi-drug-resistant bacterial infections. *ACS Cent. Sci.* 5 (8), 1366–1376. doi:10.1021/acscentsci.9b00359

Wu, L., Li, B. H., Wang, Y. Y., Wang, C. Y., Zi, H., Weng, H., et al. (2019c). Periodontal disease and risk of benign prostate hyperplasia: a cross-sectional study. *Mil. Med. Res.* 6 (1), 34. doi:10.1186/s40779-019-0223-8

Wu, Y., Zhang, X., Tan, B., Shan, Y., Zhao, X., and Liao, J. (2022). Near-infrared light control of GelMA/PMMA/PDA hydrogel with mild photothermal therapy for skull regeneration. *Biomater. Adv.* 133, 112641. doi:10.1016/j.msec.2022.112641

Wu, X., Qi, M., Liu, C., Yang, Q., Li, S., Shi, F., et al. (2023). Near-infrared light-triggered nitric oxide nanocomposites for photodynamic/photothermal complementary therapy against periodontal biofilm in an animal model. *Theranostics* 13 (7), 2350–2367. doi:10.7150/thno.83745

Wu, H., Li, Y., Shi, L., Liu, Y., and Shen, J. (2025). New advances in periodontal functional materials based on antibacterial, anti-inflammatory, and tissue regeneration strategies. *Adv. Healthc. Mat.* 14, 2403206. doi:10.1002/adhm.202403206

Xiao, J., Fiscella, K. A., and Gill, S. R. (2020). Oral microbiome: possible harbinger for children's health. *Int. J. Oral. Sci.* 12 (1), 12. doi:10.1038/s41368-020-0082-x

Xiao, L., Feng, M., Chen, C., Xiao, Q., Cui, Y., and Zhang, Y. (2024). Microenvironment-regulating drug delivery nanoparticles for treating and preventing typical biofilm-induced oral diseases. *Adv. Mat.* 37, 202304982. doi:10.1002/adma.202304982

Xu, M., Hu, Y., Xiao, Y., Zhang, Y., Sun, K., Wu, T., et al. (2020a). Near-infrared-controlled nanoplatform exploiting photothermal promotion of peroxidase-like and OXD-Like activities for potent antibacterial and anti-biofilm therapies. *ACS Appl. Mater Interfaces* 12 (45), 50260–50274. doi:10.1021/acsami.0c14451

Xu, Y., Zhao, S., Weng, Z., Zhang, W., Wan, X., Cui, T., et al. (2020b). Jelly-inspired injectable guided tissue regeneration strategy with shape auto-matched and dual-light-defined antibacterial/osteogenic pattern switch properties. *ACS Appl. Mat. Interfaces* 12 (49), 54497–54506. doi:10.1021/acsami.0c18070

Xu, H., Ye, Z., Zhang, A., Lin, F., Fu, J., and Fok, A. S. L. (2022a). Effects of concentration of sodium hypochlorite as an endodontic irrigant on the mechanical and structural properties of root dentine: a laboratory study. *Int. Endod. J.* 55 (10), 1091–1102. doi:10.1111/iej.13800

Xu, X., Fan, M., Yu, Z., Zhao, Y., Zhang, H., Wang, J., et al. (2022b). A removable photothermal antibacterial "warm paste" target for cariogenic bacteria. *Chem. Eng. J.* 429, 132491. doi:10.1016/j.cej.2021.132491

Xu, V. W., Yin, I. X., Niu, J. Y., and Chu, C.-H. (2025). Enhancing caries preventive effects of nanomaterials with phototherapy: a scoping review. *J. Func. Biomater.* 16 (9), 308. doi:10.3390/jfb16090308

Xue, Y., Zhang, L., Liu, F., Zhao, Y., Zhou, J., Hou, Y., et al. (2022). Surface bandgap engineering of nanostructured implants for rapid photothermal ion therapy of bone defects. *Adv. Healthc. Mat.* 11 (22), 2200998. doi:10.1002/adhm.202200998

Xue, Y., Zhang, L., Liu, F., Kong, L., Ma, D., and Han, Y. (2023). Fluoride releasing photothermal responsive TiO_2 matrices for antibiosis, biosealing and bone regeneration. *J. Control. Release* 363, 657–669. doi:10.1016/j.jconrel.2023.10.016

Yang, Y., Ma, L., Cheng, C., Deng, Y., Huang, J., Fan, X., et al. (2018). Nonchemotherapic and robust dual-responsive nanoagents with On-Demand bacterial trapping, ablation, and release for efficient wound disinfection. *Adv. Funct. Mat.* 28 (21), 1705708. doi:10.1002/adfm.201705708

Yang, Y., Xu, C., Xu, S., Li, Y., Chen, K. e., Yang, T., et al. (2025). Injectable hydrogels activated with copper sulfide nanoparticles for enhancing spatiotemporal sterilization and osteogenesis in periodontal therapy. *Biomater. Sci.* 13, 1434–1448. doi:10.1039/d3bm02134c

Yao, H., Turali Emre, E. S., Fan, Y., Wang, J., Liu, F., and Wei, J. (2025a). L-arginine modified mesoporous bioactive glass with ROS scavenging and NO release for periodontitis treatment. *Bioact. Mat.* 48, 200–216. doi:10.1016/j.bioactmat.2025.02.015

Yao, W., Wang, T., Sun, W., Zhang, X., Xiong, H., Yin, J., et al. (2025b). Mature biofilm-sensitive lysozyme-grafted Bi-guanidine backbone porphyrin nanorods for deep penetration and double phototherapy. *Biomaterials* 323, 123431. doi:10.1016/j.biomaterials.2025.123431

Yin, L., Ma, H., Nakayasu, E. S., Payne, S. H., Morris, D. R., and Harwood, C. S. (2019). Bacterial longevity requires protein synthesis and a stringent response. *mBio* 10 (5), e02189-19. doi:10.1128/mBio.02189-19

You, J., Li, Y., Wang, C., Lv, H., Zhai, S., Liu, M., et al. (2024). Mild thermotherapy-assisted GelMA/HA/MPDA@Roxadustat 3D-Printed scaffolds with combined angiogenesis-osteogenesis functions for bone regeneration. *Adv. Healthc. Mat.* 13 (22), 2400545. doi:10.1002/adhm.202400545

Yu, Y., Zhang, Y., Cheng, Y., Wang, Y., Chen, Z., Sun, H., et al. (2022). NIR-Activated nanosystems with self-modulated bacteria targeting for enhanced biofilm eradication and caries prevention. *Bioact. Mat.* 13, 269–285. doi:10.1016/j.bioactmat.2021.10.035

Yu, S., Xia, G., Yang, N., Yuan, L., Li, J., Wang, Q., et al. (2024a). Noble metal nanoparticle-based photothermal therapy: development and application in effective cancer therapy. *Int. J. Mol. Sci.* 25 (11), 5632. doi:10.3390/ijms25115632

Yu, Y. M., Lu, Y. P., Zhang, T., Zheng, Y. F., Liu, Y. S., and Xia, D. D. (2024b). Biomaterials science and surface engineering strategies for dental peri-implantitis management. *Mil. Med. Res.* 11 (1), 29. doi:10.1186/s40779-024-00532-9

Yuan, Z., Lin, C., He, Y., Tao, B., Chen, M., Zhang, J., et al. (2020). Near-infrared light-triggered nitric-oxide-enhanced photodynamic therapy and low-temperature photothermal therapy for biofilm elimination. *ACS Nano* 14 (3), 3546–3562. doi:10.1021/acsnano.9b09871

Zeng, J., Sun, Z., Zeng, F., Gu, C., and Chen, X. (2023). M2 macrophage-derived exosome-encapsulated microneedles with mild photothermal therapy for accelerated diabetic wound healing. *Mat. Today Bio* 20, 100649. doi:10.1016/j.mtbio.2023.100649

Zhang, C., and Chen, X. (2025). Photothermal-therapy-based targeting thrombolytic therapy. *ACS Appl. Bio Mat.* 8 (3), 1820–1834. doi:10.1021/acsabm.4c01820

Zhang, X., Cheng, G., Xing, X., Liu, J., Cheng, Y., Ye, T., et al. (2019). Near-infrared light-triggered porous AuPd alloy nanoparticles to produce mild localized heat to accelerate bone regeneration. *J. Phys. Chem. Lett.* 10 (15), 4185–4191. doi:10.1021/acs.jpclett.9b01735

Zhang, L., Wang, Y., Wang, C., He, M., Wan, J., Wei, Y., et al. (2020). Light-activable On-Demand release of nano-antibiotic platforms for precise synergy of thermochemotherapy on periodontitis. *ACS Appl. Mat. Interfaces* 12 (3), 3354–3362. doi:10.1021/acsami.9b17335

Zhang, X., Tan, B., Wu, Y., Zhang, M., and Liao, J. (2021). A review on hydrogels with photothermal effect in wound healing and bone tissue engineering. *Polymers* 13 (13), 2100. doi:10.3390/polym13132100

Zhang, B., Zheng, R., Liu, Y., Lou, X., Zhang, W., Cui, Z., et al. (2023). Perylene-mediated electron leakage in respiratory chain to trigger endogenous ROS burst for hypoxic cancer chemo-immunotherapy. *Adv. Sci.* 10 (3), e2204498. doi:10.1002/advs.202204498

Zhang, J., Tong, Z., Chen, L., Qian, Y., Lu, Y., Chen, Q., et al. (2024a). Development and applications of peri-implantitis mouse models. *Oral Dis.* 30 (6), 3788–3798. doi:10.1111/odi.14929

Zhang, S., Kong, N., Wang, Z., Zhang, Y., Ni, C., Li, L., et al. (2024b). Nanochemistry of gold: from surface engineering to dental healthcare applications. *Chem. Soc. Rev.* 53 (8), 3656–3686. doi:10.1039/d3cs00894k

Zhang, Y., Jiang, Z.-T., Wang, Y., Wang, H.-Y., Hong, S., Li, W., et al. (2024c). A supramolecular nanoformulation with adaptive photothermal/photodynamic transformation for preventing dental caries. *ACS Nano* 18 (40), 27340–27357. doi:10.1021/acsnano.4c06051

Zhang, H., Yang, M., Wu, Q., Xue, J., and Liu, H. (2025). Engineering two-dimensional nanomaterials for photothermal therapy. *Angew. Chem.-Int. Ed.* 64 (12), e202424768. doi:10.1002/anie.202424768

Zhao, J., Long, X., and Zhou, M. (2021). "Clearable nanoparticles for cancer photothermal therapy," in *Bio-nanomedicine for cancer therapy* (Cham: Springer International Publishing), 121–134.

Zhao, L., Zhu, H., Duo, Y. Y., Wang, Z. G., Pang, D. W., and Liu, S. L. (2024). A cyanine with 83.2% photothermal conversion efficiency and absorption wavelengths over 1200 nm for photothermal therapy. *Adv. Healthc. Mat.* 13 (20), 2304421. doi:10.1002/adhm.202304421

Zheng, P., Qiu, X., Zhang, L., Liu, P., Peng, Z., and Huang, Z. (2025). Comparative analysis of oral disorder burden in China and globally from 1990 to 2021 based on GBD data. *Sci. Rep.* 15 (1), 10061. doi:10.1038/s41598-025-94899-x

Zhou, B., Dong, B., Hu, S., Liu, W., Sun, L., Xu, L., et al. (2024). NIR-triggered multifunctional NO nanoplatform for conquering thermal resistance in biofilms. *Small* 20 (31), e2310706. doi:10.1002/smll.202310706

Zhu, Y., Ramasamy, M., and Yi, D. K. (2014). Antibacterial activity of ordered gold nanorod arrays. *ACS Appl. Mat. Interfaces* 6 (17), 15078–15085. doi:10.1021/am503153v

Zhu, T., Huang, Z., Shu, X., Zhang, C., Dong, Z., and Peng, Q. (2022). Functional nanomaterials and their potentials in antibacterial treatment of dental caries. *Colloid Surf. B-Biointerfaces* 218, 112761. doi:10.1016/j.colsurfb.2022.112761

Glossary

3D	Three-dimensional
Alg	Sodium alginate
ATP	Adenosine triphosphate
ATRP	Atom transfer radical polymerization
AuNPs	Gold nanoparticles
AuNRs	Gold nanorods
BA	Baicalein
BMP-2	Bone morphogenetic protein-2
BMSCs	Bone marrow-derived mesenchymal stromal cells
BP	Black phosphorus
C. albicans	*Candida albicans*
CDT	Chemical dynamic therapy
DDS	Drug delivery systems
E. coli	*Escherichia coli*
E. faecalis	*Enterococcus faecalis*
eNOS	Endothelial nitric oxide synthase
EPL	Epsilon-polylysine
EPS	Extracellular polymeric substances
F. nucleatum	*Fusobacterium nucleatum*
GelMA	Gelatin methacrylate
GNC	Gold nanocages
GO	Graphene oxide
HE	Hematoxylin-Eosin
HGFs	Human gingival fibroblasts
HSP90	Heat shock protein 90
IBD	Infectious bone defects
ICG	Indocyanine green
MgMps	Mg microparticles
MPB	Mesoporous Prussian blue
MPN	Metal-phenolic networks
mPTT	Mild photothermal therapy
MRSA	Methicillin-resistant *Staphylococcus aureus*
MSC	Mesenchymal stem cell
NIR	Near-infrared
NIR-I	Near-infrared region I
NIR-II	Near-infrared region II
NO	Nitric oxide
NPs	Nanoparticles
NSs	Nanosheets
P. gingivalis	*Porphyromonas gingivalis*
PB	Prussian blue
PC	Proanthocyanidins
PCE	Photothermal conversion efficiency
PCM	Phase-change materials
PDA	Polydopamine
PDT	Photodynamic therapy
PEG	Polyethylene glycol
PLGA	Poly lactic acid-co-glycolic acid
PLLA	Polylactic acid
POD	Photothermal and peroxidase
PTAs	Photothermal agents
PTT	Photothermal therapy
rGO	Reduced graphene oxide
RCT	Root canal therapy
RNS	Reactive nitrogen species
ROS	Reactive oxygen species
S. aureus	*Staphylococcus aureus*
S. gordonii	*Streptococcus gordonii*
S. mutans	*Streptococcus mutans*
S. oralis	*Streptococcus oralis*
S. sanguinis	*Streptococcus sanguinis*
S. sobrinus	*Streptococcus sobrinus*
SDT	Sonodynamic Therapy
SEM	Scanning electron microscopy
SNP	Sodium nitroprusside
SRP	Scaling and root planning
TC	Tetracycline
TRAP	Tartrate-resistant acid phosphatase
UBI	Ubiquicidine
VEGF	Vascular endothelial growth factor

frontiers | Frontiers in Bioengineering and Biotechnology

TYPE Original Research
PUBLISHED 16 January 2026
DOI 10.3389/fbioe.2025.1636262

OPEN ACCESS

EDITED BY
Jun Liao,
University of Texas at Arlington, United States

REVIEWED BY
Jiahui Li,
University of Pennsylvania, United States
Gizem Boztaş Demir,
University of Health Sciences Diyarbakır Gazi Yaşargil Education and Research Hospital, Türkiye

*CORRESPONDENCE
Dan Lin,
lind@sumhs.edu.cn
Xiaoqing Ma,
mxq780927@163.com

RECEIVED 27 May 2025
REVISED 30 September 2025
ACCEPTED 21 October 2025
PUBLISHED 16 January 2026

CITATION
Zeng G, Ma X and Lin D (2026) Finite element analysis of clear aligner with overhanging attachments and extended gingival coverage for interdental space closure .
Front. Bioeng. Biotechnol. 13:1636262.
doi: 10.3389/fbioe.2025.1636262

Finite element analysis of clear aligner with overhanging attachments and extended gingival coverage for interdental space closure

Guojin Zeng[1,2,3], Xiaoqing Ma[4]* and Dan Lin[1,2]*

[1]Shanghai University of Medicine and Health Sciences Affiliated Zhoupu Hospital, Shanghai, China, [2]Intelligent inspection and diagnostics health service platform, Shanghai University of Medicine and Health Sciences, Shanghai, China, [3]School of Stomatology, Xuzhou Medical University, Xuzhou, China, [4]Department of Orthodontics, Shanghai Xuhui District Stomatological Hospital, Shanghai, China

Objective: Overhanging (OH) attachments were modified clear aligner (CA) attachments with an extended portion toward the root to apply force closer to the center of resistance and enable greater control over root movement, resembling power arms. This study investigated the biomechanical effects of OH attachment and partially gingival extension of CA trimline on canine movement during the closure of extraction space via finite element analysis (FEA).
Methods: CBCT data of an adult with Angle Class I molar relationship and mild anterior crowding was applied for comparing the biomechanical effects of three attachment types (no attachment, vertical, OH) and four trimline designs (partially buccal/lingual gingival coverage). Periodontal ligament (PDL) hydrostatic stress, tooth displacement, rotational center position, and CA stress distribution were assessed via FEA.
Results: OH attachment induced increased tooth displacement and PDL hydrostatic stress (95.5 kPa) compared to regular vertical attachment (53.1 kPa) in achieving root-controlled canine movement. OH attachment combined with a buccolingual gingival extension of CA trimline on 2–6 facilitated the most translational canine movement and lowest ratio of mesio-apical to disto-occlusal displacement (0.466, compared to 0.506 in group with no attachment and trimline extension), while simultaneously avoiding excessive aligner deformation and stress concentration.
Conclusion: Overhanging attachment combined with partial gingival extension of CA trimline significantly enhanced the orthodontic force for premolar extraction cases involving space closure between canines and molars, as a more efficient and feasible design for canine bodily movement.

KEYWORDS

clear aligners, finite element analysis, overhanging attachment, bodily movement, interdental space closure

1 Introduction

Clear aligners (CA) had been increasingly being utilized in orthodontics owing to their comfort, aesthetic appeal, and ease of cleaning (Weir, 2017). Despite their popularity, challenges still remained in managing intricate tooth movements, including torque (Cheng et al., 2022a), rotation (Seo et al., 2021), and bodily movement (Zhu et al., 2022). Specifically,

during the closure of extraction spaces, torque controlling was critical to the translation of tooth and prevention of undesired tipping and rotation (Cheng et al., 2022a; Seo et al., 2021; Zhu et al., 2022).

The application of attachments was a common approach to facilitate more effective control of tooth movement (Je et al., 2023; Demir, 2024). In CA orthodontics, the standard design for closing extraction spaces involved placing attachments on canines (3) and posterior teeth (5/6/7) (Cheng et al., 2022a; Jiang et al., 2020; Liu et al., 2021; Liu L. et al., 2022; Liu J. Q. et al., 2022; Cheng et al., 2022b; Wang et al., 2022) and other auxiliaries, such as traction (Pu

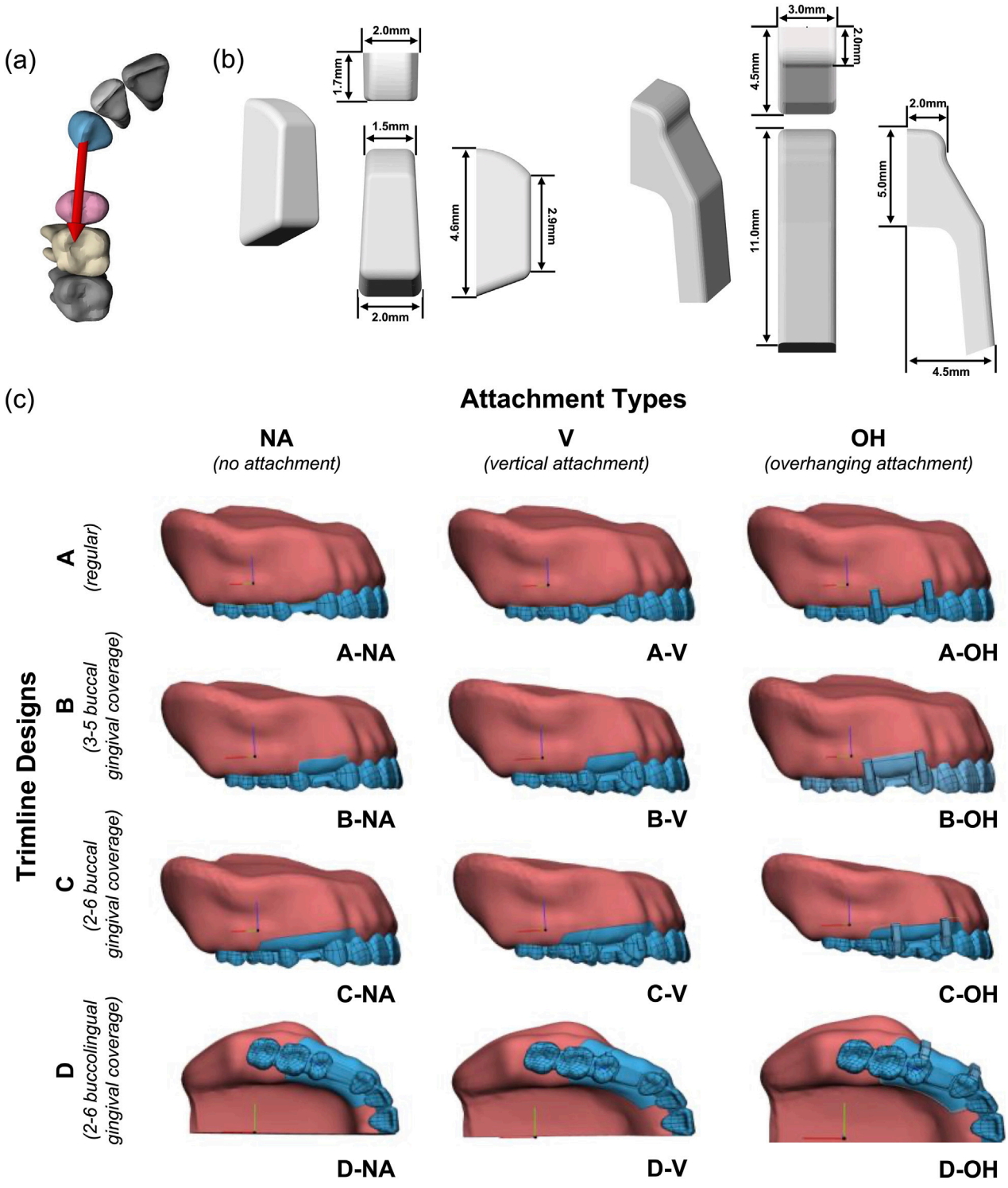

FIGURE 1
Design of CAs and attachments in Closing Extraction Spaces. **(a)** Designed tooth movement: distal movement of canines by 0.2 mm. **(b)** Shapes and dimensions of vertical attachment and OH attachment. **(c)** 12 groups of models for FEA comprising 3 attachment types and 4 CA trimline designs.

TABLE 1 12 groups of models for FEA in this study, comprising 3 attachment types and 4 CA trimline designs.

Group	Trimline designs	Attachment types
A-NA	regular CA with unextended scalloped trimline	no attachment
A-V	regular CA with unextended scalloped trimline	vertical wedge-shaped
A-OH	regular CA with unextended scalloped trimline	overhanging
B-NA	CA with scalloped trimline and 5 mm buccal extension at teeth 3~5	no attachment
B-V	CA with scalloped trimline and 5 mm buccal extension at teeth 3~5	vertical wedge-shaped
B-OH	CA with scalloped trimline and 5 mm buccal extension at teeth 3~5	overhanging
C-NA	CA with scalloped trimline and 5 mm buccal extension at teeth 2~6	no attachment
C-V	CA with scalloped trimline and 5 mm buccal extension at teeth 2~6	vertical wedge-shaped
C-OH	CA with scalloped trimline and 5 mm buccal extension at teeth 2~6	overhanging
D-NA	CA with scalloped trimline and 5 mm buccolingual extension at teeth 2~6	no attachment
D-V	CA with scalloped trimline and 5 mm buccolingual extension at teeth 2~6	vertical wedge-shaped
D-OH	CA with scalloped trimline and 5 mm buccolingual extension at teeth 2~6	overhanging

TABLE 2 Mechanical parameters (elastic modulus and Poisson's ratio) of the materials.

Material name	CA	Attachment	Gingiva	Cancellous bone	Cortical bone
Elastic Modulus/GPa	1250	1250	2.8	1370	13700
Poisson's Ratio	0.36	0.36	0.4	0.3	0.3

TABLE 3 Element types, sizes, counts, and node counts for the models. Element sizes were determined via the convergence experiment to ensure a sufficiently refined mesh for the simulation.

Component	Element type	Element size (mm)	Element count	Node count
Gingiva	C3D10H	0.2	184849	299435
PDL	C3D10H	0.2	94166	189790
Tooth	R3D3	0.2~0.8	37957	19019
Cancellous Bone	C3D10	0.2~2	169990	266400
Cortical Bone	C3D10	0.2~2	109100	185611
Attachment	C3D10M	0.2	5783	10225
CA	S4R	0.2	37777	37535

et al., 2022) and power ridges (Hong et al., 2024). These designs adjusted torque and balanced stress to precisely optimize tooth movement (Liu J. Q. et al., 2022; Wang et al., 2022; Xia et al., 2022). Root control attachments were also designed to modulate torque, including asymmetrical attachments with opposite orientations (Gomez et al., 2015; Yokoi et al., 2019) and overhanging attachments (Hong et al., 2021). An overhanging (OH) attachment was a modified CA attachment with an extended portion toward the root to apply force closer to the center of resistance and enable greater control over root movement, resembling a power arm (Hong et al., 2021). First reported in 2021 (Hong et al., 2021), an OH attachment was designed to induce bodily movement of the incisor and close scattered diastema of anterior teeth. A latest study in 2025 (Hong et al., 2025) reported the repair of gingival recession via better controlling

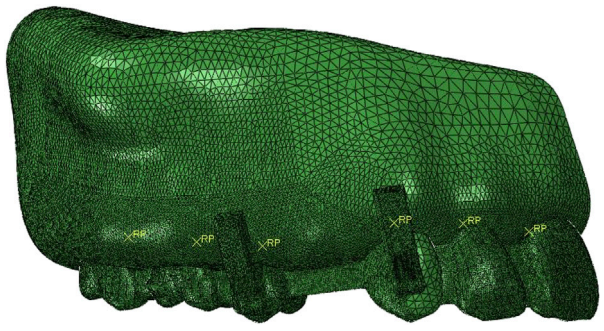

FIGURE 2
Meshed finite element model (A-OH group used as an example).

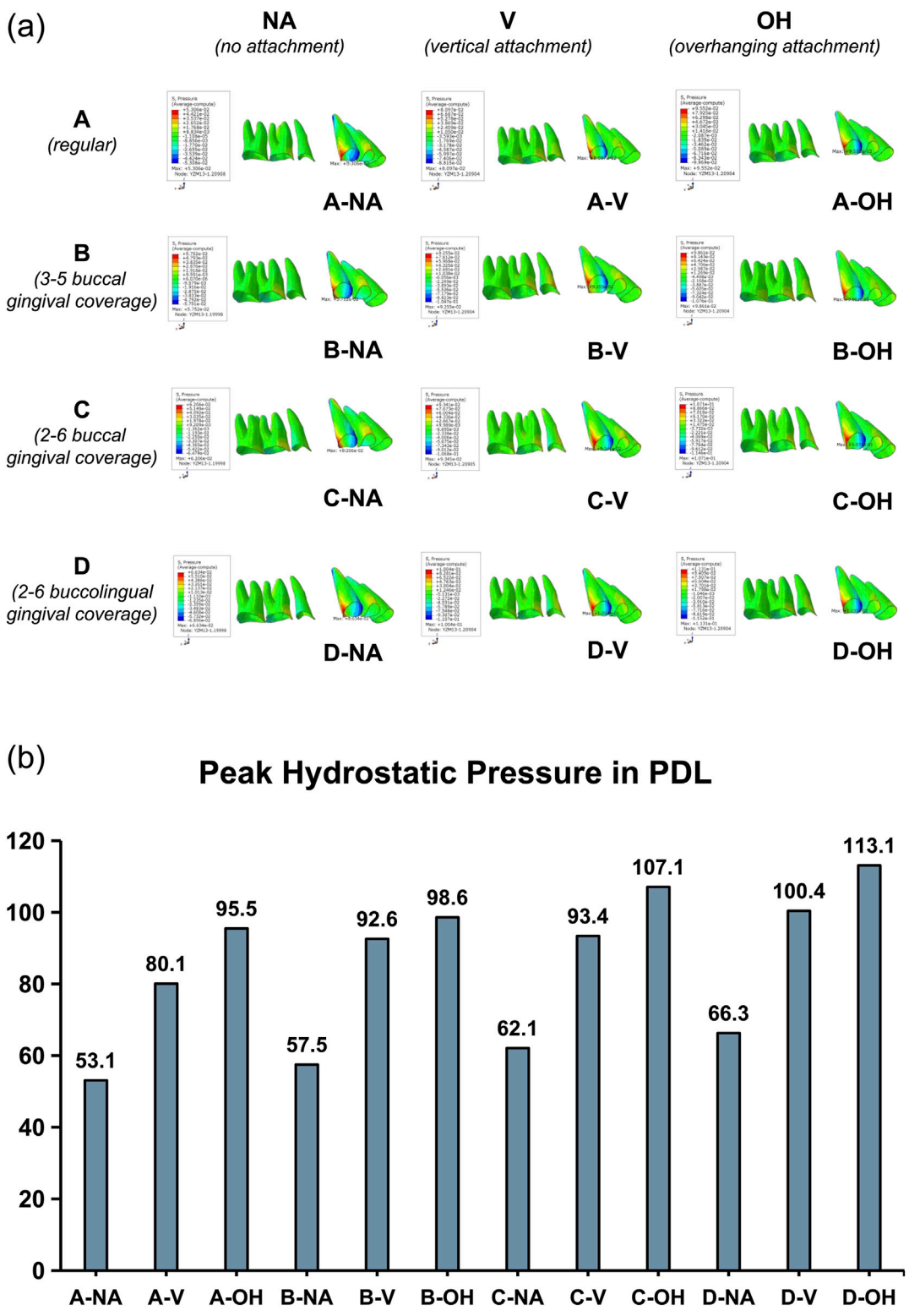

FIGURE 3
Hydrostatic pressure in PDL. **(a)** Heatmap of hydrostatic pressure in PDL, indicating compression (+) at disto-cervical and mesio-apical areas, and tension (–) at disto-apical and mesio-cervical areas. **(b)** Peak hydrostatic pressure in PDL of canine (unit: kPa). CA with 2–6 buccolingual gingival extensions and OH attachments exhibited the highest hydrostatic pressure in PDL.

TABLE 4 Maximum and mean compressive (+) and tensile (–) stress in PDL of canine (unit: kPa).

Group	Location	Maximum		Mean	
		Mesial	Distal	Mesial	Distal
A-NA	Cervical	−52.0	53.1	−39.5	41.9
	Apical	53.0	−53.1	63.3	−41.1
A-V	Cervical	−88.2	81.0	−71.1	66.6
	Apical	73.3	−79.8	63.3	−70.1
A-OH	Cervical	−99.7	95.5	−83.3	78.0
	Apical	81.0	−88.0	65.5	−74.5
B-NA	Cervical	−57.5	57.5	−46.8	43.8
	Apical	56.2	−57.2	46.6	−47.6
B-V	Cervical	−104.7	92.6	−84.1	79.8
	Apical	79.8	−89.7	65.7	−73.6
B-OH	Cervical	−107.6	98.6	−87.3	84.5
	Apical	78.5	−90.6	67.3	−72.3
C-NA	Cervical	−62.1	64.8	−54.4	51.6
	Apical	60.8	−63.8	50.5	−51.7
C-V	Cervical	−106.8	93.4	−84.9	80.2
	Apical	79.2	−91.6	63.9	−73.9
C-OH	Cervical	−114.6	107.1	−96.2	89.5
	Apical	83.1	−96.0	71.0	−78.5
D-NA	Cervical	−68.6	66.3	−54.4	53.0
	Apical	61.0	−64.9	50.7	−51.2
D-V	Cervical	−110.7	100.4	−90.6	92.5
	Apical	83.6	−95.5	71.1	−79.2
D-OH	Cervical	−115.2	113.1	−96.9	95.3
	Apical	86.0	−91.2	72.8	−76.4

root movement of lower incisor using an OH attachment. So far, there had been limited researches on OH attachments and their application in other tooth positions.

The apical extension of OH attachment necessitated the gingival extension of CA for full coverage. Extension of the trimming edges of CA had been reported to enhance control over tooth movement and improve therapeutic outcomes (Elshazly et al., 2023; Elshazly et al., 2022; Elshazly et al., 2024a; Elshazly et al., 2024b), as summarized in a recently published systematic review (Nakornnoi et al., 2024). However, despite of the widely acknowledged advantages of extended trimline, the remodeling of gingival soft tissues did not synchronize with tooth movement, and a full gingiva-covering trimline design compromised the aesthetics and comfort of CA. As a result, such trimline extensions have not gained widespread popularity in clinical practice. Reducing the gingival coverage from full to partial might avoid compromising the aesthetics and comfort of CAs, but whether equivalent effectiveness could be achieved remained unknown. Existing studies had focused on integral extension of CA trimline, with a lack of comparative research on the effects of region-specific extension of CA. Furthermore, the combined effects and biomechanical behavior of OH attachments with gingival extension of CA in closing extraction spaces remained to be explored.

In this study, finite element analysis (FEA) was employed to explore the biomechanical effects of different attachment designs (vertical/OH) combined with different gingival extension designs (buccal/lingual covering different regions) during closing extraction spaces. The effects on tooth movement, PDL stress distribution, and appliance deformation were systematically analyzed and compared to improve the effectiveness of CA and minimize adverse effects during closing extraction spaces. This study could provide guidance for future design of CA to improve the orthodontic effectiveness.

2 Materials and methods

2.1 Acquisition of dentition

The use of patient imaging data in this research was in accordance with institutional ethical standards, following informed consent and approval by the Ethical Committee of the Shanghai Xuhui District Dental Center, Shanghai, China. CBCT data of a healthy adult's dentition (with ANB angle of 4.8°, average growth pattern, Angle Class I molar relationship, and mild anterior crowding) with a slice thickness of 0.625 mm (GE Healthcare, Buckinghamshire, England) was imported into Mimics software (Version 18.0, Materialise, Leuven, Belgium) for 3 days reconstruction.

2.2 Design of CAs and attachments

As illustrated in Figure 1a, CA with a thickness of 0.5 mm was designed on the reconstructed dentition model with the distal movement of canines (3) by 0.2 mm to provide orthodontic force. Attachments were adhered in the middle of the buccal surfaces of canines (3) and second premolars (5), and the attachment designs were categorized into 3 types: vertical wedge-shaped attachment (V), overhanging attachment (OH), and no attachment (NA). As shown in Figure 1b, vertical wedge-shaped attachments were designed with the wedge surface oriented towards the occlusal direction; OH attachments were designed with 6 mm extension towards gingiva.

CA trimline designs were divided into 4 types: (A) regular CA with unextended scalloped trimline; (B) CA with scalloped trimline and 5 mm buccal extension for gingival coverage at teeth 3~5; (C) CA with scalloped trimline and 5 mm buccal extension for gingival coverage at teeth 2~6; (D) CA with scalloped trimline and 5 mm buccolingual extension for gingival coverage at teeth 2~6.

In total, 12 groups of models comprising 3 attachment types and 4 CA trimline designs were created and analyzed in this study, as shown in Table 1 and Figure 1c.

2.3 Preprocessing of 3D reconstructed models

The reconstructed maxilla and dentition were then imported into 3-Matic Medical software (Version 9.0, Materialise, Leuven,

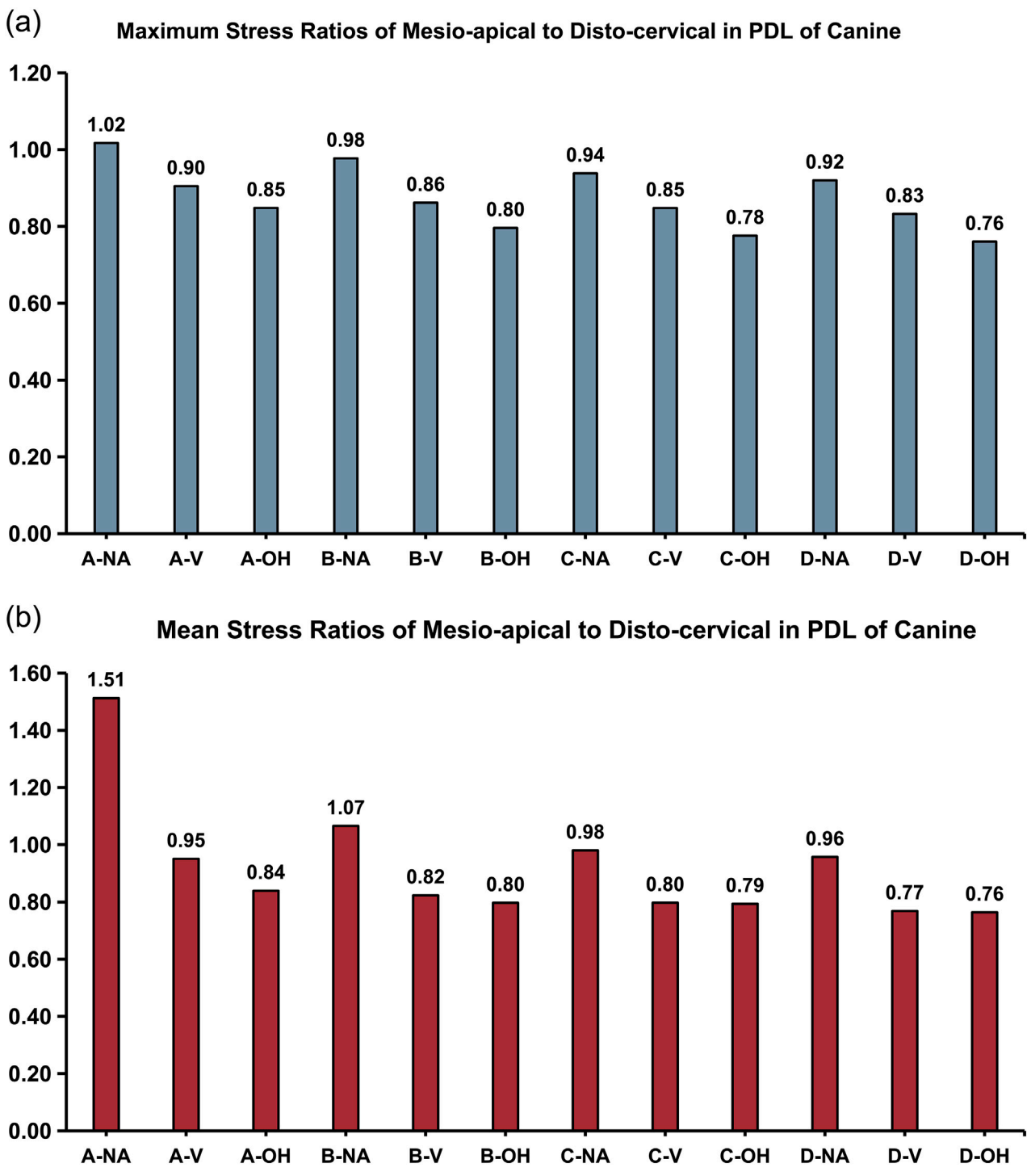

FIGURE 4
The ratios of mesio-apical to disto-cervical stress in PDL of canine, calculated using **(a)** maximum or **(b)** mean value. The closer the ratio was to zero, the closer the movement was to distal translation.

Belgium) for further processing. Both first premolars (4) were removed to simulate subtractive tooth extraction. Alveolar bone was divided into cortical bone and cancellous bone, with 2 mm thickness of cortical bone. The alveolar bone was expanded outward by 2 mm to simulate the gingiva, and the space between the teeth and alveolar bone was expanded by 0.2 mm to simulate the PDL, according to typical parameters in existing orthodontic FEA studies (Canales et al., 2013; Cao et al., 2023; Çifter and Saraç, 2011).

3D reconstructed models of maxilla, dentition, gingiva, PDL, CA, and attachment in STL format were imported into the Geomagic software (3D-SYSTEM, United States) for surface smoothing, eliminating any potential geometric imperfections and noise. Subsequently, the output file was exported as IGES

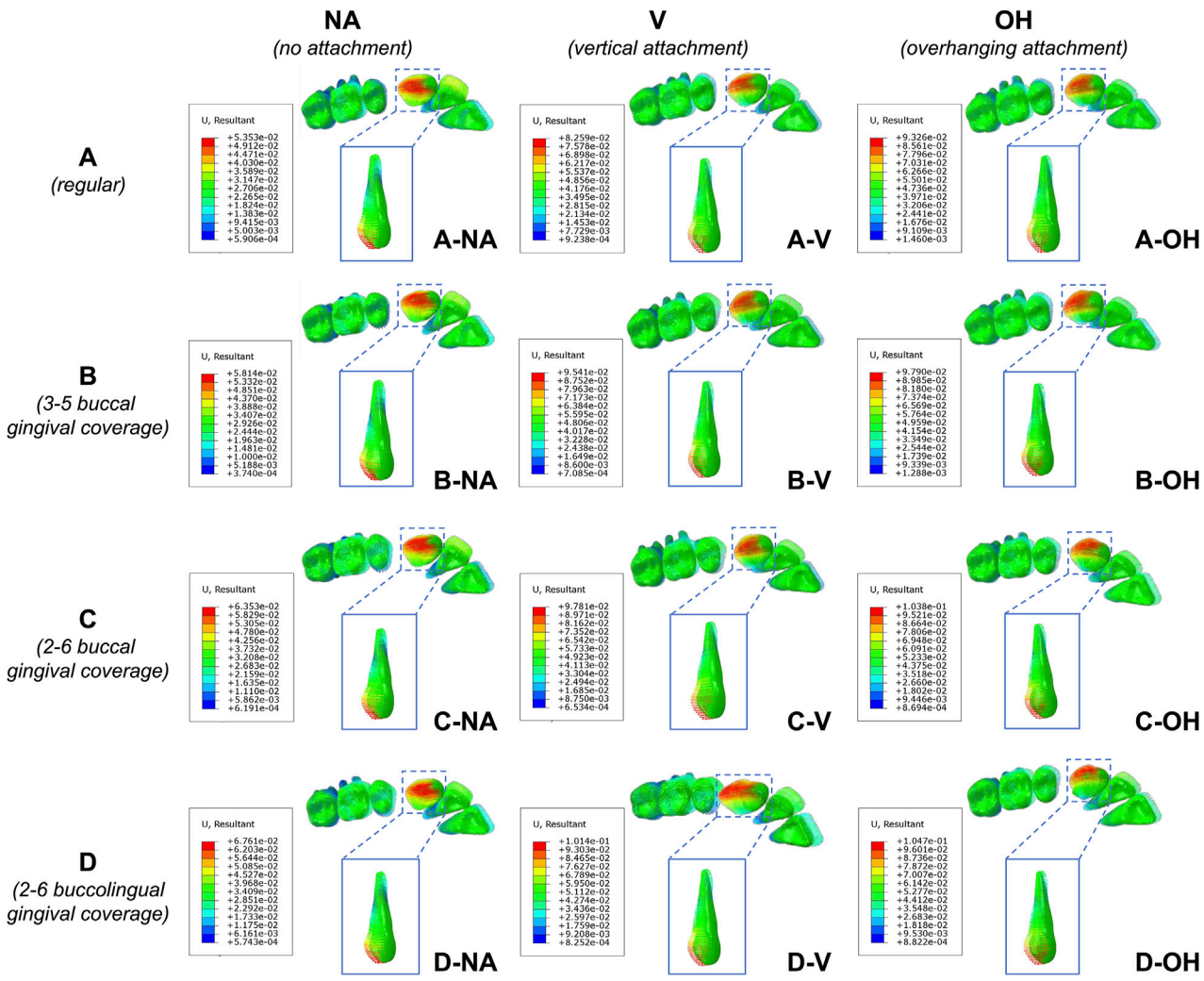

FIGURE 5
Heatmap of tooth displacement in vector diagram. Maximum values on heatmap scale revealed a trend consistent with hydrostatic pressure in PDL: OH > V > NA and D > C > B > A. **(A)** Regular CA; **(B)** CA with buccal gingival coverage from 3 to 5; **(C)** CA with buccal gingival coverage from 2 to 6; **(D)** CA with buccolingual gingival coverage from 2 to 6.

format and imported into Hypermesh software (Altair, United States) for preprocessing, including geometry repair, component organization, convergence experiment and shell meshing, material parameter setting, contact definition, and the application of boundary conditions. A symmetric dentition model with respect to the sagittal plane was adopted for analysis, with results ultimately presented as unilateral dentition.

2.4 Material properties

The material parameters used in this study were obtained from material suppliers and literature (Seo et al., 2021; Canales et al., 2013; Sarrafpour et al., 2013), as detailed in Table 2. PDL was modeled using a visco-hyperelastic-damage constitutive model (Wu et al., 2022; Natali et al., 2008). To reduce computational complexity while maintaining accuracy, the teeth were modeled as rigid bodies, as prior studies have demonstrated that the difference in predicted displacement between rigid-body and fully elastic models was less than 3%, and that tooth deformation under orthodontic forces was negligible compared to overall movement (Tamaya et al., 2021; Hamanaka et al., 2017; Kim et al., 2025).

2.5 Loading and boundary conditions

The interaction between CA and teeth was achieved via an interference fit, applying normal hard contact and tangential frictional sliding conditions, and a friction coefficient of 0.2. Tie constraints were applied between PDL and teeth, the outer layer of PDL and alveolar bone, alveolar bone and gingiva, teeth and gingiva (Natali et al., 2008; Hahn et al., 2009; Ortún-Terrazas et al., 2020; Huang et al., 2023; Goktas et al., 2011). The symmetrical model with respect to the sagittal plane was subjected to symmetrical displacement constraints.

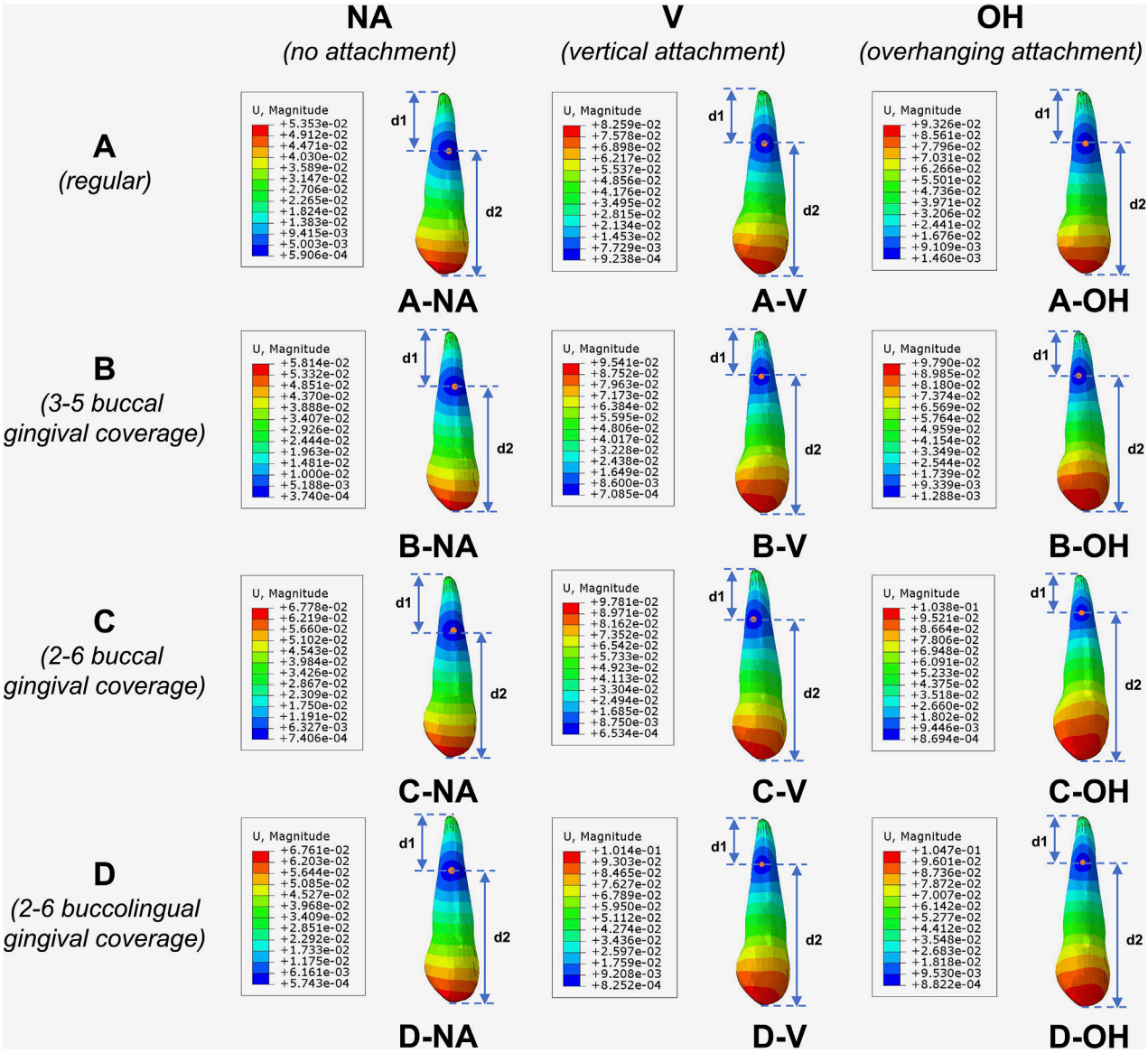

FIGURE 6
Heatmap of tooth displacement with contour. Point of minimum displacement (center of blue region) represented the center of rotation. **(A)** Regular CA; **(B)** CA with buccal gingival coverage from 3 to 5; **(C)** CA with buccal gingival coverage from 2 to 6; **(D)** CA with buccolingual gingival coverage from 2 to 6.

2.6 Construction of 3D finite element model

The general FEA software ABAQUS (DASSAULT, France) was employed as the solver and processor to perform a detailed biomechanical analysis. Element sizes of the models were determined via the convergence experiment to ensure a sufficiently refined mesh for the simulation, and the applied element types, sizes and counts, and node counts were listed in Table 3. As shown in Table 3 and Figure 2, CAs were simulated using S4R shell elements and an element size of 0.2 mm. Attachments were simulated using C3D10M elements with a size of 0.2 mm. Gingiva and PDL were modeled using C3D10H elements with a size of 0.2 mm. For alveolar bone, C3D10 elements were applied, with element sizes of 0.2 mm in regions sharing nodes with gingiva and PDL (Seo et al., 2021; AlKahlan et al., 2025), and gradual transition of element sizes to 2 mm at other regions. Dentition was simulated using R3D3 elements with a size of 0.2 mm in regions sharing nodes with PDL, and gradual transition of element sizes to 0.8 mm at other regions.

3 Results and discussions

3.1 Hydrostatic pressure in PDL

The hydrostatic pressure exerted on the PDL served as an indicator of its tensile and compressive states. Exposure to tensile or compressive stress activated the internal vascular and neural elements of the PDL under their stress conditions, thereby triggering a series of biochemical reactions and activating osteoclasts and

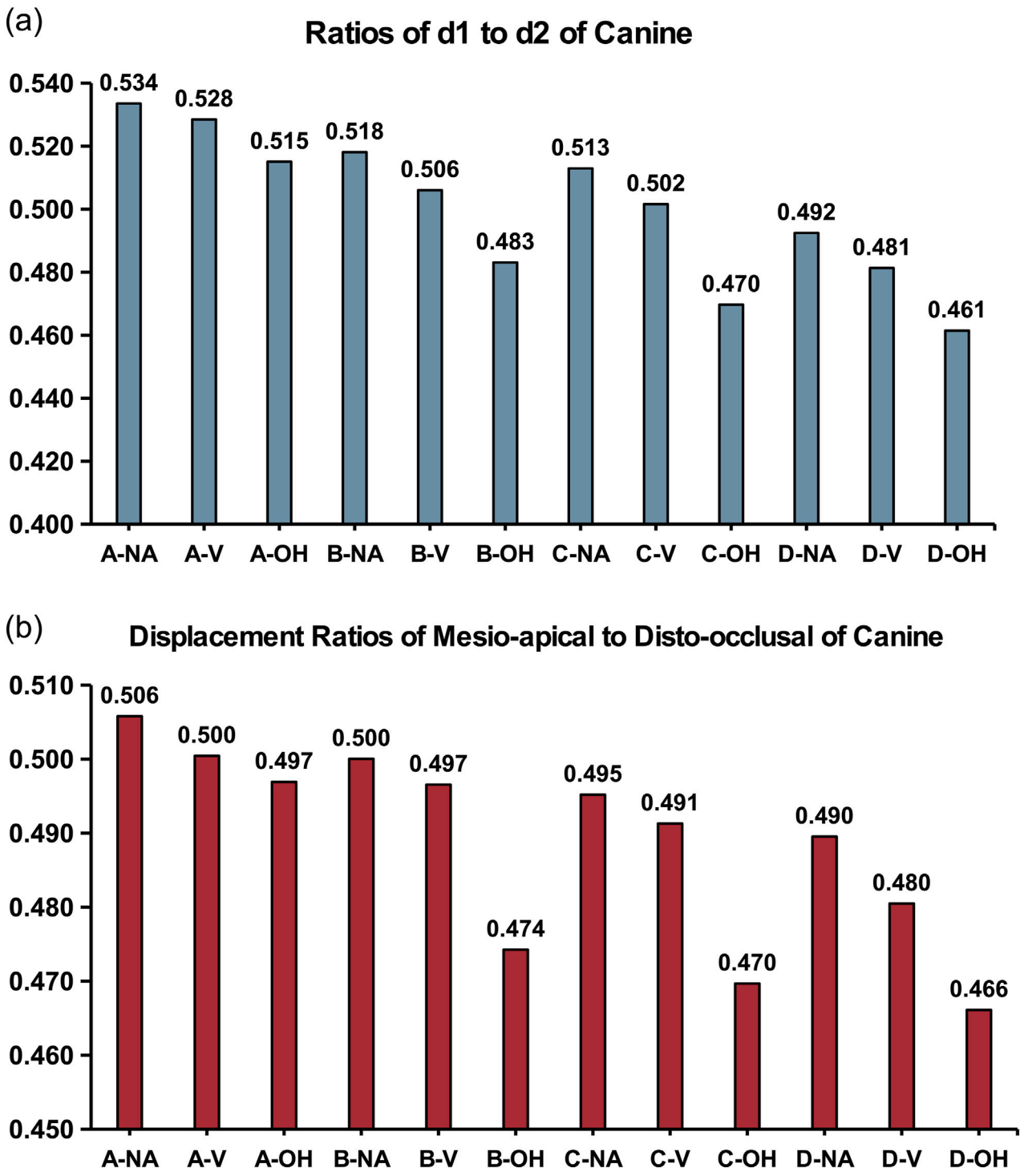

FIGURE 7
Degree of root control during canine movement. Ratios of **(a)** *d1/d2* and **(b)** mesio-apical to disto-occlusal displacement of canine. The smaller the ratios, the closer the tooth movement was to distal translation.

osteoblasts, which led to bone remodeling at the interface between the PDL and the alveolar bone. Typically, bone resorption occurred on the compression side, while bone formation took place on the tension side (Sarrafpour et al., 2013; Li et al., 2021).

As illustrated in the Figure 3a, it was evident that during the root control movement of canine (3) following the extraction of first premolar (4), the disto-cervical and mesio-apical areas of PDL near were subjected to compression (+), whereas the disto-apical and mesio-cervical areas were tension (−). The maximum and mean stress values for these regions were presented in Table 4. The comparison of the maximum hydrostatic pressure in the PDL was shown in Figure 3b. Under the same

TABLE 5 Mesio-apical and disto-occlusal displacement of canine (unit: mm).

Group	Mesio-apical displacement	Disto-occlusal displacement
A-NA	0.0532	0.0269
A-V	0.0709	0.0355
A-OH	0.0742	0.0369
B-NA	0.0561	0.0281
B-V	0.0784	0.0389
B-OH	0.0806	0.0382
C-NA	0.0620	0.0307
C-V	0.0796	0.0391
C-OH	0.0806	0.0378
D-NA	0.0639	0.0313
D-V	0.0835	0.0401
D-OH	0.0807	0.0376

CA trimline design condition, the peak hydrostatic pressure in the PDL progressively increased from the no-attachment (NA) group, to the regular vertical attachment (V) group, and further to the overhanging attachment (OH) group, with the OH group exhibiting the highest pressure. Similarly, under the same attachment design condition, the peak hydrostatic pressure also increased sequentially from the conventional CA trimline (A), to the 3~5 buccal extension (B), to the 2~6 buccal extension (C), and to the 2~6 buccolingual extension (D), with the D group presenting the maximum pressure. The application of regular attachments or OH attachments, as well as the buccal or lingual extended coverage of the CA, all enhanced the orthodontic force, thereby increasing the stress values in PDL. In all, the CA with 2~6 buccolingual gingival extensions and OH attachments exhibited the highest hydrostatic pressure in PDL.

The ratio of mesio-apical to disto-cervical stress of PDL reflected the tipping extent of the tooth (Bi and Shi, 2023). In an ideal situation when the canine moved distally and translationally, both mesio-cervical and mesio-apical hydrostatic stress were tensile (with negative value or zero), and both disto-cervical and disto -apical hydrostatic stress were compressive (with positive value or zero), resulting in a zero or negative value of the ratio of mesio-apical to disto-cervical stress. Therefore, the closer the ratio of mesio-apical to disto-cervical stress was to zero or negative value, the closer the tooth movement was to distal translation. In this study, the ratios of mesio-apical to disto-cervical stress in PDL of canine in different groups were shown in Figure 4, calculated with maximum stress value (Figure 4a) or mean value (Figure 4b). With the same CA trimline design, the ratios progressively decreased from no-attachment (NA) group, to regular vertical attachment (V) group, and further to OH attachment group, with the OH group exhibiting the lowest ratio, indicating OH attachment was the most effective for achieving bodily tooth movement among the three attachment designs. Similarly, with the same attachment design, the ratios decreased sequentially from the conventional CA trimline (A), to the 3~5 buccal extension (B), to the 2~6 buccal extension (C), and to the 2~6 buccolingual extension (D), with the D group presenting the minimum ratio. It could be concluded that the CA with 2~6 buccolingual gingival extensions and OH attachments represented the optimal configuration for facilitating translational canine movement.

3.2 Tooth displacement

Figure 5 presented the heatmap of tooth movement in vector diagram. In all groups, distal inclination of canine was observed, accompanied with labial tipping of incisors and mesial inclination of molars, as an outcome of normal anchorage effect. As evidenced by the upper limits of the heatmap scale, the trend in tooth displacement aligned with the prior findings for PDL hydrostatic pressure, following the pattern OH > V > NA and D > C > B > A.

Figure 6 presented the heatmap of tooth movement with contour, where the point of minimum displacement (the center of blue region) represented the center of rotation of canine (Seo et al., 2021). Distances from root apex and tooth cusp to the rotational center were respectively designated as *d1* and *d2*. The smaller the ratio of *d1/d2*, the closer the rotational center was to the root apex. And a ratio of zero indicated translational movement of the tooth. The ratios of *d1/d2* in different groups were shown in Figure 7a. The ratio of mesio-apical to disto-occlusal displacement of canine (Figure 7b; Table 5) also reflected the degree of root control. The smaller the ratio, the closer the tooth movement was to distal translation (Liu L. et al., 2022).

With the same CA trimline design, the ratios of *d1/d2* progressively decreased from no-attachment (NA) group, to regular vertical attachment (V) group, and further to OH attachment group, with the OH group reaching the minimum value. Similarly, with the same attachment design, the ratios of *d1/d2* decreased sequentially from the conventional CA trimline (A), to the 3~5 buccal extension (B), to the 2~6 buccal extension (C),

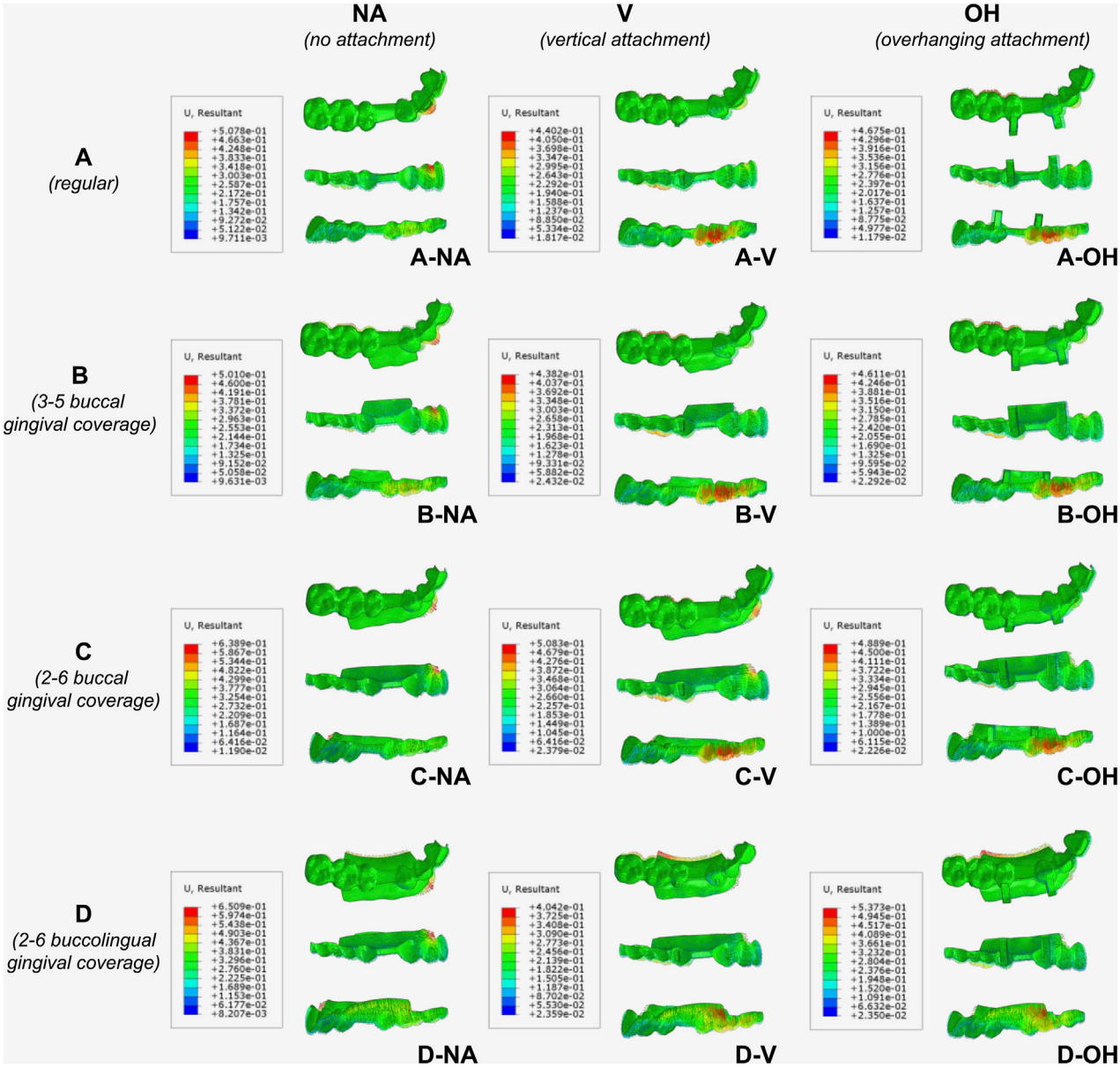

FIGURE 8
Heatmap of CA deformation in vector diagram, with occlusal, buccal, and lingual views. **(A)** Regular CA; **(B)** CA with buccal gingival coverage from 3 to 5; **(C)** CA with buccal gingival coverage from 2 to 6; **(D)** CA with buccolingual gingival coverage from 2 to 6.

and to the 2~6 buccolingual extension (D), with the D group presenting the minimum ratio. In all, D-OH group exhibited the smallest ratio of *d1/d2*. A similar trend was observed regarding the ratio of mesio-apical to disto-occlusal displacement of canine (Figure 7b; Table 5).

The CA with extended buccal and lingual gingival coverage and OH attachments effectively reduced the ratio of *d1/d2* to 0.461, which was beneficial for controlling tooth rotation and reducing the inclination of tooth during translational movement. Findings in this study were consistent with previous reports (Elshazly et al., 2023; Elshazly et al., 2022) suggesting that extending the gingival coverage of CA benefited root control movement.

3.3 Deformation of CA

The deformation of the CA was shown in Figure 8. The maximum deformation occurred at the labial side of lateral incisor in groups without attachments (NA), which was attributed to the compression caused by anchorage effect that endowed the mesial movement of canine, resulting in a labial protrusion. With attachments on 3 and 5, maximum deformation occurred around the attachment on canine, deformation of CA at the lateral incisor was reduced, and the deformation at the buccal side of molars became more pronounced. As evidenced by the upper limits of the heatmap

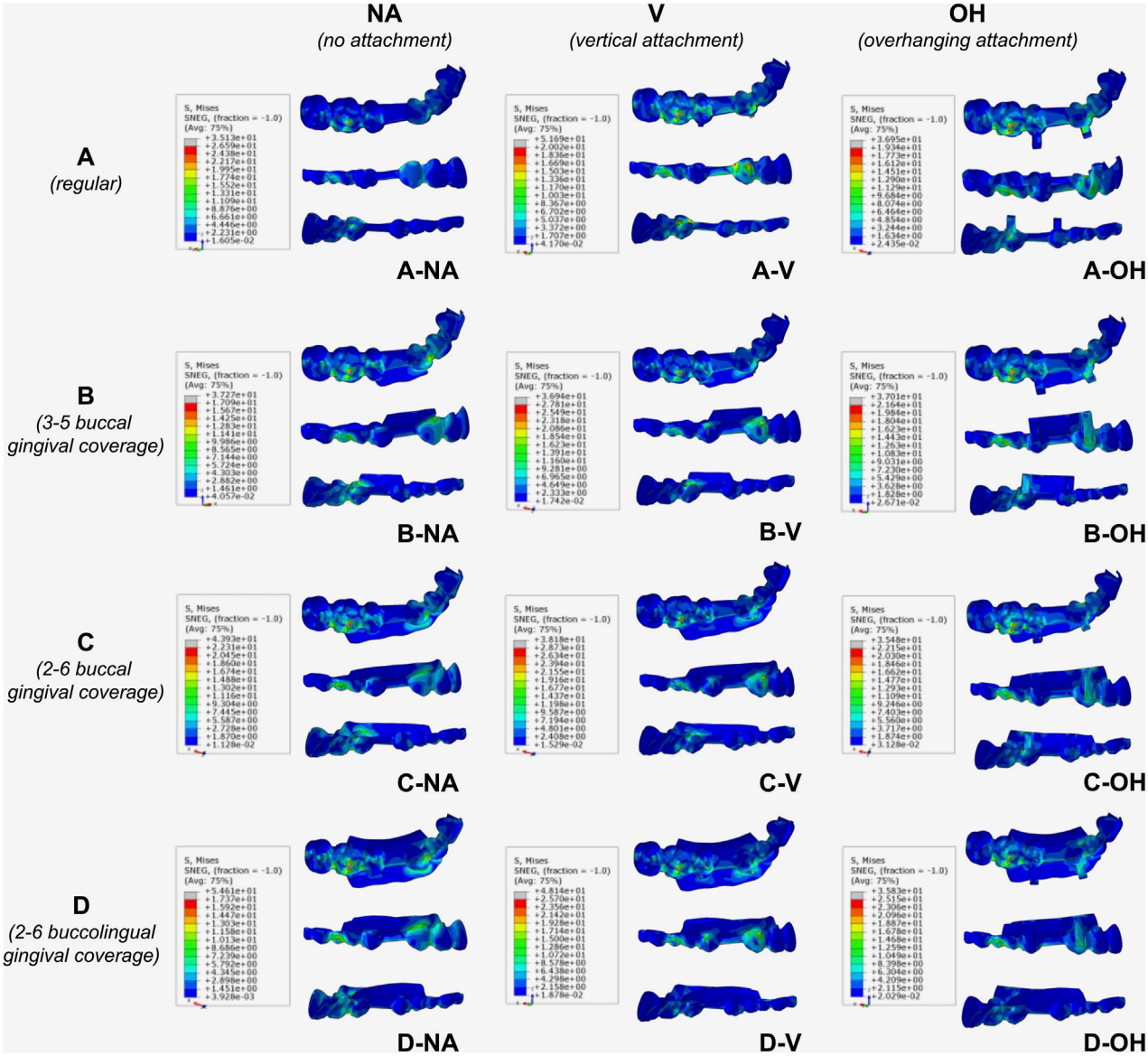

FIGURE 9
Von-Mises Stress distribution on CA. Red regions indicated the maximum stress. **(A)** Regular CA; **(B)** CA with buccal gingival coverage from 3 to 5; **(C)** CA with buccal gingival coverage from 2 to 6; **(D)** CA with buccolingual gingival coverage from 2 to 6.

scale, introduction of attachments reduced the overall maximum deformation of CA, indicating more evenly distributed orthodontic force. With buccal extended coverage on 2~6, the overall maximum deformation of CA increased, while with buccolingual extended coverage on 2~6, the overall maximum deformation of CA decreased except for the OH attachment group (D-OH). The buccolingual extension exerted a slight torsion along the dental arch curve towards the mesial direction. Moreover, upon increasing the lingual and gingival coverage, and the maximum deformation of the CA shifted to the lingual gingival extension under the first molar, resulting in a decrease in deformation of molar crowns and enhancing the retention of CA, thereby avoiding the occurrence of attachment debonding.

3.4 Stress distribution on CA

Figure 9 indicated that an increase in maximum Von-Mises stress value was observed in CAs with no attachment (NA) as the gingival coverage enlarged (D > C > B > A). Comparing A-V with A-NA, the maximum Von-Mises stress values increased after the addition of a regular vertical attachment (V), while buccal extension of CA (B-V and C-V) resulted in decreased maximum Von-Mises stress to the level of A-N. Using regular vertical attachment (V), buccolingual extension (D-V) exhibited slightly increased stress compared to buccal extension (B-V and C-V). Notably, using OH attachment, there was no significant difference in the maximum Von-Mises stress values with or without extended gingival coverage, indicating the OH attachment could minimize

stress concentration in CA. The membrane material employed in this simulation was PETG, with a yield strength of 45 MPa. All designs of CA met the material strength requirements, ensuring that no plastic deformation occurred during the wearing process.

4 Conclusion

This study first reported the biomechanical effects of overhanging attachment combined with partial gingival extension of CA trimline during closing extraction spaces. The results indicate that the overhanging attachment was more effective than the regular vertical attachment in achieving root-controlled canine movement. The highest orthodontic efficiency was observed when the overhanging attachment was combined with a buccolingual gingival extension of CA trimline on 2–6, while simultaneously avoiding excessive aligner deformation and stress concentration. This study provided theoretical bases for the clinical application of overhanging attachment. The partial gingival extension of the CA trimline proposed in this study demonstrated greater feasibility in clinical application compared to the full gingiva-covering trimline design. The methodology and findings presented here provided reference and guidance for the design of future orthodontic treatment.

Data availability statement

The original contributions presented in the study are included in the article/supplementary material, further inquiries can be directed to the corresponding authors.

Author contributions

GZ: Methodology, Visualization, Formal Analysis, Writing – original draft, Writing – review and editing. XM: Visualization, Conceptualization, Supervision, Writing – original draft, Data curation. DL: Writing – review and editing, Project administration, Visualization, Validation, Supervision, Investigation, Conceptualization, Funding acquisition.

Funding

The author(s) declare that financial support was received for the research and/or publication of this article. The authors gratefully acknowledge the support of the National Natural Science Foundation of China (32201104), and the Science and Technology Commission of Shanghai Municipality (24QA2708100).

Conflict of interest

The authors declare that the research was conducted in the absence of any commercial or financial relationships that could be construed as a potential conflict of interest.

Generative AI statement

The author(s) declare that no Generative AI was used in the creation of this manuscript.

Any alternative text (alt text) provided alongside figures in this article has been generated by Frontiers with the support of artificial intelligence and reasonable efforts have been made to ensure accuracy, including review by the authors wherever possible. If you identify any issues, please contact us.

Publisher's note

References

AlKahlan, L. A., Bindayel, N. A., Mallek, A. M., and Bendjaballah, M. Z. (2025). Extensive iterative finite element analysis of molar uprighting with the introduction of a novel method for estimating clinical treatment time. *Appl. Sci.* 15 (12), 6463. doi:10.3390/app15126463

Bi, S., and Shi, G. (2023). The crucial role of periodontal ligament's Poisson's ratio and tension-compression asymmetric moduli on the evaluation of tooth displacement and stress state of periodontal ligament. *J. Mech. Behav. Biomed. Mater* 148, 106217. doi:10.1016/j.jmbbm.2023.106217

Canales, C., Larson, M., Grauer, D., Sheats, R., Stevens, C., and Ko, C. C. (2013). A novel biomechanical model assessing continuous orthodontic archwire activation. *Am. J. Orthod. Dentofac. Orthop.* 143 (2), 281–290. doi:10.1016/j.ajodo.2012.06.019

Cao, Y., Wang, Z. W., Chen, D., Liu, L., Li, D. X., Li, N., et al. (2023). The effect of space arrangement between anterior teeth on their retraction with clear aligners in first premolar extraction treatment: a finite element study. *Prog. Orthod.* 24 (1), 39. doi:10.1186/s40510-023-00484-1

Cheng, Y., Liu, X., Chen, X., Li, X., Fang, S., Wang, W., et al. (2022a). The three-dimensional displacement tendency of teeth depending on incisor torque compensation with clear aligners of different thicknesses in cases of extraction: a finite element study. *BMC Oral Health* 22 (1), 499. doi:10.1186/s12903-022-02521-7

Cheng, Y., Gao, J., Fang, S., Wang, W., Ma, Y., and Jin, Z. (2022b). Torque movement of the upper anterior teeth using a clear aligner in cases of extraction: a finite element study. *Prog. Orthod.* 23 (1), 26. doi:10.1186/s40510-022-00421-8

Çifter, M., and Saraç, M. (2011). Maxillary posterior intrusion mechanics with mini-implant anchorage evaluated with the finite element method. *Am. J. Orthod. Dentofac. Orthop.* 140 (5), e233–e241. doi:10.1016/j.ajodo.2011.06.019

Demir, G. B. (2024). Understanding the effectiveness of attachments in clear aligner therapy: navigating design, placement, material selection and biomechanics. *Australas. Orthod. J.* 40 (2), 63–74. doi:10.2478/aoj-2024-0021

Elshazly, T. M., Keilig, L., Salvatori, D., Chavanne, P., Aldesoki, M., and Bourauel, C. (2022). Effect of trimming line design and edge extension of orthodontic aligners on force transmission: an *in vitro* study. *J. Dent.* 125, 104276. doi:10.1016/j.jdent.2022.104276

Elshazly, T. M., Salvatori, D., Elattar, H., Bourauel, C., and Keilig, L. (2023). Effect of trimming line design and edge extension of orthodontic aligners on force transmission: a 3D finite element study. *J. Mech. Behav. Biomed. Mater* 140, 105741. doi:10.1016/j.jmbbm.2023.105741

Elshazly, T. M., Bourauel, C., Chavanne, P., Elattar, H., and Keilig, L. (2024a). Numerical biomechanical finite element analysis of different trimming line designs of

orthodontic aligners: an *in silico* study. *J. World Fed. Orthod.* 13 (2), 65–71. doi:10.1016/j.ejwf.2024.01.001

Elshazly, T. M., Bourauel, C., Aldesoki, M., Salvatori, D., Alhotan, A., Keilig, L., et al. (2024b). Effect of attachment configuration and trim line design on the force system of orthodontic aligners: a finite element study on the upper central incisor. *Orthod. Craniofac Res.* 27 (Suppl. 2), 131–140. doi:10.1111/ocr.12779

Goktas, S., Dmytryk, J. J., and McFetridge, P. S. (2011). Biomechanical behavior of oral soft tissues. *J. Periodontol.* 82 (8), 1178–1186. doi:10.1902/jop.2011.100573

Gomez, J. P., Peña, F. M., Martínez, V., Giraldo, D. C., and Cardona, C. I. (2015). Initial force systems during bodily tooth movement with plastic aligners and composite attachments: a three-dimensional finite element analysis. *Angle Orthod.* 85 (3), 454–460. doi:10.2319/050714-330.1

Hahn, W., Dathe, H., Fialka-Fricke, J., Fricke-Zech, S., Zapf, A., Kubein-Meesenburg, D., et al. (2009). Influence of thermoplastic appliance thickness on the magnitude of force delivered to a maxillary central incisor during tipping. *Am. J. Orthod. Dentofac. Orthop.* 136 (1), 12.e1–12.e7. doi:10.1016/j.ajodo.2008.12.015

Hamanaka, R., Yamaoka, S., Anh, T. N., Tominaga, J. y., Koga, Y., and Yoshida, N. (2017). Numeric simulation model for long-term orthodontic tooth movement with contact boundary conditions using the finite element method. *Am. J. Orthod. Dentofac. Orthop.* 152 (5), 601–612. doi:10.1016/j.ajodo.2017.03.021

Hong, K., Kim, W. H., Eghan-Acquah, E., Lee, J. H., Lee, B. K., and Kim, B. (2021). Efficient design of a clear aligner attachment to induce bodily tooth movement in orthodontic treatment using finite element analysis. *Mater. (Basel)* 14 (17), 4926. doi:10.3390/ma14174926

Hong, Y. Y., Kang, T., Zhou, M. Q., Zhong, J. Y., and Chen, X. P. (2024). Effect of varying auxiliaries on maxillary incisor torque control with clear aligners: a finite element analysis. *Am. J. Orthod. Dentofac. Orthop.* 166 (1), 50–60. doi:10.1016/j.ajodo.2024.02.012

Hong, K. J., Baek, J. P., Park, J. J., and Park, J. H. (2025). *Repair of receded gingival tissue through lingual root movement with an overhanging attachment and clear aligners*. AJO-DO Clinical Companion.

Huang, W., Dong, L., Yu, S., Zheng, Y., Wu, H., Li, C., et al. (2023). Stress distribution of the modified clear twin-block aligner on the temporomandibular joint, alveolar bone and teeth: a finite element analysis. *Int. Orthod.* 21 (4), 100815. doi:10.1016/j.ortho.2023.100815

Jedliński, M., Mazur, M., Greco, M., Belfus, J., Grocholewicz, K., and Janiszewska-Olszowska, J. (2023). Attachments for the orthodontic aligner treatment-state of the Art-A comprehensive systematic review. *Int. J. Environ. Res. Public Health* 20 (5), 4481. doi:10.3390/ijerph20054481

Jiang, T., Wu, R. Y., Wang, J. K., Wang, H. H., and Tang, G. H. (2020). Clear aligners for maxillary anterior en masse retraction: a 3D finite element study. *Sci. Rep.* 10 (1), 10156. doi:10.1038/s41598-020-67273-2

Kim, K., Choi, Y. K., Kim, S. H., Kim, S. S., and Kim, Y. I. (2025). Multi-step finite element simulation for clear aligner space closure: a proof-of-concept compensation protocol. *Sci. Rep.* 15 (1), 22220. doi:10.1038/s41598-025-07110-6

Li, Y., Zhan, Q., Bao, M., Yi, J., and Li, Y. (2021). Biomechanical and biological responses of periodontium in orthodontic tooth movement: up-date in a new decade. *Int. J. Oral Sci.* 13 (1), 20. doi:10.1038/s41368-021-00125-5

Liu, L., Zhan, Q., Zhou, J., Kuang, Q., Yan, X., Zhang, X., et al. (2021). Effectiveness of an anterior mini-screw in achieving incisor intrusion and palatal root torque for anterior retraction with clear aligners. *Angle Orthod.* 91 (6), 794–803. doi:10.2319/120420-982.1

Liu, L., Song, Q., Zhou, J., Kuang, Q., Yan, X., Zhang, X., et al. (2022). The effects of aligner overtreatment on torque control and intrusion of incisors for anterior retraction with clear aligners: a finite-element study. *Am. J. Orthod. Dentofac. Orthop.* 162 (1), 33–41. doi:10.1016/j.ajodo.2021.02.020

Liu, J. Q., Zhu, G. y., Wang, Y. g., Zhang, B., Wang, S. c., Yao, K., et al. (2022). Different biomechanical effects of clear aligners in bimaxillary space closure under two strong anchorages: finite element analysis. *Prog. Orthod.* 23 (1), 41. doi:10.1186/s40510-022-00435-2

Nakornnoi, T., Srirodjanakul, W., Chintavalakorn, R., Santiwong, P., and Sipiyaruk, K. (2024). The biomechanical effects of clear aligner trimline designs and extensions on orthodontic tooth movement: a systematic review. *BMC Oral Health* 24 (1), 1523. doi:10.1186/s12903-024-05274-7

Natali, A. N., Carniel, E. L., Pavan, P. G., Sander, F. G., Dorow, C., and Geiger, M. (2008). A visco-hyperelastic-damage constitutive model for the analysis of the biomechanical response of the periodontal ligament. *J. Biomech. Eng.* 130 (3), 031004. doi:10.1115/1.2900415

Ortún-Terrazas, J., Cegoñino, J., and Pérez Del Palomar, A. (2020). *In silico* study of cuspid' periodontal ligament damage under parafunctional and traumatic conditions of whole-mouth occlusions. A patient-specific evaluation. *Comput. Methods Programs Biomed.* 184, 105107. doi:10.1016/j.cmpb.2019.105107

Pu, L., Zhou, J., Yan, X., Zhou, H., Liu, X., Yang, Z., et al. (2022). Orthodontic traction of an impacted maxillary third molar through a miniscrew-anchored cantilever spring to substitute the adjacent second molar with severe root resorption. *J. Am. Dent. Assoc.* 153 (9), 884–892. doi:10.1016/j.adaj.2022.05.010

Sarrafpour, B., Swain, M., Li, Q., and Zoellner, H. (2013). Tooth eruption results from bone remodelling driven by bite forces sensed by soft tissue dental follicles: a finite element analysis. *PLoS One* 8 (3), e58803. doi:10.1371/journal.pone.0058803

Seo, J. H., Eghan-Acquah, E., Kim, M. S., Lee, J. H., Jeong, Y. H., Jung, T. G., et al. (2021). Comparative analysis of stress in the periodontal ligament and center of rotation in the tooth after orthodontic treatment depending on clear aligner thickness-finite element analysis study. *Mater. (Basel)* 14 (2), 324. doi:10.3390/ma14020324

Tamaya, N., Kawamura, J., and Yanagi, Y. (2021). Tooth movement efficacy of retraction spring made of a new low elastic modulus material, gum metal, evaluated by the finite element method. *Mater. (Basel)* 14 (11), 2934. doi:10.3390/ma14112934

Wang, Q., Dai, D., Wang, J., Chen, Y., and Zhang, C. (2022). Biomechanical analysis of effective mandibular en-masse retraction using class II elastics with a clear aligner: a finite element study. *Prog. Orthod.* 23 (1), 23. doi:10.1186/s40510-022-00417-4

Weir, T. (2017). Clear aligners in orthodontic treatment. *Aust. Dent. J.* 62 (Suppl. 1), 58–62. doi:10.1111/adj.12480

Wu, B., Cheng, K., Liu, M., Liu, J., Jiang, D., Ma, S., et al. (2022). Construction of hyperelastic model of human periodontal ligament based on collagen fibers distribution. *J. Mech. Behav. Biomed. Mater* 135, 105484. doi:10.1016/j.jmbbm.2022.105484

Xia, Q., He, Y., Jia, L., Wang, C., Wang, W., Wang, C., et al. (2022). Assessment of labially impacted canines traction mode with clear aligners vs. fixed appliance: a comparative study based on 3D finite element analysis. *Front. Bioeng. Biotechnol.* 10, 1004223. doi:10.3389/fbioe.2022.1004223

Yokoi, Y., Arai, A., Kawamura, J., Uozumi, T., Usui, Y., and Okafuji, N. (2019). Effects of attachment of plastic aligner in closing of diastema of maxillary dentition by finite element method. *J. Healthc. Eng.* 2019, 1–6. doi:10.1155/2019/1075097

Zhu, C., Li, R., Yuan, L., Zheng, Y., Jin, Y., Li, H., et al. (2022). Effects of the advanced mandibular spring on mandibular retrognathia treatment: a three-dimensional finite element study. *BMC Oral Health* 22 (1), 271. doi:10.1186/s12903-022-02308-w

Frontiers in
Bioengineering and Biotechnology

Accelerates the development of therapies, devices, and technologies to improve our lives

A multidisciplinary journal that accelerates the development of biological therapies, devices, processes and technologies to improve our lives by bridging the gap between discoveries and their application.

Discover the latest Research Topics

See more →

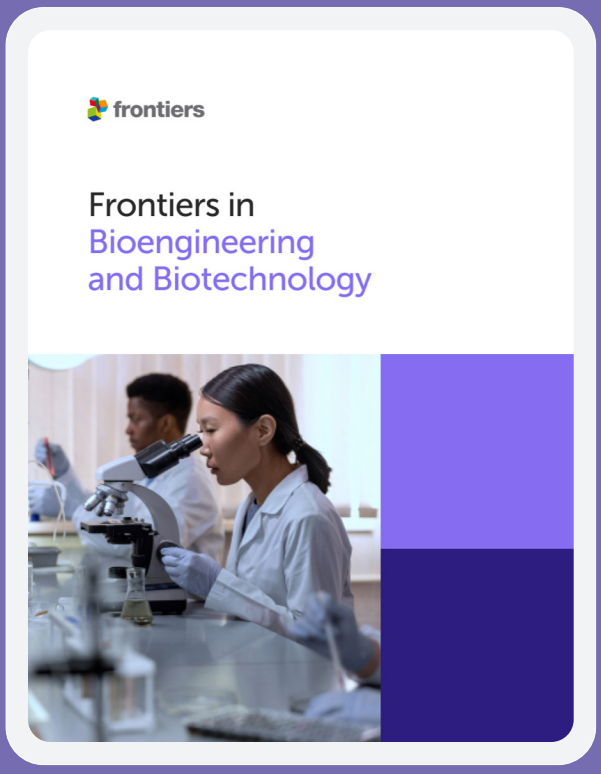

Frontiers

Avenue du Tribunal-Fédéral 34
1005 Lausanne, Switzerland
frontiersin.org

Contact us

+41 (0)21 510 17 00
frontiersin.org/about/contact